University of Nottingham
UK | CHINA | MALAYSIA

Elucidating the role of *Cdk13* and *Prkd1* in heart development and congenital heart disease

Qazi Waheed Ullah
MBBS, MPhil, MPH

Thesis submitted to the University of Nottingham for the degree of
Doctor of Philosophy
September 2023

Supervised by
Dr Siobhan Loughna
Prof J David Brook

Declaration

I hereby declare that this thesis is the result of my own work undertaken during my registered period of study for PhD in Anatomy & Cell Biology at the University of Nottingham, UK and that it has not been presented to this or any other university for the award of any degree or diploma other than for which I am a candidate.

Acknowledgements

I would like to thank my supervisors Dr Siobhan Loughna and Prof J David Brook for their utmost and constant support, guidance, and encouragement at every step of my PhD. I would also thank Siobhan for her confidence in myself optimizing the HREM technique based on her continuous guidance. I would also thank Tim Mohun, Fabrice Prin (Frances Crick Instt. London), Chris Hunter and his team from Indigo Scientific, UK, Stefan Geyer and Wolfgang J Wenninger (Medical University of Vienna) for their help regards the trouble shooting related to HREM technique and initial training. I also would thank Anna Wilsdon (previous PhD student) for having used some of her mouse hearts, (sectioned earlier by Siobhan and herself), for the initial optimization of the (post sectioning) HREM data's processing and analysis. Processing of those hearts was done by me, and phenotypic analysis was done separately by us, though some were reviewed jointly. I also extend special thanks to Dr Frances BuLock and Prof Robert Anderson for giving their expert opinions and guidance about our mouse heart phenotypes. I appreciate the help and support provided by all team members of Loughna and Brook's lab including Chrysostomos Perdios, José Sánchez, Belle, Anjani (all previous PhD students), Sophie Rochette, Sarah Buxton and Tushar Ghosh for their help always. I would also thank fellow PhD students Kawthar Alnahdi for training on W-ISH and Aseel Abbad for working in association to optimize the qPCR and W-ISH techniques in addition to having useful discussions related to our work. Regards RNA-Seq, I acknowledge the help rendered by Nadine Holmes, and thereafter Dr Fei Sang (both at

DeepSeq facility, University of Nottingham) for initial relevant bioinformatics. Luke Simpson (previous PhD student) has been helpful regards the use of R and I extend thanks to him and his late supervisor Prof Andrew Johnson for facilitation regards use of qPCR machine and Nanodrop spectrophotometer in their lab. My special thanks go to the staff of media preparation room, C-floor, QMC for their support regards media preparation, sterilization, and others.

Thank you to my sponsor, the Higher Education Department, Government of KPK, Pakistan, for funding my PhD.

At the end, I would extend my deep gratitude to my wife, Dr Samina Zahir, and our lovely baby Rayan for bearing with me to finish my thesis. Last but not the least I dedicate my all hard work to my lovely mum who is desperately waiting to hear about the news of my successful completion of PhD and my late beloved dad who had been a great motivating factor for me to excel in life.

Abstract

Congenital heart disease (CHD) is the most common congenital anomaly, with an overall incidence of approximately 1% in the United Kingdom. Genetic causes include chromosomal abnormalities, copy number variants, and point mutations. Recent studies have used whole exome sequencing (WES) in large CHD cohorts to better understand the genetic aetiology of CHD. This includes a study of 1891 probands by our group in collaboration with others, which identified three novel genes – Cyclin Dependant Kinase - 13 (*CDK13),* Protein Kinase D1 *(PRKD1)* and Chromodomain Helicase DNA Binding Protein 4 *(CHD4),* in patients with syndromic CHD. For this PhD research, two of them, *CDK13* and *PRKD1,* were selected to characterize their role in heart development and CHD. *CDK13* encodes a cyclin-dependent kinase phosphorylating the carboxyl-terminal domain (CTD) of RNA polymerase II (RNAPII) and is involved in RNA processing and splicing though its true associating partners are still unknown. *PRKD1* (also known as *PKCμ*) encodes a serine/threonine protein kinase, which is involved in a variety of fundamental cellular functions including the regulation of "rat sarcoma" (RAS) signalling, cell survival, migration, differentiation, proliferation and adhesion, and Golgi transport. Taken together, these studies demonstrate a likely critical, though uncharacterized, role for *CDK13* and *PRKD1* in the embryonic heart. To obtain a greater appreciation for the role that these essential protein kinases play in cardiogenesis and CHD, one *Cdk13* (*Cdk13*^{tm1b}) and two *Prkd1* (*Prkd1*^{em1} *&* *Prkd1*^{em2}) transgenic mouse models were analysed. The *Cdk13*^{tm1b} and *Prkd1*^{em1} carried loss of function

(LOF) mutations whereas *Prkd1*^{em2} carried the most common missense (referred to as humanised) mutation. High resolution episcopic microscopy (HREM) affords detailed morphological 3D analysis of the developing heart and provides evidence for the role of *Cdk13* and *Prkd1* in normal cardiac development and CHD. The results from this research show that homozygous mutation of *Cdk13* and *Prkd1* are associated with severe forms of CHD and are embryonically lethal. However, survival to at least postnatal day 7 is possible in case of *Prkd1*-LOF (noticed once). Moreover, six mice harbouring homozygous missense mutation (G598R) of *Prkd1* also survived to adult stage. No live-birth with homozygous *Cdk13*-LOF mutation was seen. Even in heterozygotes with LOF, cardiac differences occur, albeit at low penetrance, suggesting that one wild type allele of *Cdk13* and *Prkd1* are sufficient to support normal heart development in ~82 cases with *Cdk13*-LOF % (n = 39/47) and *Prkd1*-missense mutation (n = 53/64), and 98% cases with *Prkd1*-LOF mutation (n = 54/55). Heterozygotes with *Prkd1*-missense mutation are more deleterious in terms of CHD penetrance (coupled with reduced protein expression) than those with *Prkd1*-LOF mutation. RNA-Seq. analysis in *Cdk13*-LOF mouse comparing WT with homozygous hearts showed significant enrichment of gene ontology (GO) terms related to cardiovascular system (CVS) development and significant suppression of the morphogenetic pathways, processes related to RNA processing as well as CDK13 role as a kinase at RNA polymerase-II in the mutant hearts. Overall, this research demonstrates a vital role of *Cdk13* and *Prkd1* in heart development and the aetiology of CHD.

List of abbreviations

aa	Amino acid
Ao	Aorta
AS	Aortic stenosis/atrial septum
ASD	Atrial septal defect
ATP	Adenosine triphosphate
AV	Aortic valve or atrioventricular
AVCD	Atrioventricular canal defect
AVSD	Atrioventricular septal defect
BAV	Bicuspid aortic valve
BMP	Bone morphogenetic protein
BSA	Bovine serum albumin
BSU	Bio Support unit
Bp	Base pairs
CDK	Cyclin dependent kinase
cDNA	Complementary DNA
CHD	Congenital heart disease or defect or Chromo-domain-helicase-DNA-binding gene/protein
CHDFIDD	CHD, dysmorphic facial features, intellectual development disorder
CNCC	Cardiac neural crest cells
CS	Carnegie stage
Ct	Threshold cycle
CVN	Copy number variant/variation
CoA	Coarctation of aorta
CRD	Cysteine rich domain
CRL	Crown rump length
CTD	C terminal domain/Conotruncal defect
DA	Ductus arteriosus
DAB	3,3 diaminobenzidine

DAG	Diacylglycerol
DDD	Deciphering developmental disorders study
dH_2O	Deionized water
DICOM	Digital Imaging and Communications in Medicine
DIG	Digoxigenin
DMDD	Deciphering mechanisms of developmental disorders
DMP	Dorsal mesenchymal protrusion
DNM	De novo mutation
dNTP	Deoxynucleotide triphosphate
DORV	Double outlet right ventricle
DTT	Dithiothreitol
E	Embryonic day
E.dpc	Embryonic day post coitus
EC	Endocardial cushions
ECM	Extracellular matrix
EDTA	Ethylenediamine tetra acetic acid
EGA	Estimated gestational age
EMT	Epithelial-mesenchymal transition
EPDC	Epicardium derived cells
EUCOMM	European conditional mouse mutagenesis (program)
FC	Fold change
FDR	False discovery rate
FHF	First heart field
FS	Frame shift
GA	Gestational age
GO	Gene ontology
GOI	Gene of interest
gnomAD	The Genome Aggregation Database
HCl	Hydrochloric acid
HDAC	Histone deacetylase
HET	Heterozygous/heterozygote
HOMO	Homozygous/homozygote

HM	Humanised mutation
HREM	High resolution episcopic microscopy
HRP	Horseradish per oxidase
IAA	Interrupted aortic arch
IB	Immunoblot
ICC	Intercalated cushion
IUGR	Intrauterine growth retardation
JPEG	Joint Photographic Experts Group
iPSC	Induced pluripotent stem cells
IUGR	Intrauterine growth retardation
IVS	Interventricular septum
KO	Knockout
LA	Left atrium
LB	Lysogeny broth
LOF	Loss of function
LPA	Left pulmonary artery
LV	Left ventricle
LVOT	Left ventricular outflow tract
LVOTO	Left ventricular outflow tract obstruction
MABT	Maleic acid buffer with Tween 20
MeOH	Methanol
MS	Missense
MV	Mitral valve
n	Sample size
NaAc	Sodium acetate
NaCl	Sodium chloride
NC	Non coronary (leaflet)
NCC	Neural crest cells
NDD	Neurodevelopmental disorder/disability
NS-CHD	Non-syndromic congenital heart disease
NTD	N terminal domain
OFT	Outflow tract

P	Postnatal day
PA	Pulmonary atresia
PAS	Pulmonary artery stenosis
PBS	Phosphate buffered saline
PBS-T	PBS + 0.1% Tween 20
PCA	Principal component analysis
PCR	Polymerase chain reaction
PDA	Patent ductus arteriosus
PFA	Paraformaldehyde
PFO	Patent foramen ovale
PH	Pleckstrin homology domain
PHF	Primary heart field
PS	Pulmonary stenosis
PT	Pulmonary trunk
PTA	Persistent truncus arteriosus
PTV	Protein truncating variant
PV	Pulmonary valve
qPCR	Quantitative real time PCR
RA	Right atrium
RE	Restriction enzyme
RNA	Ribonucleic acid
RIN	RNA integrity number
RPKM	Reads per kilobase of transcript per million mapped reads
RT	Room temperature or reverse transcriptase
RT-PCR	Reverse-transcriptase PCR
RV	Right ventricle
RVOT	Right ventricle outflow tract
S-CHD	Syndromic CHD
SDS	Sodium dodecyl sulphate
SDW	Sterile deionised water
SEM	Standard error of mean

Ser	Serine
SHF	Second heart field
SNHL	Sensorineural hearing loss
SNP	Single nucleotide polymorphism
SNV	Single nucleotide variant
SSC	Saline sodium citrate
TA	Truncus arteriosus
TAE	Tris-acetate-EDTA
TBS	Tris buffered saline
TBS-T	Tris buffered saline with 1% Tween 20
TGA	Transposition of great arteries
TIFF	Tag Image File Format
Tm	Melting temperature
TOF	Tetralogy of Fallot
TV	Tricuspid valve
VS	Ventricular septum
VUS	Variant of uncertain significance
WES	Whole exome sequencing
W-ISH	Whole mount in situ hybridization
WT	Wild type
WTSI	Wellcome trust Sanger Institute

Table of Contents

Declaration ..... *ii*

Acknowledgements ..... *ii*

Abstract ..... *iv*

List of abbreviations ..... *vi*

List of figures ..... *xv*

List of tables ..... *xx*

1 INTRODUCTION *1*

1.1 Heart development 1
1.1.1 Formation of primary and secondary heart fields and heart tube 2
1.1.2 Formation of cardiac loop 7
1.1.3 Formation of endocardial cushions (EC) 9
1.1.4 Formation of cardiac septa 10

1.2 Molecular regulation of heart development 23

1.3 Congenital heart disease (CHD) 24
1.3.1 Bicuspid aortic valve (BAV) 25
1.3.2 Atrioventricular septal defect (AVSD) 26
1.3.3 Patent foramen ovale (PFO) 27
1.3.4 Ventricular septal defects (VSDs) 27
1.3.5 Pulmonary stenosis (PS) and dysplasia of the pulmonary valve 28
1.3.6 Bicuspid and quadricuspid pulmonary valves 29
1.3.7 Defects of the heart outflow tract (OFT) 29

1.4 Epidemiology of congenital heart disease 33

1.5 Causes of CHD and role of genes 34

1.6 Mouse as a model for CHD 36

1.7 Aims 39

2 MATERIAL AND METHODS *41*

2.1 Mouse lines 41
2.1.1 *Cdk13*$^{tm1b(EUCOMM)Hmgu}$ 41
2.1.2 *Prkd1*$^{em1(IMPC)Wtsi}$ 44
2.1.3 *Prkd1*$^{em2(IMPC)Wtsi}$ 44

2.2 Maintenance of mice colonies and welfare 45

2.3 Harvesting whole mouse embryos and embryonic tissue collection 46

2.4 Extraction of DNA for genotyping 49

2.5 Polymerase Chain Reaction (PCR) for Genotyping 50

2.6 Agarose gel electrophoresis 52

2.7 Polymerase Chain Reaction (PCR) for genetic sex determination in mouse 53

2.8 PCR clean up and Sanger sequencing 54

2.9 Protein extraction from mouse tissues 55

2.10 Western blot 55
2.11 High Resolution Episcopic Microscopy (HREM) 56
2.12 RNA isolation from mouse hearts 69
2.12.1 RNA isolation from mouse embryos' hearts 69
2.13 Quality control (QC) checks on extracted RNA 75
2.13.1 Nanodrop spectrophotometry 75
2.14 RNA sequencing of *Cdk13*^{tm1b} mouse heart samples 78
2.15 cDNA synthesis 79
2.16 Expression studies 80
2.16.2 Whole mount *in situ* Hybridization (W-ISH) 87
2.16.3 Statistical Analysis 103
3 ELUCIDATING THE ROLE OF Cdk13 IN HEART DEVELOPMENT AND CONGENITAL HEART DISEASE IN A MOUSE MODEL WITH LOF MUTATION 104
3.1 INTRODUCTION 104
3.1.1 *CDK13* mutations in patients 105
3.1.2 Penetrance of CHD in patients with *CDK13* mutations 108
3.1.3 Rationale for this study 118
3.2 AIM OF THIS PROJECT 118
3.2.1 Hypotheses for the project: 119
3.3 RESULTS 119
3.3.1 Mice with heterozygous mutation are viable and fertile, but homozygous mutation is embryonically lethal 119
3.3.2 External phenotyping in *Cdk13*^{tm1b} mouse line 122
3.3.3 HREM-based phenotypic analysis of E15.5 hearts collected from *Cdk13*^{tm1b} mouse line 127
3.3.4 Morphological changes in sub valvular apparatus of right (tricuspid) and left (mitral) atrioventricular valves in hearts from mice with LOF mutation of *Cdk13* 142
3.3.5 Analysis of pulmonary stenosis at pulmonary valvular and infundibular levels in *Cdk13*^{tm1b} hearts with CHD 147
3.3.6 Phenotypic analysis of *Cdk13*^{tm1b} mutant (*Cdk13*$^{tm1b/+}$) hearts at postnatal day (P) 6/7 149
3.3.7 Gender determination of *Cdk13*^{tm1b} mutant mice with CHD 154
3.3.8 X-Gal staining for expression of *Cdk13* at different ages 154
3.3.9 Quantitative RT-PCR to explore gene expression of *Cdk13* at different embryonic ages 159
3.3.10 Immunoblot for CDK13 protein expression in adult mouse tissues . 166
3.3.11 RNA-Sequencing on whole hearts from E12.5 mouse 167
3.3.12 qPCR for genes related to morphogenesis of cardiovascular system 177
3.3.13 Whole mount *in Situ* hybridization (W-ISH) for GOI 178
3.4 DISCUSSION, CONCLUSIONS AND PERSPECTIVES FOR FUTURE WORK 186
4 CHARACTERIZATION OF THE ROLE OF Prkd1 IN HEART DEVELOPMENT AND CHD IN A MOUSE MODEL WITH LOSS OF FUNCTION (LOF) MUTATION 203
4.1 INTRODUCTION 203
4.1.1 Expression of PRKD1 205

4.1.2 Structure of PRKD1 and mechanism of its activation 207
4.1.3 Activity of PRKD1 in ventricular myocardium and its role in cardiac hypertrophy 211
4.1.4 Regulatory role of PRKD1 in various clinical conditions 211
4.1.5 Reported PRKD1 mutations in patients 212
4.1.6 Previous *Prkd1* mouse models 224
4.1.7 *Prkd1* mouse models used in this work 225
4.2 HYPOTHESIS AND AIM OF THIS PROJECT 226
4.2.1 Specific aim of this project 226
4.2.2 Hypotheses for the project: 227
4.3 RESULTS 227
4.3.1 Mice with heterozygous (*Prkd1*$^{em1/+}$) mutation are viable and fertile, but homozygous mutation (*Prkd1*$^{em1/em1}$) is embryonically lethal 227
4.3.2 External phenotyping of E12.5 and E15.5 embryos collected from *Prkd1*^{em1} mouse line 230
4.3.3 HREM based phenotypic analysis 233
4.3.4 Morphological changes in sub valvular apparatus of right and left) AV valves in E15.5 hearts from *Prkd1*^{em1} mice 241
4.3.5 Expression analysis of *Prkd1, Prkd2* and *Prkd3* in E12.5 hearts by RT-qPCR 255
4.3.6 Significant reduction in PRKD1 protein expression was observed in *Prkd1*$^{em1/em1}$ (HOMO) hearts compared with WT 261
4.4 Discussion, conclusions, and perspectives for future work 264
5 CHARACTERIZATION OF THE ROLE OF Prkd1 IN HEART DEVELOPMENT AND CHD IN A MOUSE MODEL WITH HUMANISED MUTATION (HM) 276
5.1 INTRODUCTION 276
5.1.1 Rationale for the study 276
5.1.2 The *Prkd1* mouse model with humanised mutation 277
5.2 HYPOTHESIS AND AIM OF THIS PROJECT 277
5.2.1 Hypotheses for the project: 277
5.3 RESULTS 278
5.3.1 In silico analysis of PRKD1-G592R mutation 278
5.3.2 Mice with heterozygous (*Prkd1*$^{em2/+}$) mutation are viable and fertile, but homozygous mutation (*Prkd1*$^{em2/em2}$) is embryonically lethal 281
5.3.3 Pups' survival ratios at pre-weaning (pre-genotyping) and post weaning stages 284
5.3.4 External phenotyping of E15.5 embryos collected from *Prkd1*^{em2} mouse line 285
5.3.5 HREM-based phenotypic analysis of E15.5 hearts collected from *Prkd1*^{em2} mouse line 289
5.3.6 Morphological changes in sub valvular apparatus of right (tricuspid) and left (mitral) atrioventricular valves in hearts from mice with HM mutation of PRKD1 (*Prkd1*^{em2}) 298
5.3.7 Dimensions of RVOT and pulmonary annulus in *Prkd1*^{em2} hearts with CHD 302
5.3.8 HM mutation of *Prkd1* causes significant change in total heart and left ventricular volumes at E15.5 305
5.3.9 Exploring CHD phenotypes in mouse neonates 315
5.3.10 Heterozygous humanised mutation of *Prkd1* is not associated with a significant change in heart size and heart chambers' volumes in P6 *Prkd1*^{em2} neonates 320
5.3.11 Gender determination of *Prkd1*^{em2} mutant mice with CHD 324

5.3.12 RT-qPCR to explore gene expression of *Prkd1*, *Prkd2* and *Prkd3* in *Prkd1*^{em2} mouse hearts at E15.5 325
5.3.13 Immunoblot for PRKD1 protein expression in *Prkd1*^{em2} hearts at E15.5 331
5.4 DISCUSSION, CONCLUSIONS AND PERSPECTIVES FOR FUTURE WORK 335
6 SUMMARY AND IMPLICATIONS FOR FURTHER RESEARCH 347
7 APPENDIX 358
8 REFERENCES 359

List of figures

Figure 1:1 Three different types of precursor cells population related to heart development..... 2
Figure 1:2 Primitive stage of heart development.. 3
Figure 1:3 Formation of the endothelial tubes and cephalic folding of the embryo.. 4
Figure 1:4 Lateral folding of the embryos and fusion of the heart tubes.. 5
Figure 1:5 Contribution of the PHF and SHF in the heart development. 7
Figure 1:6 Cardiac looping.. 8
Figure 1:7 Development of the sinus venosus..... 9
Figure 1:8 Origin and fate of the endocardial cushions.. 10
Figure 1:9 Formation of the atrial septum..... 13
Figure 1:10 Septation of the cardiac OFT..... 17
Figure 1:11 Development of the aortic arches and their remodelling... 19
Figure 1:12 Formation of AV valve and chordae tendinae..... 20
Figure 1:13 Successive remodelling of the cardiac valves.. 21
Figure 1:14 Comparison of the genes involved in cardiac septation and development of cardiac valves.. 22
Figure 1:15 Different stages of heart development and the key regulators.. 24
Figure 1:16 Different types of BAV.. 25
Figure 1:17 Partial and complete AVSD..... 26
Figure 1:18 Different components of the ventricular septum and types of VSD..... 28
Figure 1:19 Mal-alignment of the OFT resulting in OA or DORV..... 31
Figure 1:20 Spectrum of the outflow tract defects. 33
Figure 2:1 Generation of tm1b allele from tm1a allele and Cdk13^{tm1b} mouse model..... 43
Figure 2:2 Prkd1^{em1} mouse model and location of primers used for genotyping..... 44
Figure 2:3 Location of the screening primers used for genotyping of Prkd1^{em2} mouse..... 45
Figure 2:4 Determining genetic sex of mouse embryos..... 54
Figure 2:5 JB4 infiltration..... 59
Figure 2:6 JB-4 embedding.. 61
Figure 2:7 Baking of JB4 blocks prior to sectioning..... 62
Figure 2:8 Locating and identifying the hearts in the JB4 block..... 63
Figure 2:9 Key parts of HREM system and the sectioning process. .. 65
Figure 2:10 Summary of the main steps of HREM technique for morphologic analysis of mouse heart at E15.5..... 68
Figure 2:11 RNA extraction from adult heart sample as per supplier's protocol..... 72
Figure 2:12 Improvement of RNA extraction from adult heart sample through modification of the protocol..... 73
Figure 2:13 Spectrophotometry of RNA sample on NanoDrop™.. 76
Figure 2:14 Abnormal second peak on NanoDrop spectrophotometry.. 76
Figure 2:15 Gel electrophoresis of RNA samples..... 77

Figure 2:16 RNA samples extracted from Cdk13^{tm1b} mouse hearts at E12.5.. 78
Figure 2:17 qPCR primer optimisation using Cdk13 primers and making standard curve.. 84
Figure 2:18 Gel image after gradient PCR.. 87
Figure 2:19 Gel electrophoresis after PCR on two bacterial colonies.. 89
Figure 2:20 Alignment of plasmid sequence to GOI sequence on NCBI.. 92
Figure 2:21 Identifying the restriction enzymes which should not cut through the plasmid. 93
Figure 2:22 Gel after plasmid linearization. 95
Figure 2:23 Gel electrophoresis to check probes integrity.. 97
Figure 3:1 Phosphorylation by CDK13.. 104
Figure 3:2 Expression of CDK13 in different adult tissues in human.. 105
Figure 3:3 Missense mutations of CDK13 as reported for the first time in seven unrelated patients.. 106
Figure 3:4 Schematic representation of the domain structure of CDK13 and location of the reported SNVs.. 107
Figure 3:5 Cdk13^{tm1b} genotyping.. 121
Figure 3:6 Intrauterine growth retardation and lobster claw deformity of right hand in Cdk13^{tm1b} mouse.. 124
Figure 3:7 Midfacial aplasia seen in Cdk13$^{tm1b/tm1b}$ (HOMO) hearts at E12.5.. 125
Figure 3:8 Hydrocephaly and brain atrophy.. 126
Figure 3:9 Pericardial effusion.. 126
Figure 3:10 Anophthalmia.. 127
Figure 3:11 Perimembranous VSD with DORV. 130
Figure 3:12 Muscular VSD. 131
Figure 3:13 Bicuspid aortic valve.. 133
Figure 3:14 Quadricuspid pulmonary valve, BAV and muscular VSD.. 135
Figure 3:15 Complete AVSD with DORV. 138
Figure 3:16 Pulmonary stenosis.. 139
Figure 3:17 DORV with complete AVSD, muscular VSD, deficient second interatrial fold (the so-called septum secundum) and failure of development of the outlet septum. 141
Figure 3:18 Papillary muscles of tricuspid valve, their morphology, and attachments in Cdk13^{tm1b} hearts at E15.5.. 144
Figure 3:19 Papillary muscles of mitral valve, their attachments and morphology in Cdk13^{tm1b} hearts at E15.5.. 146
Figure 3:20 Right ventricular outflow tract obstruction and pulmonary stenosis. 148
Figure 3:21 Patent foramen Ovale (PFO). 151
Figure 3:22 Increased heart walls' thickness and narrowed ventricular chambers. 152
Figure 3:23 Supernumerary coronary ostia in left aortic sinus. 153
Figure 3:24 Spontaneously closed muscular ventricular septal defects in P6 neonates.. 153
Figure 3:25 X-Gal staining to show Cdk13 expression in E10.5 Cdk13$^{tm1b/+}$ (HET) embryos.. 156

Figure 3:26 X-Gal staining to show Cdk13 expression in E12.5 embryos.. 157
Figure 3:27 X-Gal staining to show Cdk13 expression in E15.5 hearts.. 158
Figure 3:28 X-Gal staining to show Cdk13 expression in Adult hearts. 159
Figure 3:29 Expression of Cdk13 by RT-qPCR in E10.5 hearts from Cdk13$^{tm1b/+}$ mouse line..... 161
Figure 3:30 Transcript expression of Cdk13 by RT-qPCR in E12.5 hearts from Cdk13$^{tm1b/+}$ mouse line..... 163
Figure 3:31 Transcript expression of Cdk13 in E15.5 hearts from Cdk13^{tm1b} mouse line by RT-qPCR.. 164
Figure 3:32 Transcript expression of Cdk13 in adult hearts from Cdk13^{tm1b} mouse line by RT-qPCR. 165
Figure 3:33 Trial for CDK13 protein detection in mouse tissues..... 167
Figure 3:34 Assessment of intra- and intergroup variability..... 169
Figure 3:35 Differentially expressed genes in hearts from Cdk13^{tm1b} mouse comparing WT with HOMO..... 170
Figure 3:36 Chord diagram showing functional enrichment analysis of the DEGs..... 171
Figure 3:37 Heatmap showing results of gene set enrichment analysis for all samples using gene set of GO biological processes..... 173
Figure 3:38 Heatmap showing results of gene set enrichment analysis for all samples using gene set of GO molecular processes.. 174
Figure 3:39 Visual tree representation of the effects of the differential expression of GO terms for cellular processes..... 175
Figure 3:40 Differential expression of the genes in Cdk13^{tm1b} RNA-Seq data, selected for downstream analyses.. 176
Figure 3:41 qPCR validation of the log_2FC of the differentially expressed genes from RNA-Seq data of Cdk13^{tm1b} mouse, comparing Cdk13$^{+/+}$ (WT) with Cdk13$^{tm1b/tm1b}$ (HOMO) hearts.. 178
Figure 3:42 Whole mount In Situ hybridization for Eln expression in E12.5 mouse heart..... 181
Figure 3:43 W-ISH to locate transcript expression of Sall4 in E12.5 Cdk13^{tm1b} heart..... 182
Figure 3:44 Transcript expression of Notch2 in E12.5 Cdk13^{tm1b} mouse heart.. 184
Figure 3:45 Interactions among proteins of some key heart related genes in relation to pulmonary stenosis. 196
Figure 4:1 Schematic structure of the three paralogues of human PRKD. 204
Figure 4:2 The protein expression pattern of PRKD1 in different body tissues in human..... 206
Figure 4:3 Dimerization of PRKD1..... 209
Figure 4:4 Role of PRKDs in various conditions..... 212
Figure 4:5 Missense mutations of PRKD1..... 213
Figure 4:6 High-confidence protein-protein interactions among the top order CHD-associated genes (FDR < 50%) of the WES dataset as found in the STRING database.. 214

Figure 4:7 Schematic structure of the human protein kinase D1 (PRKD1) gene and protein and location of the reported PRKD1 mutations..... 216
Figure 4:8 Agarose gel for genotyping of mouse embryos collected at E15.5.. 229
Figure 4:9 Intrauterine growth retardation in Prkd1$^{em1/em1}$ (HOMO) mice at E12.5 and E15.5..... 231
Figure 4:10 Oedema of the back at E15.5..... 232
Figure 4:11 Hemopericardium in Prkd1$^{em1/+}$ (HET) mouse.. 232
Figure 4:12 One heterozygous Prkd1^{em1} E15.5 heart had a congenital heart defect.. 234
Figure 4:13 Morphology of abnormal valves in outflow vessels in E15.5 Prkd1$^{em1/em1}$ (HOMO) hearts.. 237
Figure 4:14 AVSD is seen in two E15.5 Prkd1$^{em1/em1}$ (HOMO) hearts.. 240
Figure 4:15 Comparison of trabeculae and papillary muscles in E15.5 Prkd1^{em1} hearts.. 242
Figure 4:16 Abnormal external appearance of Prkd1$^{em1/em1}$ (HOMO) hearts.. 243
Figure 4:17 Volumetric analyses of Prkd1^{em1} mouse hearts at E15.5.. 248
Figure 4:18 Bicuspid aortic valve is seen in P7 Prkd1$^{em1/+}$ (HET) heart.. 250
Figure 4:19 Comparison of Prkd1$^{+/+}$ and Prkd1$^{em1/em1}$ hearts at P7.. . 251
Figure 4:20 Volumetric analysis of Prkd1^{em1} neonatal hearts..... 254
Figure 4:21 Comparison of Prkd1 expression in Prkd1^{em1}hearts..... 257
Figure 4:22 Comparison of Prkd2 expression in Prkd1^{em1}hearts..... 258
Figure 4:23 Comparison of Prkd3 expression in Prkd1^{em1}hearts..... 260
Figure 4:24 Immunoblot of E12.5 Prkd1^{em1}mouse heart..... 261
Figure 4:25 Expression of PRKD1 protein in Prkd1^{em1} hearts.. 262
Figure 4:26 The protein-protein interaction of PRKD1 with others using the STRING database. 273
Figure 5:1 The 3D structure of human PRKD1..... 281
Figure 5:2 Prkd1^{em2} genotyping..... 282
Figure 5:3 Resorbed embryo..... 284
Figure 5:4 Oedema at the back. 287
Figure 5:5 Exencephaly, brain hypertrophy, anophthalmia and oedema at the back in Prkd1$^{em2/+}$ (HET) embryo collected at E15.5..... 288
Figure 5:6 Intrauterine growth retardation.. 289
Figure 5:7 Perimembranous VSD with OA.. 292
Figure 5:8. Perimembranous VSD with DORV and muscular VSD.. . 293
Figure 5:9 Muscular VSD as an isolated defect..... 294
Figure 5:10 Perimembranous VSD with DORV.. 296
Figure 5:11 Perimembranous and muscular VSD. 297
Figure 5:12 Perimembranous VSD with OA... 298
Figure 5:13 Papillary muscles of tricuspid valve, their morphology, and attachments in Prkd1^{em2} hearts at E15.5..... 299
Figure 5:14 Papillary muscles of mitral valve, their attachments and morphology in Prkd1^{em2} hearts at E15.5. b..... 301
Figure 5:15 Right ventricular outflow tract obstruction and pulmonary stenosis.. 303

Figure 5:16 Comparison of heart size and muscle volume in E15.5 Prkd1^{em2} hearts.. 310
Figure 5:17 Volumetric analyses of Prkd1^{em2} hearts collected at E15.5. 312
Figure 5:18 Volumetric analysis of Prkd1$^{em2/em2}$ (HOMO) hearts without CHD collected at E15.5.. 314
Figure 5:19 Patent foramen Ovale (PFO).. 317
Figure 5:20 Spontaneous correction of ventricular septal defect in P6 Prkd1^{em2} neonates. 318
Figure 5:21 Probe patency of foramen Ovale and spontaneously closed muscular VSD..... 319
Figure 5:22 Quantitative analysis of the Prkd1^{em2} neonatal hearts collected at P6.. 324
Figure 5:23 Expression of Prkd1 in E15.5 hearts from Prkd1^{em2} mouse.. 327
Figure 5:24 Expression of Prkd2 in E15.5 hearts from Prkd1^{em2} mouse line.. 329
Figure 5:25 Expression of Prkd3 in E15.5 hearts from Prkd1^{em2} mouse line.. 330
Figure 5:26 Immunoblot of E15.5 mouse heart with point mutation (G598R) in Prkd1 (Prkd1^{em2}).. 332
Figure 5:27 Comparison of normalised protein expression of PRKD1 in E15.5 mouse hearts from Prkd1^{em2} mouse line.. 333
*Figure 5:28 Interaction between PRKDs and actin cytoskeleton to regulate directed cellular migration.
. ..... 358*

List of tables

Table 1:1 The adult derivatives of the different parts of heart tube..... 6
Table 1:2 Major cardiac morphological differences between mouse and human.. 36
Table 1:3 Stages of development in the mouse heart are outlined..... 37
Table 2:1 PCR reaction cocktail for genotyping..... 51
Table 2:2 Mouse genotyping primers. 51
Table 2:3 Amplification conditions for Cdk13^{tm1b}, Prkd1^{em1}, Prkd1^{em2} for genotyping..... 52
Table 2:4 Mouse primers for genetic sex determination.. 54
Table 2:5: Amount of the ingredients in the JB-4 dye mix. 57
Table 2:6 Criteria for primer designing for qPCR and W-ISH. 81
Table 2:7 Primers used in qPCR and W-ISH..... 82
Table 2:8 Reaction mix for the qPCR standard curve as well as relative quantification.. 83
Table 2:9 Thermal cycler conditions employed for primers' optimisation as well as comparative qPCR..... 83
Table 2:10 Efficiency of primers used for transcript expression of the respective genes by RT-qPCR.. 85
Table 2:11 Reagents used in RT-PCR reaction..... 86
Table 2:12 PCR conditions used for RT-PCR.. 87
Table 2:13 Concentration of plasmids with gene inserts on NanoDrop™ spectrophotometer..... 91
Table 2:14 Restriction enzymes used for linearization of plasmids.. ... 93
Table 2:15 Reagents used for linearisation reaction for plasmids with GOI-insert..... 94
Table 2:16 Restriction enzymes used for plasmid linearisation and post linearisation concentration..... 95
Table 2:17 RNA polymerases used for in vitro transcription for riboprobe synthesis. 96
Table 2:18 Reaction set up for riboprobe synthesis using Riboprobe® in vitro Transcription systems (Promega)..... 96
Table 2:19 Dehydration of heart samples through graded series of alcohol concentration after overnight fixation in 4% PFA, for onward W-ISH. 98
Table 2:20 Pre- and post-hybe reagents made in-house for ISH.. 99
Table 2:21 Post hybridization steps during W-ISH. 100
Table 2:22 Reagents used to prepare BCL III buffer in-house. 100
Table 2:23 Ingredients of X-Gal Rinse buffer.. 102
Table 2:24 X-Gal staining solution..... 102
Table 3:1 Reported patients with CDK13 SNVs. 116
Table 3:2 Genotype distribution of Cdk13^{tm1b} embryos.. 121
Table 3:3 Abnormal external phenotypes of Cdk13^{tm1b} embryos..... 123
Table 3:4 Cdk13^{tm1b} hearts collected at embryonic stage E15.5 and analysed by HREM..... 128
Table 3:5 Phenotypes of the E15.5 mouse hearts with heterozygous (Cdk13$^{tm1b/+}$) mutation. 129

Table 3:6 Phenotypic analysis of E15.5 hearts from mice with LOF mutation in both alleles of Cdk13 (Cdk13$^{tm1b/tm1b}$)..... 136
Table 3:7 Phenotypes in hearts collected from Cdk13$^{tm1b/+}$ (HET) mouse neonates at sixth postnatal day (P6). 150
Table 3:8 Comparative mean Cdk13-transcript expression in E10.5 hearts from Cdk13$^{tm1b/+}$ mouse line..... 161
Table 3:9 Comparative mean Cdk13-transcript expression in E12.5 hearts from Cdk13^{tm1b} mouse line. 163
Table 3:10 Comparative mean Cdk13 expression in E15.5 hearts from Cdk13^{tm1b} mouse line. 164
Table 3:11 Comparative mean Cdk13 expression in adult hearts from Cdk13^{tm1b} mouse line.. 165
Table 3:12 qPCR validation of the differentially expressed GOI from RNA-Seq data of Cdk13^{tm1b} mouse hearts.. 177
Table 4:1 Reported patients with SNVs in Prkd1..... 222
Table 4:2 The prevalence of different types of CHD in humans with SNVs in Prkd1.. 224
Table 4:3 Genotype distribution of Prkd1^{em1} embryos from HET X HET crosses, collected at E15.5..... 229
Table 4:4 Abnormal external phenotypes of Prkd1^{em1} embryos.. 230
Table 4:5 Prkd1^{em1} mouse hearts collected at embryonic age E15.5 and analysed by HREM..... 233
Table 4:6 Ventricular septal defect (VSD) in one Prkd1$^{em1/+}$ (HET) heart at E15.5. 234
Table 4:7 Phenotypes in Prkd1$^{em1/em1}$ (HOMO) mice..... 235
Table 4:8 HREM analysis of hearts collected from Prkd1^{em1} mouse neonates at P6/P7.. 249
Table 4:9 Volumetric analysis of Prkd1^{em1} neonatal hearts comparing WT with HET hearts.. 253
Table 4:10 Comparison of Prkd1 expression in Prkd1^{em1}hearts.. 257
Table 4:11 Comparison of Prkd2 expression in Prkd1^{em1}hearts. 259
Table 4:12 Comparison of Prkd3 expression in Prkd1^{em1}hearts. 260
Table 4:13 Expression of PRKD1 protein in Prkd1^{em1} hearts. 262
Table 5:1 In silico analysis of PRKD1-G592R single point mutation.. 280
Table 5:2 Genotype distribution of Prkd1^{em2} embryos from HET X HET crosses, collected at E15.5..... 283
Table 5:3 Prkd1$^{em2/em2}$ live-born pups from HET X HET crosses.. 283
Table 5:4 Abnormal external phenotypes of Prkd1^{em2} embryos at E15.5. 286
Table 5:5 Prkd1^{em2} hearts collected at embryonic stage E15.5 and analysed by HREM..... 290
Table 5:6 Phenotypes of the E15.5 mouse hearts with heterozygous (Prkd1$^{em2/+}$) mutation.. 291
Table 5:7 Phenotypic analysis of hearts from mice with humanised (missense/point) mutation in both alleles of Prkd1 (Prkd1$^{em2/em2}$)..... 295
Table 5:8 Comparison of pulmonary valvular and infundibular diameters..... 304
Table 5:9 Phenotypes in hearts collected from Prkd1$^{em2/+}$ (HET) mouse neonates at P6. 316

Table 5:10 Comparative mean Prkd1-transcript expression in E15.5 hearts from Prkd1^{em2} mouse line 327
Table 5:11 Comparative mean Prkd2 expression in E15.5 hearts from Prkd1^{em2} mouse line. 329
Table 5:12 Comparative mean Prkd3 expression in E15.5 hearts from Prkd1^{em2} mouse line.. 331
Table 5:13 Comparative mean PRKD1 protein expression in E15.5 hearts from Prkd1^{em2} mouse line.. 333

1 INTRODUCTION

In embryonic life, cardiovascular system (CVS) is the first vital system which starts functioning [1]. Heart development involves a series of well-orchestrated events running in parallel and in a finely tuned fashion. A network of large number of genes (encoding transcription factors, structural proteins, signalling proteins and several others) orchestrate the events pertaining to heart development and functioning [2]. A slight perturbation of any of these event(s) can lead to congenital heart disease (CHD)[3].

Throughout this introduction, human developmental age is mentioned as determined from the date of fertilization.

1.1 Heart development

Heart development is initiated at gastrulation with appearance of its primordium whereas the primitive heart starts functioning by the beginning of the fourth week in human owing to the increased functional demands of the growing number of cells [4]. There are three types of precursor cells which are related to heart development. These include cardiac mesodermal cells, the proepicardium, and neural crest cells [5] (Figure 1:1). Fully developed heart comprises of three different layers (inner to outer): endocardium, myocardium and epicardium [6].

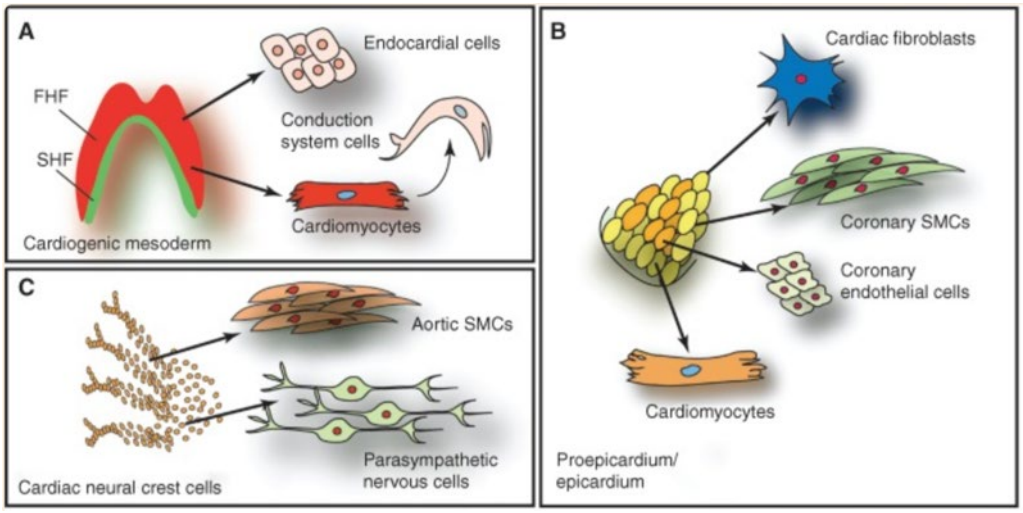


Figure 1:1 Three different types of precursor cells population related to heart development. A: derivatives of cardiogenic mesoderm; B: structures derived from proepicardium; C: derivatives of neural crest cells in heart. Reproduced from [5].

1.1.1 Formation of primary and secondary heart fields and heart tube

Gastrulation is the process of formation of three germ layers (ectoderm, mesoderm, endoderm) in the third week of development in human (E 6.25 to E9.5 in mouse). These germs layers then give rise to different tissues and organs in the body [7]. Formation of the primitive streak on bilaminar germ disc is the key prerequisite step for gastrulation to happen [8]. Epiblast cells, through the process of invagination through the primitive streak, migrate inward giving rise to these different germ layers in the developing embryo [8]. The heart progenitor cells originate in the posterolateral region of epiblast which by invagination through the primitive streak reach the splanchnic layer of lateral plate mesoderm [9]. Within the lateral plate mesoderm, the first population of these cells arrange themselves in a horseshoe pattern, forming the primary heart field (PHF) which later forms the linear heart tube (Figure 1:2) and subsequently the

left ventricle and atrial chambers [10, 11] (Figure 1:5). Moreover, another population of heart progenitor cells originate subsequently in the epiblast which migrate towards the area of the PHF, to arrange anterior and medial to the PHF, and give rise to the secondary heart field (SHF) [12, 13]. SHF will develop into the outflow tract and right ventricle [12, 13] (Figure 1:5).

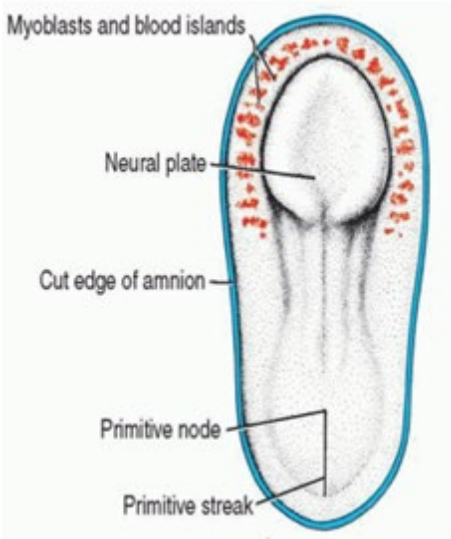


Figure 1:2 Primitive stage of heart development. Cardiac progenitor cells after migrating through the primitive streak arrange themselves as horseshoe shaped heart field in splanchnic mesoderm [8].

The cells of the heart fields are controlled by opposing signals from notochord and underlying endoderm [14]. Endoderm, through bone morphogenetic protein (BMP), stimulates differentiation of these cardiac progenitor cells into heart myoblasts whereas WNT-mediated signalling from notochord inhibits these [14]. In the meantime, within the heart fields (in the splanchnic layer of lateral plate mesoderm), blood islands appear (Figure 1:3 A-B) [15]. These contain erythroblasts and angioblasts (premature endothelial cells) which give rise to blood cells, and blood vessels (by vasculogenesis) respectively [15]. This process gives rise to endothelial lined tubes, one on each side, which are then surrounded by the

cardiac myoblasts derived from heart fields [16]. The intraembryonic cavity (formed due to splitting of the lateral plate mesoderm) over this area of cardiogenesis (Figure 1:3 A) on each side develops into pericardial cavity [8]. The location of this heart-forming area is initially anterior to the oropharyngeal membrane (Figure 1:3 B) [8]. The gradual development of brain accompanied by cephalic folding of the embryo (denoted by black and white arrows in Figure 1:3 B-E) results in migration of this developing heart and pericardial cavity, on each side, first into the cervical and finally into the thoracic region [8].

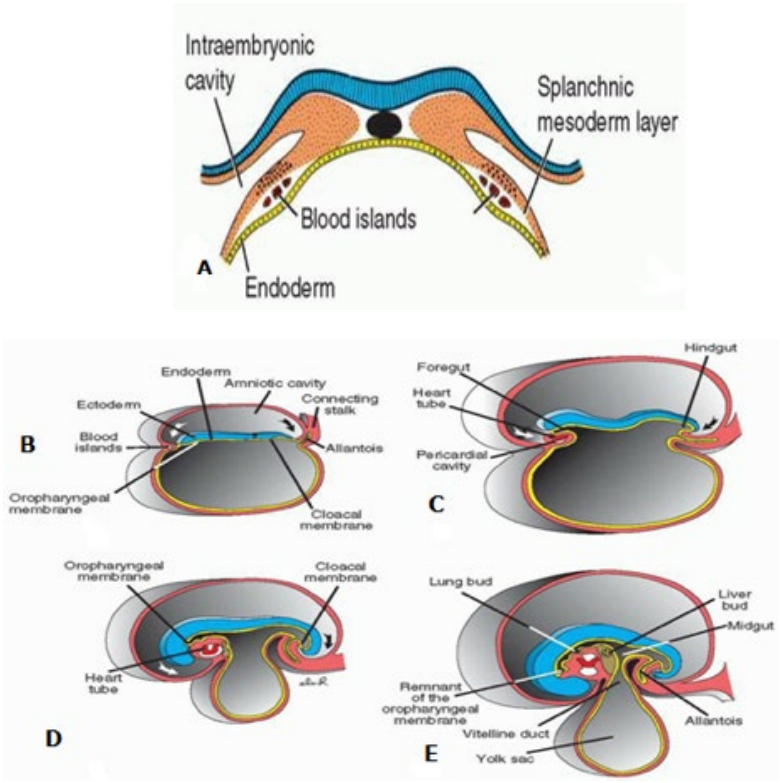


Figure 1:3 Formation of the endothelial tubes and cephalic folding of the embryo. Blood islands appearing in the splanchnic mesoderm (A-B) will result in the formation of endothelial tubes, which will then be surrounded by myoblasts to form heart tubes (C-D). Intraembryonic cavity, developed due to splitting of lateral plate mesoderm, will contribute pericardial cavity around these heart tubes (C-E). The gradual development of brain accompanied by cephalic folding of the embryo (denoted by black and white arrows in B-E) results in migration of this developing heart and pericardial cavity, on each side, first into cervical and finally into thoracic region. Figure reproduced from [8].

Moreover, embryonic development also involves lateral folding which causes the endocardial heart tubes to approach each other and finally fuse (Figure 1:4-B) (Day 21 in human and E8.25 in mouse), giving rise to a single heart tube and pericardial cavity (Figure 1:4-C)[17]. The caudal most ends of these endocardial tubes however do not fuse, making the heart tube to have an inverted Y-shape (Figure 1:4-C) [18].

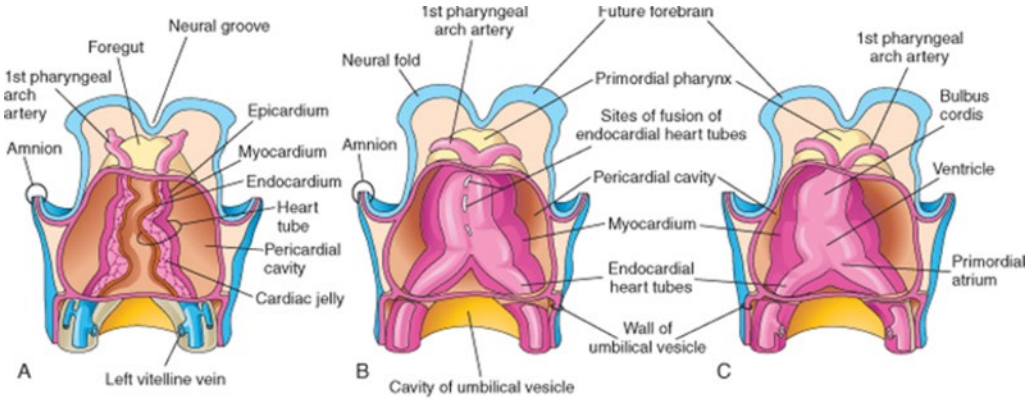


Figure 1:4 Lateral folding of the embryos and fusion of the heart tubes. The initially paired heart tubes fuse to form a single tubular heart surrounded by pericardial cavity. Reproduced from [18].

This heart tube keeps expanding due to the contribution of the SHF cells, and at this stage, it has bilaterally symmetrical appearance. The heart tube formed comprises of endocardium and myocardium, separated by cardiac jelly (extracellular matrix) [19]. The epicardium forming the outer layer of heart tube is derived from proepicardium which is derived from the lateral plate mesoderm and embryonic mesothelial cells [20]. These cells reach the endocardial heart tubes during looping to form the covering epicardial layer for them [21]. These proepicardial cells also contribute to the development of coronary arteries, muscular part of atrioventricular septum and cardiac fibroblasts [22-25]. Molecular interaction of epicardium with myocardium is vital for the development of ventricles [5] (including its trabeculae), cardiac septa, valves and conducting system of

heart [26]. Interruption of such interaction results in growth disruption of myocardium with thinning of the compact layer [27]. There is also a crucial cross-talk between endocardium and myocardium during development [28]. An example of such interaction is the one mediated by cardiac jelly (produced mainly by myocardium) which ensures normal development of ventricular trabeculae between E9.5-E13.5 in mouse [28] (Day 28-50 or CS 13-21 in human). Thereafter, the level of such interaction should normally decrease [29] or else can result in excessive trabeculation of the ventricles [29].

The fused heart tube has five recognisable parts, each of which gives rise to the structures of adult heart. Craniocaudally, they are truncus arteriosus, bulbus cordis, primitive ventricle, primitive atrium, and sinus venosus (Table 1:1). Atria and ventricles undergo expansion by ballooning out from the primitive heart tube to form the atrial appendages and ventricular apices respectively [30, 31].

Embryonic dilatation	Adult structure
Truncus arteriosus	Ascending aorta Pulmonary trunk
Bulbus cordis	Proximal part forms trabeculated part of right ventricle Distal part (conus cordis) will form the OFT of both ventricles
Primitive ventricle	Trabeculated part of left ventricle (LV)
Primitive atrium	Trabeculated part of right atrium Trabeculated part of left atrium
Sinus venosus	Smooth part of right atrium* Coronary sinus Oblique vein of left atrium
*Smooth part of left atrium is formed by incorporation of pulmonary veins into the wall of left atrium. The junction between smooth and trabeculated parts of right atrium is internally demarcated by crista terminalis and externally by sulcus terminalis.	

Table 1:1 The adult derivatives of the different parts of heart tube. Reproduced from [8].

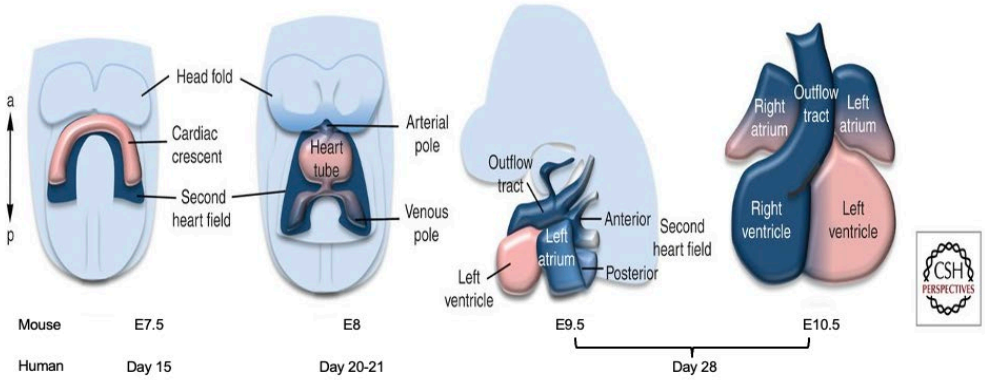


Figure 1:5 Contribution of the PHF and SHF in the heart development. The images from mouse embryo showing the contribution by the PHF (pink) and SHF (blue) in the development of the different parts of heart. Reproduced from [12] [5, 32].

1.1.2 Formation of cardiac loop

The developing heart elongates and then undergoes bending called as cardiac looping which starts by about day 23 in human (E8.5 in mouse) [5, 8]. The cardiac looping will change the symmetrical appearance of heart tube to an asymmetrical one [33]. The cranial portion of the heart tube bends downwards, forwards and slightly in the rightward direction [8]. In contrast, the caudal part of the heart tube bends in upwards, backwards and in the leftward direction, resulting in incorporation of large parts of the developing heart tube into the pericardial cavity [8]. This process is completed by approximately day 28 in human (E9.5-E10.5 in mouse) [8] (Figure 1:6). Cardiac looping happens due to unidirectional (leftward) movement of epiblast cells through the primitive node part of the primitive streak [34]. This results in induction and increased expression of NODAL (TGF beta subfamily), PITX2 and LEFTY on left side [35, 36]. Other factors such as BMP4 and BMP2 (TGF beta subfamily), GDF, CITED2 and WNT also have role in determining laterality [37-39].

Furthermore, cSNR (inhibits PITX2), FGF8 and NKX2.5 act on right hand side, whereas Shh, Nodal, Lefty1 and 2, PITX2, BMP2, NKX3.2 and NKX2-5 act on left hand side ensuring the correct laterality [40].

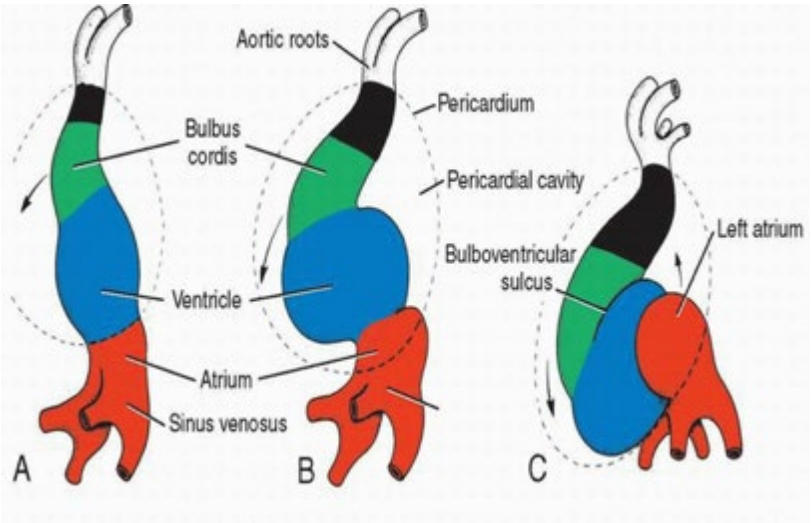


Figure 1:6 Cardiac looping. Elongated heart tube (A) due to expansion starts dextral (rightward) bending at day 23 in human (E8.5 in mouse) (B). During this phase of cardiac morphogenesis, the cranial portion of the heart tube (black-conus cordis, green-bulbus cordis) bends downward, forward and to the right whereas the caudal part (blue-primitive ventricle & red-primitive atrium and sinus venosus) bends upwards, backwards and to the left, thereby creating a cardiac loop (C). This also results in incorporating greater parts of the heart tube inside the pericardial cavity (dotted line) by day 28 in human (E9.5-E10.5 in mouse). Reproduced from [8].

Sinus venosus develops two horns – right and left, by the 4th week in human (E9.5-E10.5 in mouse) [8]. The right horn of sinus venosus gets incorporated into the right atrium to form the smooth part of right atrium (sinus venarum) whereas the left horn becomes the coronary sinus and great cardiac vein [8] (Figure 1:7). Coronary sinus drains venous blood from the myocardium into the right atrium through a valve-guarded sino-atrial orifice [41, 42].

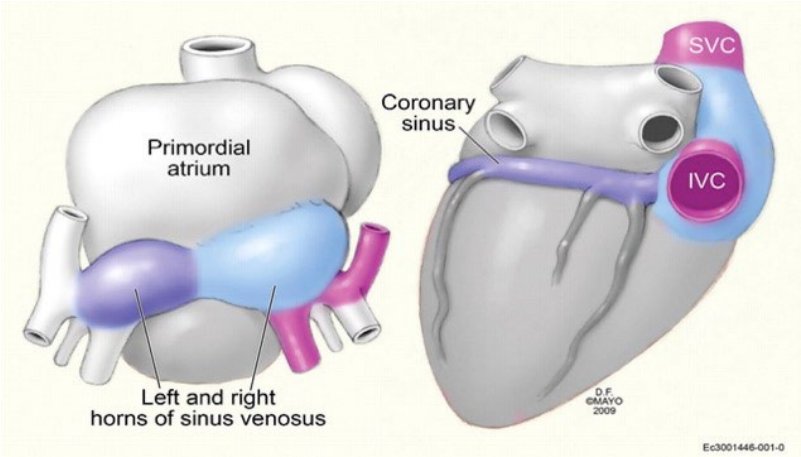


Figure 1:7 Development of the sinus venosus. Right horn of sinus venosus is incorporated into the right atrium (light blue) whereas the left horn develops into coronary sinus and great cardiac vein (dark blue/purple). Reproduced from [41].

1.1.3 Formation of endocardial cushions (EC)

After the formation of heart tube, cardiac jelly is formed between endo- and myocardium (Figure 1:8-A). The cardiac jelly is rich in extracellular matrix (ECM) [43]. Amount of this cardiac jelly increases when cardiac looping occurs which results in forming masses of tissues at AV junction and OFT which will later on develop into endocardial cushions [43]. These cushions increase in size due to the invasion of endocardial cells, followed by their endocardial-mesenchymal transition – the process which is regulated by *NOTCH* and *TGFβ* signalling [10]. The endocardial cushions develop by the end of week 4 of development in humans (E9.5-E10.5 in mouse) and contribute to the formation of separate AV canals, interatrial and interventricular septa, heart valves and segregation of aortic and pulmonary channels [44].

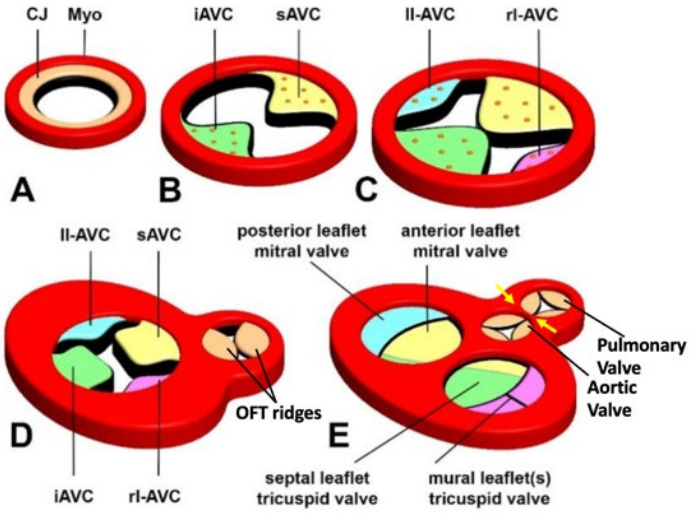


Figure 1:8 Origin and fate of the endocardial cushions. The sequential stages of AV and OFT cushions formation. (A) When the heart tube is formed, cardiac jelly accumulates between endocardium and myocardium, resulting in the formation of major (superior and inferior) and lateral AV cushions (B-C). These cushions fuse together to result in partitioning of the common AV canal into right and left AV orifices as well as the formation of the leaflets of the AV valves to guard these orifices against backflow of blood (D,E). Endocardial cushions in the OFT give rise to the OFT ridges which fuse to segregate aorta and pulmonary artery (yellow arrows) and give rise to the respective semilunar valves (D-E). Myo, myocardium; CJ, cardiac jelly; OFT: outflow tract; iAVC, inferior AV cushion; sAVC, superior AV cushion; rlAVC, right lateral AV cushion; ll-AVC, left lateral AV cushion. Reproduced from [43].

1.1.4 Formation of cardiac septa

After the completion of cardiac looping, septum formation in the heart occurs in the 4th and 5th weeks (27th and 37th days) of development in humans (E10.5 - E13.5 in mouse) [17]. This involves contribution of mesenchyme derived from endocardium, epicardium, cardiac neural crest cells, and cells from the second heart field (i.e. the dorsal mesenchymal protrusion - DMP) [45].

1.1.4.1 Formation of the septum in AV canal

By the end of week 4 of development in human (E9.5-E10.5 in mouse), the AV canal which was giving access only to primitive left ventricle until

now, enlarges to the right to ensure that the blood passing through AV orifice can now enter into both right and left ventricles [44]. By the end of 5th week in humans (E13.5 in mouse), the superior and inferior endocardial cushions normally fuse to divide the common AV canal into right and left AV canals [46] [47] (Figure 1:8-B). After the formation of superior and inferior endocardial cushions, two more – right and left lateral AV endocardial cushions are formed (Figure 1:8-C)[46, 48]. Endocardial cells, lining these cushions, then invade these cushions and undergo endocardial-mesenchymal transition (EMT) giving rise to fibroblasts in the developing AV valves. All these cushions hence also contribute to the formation of the AV valves' leaflets (Figure 1:8 D-E) [43]. Moreover, epicardium-derived cells in the AV region also contribute to the AV valve formation, after undergoing "epicardium-mesenchyme" transition (EMT). These cells invade the lateral endocardial cushions as well [49].

1.1.4.2 Formation of the interatrial septa

For the formation of atrial septum, different structures collectively contribute. These are the superior and inferior atrioventricular (AV) endocardial cushions (with contribution from endo- and epicardium), the dorsal mesenchymal protrusion (DMP), and primary atrial septum with a mesenchymal cap (derived from endocardium) [45]. The AV endocardial cushions and mesenchymal cap are derived from endocardium by endocardial-mesenchymal transition (EMT) [50-52]. There is no known role of cardiac neural crest cells in atrial septation [45].

By the end of 4th week in human (E9.5-E10.5 in mouse), the septum primum, in the form of a sickle shaped muscular crest, grows from the roof

of common atrium into the lumen [8] (yellow area in Figure 1:9 A-C). At its lower free leading edge, there is a mesenchymal cap (white rim in Figure 1:9 A-C) which grows inferiorly to fuse with the superior AV endocardial cushion (denoted by blue asterisk in Figure 1:9 A-C)[53]. From the posterior wall of the common atrium, the DMP (also called as vestibular spine) (denoted by purple area in Figure 1:9 A-C) grows toward the inferior AV endocardial cushion (denoted by yellow asterisk in Figure 1:9 A-C) [54]. At this stage of development, among these three AV mesenchymal structures, there is still an opening left, called as the ostium primum (black arrows in Figure 1:9 A-B) [55]. However, gradual fusion of these structures results in closure of the ostium primum by the 7th week in human (E13.5 in mouse), (green arrow pointing at white area in Figure 1:9C), followed by myocardialization of the vestibular spine/DMP and mesenchymal cap to form the muscular anteroinferior rim of the fossa ovalis [55] which is the true “septum secundum” (Lecture by Prof. Robert Anderson in Congenital Heart Academy’s series). At this time, the two AV cushions also fuse to form an intermediate septum dividing the common AV canal into two – right and left AV valvar orifices (single yellow dotted line in Figure 1:9C) [56]. Prior to the complete closure of the ostium primum, cell death starts in the cranial part of septum primum, producing perforations in it (light blue area in Figure 1:9B). These perforations fuse together to form ostium secundum (dark blue area in Figure 1:9C), which ensures free flow of blood from right to left side of primitive atrium [56]. In the next step to complete the atrial septum formation, between the days 36-42 in human (E12.5 in mouse), another muscular fold (the so-

called septum secundum as traditionally called) extends from the posterosuperior part of the roof of the common atrium between the pulmonary venous sinus and right atrium (denoted by light blue arrow in Figure 1:9 A-C) towards the right-hand side of the septum primum [8]. This will serve as a support for the flap of the valve of foramen ovale (i.e., the septum primum) to fuse with after birth when the interatrial communication would get closed [56].

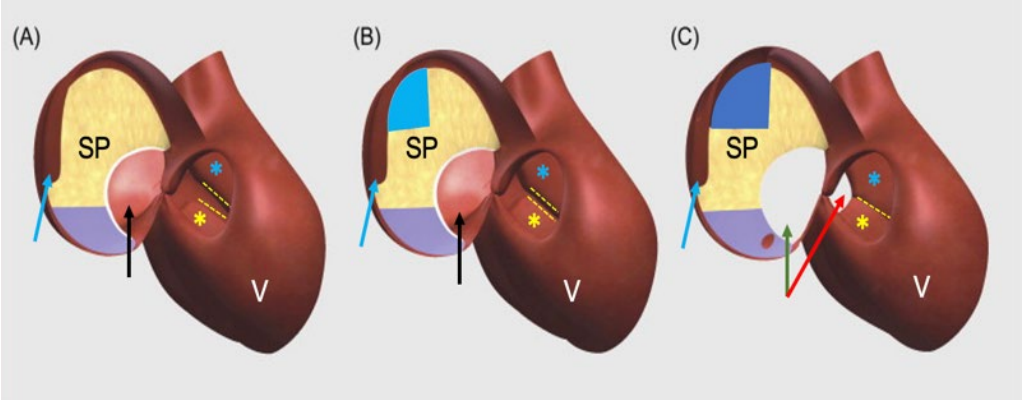


Figure 1:9 Formation of the atrial septum. A: The septum primum (SP) (in yellow) has a mesenchymal cap (white rim) at its leading edge. DMP (purple area) is extending from the posterior wall of the common atrium towards the inferior AV cushion (denoted by yellow asterisks). These is an interatrial communication (black arrow) at this stage. B: A second interatrial communication - ostium secundum starts developing (light blue) due to programmed cell death in the superior part of the septum primum. C: Ostium secundum has formed (dark blue). The septum secundum as a muscular flap (blue arrow) extends from the roof of the atrium to the right had side of the septum primum. Ostium primum has closed (white area pointed by green arrow) due to the AV mesenchymal complex which also has contributed to the inlet septum further down (white area pointed with red arrow). Yellow dotted lines denote gradual fusion of the two AV cushions (denoted by yellow and blue asterisks) to form an intermediate septum (after the formation of a single yellow dotted line as in C), dividing the common AV canal into right and left AV orifices. SP: septum primum; V: ventricle; yellow asterisk (*): inferior endocardial cushion; blue asterisk (*): superior endocardial cushion; purple area: dorsal mesenchymal protrusion (DMP); light blue area: developing ostium secundum; dark blue: developed ostium secundum. Adapted and modified from [56].

TBX5, TBX20, NKX2-5, GATA4 are reported to be some of the important genes for the formation of atrial septum and patients with mutations in these presented with ASDs and AVSDs [57-60]. Intriguingly, ASDs (and even VSDs) were also observed in patients with mutations in sarcomeric genes such as *MYH6,* and *ACTC1* [61] [62]. Moreover, defective formation of DMP due to deletion of *Alk3* (receptor for BMP) was associated with ostium primum ASD (a key feature of AVSDs) [63].

1.1.4.3 Formation of the interventricular septum

By the end of 4th week of development in human (E9.5-E10.5 in mouse), the primitive ventricles begin to expand (by ballooning) which results in gradual apposition and merging of medial walls of these ventricles forming the muscular part of interventricular septum (IVS) and which extends towards the AV endocardial cushions [44, 52]. At this stage, there is a space between the free rim of the muscular IVS (inferiorly) and the endocardial cushions (superiorly), enabling communication between the two ventricles in the earlier stages of development in the form of interventricular foramen which thereafter shrinks after the formation of the conus septum [52]. The closure of this foramen occurs when superior, inferior, and the two lateral endocardial cushions fuse while extending towards the free rim of the muscular part of the IVS [52]. During the same process, ostium primum is also closed (Figure 1:9-C) [52]. The muscular IVS also fuses with the (NCC-derived) endocardial cushions (and the derived aorticopulmonary septum) in the outflow tract of the heart (section 1.1.4.4) which results in complete separation of the right and left ventricles and their outlets [50]. Membranous interventricular septum is formed mainly

by the AV endocardial cushions, however, this down growth of aorticopulmonary septum contributes to the outlet septum [50] [64]. Hence, complete ventricular septation depends upon fusion of the OFT ('s conotruncal) septum, muscular IVS and AV endocardial cushions [17].

Many genes such as *Tbx5*, *Sall4*, *Gata4*, *Nkx2-5*, *Hand* (transcription factors) have a role in the development of interventricular septum (IVS) [65, 66] and their mutations are reported to result in septal defects [2].

1.1.4.4 Septation of the outflow tract (OFT)

OFT of the heart tube will differentiate into aorta and pulmonary trunk after septation which happens during the 7th and 8th weeks of development in human (E11.5 – E13.5 in mouse) [8]. This involves the formation of truncal and bulbar (conus) ridges/cushions in the 5th week of development in human (E11.5 in mouse) [17]. Bulbar ridge is in the bulbus cordis and truncus ridge is located distally in the truncus arteriosus [10]. Proliferation of mesenchymal cells result in formation of these ridges [47] (Figure 1:8 D). OFT of heart has resident population of PHF cells whereas the SHF cells subsequently migrate to it [67]. Anterior SHF cells form myocardium of the OFT [68] as well as the sub-pulmonary conus (infundibulum) [69]. Thereafter, the cardiac neural crest cells (CNCC), from dorsal neural tube (between 1st and 3rd somite), migrate via III, IV and VI pharyngeal arches into the truncal cushions (the right-superior and left-inferior) to form their mesenchyme (Figure 1:10-A) [50]. On the other hand, the conus cushions (the right-posterior and left-anterior) are derived from the mesenchyme derived from endocardium through EMT [70]. The proximally located conus (endocardial) cushions merge to

divide the heart outflow region into the right and left ventricular outflow regions (called as RV infundibulum and aortic vestibule respectively) (Figure 1:10-D)[71]. It also forms the outlet septum before developing into the RV's infundibulum [72]. The distally positioned truncal cushions merge to form the septum which segregates the aorta and pulmonary tract (Figure 1:10-D)[73]. The conal cushions extend distally towards the truncal cushions to fuse with them in a spiral pattern (180 degrees counter clockwise) (Figure 1:10 C-D). The conus part of the septum extends further proximally to get fused with the AV endocardial cushions, and the ventricular septum (to form the outlet septum) [50]. This results in complete separation of the right and left sides of the heart.

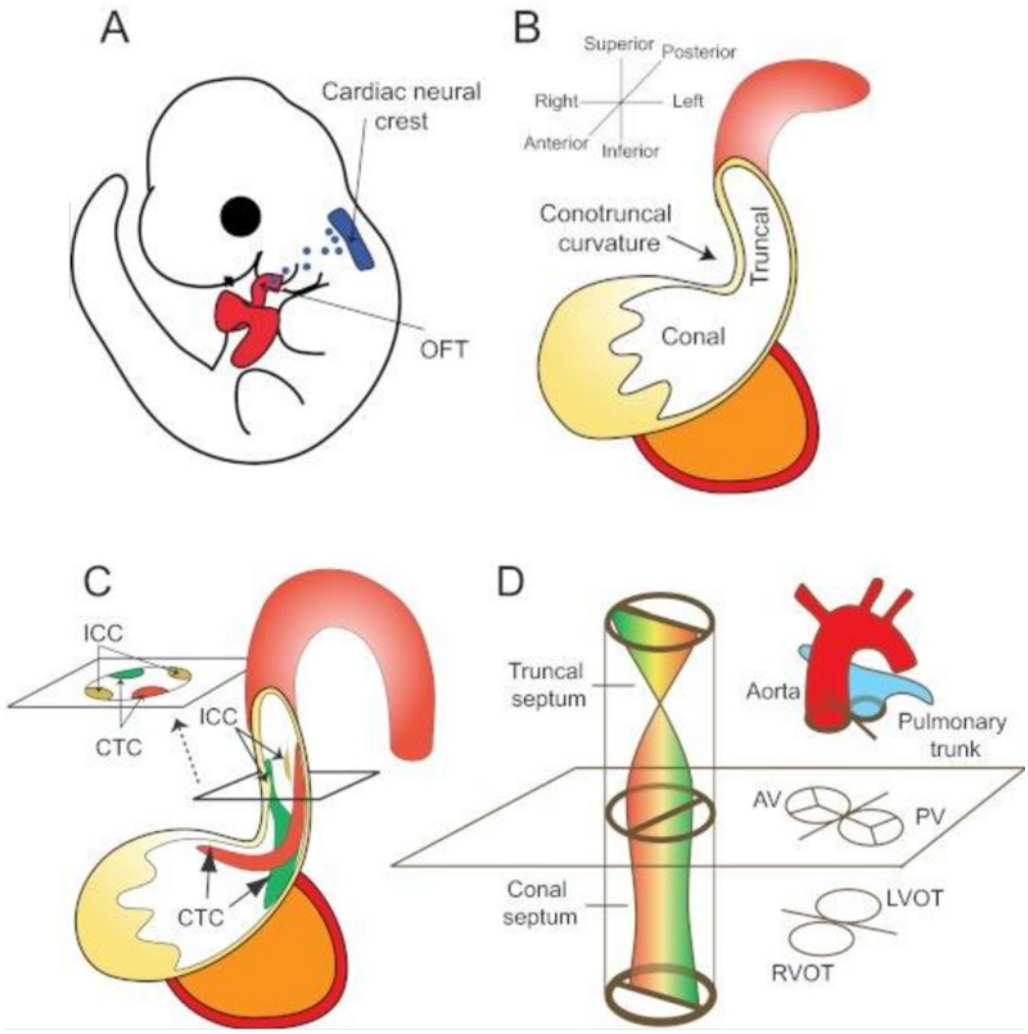


Figure 1:10 Septation of the cardiac OFT. (A) in the E10 stage mouse embryo (5-7 weeks in human), cardiac neural crest cells (blue) migrate from the dorsal neural tube to the distal (truncal cushions) part of the heart OFT. (B-C) The OFT contains conal (proximal) and truncal (distal) cushions which fuse in a spiral pattern to septate the OFT, as shown in (D). The truncal part of it divides the OFT into aorta and pulmonary trunk, whereas the conal part septate the OFT into aortic vestibule (left) and RV infundibulum (right). The aortic valves (AV) and pulmonary valves (PV) develop where the truncal and conal cushions meet. ICC: intercalated cushions which form anterior and posterior leaflets of semilunar valves; CTC: conotruncal cushions; RVOT: right ventricular outflow tract; LVOT: left ventricular outflow tract; AV: aortic valve; PV: pulmonary valve. Reproduced from [50].

Different genes have been reported to have a role in the outflow tract septation such as *FOXC1/C2, BMP2, NKX2-5, TBX1, SHH, FG8, FGF10* and *PITX2*. Mutations in these can result in developmental anomalies

such as overriding aorta (OA), transposition of great arteries (TGA), double outlet right ventricle (DORV), Tetralogy of Fallot (TOF), Ventricular septal defect (VSD), interrupted aortic arch (IAA) and common arterial trunk [66]. Cardiac neural crest cells are vital for the OFT septation and development [70, 74]. HAND1 and HAND2 transcription factors have been implicated previously in humans with OFT defects [75]. These transcription factors regulate OFT development through BMP-GATA mechanism by localizing cardiac neural crest cells in the OFT [75].

1.1.4.5 Aortic sac and aortic arches

Aorta development start in the 3rd week of development in human (E8.25 in mouse) as part of the developing heart tube when two dorsal and two ventral aortae connected by an arch are formed [76]. Truncus arteriosus, after OFT septation, will form the ascending part of the aorta (in addition to pulmonary trunk) [50]. This (ascending) aorta has aortic sac located superior to it which is formed by merging of the two ventral aortae whereas, inferiorly, the two dorsal aortae fuse to form the midline descending thoracic aorta [77]. Aortic sac is the distal part of the truncus arteriosus [17]. The aortic sac will then split into two horns [78]. Initially, five paired aortic arches (called as pharyngeal arch arteries) arise from the aortic sac between the paired dorsal and ventral aortae though some of these arteries regress as development progresses and all are never present at the same time [78]. Fifth aortic arch never forms [79] (though commonly it is said that it forms incompletely and then regresses [77]. The left 4th aortic arch along with the left horn of the aortic sac forms the arch of the aorta whereas the right horn of the aortic sac forms the

brachiocephalic trunk [78]. The 6th aortic arch is also called pulmonary arch. The proximal part of the right sixth arch contributes to the formation of the right pulmonary artery whereas its distal portion disappears. On the left, the 6th aortic arch persists to develop into left pulmonary artery and ductus arteriosus (Figure 1:11) [78]. After the partitioning of truncus arteriosus, the main pulmonary artery develops from the pulmonary trunk [77, 78].

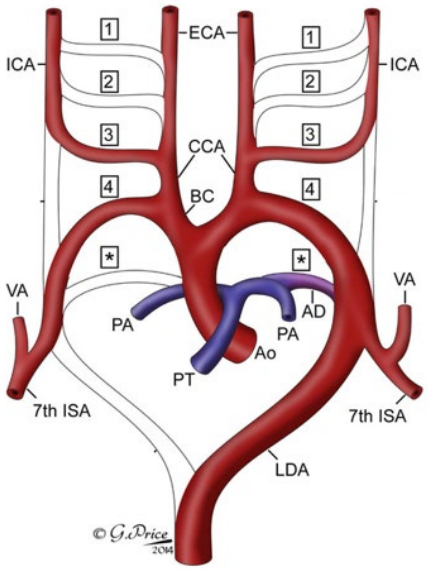


Figure 1:11 Development of the aortic arches and their remodelling. The pharyngeal arch arteries originate bilaterally symmetrically but most of them regress as the development progresses. Those remaining develop into the ultimate branches of aorta. The numbers denote the respective pharyngeal arches. Asterisk (*) denotes the 6th arch from which the proximal parts of pulmonary arteries and ductus arteriosus/arterial duct (AD) develop, though the distal part of the 6th arch regresses on right side. The arteries obtained after the remodelling are labelled. Abbreviations: AD, arterial duct (i.e., ductus arteriosus); Ao, aorta; BC, brachiocephalic trunk; CCA, common carotid artery; CD, carotid duct; ECA, external carotid artery; ICA, internal carotid artery; ISA, intersegmental artery; LDA, left dorsal aorta; PA, pulmonary artery; PT, pulmonary trunk; RDA, right dorsal aorta; VA, vertebral artery. Reproduced and adapted from [78].

1.1.4.6 Formation of cardiac valves

1.1.4.6.1 Formation of the AV Valves

The AV valves develop between 5th-8th week of development in humans (E10.5–E17.5 in mouse) [50, 80] though ECM remodelling continues in postnatal life [81, 82]. Bilaterally, AV orifices are surrounded by endocardial cushions (see section 1.1.3) These endocardial cushions not only divide the common AV canal into right and left AV canals but also give rise to the AV (mitral and tricuspid) valves [50]. To develop into AV valves, these endocardial cushions undergo remodelling which involves apoptosis at their bases and increased proliferation at the tip [83]. They become hollowed out and thinned on the ventricular surface, resulting in their delamination [84] (Figure 1:12-C). Initially these AV valves stay connected to the ventricular wall by muscular cords which subsequently become dense connective tissue/fibrous cords (Figure 1:12-C compared with A&B). Finally, the valves are connected to the ventricular trabeculae, papillary muscles, through chordae tendineae (Figure 1:12-C) [8, 85].

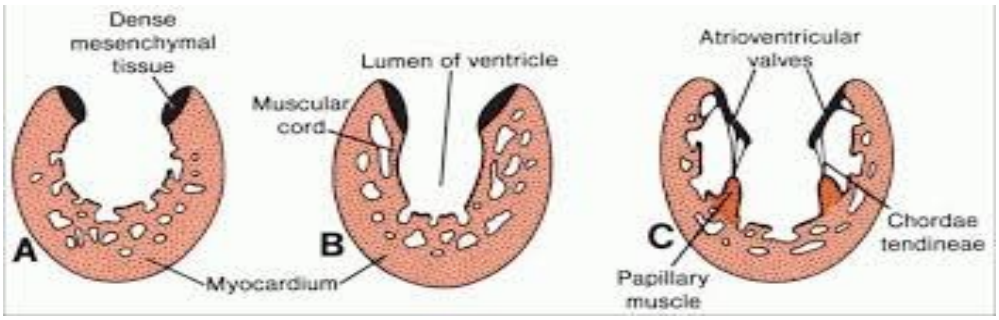


Figure 1:12 Formation of AV valve and chordae tendinae. Valves hollowed out on their ventricular surface (A) but remained connected to ventricular wall initially by muscular cords (B) and subsequently by chordae tendinae and papillary muscles (C). Reproduced from [8].

1.1.4.6.2 Formation of the semilunar valves

Semilunar (aortic and pulmonary) valves start developing in 6th week in human (E12.5 in mouse) from the two conotruncal cushions, and two intercalated cushions (ICC) – the left-anterior and right-posterior (Figure 1:10C) [86, 87]. The ICCs give rise to anterior cusp of pulmonary and non-coronary cusp of aortic valves [52, 86]. However, no confirm information is available regards its origin [88]. These swellings undergo excavation on its superior surface, as part of the remodelling, giving rise to the semilunar valves in aortic and pulmonary channels (Figure 1:13) [85, 89, 90]. Development of semilunar valves requires endocardium-derived as well as the cardiac neural cells-derived mesenchyme (through EMT) [50].

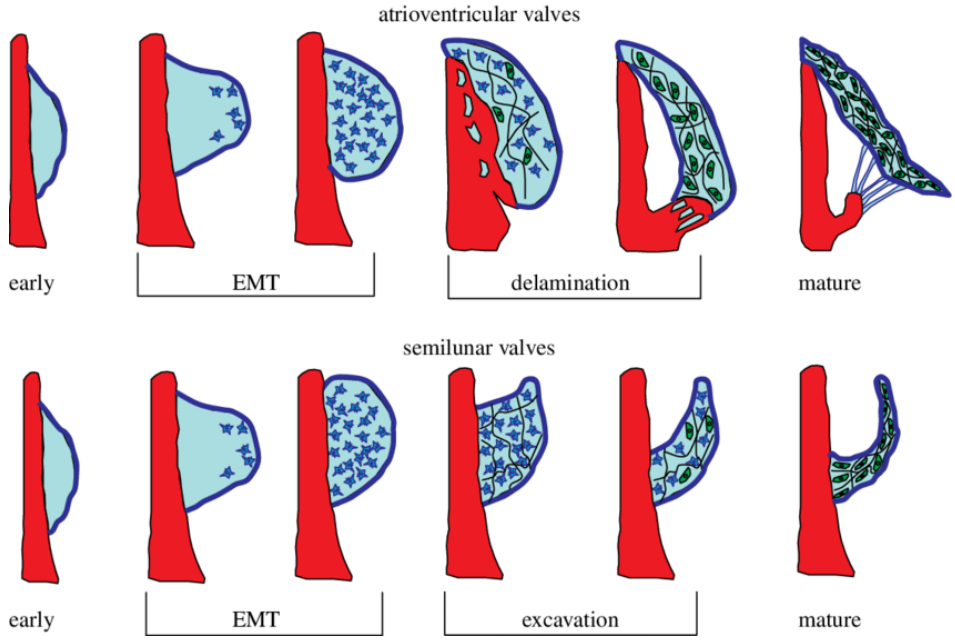


Figure 1:13 Successive remodelling of the cardiac valves. The AV valves undergo delamination from the muscular ventricular walls, whereas in case of semilunar valves the cushions get excavated from the aortic side inward. Reproduced from [85].

There is a great similarity between the genes and pathways involved in the AV canal and OFT septation and development of cardiac valves [50]

(Figure 1:14). However, there are some differences reported as well in these processes happening at the two sites. For example, VEGF signalling through VEGFR1 is required for differentiation of valves formed by EMT in OFT, whereas, in the AV canal's endocardial cushions, VEGF acts through VEGFR2 receptors to cause EMT as needed for morphogenesis of AV valvular leaflets [91].

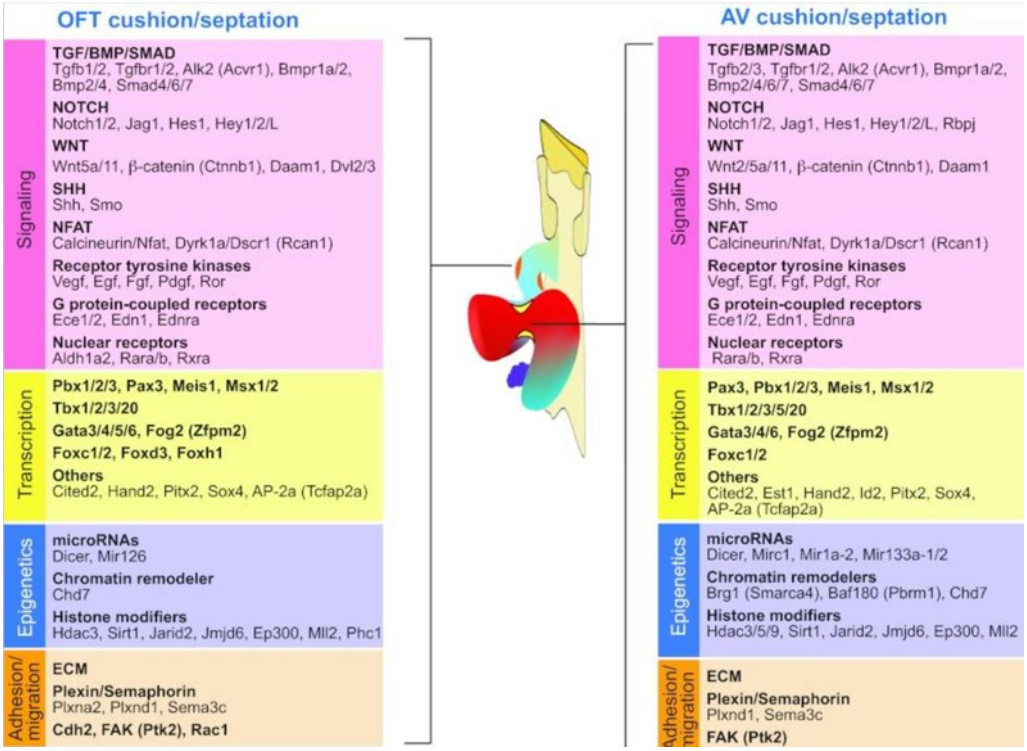


Figure 1:14 Comparison of the genes involved in cardiac septation and development of cardiac valves. There is a great similarity between the genes and pathways involved in septation of the AV canal and OFT and development of cardiac valves. However, there are some differences reported as well in these processes happening at the two sites. Reproduced from [50].

1.1.4.7 Foetal circulation and the changes after birth

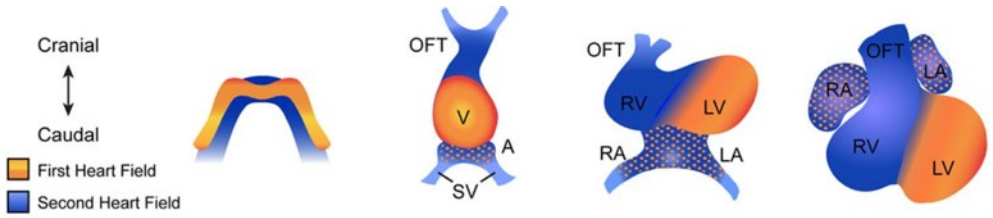
Heart starts beating by 21st/22nd day in human (E8.25 in mouse) [92] though the first heartbeat occurs even earlier i.e., at E8 in mouse (Day 16 in human) as required for normal heart development [93]. From the start of heart beating by 21st/22nd day in human (E8.25 in mouse) until

the end of the organogenesis (9th week in human and, just prior to birth in mouse i.e., ~E20), yolk sac through vitelline circulation and placenta through umbilicoplacental circulation provide gaseous exchange and nutrients supply [94]. However, after 9th week (in human), placental circulation dominates [94, 95]. Placental circulation brings oxygenated blood to the developing foetus which is distributed to all the body tissues bypassing the non-functional lungs at this stage [95]. This involves different shunts which are the oval foramen, ductus arteriosus, ductus venosus and placenta [95]. Moreover, factors such as Prostaglandins (PGs) and Endothelin1 (Edn1) are responsible for increasing pulmonary vascular resistance [96]. However, after birth, structural, physiological, and biochemical changes happen to support the neonate's cardiovascular system to take over the role of body oxygenation [95, 97]. This pulmonary vascular resistance disappears with the release of bradykinin (which stimulates nitric oxide release from the endothelium, causing vasodilation) [98]. This enables pulmonary circulation to begin as is needed for blood oxygenation postnatally. Moreover, the shunts get closed after birth to keep separate the oxygenated and deoxygenated blood [99, 100].

1.2 Molecular regulation of heart development

Heart formation is a very complex process involving a range of important signalling pathways [101]. These include Nodal, Wnts, bone morphogenic proteins (BMPs), NOTCH, Sonic hedgehog (SHH), neuregulin, retinoic acid (RA), fibroblast growth factors (FGFs), and others [102-105]. These signalling molecules regulate cardiogenesis through cardiac

transcription factors such as NKX2.5, MESP1, GATA4, ISL1, HAND1, HAND2, and various TBX transcription factors [102-105] (Figure 1:15).



Stage	Cardiac Crescent	Linear Heart Tube	Looping Heart	Chamber Specialization/ Septation
Mouse Embryo Stage	E7.5	E8.0	E9-12	E10+
Human Embryo Stage	Day 15	Day 20	Day 28-30	Day 32+
Key Regulators	GATA4 NKX2.5 MESP1/2 ISL1 BAF60C MEF2C	GATA4 NKX2.5 TBX5 TBX20 MEF2C	GATA4 NKX2.5 TBX5 MEF2C HAND1/2	GATA4 NKX2.5 TBX5 PITX2 TBX1

Figure 1:15 Different stages of heart development and the key regulators. OFT: outflow tract; SV: sinus venosus; V: primitive ventricle; A: primitive atrium; RA: right atrium; LA: left atrium; LV: left ventricle; RV: right ventricle. Reproduced from [106].

1.3 Congenital heart disease (CHD)

Congenital heart disease affects ~1% of infants born [107] and is the most common anomaly present at birth [108]. This can be in the form of isolated defects such as septal defects/holes in the chambers or complex defects with higher lethality [109]. Heart defects due to initial insult (e.g., genetic, environmental) can be further compounded by the added hemodynamic changes. For example, hypoplasia of heart (with compromised ventricular trabeculation) can happen due to reduced blood flow because of atresia/stenosis of AV and semilunar valves [101]. A brief account of some common CHDs is given here.

1.3.1 Bicuspid aortic valve (BAV)

BAV is the most common CHD, occurring in 1- 2% of the population [110]. There are three main types of BAV, which vary in the morphology of the leaflets and the number of sinuses. They are (i) fused type with two cusps, three sinuses, two commissures and raphe, (ii) 2-sinus BAV which has 2 sinuses, 2 cusps and 2 commissures and no raphe, (iii) partial fusion BAV (forme fruste) in which there are 3 cusps, 3 sinuses and 3 commissures, where two commissures are normal and the third one is <50% fused and there is a small/mini-raphe (Figure 1:16) [111].

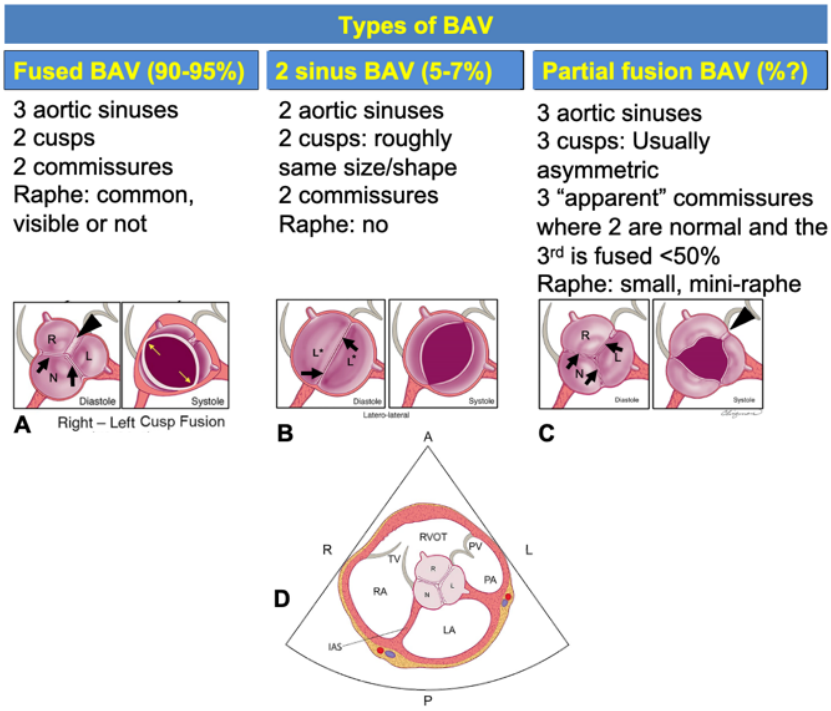


Figure 1:16 Different types of BAV. A: fused type BAV where the right and left cusps are fused with raphe (denoted by black arrowhead) but two commissures (denoted by black arrows) and three sinuses can be appreciated. B: The two-sinus type BAV with two cusps. There are two lateral cusps (denoted by L), two commissures (denoted by black arrows) and two sinuses in this condition. C: Partial fusion type of BAV has three cusps and sinuses. There are three apparent commissures (denoted by black arrows) but the third one is fused by less than 50% and a small raphe (denoted by black arrowhead) can be seen. D: represents the normal aortic valve with three cusps as oriented in a parasternal short axis view for comparison of the aortic valves shown in A-C. Adapted from [111].*

1.3.2 Atrioventricular septal defect (AVSD)

An AVSD is a complex type of CHD, which occurs in approximately 0.05% of live-births in humans and approximately 50% of these are found in individuals with Trisomy 21 [112]. The AVSD can be either complete or partial. In complete AVSD, there is a failure of the dorsal mesenchymal protrusion (DMP) to fuse with the mesenchymal cap and the atrioventricular (AV) endocardial cushions [113, 114]. This results in ostium primum defect, inlet VSD and common AV canal guarded by common AV valve (Figure 1:17A) [45, 115]. The cause of inlet VSD is the deficiency of the AV component of the membranous septum [115]. The AV component of membranous septum is normally present between the right atria and left ventricle and has membranous and muscular parts [115].

In partial AVSD, there is an ostium primum defect [116]. In this case, there is shunting of blood between the atria but the AV valve's bridging leaflets are fused to the crest of ventricular septum resulting in two separate AV orifices in contrast to the complete AVSD (Figure 1:17B) [117].

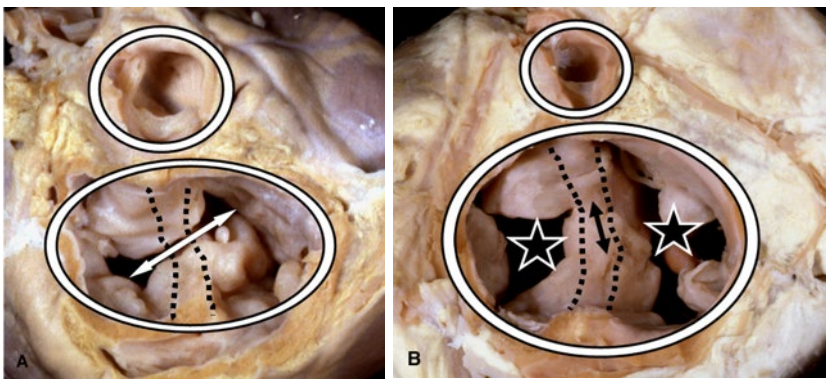


Figure 1:17 Partial and complete AVSD. The images show short axis superior view of the two different hearts after removal of atria. There is a common atrioventricular orifice (white arrow) and occurs in complete AVSD (A) whereas in partial/incomplete AVSD (B), there are two AV orifices (stars) due to fusion of AV valves' tissue (black arrow). There is associated ostium primum defect (not shown). Ventricular septum is denoted by dotted lines. Reproduced from [115].

1.3.3 Patent foramen ovale (PFO)

Patent foramen ovale (PFO) is a defect of interatrial septum when the interatrial communication persists after birth [118]. Normally, due to increased left atrial pressure after birth, the flap valve should fuse spontaneously with the septum secundum to close off this communication [119]. However, in 15-35% of adult population, this communication persists as PFO [120]. PFO has been associated with thromboembolism leading to cryptogenic stroke, migraine, decompression sickness (in divers) [121-124]. This makes this condition of clinical significance.

1.3.4 Ventricular septal defects (VSDs)

VSDs account for about 36% of CHDs [125]. During septation of the ventricles, aorta is shifted toward the LV which brings the OFT's septation-cushions near the ridge of the muscular part of ventricular septum [126], resulting in reduction of the size of the interventricular foramen. The final closure of the interventricular foramen is then carried out by the AV endocardial cushions [44]. If this process fails, VSD will occur [44]. Abnormal interventricular communication can also involve the muscular part of the ventricular septum, where the failure of fusion of the ventricular trabeculae would result in abnormal communication between the two ventricles [127]. The different parts of ventricular septum are shown in Figure 1:18. VSDs can be of inlet, outlet, trabecular and perimembranous types [128]. Perimembranous type occurs when there is added involvement of surrounding inlet, outlet and/or some trabecular parts as well) [129]. However, the inlet VSD is in the part of AV septum which separates inlet of RV and outlet of LV and hence would be more appropriate to label as

"inlet/outlet" VSD [115, 130]. RV outlet is between the limbs of septomarginal trabeculation and pulmonary root; between the right and noncoronary aortic sinuses is membranous interventricular septum [72]. Infundibular part of the interventricular septum separates the outflow tracts of both ventricles [131] and defect in here would be the outlet VSD.

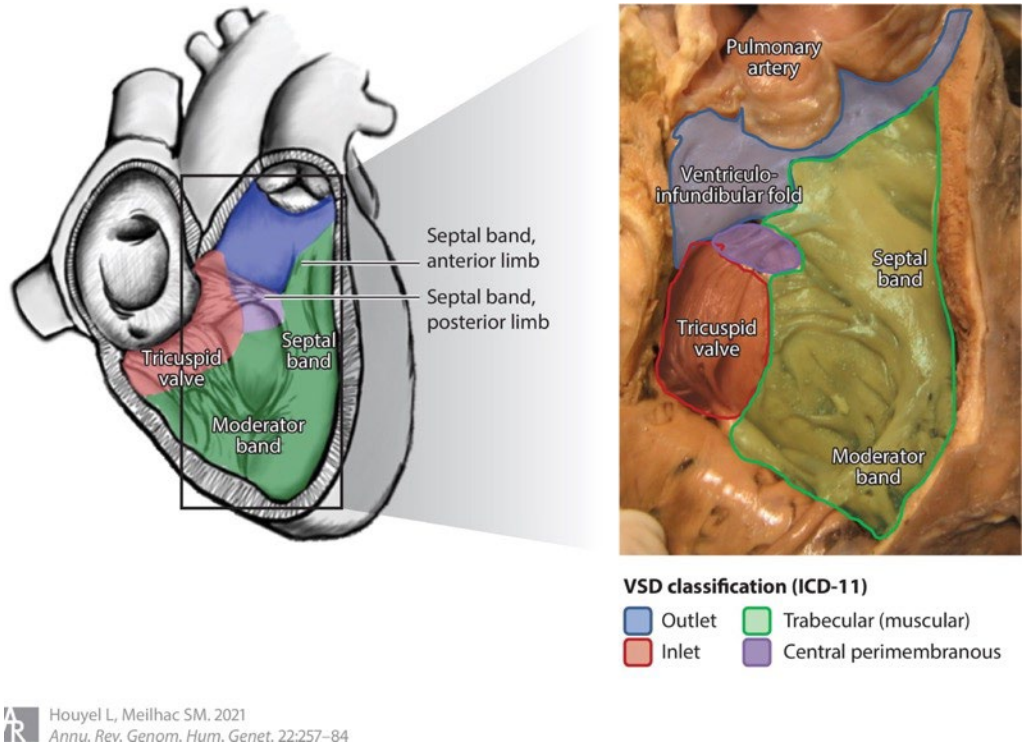


Figure 1:18 Different components of the ventricular septum and types of VSD. According to international classification of diseases (ICD), version 11, VSDs can be of inlet, outlet, trabecular and perimembranous types. This specification helps to locate the VSDs to specific location in the VS. Reproduced from [128].

1.3.5 Pulmonary stenosis (PS) and dysplasia of the pulmonary valve

PS is reported to occur in 8% of CHD cases [132]. Pulmonic stenosis can occur either at valvular, subvalvular (infundibular) or supravalvular levels [133] and occurs in tetralogy of Fallot (TOF). It is commonly associated with other CHDs as well [134].

Dysplasia of the pulmonary valve is considered one of the types of valvular PS [135]. It occurs when the cusps are thickened with no commissural fusion of the cusps and narrow pulmonary annulus [135].

1.3.6 Bicuspid and quadricuspid pulmonary valves

Bicuspid and quadricuspid pulmonary valves are rare anomalies with incidence of 0.1% and 0.2% respectively[136]. In TOF, PV is mainly bicuspid [137]. Being quadricuspid (having four cusps) is a rare anomaly of the pulmonary valve [138].

1.3.7 Defects of the heart outflow tract (OFT)

Cardiac outflow tract defects account for 30% of all CHDs [139]. These defects present as double outlet right ventricle (DORV), overriding aorta (OA), discordant ventriculoarterial (VA) connection/transposition of the great arteries (TGA), persistent truncus arteriosus (PTA), coarctation or dilatation of aorta [139, 140]. These OFT anomalies happen due to defects of rotation, alignment and unbalanced septation during the morphogenesis of the conotruncal and conoventricular parts of the embryonic hearts [128] (Figure 1:20). OFT defects have an associated outlet VSD with except of some TGAs [128].

Double outlet right ventricle (DORV)

DORV is a rare condition accounting for about 1-1.5% of all congenital heart defects [141]. In DORV, both aorta and pulmonary originate totally or predominantly (based on 50% rule) [142]) from the right ventricle. However, both aorta and pulmonary artery are already separated due to the formation of septum in between [143]. There is always an associated

VSD with DORV [142]. Location of VSD in this condition is critical to determine the right surgical approach [143]. The VSD can therefore, be subaortic, sub-pulmonary non-committed or doubly committed [144-146]. Doubly committed and non-committed VSDs are labelled so based on the proximity of the upper edge of the VSD to the centre of the respective arterial valves [143]. Distance of the VSD if more than the diameter of the aortic valve is generally considered as a non-committed VSD [146].

Overriding aorta (OA)

Overriding aorta is a malalignment defect of the OFT [147]. It occurs when the aortic root does not normally wedge between the mitral and tricuspid valves due to defect of OFT lengthening during cardiac looping [147]. Normally, aortic valve leaflets should be exclusively extended/supported in the LV. In OA, 50% of the aortic root circumference is supported within the RV and 50% within LV (Figure 1:19-B compared with A) [148]. The presence of VSD is a prerequisite for the OA to occur [149]. If more than 50% of aortic root is supported by the RV, then it becomes the DORV [149] (Figure 1:19-C compared with A).

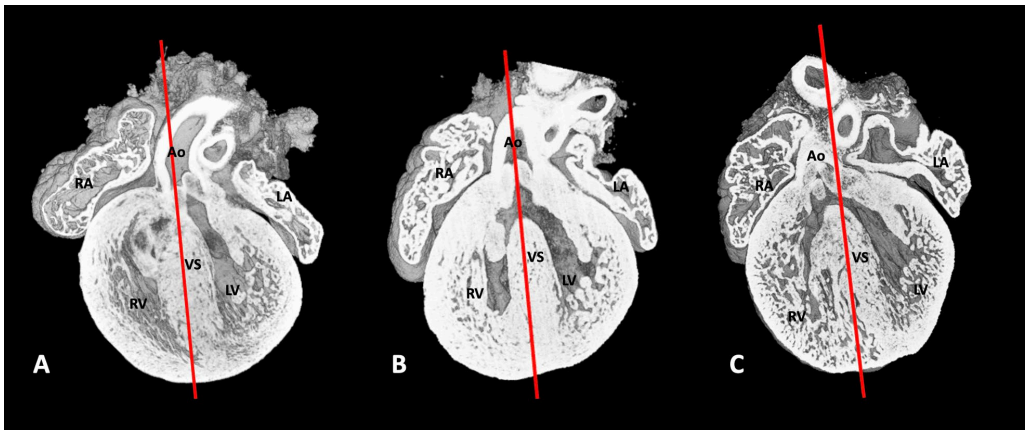


Figure 1:19 Mal-alignment of the OFT resulting in OA or DORV. Normally, aortic valve leaflets should be exclusively extended/supported in the LV (A, WT). In OA, 50% of the aortic root circumference is supported within the RV and 50% within LV (B). If more than 50% of aortic root is supported by the RV, then it becomes the DORV (C). RA: right atrium; RV: right ventricle; LA: left atrium; LV: left ventricle; VS: ventricular septum; Ao: aorta.

Transposition of great arteries (TGA)

TGA is a congenital anomaly due to defect of the spiralling mechanism of the conotruncal septum such that it fails to follow carry out spiralling [150]. This results in ventriculoarterial discordance, with aorta arising from the right and pulmonary trunk from the left ventricle [150]. This is commonly associated with VSD but ASD and PDA can also occur to enable mixing of the blood from systemic and pulmonary circulations [150, 151].

Persistent truncus arteriosus (PTA)

Persistent truncus arteriosus (PTA) is a condition when the OFT fails to septate, resulting in a single arterial trunk [139, 140]. It is characterised by the presence of VSD, truncus with a single valve and a common heart outflow channel [152]. Cardiac neural crest cells have a key role in the septation of OFT [64].

Coarctation of aorta (CoA)

CoA occurs due to abnormal intrauterine development of aortic arches [153]. In this condition, there is the narrowing of aorta typically in the descending aorta immediately distal to the origin of left subclavian artery [154]. It accounts for about 3.5% of CHDs [125]. It is commonly associated with other defects such BAV, VSD and complex types of CHDs [155]. Interruption of the aortic arch (IAA) is considered as the severe form of CoA [153, 156] which is associated with other CHDs such as VSD, TA and PDA [157].

Tetralogy of Fallot (TOF)

TOF is characterised to have 4 interrelated defects such as RVOT obstruction, RV hypertrophy, VSD and overriding aorta (OA). There could be other associated defects such as cleft lip and palate [158].

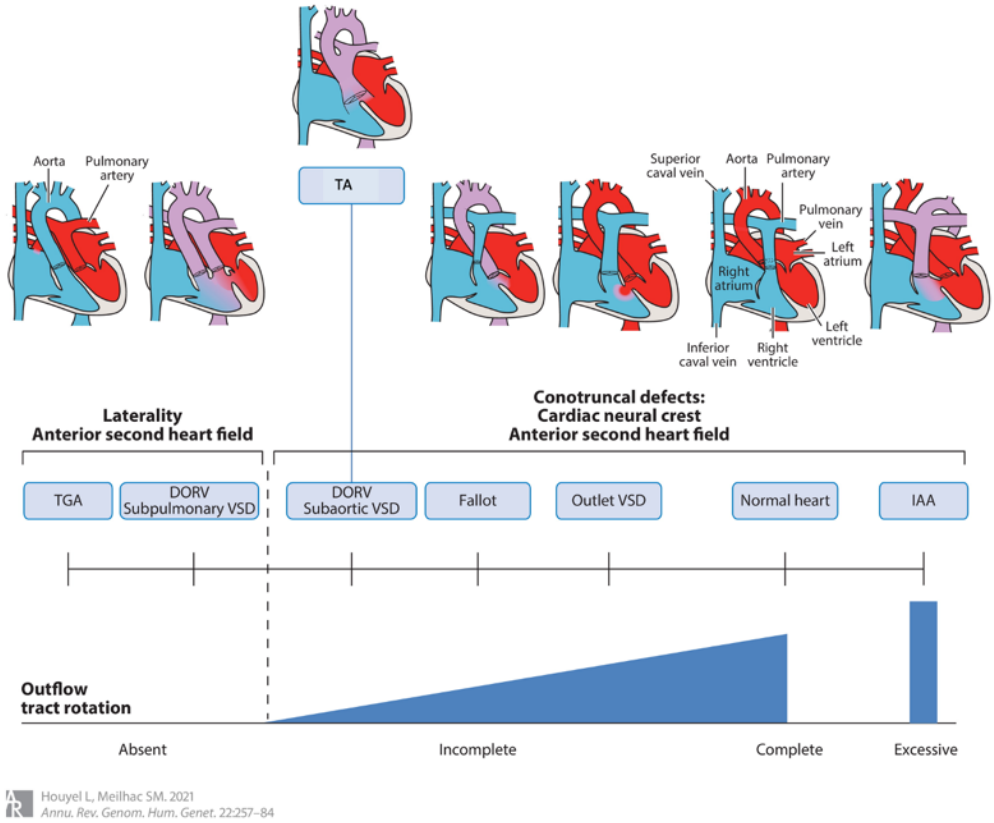


Figure 1:20 Spectrum of the outflow tract defects. The figure shows anomalies resulting from an abnormal rotation of the outflow tract, which may be absent (in DORV with a subpulmonary VSD, TGA, and CAT), incomplete (in DORV with a subaortic or doubly committed VSD, tetralogy of Fallot, or outlet malalignment VSD), or excessive (IAA type B). With the exception of some TGAs, these defects share the same anatomical type of VSD—namely, an outlet VSD with a misaligned and/or fibrous outlet septum. The anterior second heart field is involved in all outflow tract anomalies, in association with laterality abnormalities in TGA and DORV with a subpulmonary VSD, or in association with defective cardiac neural crest in a category commonly referred to as conotruncal defects. Abbreviations: TA, truncus arteriosus (common arterial trunk); DORV, double-outlet right ventricle; IAA, interrupted aortic arch; TGA, transposition of the great arteries; VSD, ventricular septal defect. Reproduced from [128].

1.4 Epidemiology of congenital heart disease

Congenital heart disease (CHD) constitutes the most commonly diagnosed congenital defect in new-borns, affecting 0.8-1.2% of all live-births [159] [101]. CHD affects one out of 150 babies born in the United Kingdom, with an average of 13 cases per day [160]. The commonest type of CHD is considered to be BAV however its true prevalence remains

underestimated due to it getting medical attention, mostly, only incidentally [161]. With adding BAV to the CHD-figures, the prevalence of CHD rises to 1.9% [162]. Moreover, if the small muscular VSDs and other minor cardiac anomalies are also accounted for, this value rises to 7.5% [162]. VSDs and ASDs are the next most common types of CHD accounting for 29.6 % of all the CHD cases [163]. The prevalence of CHD stays same for the last more than 3 decades which suggests that no improvement could be made to prevent CHD [163] [164]. However, with improvement in healthcare, prevalence of CHD in population is increasing as 95% people with CHD survive to adult age [165] [166].

1.5 Causes of CHD and role of genes

CHDs have quite a complex aetiology, involving both genetic and environmental causes which are responsible for 20-30% of cases [167]. It is heterogeneous condition and genetic causes have been identified in 33-39% of infants with CHD [168, 169]. CHD mostly occurs as a “one off” phenomenon in a family and so far, more than 55 genes have been implicated in human cases [170]. The mice studies with targeted deletions report more than 500 genes which when mutated could lead to CHDs (http://www.informatics.jax.org) [170]. However, no conclusive phenotype-genotype association could be established [170, 171]. More recently, studies have focussed on whole exome sequencing (WES) of large cohorts having CHD, aiming to find some novel genes. A WES study by Zaidi *et al* focussed on 4169 (Higher Heart Expression, HHE) genes and found that *de novo* mutations (DNM) were responsible for almost 10% of the severe CHD [172]. Following this study, Homsy *et al*

compared the number of DNM in 1213 CHD trios with 900 healthy trios and noted a significant (1.4 fold) enrichment of *de novo* deleterious variants in the CHD cohort, more so in syndromic-CHD (S-CHD) [173]. Moreover, there was 2.4-fold increase in the deleterious variants in top quartile of HHE genes [173]. This study supported the results of Zaidi et al [172] that DNMs are often the cause of CHDs [173]. A more recent study from the same collaboration which carried out WES of 2874 CHD probands reported that DNM account for 8% of CHD cases including ~28% of S-CHD and ~3% of non-syndromic CHD (NS-CHD) cases [174]. Their study shows that many of the key genes are jointly expressed in heart as well as brain and hence indicates shared causative genetic mutations as a cause of CHD and neurodevelopmental disorder, though with variable expression [175]. Homsy *et al* also listed 21 genes with DNM as a cause of CHD, some of which were reported previously as well, as a cause of CHD such as *MYH6* (atrial septal defects, cardiomyopathy), *PTPN11* (Noonan syndrome), *KMT2D* (Kabuki syndrome), *ZEB2* (Mowat Wilson syndrome), *JAG1* (Alagille syndrome), and *NOTCH1* (associated with disease of the aortic valve & Adams Oliver syndrome), *CHD7* (CHARGE syndrome), and *RBFOX2 (*Hypoplasia of left heart*)* [173]. All these earlier studies however could not explain the underlying mechanism of NS-CHD which constitute the largest CHD group.

In order to explore the genetic mechanism underlying the NS-CHD, WES of 1891 probands with NS-CHD and S-CHD was carried out through widespread collaboration under the umbrella of the Deciphering Developmental Disorders (DDD) study to which our lab was part of [176]. This

study reported that there was a role of inherited mutations in the occurrence of NS-CHD [176]. It showed that in S-CHD cohort, there was significant excess in *de novo* protein truncating variants (PTVs) and missense mutations in genes previously known to have a role in causing autosomal dominant CHD whereas in NS-CHD cohort, the burden of these variants was lower [176]. This study came up with the identification of three novel human S-CHD genes: cyclin dependant kinase 13 (*CDK13)* (7p14.1), chromodomain helicase DNA binding protein 4 *(CHD4)* (12p13.31), and protein kinase D1 (*PRKD1)* (14q12) [171, 176].

1.6 Mouse as a model for CHD

Mouse resembles humans in terms of genome (99%) and the various developmental processes and the associated genetic control [128, 177]. Mouse heart anatomy greatly resembles that of human, with some of the differences mentioned in Table 1:2 [92].

Cardiac morphological differences between mouse and human		
No.	**Mouse**	**Human**
1.	Bilateral SVC	Single right sided SVC
2.	Septal leaflet of TV fails to delaminate *in utero*	Delamination occurs *in utero*
3.	AV septum is thick & muscular	AV septum is thin & fibrous
4.	Similar pattern of trabeculation in both ventricles	Smooth trabeculations in the left & coarse in the right ventricles.
5.	Absence of identifiable moderator band	Moderator band identifiable
6.	Single pulmonary venous orifice	Two to four pulmonary venous orifices
7.	Atrial appendage more prominent	Atrial appendage less prominent

Table 1:2 Major cardiac morphological differences between mouse and human. AV: atrioventricular; TV: tricuspid valve; SVC: superior vena cava. Reproduced from [92].

The course of developmental events in mouse heart is also quite similar to that in human [92] (Table 1:3). All major cardiac structures are identifiable by E14.5 (corresponding to day 50 in human) [81, 82]. From E15.5 to E17.5 in mouse (GA 21 weeks in human) and onwards, semilunar and AV valves undergo refinement [81, 82] whereas myocardium undergoes progressive compaction [32]. In mouse, papillary muscles appear by E14.5 (day 50 in human) whereas the anterior leaflet of tricuspid and posterior leaflet of mitral valves are released by E15 in mouse (corresponding to GA after 7th week and prior to 21 weeks in human) [47]. Mouse embryonic age E15.5 - E17.5 corresponds to 21 weeks in human [92]. The septal leaflet of tricuspid valve is not delaminated in utero, in mouse [92, 178]. By E16 in mouse (~21 weeks in human), main branches of coronary arteries appear [47]. Chordae tendineae appear by E16.5 (21 weeks in human).

Mouse developmental stage (E. dpc)	E 9.5	E 10.5	E 11.5	E 12.5	E 13.5
Carnegie stage	13	14	15	16	17
1. Cardiac loop					
2. Atrial septation					
A. Septum primum					
B. Septum secundum					
3. Interventricular foramen					
4. Ventricular septation					
A. Muscular interventricular septum					
B. Inlet interventricular septum					
C. Outlet interventricular septum					
5. Atrioventricular junction/valve formation					
A. Mitral valve					
B. Tricuspid valve					
6. Outflow septation					
7. Semilunar valve formation					
A. Aortic valve					
B. Pulmonary valve					

Table 1:3 Stages of development in the mouse heart are outlined. E.dpc: Embryonic day post coitus. Reproduced from [92] and [179].

In order to study CHD, mouse is quite a useful model [92] and genetic mutation in mouse can often recapitulate the effect of such mutations in human [180]. Moreover, the same standard CHD nomenclature can be applied as in human [128]. The genetically engineered mouse models have been used to characterise gene function as relevant to human health and disease [177]. The phenotype data of the various such mouse models are available at https://www.mousephenotype.org/ [181].

There are certain limitations to mouse model as well. Knowledge of the similarities and differences between the mouse and human is important to make best use of the mouse model for studying human biology and disease. For example, septation in mouse and human heart is similar with no major differences [52, 92] therefore mouse is a good model to study heart septal defects. However, owing to differences between mouse and human in normal pattern of trabeculation [92], modelling and interpreting cardiomyopathic/trabeculation changes could be challenging. Moreover, there are no specific comparable stages in human corresponding to mouse after E17.5 till birth [92]. The longer gestation in human compared to mouse may result in additional cardiac features due to CHD-associated hemodynamic remodelling [92]. Some cardiac anomalies such as Ebstein's anomaly, pulmonary stenosis and hypoplastic left heart syndrome with aortic stenosis might not be identified in mouse models due to temporal differences between mouse and human development [182-184].

Other than these, differences exist between mouse and human in terms of gene expression, coding sequence (making proteins with different

properties), differing interaction of genes in a network, higher metabolic and heart rates in mice etc [185]. Nevertheless, more than 50% of the interactions between transcription factors (crucial for gene expression and thence tissue specificity) are conserved between mouse and human [186].

1.7 Aims

The aim of this thesis was to characterize the role of two of the three novel genes (*CDK13 and PRKD1*), identified in the previous work from our lab [176], using mouse models. The third novel gene was *CHD4* on which a previous PhD student in the lab worked. Heart morphogenesis was analysed in the three genetically engineered mouse models (two for *Prkd1* and one for *Cdk13*) obtained from the Wellcome Trust Sanger Institute (*Wtsi*) UK and European Conditional Mouse Mutagenesis (EUCOMM) program. These mice were bred at the University of Nottingham, UK on C57BL/6N background. The main aim of this mouse work was to phenotypically characterise the role of different genes in heart development and CHD. However, it also aimed to lay a basis for the identification of potential pathways related to heart morphogenesis and CHD pathogenesis.

The main aims were:

1. To carry out lethality assessment in the three mutant mouse lines comparing WT with HET and HOMO mice.
2. Gross/external phenotyping of embryos after collection for any visible developmental anomaly involving other systems.

3. Phenotypic analysis of the hearts from all three mouse models to compare hearts using high resolution episcopic microscopy (HREM) technique followed by 3D heart modelling [187];
4. Comparison of the differential expression of these GOIs (i.e., *Cdk13* and *Prkd1*) among WT, HET and possibly HOMO mice (based on tissue availability in relation to lethality), using qPCR, X-Gal staining (*Cdk13* only) and western blotting.
5. RNA-Seq transcriptome analysis to identify downstream targets comparing WT with HOMO hearts.
6. Identification and validation of some of the *Cdk13*-targets related to heart development by RT-qPCR and whole mount *in situ* hybridization (W-ISH). The transcriptomic analyses would help establish the role of *Cdk13* in heart development and its relationship to others thereby help establishing a road map of cardiac development.

2 MATERIAL AND METHODS

2.1 Mouse lines

Three different transgenic mouse lines were used for this work. They were *Cdk13^{tm1b}, Prkd1^{em1} and Prkd1^{em2}* as detailed below:

2.1.1 *Cdk13$^{tm1b(EUCOMM)Hmgu}$*:

The *Cdk13* transgenic mouse line, carrying the loss of function (LOF) mutation allele, *Cdk13^{tm1b}*(EUCOMM)Hmgu, used for this project was generated by the European Conditional Mouse Mutagenesis (EUCOMM) program. The mouse carried *LacZ* tagged null allele (*tm1b*) and was considered a true knockout because skipping over the *LacZ* cassette would not be able to restore gene expression. In the *LacZ* tagged null allele (*tm1b*), *Lacz loxP* cassette was inserted through homologous recombination followed by Cre-mediated replacement of *Cdk13* exons 3 and 4 (critical exons) (171 base pairs and 140 base pairs, respectively) with *LacZ* (i.e., a true knock out). Moreover, the knock-in cassette carried *LacZ*, expression of which was found in tissues with knock out of the gene of interest (GOI) i.e., *Cdk13*. Presence of *LacZ* cassette is commonly utilised for following the expression of GOI after β-galactosidase staining and hence was utilised for the same purpose in this study. The missing exons in this *Cdk13^{tm1b}* were exon-3 (171bp) and exon-4 (140bp). The Figure 2:1 shows the generation of allele *tm1b* from *tm1a* after Cre-loxP recombination when the critical exons (3 and 4) along with flanking loxP, FRT and neomycin were excised. Genotyping of *Cdk13 ^{tm1b}* mouse include combination of different PCR reactions. For detecting gene specific WT allele,

Cdk13-F (*Cdk13_84881_F)* and *Cdk13*_R (*Cdk13_84881_R)* primers were used (Table 2:2). For detecting the specific sequence in mutant allele, *Cdk13*-F (*Cdk13_84881_F)* and CAS_R1_Term primers were used (Table 2:2). The *LacZ* cassette was present in mutant allele only and its presence was identified by *LacZ* specific primers *(LacZ_2_small_F and LacZ_2_small_R)* shown as *LacZ*-F and *LacZ*-R (Figure 2:1, Table 2:2). In case of HET mutation, there will be a WT band (250bp), mutant band (200bp) and a *LacZ* band (108bp) on gel electrophoresis, whereas homozygous mutation would give bands both in the mutant as well as the *LacZ* lanes (Figure 3:5).

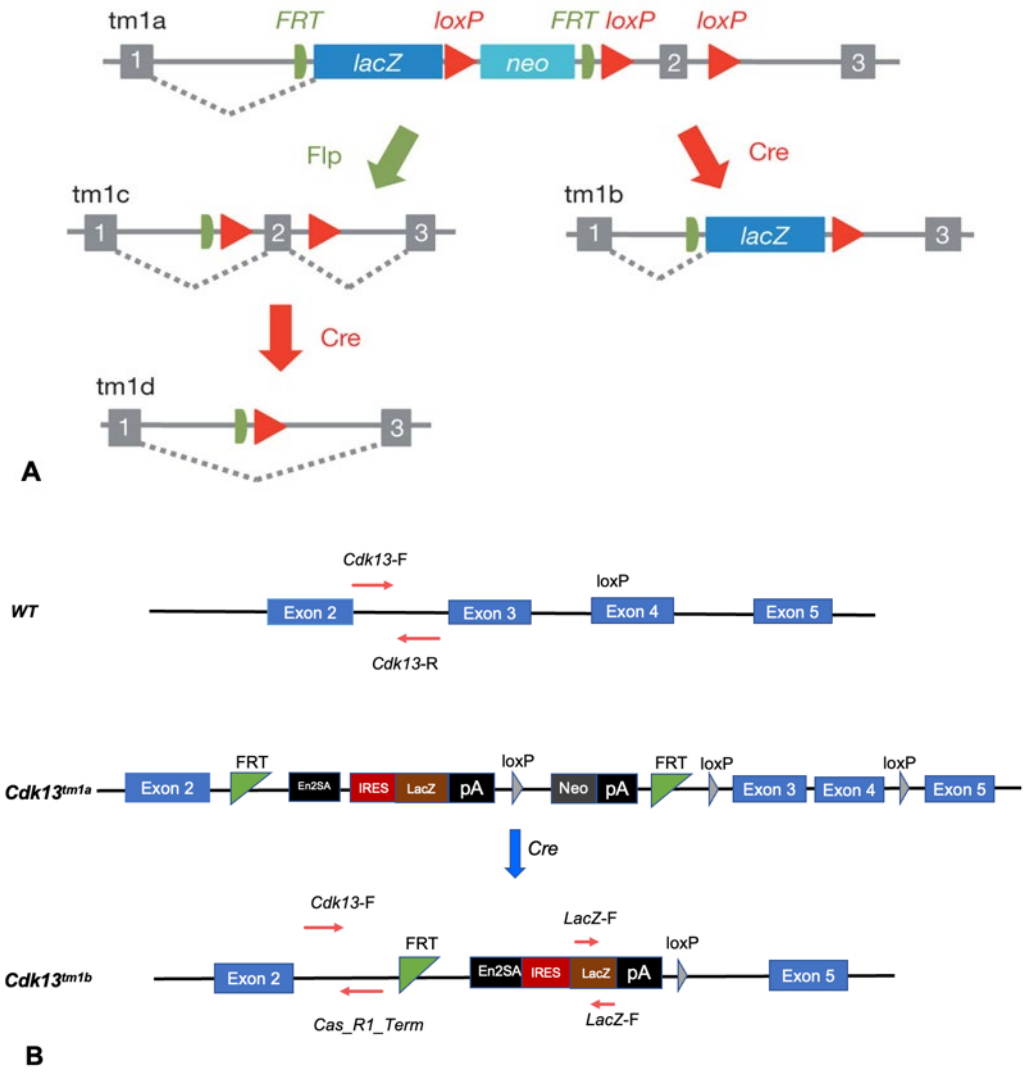


Figure 2:1 Generation of tm1b allele from tm1a allele and Cdk13^{tm1b} mouse model. A: There is Cre-mediated replacement of critical exons with LacZ. The critical exons along with the two flanking loxP sites, FRT and neomycin cassette in tm1a allele are excised by Cre-recombinase to give rise to tm1b allele. Tm1d allele is a frame shift mutation produced if Cre recombinase excise the floxed exon of tm1c allele. B: In case of Cdk13 ^{tm1b}, critical exons excised are 3 and 4 and the allele contains LacZ cassette inserted into the intron 2. WT mouse showing location of the genotyping primers in intron 2 whereas Cdk13^{tm1b} mouse shows location of primers used for detection of mutant allele located in the intron 2, but the WT sequence finishes before the Cas_R1_Term primer (mutant reverse primer). Primers for detection of LacZ cassette in mutant allele are also shown. Image A is adapted from [188]. FRT: flippase recognition target; Tm: target mutation; EUCOMM: European Conditional Mouse Mutagenesis Program; IRES:lacZ trapping cassette: internal ribosome entry site upstream of lacZ; En2SA, Engrailed 2 gene splice acceptor; loxP (locus of crossover (x) in bacteriophage P1); pA: polyA tail.

2.1.2 *Prkd1*$^{em1(IMPC)Wtsi}$:

This LOF allele was generated at the Wellcome Trust Sanger Institute (Cambridge, UK), employing CRISPR/Cas9 genome editing technology to delete exon 2 of this gene. Exon 2 encodes part of the CRD region of PRKD1 protein. Three primers were used for genotyping this mouse (Figure 2:2 and Table 2:2). Two PCR reactions were carried out to genotype this mouse. DF1 and ER1 primer pair gave band (of 233bp) only if the allele was WT whereas, to detect the mutant allele, DF1 and DR1 in combination gave a band of 397bp. Occasionally, an additional band of 1360bp was also detected in the mutant lane in case of HET mutation (due to the presence of one WT allele in there).



Figure 2:2 Prkd1^{em1} mouse model and location of primers used for genotyping. DF1 and ER1 were used to detect WT allele whereas DF1 and DR1 detected mutant allele. DR1 was in intron 1 whereas DF1 and ER1 were located in intron 2 of Prkd1 (GRCm39).

2.1.3 *Prkd1*$^{em2(IMPC)Wtsi}$:

It is the humanized mutation (HM) allele generated at the Wellcome Trust Sanger Institute (Cambridge, UK). This specific CHD-causing HM was chosen based on the phenotypes of the affected population previously reported [176]. The mouse had base change mutation in chromosome 12 (at 50385167 G/A-1) giving missense mutation. *PRKD1* gene in both

human and mouse has 19 exons and this mutation lies in exon 13 in both (Figure 2:3). The mutation translates into a protein with G598R substitution which is equivalent to human G592R substitution as reported in two patients with ASD and pulmonary valve abnormality in the study which formed basis for this work [176]. The screening primers used for the genotyping of this mouse are shown in Figure 2:3 and Table 2:2.



263734	ttcaaaatattataggaatgtaatttgaatattatagccattgaaattttatccgacatttagaagtgttaaatgagctttggaatgtttaattatatttctgttcaatcagctaatagc	263853
263854	aattataattataaaatgtaataggattaaagcttgtctcccctcccctttctttgtctttctctgggtatgcacctgtag	263933
263934	GATATCAGCACAGTCTATCAAATATTTCCTGATGAAGTTCTGGGTTCCGGACAGTTTGGAATTGTTTATGGAG	264006
264007	gtgagtaggttcaatgtgggttttttctatgaacttaaaaatgtaagcacttatgtgtaaaagtattatagtaccaagacaaatataaataaaaaaaggatatgaatctgtgtgtctcgg	264126
264127	agtcaccttcagagaagcttcctctgagatagccattcttttaaagatctagttatttcatgtatatgccttcaggcacaccagaagaggggcatgggattccattacagatggttgtga	264246

Figure 2:3 Location of the screening primers used for genotyping of Prkd1^{em2} mouse. Exon 13 is shown in capital letters whereas introns 12 and 13 are shown in lower case letters. Forward and reverse primers are highlighted in green and pink, located in the introns 12-13 and 13-14. The site of base mutation is highlighted in red. i.e., "G" is changed to "A" in the mutant mouse model translating into G598R. The part of Prkd1 sequence shown is from Ensembl (GRCm39).

2.2 Maintenance of mice colonies and welfare

The mutant mouse lines received from the respective suppliers were bred and maintained in the BioSupport Unit (BSU) at the University of Nottingham, UK in accordance with the regulations and guidelines of the Home Office, UK as well as the research ethics pertaining to animals use in research, ensuring best practices. The breeding of these mice and the

experimental procedures related to the project were as per the regulations of the Animal Scientific Procedures Act (ASPA) 1986, under the project license number P375A76FE (Nottingham) issued by the Home Office, UK on August 22, 2018.

Wild type mice (C57BL/6N) were obtained from Charles River, UK and Europe. Heterozygous mice for each line were backcrossed with the wild type mice for colony maintenance. Three WT X HET breeding pairs were set up to maintain the colony of each strain. For experiments i.e., for timed pregnancies, mating (mostly two females with a single male in a same cage) were set up in the late afternoon and mice checked next morning for vaginal plug by personnel of the BSU and communicated to us. The presence of vaginal plug would make this stage of embryos designated as E0.5. To obtain HOMO embryos for transcriptomic, proteomic as well phenotypic analyses, HET X HET timed-matings were set up.

2.3 Harvesting whole mouse embryos and embryonic tissue collection

Embryos for HREM analysis were collected at E15.5 as the outflow tract and the ventricular chambers have normally completed septation to form a four chambered structure with correctly aligned outflow vessels[189], so most of the common CHDs could be detected. For transcriptomics and expression studies, mouse age E12.5 was selected being within the potential survival window (E11.5 - E15.5) and being the age when important heart structural features are in the early process of development [32, 179]. Also this age was expected to give us enough tissue for our analyses coupled with ease of collection.

For HREM analysis, the number of mouse embryos collected were: *Cdk13*^{tm1b} (n = 51), *Prkd1*^{em1} (n = 61) and *Prkd1*^{em2} (n = 79) in addition to n = 74 WT of C57BL/6N background. After culling the female mouse humanely by cervical dislocation, the whole mouse body was douched with 70% ethanol and thereafter placed on a dissection bench lying on its back. The abdomen was opened with the help of a pair of surgical scissors and forceps, giving a U-shaped incision, and extending superiorly until the thorax and then cutting through the lateral wall of the rib cage. The two horns of uterus containing embryos (which appeared like beads), were resected and placed in a petri dish containing Phosphate Buffered Saline (PBS) at 37°C. Surgical pair of scissors was used to cut through the wall of the uterus and segregating each embryo in a separate PBS-containing petri dish. Each embryo was then gently harvested under the dissecting microscope (Carl Zeiss Stemi SV11 and Zeiss Discovery V8), cutting through the umbilical cord, carefully removing placenta and other extraembryonic membranes. At this point, any abnormality in the gross phenotype was noted, and imaged where possible. Thereafter, the embryos were decapitated prior to dissection (as a requirement of ASPA, 1986). The thoracic cavity was opened in order to harvest the heart, using a pair of surgical scissors to cut through its lateral parts on both sides, gently reflecting the anterior thoracic wall and then resecting it to expose the thoracic cavity. Forceps were then gently applied underneath the heart in order to reflect it forward and then passed further up as far away from the outflow tract (OFT) as possible. While preserving the OFT, heart would be released and removed from the thoracic cavity by cutting

through the neck region. The heart would then be cleaned of any extra tissue like lungs, trachea, thymus etc using a very delicate pair of forceps. The embryo carcass (mostly limb) was collected for genotyping.

For HREM, embryos collected would be immediately transferred to a prelabelled 50ml Falcon™ tube containing warm PBS (37ºC) which would then be shaken well (up and down or rolling movements), but gently, in hands for 15 min by a second person/helper. To make the process more independent, a shaking system was designed consisting of a plastic container, ¾ filled with warm water (37ºC) and glued to an electric shaker. The falcon tubes were then placed in a tube-rack within this waterfilled plastic container on the shaker. The gentle shaking like this was intended to get rid of as much blood as possible while the hearts would still be beating, in order to get cleaner hearts for HREM. Thereafter, these hearts were fixed in 4% (w/v) paraformaldehyde (PFA) (pH 6.8-7.4) and left for 25 min before subjecting them to further repeated (4x15min) washings in distilled water on the dancing roller bars in order to clean its chambers of any blood. The distilled water-washings would be carried out for maximum of 1 hour and were preferably stopped even earlier if the blood lysed sooner and heart seemed reasonably clean/white. After these washes, the heart samples were again fixed in 4% PFA and stored at 4ºC overnight or until further processing. For collecting hearts from neonates for HREM, all the steps mentioned so far were the same right from decapitation until final fixation in 4% PFA. However, the tissues including rib cage in neonates were much harder/denser.

The embryos and the hearts intended for RNA and protein extraction from *Cdk13*^{tm1b} (n = 189), *Prkd1*^{em1} (n = 129) and *Prkd1*^{em2} (n = 48) mouse lines, after collection from the uterine horns and prior to and even during dissection, were placed in cold (4 ºC) DEPC-PBS (prepared prior by adding 1 mL of DEPC,(diethyl pyrocarbonate) per 1L of PBS, and then autoclaved). After dissection, and imaging where needed and possible, hearts would be collected and immediately put in a pre-labelled 1.5ml Eppendorf tube, snap frozen in liquid nitrogen and then stored at -80°C for subsequent expression analyses. Adult mouse tissues for various experiments in this thesis were collected opportunistically from spare adult mice (both male and female) no more required for breeding/colony maintenance.

All the steps for HREM starting from culling until fixation in 4% PFA had to be performed very swiftly to avoid blood clotting in the heart. Nevertheless, the hearts for expression studies equally required expeditious collection and snap freezing.

2.4 Extraction of DNA for genotyping

Mice genotyping was carried out using ear notches (collected by one of the personnel at the BSU) for adults and pups, and embryonic carcass for embryos. These would be put in 1.5ml Eppendorf tube. 500µl lysis buffer (100Mm Tris-HCl Ph 8.8, 5Mm EDTA pH 8.0, 0.2% SDS, 200Mm NaCl) and 25µl of 10mg/ml proteinase K (Cat. No. 183988 MP-Bio, UK) were added to the Eppendorf tube containing the sample and placed in a water bath at 55ºC overnight (12-24 hours). The next day, the samples were quickly vortexed followed by spinning down at 10000 rpm for 10

min. The supernatant (~500µl) was collected in a clean 1.5ml Eppendorf tube. In order to precipitate DNA, an equal amount (500µl) of 100% Isopropanol (4ºC) was added to this supernatant and the tube contents thoroughly mixed by repeated inversion followed by centrifuging for 30 min at 13000 rpm at 4ºC. The supernatant was discarded whereas the leftover DNA pellet at the bottom of the tube was washed with 500µl of 70% ethanol (4ºC) and centrifuged again at 13000 rpm for 15 min at 4ºC. The supernatant was discarded, and the genomic DNA sample was left to dry at room temperature for ~30 minutes. Once dried, 30µl standard distilled water was added to it, followed by measuring its concentration by NanoDrop™ 1000 Spectrophotometer (Thermo Fisher Scientific®) and thereby diluting the DNA sample to 100ng/µl working solution, to use for genotyping.

Genotyping of the mouse embryos, pups and adult mice was carried out by end point PCR using genomic DNA obtained from embryo carcass, tail notches and ear notches respectively.

2.5 Polymerase Chain Reaction (PCR) for Genotyping

The working solution of extracted genomic DNA from the mouse samples are subjected to genotyping by PCR amplification of the target allele as per the protocol provided by Wellcome Trust Sanger Institute (Cambridge, UK) using Promega® Mastermix (Cat. No. M7505, Promega Corporation, USA), a premixed 2X solution of Taq DNA Polymerase, dNTPs and Reaction Buffer. The ingredients of the PCR reaction cocktail and their respective volumes for each reaction (25 µl) are mentioned in the

Table 2:1 whereas the sequences of the different primers used for the different mouse lines are shown in Table 2:2.

S.No.	Ingredients	Volume
1.	Sterile deionized water	11.5µl
2.	Forward primer (10µM)	1µl
3.	Reverse primer (10µM)	1µl
4.	Promega® master mix	10.5µl
5.	Genomic DNA (50ng/µl)	1µl
	Total	25µl

Table 2:1 PCR reaction cocktail for genotyping. Volumes of the different ingredients of the reaction cocktail for a single PCR reaction to amplify the target allele for genotyping.

Cdk13^{tm1b}			
Assay	**Primer ID**	**Primer Sequence (5' to 3')**	**Size (bp)**
Wildtype	*Cdk13_84881_F*	GCTCTAAGGGCAACCTTGAA	250
	Cdk13_84881_R	AGCTGGGAAGATGGTGTTGT	
Mutant	*Cdk13_84881_F*	GCTCTAAGGGCAACCTTGAA	200
	CAS_R1_Term	TCGTGGTATCGTTATGCGCC	
Cassette	*LacZ_2_small_F*	ATCACGACGCGCTGTATC	108
	LacZ_2_small_R	ACATCGGGCAAATAATATCG	
Prkd1^{em1}			
Assay	**Primer ID**	**Primer Sequence (5' to 3')**	**Size (bp)**
Wild type	*Prkd1_DF1*	GGCATGGCTGGACCTAATCT	223
	Prkd1_ER1	CACCCATGCCCTCAAGTATC	
Mutant	*Prkd1_DF1*	GGCATGGCTGGACCTAATCT	397
	Prkd1_DR1	GCTTGACACTGGAAATGGAA	
Prkd1^{em2}			
Assay	**Primer ID**	**Primer Sequence (5' to 3')**	**Size (bp)**
Screening*	*Prkd1_Gly592_F*	GACTCCGAGACACACAGATTCA	362
	Prkd1_Gly592_R	GCCATTGAAATTTTATCCGACA	

Table 2:2 Mouse genotyping primers. Primers used for genotyping by PCR followed by gel electrophoresis are shown in the tabulated form. The expected size bands are also shown. These primers' sequences were provided by the mouse line supplier and the primers were supplied by Sigma Aldrich®. The postfix "F" where shown denotes the respective forward, whereas "R" denotes the reverse primers. The postfix "Term" denotes reverse primer for mutant Cdk13 allele (Cdk13^{tm1b}). In Prkd1^{em1} mouse, the DF1, ER1 represent forward and reverse primers respectively for WT allele whereas the primer with DR1 is a reverse primer for mutant allele of Prkd1 (with deletion). In case of Prkd1^{em2}(HM), mice were

sequence-verified with the screening primers in order to confirm genotyping.

The final reaction volume of 25 µl was added in 0.2 ml thin-walled PCR tubes. The DNA was amplified using the T100™ Thermal Cycler (BIO-RAD), according to the protocol in Table 2:3. The PCR was run for 34 cycles.

Step	Conditions	Time	
Initial denaturation	94°C	5 min	
Denaturation	94°C	30 sec	32 cycles
Annealing	58°C	30 sec	
Extension	72°C	45 sec	
Final extension	72°C	5 min	
Hold	12°C	Continuous	

Table 2:3 Amplification conditions for Cdk13^{tm1b}, Prkd1^{em1}, Prkd1^{em2} for genotyping.

2.6 Agarose gel electrophoresis

1% agarose gels were prepared by mixing agarose powder (Cat. No. A9539, Sigma-Aldrich, USA) in 1xTAE buffer solution (comprising 40 mM Tris, 20 mM acetic acid, and 1 mM EDTA) in a glass flask, followed by heating to boil in a microwave oven. After cooling it down to a temperature acceptable to hand-touch, 10µl of 10mg/mL ethidium bromide solution (Cat. No. E1510, Sigma-Aldrich, USA), meant to visualise DNA during electrophoresis, was added to the glass flask containing agarose gel and thereby mixed thoroughly. Thereafter, the mixture was poured into a gel cassette and left to solidify for 20 minutes at room temperature. Thereafter, all the DNA samples were added with gel loading dye, Purple (6X) (Cat. No. B7021S, New England Biolabs, USA), which was premixed loading buffer comprising of a mix of red and blue dyes, SDS and Ficoll®,

meant to make the DNA dense and make its bands in gel colourful, brighter and sharper (specially attributed to Ficoll and SDS). It also contained EDTA used to chelate magnesium ions to stop the reaction. A 100bp DNA Ladder (Cat. No. 15628019 Invitrogen®) was added in one of the wells. The gels would be run at 95 V for 45 minutes which would be then imaged on Gel Doc system (Bio-Rad®, USA) using imaging software *GeneSnap* from SynGene® to determine the genotype.

2.7 Polymerase Chain Reaction (PCR) for genetic sex determination in mouse

The male specific region on Y chromosome in mouse has some additional X chromosome genes with acquired & amplified gametologs on Y chromosome [190]. Two-copy *Rbm31y* (Y-linked) and the single copy *Rbm31x* (X-linked) are two of these unique Y chromosome gametologs which have great sequence homology. However, there is an 84bp deletion in *Rbm31x* versus *Rbm31y [191].* Sex of the mouse embryos', with CHD and gDNA available (*Cdk13*^{tm1b}, n = 9; *Prkd1*^{em1}, n = 3 and *Prkd1*^{em2}, n = 17), was determined by amplifying *Rbm31x/y* gene. The embryos' gDNA (already extracted as in section 2.4) was utilised for genetic sex determination using the PCR ingredients as used for genotyping (Table 2:1) but with primers as previously published for genetic sex determination (given in Table 2:4) [191]. The primers flanked the deleted 84bp deletion. The thermocycler conditions used were the same as in Table 2:3, followed by gel electrophoresis (as mentioned in section 2.6) and shown in Figure 2:4.

Primer		Primer Sequence (5' to 3')
Forward		CACCTTAAGAACAAGCCAATACA
Reverse		GGCTTGTCCTGAAAACATTTGG
Size	*From Rbm31x*	269bp
	From Rbm31y	353bp

Table 2:4 Mouse primers for genetic sex determination. These primers were taken from published literature [191] to determine the genetic sex of mouse embryos by simplex PCR followed by gel electrophoresis. The expected size bands are shown. The primers were supplied by Sigma Aldrich®.

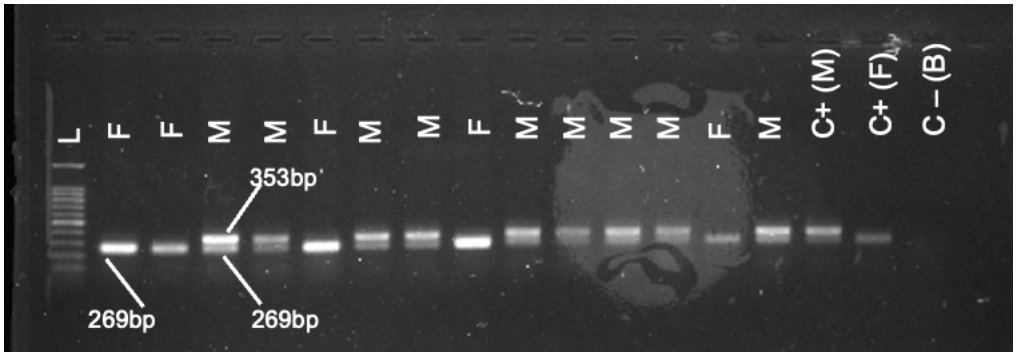


Figure 2:4 Determining genetic sex of mouse embryos. Agarose gel picture showing results for determining genetic sex of mouse embryos. A known male and female samples were used as positive controls and water-only sample as a negative control, with ladder (L) at the left end of the gel. Expected bands and their sizes were: 269 and 353bp in male, and only 269bp in female. Ladder: 100bp (Invitrogen®).

2.8 PCR clean up and Sanger sequencing

PCR clean-up was carried out using GenElute™ PCR Clean-Up Kit (Cat. No. NA1020, Sigma-Aldrich) following supplier's protocol, prior to sending for Sanger sequencing which was mainly performed by Source Biosciences (www.sourcebioscience.com) and Eurofins Genomics UK Limited (www.eurofinsgenomics.com) for *Prkd1*^{em2} genotyping. However, for small number of samples for some other experiments, Sanger sequencing was also performed by Mr Matthew Carlile at the DeepSeq facility of the University of Nottingham (https://www.nottingham.ac.uk/deepseq/index.aspx). For this purpose, 5μl of the purified PCR products would be

sent at a concentration of 100ng//μl, along with 5μl primers at a concentration of 3.2pmol/μl. The results of the sequencing would be received in *.ab1* format which would then be analysed by the *Chromas* software (https://technelysium.com.au/wp/chromas/).

2.9 Protein extraction from mouse tissues

Tissues stored at -80°C were collected from the freezer and thawed (keeping the sample on ice) to get a small piece of it and weighed out in an Eppendorf. For extracting protein from embryonic mouse heart (n = 3 each of WT, HET and HOMO from *Prkd1*^{em1} and *Prkd1*^{em2}) and from adult *Cdk13*^{tm1b} mouse brain, muscle and heart tissue (n = 3 WT & 3 HET), cold extraction buffer (Tris. HCl buffer-Ph-7.6 containing 8M urea), roughly 1 ml /200mg tissue and 1X protease inhibitor (cell signalling technology, Cat. No. 5872) were added to the sample in the tube. The solution was homogenized with a tissue homogenizer for 20 secs and then centrifuged at 12,000g for 20 minutes at 4ºC to collect a clear supernatant. The clear supernatant was removed, aliquoted into a clean Eppendorf tube and stored at -80°C until further use. 15-20µl was also set aside for protein estimation by quick start Bradford method (Biorad® Quick Start™ Bradford 1x Dye Reagent, Cat. No. 5000205).

2.10 Western blot

20µg of tissue extract was mixed with 1X LDS sample buffer (NuPAGE™, Cat. No.NP0007) and 1X reducing agent (NuPAGE™, Cat. No. NP0004). The solution was heated at 95°C for 5 minutes before loading onto the NuPAGE™ 10%, Bis-Tris Protein Gel (Cat. No. NP0301BOX, Invitrogen™). Proteins were fractionated using 1X NuPAGE MOPS SDS

Running Buffer (Cat. No. NP0001, Invitrogen™) at 200V for 55 minutes. Precision Plus dual-stain protein standard (Cat No. 1610376, Biorad®) was loaded to a well on one end of the gel. Proteins were then transferred from gel to a Polyvinylidene fluoride (PVDF) membrane (Cat.No. LC2002, Invitrogen™) at 25V for 90 minutes. For this purpose, 1X Tris-Glycine transfer buffer (Cat. No.LC3675, Invitrogen™) and Blot Module (XCell II™ Cat.No. EI9051, Invitrogen™) were used. The membrane was then processed for immunodetection of the proteins. The primary antibodies used were rabbit monoclonal anti-PKCmu/PKD1 (Cat. No. ab51246, Abcam®) for PRKD1, rabbit anti-CDK13 polyclonal antibody (Cat. No. 67681, Invitrogen®) for CDK13, and rabbit anti-GAPDH polyclonal antibody (Cat. No. ab9485, Abcam®) for GAPDH. Anti-PKCmu/PKD1 and anti-CDK13 antibodies were used at 1:1000 dilution whereas anti-GAPDH was used at 1:2500 dilution. Goat anti-rabbit horse-radish peroxidase (HRP) (Cat. No. ab6721, Abcam®) was used as a secondary antibody in 1:2000 dilution. All the dilutions for these antibodies were prepared in freshly prepared 5% BSA-TBST solution. For protein detection, *Clarity Western ECL Substrate* (Cat #1705061, Biorad®) was used whereas the chemiluminescent images were captured digitally on a *LAS-3000* Imager (Fujifilm®).

2.11 High Resolution Episcopic Microscopy (HREM)

In order to embed and subsequently section mouse hearts, the samples needed to be dehydrated and then infiltrated with JB-4 resin dye-mix followed by embedding and then sectioning.

1.1.1.1 Preparation of JB-4 dye mix

JB-4 is a water-soluble glycerol methacrylate-based embedding medium for high resolution microscopy. In order to prepare JB-4 dye mix, A JB-4 kit (Sigma Aldrich EM0100-1KT), containing JB-4 solution A (J4954) – monomer and Benzoyl peroxide (J0455) - acting as a catalyst, was used (Solution B in the kit was used at a later step, as mentioned under "embedding"). Other ingredients of the JB-4 dye mix, which were ordered separately than the kit, were Eosin B (Cat. No. 861006, Sigma Aldrich) and Acridine orange (Cat. No. 318337, Sigma Aldrich). The exact volumes of each ingredient needed to prepare the required volume of total JB-4dye mix are very important for optimal results and are shown in the Table 2:5.

Total volume of dye mix	100ml	200ml	300ml
Solution A (ml)	100	200	300
Benzoyl peroxide (g)	1.25	2.50	3.75
Eosin B (g)	0.275	0.550	0.825
Acridine orange (g)	0.056	0.113	0.169

Table 2:5: Amount of the ingredients in the JB-4 dye mix. The ingredients of the JB-4 dye mix need to be in the right amount to produce optimal results in terms of proper infiltration, embedding and sectioning of samples as well as production of high-resolution images.

All the instruments and equipment (weighing scale, stirrer, and glassware etc.) needed for preparing the JB4-dye mix were prior shifted to the fume hood. After measuring out the Solution-A, it was transferred to a glass bottle containing mixer stir bar and placed on a magnetic stirrer. The required amount of Benzoyl peroxide was added very slowly to the solution-A so as to avoid clumps formation. This was followed by slow addition of accurately measured amounts of Eosin B and Acridine orange dyes to

the solution and the whole solution was left on the stirrer overnight inside the fume hood at room temperature. The next morning, the JB4-dye mix was filtered through Polyether sulfone (PES) membrane (Cat. No. 431153, Corning, USA) with the pore size of 0.22 µm in order to remove any undissolved ingredients of the mix. Once the whole solution was filtered through, the JB4-dye mix was stored at 4ºC after labelling it along with the date, for its use over the next 3 weeks.

1.1.1.2 Dehydration of heart samples

To embed the heart samples in JB4 require prior dehydration of these through a graded series of methanol (MeOH). In order to do this, the samples fixed in 4% PFA overnight were transferred to 24 well plates (Cat. No. 353935, Corning Falcon, USA), with wells labelled on the lid of the plate. A photo of the lid was taken for record in case the labels disappear later during washes. All samples in the wells were then washed in PBS (4x30min) at room temperature over the belly dancer. Thereafter, the samples were washed in a graded series of MeOH/PBS solutions in ascending order (10%, 20%, 30%, 40%, 50%, 60%, 70%, 80%, 90%, 95% and 100% MeOH), 45min each, at room temperature while on the belly dancer. During all the MeOH washes, the multi-well plate was wrapped in a cling film (to avoid drying up of sample). During and in between all the washes, it was ensured that the samples stay immersed in the solution.

2.11.1.1 Infiltration of samples with JB-4 dye mix

The MeOH washing was followed by infiltration of the samples with JB-4 dye mix. To do this, the samples, while still in the multi-well plates, were

incubated in a solution of MeOH and JB-4 dye mix in 50:50 ratio and left overnight at 4ºC. The next day, the MeOH and JB-4 dye mix in (50:50) in the wells was replaced with 100% JB-4 dye mix and the heart samples were left to incubate overnight in it at 4ºC, to allow removal/replacement of all alcohols and infiltration of JB-4 dye mix before embedding (Figure 2:5). The neonatal hearts were left for 2 nights in pure JB4-4 dye mix to allow for much thicker/firmer heart walls in neonates. However, despite this, the luminal half of the heart walls still seemed to have less dye penetration during analysis.

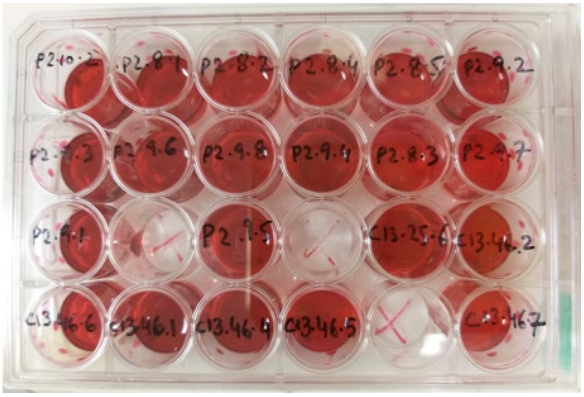


Figure 2:5 JB4 infiltration. After lying in the MeOH and JB-4 dye mix in 50:50 ratio for a night, hearts were left overnight (longer in case of neonates) to infiltrate with pure JB4. The image shown is of the plate at the end of pure JB4 infiltration of hearts when they were embedded using JB4 embedding medium. The labels for each heart specimen (in respective well) can be seen on the corresponding site on the plate-lid. These labels need refreshing during all dehydration steps since MeOH can get away with these.

1.1.1.3 Embedding of samples using JB-4 embedding medium

After infiltration with JB-4 dye mix overnight (longer in case of neonates), samples were embedded in JB-4 plastic resin. To achieve this, embedding solution was prepared. 0.6 ml of Solution B - accelerator (Cat. No. J0330, Sigma-Aldrich, USA) (stored at room temperature) was added to 10ml of JB-4 dye mix (stored at 4ºC) and mixed thoroughly but trying to

avoid bubble formation which could interfere with the embedding process later. At any one time, one well in a plastic mould (Electron microscopy Sciences, USA) was filled with the freshly prepared polymerising mixture and heart (immersed until now in 100% JB-4 dye mix) was picked from the multi-well plate with a plastic dropper and dropped gently into the well of the plastic mould. Three E15.5 hearts per well of the plastic mould were embedded, by carefully noting the IDs of each sample. After sinking into the well, the respective hearts were positioned on the respective hand side, using blunt-ended glass capillaries while observing under the stereomicroscope. The heart apex would face up whereas the OFT would be sitting on the bottom of the well. This manipulation needed to be done very quickly before the polymerization of JB-4 started. After each heart was positioned as required, a pre-labelled plastic chuck (Indigo Scientific, UK) was placed on the top of the well. The chuck would also have RHS marked on it on the side where there would be a single heart. The IDs as well as positions of the individual hearts in each block were also noted in the embedding register. After placing the plastic chuck, polymerising mixture would be topped up into its compartments so that it is properly bound to the tissue-containing resin in the well underneath. The resin was left to set at room temperature for an hour followed by instilling few drops of mineral oil into the different compartments of the chuck to prevent air interfering with the polymerisation process. Thereafter, the mould containing resin-embedded hearts was placed in the fume hood over night at room temperature to allow polymerisation to complete, resulting in a hard block to have formed (Figure 2:6).

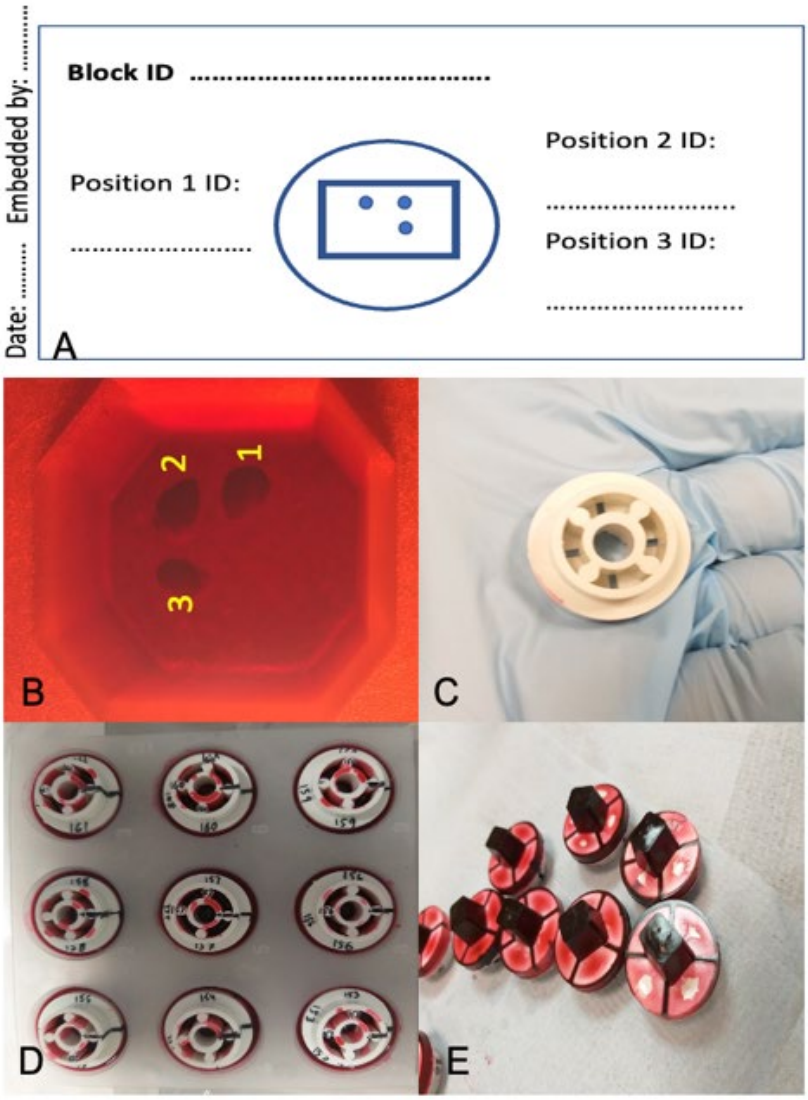


Figure 2:6 JB-4 embedding. Under stereomicroscopic observation, three hearts are placed in JB4 embedding medium prepared afresh (B), as per the predetermined site allocation shown in (A) and the plastic chuck (C) is placed on top of it. This chuck needs to be prelabelled with block ID (as well as LHS-marked) before its placement (D). The mark on the chuck is on the left-hand side, corresponding to the image in (A). The JB-4 block is hardened after the overnight polymerisation of JB4 in the fume hood. This is removed from the mould through application of reasonable pull straight up with a plier without twisting. As shown in the figure (E), the base of the polymerised block faces up and the chuck faces down. Each of the block contains three E15.5 and one P6/P7 mouse heart and they lie near the base of the block. The polymerised JB4 blocks need to be baked overnight before they can be sectioned.

1.1.1.4 Preparing the JB-4 Blocks for sectioning

The next day, JB-4 blocks were removed from the plastic mould using an adjustable wrench to pull them off straight avoiding any twisting

movement. The extra JB-4 material around the circumference of the chuck was removed using a blunt knife. Thereafter, the resin blocks were placed in the oven to bake at 95ºC overnight Figure 2:7). The next morning, the blocks were placed in fridge (4ºC) to cool down for few hours as required to make them hard enough for sectioning afterwards.



Figure 2:7 Baking of JB4 blocks prior to sectioning. JB4 blocks, after pulling out from the plastic moulds, are baked in the oven at 95ºC overnight, followed by leaving at 4ºC for few hours. At the end of this, the blocks are hard enough to section for HREM.

1.1.1.5 Sectioning and imaging on High resolution episcopic microscope (HREM)

The baked JB-4 block containing heart samples was mounted on the stage of HREM apparatus (Indigo Scientific, UK) comprising of motorised microtome with a tungsten carbide blade (Leica, Germany), stereomicroscope and camera (Jenoptik ProGres Gryphax, Germany), a fluorescence optical system, all connected to Optical-HREM software which controls the operation of this machine including focus, sectioning as well storage of sequential imaging data as z-stack on the connected computer's hard drive. The JB-4 plastic resin block after removing from the 4°C is hard enough to allow serial sections of as small as 2µ thickness

on HREM working at room temperature. The block was examined in bright light and under a stereomicroscope (Nikon, Japan) to locate the hearts and to measure their cutting/location depth inside the block (Figure 2:8).

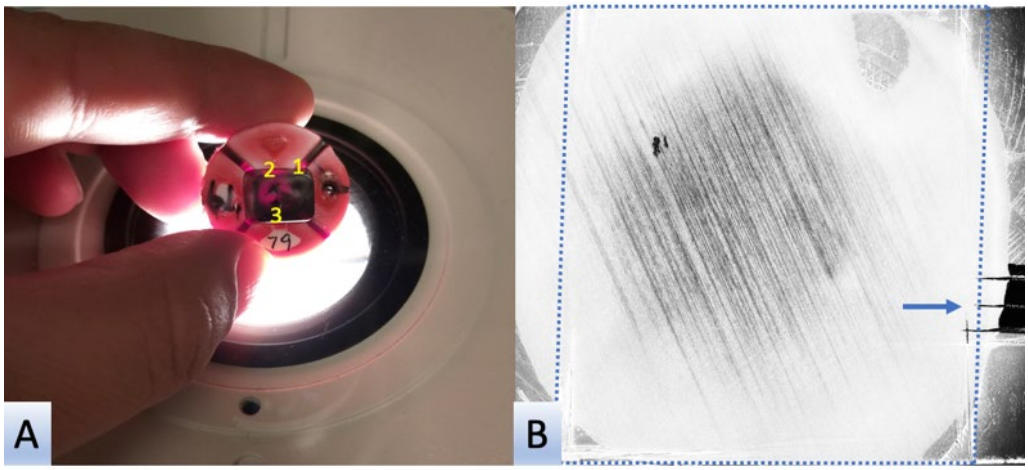


Figure 2:8 Locating and identifying the hearts in the JB4 block. (A) It is very important to locate the three hearts within the block which is done easily in bright light as shown in the figure, using microscope light. (B): Thereafter, bounding box (blue dotted lines) and scratch mark on the left-hand side (as a reference for heart position), denoted by blue arrow, are made on the block surface (base) under the microscope. This scratch mark is at the same location as the mark made on the chuck while embedding. Moreover, the depth of the hearts within the block is determined. The depth of the deepest heart will determine the total depth of the block to section. The photo of the bounding box and scratch mark on the block surface in (B) is from the HREM camera taken of one of the earliest sections.

Then using a bright light (of cell phone torch) shone from the base of the chuck, a bounding box encompassing all the hearts in the block was made on the block surface, using a blade. A scratch mark was also made on the block surface to identify the left-hand side of the block as that was necessary to identify which heart is which. The block was then mounted on a fixed stage with the block-base facing up. The tungsten carbide blade (Leica, Germany) was fixed to a movable socket sitting above the block. Before starting auto-sectioning by the blade, relative gap between

the cutting edge of the blade and the block surface was reduced to the least possible by constant visual monitoring through a glass window provided on the side of the machine (Figure 2:9). While fixed in the stage, the upper most segment of the block base above the tissue level was get rid of by controlled sectioning through continuous monitoring. Once the level of the block with tissue reached, the scope would be zoomed in to the bounding box and the focus (mainly fine) knobs were used to fine focus on the bit of the tissue within it. Exposure was adjusted accordingly as well. First picture showing scratch mark was taken and saved as “orientation image” in a predetermined location/folder for the imaging data of that block. Onto the window of the Optical-HREM software, the desired cutting thickness (to 2µ for E15.5 and 3µ for P6/P7 neonatal hearts) and total depth to section (already determined on stereomicroscope, minus the thickness of the removed extra bit of block base) was entered. After entering the details of the destination folder, sectioning would be started. The camera would take sequential images of the block surface, one after every section to make a stack of perfectly aligned 2D images of high resolution and quality. The vacuum pump was supposed to remove the cut section from the block surface immediately after each section, to keep the block surface clear for imaging (Figure 2:9). There was an option to pause the process and adjust the focus as and when desired and resume from thereon. Once the block was completely sectioned, the sectioning process was stopped and a graticule image was taken, as needed later during the image processing/visualization to get the image stack into cubic size.

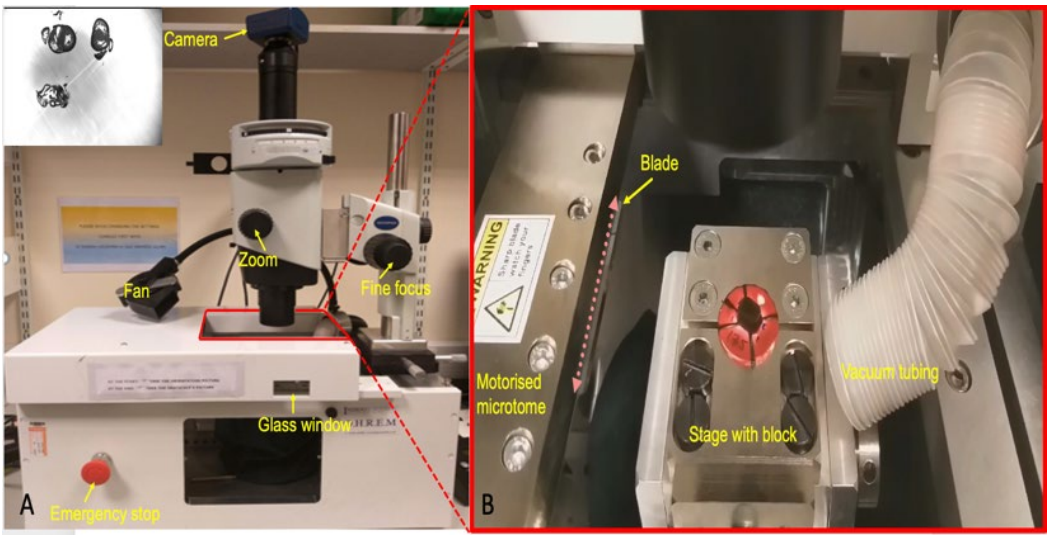


Figure 2:9 Key parts of HREM system and the sectioning process. A) HREM set up includes a high-resolution camera attached and knobs for adjusting zoom and fine focussing, as monitored on the computer screen (shown in inset). The glass window in the machine is used to follow the decreasing gap between the blade and the block surface during preparatory/pre-sectioning phase. B) Close up of the red marked area in A to show the parts directly involved in sectioning, the sectioning process and relation of the blade to the block. JB-4 block is tightly fixed in the HREM stage. The moving blade of the motorised microtome braces the block surface at a predetermined speed to section at a pre-set thickness. Camera captures high resolution image of the block surface after each section to produce a z-stack of 2D-images. The hose pipe overhanging it and connected to the vacuum pump sucks in the tissue section after each section, prior to the image taken by the camera. Fan can also be used to get the cut section off the way after each section, allowing the camera to capture a clear image.

1.1.1.6 Processing of HREM-images dataset and 3D Modelling

The z-stack of perfectly aligned 2D images from HREM was transferred to iMac for downsizing the data and further processing to make 3D models of the hearts. Downsizing was important for reducing the memory/space consumption as well as for handling by the imaging software since the suggested data size for 3D modelling by Osirix was 250MB. This involved the use of GraphicConverter® v 9 (Lemkesoft, Germany) to make QuickTime video and downsizing the dataset to 50%. An image (with three hearts) from almost the middle of the block would be

opened in Adobe Photoshop® CC 2019 (version 20.0). Using Guide-Liner® tool v1.26 (MK Software, Kirchlengern, Germany), the individual heart would be selected for cropping with the help of the superimposed and perfectly aligned QuickTime movie made in the earlier step. Thereafter, an action was designed in the Photoshop to crop out the individual heart from the trio. To carry out image adjustments on this heart data, more actions such as “level” and “curves” were designed in the Photoshop as well. All these actions were then applied to the trio-dataset and the output saved in a distinctly labelled separate folder for that heart. Thereafter, “invert” action was applied to this latest folder and the output was saved in a new folder labelled as “invert folder”. The size of this folder was checked to see how it differed from the target size of 250MB. In order to achieve the target size, it had to be sub-scaled by a factor as per the calculations developed by Prof Tim Mohun (retired from The Francis Crick Institute, London, UK in 2019). This scale factor was determined as: square root of “Size of your (inverted) data stack in Mb÷250 Mb” = e.g., 0.8. This would suggest scaling down the data to 80% which was done in ImageJ® v1.52. This would also take into account the graticule pixels to get the data cubic. The output data from this sub scaling in ImageJ® was saved as a new folder with the postfix of “80%” attached to the name. This sub scaled data folder was now ready for its import into another software - OsiriX™ 11.0 (Pixmeo SARL, Switzerland) or Horos™ to make 3D model of the heart. (Horos™ is a free version of OsiriX™ that is distributed under the LGPL license at Horosproject.org and sponsored by Nimble Co LLC d/b/a Purview in Annapolis, MD USA)

(https://horosproject.org). The data would be imported as DICOM (Digital Imaging and Communications in Medicine) files into these imaging software/progrmas. The various in-built tools in these allowed morphological analysis of the 3D heart model in various planes. The images of the defects were saved as JPEG (Joint Photographic Experts Group) or TIFF (Tag Image File Format) files as well, where possible. All main steps involved in HREM based analysis are summarised in Figure 2:10.

The volumetric analyses of the different chambers of the heart were carried out on HREM data after importing as DICOM files into 3D slicer, an open-source image visualisation and analysis software [192] (www.slicer.org). This involved segmentation of the part of the heart using “segment editor” module and thereby calculating its volume using “segmentation statistics” module.

The diameters were measured using measurement tool in OsiriX™ and Horos™, in the coronal plane, taking the largest diameter.

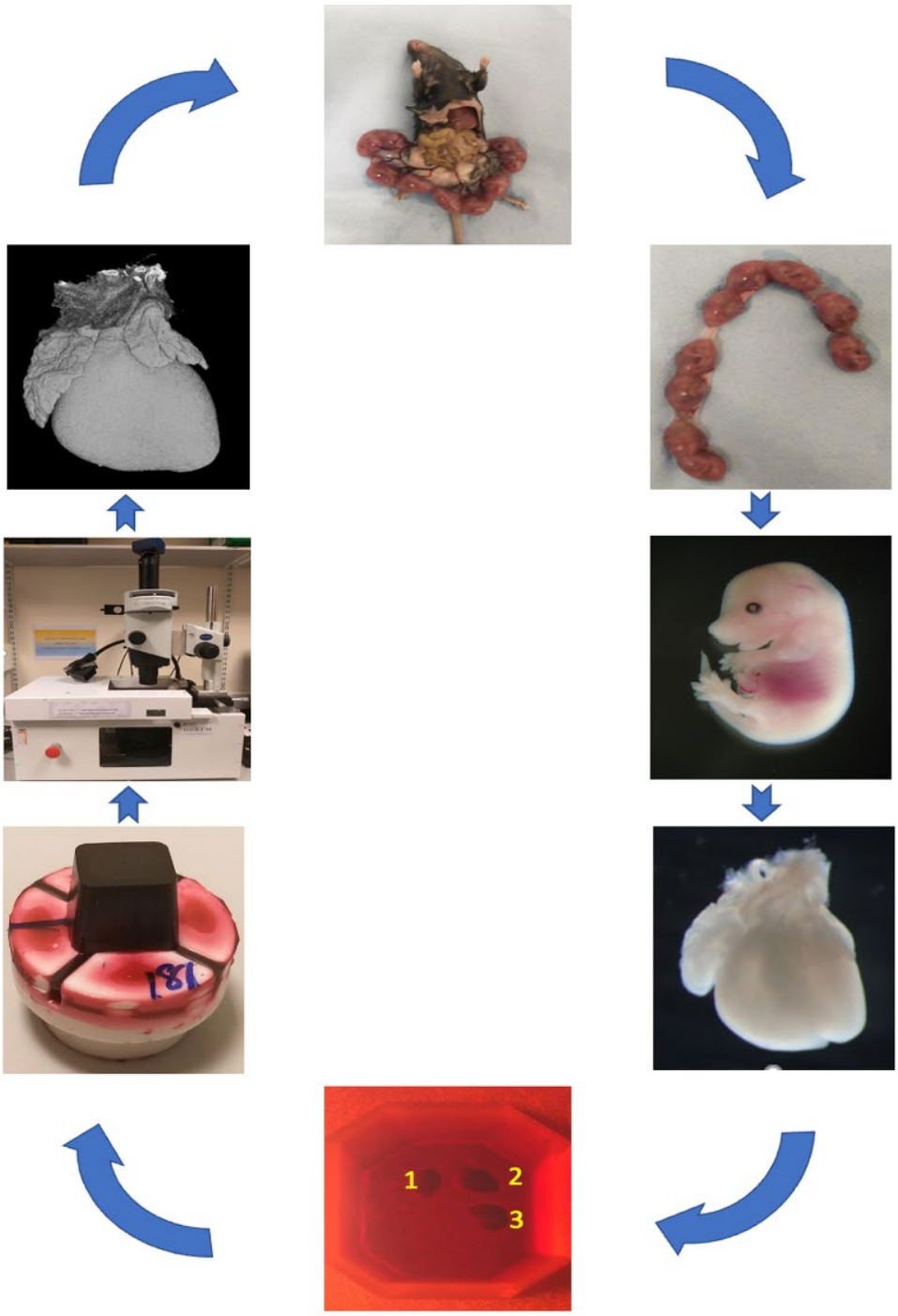


Figure 2:10 Summary of the main steps of HREM technique for morphologic analysis of mouse heart at E15.5. Pregnant dam after having culled by schedule 1 procedure undergoes laparotomy to excise it's both uterine horns containing embryos resembling beads. Embryos are retrieved from the uterus and their hearts are harvested one by one. Extra tissues surrounding the heart are cleaned by fine dissection, followed by PFA fixation. After series of dehydration and JB4 infiltration, the hearts (3 in each block) are embedded in JB4 embedding medium. The block after baking is sectioned on HREM machine. The z-stack images captured by its camera are processed further on different imaging software to provide 3D volume rendered heart which is then analysed in different planes.

2.12 RNA isolation from mouse hearts

2.12.1 RNA isolation from mouse embryos' hearts

RNA from mouse hearts (*Cdk13*^{tm1b}, n = 36; *Prkd1*^{em1}, n = 8 and *Prkd1*^{em2}, n = 6) was extracted using RNeasy® Micro Kit (Cat. no. 74004, Qiagen). RNA was extracted from each individual E12.5 mouse embryo hearts and not pooled up so as to avoid any possible masking of small alterations in individual hearts due to this.

RNA was extracted following mainly the supplier's protocol provided with the kit. 350µl of Buffer RLT, containing guanidine thiocyanate (inhibits RNases) (at room temperature) was added to 1.5ml Eppendorf tube containing the previously collected heart samples (stored at -80°C) and the electric homogenizer was used to disrupt the tissue to get a homogenous mixture. The tube was centrifuged for 3 min at a max. speed (17200 RCF). Then 1 volume (350µl) of 70% Ethanol (prepared in RNase free water) was added to the Eppendorf tube and mixed well by pipetting up and down. All the contents of the sample tube were then transferred to an RNeasy MinElute spin column in a 2 ml collection tube (4°C). After closing its lid, it was centrifuged at 10000 RCF at 4°C for 30 seconds and the flow-through obtained at the end was discarded. As a next step, 350µl of Buffer RW1 was added to the MinElute spin column, lid closed and centrifuged for 30 seconds at 10000 RCF at 4°C, discarding the flow-through at the end. Buffer RW1 contained guanidine salt (like the buffer RLT) and ethanol, acting as a strong washing buffer to remove carbohydrates, proteins, fatty acids etc. from the sample. At this time, DNase I incubation mix had to added which would ideally be prepared during the

waiting time between the pervious steps. DNase I incubation mix would be prepared for all the samples in a single eppendorph, such that for each sample, 70 µl RDD buffer was mixed with 10µl of DNase I stock solution by inverting the tube. Once mixed, the 80ul mix was added directly to each RNeasy MinElute spin column membrane. The tube lid was closed, and it was left on the benchtop for 15 min at room temperature. During this interval, the dry block heater would be turned on and an eppendorph with nuclease free water would be placed in it to heat it to 62°C for later use. After the 15 min post-DNase I incubation, 350µl Buffer RW1 was added to MinElute spin column and centrifuged at 10000 RCF for 30 sec at 4°C. At the end of this, the collection tube containing the flow-through was discarded. Buffer RW1 contained a guanidine salt and ethanol and was used as a stringent washing buffer to remove carbohydrates, proteins, fatty acids etc., that are non-specifically bound to the membrane. The MinElute spin column was then placed in another collection tube and 500µl RPE Buffer was added to the spin column. RPE is a mild washing buffer and was used to remove any left-over traces of salts on the column. After closing the lid, it was centrifuged at 10000 RCF for 30 sec at 4°C and the flow-through was discarded. As a next step, 500 µl of 80% ethanol (prepared in RNase free water, -20C) was added to the RNeasy MinElute spin column, and with lid closed was centrifuged at 10000 RCF for 2 min. At the end of this step, the collection tube was discarded. The MinElute spin column was then placed in a new collection tube. The lid of the spin column was now left open and then centrifuged at 17200 RCF for 5 min to facilitate drying up of the membrane inside the spin column.

At the end of the centrifugation, the collection tube containing the flow-through was discarded. The opened lids within the centrifuge were positioned such that they trailed behind during the rotor movement, following direction of the spin. This would avoid breaking the lids off during the centrifugation. The RNeasy MinElute spin column was then placed in a new 1.5 ml Eppendorf tube and RNase free water (62°C) was added to the centre of the spin column membrane under direct observation as 10 µl, 5µl and then 5µl making sure to cover all the membrane. After closing the lid of the spin column, it was centrifuged at 17200 RCF for 1 min to elute the RNA (~16µl) in the collection (Eppendorf) tube whereas the spin column was discarded at the end. The RNA obtained would be placed on ice. To avoid repeated freezing-thawing cycles of the stock solution, it was aliquoted into smaller volumes, including two separate aliquots of 2µl and 3µl. The 2µl and 3µl aliquots were used to performing some QC checks on the extracted RNA. These were stored at -20°C whereas the rest of the aliquots were shifted to -80°C for longer storage. RNA was always kept on ice while out of the fridge/freezer.

1.1.2 RNA extraction from adult mouse heart samples

In case of adult heart tissues (n = 3 WT and 3 HET for each of *Cdk13*^{tm1b}, *Prkd1*^{em1}, and *Prkd1*^{em2}), with tissues quite firm, using the RNeasy kit and its protocol on its own did not work, giving poor concentration and quality of RNA from the adult heart tissue (Figure 2:11).

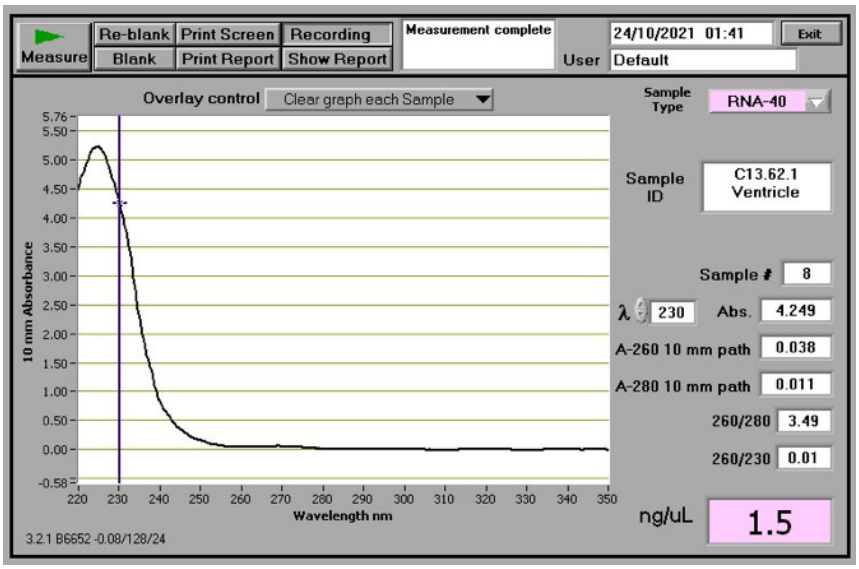


Figure 2:11 RNA extraction from adult heart sample as per supplier's protocol. RNeasy micro kit worked well for RNA extraction in embryonic heart samples but in case of adult heart samples, the tissue didn't lyse well, and RNA obtained was unbelievably negligible.

The RNeasy protocol was therefore edited by adding Proteinase K to it as suggested by Dr Rudolf Billeter Clarke, Medical School, University of Nottingham, UK. The results were surprising being so good. From the same heart, a fresh and almost same amount of sample was taken for RNA extraction using this modified protocol and the RNA concentration and quality obtained was great (Figure 2:12) and had no match to the earlier reading.

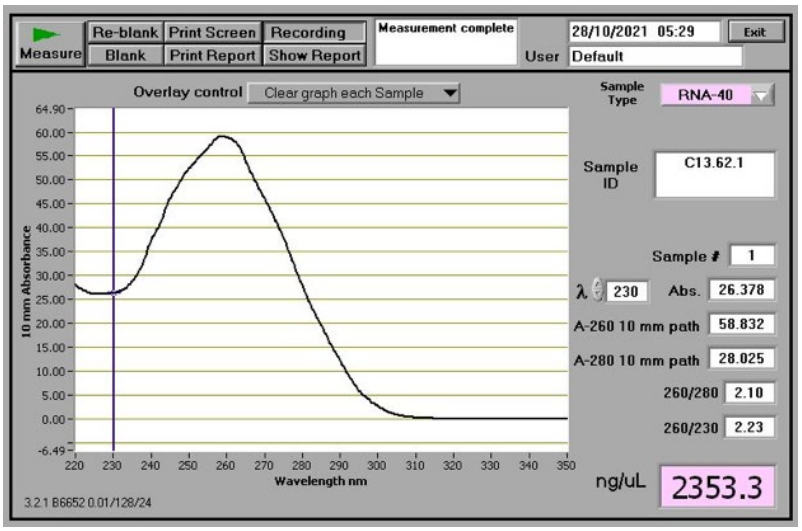


Figure 2:12 Improvement of RNA extraction from adult heart sample through modification of the protocol. RNeasy micro kit worked well for RNA extraction in embryonic heart samples but for adult heart samples, the protocol needed amendment to be useful. The amended RNeasy micro kit's protocol for adult tissues gave enormous amount of RNA.

After collecting the heart tissue in a 1.5ml eppendorph, 150µl of Buffer RLT (at room temperature) was added to it. Plastic piston as part of the RNase-Free Pellet Pestles (Cat. No. 12-141-368, Fisherbrand™) was used to manually macerate the tissue, followed by electric homogenization using Pellet Pestles cordless adapter (Cat. No. 12-141-361, Fisherbrand™) so as to get a homogenised sample. After this, 285 µl of nuclease free water was added to the eppendorph by making it run over the piston tip and then quickly vortexed. Thereafter, 15µl of 10mg/ml proteinase K (Cat. No. 183988 MP-Bio, UK) was added to the eppendorph and incubated at 55°C for 15 minutes, by centrifuged for 3 min at a max. speed (17200 RCF). The supernatant was transferred into a new eppendorph tube which was about 450µl. To this tube, 450µl more volume of buffer RLT was added to the column, followed by adding 450µl of 100% ethanol (4°C) and vortexed. All the contents of the sample tube were then

transferred to RNeasy MinElute spin column in a 2 ml collection tube (4°C). However, the spin column being smaller for sample volume, the tube contents were transferred in two steps, followed by centrifuge at 10000 RCF at 4°C for 15 seconds each time (allowing RNA binding to the column membrane). The flow-through obtained at the end was discarded. As a next step, 600µl of Buffer RW1 (wash solution) was added to the MinElute spin column, lid closed. After incubation for a minute, the tube was centrifuged for 15 seconds at 10000 RCF at 4°C, discarding the flow-through at the end. Another volume of 350µl of Buffer RW1 was added to the MinElute spin column, centrifuged for 15 seconds, and discarded the flow through. At this time, DNase I incubation mix (70 µl RDD buffer and 10µl of DNase I) was added directly to the membrane and the tube was left on the benchtop for 15 min at room temperature. To wash away the DNase mix, another 350µl of RW1 buffer was added to the column, centrifuged for 15 seconds, and discarded the flow through. As a next step, an additional wash step, 500ul of RPE buffer was added to the column, centrifuged for 15 sec, and discarded the flow through. The final wash was by 80% ethanol (4°C,prepared in RNase free water) was added to the column and centrifuged for 2 minutes. The flow through and the collection tube were discarded. The spin column was placed in new 1.5ml collection stube. The lids of spin columns are opened and as such were centrifuged for 5 minutes to get the column membrane completely dry as any left-over ethanol will interfere with RNA solubilisation. The RNeasy MinElute spin column was then placed in a new 1.5 ml Eppendorf tube and RNase free water (62°C) was added to the centre of the

spin column membrane under direct observation as 10 µl, 5µl and then 5µl making sure to cover all the membrane. After closing the lid of the spin column, it was centrifuged at 17200 RCF for 1 min to elute the RNA (~16µl) in the collection (Eppendorf) tube. I rotated the columns in the rotor and centrifuged for 1 more minute. At the end of this, the spin column was discarded. The RNA obtained would be placed on ice. After collecting aliquots for QC checks and measuring concentration (stored at -20°C), rest of the RNA was stored at -80°C.

2.13 Quality control (QC) checks on extracted RNA

2.13.1 Nanodrop spectrophotometry

As a part of total RNA QC-work up, the 2 µl aliquot of RNA sample was used to measure RNA concentration and purity on NanoDrop™ spectrophotometer (ND1000, Thermo Fisher Scientific®), and running PCR and gel electrophoresis for any genomic DNA contamination.

On NanoDrop™ spectrophotometer, ultraviolet absorbance is measured at 260 and 280nm. RNA concentration reading provided by it is based on the UV absorbance at 260 nm. The 260/280 and 260/230 ratios and the shape of the curve identify potential contamination. For RNA, the 260/280 ratio of ~2.0 and the 26/230 ratio of ~ 2.0-2.2 were generally recommended and hence were considered as acceptable checks of purity (Figure 2:13). The lower value would indicate protein contamination (Figure 2:14).

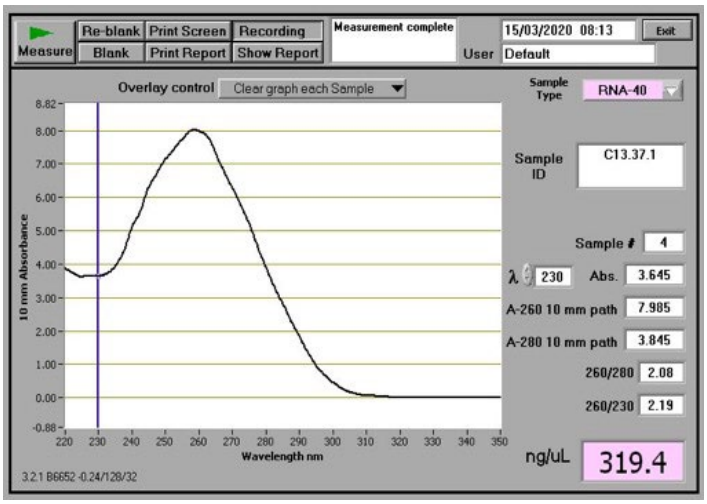


Figure 2:13 Spectrophotometry of RNA sample on NanoDrop™. Determining the purity and concentration of extracted RNA from single E12.5 Cdk13+/+ mouse heart. For RNA, the 260/280 ratio of ~2.0 and the 260/230 ratio of ~ 2.0-2.2 are generally considered as acceptable checks of purity by this method. The shape of the curve as well as presence of additional curves also helps to determine the quality/purity of RNA sample.

During initial optimization, I had the issue of getting second peak, along with low 260/230 nm absorption ratios due to potential salt-carry over. That was sorted to a greater extent in subsequent extractions by an additional wash of MinElute spin column membrane with 80% ethanol after the RPE washes, using the RNeasy® Micro kit.

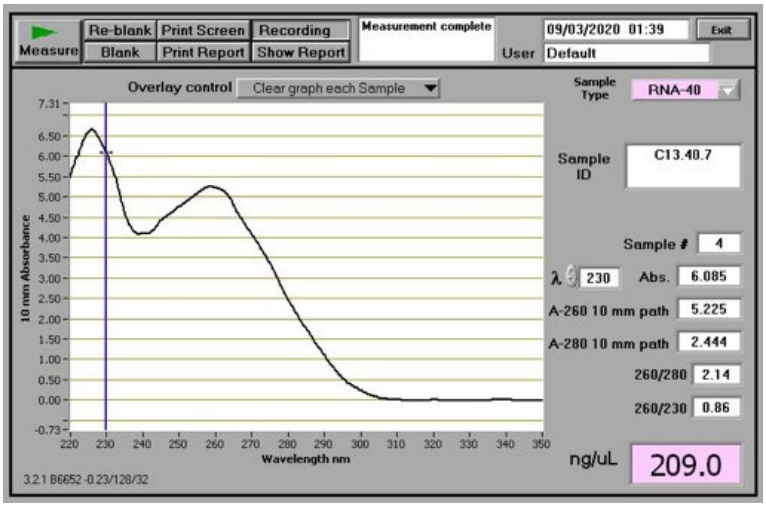


Figure 2:14 Abnormal second peak on NanoDrop spectrophotometry. The figure from Nanodrop spectrophotometer (ND1000®) showing RNA concentration obtained from a single WT mouse heart at E12.5. The value of 260/230 is very low; moreover, the second peak in a curve can be seen, due potentially to salts carry over.

To exclude any genomic DNA contamination of the RNA sample, PCR amplification was carried out using *Prkd*$^{-em1}$ wild type primers, followed by visualisation of the bands on gel electrophoresis (Figure 2:15).

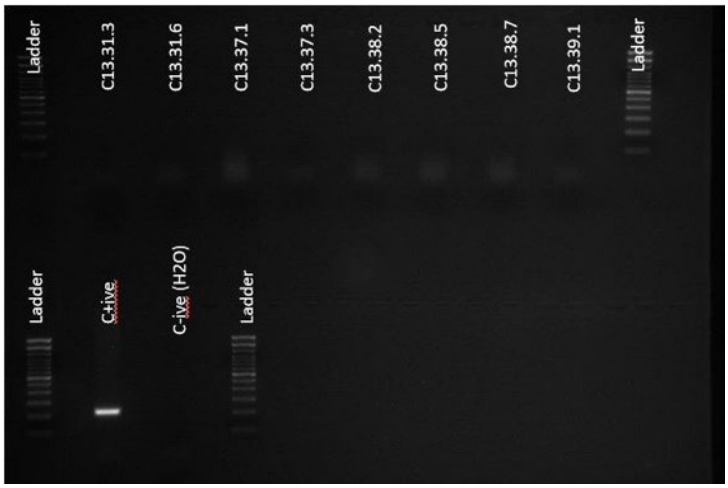
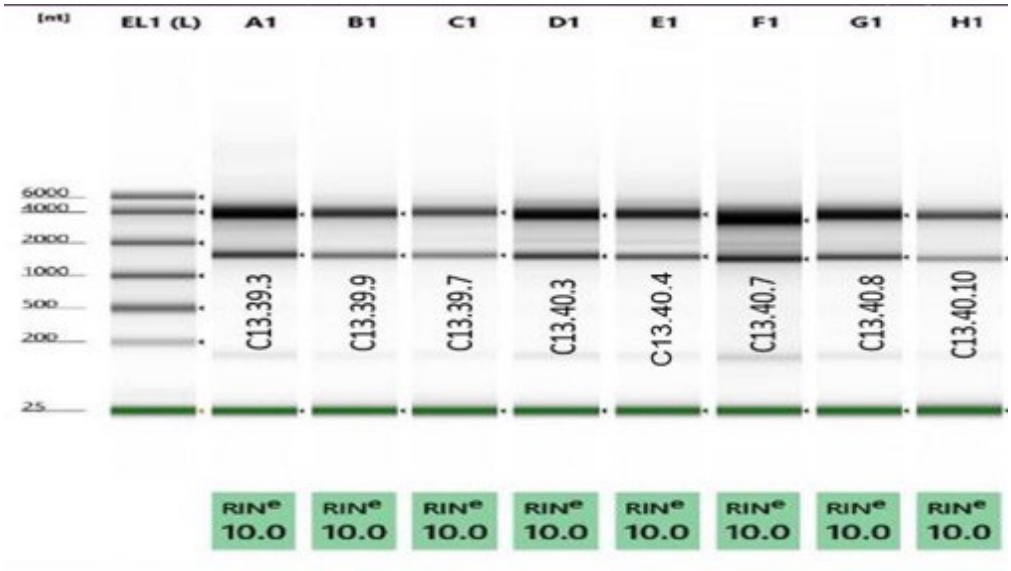


Figure 2:15 Gel electrophoresis of RNA samples. A representative image of electrophoresis gel of RNA samples from E12.5 mouse hearts after PCR amplification is shown. WT primer pair of one of the mouse lines was used for PCR amplification. No abnormal band is visible in any experimental sample's lane, thereby excluding any gDNA contamination of these RNA samples. C+ive = positive control; C-ive = negative control (RNase free water).

1.1.3 QC checks on extracted RNA prior to sequencing

After the initial analysis of RNA samples to determine their concentration and purity by Nanodrop followed by gel electrophoresis, as described above, a 3µl aliquot of each RNA sample was sent to DeepSeq facility, Medical School, University of Nottingham. They carried out further analysis of these RNA samples by ScreenTapeStation system® (Agilent, USA) to get accurate information about the integrity and quantity of RNA in each sample. This prior analysis was mandatory prior to RNA sequencing. The information about RNA degradation was provided as an RNA Integrity Number (RIN^{e}). Moreover, report from the RNA ScreenTapeStation system® (Agilent, USA) also mentioned concentration of RNA in

the sample and this value was then considered for subsequent cDNA synthesis (Figure 2:16).



Well	RINe	28S/18S (Area)	Conc. [ng/µl]	Sample Description	Alert	Observations
EL1	-	-	84.9	Electronic Ladder		Ladder
A1	10.0	2.7	148	C13-39-3		
B1	10.0	2.4	76.4	C13-39-9		
C1	10.0	2.2	59.8	C13-39-7		
D1	10.0	2.6	126	C13-40-3		
E1	10.0	2.6	93.2	C13-40-4		
F1	10.0	3.1	188	C13-40-7		
G1	10.0	2.9	107	C13-40-8		
H1	10.0	2.4	48.4	C13-40-10		

Figure 2:16 RNA samples extracted from Cdk13tm1b mouse hearts at E12.5. A representative analysis report of RNA ScreenTapeStation system® (Agilent, USA) showing information about RNA integrity in terms of RNA integrity number (RIN).The higher the RIN, the better the RNA is. The maximum possible value for RIN in any sample is 10 and hence all the samples shown are of the best quality making them highly suitable for RNA-Seq. The concentration of RNA in each sample is also mentioned in the report.

2.14 RNA sequencing of *Cdk13^{tm1b}* mouse heart samples

RNA-Seq of *Cdk13^{tm1b}* mouse heart samples (n = 6 WT, 5 HOMO samples) and its related initial bioinformatic analysis was carried out by Dr Fei Sang of the DeepSeq facility, Life Sciences, University of Nottingham. *RNA-Seq* was carried out on Illumina NextSeq500. QuantSeq kit was used for generating library of sequences at 3' end of poly A RNA. Data

analysis was carried out on BlueBee® Genomics Platform. The low-quality reads were trimmed by setting minimum threshold. Thereafter, the sequence reads were mapped to the reference mouse genome (GRCm39) and those uniquely mapped were noted as .bam files. The unique and accurately aligned reads were then counted using HtSeq-count in BlueBee®. The total read counts of a gene in a sample once determined were then divided by 1,000,000 to give a “per million” scaling factor. The total gene read counts for each gene were then divided by this scaling factor to give us reads per million (RPM); this normalises for the sequencing depth. The RPM values obtained were divided by total gene length (in kilobases) to give reads per kilobase of transcript per million (RPKM). The RPKM for each gene obtained were then normalised to the total number of mapped reads [193]. Principal Component Analysis (PCA) was done to determine that the biological replicates were closely related to each other, allowing subsequent deferential expression analysis. Differential expression of genes (DEGs) was analysed by using DESeq2 package (version 1.24.0) in R, with a false discovery rate (FDR) <0.05 [194]. Gene ontology (GO) enrichment analysis was carried out using GOSeq (version 1.4.0), also an R software package [195]. Additionally, functional enrichment analysis was also carried out using a bioinformatics’ web-based application for integrated differential expression and pathway (iDEP) analysis [196].

2.15 cDNA synthesis

RNA isolated from embryos (*Cdk13*^{tm1b}, n = 36; *Prkd1*^{em1}, n = 8 and *Prkd1*^{em2}, n = 6) and adult heart tissues (n = 3 WT and 3 HET for each of

the *Cdk13*^{tm1b}, *Prkd1*^{em1}, and *Prkd1*^{em2} mice), was reverse transcribed to cDNA for further experiments. SuperScript™ II Reverse Transcriptase kit (Cat. No.18064014, Invitrogen™) was used for this purpose. This involved carrying out two reactions for each sample i.e., one was RT- positive whereas the other being RT- negative (control). To a 1.5ml eppendorph, 1 µl of hexamers, 1µl of dNTP mix and 500 ng of total RNA were added. Nuclease free water was added to make the volume 13 µl. This mixture was place on pre-heated dry heat block to heat it to 65°C for 5 minutes and then quickly chilled on ice for 15 seconds. Thereafter, 4ul of first strand buffer (5X) and 2 µl of DTT were added to this mixture and gently mixed by pipetting up and down. The mixture was then left to incubate in pre-set and heated thermal cycle at 25° C for 2 minutes. After this, SuperScript™ II Reverse Transcriptase (1µl) was added to the RT-positive sample whereas 1µl of nuclease free water was added to the RT-negative samples. The mixture, 20µl, was then incubated in a pre-set and heated thermal cycle at 25° C for 10 minutes, 42° C for 50 minutes and 70° C for 15 minutes. At the end of this, cDNA was stored in freezer (-20C) to use in subsequent experiments.

2.16 Expression studies

1.1.4 Primer designing

All the primer pairs for expression studies (qPCR and W-ISH) were designed by employing the freely available tool i.e., Primer-BLAST, accessible via https://www.ncbi.nlm.nih.gov/tools/primer-blast/). The different filters applied while designing the primers are given in Table 2:6. For W-ISH primers, the filter applied for amplicon size was 450-850bp. After

designing the intended primers, they were counter checked for binding specificity using the BLAST tool.

Criteria for primer designing	
Spanning exon-exon junction	Yes
Product size for qPCR primers	70-250bp
Product size for W-ISH primers	450-850bp
Melting temperature (Tm)	57°C-63°C
GC content	50-55%
Maximum difference in Tm between primer pairs	3°C

Table 2:6 Criteria for primer designing for qPCR and W-ISH. The different filters as above applied in the BLAST tool resulted in appropriate primers for the qPCR and W-ISH experiments. For W-ISH, primers giving bigger amplicon size were designed.

The different primers designed for qPCR, RT-PCR/W-ISH analyses and their expected amplicon size are given in the Table 2:7. The reference genes selected were those reported earlier to be the best for mouse heart [197].

Gene	Sequences 5' to 3'	Amplicon (bp)
Cdk13 (qPCR)	F: TGCCATGCTAGAGGAAAGGG R: CTGGTTCTGGTGTCAGCTCC	149
Prkd1 (qPCR)	F: ATGTATCCACCCAACCCGTG R: CCACCTGGAGTCATCGCTTT	213
Prkd2 (qPCR)	F: GTGAGCCTTAGTGGCACGTT R: GTCAAGCCACGTCTGGTACT	219
Prkd3 (qPCR)	F: CCACCAAATCCATGGCGAGA R: CCAGATTGTGCGTGTATGCG	235
Sall4 (qPCR)	F: ACCACGAAAGGCAACCTGAA R: TCCTTGGAAAACACCTCGGG	146
Sall4 (W-ISH)	F: CAGGAGTGTCAGAGCCGAAG R: CTTTTCTCCGTTCCCGCTCA	795
Vegfa (qPCR)	F: CCAAGATCCGCAGACGTGTA R: CTTTCCGGTGAGAGGTCTGG	172
Vegfa (W-ISH)	F: CCTTGGGATCTTGCATCGGA R: GCTTCGCTGGTAGACATCCA	710
Cdkn1a (qPCR)	F: TGTCGCTGTCTTGCACTCTG R: GACCAATCTGCGCTTGGAGT	128
Edn1 (qPCR)	F: GGCCCAAAGTACCATGCAGA RV: GATGGCCTCCAACCTTCGTA	127
Ednra (qPCR)	F: CACCTCAAACAGCGTCGAGA R: TGCCAGGTTAATGCCGATGT	186
Notch2 (qPCR)	F: AGCAGGAGGTGATAGGCTCT R: TGGGCGTTTCTTGGACTCTC	187
Notch2 (W-ISH)	GATGAAGGACCCCAGCCAAA GGCCGCTTCATAACTTCCCT	795
Eln	F: ATTCCTGGGATTGGAGGCATTG	104

(qPCR)	R: ACTAAACCTCCAGCAGCTCCATA	
Eln (W-ISH)	F: ATTGGTGGCATCGGTGGCTTA R: AGCACCTGGGAGCCTAACT	657
**Pgk1 (qPCR)*	FW: GTCGTGATGAGGGTGGACTT RV: AAGGACAACGGACTTGGCTC	126
**Rpl4 (qPCR)*	FW: GCCGCTGGTGGTTGAAGATAA RV: CGTCGGTTTCTCATTTTGCCC	150
**Eef1e1 (qPCR)*	FW: TCCAGTAAAGAAGACACCCAGA RV: GACAAAACCAGCGAGACACA	187

*Table 2:7 Primers used in qPCR and W-ISH. The sequences used in qPCR and RT-PCR/W-ISH and the amplicon sizes are given. The amplicon size for qPCR primers was less than 250bp whereas for W-ISH, it was between 450-850bp. * The primers for these reference genes were taken from literature [197].*

1.1.5 qPCR standard curve and relative quantification

2.16.1.1 qPCR primer optimisation

Primers were designed by using NCBI PrimerBlast program. For this purpose, RNA was extracted from a WT E12.5 mouse hearts which was converted to cDNA by in vitro reverse transcription (RT). To get a standard curve for each qPCR's primer pair, a six point and three-fold (1:3) dilution of the WT cDNA template was carried out, started with the undiluted RT+ sample. For each dilution, two technical replicates were used along with undiluted RT- and blank (nuclease free water) controls. The reaction volume was 10μl. The different concentrations for undiluted reactions are given in the Table 2:8 and thermal cycler conditions for primer optimisation/standard curve are given in Table 2:9.

Reagent	RT+ and RT- Volume	Water control Volume
iTaq™ Universal SYBR® Green Supermix (Cat. No. 1725121, BIORAD)	5μl	5μl
Primer pair (Sigma-Aldrich) (10μM)	0.25 or 0.5μl	0.25 or 0.5μl
Template from RT+ or RT-	1μl	-
Nuclease free water (to top up to 10 μl)	3 or 3.5μl	4 or 4.5μl
Total reaction volume	10μl	10μl

Table 2:8 Reaction mix for the qPCR standard curve as well as relative quantification. The table is showing different reagents used to determine standard curve and primer efficiency. Primers' concentrations at which the efficiency was most optimal were 250 or 500nM, as determined individually for each of the primer used.

Steps	Temperature (°C)	Time (sec)
Holding stage	50	120
	95	60
Cycling stage (40 cycles)	95	15
	60	60
Melt curve stage	95	15
	60	60
	95	30
	60	15

Table 2:9 Thermal cycler conditions employed for primers' optimisation as well as comparative qPCR.

qPCR standard curves and melt curves were examined using 7500 software v2.0.6. The cut off value set for primer efficiency was between 85% and 110% with an $R^2 \geq 0.95$ (or $R \geq 0.990$). The standard curve (Figure 2:17-A) was used to calculate the relevant abundance of our target gene compared with the unknown samples. The melting curve for each dilution was a single overlapping peak (Figure 2:17-B). Smaller peak(s) at lower temperatures in addition to the main peak are due to primer dimers and were deemed acceptable if the primer efficiency and R^2 were within the acceptable range. Higher peak(s) at higher temperature if any would be due to genomic DNA contamination and were not considered acceptable.

However, prior DNase treatment as well as the designing of intron-spanning primers should have excluded presence and/or amplification of any gDNA and hence were not detected. The primer efficiency and "R^2" for the primer pairs used are given in the (Table 2:10). The workflow as well as the figures of melt curve and standard curve are given only for *Cdk13* here. However, the same protocol was used for all the genes studied.

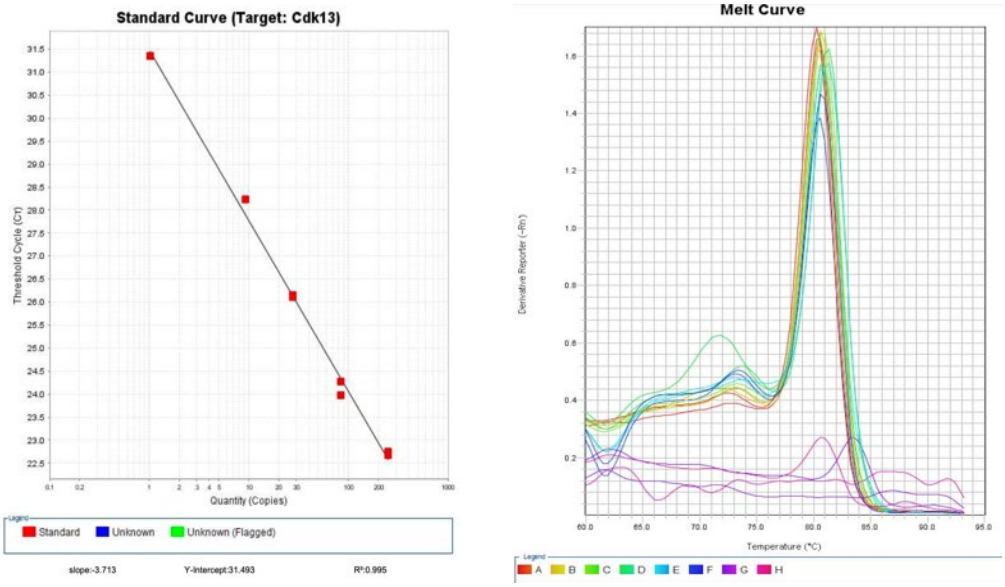


Figure 2:17 qPCR primer optimisation using Cdk13 primers and making standard curve. A: The standard curve in which threshold cycle (Ct) is plotted against the log of the starting quantity of cDNA template for each dilution in the 1:3 dilution series. R2 represents correlation coefficient and should normally be > 0.995. The slope "m" of the standard curve indicates PCR efficiency E and was calculated by the software of the qPCR equipment. B: the Melting curve graph showing melt curve for a single experiment, plotted against the negative derivative (-Rn) of the normalised fluorescence of each well versus the melting temperature.

Primer pairs	Efficiency (%)	Slope	R^2
Cdk13	85.92	-3.713	0.99
Prkd1	98.96	-3.347	0.966
Prkd2	99.75	-3.328	0.98
Prkd3	86.187	-3.704	0.987
Sall4	107.5	-3.154	0.992
Vegfa	103.5	-3.239	0.995
Eln	93.32	-3.493	0.986
Notch2	92	-3.527	0.988
Cdkn1a	95	-3.444	0.996
Ednra	0.98	-3.101	110
Edn1	105.8	-3.190	0.969
Pgk1	108.99	-3.123	0.99
Rpl4	109.49	-3.113	0.99
Eef1e1	93.38	-3.4916	0.98

Table 2:10 Efficiency of primers used for transcript expression of the respective genes by RT-qPCR. The table showing primer efficiency, slope and R2 values of the primers used for RT-qPCR. Transcript expression was normalised to two of the three reference genes i.e., Pgk1, Rpl4 and Eef1e1 run in every qPCR plate.

2.16.1.2 Relative quantification by qPCR

Relative quantification for each gene of interest (GOI) was performed by running three technical replicates for each biological sample. For each group, three biological samples were used. RT- negative (RT -) and no template control (NTC)/water were used as negative controls in each qPCR-plate for each GOI. The reagents and their concentrations used were the same as in Table 2:8. To load 10μl of each sample, MicroAmp™ Optical 96-Well Reaction Plate (Applied Biosystems™) was used. The plate was finally sealed with a Microseal 'B' Adhesive Sealing Film (Cat. No. MSB1001, Biorad). qPCR was carried on 7500 Fast Real-Time PCR system (Applied Biosystems™). The PCR settings used are as shown in Table 2:9. Comparative qPCR data of gene expression obtained were normalised to *Pgk1 or Eef1e1* and *Rpl4* and analysed using modified Pfaffl method [198] as described previously [199] [200]. For statistical

analysis of expression data and making relevant graphs, GraphPad Prism 9.2.0 (www.graphpad.com) was used.

1.1.6 RT-PCR for the W-ISH probes

By running RT-PCR, cDNA synthesised earlier was amplified by using the thermal cycler (T100™, Bio-Rad). The final reaction volume for PCR was 25μl (Table 2:11). 1.3% agarose gel was made with 1X TAE and SYBR™ Safe DNA gel stain (Cat. No. S33102, Invitrogen™) in 1:1000 dilution. Samples along with 1kb ladder (Cat. No. 10787018, Invitrogen™) were loaded onto the gel and run at 80V for 90 minutes.

Reagents	Volume (μl)
Promega® PCR Mastermix (2X)	10.5
Forward primer (10μM)	1
Reverse primer (10μM)	1
Nuclease free water	11.5
RT+ (cDNA) (500ng)	1
RT- (RNA) (500ng)	1
Blank (Nuclease free water)	NA

Table 2:11 Reagents used in RT-PCR reaction. The table shows the reagents used in different proportions to make a 25μl reaction.

To generate PCR template for the W-ISH probes, first, three PCR reactions were carried out to in the gradient thermal cycler to determine the most optimal annealing temperature for the respective primer. The gradient temperature options varied by 2-3 degrees and the bands obtained on gel electrophoresis were analyzed to select the most optimal annealing temperature (Figure 2:18). Thereafter, at the selected annealing temperature, five more PCR reactions were carried out together (Table 2:12) to get sufficient product/template for subsequent steps of probe synthesis for W-ISH. All reactions were mixed up at the end of PCR. 15μl from this

total product was used for gel electrophoresis whereas the rest was used for PCR-clean up.

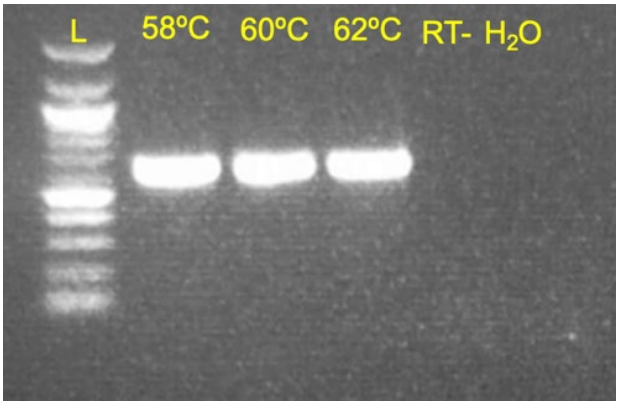


Figure 2:18 Gel image after gradient PCR. A representative gel image of 3 PCR reactions for a primer pair for a specific gene after running gradient PCR to determine the optimal annealing temperature for the primers. For this specific gene, all the bands were reasonably good at all these differential temperatures, however the band at 62°C seemed much sharper and hence was selected as the annealing temperature.

PCR steps	Temperature (°C)	Duration (min)
1	95	3
2 (36 cycles)	95	0.5
	Annealing Temperature	0.5
	72	1
3	72	5

Table 2:12 PCR conditions used for RT-PCR. Annealing temperature was specific for specific primer pair. Amount of cDNA used was 500ng whereas the extension time selected was 1 minute.

2.16.2 Whole mount *in situ* Hybridization (W-ISH)

2.16.2.1 PCR clean-up

After the cDNA synthesis, it was cleaned up by column precipitation to purify the product using GenElute™ PCR Clean-Up Kit (Cat. No. NA1020, Sigma-Aldrich) following supplier's protocol. Thereafter the concentration of the purified product was measured by Nanodrop™ Spectrophotometer (ThermoFisher Scientific) and thereby stored at -20° C for subsequent use as a template for ligation reactions.

2.16.2.2 Ligation and transformation

In order to perform ligation of fragments of GOI and transformation, pGEM-T Easy Vector Systems (Cat. No. 1360, Promega, UK) kit and the supplied protocol was used. Three ligation reactions were carried out for each gene, with three ratios of insert:vector (3:1, 5:1, 7:1). The final volume of the reaction was 20μl which was placed at 16°C overnight in the thermal cycler. Thereafter, the ligation product was wither stored at -20°C or directly used for the transformation reaction.

Transformation involved mixing 30μl of DH5-alpha competent cells (in house stock stored at -80°C) with 2μl of the ligation reaction. DH5-alpha cells are engineered E. coli cells. The mixture was incubated on ice for 20 minutes, followed by heat shock of the cells at 42°C for 50 seconds and then incubation again on ice at 2 minutes. To this mixture, 950μl of SOC medium was added, followed by incubation for 90 minutes at 37°C. Thereafter, the tube with the mixture was centrifuged at 4000rpm for 10 min. About 800μl of the supernatant was discarded and 100μl of the mixture was collected from the bottom of the tube to spread it, under sterile conditions, on plates containing Lysogeny broth (LB) agar (in house) and 0.1mg/ml Ampicillin (Sigma-Aldrich). The plates were incubated at 37°C overnight. The next day, colonies were checked if they were pink/white or red. Those with an insert were in pink/white in colour. Out of the pink/white coloured colonies, those present as single colonies were selected and scrapped. Each colony was incubated in 4ml LB high salt (HS) medium in an incubator at 37°C overnight, at 200rpm. The next day, the tubes with bacterial culture were cloudy as expected. To confirm if the

colony cells/transformants carry the right insert, a 25μl PCR reaction was carried out with primers, using template (1μl) from the cloudy bacterial culture tube. PCR conditions were the same as mentioned before (Table 2:12) except the step 1 which was of 18 minutes (instead of 3 minutes) at 95°C to allow time to lyse bacteria. Gel electrophoresis was done as previously described to see if the band was of the correct size (Figure 2:19). The gel was imaged using GeneGenius Bioimaging System (Syngene, UK).

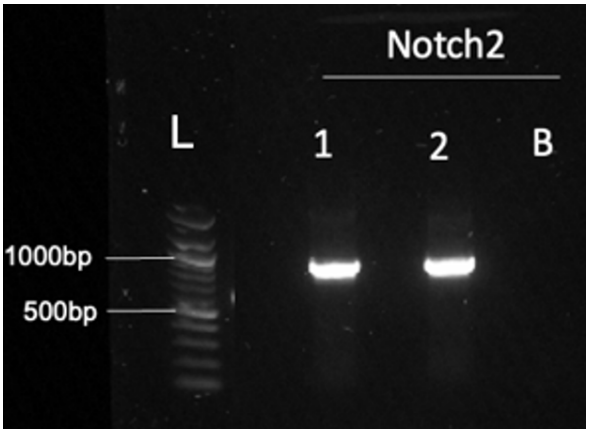


Figure 2:19 Gel electrophoresis after PCR on two bacterial colonies. Representative image of the post PCR gel of the bacterial colonies with insert of one of the genes of interest (Notch2), showing the right size band (795bp) in both colonies. L: 100b ladder; B: blank.

2.16.2.3 Midiprep

To isolate transfected/transformed plasmid from *E.Coli,* midi prep was carried out using Plasmid Midi kit (Cat. No. 12143, Qiagen) following the manufacturer's protocol. After confirming (in the previous step) that the colonies had the right insert, 800ul of bacterial culture was added to a 100ml conical flask containing LB HS broth and Ampicillin (0.1mg/ml) and left on shaker overnight at 37°C and 200rpm. The next day, flask was expected to have a cloudy medium. Optical density of the culture was

determined using spectrophotometer (SmartSpec 3000, BIORAD). A cell mass of 100 (OD_{600} x ml of culture) was put in Oak Ridge centrifuge tubes and centrifuged in a high-speed centrifuge (Avanti J-25 Rotor – Ja25.50) at 5000 x g for 10 minutes at 4°C. The supernatant was discarded, and the remaining pellet was resuspended using in 1.2ml of the resuspension solution (stored at 4°C), followed by rubbing the tube vigorously against a corrugated surface to get a homogenous milky solution. Thereafter, to lyse bacterial cells to release plasmid, 1.2ml of lysis solution was added to the tube and mixed by gently inverting 6-8 times until the solution was clear and viscous (but in no case for more than 5 minutes to avoid plasmid digestion). In the next step, 1.6ml of neutralising solution was added to stop the lysis reaction and mixed by gently inverting the tube 6-8 times as above. The tube was then centrifuged at 15000 x g for 15min at 4°C. The pellet obtained will have bacteria.

Thereafter, binding column was prepared by placing it a 15 ml Falcon® collection tube and 3ml of column preparation solution was added to it. The binding column was then centrifuged at 5000 x g at 4°C for 2min with no lid on and the flow through was discarded. This step was intended to charge the filter to allow plasmid binding to it. The lysate obtained at the end of the neutralisation step was now added to this pre-prepared column and centrifuged at 5000 x g for 2 min at 4°C. Flow through was discarded followed by adding 3ml of wash solution to the binding column. The column was then centrifuged at 5000 x g for 5 minutes with no lid on, followed by an additional spin of 2 minutes to remove all wash solution completely. In the next step to elute DNA (plasmid), the binding column was

then placed in a new 15ml Falcon tube, to which 600µl of preheated (65°C) nuclease free water was added. The binding column as such was left for 10 minutes at room temperature before centrifugating it at 4000 x g for 5 minutes. The eluate obtained at the end contained plasmid, of which the concentration was measured by NanoDrop™ 2000c spectrophotometer at 260nm absorbance (Table 2:13) and was then stored at -20°C.

Plasmid with GOI	Conc. on NanoDrop™ (ng/µl)
Eln	400.8
Notch2	760
Sall4	525.5
Vegfa	500

Table 2:13 Concentration of plasmids with gene inserts on NanoDrop™ spectrophotometer.

2.16.2.4 Sequencing and linearisation of plasmid

Plasmid obtained at the end of midiprep was sent for sequencing, using T7 promoter forward primer, to Deep sequencing facility at Medical School, University of Nottingham where it was sequenced on 3130xl ABI PRISM Genetic Analyser (Life Technologies). Sequencing was needed to determine the direction of the insert in the vector since orientation of the plasmid could be 5' to 3' or 3' to 5'. The sequence obtained was therefore aligned to the gene sequence from NCBI using MultAlin [201] (http://multalin.toulouse.inra.fr/multalin/) (Figure 2:20).This also helped to determine which restriction enzyme and promotor to use to get the antisense probe. If it mapped to the obtained NCBI sequence, it would be sense probe but if mapped to the complimentary sequence, then would be antisense probe.



Figure 2:20 Alignment of plasmid sequence to GOI sequence on NCBI. MultAlin free software [201] was used for aligning the obtained sequence to the gene sequence on NCBI. The example shows obtained sequence for Elastin (Eln) (labelled as "Seq") and aligned to its sequence on NCBI database (labelled as "Eln").

Thereafter, the sequence was mapped on the pGEM-T easy vector using SerialCloner 2.6.1 (http://serialbasics.free.fr/Serial_Cloner.html) (Figure 2:21) to determine the restriction enzymes (RE) needed for isolating the probe from sense or antisense RNA transcription promotor, i.e., to produce the antisense and sense strands, without cutting through the inserted fragment of GOI (Table 2:14).

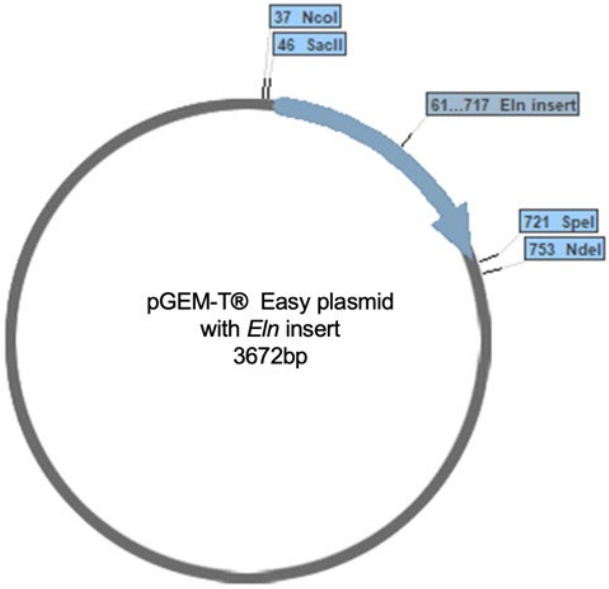


Figure 2:21 Identifying the restriction enzymes which should not cut through the plasmid. A representative image of plasmid with insert of one of the genes of interest (Elastin) (grey arrow and box) and the restriction enzymes (blue boxes). A freely available software was used for this purpose. i.e., SerialCloner 2.6.1 (http://serialbasics.free.fr/Serial_Cloner.html). All the restriction enzymes lie outside the inserted plasmid. NdeI and NCoI were selected for sense and antisense Eln probes respectively.

Plasmid with GOI	Sense RE	Antisense RE
Eln	NdeI	NcoI
Notch2	NdeI	SacII
Sall4	ApaI	MluI-HF
Vegfa	NcoI	NdeI

Table 2:14 Restriction enzymes used for linearization of plasmids. GOI: gene of interest, RE: restriction enzyme.

The pGEMT-T® Easy plasmid was then linearized so as to stop the T7 or SP6 polymerase to transcribe anything else than the insert. This was done by using 5µl of CutSmart® buffer (Cat. # B7204, NEB), 2-5 µl of RE (NEB), 15 µg of plasmid and topped up to 50 µl with DEPC ddH2O to make 50µl of the (linearization) reaction (Table 2:15). The reaction was then incubated at 37° C for 4 hours.

Reagents	*Eln*	*Notch2*	*Sall4*	*Vegfa*
DEPC treated dH2O *(µl)*	5.6	22.3	11.5	10
CutSmart® buffer*(µl)*	5	5	5	5
Plasmid DNA (15 µg) *(µl)*	37.4	19.7	28.5	30
RE (NEB) *(µl)*	2	3	5	5
Total reaction volume *(µl)*	50	50	50	50

Table 2:15 Reagents used for linearisation reaction for plasmids with GOI-insert. Total reaction volume is 50µl and amount of plasmid DNA for each GOI is 15 µg. The column for each GOI is showing the volume of each reagent.

Thereafter, to extract plasmid DNA, 425µl of nuclease free water and 500µl of phenol chloroform isoamyl alcohol were added to the reaction, mixed, and then centrifuged at 11000 x g for 9 minutes. To precipitate the plasmid DNA, the supernatant was then collected and mixed with 3M sodium acetate (NaOAc) (Cat. No. S8625, Sigma), pH 5.2 in a 10:1 (DNA:NaOAc) ratio and with 100% ethanol in a 1:2 (DNA:EtOH) ratio. The mixture was left overnight at -20°C. As a next step, the mixture was then centrifuged at 17200 x g for 10 minutes at 4°C. The supernatant was discarded whereas the pellet was washed with 300µl of 70% ethanol followed by centrifuge at 17200 x g for 15minutes at 4°C. At the end of this, ethanol was removed and 11µl nuclease free water was added to the tube containing pellet. Concentration was checked by NanoDrop™ spectrophotometer (Table 2:16). An aliquot of the linearized plasmid was run on 1% agarose gel to confirm that linearization was successful (Figure 2:22). Thereafter, the sample was stored at -20°C.

Linearized plasmid with RE		Conc. On NanoDrop™ (ng/μl)
Eln	NdeI	844.5
	NcoI	881.3
Notch2	SacII	735.2
	NdeI	878.4
Sall4	MluI-HF	946
	ApaI	690
Vegfa	NdeI	555.5
	NcoI	830.3

Table 2:16 Restriction enzymes used for plasmid linearisation and post linearisation concentration.

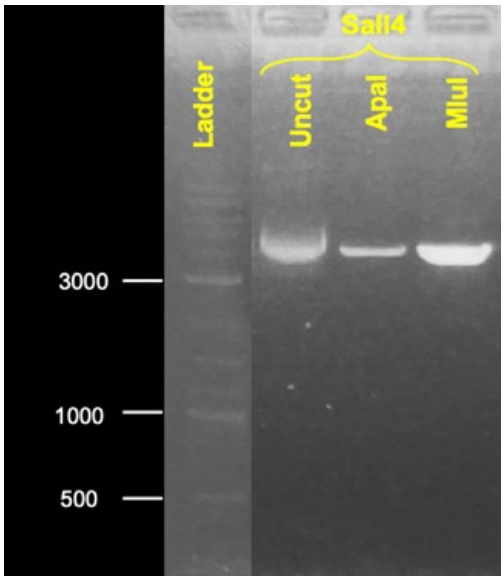


Figure 2:22 Gel after plasmid linearization. A representative image of the gel after linearization showing Uncut, sense and antisense linearized plasmid for a riboprobe. Both sense and antisense templates for the for Sall4 riboprobe has a correct band size of 3810bp. Both sense and anti-sense linearized plasmids need to be of the same size (PGEM-T vector size = 3015bp plus insert size). Uncut would give two bands: circular (higher size) and supercoiled (lower size). No other bands can be seen as in sense and antisense template which means that the plasmid has been completely linearized. Irrelevant lanes were excluded. Ladder = 1kb.

2.16.2.5 Synthesis and purification of riboprobe

To synthesize digoxygenin (DIG) labeled RNA probe, the linearized plasmid was used as a template for in vitro transcription, using SP6 and T7 RNA polymerases (Table 2:17). The reaction was carried using reagents from Riboprobe® in vitro Transcription systems (Promega) (Table 2:18).

The final reaction volume was 33.6µl which was incubated for 2.25 hours at 37°C.

Plasmid with GOI	Sense polymerase	Antisense polymerase
Eln	T7	SP6
Notch2	T7	SP6
Sall4	SP6	T7
Vegfa	T7	SP6

Table 2:17 RNA polymerases used for in vitro transcription for riboprobe synthesis.

Reagents	Volume (µl)
Trans Buffer	6
DEPC treated ddH_2O	**
DTT (100nM)	3
rRNasin (40U/µl)	1
10X DIG mix	3
3µg Plasmid DNA	*
RNA polymerase (SP6/T7)	3
Total reaction volume	33.6

Table 2:18 Reaction set up for riboprobe synthesis using Riboprobe® in vitro Transcription systems (Promega).

Thereafter, the transcription product (riboprobe) was purified by using illustra™ ProbeQuant™ G-50 Micro Columns (Cat. No. 28903408, SLS) by following the manufacturer's protocol. The column was prepared which involved vortexing to resuspend the resin, removing the bottom closure and loosening the cap by quarter of a turn. This column was then placed in a collection tube and centrifuged at 735 x g for 1 minute. Thereafter, the column was placed in a new collection tube and the riboprobe mixture prepared in the previous step was applied to the center of the resin. The column within the collection tube was then centrifuged at 735 x g for 2 minutes to get the eluate containing riboprobe. 20µl of prehybe buffer (Table 2:20) was then added to this eluate and the purified riboprobe was aliquoted and stored at -80°C.

In order to check the integrity of the probe, 2.5µl of this riboprobe-prehybe mixture was mixed with 7.5µl of RNA denaturing buffer (prepared in house) and 2µl of gel loading dye (NEB). The sample was left to incubate for 8 minutes at 67°C and then loaded on to 1% agarose gel to run at 4°C for 90 minutes at 70 V. A pGEM-T express positive control (Promega) was used as a positive control and a ladder (Figure 2:23).

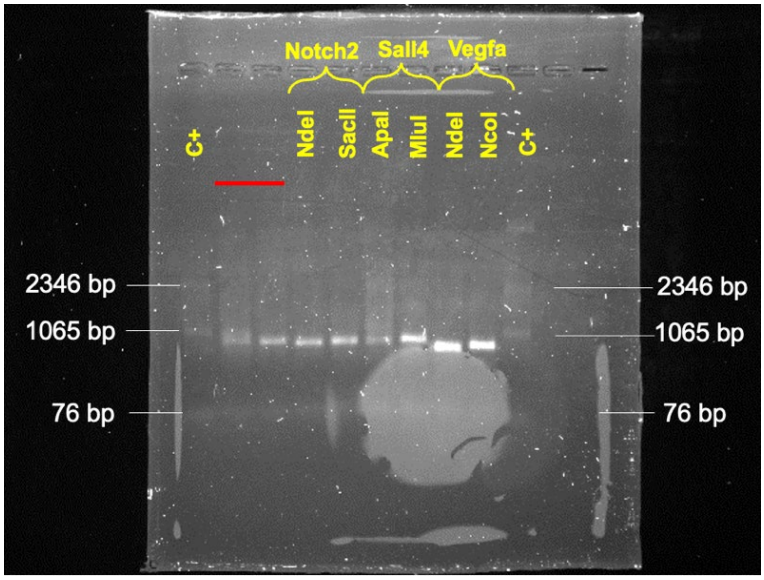


Figure 2:23 Gel electrophoresis to check probes integrity. A pGEM-T express positive control (Promega) was used as a positive control (C+) and ladder, having two bands of 1065 and 2346bp. The band at 76bp is due to tRNA present in prehybe. The sense and antisense probes have the same (expected) sizes. i.e., 795bp for Notch2 and Sall4, and 710bp for Vegfa. Redline denotes irrelevant probes.

2.16.2.6 Tissue processing for W-ISH

For W-ISH, hearts were collected from *Cdk13*^{tm1b} mouse (n = 3 each of WT and HET) at E12.5. The heart samples were collected in DEPC-PBS (4°C) and then fixed in 4% PFA (in DEPC-PBS) at 4°C overnight. The next day, fixed heart samples were dehydrated through the graded series of Methyl alcohol (MeOH) concentrations (-20°C) (Table 2:19), and finally was stored at -20°C in absolute MeOH for further processing.

Washes	Duration (min)	Repeats
RNase free PBS	10	2
25% MeOH (in DEPC-PBS)	10	2
50% MeOH (in DEPC-PBS)	10	2
75% MeOH (in DEPC-PBS)	10	2
95% MeOH (in DEPC-PBS)	10	2
100% MeOH (in DEPC-PBS)	10	2
100% MeOH (in DEPC-PBS)	10	2

Table 2:19 Dehydration of heart samples through graded series of alcohol concentration after overnight fixation in 4% PFA, for onward W-ISH.

2.16.2.7 Whole mount in situ hybridization (W-ISH)

For W-ISH, the hearts were rehydrated through decreasing concentration of methanol (75%, 50%, 25%), prepared in DEPC PBS, at 4°C for 5 mins each and then washed twice in PBS (4°C) for 5 mins each. They were then treated with Proteinase K (0.02mg/ml) (37°C) for 8 min to increase permeability of the tissue. The activity of Proteinase K was stopped by washing twice with glycine (2mg/ml in PBS-T) (4°C) for 5 min each time. This was followed by washings in PBST twice for 5 min at 4°C. The hearts were then refixed in 4% PFA (DEPC PBS) for 20 min at 4°C followed by three PBST washes for 5 minutes each. Hearts were then treated with 75% posthybe solution for 30 min and then in prehybe solution (Table 2:20) for 3 hours at 65°C (after one quick wash with 1ml prehybe). Thereafter, hearts were incubated, for 24 hours at 65°C, with DIG-labelled riboprobes added to prehybe in a concentration of 530ng/µl.

Reagents	Stock conc.	Working conc.
Deionised formamide	100%	50%
SSC 20X	20X	5X
Citric acid (C/6200/60; M.W. = 210.15)	1M	9.2mM
EDTA (D/0700/53; M.W. = 372.24)	0.5M	5mM
CHAPS (C3023, Sigma)	10%	0.1%
tRNA* (10109525001, Sigma)	100mg/ml	1mg/ml
Heparin* (CAS 9041-08-1 Fisher)	100mg/ml	50ug/ml
Tween20 (P9416, Sigma)	20%	0.1%
DEPC treated dH_2O	**	**

Table 2:20 Pre- and post-hybe reagents made in house for ISH. The reagents with single asterisk (*) will be absent from the post-hybe solution. Water (**) was added as required based on calculations.

After hybridization, the hearts were sequentially washed as in Table 2:21. BCL III buffer used was prepared in house (Table 2:22). Photographs were taken after the 100% glycerol step using microscopes (Carl Zeiss Stemi SV11 and Zeiss Discovery V8) with attached camera.

Washes	Temp.	Duration (min)	No. of washes
50% Posthybe	65°C	20	2
Saline sodium Citrate (SSC) X2		20	3
SSC X0.2		20	4
SSCX2: Maleic Acid Buffer with Tween20 (MABT) (1:1)	RT	20	1
MABT			
RNase A (EN0531, Thermo Scientific™) (100ug/ml) solution in MABT - to eliminate non-specific bound probe	37°C	30	1
MABT		10	3
2% Boehringer bocking reagent (No. 11096176001, Roche) in MAB, plus 20% sheep serum (S3772, Sigma)	RT	120	3
Anti-Digoxigenin-AP Fab fragments (Cat. No.11093274910, Roche) in MAB-blocking buffer (in ratio of 1:2500)	4°C	Overnight	-
MABT – to remove unbound antibody	RT	60	5
BCL buffer III and levamisole	RT	5	3
50% BM purple™ (Cat # 11442074001, Roche) - BCL buffer III: BM purple™ (1:1) - to detect the colour development while on rocker	RT	180 (then monitoring colour development every 15-30 min)	Used >50% concentration if staining was not good (but before the 4% PFA step).
PBST (To stop reaction after colour development)	RT	15	3
4% PFA – to fix the signal	RT	15	-
50% glycerol (in PBS)	RT	15	-
100% glycerol	4°C	Overnight	-

Table 2:21 Post hybridization steps during W-ISH.

Reagents	Stock conc.	Working conc.
Tris HCl (pH 9.5)	1M	0.1M
NaCl	5M	0.1M
$MgCl_2$	0.5M	0.05M
Tween20	20%	0.1%
dH_20	*	*

*Table 2:22 Reagents used to prepare BCL III buffer in-house. *water was added as required.*

1.1.7 Beta galactosidase staining of mouse embryos and adult tissues

Beta galactosidase/X-Gal/LacZ staining was carried out on *Cdk13*^{tm1b} mouse since it had the LacZ cassette (Figure 2:1). This technique was used to explore expression of *Cdk13* in mouse embryos at different developmental ages (E10.5, 12.5, 15.5) as well as in adult tissues (n = 3 WT and 3 HET at each age). At E10.5 and 12.5, whole embryos were stained, whereas at E15.5 and in adult mice, individual tissues were harvested and then processed for X-Gal staining. Hearts were collected opportunistically from adults (both male and female) which were no more required for breeding/colony maintenance. The protocol used was mainly based on those previously reported https://wythelab.squarespace.com/s/Whole-mount-lacZ-Staining.docx , [202, 203]. Mouse (embryos and adult) dissection was carried out in ice cold 1XDEPC-PBS immediately after culling. The embryos and tissues were then transferred to individual (labelled) wells in a 24 well plate and fixed in 3.7% PFA (4°C) on ice for 20-50 minutes (allowing time for dissecting and fixing all embryos in a litter). Adult tissues were left in the fixative for 40-50 minutes.

In the next step (permeabilization), the embryos/tissues were rinsed twice in ice cold DEPC-PBS to remove the fixative. After this, permeabilization solution/rinse buffer (Table 2:23), at 4°C, was added to the embryos/tissues in the wells to rinse and then washed thrice for 20 minutes each with it at 4°C while on rocker. After this, fresh permeabilization solution was added to each well and the plate was left overnight at 4°C on rocker.

X-Gal staining was carried out the next day at 37°C in incubator overnight using freshly prepared X-Gal staining solution (1mg/ml), prepared from 20mg/ml X-Gal stock (Cat. No. R0941,Thermo Scientific™) in 3mM rinse buffer (Table 2:24). The working X-Gal solution was prepared immediately before use. The 24-well plate with tissues completely submerged in was wrapped in cling and aluminium foils before placing in incubator to avoid tissue drying out. The next day, samples were rinsed twice with rinse buffer, and then washed twice with it for 20min on rocker to remove any residual stain. The samples were then fixed in 3.7% PFA (in 1X DEPC-PBS) at 4°C overnight. Thereafter, the samples were placed in 50% glycerol (prepared in 1X PBS) at 4°C overnight for imaging next day. Imaging was performed by using microscopes (Carl Zeiss Stemi SV11 and Zeiss Discovery V8) with attached camera. All washing steps were performed with 200µl for each well.

Reagents	Working conc.
Sodium phosphate dibasic (0.5 M; pH 7.0–7.5)	0.1 M
Sodium phosphate monobasic (0.5 M; pH 7.0–7.5)	5 mM
$MgCl_2 \cdot 6H_2O$ (1 M)	3 mM
Sodium deoxycholate	1.5 mM
Octylphenoxypolyethoxyethanol (IGEPAL CA-630)	3.0%
X-Gal rinse buffer was prepared in DEPC-PBS.	

Table 2:23 Ingredients of X-Gal Rinse buffer [203]. Rinse buffer was also used to make X-Gal staining solution.

Reagent	Final concentration
Potassium ferricyanide (200mM)	5 mM
Potassium ferrocyanide (200mM)	5 mM
X-Gal – 'ready to use' solution (20mg/ml)	1 mg/mL
X-Gal staining solution was prepared in X-Gal rinse buffer.	

Table 2:24 X-Gal staining solution. It was prepared fresh immediately before use.

2.16.3 Statistical Analysis

For quantitative data, to compare the three groups with normal data distribution, one-way ANOVA ($P \leq 0.05$) was applied followed by post hoc-Tukey (multiple comparisons) test. In case of data not normally distributed, Kruskal-Wallis's test was applied instead of one-way ANOVA, followed by Dunn's multiple-comparison test. Two group means with normal data distribution were compared using independent samples t test whereas, in case abnormal data distribution, Mann Whitney test was applied. All these tests were applied using GraphPad Prism 9.2.0 (www.graphpad.com). To carry out lethality assessment in mice, Chi-square (x^2) test was applied using MS-Excel. All the statistical tests used were two-tailed and had cut off value for significance being $P < 0.05$. All the results were calculated from minimally three independent experiments with three technical repeats and expressed as Means $\pm$ Standard error of Mean (SEM).

3 ELUCIDATING THE ROLE OF *Cdk13* IN HEART DEVELOPMENT AND CONGENITAL HEART DISEASE IN A MOUSE MODEL WITH LOF MUTATION

3.1 INTRODUCTION

Cyclin dependant kinase-13 (CDK13) belongs to the family of serine/threonine protein kinases. Human CDK13 protein comprises of 1512 amino acids with surrounding C- and N-terminal arms whose functions are undefined [204]. Its actions are ATP-dependent and is involved in the regulation of various genes and progression of cell cycle [205]. CDK13 requires Cyclin K for its activation. Once activated, it phosphorylates serine 2 (Ser 2) and serine 5 (Ser 5) present within the heptapeptides $Y^1S^2P^3T^4S^5P^6S^7$ of the carboxyl-terminal domain of RNA polymerase II (Figure 3:1) [206] and hence is required for alternative RNA splicing [207, 208]. CDK13 has C-terminal extension helix which is a characteristic feature of the kinases involved in transcription elongation [209].

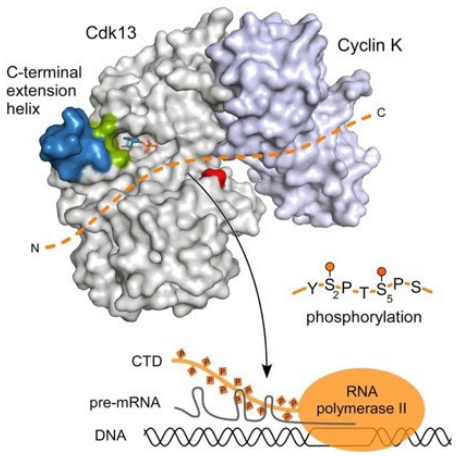


Figure 3:1 Phosphorylation by CDK13. Cyclin-dependent kinase-13 regulates transcription through phosphorylation of serine 2 (Ser 2) and serine 5 (Ser 5) present within the heptapeptides Y1S2P3T4S5P6S7 of the carboxyl-terminal domain (CTD) of RNA polymerase II. Reproduced from [210].

There is very limited data available currently about CDK13 expression. A mouse study showed CDK13 protein expression by western blot in the heart of embryos and neonates [211]. Chen *et al* reports its ubiquitous expression except in heart, as determined by W-ISH at stages E6.5-9.5 [212]. Human Protein Atlas shows that CDK13 is expressed in a wide variety of body tissues however, in myocardium, its expression (as transcript) is low (Figure 3:2).

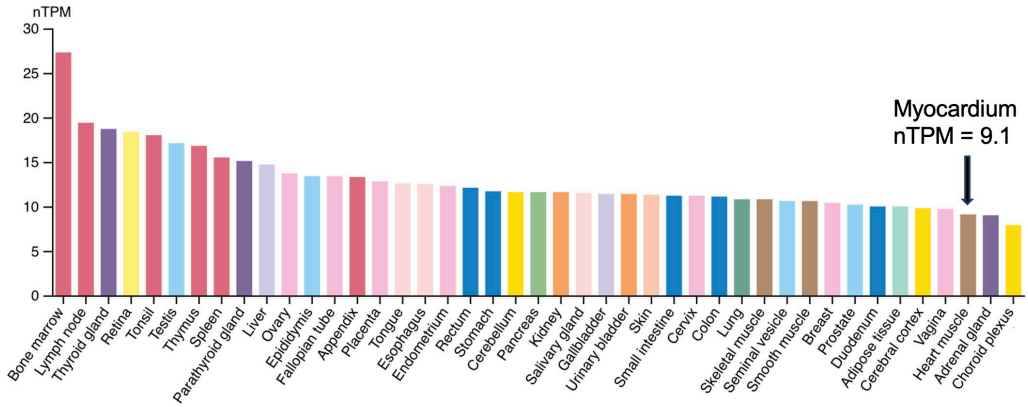


Figure 3:2 Expression of CDK13 in different adult tissues in human. Expression pattern in various tissues is shown as normalised transcripts per million (nTPM) shown along y-axis corresponding to the tissues shown along x-axis. Highest expression is in bone marrow and lymphoid tissues (28.1 nTPM) whereas in myocardium it is 9.1 nTPM (denoted by black arrow). The RNA expression shown is derived from consensus dataset in human protein atlas (HPA) which includes a combined expression data from both HPA and GTEx (Genotype-Tissue transcriptome expression) databases. nTPM denotes means expression values from different samples of the same tissue. Colour coding is based on grouping of tissues based on having common functional features. Image credit: Human Protein Atlas, version 22. (https://www.proteinatlas.org/ENSG00000065883-CDK13/tissue#rna_expression).

3.1.1 *CDK13* mutations in patients

Association of mutations in *CDK13* with human developmental disorders was reported by a whole exome sequencing (WES) study of 1891 probands, to which our lab was part of [176]. This study identified *CDK13* mutations in seven patients which manifested as syndromic type of CHD

[176]. These mutations were of *de novo* missense type in six of them whereas for the seventh patient, it was undetermined. These mutations were clustered in protein kinase domain (PKD) of CDK13 and all patients had characteristic facial features such as high arched eyebrows, broad forehead and nasal root and drooping eyelids. All these patients also had CHD (ASD n = 5, VSD n = 2, pulmonary valve abnormality n = 2) as well as developmental delay. These findings in CDK13-patients led to labelling this as CHDFIDD (congenital heart disease, dysmorphic facial features, intellectual developmental disorder) and CDK13-related disorder later on [213]. Some other features such as microcephaly, structural brain lesions, clinodactyly, hypermobility of joints and hypotonia were also noted in some of them (Figure 3:3).

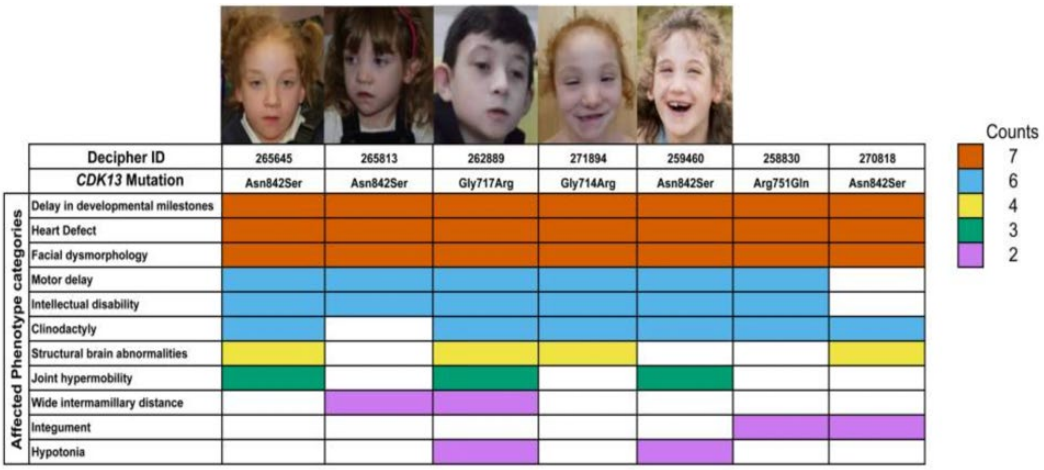


Figure 3:3 Missense mutations of CDK13 as reported for the first time in seven unrelated patients. All cases were having CHD along with specific facial features and developmental delay. In six of them, there was motor delay, intellectual disability, and clinodactyly. Structural brain anomalies were present in 4 of them whereas other features such as widely spaced nipples, defects of integumentary system and hypotonia were each present in two out of six patients. The orange colour shade of the cells denotes if all seven probands share a particular phenotype whereas blue, yellow, green and purple shades represent if only six, four, three or two of the seven probands share that specific phenotype. The photos of the five probands are shown for which prior consent was obtained from parents before publication in the article [176].

After this publication reporting 7 patients, 136 more patients with CDK13 mutations were reported and CHD was present in 58 of them [175, 213-225]. So far, 59 different types of *CDK13*-SNVs have been reported and 36 are clustered in the serine/threonine protein kinase domain (Figure 3:4). The most common CDK13 missense mutation reported to date is N842S which was present in 49 unrelated cases, and 25 of these had a CHD (Table 3:1).

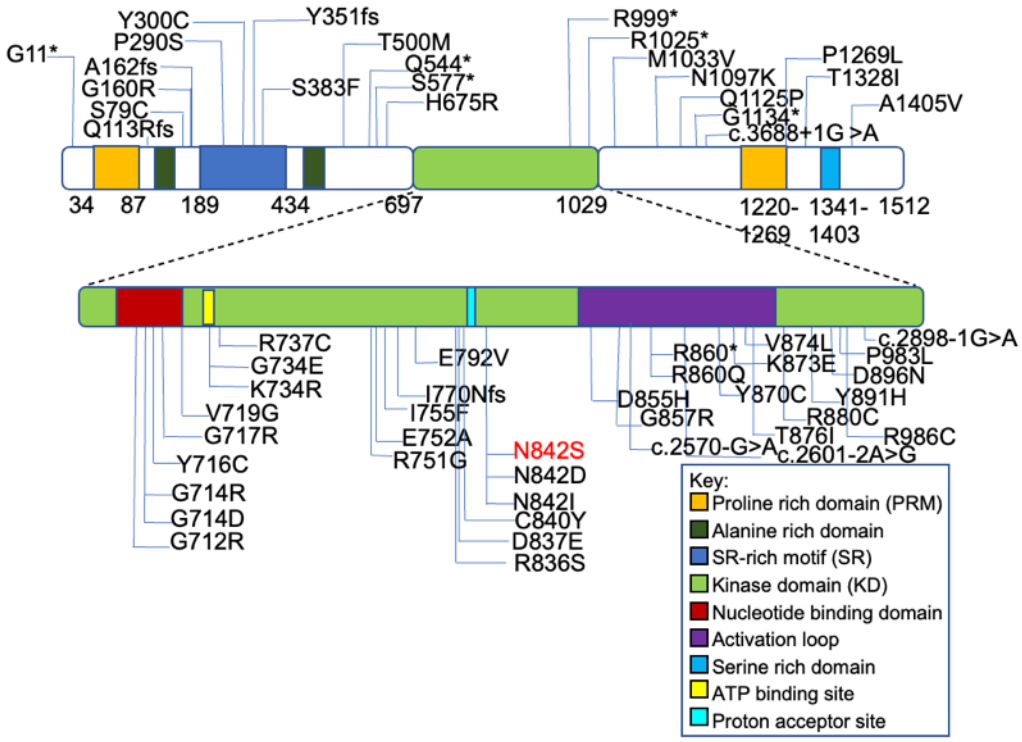


Figure 3:4 Schematic representation of the domain structure of CDK13 and location of the reported SNVs. The N-terminal end contain extended region of serine-arginine (SR) motifs which are involved in RNA processing. Proline-rich motifs (PRMs) are also present which are involved in intracellular protein-protein interaction. At the centre is the kinase domain (KD). Notably most (n = 36) of the variants are clustered into KD. Mutations in CDK13 are associated with syndromic congenital heart defects (s-CHDs) along with developmental delay and slight to moderate microcephaly. The most common mutation (N842S) is shown in red.

Inspecting the Genome Aggregation Database (gnomAD) [226] 41 out of the total 59 *CDK13-SNVs* in patients are not reported to occur (for those reported, allele frequency is mentioned in Table 3:1). The absence of most of these SNVs supports the pathogenicity of these [226, 227]. The constraint metric (i.e., observed / expected metric) for LOF type of SNVs in *CDK13* was 0.32. This indicates that *CDK13* is under selective pressure against LOF type of SNV. For missense type of SNVs in *CDK13,* the constraint metric was 1.08 which indicates that *CDK13* is tolerant to missense mutations [226]. However, the different regions of the protein might have different tolerance to mutations [214]. Within gnomAD, there are only 5 SNVs (with allele frequency reported) in protein kinase (PK) domain and are pathogenic/likely pathogenic [226], which means that PK domain of CDK13 is under great selective pressure against missense variation [214].

3.1.2 Penetrance of CHD in patients with *CDK13* mutations

In all 143 cases with *CDK13* mutation, CHD was present in 58 (40.5%) of them. The predominant CHD was ASD present in 29 individuals, followed by VSD present in 10, pulmonary stenosis (PS) in 10, pulmonary valvular defect in 2, PDA in 4, BAV in 6, LVOTO including AS in 4, hypoplasia of left pulmonary artery (LPA) in 2, patent foramen ovale (PFO) in 2, and dilated pulmonary artery (PA), left ventricular non-compaction (LVNC) each in 1 individual [175, 176, 213-225, 228, 229]. Based on the gender, where reported, for these patients, 64 males (41 being without CHD) and 64 females (32 without CHD) had mutations in *CDK13*.

All the human studies reporting *CDK13*-mutations suggest that even heterozygous mutation of *CDK13* result in developmental disorders affecting predominantly the heart, brain and facial skeleton but with incomplete penetrance [176, 213, 214]. However, homozygous mutation result in syndromic form of CHD with complete penetrance as reported by Acharya *et al* [223] when all siblings with homozygous missense mutation (p.Asn1097Lys) developed BAV along with sensorineural hearing loss, diabetes mellitus and insipidus, gastrointestinal abnormalities and others. Another group working to characterise the role of CDK13 in *Cdk13* knockout mouse recently showed that homozygous LOF mutation is not compatible with life [211]. The deleterious effects of mutated *CDK13* potentially could be due to the less protein present [211] or possible inactivation of its role as a kinase which could even be due to inhibition of Cyclin K-binding to it [206, 207, 214]. Nevertheless, some of the *CDK13* mutations in humans were predicted to have Cyclin K binding but its role as a catalyst was still compromised, hence manifesting as dominant negative mutation [214]. Evidence regards the confirmed role of CDK13 in developmental pathways, and even in other diverse biological processes such as oncogenesis is still lacking and hence is speculation-based [230-232]. Studies regarding molecular characterization of the role of *CDK13* suggest that CDK13 could be involved in the regulation of genes needed at any specific stage of development or in the specific types of body cells [233]. Moreover, normal heart development entails the interaction of several well-regulated signalling pathways which work in coordination with several diverse development networks [2]. Genetic mutations which

result in potential interfering with the functioning of these complex signalling pathways possibly end up as CHD. Such genetic mutations could not only have adverse effect on factors within any specific network but on various other interacting networks [234].

	Mutation	ID	Type	Variant classification	Location	Phenotype/CHD	Reference
1.	p.Gly11*	C2 (F)	NS (*De novo*)	Pathogenic	-	No CHD	Rouxel et al 2022
2.	p.Ser79Cys	301167 (M)	MS	Likely benign	-	VSD; AS	DDD 2017
3.	p.Gln113Argfs* (2.59e-6)	Patient 41 (M)	FS (*De novo*)	Pathogenic	-	No CHD	Morison et al 2023
4.	p.Gly160Arg (9.15e-7)	Patient 29 (F)	MS	Pathogenic VUS (gnomAD)	-	No CHD	Morison et al 2023
5.	p.Ala162Glyfs*108 (4.22e-5)	#1 (11y F)	FS (*De novo*)	Pathogenic	Near the site for canonical arginine salt bridging (p.T160)	No CHD	Van Den Akker et al 2018
6.		#12 (13y M)				No CHD	Van Den Akker et al 2018
7.		Patient 40 (F)	FS			ASD, VSD, PDA, ToF, PA[#]	Morison et al 2023
8.		# 13 (54y M)	FS			No CHD	Van Den Akker et al 2018
9.	p.Pro290Ser (1.45e-6)	265075 (M)	MS	Uncertain	Arginine/ serine rich domain	No CHD	DDD 2017
10.	p.Tyr300Cys (7.22e-7)	293576 (M)	MS	Uncertain	Arginine/ serine rich domain	No CHD	DDD 2017
11.	p.Tyr300*	Male fetus. - 24weeks	NS (*De novo*)	Uncertain	Arginine/ serine rich domain	No CHD (detected on U/S as cystic hygroma with nuchal fold thickening)	Gibbs et al 2023
12.	p.Tyr351Ilefs*93	1 (F)	FS	Pathogenic	Arginine/ serine rich domain	No CHD	Trinh et al 2019
13.	p.Ser383Phe (6.83e-6)	411755 (M)	MS	Uncertain	Arginine/ serine rich domain	No CHD	DDD 2017
14.	p.Thr500Met (3.08e-5) (This patient had mutation in *FOXG1* too)	2 (F)	MS (*De novo* – for *CDK13* but not for *FOXG1*)	Likely benign	-	VSD	Trinh et al 2019
15.	p.Gln544*	3 (M)	NS (*De novo*)	Pathogenic	-	No CHD	Trinh et al 2019
16.		Patient 39 (M)	NS (*De novo*)	Pathogenic	-	No CHD	Morison et al 2023
17.	p.Ser577* (1.20e-6)	-	NS (*De novo*)	Pathogenic		LVOTO	Jin et al, 2017
18.	p.His675Arg	4 (M) (sibling below also had same mutation)	MS	VUS - Non-pathogenic	-	Not available	Trinh et al 2019
19.		Sibling of above			-	Not available	Trinh et al 2019
20.	p.Gly712Arg	5 (M)	MS (*De novo*)	Likely pathogenic	protein kinase domain	No CHD	Trinh et al 2019
21.	p.Gly714Cys	A10 (M)	MS (*De novo*)	Probably damaging	protein kinase domain	No CHD	Rouxel et al 2022
22.	p.Gly714Arg c.2140G>C	271894 (F)	MS (*De novo*)	Probably damaging	Nucleotide binding domain of protein kinase domain	ASD	Sifrim et al 2016
		Patient 1					Hamilton et al 2018

23.	p.Gly714Asp	Individual 6 (11y F)	MS (*De novo*)	Probably damaging	PK domain	ASD	Van Den Akker et al 2018
24.		A9 (F)	MS (*De novo*)	Probably damaging		CHD (PAS)	Rouxel et al 2022
25.	p.Gly714Arg	Patient 24 (M)	MS	Probably damaging		No CHD	Morison et al 2023
26.	p.Tyr716Cys	6 (M)	MS (*De novo*)	Likely pathogenic		No CHD; Abnormal facial shape	Trinh et al 2019
27.	p.Gly717Arg	Patient 1 (male)	MS (*De novo*)	Pathogenic	Nucleotide binding domain of protein kinase domain	No CHD	Uehara et al 2018
28.		Patient 3 (M)				No CHD;	Uehara et al 2018
29.		262889 (DDDP111394)				CHD (VSD & Pulmonary valve abnormality)	Sifrim et al 2016
		Patient 2 (Male)					Hamilton et al 2018
30.	p.Gly717Arg mosaic	DDD4K.02553 (259077) (patient 3-F)				No CHD	Hamilton et al 2018
31.	p.Gly717Arg	260858 (M)				No CHD	DDD 2017
32.		261734 (M)				No CHD	DDD 2017
33.		304462 (M)				ASD; PS	DDD 2017
34.		383341 (F)				No CHD	DDD 2017
35.		Mother				No CHD	Cui et al 2021
36.		Son				No CHD	Cui et al 2021
37.		B2 (M)				ASD	Rouxell et al 2022
38.		Patient 19 (F)			Nucleotide binding domain of protein kinase domain	No CHD	Morison et al 2023
39.		Patient 20 (F)				No CHD	Morison et al 2023
40.		Patient 21 (F)				No CHD	Morison et al 2023
41.		Patient 22 (F)				ASD, PS, aortopulmonary window	Morison et al 2023
42.	p.Val719Gly	DDD4K.04200 (261411) (Patient 4 – F)	MS(*De novo*)	Pathogenic	Nucleotide binding domain of protein kinase domain	No CHD	Hamilton et al 2018
43.	p.Ala732Thr	A1 (M)	MS (*De novo*)	Probably damaging	ATP binding site of PK domain	CHD (PDA)	Rouxell et al 2022 Morison et al 2023
44.	p.Lys734Arg	DDD4K.00408 264961 (patient 5 – F)	MS (*De novo*)	Probably damaging	ATP binding site of PK domain	No CHD	Hamilton et al 2018
45.		Patient 30 (F)	MS (*De novo*)	Probably damaging	ATP binding site of PK domain	No CHD	Morison et al 2023

46.	p.Lys734Glu	1008 (M)	MS (*De novo*)	Probably damaging	ATP binding site of PK domain	ASD; Abnormal TV, Ebstein's anomaly;	Bostwick et al 2017
47.	p.Arg737Cys	Individual 7 (13y F)	MS (*De novo*)	Probably damaging	PK domain	No CHD	Van Den Akker et al 2018
48.	p.Arg751Gln (2.41e-6)	258830 (Patient 6 –F)	MS (*De novo*) (also had de novo missense variant in TCF12)	Pathogenic		ASD, VSD	Sifrim et al 2016 Hamilton et al 2018
49.	p.Glu752Ala	A4 (F)	MS (*De novo*)	Probably damaging		No CHD	Rouxel et al 2022
50.	p.Ile755Phe	Patient 34 (M)	MS	Probably damaging		PFO with heart murmur	Morison et al 2023
51.	p.Ile770AsnfsTer4 (769 E/EX)	259855 (M)	FS	Uncertain		No CHD	DDD 2017
52.	p.Glu792Val	Not mentioned in the article except in the schematic	MS	Probably damaging		Not mentioned in the article	McRae J et al DDDS Nature 2017
53.	p.Arg836Ser	307568 (F)	MS (HET)	Pathogenic		PDA	DDD 2017
54.	p.Asp837Glu	Patient 32 (M)	MS			No CHD	Morison et al 2023
55.	p.Cys840Tyr	Patient 36 (F)	MS			No CHD	Morison et al 2023
56.	p.Asn842Ser	265645 (Patient 7 – F)	MS (*De novo*)	Probably damaging		VSD	Sifrim et al 2016 Hamilton et al 2018
57.		265813 (Patient 8 – F)				ASD, PS	Sifrim et al, 2016 Hamilton et al 2018
58.		270818 (Patient 10 – M)				ASD	Sifrim et al 2016 Hamilton et al 2018
59.		259460 (Patient 9 – F)				Secundum ASD	Sifrim et al 2016 Hamilton et al 2018
60.		1001(F)				ASD, hypoplastic LPA	Bostwick et al 2017
61.		1002 (F)				ASD	Bostwick et al 2017 Morison et al 2023
62.		1003 (M)				No CHD	Bostwick et al 2017
63.		1004 (M)				Hypoplastic LPA, dilated PA	Bostwick et al 2017
64.		1005 (F)				No CHD	Bostwick et al 2017

65.		1006 (F)				VSD,TOF	Bostwick et al 2017
66.		1007 (M)				No CHD	Bostwick et al 2017
67.		Patient 2 (F)				No CHD	Uehara et al 2018
68.		Individual 1 (M)				No CHD	Van Den Akker et al 2018
69.		Individual 2 (F)				No CHD	Van Den Akker et al 2018
70.		Individual 3 (F)				No CHD	Van Den Akker et al 2018
71.		Individual 4 (female)				No CHD	Van Den Akker et al 2018
72.		Individual 5 (M)				No CHD	Van Den Akker et al 2018
73.		7 (A8) (M)				No CHD	Trinh et al 2019
74.		Single patient – (F) (Case report)				No CHD	Yakubov et al 2019
75.		276658 (M)				No CHD	DDD 2017
76.		304950 (M)				No structural CHD; endocarditis	DDD 2017
77.		328104 (F)				ASD	DDD 2017
78.		384040 (F)				ASD	DDD 2017
79.		A3 (F)				ASD	Rouxel et al 2022
80.		A6 (F)				CHD (PFO)	Rouxel et al 2022
81.		A8 (M)				No CHD	Rouxell et al 2022 Morison et al 2023
82.		B1 (F)				ASD; PAS	Rouxell et al 2022
83.		B3 (F)				No CHD	Rouxell et al 2022
84.		B7 (F)				No CHD	Rouxell et al 2022 Morison et al 2023
85.		B10 (F)				CHD (PS)	Rouxell et al 2022
86.		C1 (M)				CHD (VSD & BAV)	Rouxell et al 2022
87.		331720 (Patient 12-F) (non-DDD)-by WES at Bergen	MS (*De novo*)	Probably damaging		CHD (ASD and/or VSD)	Hamilton et al 2018
88.		NA (Patient 11-F) (non-DDD)-by WES at MRC oxford				CHD (ASD and/or VSD);	Hamilton et al 2018

89.	p.Asn842Ser	1009 (M) adult 38yrs	MS			BAV, AS and aortic insufficiency, LVNC; sick-sinus syndrome.	Bostwick et al 2017 Morison et al 2023
90.		Patient 1	MS			No CHD	Morison et al 2023
91.		Patient 2				No CHD	Morison et al 2023
92.		Patient 2				No CHD	Morison et al 2023
93.		Patient 4 (M)				IA communication	Morison et al 2023
94.		Patient 6				No CHD	Morison et al 2023
95.		Patient 8 (M)				ASD, PS	Morison et al 2023
96.		Patient 10 (M)				ASD	Morison et al 2023
97.		Patient 11				No CHD	Morison et al 2023
98.		Patient 12 (M)				IA communication, PS	Morison et al 2023
99.		Patient 13				No CHD	Morison et al 2023
100.		Patient 14 (M)	MS			ASD	Morison et al 2023
101.		Patient 15	MS			No CHD	Morison et al 2023
102.		Patient 16 (M)				ASD	Morison et al 2023
103.		Patient 17				No CHD	Morison et al 2023
104.		-	MS (*De novo*)			CTD	Jin et al, 2017
105.	p.Asn842Ile	8 (F)	MS	Likely pathogenic		ASD	Trinh et al 2019
106.	p.Asp855His	Patient 8 (F)	MS (*De novo*)	Likely pathogenic	Activation loop of PK domain	No CHD	Carneiro et al 2018
107.		259845 (M)				No CHD	DDD 2017
108.		287314 (M)				No CHD	DDD 2017
109.	p.Arg855Cys	Patient 37 (M)		Likely pathogenic		No CHD	Morison et al 2023
110.	p. Gly857Arg	B6 (M)		Likely pathogenic		ASD; PAS	Rouxell et al 2021
111.	p.Arg860Gln	DDDK.00381 (264613 – Patient 13 F)		Probably damaging		No CHD	Hamilton et al 2018
112.		Patient 28 (F)	MS (*De novo*)			PDA	Morison et al 2023
113.	p.Arg860* (*de novo* missense variant in the SHANK2 gene too) (1.37e-6)	-	NS (Paternally transmitted)	Probably damaging		unknown	Wang et al 2020
114.	p.Tyr870Cys (1.59e-6)	C3 (F)	MS (*De novo*)	Pathogenic		ASD	Rouxel et al 2022 Hildebrand et al 2020 Morison 2023
115.	p.Lys873Glu	300881(M)	MS	Likely pathogenic		Sub valvular AS	DDD 2017
116.	p.Val874Leu	DDD4K.02539 (270857- Patient 14 F)	MS (*De novo*)	Possibly damaging		No CHD	Hamilton et al 2018
117.	p.Thr876Ile	A7 (M)	MS (*De novo*)	Probably damaging	PK domain	CHD (ASD; PAS)	Rouxel et al 2022
118.	p.Arg880Cys	Individual 8 (9y 10m M)	MS (*De novo*)	Probably damaging		No CHD	Van Den Akker et al 2018
119.		Patient 25 (F)	MS	Probably damaging		ASD[#]	Morison et al 2023

120.		Patient 26 (M)	MS	Probably damaging		No CHD	Morison et al 2023
121.	p.Tyr891His	284153 (M)	MS (*De novo*)	Pathogenic		No CHD	DDD 2017
122.	p.Asp896Asn (6.57e-6)	301509 (Patient 15 F)	MS (*De novo*)	Probably damaging		No CHD	Hamilton et al 2018
123.	p.Pro983Leu	355599 (F)	MS (*De novo*)	Likely pathogenic		TGA with VSD	DDD 2017
124.	p.Arg986Cys	Patient 35 (M)	MS	Likely pathogenic		No CHD	Morison et al 2023
125.	p.Arg999* (1.33e-5)	Individual 14 (9y M)	NS (*De novo*)	Possibly pathogenic		No CHD	Van Den Akker et al 2018
126.	p.Arg1025*	Individual 15 (3y 4m F)	NS (*De novo*)	Possibly pathogenic		No CHD	Van Den Akker et al 2018
127.	p.Met1033Val (5.58e-6)	9 (M)	Start_lost	VoUS/Benign	-	No abnormal phenotype	Trinh et al 2019
128.	p.Asn1097Lys (3.41e-5)	(Patient V1: F)	MS (HOMO) – inherited from unaffected parents	Possibly damaging	-	BAV; died due to cardiac arrest	Acharya et al 2021
129.		(Patient V3: F)				BAV	Acharya et al 2021
130.		(Patient V4: F)				BAV	Acharya et al 2021
131.		(Patient V2: M)	MS (HET)			Normal	Acharya et al 2021
132.	p.Gln1125Pro (3.10e-5)	10 (M)	MS	Benign/(VoUS)	_	No abnormal phenotype	Trinh et al 2019
133.	p.Gly1134*	-	NS (LOF)-HET	VoUS	-	LVOTO	Jin et al, 2017
134.	p.Pro1269Leu (8.68e-6)	281338 (M)	MS	Uncertain	Proline rich region	No CHD	DDD 2017
135.	p.Thr1328Ile	Not mentioned	MS	VoUS	-	Not available	Trinh et al 2019
136.	p.Ala1405Val (6.84e-7)	301623 (F)	MS (*De novo*)	Uncertain	-	No CHD	DDD 2017
137.	c.2898-1G>A	DDD4K.02000 (271710- Patient 16) (F)	Canonical Splice acceptor site variant (*De novo)*	VoUS	Splice site	No CHD	Hamilton et al, 2018
138.	c.2570-G>A	A2 (M)	*De novo* variant	VoUS	PK domain	ASD	Rouxell et al 2022
139.	c.2601-2A>G	Individual 9 (13y F)	Splice-acceptor variant (*De novo*)	Pathogenic	Splice-acceptor site in PK domain	PDA	Van Den Akker et al 2018
140.		Individual 10 (13y F)	Splice-acceptor variant (*De novo*)	Possibly Pathogenic	Splice-acceptor site in PK domain at aa 867	No CHD	Van Den Akker et al 2018
141.	c.3688 + 1 G > A	Patient 38 (M)	Splice-acceptor variant (*De novo*)	Possibly Pathogenic	-	BAV with dilated aortic root & dilated ascending aorta	Morison et al 2023
142.	*CDK13* Het mutation (specific mutation not reported)	Single patient (8y M)	_	_	-	Pulmonary valve defect	Kacpura et al 2021 (Conference abstract)/ Molecular Genetics and Metabolism (2021)
143.	*CDK13* mutation (Details not known)	1 patient (gender unknown)	_	_	_	Valvular PS	Weaver et al 2022

Table 3:1 Reported patients with CDK13 SNVs. ASD: atrial septal defect; VSD: ventricular septal defect; AS: aortic stenosis; PS: pulmonary stenosis; PDA: patent ductus arteriosus; LPA: left pulmonary artery; PAS: pulmonary artery

stenosis; CHD: congenital heart disease; CTD: conotruncal defect; VoUS: variant of unknown significance; BAV: bicuspid aortic valve; TGA: transposition of great arteries; PFO: patent foramen ovale; PA: pulmonary atresia; PAS: pulmonary artery stenosis; LNVC: left ventricular non-compaction; LVOTO: left ventricular outflow tract obstruction, het: heterozygous; homo: homozygous; MS: missense; NS: non-sense; FS: frameshift; LOF: loss of function; SNV: single nucleotide variant. M/F in the ID column denotes gender of the patient where known. Age of the patient also shown where known. "-" denotes unavailability of the information. Allele frequency from gnomAD where available is given within parentheses in the column for "mutation".

3.1.3 Rationale for this study

Whole exome study on S-CHD and NS-CHD patients conducted by Sanger Institute in collaboration with our lab discovered *CDK13* as one of the three novel genes (others being *PRKD1* and *CHD4*) associated with CHD[176]. This project aimed at characterizing the role of CDK13 in heart development and CHD in case of loss of function (LOF) mutation of *Cdk13*, using *Cdk13*^{tm1b} mouse model (as described in section 2.1.1, Figure 2:1).

3.2 AIM OF THIS PROJECT

In order to characterise the role of CDK13 in heart development and CHD, *in vivo* studies on transgenic mouse model carrying LOF mutation were carried out. For phenotypic characterisation of the role of CDK13 in heart development and CHD, a recently acquired HREM equipment was used which enabled viewing the 3D morphology of mouse hearts with high resolution.

Moreover, it seemed highly pertinent to identify the targets that were regulated by *Cdk13*. The use of a mouse model to decipher the molecular pathways regulated by *Cdk13* was expected to be very useful in understanding the normal heart development as well as the development of CHD. In order to achieve this, RNA-Seq transcriptome analysis was planned to elucidate the role of *Cdk13* downstream in heart development and CHD. The results obtained from this were aimed for planning further experiments to provide insights into the role of *Cdk13* downstream.

3.2.1 Hypotheses for the project:

Hypotheses for this project were:

1. LOF-mutation in one or both alleles of *Cdk13* would result in CHD with variable penetrance.
2. LOF mutation of *Cdk13* in heterozygous state would be compatible with life, whereas the homozygous LOF mutation of *Cdk13* would cause embryonic lethality.
3. *Cdk13* mutation would modulate expression of the downstream targets as relevant to the heart development and CHD.

3.3 RESULTS

3.3.1 Mice with heterozygous mutation are viable and fertile, but homozygous mutation is embryonically lethal

The goal for this project was to set up HET X HET crosses to get homozygous null (*Cdk13*$^{tm1b/tm1b}$) embryos in addition to WT (*Cdk13*$^{+/+}$) and heterozygous (*Cdk13*$^{tm1b/+}$) embryos whereas for maintaining the colony, HET X WT crosses were set up. Figure 3:5 is a representative image of a typical result of genotyping of the *Cdk13*^{tm1b} mouse line. For each sample, three different PCR reactions were performed: a WT reaction for the WT allele, a MUT reaction for the detection of the mutant allele and a LacZ reaction was performed to detect the presence of *LacZ* in the mutant allele. In WT sample, only WT band was visible whereas in *Cdk13*$^{tm1b/+}$ (HET), WT, MUT as well as the LacZ bands were seen (Figure 3:5). Genotype distribution of the collected embryos at E12.5 (for transcriptomics) and E15.5 (for HREM) is shown in Table 3:2. The total

number of embryos collected at E12.5 from HET X HET crosses were 267, of which 70 (26.2%) were WT, 164 (61.4%) were HET and 33 (12.4%) were HOMO. At E15.5, the total embryos collected were 141 which included 52 (36.9%) WT, 81 (57.4%) HET and 8 (5.7%) HOMO. On lethality assessment based on genotype of the embryos collected, we found that the observed ratios were less than the expected Mendelian ratios and that this difference was statistically significant at both E10.5 and E15.5 (P = 0.000005 & P = 0.0000002 respectively, Chi square test), indicating that loss of both alleles of *Cdk13* is not compatible with life (Table 3:2). Comparing the two stages, it was observed that very few homozygous mice survive to E15.5 and the difference was significant (P = 0.0196, Pearson's Chi square test) (Table 3:2). After breeding and genotyping 866 mice (excluding the 267 and 141 embryos at E12.5 and E15.5, Table 3:2) from this colony (data obtained from BSU), no live-born homozygous ($Cdk13^{tm1b/tm1b}$) pups were obtained, but in the age window of E10.5 to E15.5, forty nine surviving null embryos (E10.5=7; E11.5 = 1; E12.5 = 33; E15.5 = 8) were isolated.

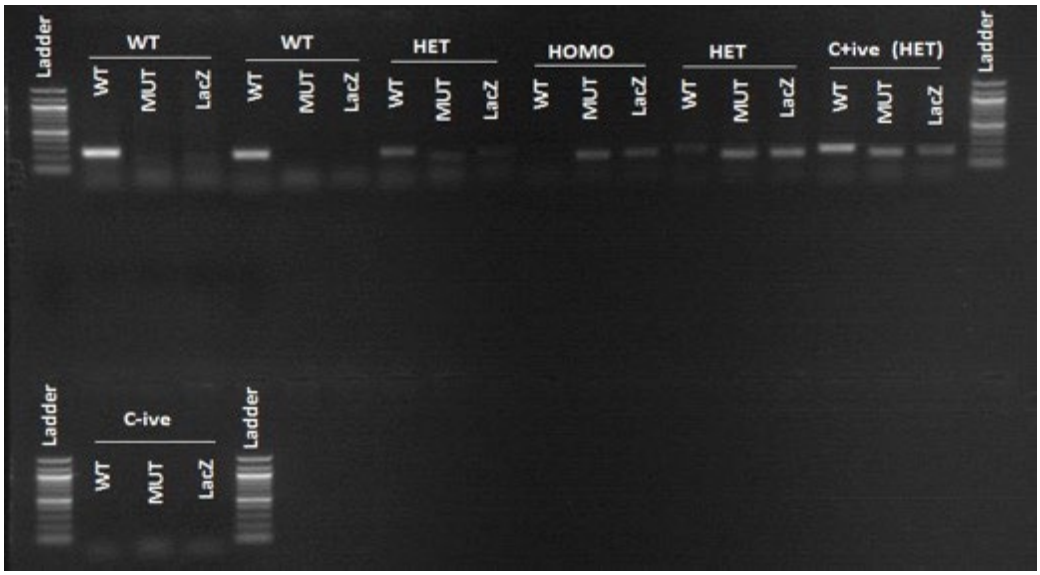


Figure 3:5 Cdk13^{tm1b} genotyping. Agarose gel picture showing genotyping results for WT, HET and HOMO samples. A HET sample is used as positive control and water-only sample as negative control, with ladder at the beginning and end of each gel lane. Expected band sizes are: WT=250bp, MUT= 200bp and LacZ = 108bp. Ladder: 100bp (Invitrogen®).

	HET X HET		WT	HET	HOMO	Chi-square test
Cdk13^{tm1b}	**E12.5**	**Expected**	66.75 (25%)	133.5 (50%)	66.75 (25%)	*P* = 0.000005
		Observed	70 (26.2%)	164 (61.4%)	33 (12.4%)	
	E15.5	**Expected**	35.25 (25%)	70.5 (50%)	35.25 (25%)	*P* = 0.0000002
		Observed	52 (36.9%)	81 (57.4%)	8 (5.7%)	
Pearson's Chi square test				*P* = 0.0196		

Table 3:2 Genotype distribution of Cdk13^{tm1b} embryos. Cdk13^{tm1b} mouse embryos were collected from HET X HET crosses at E12.5 and E15.5. Chi-square test shows that there is statistically significant difference between the observed and expected (Mendelian) ratios at both E12.5 and E15.5 (P < 0.05). Comparing the genotype ratios at both stages shows that fewer homozygous embryos are obtained at E15.5 than E12.5 (P < 0.05, Pearson's Chi square test).

3.3.2 External phenotyping in *Cdk13*^{tm1b} mouse line

External phenotyping of E12.5 (n = 70 WT, 164 HET, 33 HOMO) and E15.5 embryos (n = 52 WT, 81 HET, 8 HOMO) from *Cdk13*^{tm1b} mouse line was carried out at the time of tissue collection (**Table 3:3**). This phenotyping was carried out before genotyping.

#	ID	Age	Genotype	External Phenotype
1.	C13.17.8	E15.5	HOMO	Midfacial aplasia; sac like big atria
2.	C13.20.9	E15.5	HOMO	Growth retarded - abnormal looking embryo; dead - white heart
3.	C13.20.109	E15.5	HOMO	Growth retarded; dead in utero - heart very white
4.	C13.27.3	E12.5	HET	Growth retarded; white - limb plates visible
5.	C13.27.7	E12.5	HET	Growth retarded – dead embryo
6.	C13.29.5	E12.5	HET	Boot shaped heart; growth retarded
7.	C13.31.3	E12.5	HOMO	Massive pericardial effusion; growth retarded; boot shaped heart
8.	C13.31.6	E12.5	HOMO	Pericardial effusion; growth retarded
9.	C13.31.7	E12.5	HET	Massive pericardial effusion extending to liver
10.	C13.33.6	E12.5	HOMO	Growth retarded; heart was U-shaped,
11.	C13.34.2	E12.5	HOMO	Growth retarded; very tiny heart collected
12.	C13.35.9	E12.5	HET	Growth retarded; white/dead embryo
13.	C13.36.1	E12.5	HOMO	Growth retarded but alive
14.	C13.36.8	E12.5	HOMO	Growth retarded but alive
15.	C13.37.2	E12.5	HET	Growth retarded but alive
16.	C13.37.6	E12.5	HET	Growth retarded and dead in utero
17.	C13.38.9	E12.5	HET	Mildly growth retarded
18.	C13.39.1	E12.5	HOMO	Growth retarded
19.	C13.39.7	E12.5	HOMO	Hydrocephalus & mid facial aplasia
20.	C13.39.9	E12.5	HOMO	Mid facial aplasia
21.	C13.40.8	E12.5	HOMO	Growth retarded - smaller size as compared to others in the litter
22.	C13.40.10	E12.5	HOMO	Mid facial aplasia
23.	C13.42.7	E12.5	HET	Incompletely fused maxillae – midfacial cleft
24.	C13.46.7	E15.5	HOMO	Growth retarded with midfacial aplasia; white(dead?; fresh blood can be seen)
25.	C13.53.3	E12.5	HOMO	Mid facial aplasia
26.	C13.56.5	E12.5	HET	Oedema at the back
27.	C13.56.7	E12.5	HOMO	Haemorrhagic spots in cranial region & back of neck; growth retarded
28.	C13.56.8	E12.5	HOMO	Growth retarded; mid facial aplasia – pericardial effusion
29.	C13.57.8	E15.5	HET	Right side anophthalmia, tongue protruded, mildly growth retarded
30.	C13.58.6	E12.5	HOMO	Growth retarded and dead in utero
31.	C13.65.3	E12.5	HOMO	Growth retarded

32.	C13.65.4	E12.5	HET	Growth retarded
33.	C13.88.1	E15.5	HOMO	Growth retarded, Dead
34.	C13.93.8	E15.5	HOMO	Growth retarded - probably dead, mid facial aplasia; lobster claw-right hand/ectrodactyly
35.	C13.100.1	E12.5	HOMO	Growth retarded; midfacial aplasia
36.	C13.104.2	E15.5	WT	Left side anophthalmia/fused eyelids
37.	C13.108.5	E12.5	HOMO	Midfacial aplasia
38.	C13.111.2	E12.5	HOMO	Growth retarded
39.	C13.111.8	E12.5	HOMO	Growth retarded, midfacial aplasia,
40.	C13.115.6	E12.5	HOMO	Growth retarded; midfacial aplasia
41.	C13.115.8	E12.5	HOMO	Growth retarded/dead; delicate tissues

Total WT (E12.5 & E15.5)		Total HET (E12.5 & E15.5)		Total HOMO (E12.5 & E15.5)	
122		245		41	
Normal WT	**Abnormal WT**	**Normal HET**	**Abnormal HET**	**Normal HOMO**	**Abnormal HOMO**
121	**1**	**233**	**12**	**13**	**28**

Table 3:3 Abnormal external phenotypes of Cdk13^{tm1b} embryos. Table showing abnormal phenotypes as noted in Cdk13^{tm1b} mouse embryos harvested at E12.5 & E15.5 (n = 122 WT, 245 HET and 41 HOMO). Based on external phenotyping, only 1 out of 121 WT embryos looked abnormal whereas 12 (out of 233) HET embryos and 28 (out of 41) HOMO embryos were having abnormal external phenotype. "E" denotes embryonic day in mouse.

At the time of collection at E12.5 and E15.5, 9 out of 245 heterozygous (*Cdk13$^{tm1b/+}$*) and 21 out of 41 homozygous (*Cdk13$^{tm1b/tm1b}$*) embryos were growth retarded and/or dead (Figure 3:6-B compared with A). Some of these and remaining homozygous (*Cdk13$^{tm1b/tm1b}$*) embryos were having mostly other abnormalities, commonly midfacial aplasia, and/or pericardial effusion (Table 3:3). In one homozygous (*Cdk13$^{tm1b/tm1b}$*) embryo, lobster claw deformity of hand was also noted (yellow arrow in Figure 3:6-G).

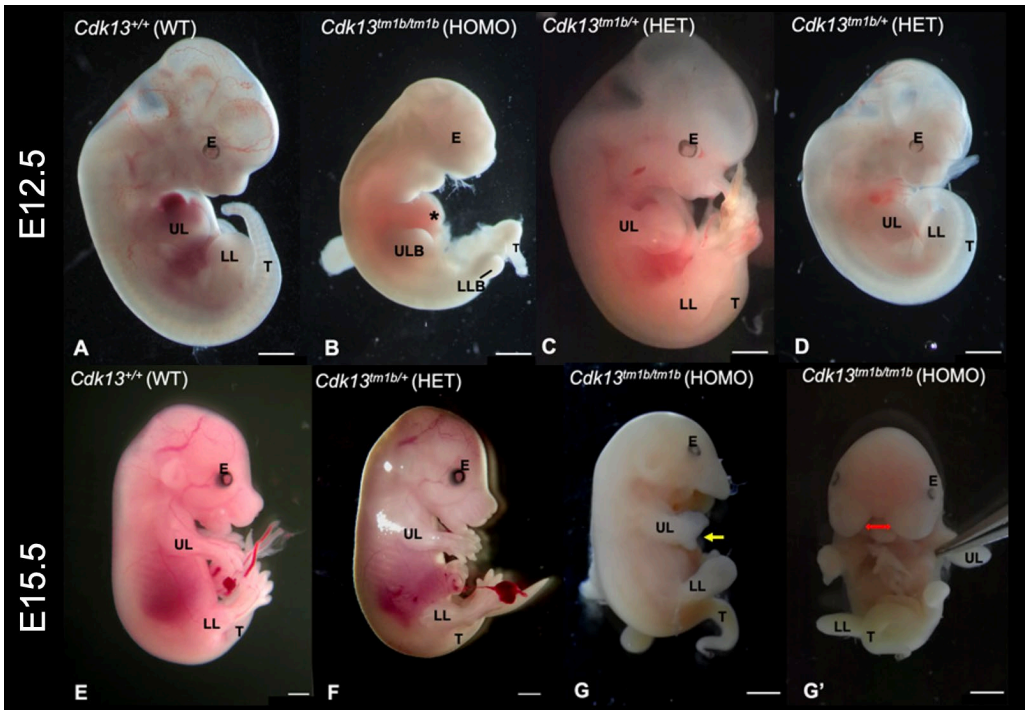


Figure 3:6 Intrauterine growth retardation and lobster claw deformity of right hand in Cdk13^{tm1b} mouse. A-D: Representative images of WT (A), Cdk13$^{tm1b/tm1b}$ (HOMO) (B) and Cdk13$^{tm1b/+}$ (HET) embryos (C), collected at E12.5. Some of the Cdk13$^{tm1b/+}$ (HET) embryos at E12.5 were growth retarded (D). E-G,G': Representative images of WT (E), Cdk13$^{tm1b/+}$ (HET) (F) and Cdk13$^{tm1b/tm1b}$ (HOMO) embryos (G,G'), collected at E15.5. The embryo in G (lateral view) & G' (ventral view) is retarded and has midfacial cleft (denoted by red arrow in G'). The same embryo has lobster claw deformity as well (denoted by yellow arrow in G). Scale bar: 1mm for all images. ULB: upper limb bud; UL: upper limb; LLB: lower limb bud; LL: lower limb; T: tail; E: eye.

Mid-facial aplasia/cleft was observed in 13 *Cdk13$^{tm1b/tm1b}$* (HOMO) embryos (Figure 3:6-G', Figure 3:7), whereas in only one *Cdk13$^{tm1b/+}$* (HET) embryo, there was a groove (shallow depression) at the same site i.e., the site of fusion of medial nasal prominences (Table 3:3).

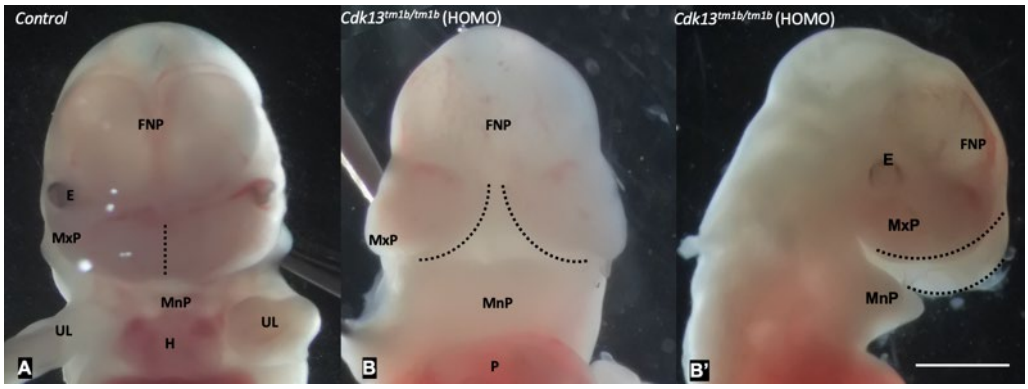


Figure 3:7 Midfacial aplasia seen in Cdk13$^{tm1b/tm1b}$ (HOMO) hearts at E12.5. There is non-fusion of medial nasal prominences (dotted lines in B & B') denoted by a gap between the dotted lines in the Cdk13$^{tm1b/tm1b}$ (HOMO) heart. The medial nasal processes are growing laterally instead of medially leading to non-fusion of medial nasal processes (MNP) and resulting is midfacial cleft. In WT mouse (A), maxillary prominences (MxP) from peripheral regions are extending forward to fuse with nasal prominences and thereby contribute to the formation of maxilla. The nasal prominences also fuse together as part of the normal face development. Heart is visible in control heart but is invisible due to pericardial effusion in the Cdk13$^{tm1b/tm1b}$ (HOMO) heart. Scale bar: 1mm for all images. Mxp: maxillary prominence, MnP: mandibular prominence, FNP: frontonasal prominence, H: heart, P: pericardial cavity, UL: upper limb, LL: lower limb, E: eye.

Hydrocephaly was observed in one adult female *Cdk13$^{tm1b/+}$* (HET) and one E12.5 *Cdk13$^{tm1b/tm1b}$* (HOMO) embryo. Hydrocephaly in adult female *Cdk13$^{tm1b/+}$* (HET) was so severe that it caused pressure atrophy of the brain making the mouse very ill and therefore had to be culled (Figure 3:8).

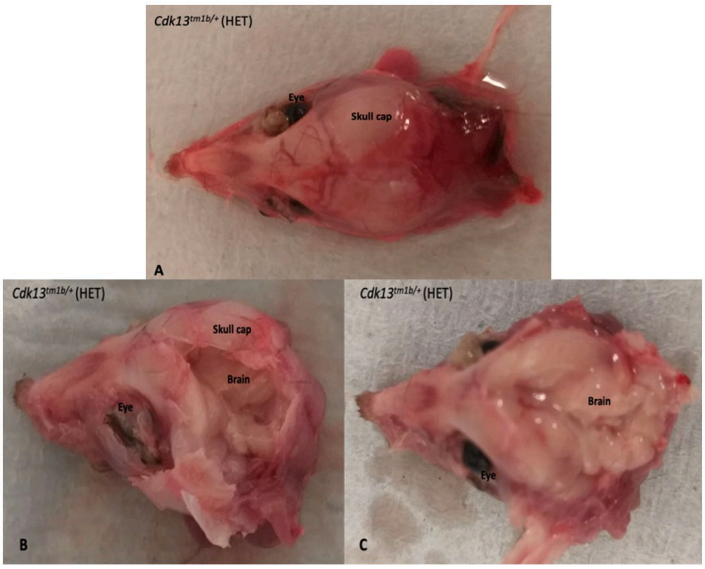


Figure 3:8 Hydrocephaly and brain atrophy. A) superior view of the head with skin/scalp removed collected from adult Cdk13tm1b/+ (HET) female. Removing the cranial vault revealed severe brain atrophy after the cerebrospinal fluid gushed out, leaving an empty space inside the cranial cavity. B-C) Severely atrophied brain tissue visible after moving the bony cranial vault.

In one *Cdk13*$^{tm1b/+}$ (HET) and three *Cdk13*$^{tm1b/tm1b}$ (HOMO) hearts at

E12.5, pericardial effusion was noted (Figure 3:9).

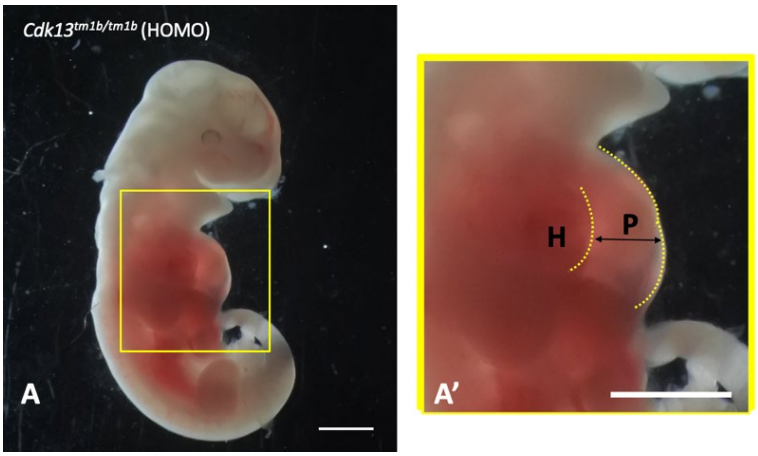


Figure 3:9 Pericardial effusion. In case of Cdk13 mutation, pericardial effusion, as a sign of cardiac failure was noticed commonly in case of Cdk13$^{tm1b/tm1b}$*(HOMO) mutation but was also noticed in case of Cdk13*$^{tm1b/+}$*(HET) mutation. The gap between the dotted lines (black arrow in A') is the distended pericardial cavity. The same embryo was developmentally delayed and there was non-fusion of medial nasal prominences causing mid facial cleft (A). A' is the zoomed-in view of the area bounded by yellow box in image A. Scale bar: 1mm for each image. H: heart, P: pericardial cavity.*

In another *Cdk13*$^{tm1b/+}$ (HET) and one *Cdk13*$^{+/+}$ (WT), anophthalmia was noticed when no palpebral fissure and no ophthalmic tissues could be seen on gross examination (Figure 3:10). No histological assessment was carried out and hence we were unable to comment about presence or absence of ophthalmic tissues inside the orbit.

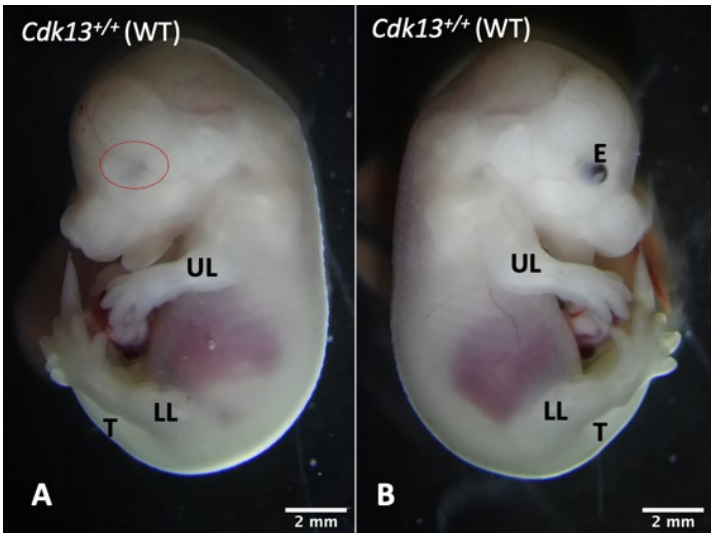


Figure 3:10 Anophthalmia. Representative images of anophthalmia as seen in one WT (A-B – red oval) mouse embryo of left side at E15.5 on gross examination. Scale bar = 2mm. UL: upper limb, LL: lower limb, T: tail, E: eye.

3.3.3 HREM-based phenotypic analysis of E15.5 hearts collected from *Cdk13*^{tm1b} mouse line

E15.5 hearts from *Cdk13*^{tm1b} mice were analysed after generating their 3D models from the z-stack of high resolution 2D images. This analysis was carried out while blind to the genotype. Using HREM, the heart was analysed both externally and internally in different planes. All chambers including the valves were analysed to exclude any morphological abnormality such as an abnormal communication between the different chambers or any pathology related to the valves structure. Interatrial (IA)

communication as open-foramen-ovale was expected to be present as normal finding in all embryos at E15.5 unless there was partial or complete deficiency of the septum primum and/or secundum.

The *Cdk13^{tm1b}* mouse hearts collected at E15.5 and analysed by HREM are detailed in the (Table 3:4).

Genotype	WT	HET	HOMO	Total
Cdk13^{tm1b} (LOF)				
Number (n)	74	47	4	125

Table 3:4 Cdk13^{tm1b} hearts collected at embryonic stage E15.5 and analysed by HREM. HREM-based phenotypic comparison was carried out among Cdk13$^{+/+}$(WT) (n = 74), Cdk13$^{tm1b/+}$ (HET) (n = 47) and Cdk13$^{tm1b/tm1b}$ (HOMO) (n = 4) hearts.

3.3.3.1 The CHD penetrance in heterozygous (*Cdk13$^{tm1b/+}$*) hearts at E15.5 and the observed phenotypes

The penetrance of CHD was 17% (8/47) in *Cdk13$^{tm1b/+}$* (HET) hearts. CHD was not observed in WT hearts at the same stage. The phenotypes observed in HET hearts are given in the Table 3:5.

Cdk13$^{tm1b/+}$ hearts with phenotype			
No.	**Sample ID**	**Phenotype**	**Penetrance**
I.	SID8145_A	pMem. VSD (outlet), BAV (2-sinus type with 2 leaflets, 2 sinuses)	8/47 (17.02%)
II.	SID8145_C	pMem. VSD (inlet and outlet), DORV	
III.	SID8153_B	pMem. VSD (outlet)	
IV.	NID0009_A	pMem. VSD (outlet)	
V.	NID0010_B	pMem. VSD (inlet and outlet), DORV	
VI.	NID0018_B	BAV (2-sinus type with 2 leaflets, 2 sinuses)	
VII.	NID0047_A	Musc. VSD	
VIII.	NID0095_B	Stenotic BAV (2-sinus type with 2 leaflets, 2 sinuses), Quadricuspid PV, Spongy lower VS with small musc.VSD,	

Table 3:5 Phenotypes of the E15.5 mouse hearts with heterozygous (Cdk13$^{tm1b/+}$) mutation. Phenotypic analysis of hearts from mice with Cdk13$^{tm1b/+}$ (HET) mutation showed CHD penetrance of 17% in these hearts. pMem. type of VSD was the most common type of CHD along with other defects such as muscular VSD, DORV, BAV observed in the same or different hearts. However, ~83% hearts with heterozygous (Cdk13$^{tm1b/+}$) LOF-mutation did not show any CHD. RV: right ventricle; PV: pulmonary valve; pMem, perimembranous; Musc, muscular; VS: interventricular septum; VSD: ventricular septal defect; DORV: double-outlet right ventricle; BAV: bicuspid aortic valve.

3.3.3.2 VSD was the most common phenotype in *Cdk13$^{tm1b/+}$* (HET) hearts at E15.5

CHD was noted in 8 out of 47 *Cdk13$^{tm1b/+}$* (HET) hearts and VSD was present in 7 of these 8 hearts, making it as the most common phenotype in these hearts. It was of perimembranous type in 5 hearts (Figure 3:11-B compared with A) and of muscular type in 2 others (red arrow in Figure 3:12 B-D compared with A).

DORV was found in two of these 8 *Cdk13$^{tm1b/+}$* (HET) hearts and in both, there was an associated perimembranous VSD as well (Figure 3:11-B compared to A).

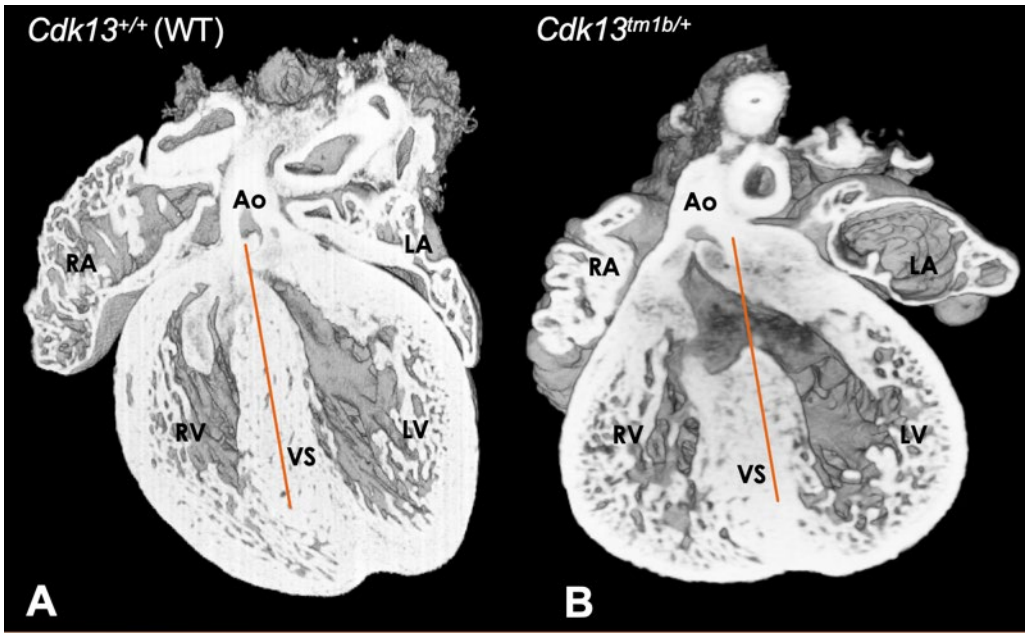


Figure 3:11 Perimembranous VSD with DORV. (A) A coronal section of E15.5 WT mouse heart showing the left and right ventricular chambers separated from each other by VS and aorta originating from LV. (B) Coronal section of a Cdk13$^{tm1b/+}$ (HET) mouse heart (NID8145_C) collected at E15.5 showing pMem. VSD and >50% of the diameter of annulus of aortic valve connecting to morphologic RV instead of LV (based on the orange line extending from VS). RA: right atrium, RV: right ventricle, LA: left atrium, LV: left ventricle, VS: interventricular septum, Ao: aorta.

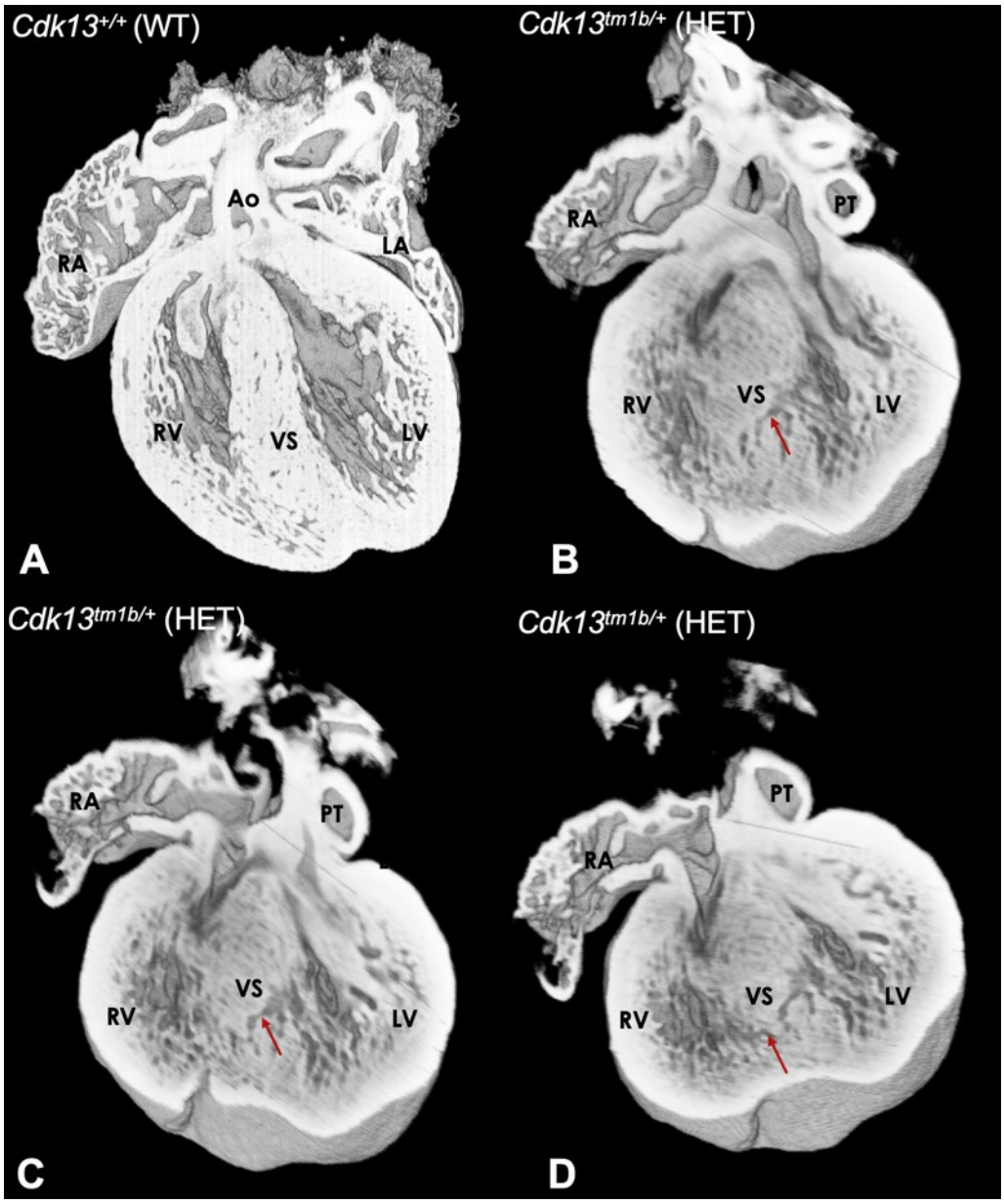


Figure 3:12 Muscular VSD. (A) Coronal section of E15.5 WT mouse heart showing the left and right ventricular chambers separated from each other by VS. (B) Anterior view of a Cdk13$^{tm1b/+}$ (HET) mouse heart collected at E15.5 showing interventricular communication in the muscular part of VS (arrow). (C-D) Anterior of the same Cdk13$^{tm1b/+}$ (HET) heart shown in B viewed in different planes to explore the muscular VSD which has somewhat serpentine course. RA: right atrium, RV: right ventricle, LA: left atrium, LV: left ventricle, VS: interventricular septum.

3.3.3.3 BAV was observed in *Cdk13*$^{tm1b/+}$ (HET) hearts at E15.5

BAV was found in 3 of these 8 *Cdk13*$^{tm1b/+}$ (HET) hearts (Figure 3:13 B-C compared with A) as an isolated defect in one and in combination with perimembranous or muscular VSD in the two others.

The aortic valve leaflets/cusps are normally arranged as right, left and non-coronary, and these were readily seen in both the control and most of the heterozygous hearts (Figure 3:13 A', boxed area in A). However, in three heterozygous (*Cdk13*$^{tm1b/+}$) hearts, the aortic valve was 'bicuspid'. There are three main types of BAV, which vary in the morphology of the leaflets/cusps and the number of sinuses. They are (i) fused type with two cusps/leaflets, three sinuses, two commissures, (ii) 2-sinus BAV which has 2 sinuses, 2 cusps/leaflets and 2 commissures and no raphe, (iii) partial fusion BAV (forme fruste) where there are 3 cusps/leaflets, 3 sinuses and 3 commissures where two commissures are normal and third one is fused (<50%), and there is a small/mini-raphe [111]. In this study, all three (SID8145A, NID18B, & NID95B) E15.5 *Cdk13*$^{tm1b/+}$ (HET) hearts had type 2 BAV (i.e., 2-Sinus BAV), characterised by having two cusps/leaflets and two sinuses, two commissures and absent raphe as shown in Figure 3:13 B & B' (SID8145)_A) and C & C' (NID18_B) compared with A & A' (WT), and Figure 3:14 B and b (NID95_B) compared with A and a (WT). This type of BAV accounts for 5-7% of cases in humans [235]. The left and noncoronary cusps were fused in SID8145A, whereas in NID18B & NID95B, the specific subtype of the 2-sinus BAV was "anteroposterior" with two lateral aortic cusps/leaflets [111]. The left and right coronary arteries were patent in these *Cdk13*$^{tm1b/+}$ (HET) hearts

and were originating separately from both sinuses (red arrows in Figure 3:13 A', B' & C').

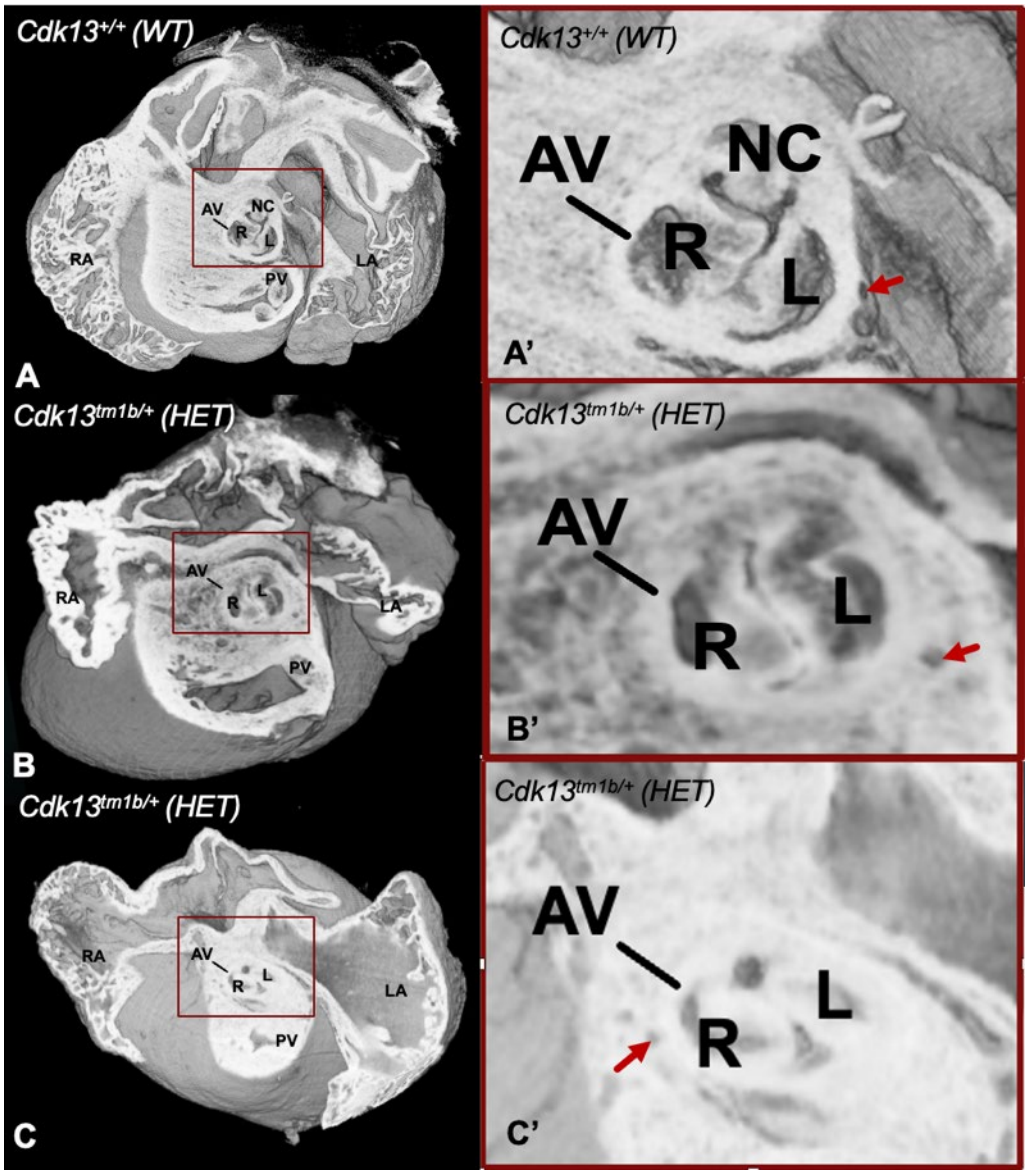


Figure 3:13 Bicuspid aortic valve. A: A superior view of the WT heart showing aortic valve having three leaflets and corresponding three sinuses – right (R), left (L) and non-coronary (NC) sinuses. B-C: Cdk13$^{tm1b/+}$ (HET) hearts having BAV of type 2 (i.e., 2-sinus BAV) [111], characterised by having two cusps and two sinuses, two commissures and absent raphe. A', B' and C' represent the magnified views of the boxed areas shown in A, B & C respectively. Red arrow indicates origin of left coronary artery in A' & B' and of right coronary artery in C'. Both coronary arteries were not feasible to show in the specific planes as selected to show the BAV. RA: right atrium; LA: left atrium; PV: pulmonary valve, AV: aortic valve, R: right AV leaflet and sinus, L: left AV leaflet and sinus, NC: non-coronary AV leaflet and sinus.

3.3.3.4 Quadricuspid pulmonary valve was seen in a heterozygous (*Cdk13*$^{tm1b/+}$) heart at E15.5

A normal pulmonary valve should have 3 leaflets i.e., right, left, and anterior leaflets (Figure 3:14 A and a). In one heterozygous (*Cdk13*$^{tm1b/+}$) heart at E15.5, pulmonary valve with 4 leaflets was seen (Figure 3:14 B and b, denoted by red asterisks). This heart additionally had “2-Sinus” BAV (Figure 3:14 B and b, denoted by black asterisks), spongy ventricular septum in its lower part with a small musc.VSD and prominent trabeculae in right ventricle (Figure 3:14 C-D,d).

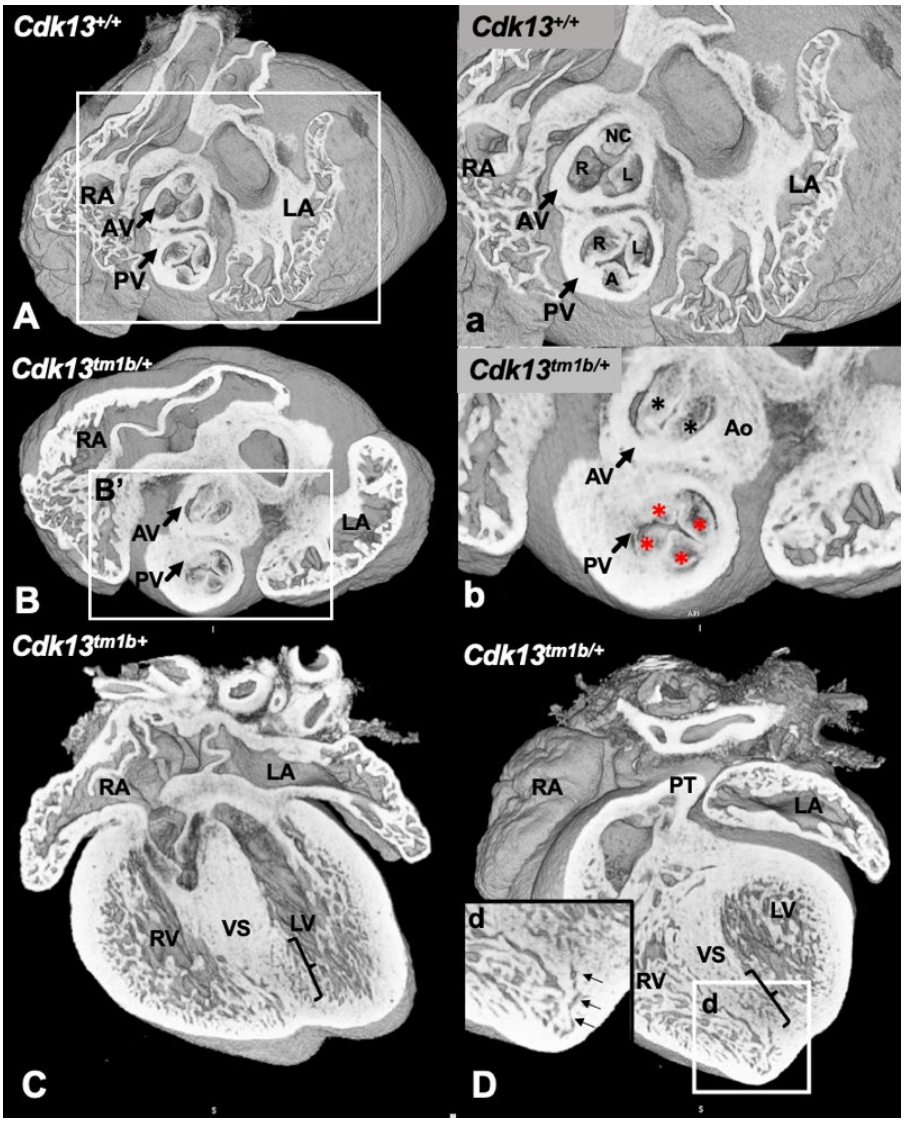


Figure 3:14 Quadricuspid pulmonary valve, BAV and muscular VSD. Superior views of a Cdk13$^{+/+}$ (WT) (A & a) and Cdk13$^{tm1b/+}$ (HET) (B & b) hearts show that the WT heart has normal valves in the outflow region, with 3 valve leaflets (right, left and anterior) in the pulmonary trunk and three leaflets (right, left and non-coronary) can be seen in the aortic valve (a, boxed area in A). In contrast, the heterozygous (Cdk13$^{tm1b/+)}$ heart has an abnormal pulmonary valve where 4 leaflets of the pulmonary valve can be seen (b, boxed area in B, denoted by red asterisks). Additionally, this heart also had 2-Sinus BAV (B and b; denoted by black asterisks). A four-chamber view of a normally septated heterozygous (Cdk13$^{tm1b/+)}$ heart (C) appears to have a spongier interventricular septum in its lower region (denoted by bracket). This spongy interventricular septum can also be seen in a more ventral view in the same heart (D; see bracket). In addition, the boxed area (d) denotes a small muscular ventricular septal defect (shown by black arrows). RA, right atrium; RV, right ventricle; LA, left atrium, LV, left ventricle; VS, interventricular septum; Ao, aorta; PT, pulmonary trunk; AV, aortic valve; PV, pulmonary valve; R, right; L, left; NC, non-coronary.

3.3.3.5 The CHD penetrance in homozygous (*Cdk13$^{tm1b/tm1b}$*) hearts at E15.5 and the observed phenotypes

In case of homozygous LOF mutation of *Cdk13* (*Cdk13$^{tm1b/tm1b}$*), CHD penetrance was 100% (4/4). The different phenotypes seen are given in the Table 3:6 and described in next sections.

Cdk13$^{tm1b/tm1b}$ E15.5 hearts with phenotype			
#	**Sample ID**	**Phenotype**	**Penetrance**
I.	SID8144_A	Complete AVSD (with inlet and outlet VSD) and DORV with doubly committed sub arterial extension of VSD, spongy myocardium.	4/4 (100%)
II.	NID0012_A	Complete AVSD (with inlet & outlet i.e., confluent VSD) and DORV; spongy myocardium with Musc VSD; doubly committed sub arterial extension of VSD.	
III.	NID0016_B	AVSD (with inlet and outlet VSD); DORV; stenotic PA and dilated/large aorta; spongy myocardium with muscular IV communications.	
IV.	NID0099_A	Complete AVSD (with inlet and outlet VSD) and DORV.	

Table 3:6 Phenotypic analysis of E15.5 hearts from mice with LOF mutation in both alleles of Cdk13 (Cdk13$^{tm1b/tm1b}$). Complete AVSD accompanied by DORV was the most common type of CHD. In one HOMO heart, there was associated Musc. VSD due to spongy myocardium. AVSD: atrioventricular septal defect; VSD: ventricular septal defect; pMem: perimembranous; Musc: muscular; DORV: double-outlet right ventricle; BAV: bicuspid aortic valve.

3.3.3.6 Complete AVSD with DORV was the most common phenotype in homozygous (*Cdk13$^{tm1b/tm1b}$*) hearts at E15.5

Complete AVSD with DORV was the most common phenotype in *Cdk13$^{tm1b/tm1b}$* (HOMO) hearts and was present in three out of four *Cdk13$^{tm1b/tm1b}$* (HOMO) hearts. In complete AVSD, there is failure of fusion of DMP (vestibular spine) with mesenchymal cap and AV

endocardial cushions, forming ostium primum defect, inlet VSD (due to deficiency of AV component of membranous septum) and common AV canal (with a common AV valve). The *Cdk13*$^{tm1b/tm1b}$ (HOMO) hearts were abnormal shaped on external examination. In one such *Cdk13*$^{tm1b/tm1b}$ (HOMO) heart, the size of RVOT was very enlarged (Figure 3:15 B compared with A). In the *Cdk13*$^{tm1b/tm1b}$ (HOMO) hearts with AVSD, the superior and inferior endocardial cushions (red asterisks in Figure 3:15 -G) were not fused, (yellow arrow in Figure 3:15-G), resulting in common AV canal, making it a complete AVSD. Additionally, in these hearts, an outlet VSD was also present when the interventricular communication was visibly located ventral to the ventral/superior endocardial cushion (blue arrow in Figure 3:15-F&G).

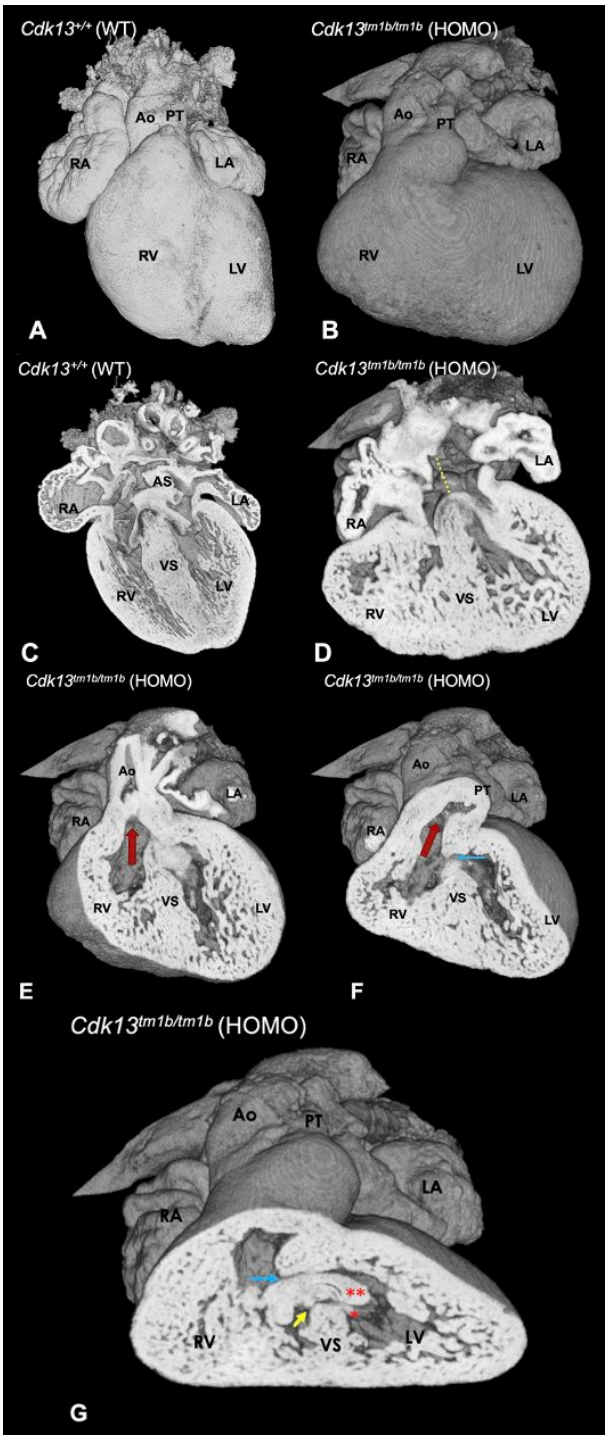


Figure 3:15 Complete AVSD with DORV. On external examination, the HOMO heart (B) is quite abnormal in size and shape compared with WT (A). C-D: Coronal sections show that Cdk13$^{tm1b/tm1b}$ (HOMO) heart (D) has absent atrial septum (yellow dotted line) unlike in WT heart (C) where AS is present. Cdk13$^{tm1b/tm1b}$ (HOMO) heart (E-G) shows that both aorta and PT are originating from RV (red arrows) and there are outlet (blue arrow) and inlet VSDs (yellow arrow). RA: right atrium, RV: right ventricle, LA: left atrium, LV: left ventricle, AS: atrial septum; VS: ventricular septum, Ao: aorta, PT: pulmonary trunk.

In the fourth homozygous (*Cdk13*$^{tm1b/tm1b}$) heart (NID16_B), there was DORV and perimembranous VSD but atrial septation appeared normal. On external examination, there was a little bulge of the pulmonary valve more anteriorly and superiorly, almost at an angle with aortic valve. Spiralling seemed absent and there was no outlet septum as well (similar to that denoted by red arrow in Figure 3:17-C). This heart had stenotic pulmonary artery and large/dilated aorta due to probably unequal separation of vessels beyond valves, like TOF without outlet VSD. The pulmonary artery was very smaller (Figure 3:16-B compared with A).

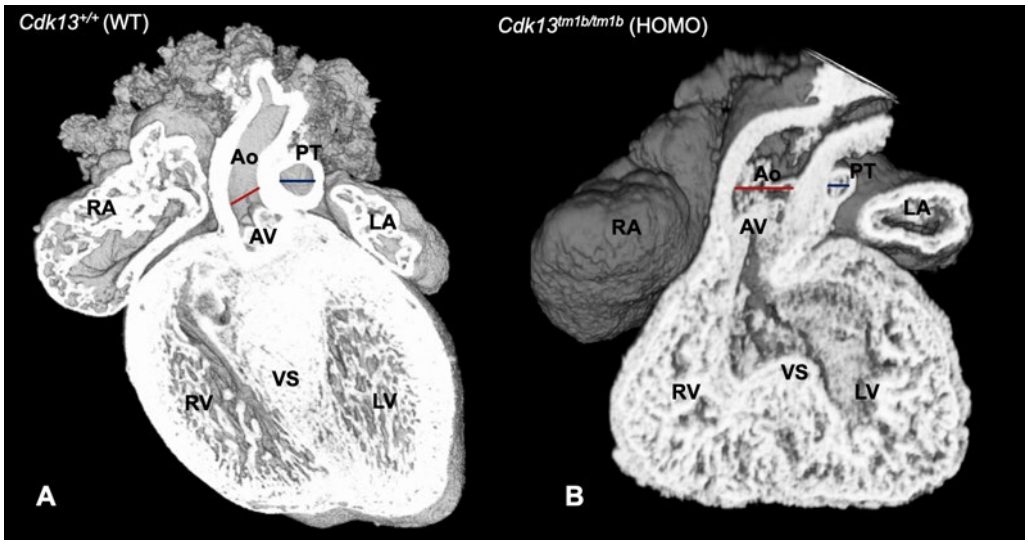
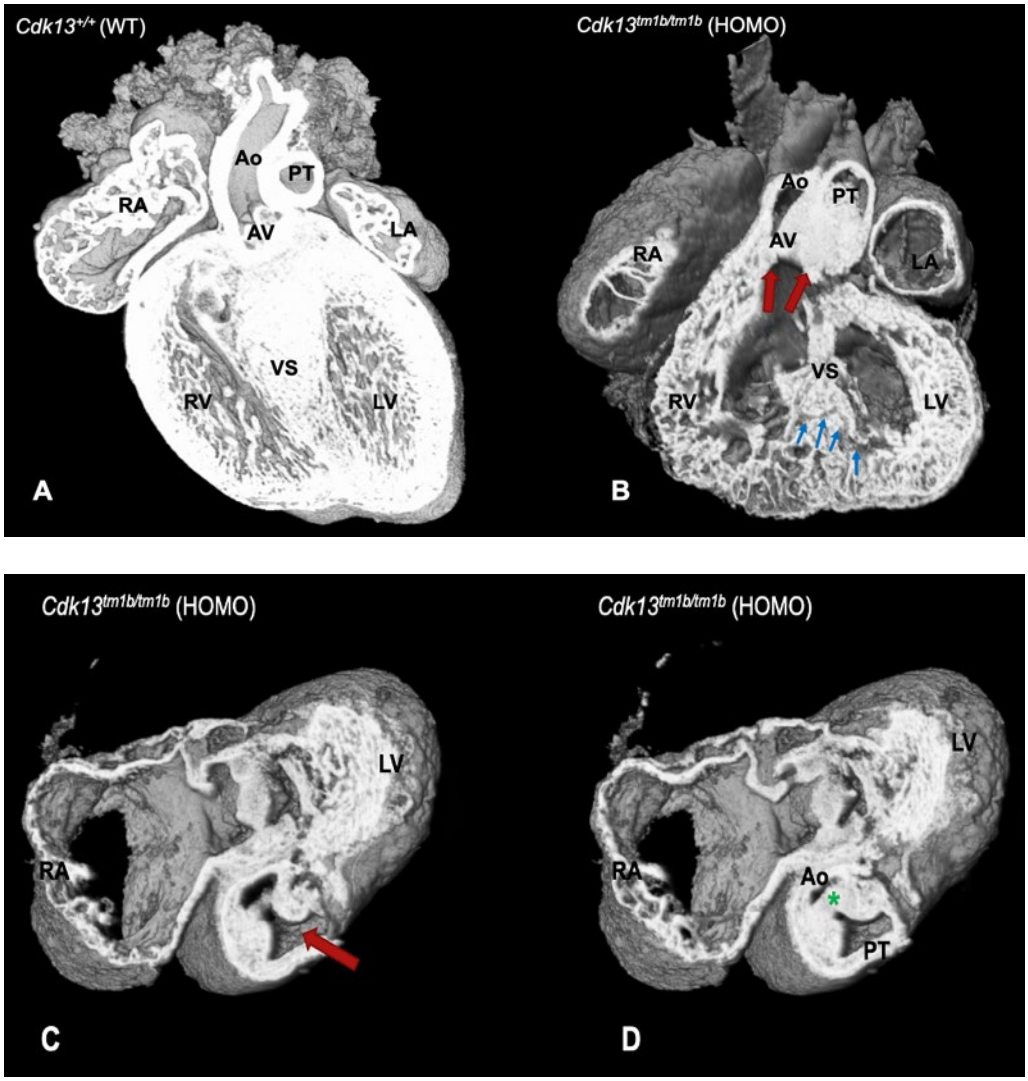


Figure 3:16 Pulmonary stenosis. A Cdk13$^{tm1b/tm1b}$ *(HOMO) heart (B) with DORV & AVSD had very narrow pulmonary trunk (navy-blue line) and correspondingly, lumen of aorta (red line) was much wider compared to WT (A). RA: right atrium, RV: right ventricle, LA: left atrium, LV: left ventricle, VS: interventricular septum, AV: aortic valve, Ao: aorta, PT: pulmonary trunk.*

In one heart (NID12A) with complete AVSD & DORV (Figure 3:17-B&F), muscular VSD was also noted when the ventricular septum was spongy/vacuolated and the trabeculae lacked fusion to create tracks enabling IV communication (blue arrows in Figure 3:17-B). The VSD was

both as inlet and outlet types i.e., confluent VSD. There was doubly committed subarterial extension of AVSD (Figure 3:17-B) and failure of development of the outlet septum (red arrow in Figure 3:17-C). Further distally, however, aorta and pulmonary arteries were separated (green asterisk in Figure 3:17-D)and had separated valves. In case of atrial septum, the second interatrial tissue fold (the so-called septum secundum) was deficient to provide support to the flap of foramen ovale (yellow arrow in Figure 3:17-F).



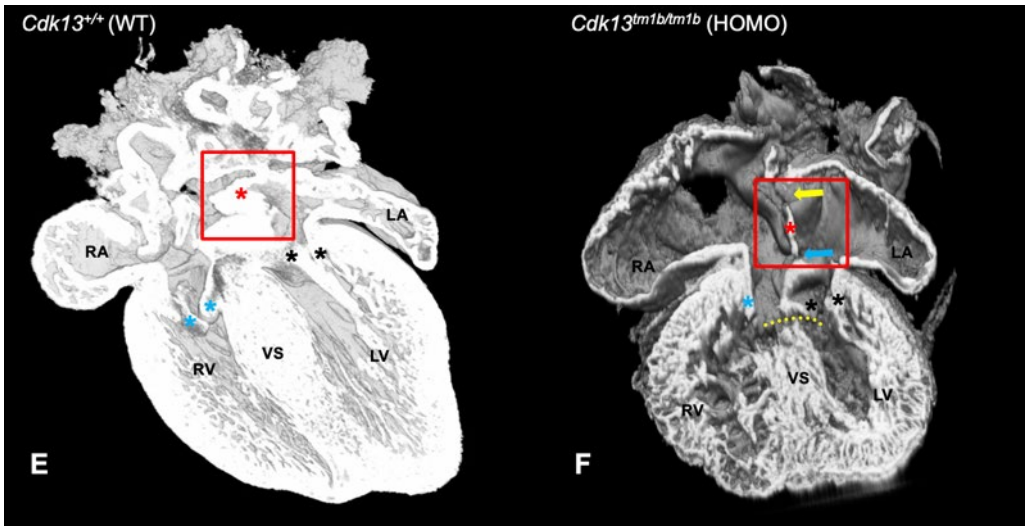


Figure 3:17 DORV with complete AVSD, muscular VSD, deficient second interatrial fold (the so-called septum secundum) and failure of development of the outlet septum. (A) Coronal section of E15.5 WT mouse heart showing the left and right ventricular chambers separated from each other by VS. (B) Anterior view of a Cdk13$^{tm1b/tm1b}$ (HOMO) mouse heart collected at E15.5 showing aorta and pulmonary trunk originating from RV (red arrows) and there is visible through and through interventricular communication in the muscular part of VS (blue arrows). (C-D) Looking at the superior aspect of axial section at the level of outflow region of the heart shows absent outflow septum (red arrow) when the partitioning between aorta and pulmonary artery is absent, proximally. However, distally, the aorta and pulmonary artery separate due to the formation of aorticopulmonary septum (green asterisk). (E-F) In the same HOMO heart, as part of AVSD, ostium primum (blue arrow) defect was present. Common atrioventricular valves are shown as blue and black asterisks. The yellow dotted line denotes inlet VSD. In homozygous (Cdk13 $^{tm1b/tm1b}$) hearts, the ventricular myocardium of both ventricles and the interventricular septum was spongy (B compared with A). RA: right atrium, RV: right ventricle, LA: left atrium, LV: left ventricle, VS: interventricular septum, Ao: aorta, AV: aortic valve, PT: pulmonary trunk.

3.3.3.7 Spongy myocardium in homozygous (*Cdk13$^{tm1b/tm1b}$*) hearts at E15.5

In homozygous *(Cdk13$^{tm1b/tm1b}$)* hearts, the ventricular myocardium of both ventricles and the interventricular septum was spongy (with coarse, deeply crypted trabeculae) (Figure 3:17B), in comparison to the WT heart (Figure 3:17A). There were several openings present in the muscular interventricular septum (blue arrows in Figure 3:17B compared with A). In

homozygous *(Cdk13$^{tm1b/tm1b}$)* hearts, along with this spongy myocardium, there was a thin layer of compact myocardium as well. However, clinically this phenotype (thinner layer of compact myocardium) has not been reported in patients. Obviously, the patients are older than the mouse stage we looked at.

3.3.4 Morphological changes in sub valvular apparatus of right (tricuspid) and left (mitral) atrioventricular valves in hearts from mice with LOF mutation of *Cdk13*

Since trabeculae carneae are the source of the papillary muscles [236], and the myocardium was spongy in case of homozygous mutation (*Cdk13$^{tm1b/tm1b}$*), these (n = 4) and HET (*Cdk13$^{tm1b/+}$*) hearts (n = 8) with CHD were analysed for any changes in the papillary muscles compared to WT (n = 3). It was observed that chordae tendineae were not discernible, and papillary muscles at this stage were found to be attached directly to the valve leaflets without chordae tendinea in both WT and mutant hearts. In case of both *Cdk13$^{tm1b/+}$* (HET) and *Cdk13$^{tm1b/tm1b}$* (HOMO) hearts, most (4/8 & 4/4 respectively) had thickened and/or dysplastic papillary muscles and the trabeculae were much coarser (even more disorganised and coarser in HOMO) (Figure 3:18 B&C compared with A, Figure 3:19 B&C compared with A).

On visual/qualitative analysis, the papillary muscles in *Cdk13$^{tm1b/+}$* (HET) hearts related to tricuspid valve (anterior and inferior) were thicker in 4 out of 8 hearts (red line in Figure 3:18-B compared to A) and were extending from the tricuspid valve to the ventricular septum (VS) (red arrow

in Figure 3:18-B). In *Cdk13*$^{tm1b/tm1b}$ (HOMO) hearts, the papillary muscles instead were more dysplastic due to spongy nature of the myocardium in these hearts (Figure 3:18-C compared with A&B). From the VS, the trabeculae, which were coarser in mutant hearts, extended to the ventricular walls (black arrows in Figure 3:18A-C).

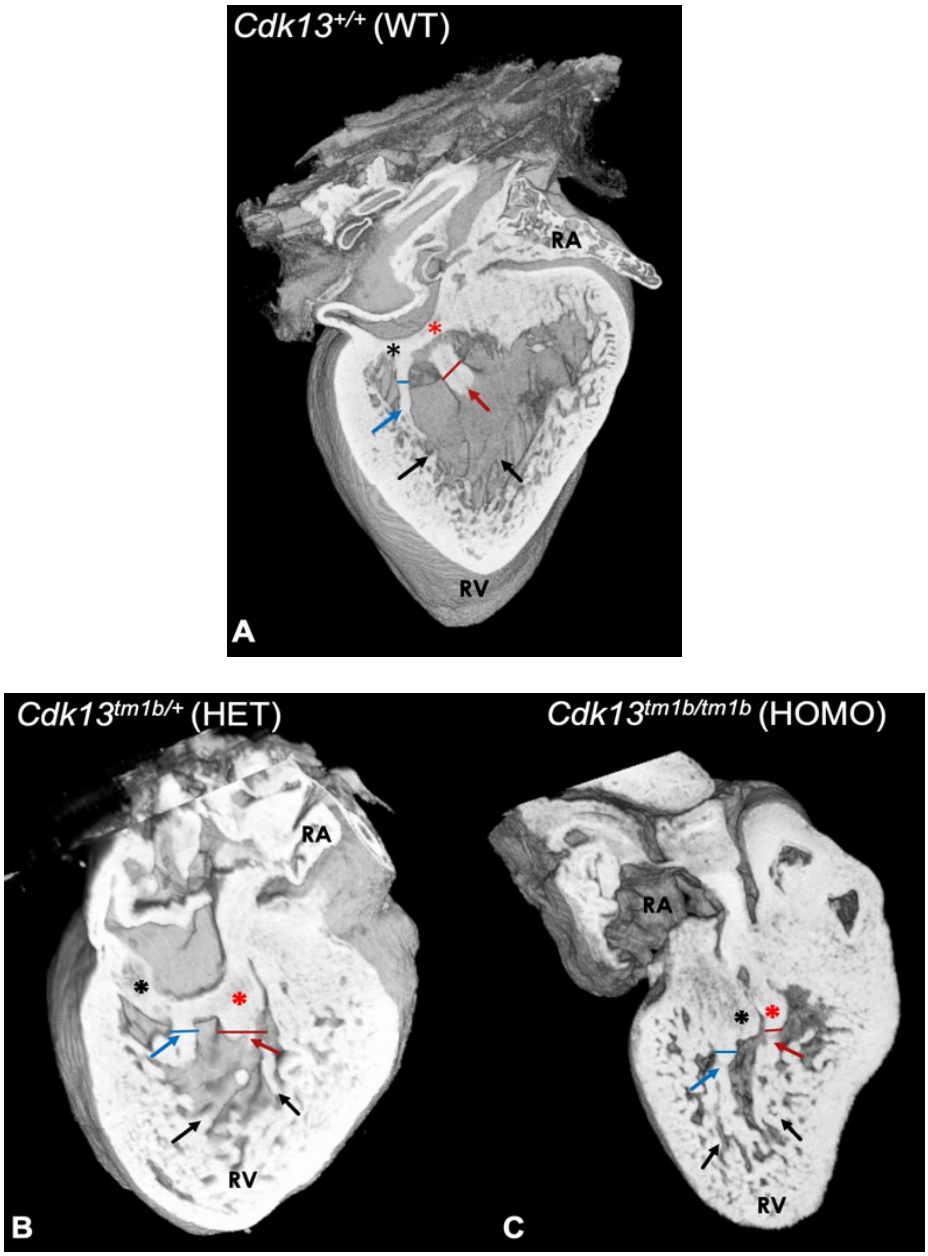


Figure 3:18 Papillary muscles of tricuspid valve, their morphology, and attachments in Cdk13^{tm1b} hearts at E15.5. Representative images of right sagittal sections of Cdk13^{tm1b} hearts (right ventricular view) showing papillary muscles which are directly attached to the leaflets of tricuspid valve (red and black asterisk) without intervening chordae tendineae. The papillary muscles are thicker (blue and red lines) in Cdk13$^{tm1b/+}$ (HET) (B) compared to Cdk13$^{+/+}$ (WT) (A). In Cdk13$^{tm1b/tm1b}$(HOMO) hearts (C), the papillary muscles instead are more dysplastic due to the spongiform myocardium in these hearts compared to (A) and (B). RA: right atrium, RV: right ventricle, red asterisk (*): anterior leaflet, black asterisk (*): inferior (aka posterior) leaflet, blue arrow: inferior papillary muscle, red arrow: anterior papillary muscle; black arrow: distal attachment of the papillary muscles as trabeculae carneae to the ventricular wall. Redline denotes the thickness of the anterior papillary muscle.

In case of mitral valve, the anterolateral and posteromedial papillary muscles were directly attached to the two leaflets of the mitral valve (like in tricuspid valve) at this stage (anterolateral and posteromedial leaflets of mitral valve denoted by red and black asterisks and their respective papillary muscles by red and blue arrows respectively in Figure 3:19A-C). Inferiorly, the ends of the two types of the papillary muscles fused to form an arcade and the trabeculae carneae extended from this arcade towards the ventricular walls (black arrows in Figure 3:19 A-C). The papillary muscles as well as the arcade they form were thicker (red and blue lines in Figure 3:19 A-C) and much coarser in *Cdk13*$^{tm1b/+}$ (HET) and *Cdk13*$^{tm1b/tm1b}$ (HOMO) hearts compared with *Cdk13*$^{+/+}$ (WT), where they were thin, elongated and clearly defined (Figure 3:19 B&C compared with A).

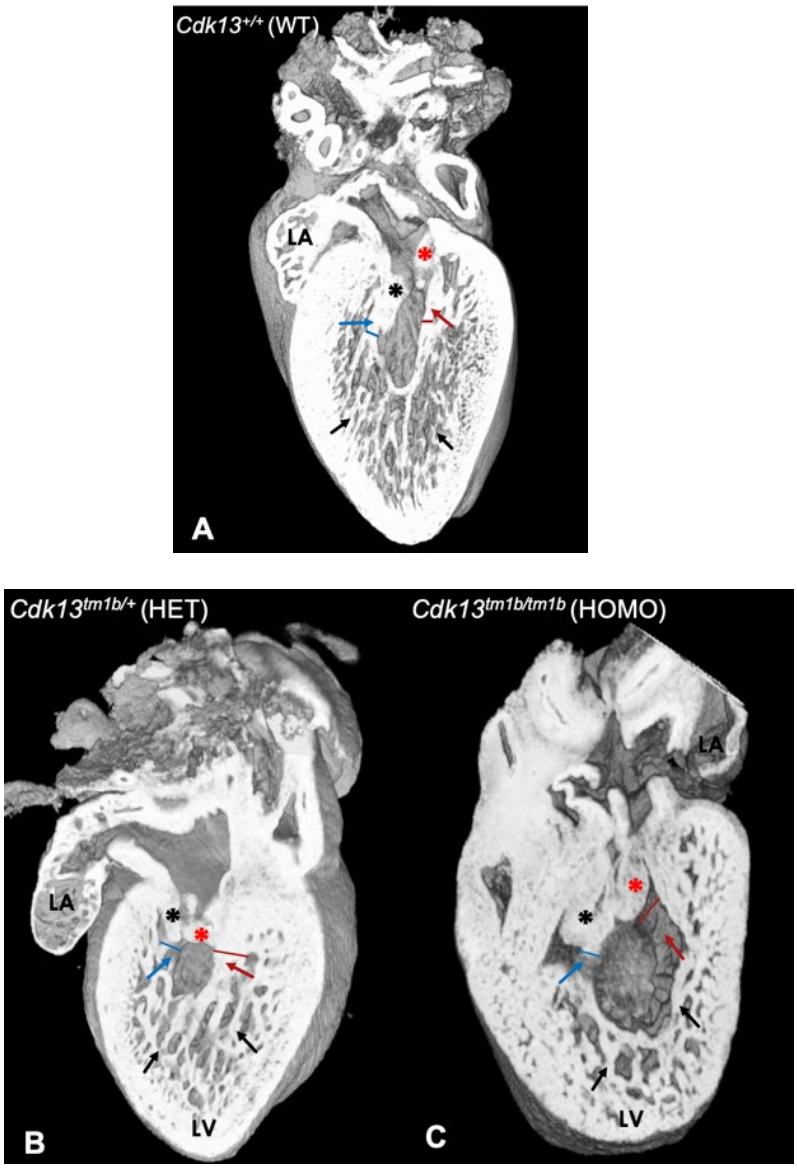


Figure 3:19 Papillary muscles of mitral valve, their attachments and morphology in Cdk13^{tm1b} hearts at E15.5. Representative images of left sagittal sections of Cdk13^{tm1b} hearts (left lateral view) showing thicker papillary muscles and the trabeculae are much coarser in Cdk13$^{tm1b/+}$ (HET) (B) and Cdk13$^{tm1b/tm1b}$ (HOMO) hearts (C) compared to Cdk13$^{+/+}$ (WT) (A). The papillary muscles are directly attached to the mitral valve leaflets without intervening chordae tendineae at this stage (in both WT and mutant hearts). Inferiorly, the papillary muscles form arcade when the two types of papillary muscles fuse, and from this arcade, trabeculae extend towards their insertion into the ventricular walls. LA: left atrium, LV: left ventricle, red asterisk (*): anterolateral leaflet, black asterisk (*): posteromedial leaflet, blue arrow: posteromedial papillary muscle, red arrow: anterolateral papillary muscle, black arrow: distal attachments of the papillary muscles through trabeculae carneae (and not directly) to the ventricular wall. Redline denotes the thickness of the anterolateral papillary muscle.

3.3.5 Analysis of pulmonary stenosis at pulmonary valvular and infundibular levels in *Cdk13^{tm1b}* hearts with CHD

Pulmonary abnormalities including stenosis were reported in patients with *CDK13* mutations [176, 214, 220, 225, 237]. Moreover, pulmonary stenosis, either at valvular or subvalvar (infundibular) level forms one of the components of the tetralogy of Fallot [133]. In one *Cdk13$^{tm1b/tm1b}$* (HOMO) heart as well, there was apparent pulmonary stenosis on HREM analysis (Table 3:6, Figure 3:16 B compared to A). Therefore, hearts from all three groups (WT = 3, HET = 5, HOMO = 4) were quantitatively analysed for any associated obstruction to the outflow of right ventricle at pulmonary valvular as well as infundibular levels, looking for the widest diameter. Diameter at infundibulum was significantly reduced in homozygous (*Cdk13$^{tm1b/tm1b}$*) hearts compared to WT (P = 0.0407), whereas, at pulmonary annulus level, the difference was not significant in HET (*Cdk13$^{tm1b/+}$*) and HOMO (*Cdk13$^{tm1b/tm1b}$*) hearts compared with WT (P = 0.9112) (Figure 3:20D). However, there were 2 out of 5 *Cdk13$^{tm1b/+}$* (HET) hearts (with CHD) which had narrowing at pulmonary annulus (with diameter less than the mean value ± SEM of 0.5467 ± 0.079mm in WT) (black arrow in Figure 3:20-B compared with A). Four out of five *Cdk13$^{tm1b/+}$* (HET) hearts with CHD had infundibular diameter less than the mean value ± SEM of 0.566 ± 0.0452mm as in WT (yellow arrow in Figure 3:20-B compared with A) but the difference was not significant (P > 0.05) (Figure 3:20-D). In case of *Cdk13$^{tm1b/tm1b}$* (HOMO) hearts, all 4 had narrowing at infundibular level and 1 out of 3 had narrowing at

pulmonary annulus level (diameters less than their mean values in WT). In the 4th *Cdk13$^{tm1b/tm1b}$* (HOMO) heart, the narrowing of pulmonary trunk and potentially of the annulus was apparent on gross analysis however, owing to poor tissue integrity, presence of clotted blood and hence inappropriate/suboptimal image resolution did not allow measuring the diameter of pulmonary annulus (Figure 3:20-C&C').

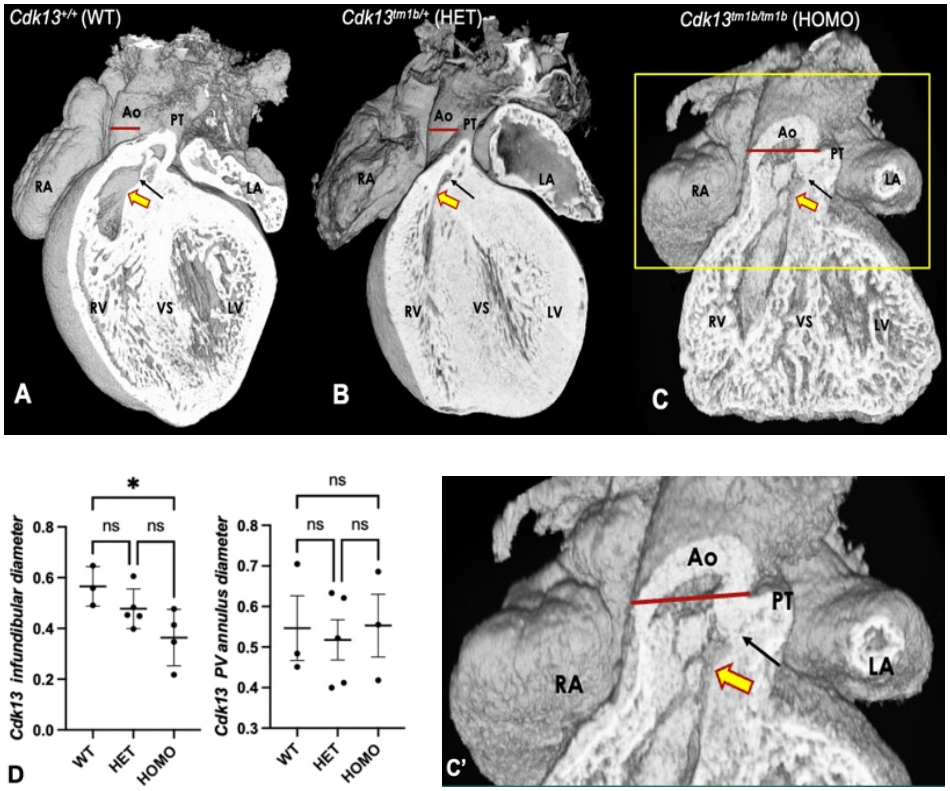


Figure 3:20 Right ventricular outflow tract obstruction and pulmonary stenosis. In some Cdk13$^{tm1b/+}$ (HET) and Cdk13$^{tm1b/tm1b}$ (HOMO) hearts, narrowing at infundibular (sub-valvar) region (yellow arrow) and at pulmonary annulus levels (black arrow in A-C, C') were observed. The difference was significant in homozygous hearts in case of infundibular diameter (P = 0.0407) but insignificant in case of pulmonary annulus diameter (P = 0.9112) (D). In the Cdk13$^{tm1b/tm1b}$ (HOMO) heart (C), in addition to severe narrowing at infundibular and pulmonary valve-annulus regions, the size of aorta was quite large compared to HET and WT (red line). This was probably due to unequal fusion of the OFT cushions and hence unequal separation of the aorta and pulmonary artery beyond the valves. This HOMO heart had confluent VSD, DORV and spongy myocardium as well. C' is the magnified view of the yellow boxed region in panel C, showing narrowing at the level of infundibulum, pulmonary annulus, and pulmonary trunk.

3.3.6 Phenotypic analysis of *Cdk13^{tm1b}* mutant (*Cdk13$^{tm1b/+}$*) hearts at postnatal day (P) 6/7

3.3.6.1 Selection of P6/P7 day for exploring CHD phenotypes postnatally

In order to look for association of PFO with *Cdk13* mutation, postnatal day 6 or 7 (P6/P7) was selected based on previous literature according to which the interatrial communication should have closed off normally in the region of foramen ovale due to the fusion of septum primum and secundum [238]. Additionally, these hearts were analysed morphologically for all the structures including ventricular septum (VS), aortic valve (AV), pulmonary valve (PV), mitral valve (MV), tricuspid valve (TV), in addition to the atrial septum (AS). Our results showed that in *Cdk13$^{+/+}$* (WT) hearts (n = 6), the foramen ovale was patent in two hearts and partially fused in two more hearts whereas it was closed in the remaining two hearts. Observation of patency of foramen ovale in *Cdk13$^{+/+}$* (WT) hearts at P6/P7 day makes this point in time inappropriate for PFO analysis. However, other phenotypes observed in these hearts are mentioned below and in Table 3:7.

3.3.6.2 CHD phenotypes in *Cdk13$^{tm1b/+}$* neonatal hearts at P6/P7 by HREM analysis

Postnatal hearts from *Cdk13$^{tm1b/+}$* (HET) mice (n = 9) compared with WT (n = 6) at P6/P7 were analysed after generating their 3D models from a z-stack of high resolution 2D HREM images. The phenotypes observed in these P6 *Cdk13$^{tm1b/+}$* (HET) hearts are shown in the Table 3:7:

Cdk13$^{tm1b/+}$ (HET) neonatal hearts at P6	
Sample ID	**Phenotype**
NID179-A	Closed FO; thick RV & LV wall and VS; PS
NID0185-A	Very thick ventricular walls and narrow ventricular cavities; PS; Partially closed FO
NID0185-B	Closed FO
NID186-A	Closed FO; less dense areas in the muscular part of VS – spontaneously closed Musc. VSDs?; two coronary ostia in left and one in right coronary sinus (i.e., supernumerary coronary ostia)
NID186-B	Severely thick ventricular walls; PFO
NID187-A	PFO
NID187-B	Closed FO
NID190-A	PFO
NID190-B	PFO

Table 3:7 Phenotypes in hearts collected from Cdk13$^{tm1b/+}$ (HET) mouse neonates at sixth postnatal day (P6). PFO was noted in four Cdk13$^{tm1b/+}$ (HET) hearts, and in one Cdk13$^{tm1b/+}$ (HET) heart, there was spontaneously closed muscular VSDs when the specific sites were less dense than the rest of the muscular interventricular septum. In 5 out 9 hearts, the FO was closed. FO: foramen ovale; VSD: ventricular septal defect, PFO: patent foramen Ovale; Musc: muscular; VS: interventricular septum; RV: right ventricle; LV: left ventricle.

In four out of nine neonatal hearts from mice with *Cdk13$^{tm1b/+}$* (HET) mutation, the septum primum was not fused with septum secundum, resulting in persistent communication between the two atria i.e., patent foramen ovale (PFO) (Figure 3:21-B compared with A). In *Cdk13$^{+/+}$* (WT) hearts at P6, these two septa were not fused in 2 out of 6 hearts analysed. This suggests that such analysis for PFO be carried at a much later stage in future studies e.g., around weaning.

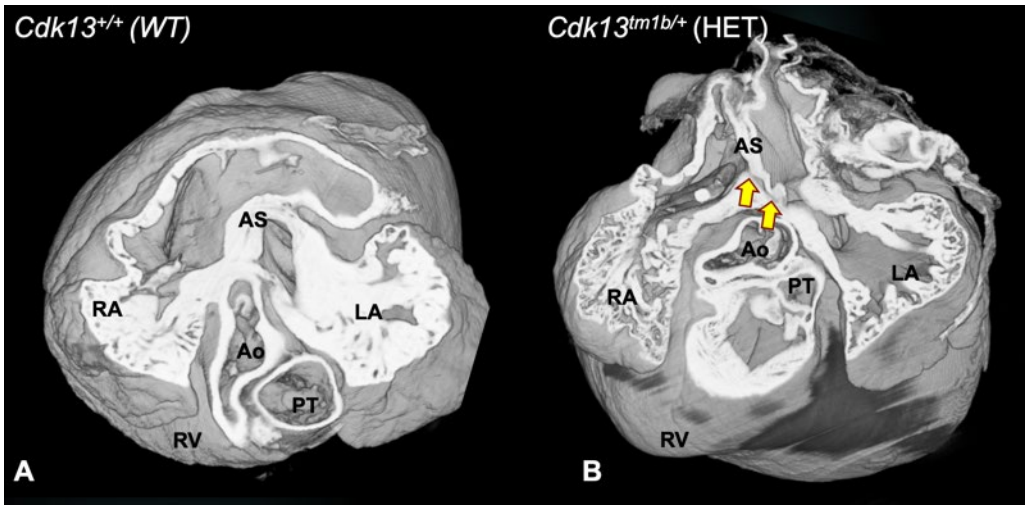


Figure 3:21 Patent foramen Ovale (PFO). A&B - Axial sections (superior view) of the outflow region of Cdk13$^{+/+}$(WT) and Cdk13$^{tm1b/+}$ (HET) hearts at postnatal day 6. A: Cdk13$^{+/+}$(WT)) mouse heart showing the closed interatrial communication after the fusion of septum primum and secundum to give rise to atrial septum; B: Cdk13$^{tm1b/+}$ (HET) heart showing non-fusion of septum primum and secundum, leaving a gap (yellow arrows) to allow interatrial communication in the region of fossa ovalis as patent foramen ovale. RA: right atrium; LA: left atrium; RV: right ventricle; LV: left ventricle; AS: atrial septum; PT: pulmonary trunk; Ao: aorta.

In three of the nine *Cdk13*$^{tm1b/+}$ (HET) hearts analysed, there was heart wall thickening, resulting in narrowing of the ventricular lumina (Figure 3:22-B&C compared with A).

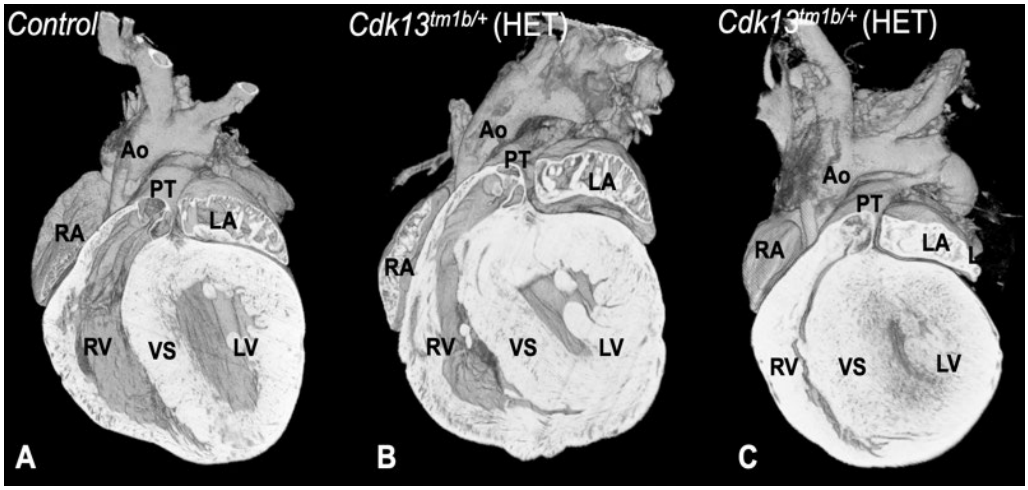


Figure 3:22 Increased heart walls' thickness and narrowed ventricular chambers. Coronal sections of the P6 neonatal Cdk13$^{tm1b/+}$ *(HET) hearts (B-C) having thickened walls compared to control (A). Three of the nine Cdk13*$^{tm1b/+}$ *(HET) hearts analysed showed increased wall thickness resulting in narrowing of the ventricular lumina as well as the outflow regions of both ventricles (B-C) compared to WT (A). RA: right atrium; LA: left atrium; RV: right ventricle; LV: left ventricle; VS: ventricular septum; Ao: aorta; PT: pulmonary trunk.*

In one P6 *Cdk13*$^{tm1b/+}$ (HET) heart, there were three coronary ostia in the aortic sinuses i.e., one for the right coronary artery (RCA) in the right sinus (red arrow) and two in the left coronary sinus - one each for the left main coronary and anterior interventricular arteries (denoted by blue arrows in Figure 3:23-B compared with A).

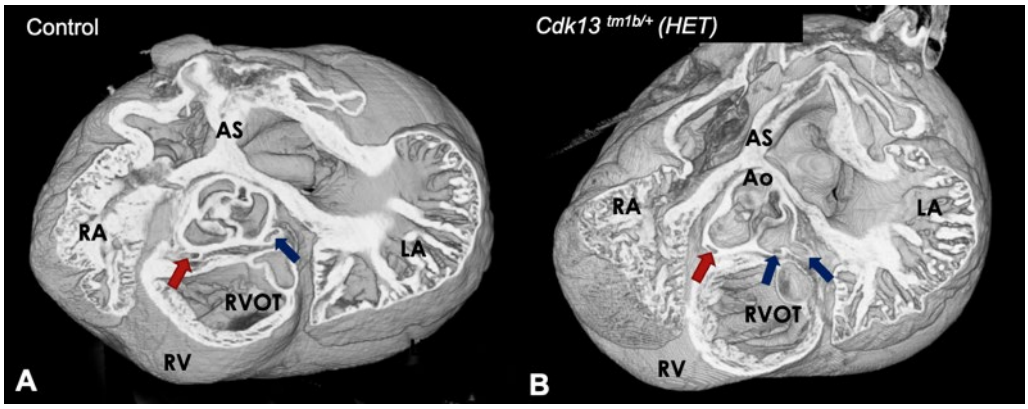


Figure 3:23 Supernumerary coronary ostia in left aortic sinus. Superior view of the axial sections of the P6 neonatal Cdk13^{tm1b} hearts, comparing coronary ostia of Cdk13$^{tm1b/+}$ (HET) (B) with control heart (A). Cdk13$^{tm1b/+}$ (HET) heart (B) shows two coronary ostia in the left aortic sinus (blue arrows), instead of one, and a single ostium in right coronary sinus (red arrow). RA: right atrium; LA: left atrium; RV: right ventricle; AS: atrial septum; Ao: aorta; RVOT: right ventricular outflow tract.

In the same *Cdk13$^{tm1b/+}$* (HET) heart, potential spontaneously closed muscular VSDs were noted. These were labelled as probably spontaneously closed VSDs based on the tissue density being less than the rest of the ventricular septum (Figure 3:24-B compared with A).

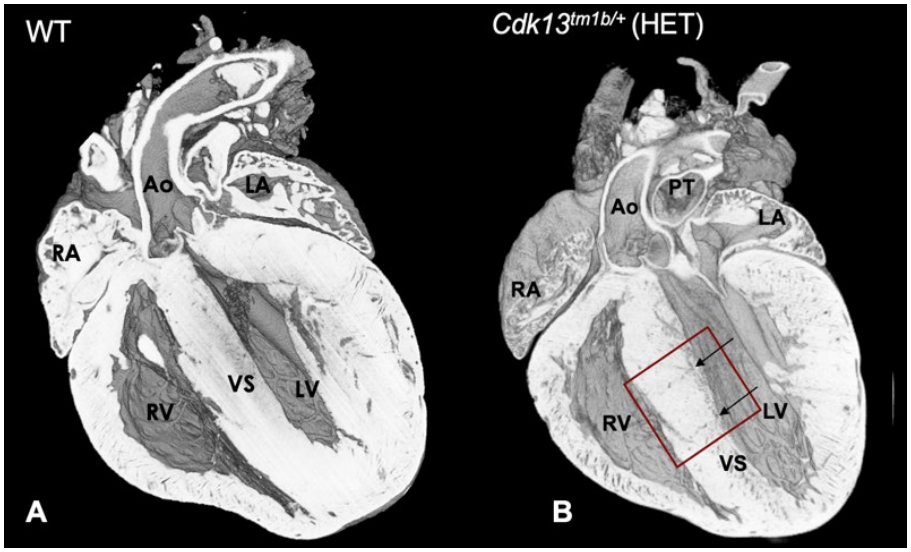


Figure 3:24 Spontaneously closed muscular ventricular septal defects in P6 neonates. A Cdk13$^{tm1b/+}$(HET) heart (B) having less dense areas in the muscular part of the ventricular septum (black arrows) compared to WT (A). This is suggested to be spontaneously closing/recently closed muscular VSD. RA: right atrium; LA: left atrium; RV: right ventricle; LV: left ventricle; VS: ventricular septum; Ao: aorta; PT: pulmonary trunk.

No liveborn *Cdk13*$^{tm1b/tm1b}$ (HOMO) pups were obtained and hence no *Cdk13*$^{tm1b/tm1b}$ (HOMO) hearts were available postnatally for comparative morphologic analysis with *Cdk13*$^{+/+}$ (WT) and *Cdk13*$^{tm1b/+}$ (HET) hearts.

3.3.7 Gender determination of *Cdk13*^{tm1b} mutant mice with CHD

Gender was determined of both *Cdk13*$^{tm1b/+}$ (HET) (n = 6) and *Cdk13*$^{tm1b/tm1b}$ (HOMO) (n = 3) mice with CHD. However, gDNA was not available for 3 *Cdk13*$^{tm1b/+}$ (HET) mice and therefore their gender could not be determined. Out of the (available) total nine *Cdk13*-mutant mice with CHD, 6 (4 HET + 2 HOMO) were males and 3 (2 HET + 1 HOMO) were females.

3.3.8 X-Gal staining for expression of *Cdk13* at different ages

There is a limited data available regards *Cdk13* expression [211]. Previous preliminary work carried out by José Aparicio Sánchez (a previous PhD student) from this lab performing X-Gal staining of *Cdk13*$^{tm1b/+}$ heterozygous mouse hearts (n = 5) showed that *Cdk13* was expressed in developing heart in the E12.5 and E13.5 in a ubiquitous manner. These preliminary *Cdk13* expression studies needed to be confirmed through further experiments.

With the aim to identify the expression of *Cdk13* during heart development, X-Gal staining was carried out at E10.5, E12.5, E15.5 and in adult mice, aimed to compare HETs with WT (minimally n = 3 each at each stage). At E10.5 and E12.5, whole embryos (instead of just hearts as in case of E15.5 and adult mice) were subjected to X-Gal staining as the

heart were very small/delicate at these stages and could be damaged if harvested from the embryo. At E10.5, three HETs, whereas at E12.5 eleven HETs were compared to 3 WT at each stage. Moreover, there were two HOMO embryos at E12.5 available as well which were also subjected to X-Gal staining. The results of the staining were quite interesting. As shown in Figure 3:25 (B-C), the expression of *Cdk13* at E10.5 was quite distinctly localised and ubiquitous in heart/pericardium and in the 1st pharyngeal arch area (mandibular and maxillary processes/facial skeleton). In the Figure 3:25 (C), in ventral view of the embryo, expression can be seen in the heart, neck structures including laryngeal cartilages (yellow asterisk) and trachea (blue arrow) further inferiorly. Laryngeal cartilages develop from second, third and fourth pharyngeal arches [8].

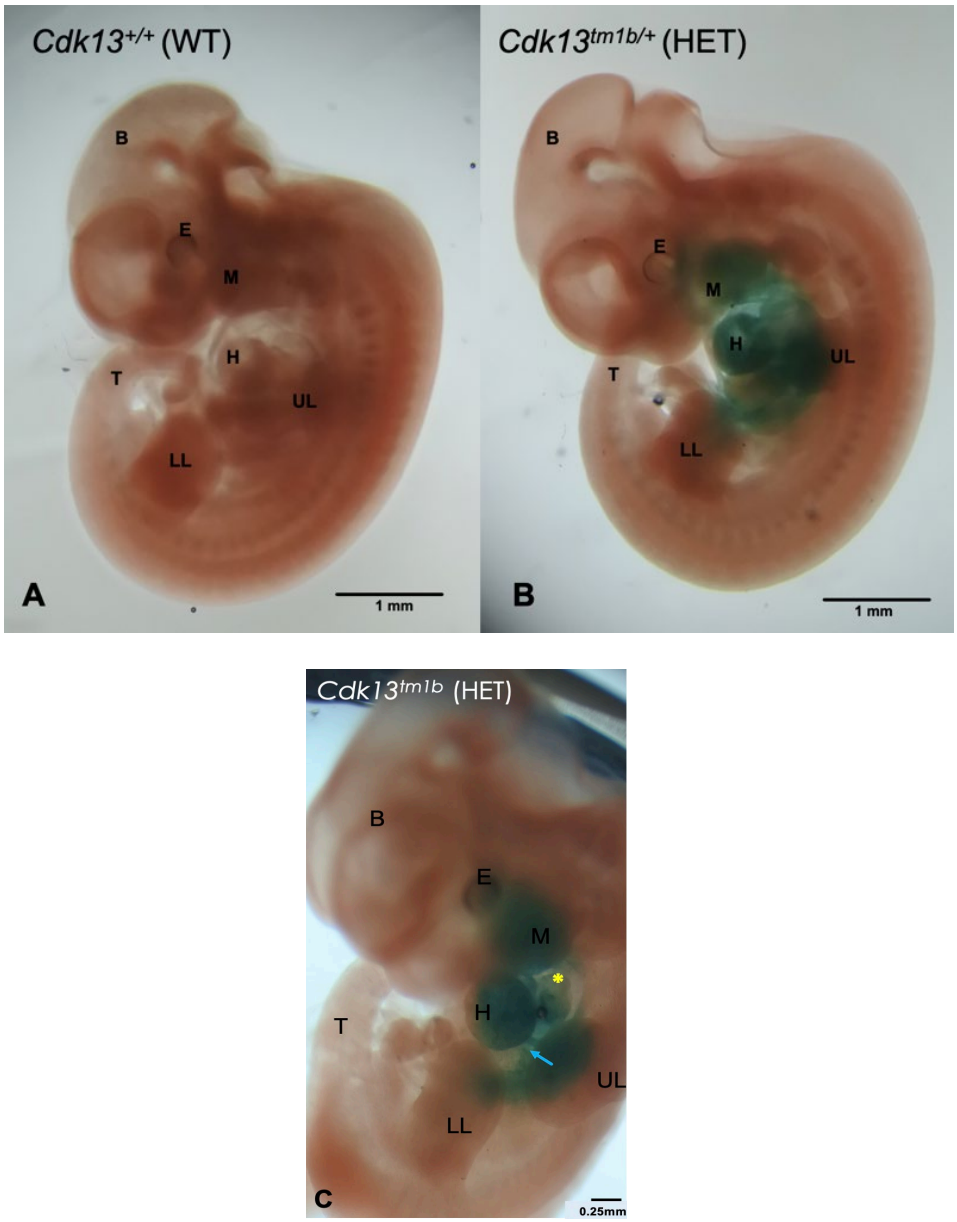


Figure 3:25 X-Gal staining to show Cdk13 expression in E10.5 Cdk13$^{tm1b/+}$ (HET) embryos. Cdk13 expression is very distinct and localised to facial skeleton (maxillary and mandibular processes of 1st pharyngeal arch), neck, heart and pericardium (B-C). Image A is shown as a control. (C): Magnified ventral view of the embryo shown in (B) shows more clearer expression of Cdk13 in heart, neck structures including laryngeal cartilages (yellow asterisk) and trachea (blue arrow) further inferiorly. B: brain; E: eye; M: maxillary and mandibular processes of 1st pharyngeal arch; H: heart in pericardial cavity; UL: upper limb bud; LL: lower limb bud; T: tail. Scale bar = 1mm for A-B, and 0.25mm for C.

X-Gal staining of whole embryos at E12.5 showed that *Cdk13* expression was ubiquitous as well as very strong throughout the embryo

(Figure 3:26), unlike at E10.5 when it was more restricted at the sites of developing heart as well as the pharyngeal arches Figure 3:25 (B-C).

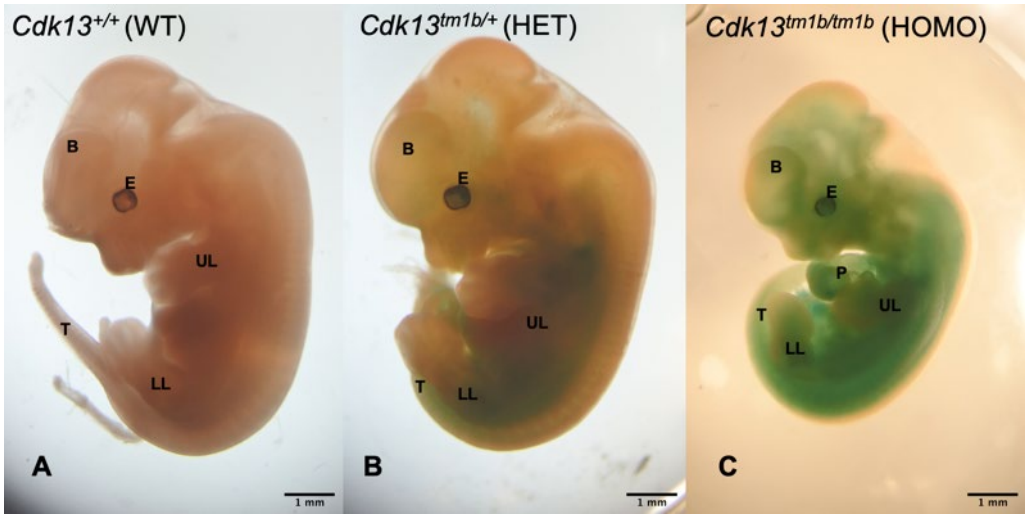


Figure 3:26 X-Gal staining to show Cdk13 expression in E12.5 embryos. Representative images of Cdk13 expression in E12.5 Cdk13$^{tm1b/+}$(HET) and Cdk13$^{tm1b/tm1b}$ (HOMO) embryos (B-C), compared to control (A). The expression of Cdk13 is ubiquitous at this stage as can be seen in the brain, viscerocranium, heart and rest of the body (B-C). B: brain; E: eye; P: pericardial cavity; UL: upper limb bud; LL: lower limb bud; T: tail. Scale bar = 1mm.

At E15.5, since the embryos covering body wall/tissues were too dense to allow easy and appropriate penetration of the X-Gal staining reagents, hearts were harvested from these embryos and thereby stained to explore cardiac expression of *Cdk13* at this stage. The results showed that at E15.5, *Cdk13* expression was very strong, and like E12.5, it was present throughout the heart (Figure 3:27-B compared to A).

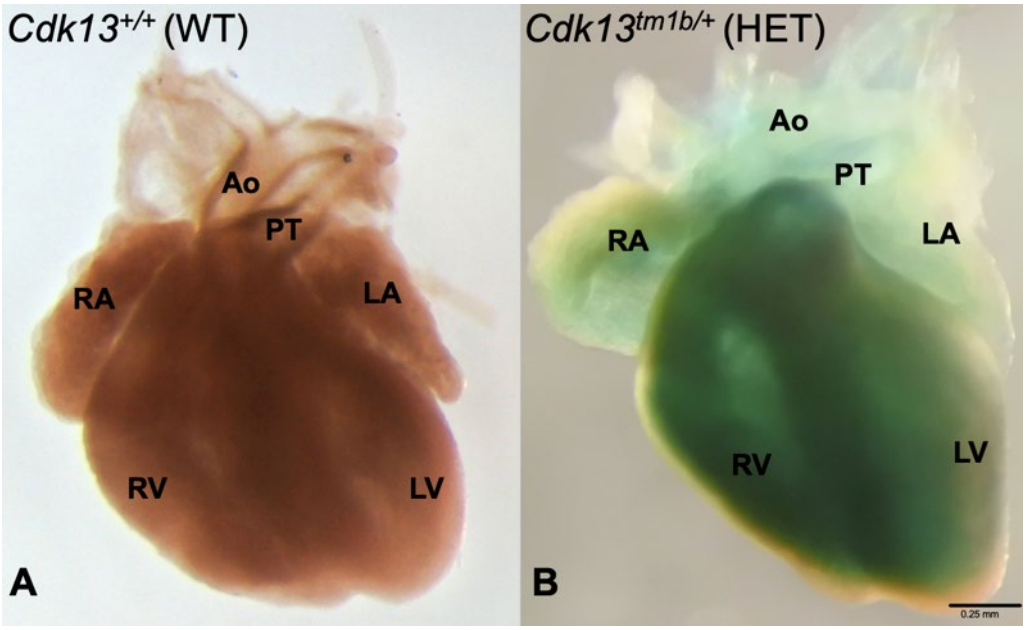


Figure 3:27 X-Gal staining to show Cdk13 expression in E15.5 hearts. Representative image of Cdk13 expression in E15.5 Cdk13$^{tm1b/+}$(HET) hearts (B), compared to control (A). The expression of Cdk13 is very strong as well as ubiquitous in heart. RA: right atrium; LA: left atrium; RV: right ventricle; LV: left ventricle; Ao: aorta; PT: pulmonary trunk. Scale bar = 0.25mm.

Moreover, hearts were collected from adult mice to see if *Cdk13* expression resembles that in the intrauterine life/embryonic stages. Adult hearts were collected opportunistically from spare adult mice no more required for breeding. X-Gal staining of adult *Cdk13*$^{tm1b/+}$ (HET) hearts showed that there was a strong expression of *Cdk13* in atria, pulmonary trunk and aorta. Increased expression in ventricles cannot be excluded though as probably the ventricular tissues were much firmer in adult mice presenting increased resistance to penetration of X-Gal staining reagents (Figure 3:28-B compared with A).

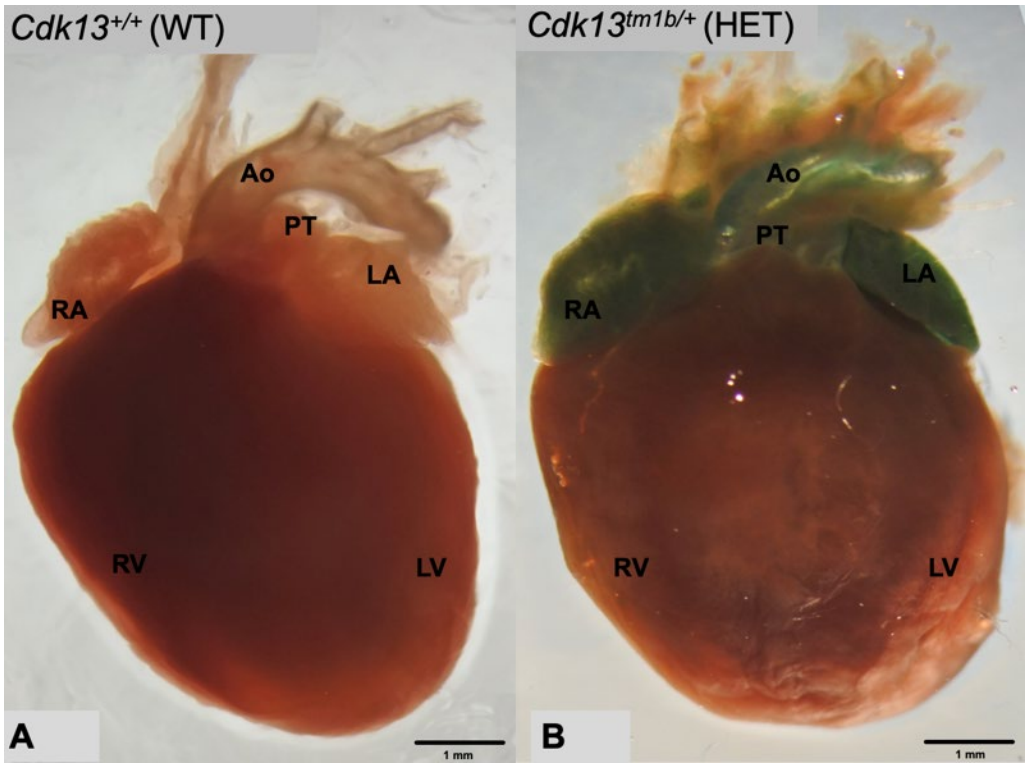


Figure 3:28 X-Gal staining to show Cdk13 expression in Adult hearts. Representative images of Cdk13 expression in Adult Cdk13$^{tm1b/+}$(HET) hearts (B), compared to WT control (A). The expression of Cdk13 is strong in both atria, aorta, and pulmonary trunk. The expression is not detected in ventricles at this stage probably due to firmer ventricular tissues at this stage resisting easy penetration of X-Gal staining reagents. RA: right atrium; LA: left atrium; RV: right ventricle; LV: left ventricle; Ao: aorta; PT: pulmonary trunk. Scale bar = 1mm

3.3.9 Quantitative RT-PCR to explore gene expression of *Cdk13* at different embryonic ages

3.3.9.1 Tissue collection, RNA extraction and cDNA synthesis

Quantification of the transcript of *Cdk13* was carried out by reverse transcriptase-quantitative polymerase chain reaction (RT-qPCR) technique comparing *Cdk13*$^{+/+}$ (WT) with *Cdk13*$^{tm1b/+}$ (HET) and *Cdk13*$^{tm1b/tm1b}$ (HOMO) heart samples collected at E10.5, E12.5, E15.5 and adult ages. E10.5 and E12.5 were selected to give an idea about *Cdk13* expression

and its role when key heart morphogenetic events like septation of chambers and outflow tracts were happening and which complete by the end of E14.5 [92]. Therefore E15.5 was selected as another stage for qPCR and also was the same age as the one selected for HREM analysis. To determine *Cdk13* expression in E10.5, E12.5, E15.5 and adult mouse hearts, RNA was extracted from *Cdk13*$^{+/+}$ (WT), *Cdk13*$^{tm1b/+}$ (HET) and *Cdk13*$^{tm1b/tm1b}$ (HOMO) hearts (n = 3 each) at E10.5 and E12.5, and from WT and *Cdk13*$^{tm1b/+}$ (HET) (n = 3 each group) in case of E15.5 and adult mice. cDNA obtained after reverse transcription was used as a template for the qPCR. Expression data, normalised to *Pgk1 or Eef1e1* and *Rpl4,* was analysed by using modified Pfaffl method [198]. The primers used, their standard curve, optimisation and their efficiency calculations made are mentioned in the methods section.

3.3.9.2 Gene expression analysis of *Cdk13* in *Cdk13*^{tm1b} hearts at E10.5, shows significant change in HOMO compared to WT and HET hearts

The data for *Cdk13*$^{+/+}$ (WT) ($W = 0.9333$, $P = 0.5013$), *Cdk13*$^{tm1b/+}$ (HET) ($W = 0.8908$, $P = 0.3568$) and *Cdk13*$^{tm1b/tm1b}$ (HOMO) ($W = 0.9615$, $P = 0.6227$) groups were normally distributed. Comparing the three groups, we found that there was significant difference among the means of *Cdk13* expression (log_2FC) of these groups ($P = 0.0120$). Multiple comparisons' (Tukey) test showed no significant difference in terms of *Cdk13* expression, comparing *Cdk13*$^{+/+}$ (WT) with *Cdk13*$^{tm1b/+}$ (HET) ($P = 0.7023$) but the difference was significant comparing *Cdk13*$^{+/+}$ (WT) with

Cdk13$^{tm1b/tm1b}$ (HOMO) (*P* = 0.0129), and *Cdk13*$^{tm1b/+}$ (HET) with *Cdk13*$^{tm1b/tm1b}$ (HOMO) (*P* = 0.0330). (Table 3:8, Figure 3:29).

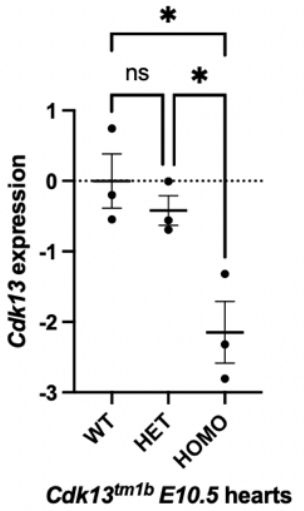


Figure 3:29 Expression of Cdk13 by RT-qPCR in E10.5 hearts from Cdk13$^{tm1b/+}$ *mouse line. The log*$_2$*FC of Cdk13 (mean with SE) in Cdk13*$^{tm1b/+}$ *(HET) and Cdk13*$^{tm1b/tm1b}$ *(HOMO) hearts collected at E10.5, compared with WT (Cdk13*$^{+/+}$*) hearts of the same age. As shown in the scatter plot, using one way-ANOVA and posthoc-Tukey test, no statistically significant difference is present in the level of Cdk13 transcript in Cdk13*$^{tm1b/+}$ *(HET) compared to WT (Cdk13*$^{+/+}$*) hearts. But the difference is significant in Cdk13*$^{tm1b/tm1b}$ *(HOMO) compared to WT (Cdk13*$^{+/+}$*) and Cdk13*$^{tm1b/+}$ *(HET) hearts. ns: not significant.*

Groups comparison	Mean *Cdk13* expression (log_2FC)		Mean difference in log_2FC	SE of difference	95% CI of difference	Adjusted p-value
WT Vs HET	WT 0.000	HET -0.4184	0.4184	0.5069	-1.137 to 1.974	0.7023 (n.s.)
WT Vs HOMO	WT 0.000	HOMO -2.147	2.147	0.5069	0.5921 to 3.703	0.0129 (sig.)
HET Vs HOMO	HET -0.4184	HOMO -2.147	1.729	0.5069	0.1737 to 3.284	0.0330 (sig.)

Table 3:8 Comparative mean Cdk13-transcript expression in E10.5 hearts from Cdk13$^{tm1b/+}$ *mouse line. Multiple comparisons of log*$_2$*FC of Cdk13 among the three E10.5 groups (n = 3 each) from Cdk13*^{tm1b} *mouse line using Post-hoc (multiple-comparisons) Tukey test. There is no significant difference between WT and HET (P = 0.7023) but the difference was significant between WT and HOMO (P = 0.0129), and between HET and HOMO hearts (P = 0.0330). The log*$_2$*FC in HET and HOMO are compared to log*$_2$*FC of "zero" in WT. The reference genes used were Pgk1 and Rpl4. n.s = not significant. SE = standard error*

3.3.9.3 Gene expression analysis of *Cdk13* in *Cdk13^{tm1b}* hearts at E12.5, shows significant change in HOMO compared to WT and HET hearts

To find out if there was any change in the transcript level of *Cdk13* in the *Cdk13$^{tm1b/+}$* (HET) and *Cdk13$^{tm1b/tm1b}$* (HOMO) hearts collected at E12.5 stage, comparative qPCR was carried out for *Cdk13*-transcript quantification. Data obtained from all the three groups – *Cdk13$^{+/+}$* (WT) (W = 0.8496, *P* = 0.2394) *Cdk13$^{tm1b/+}$* (HET) (W = 0.8658, *P* = 0.2837) and *Cdk13$^{tm1b/tm1b}$* (HOMO) (W = 0.9043, *P* = 0.3992) was normally distributed. One-way ANOVA showed that there were significant differences between the genotypes (*P* = 0.0074). Post-hoc-Tukey (multiple comparisons) test also showed that the comparisons resulted in no significant difference between *Cdk13$^{+/+}$* (WT) & *Cdk13$^{tm1b/+}$* (HET) (*P* = 0.5049), but the difference was significant between *Cdk13$^{+/+}$* (WT) & *Cdk13$^{tm1b/tm1b}$* (HOMO) (*P* = 0.0073) and between *Cdk13$^{tm1b/+}$* (HET) & *Cdk13$^{tm1b/tm1b}$* (HOMO) (*P* = 0.0263) hearts (as shown in Figure 3:30 and Table 3:9).

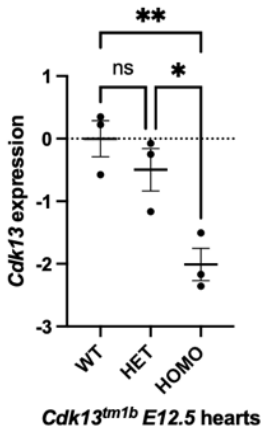


Figure 3:30 Transcript expression of Cdk13 by RT-qPCR in E12.5 hearts from Cdk13$^{tm1b/+}$ mouse line. The log$_2$FC of Cdk13 (mean with SE) in Cdk13$^{tm1b/+}$ (HET) and Cdk13$^{tm1b/tm1b}$ (HOMO) hearts collected at E12.5, is compared to WT (Cdk13$^{+/+}$) hearts of the same age. As shown in the scatter plot, using one way-ANOVA and posthoc-Tukey test, no statistically significant difference is present in the level of Cdk13 transcript in Cdk13$^{tm1b/+}$ (HET) compared to WT (Cdk13$^{+/+}$) hearts. But the difference is significant in Cdk13$^{tm1b/tm1b}$ (HOMO) compared to WT (Cdk13$^{+/+}$) and Cdk13$^{tm1b/+}$ (HET) hearts. ns: not significant.

Groups comparison	Mean *Cdk13* expression (*log$_2$FC*)		Mean diff. in *log$_2$FC*	SE of diff.	95% CI of difference	Adjusted p-value
WT Vs HET	WT 0.000	HET -0.4964	0.4964	0.4201	-0.7925 to 1.785	0.5049 (n.s.)
WT Vs HOMO	WT 0.000	HOMO -2.010	2.010	0.4201	0.7209 to 3.299	0.0073 (sig.)
HET Vs HOMO	HET -0.4964	HOMO -2.010	1.513	0.4201	0.2244 to 2.802	0.0263 (sig.)

Table 3:9 Comparative mean Cdk13-transcript expression in E12.5 hearts from Cdk13^{tm1b} mouse line. Multiple comparisons of log$_2$FC of Cdk13 among the three E12.5 groups (n = 3 each) from Cdk13^{tm1b} mouse line using Post-hoc (multiple-comparisons) Tukey test. There was no significant difference between Cdk13$^{+/+}$ (WT) and Cdk13$^{tm1b/+}$ (HET) hearts (P = 0.5049) but the difference was significant between Cdk13$^{+/+}$ (WT) and Cdk13$^{tm1b/tm1b}$ (HOMO) hearts (P = 0.0073), and between Cdk13$^{tm1b/+}$ (HET) and Cdk13$^{tm1b/tm1b}$ (HOMO) hearts (P = 0.0263). The log$_2$FC in Cdk13$^{tm1b/+}$ (HET) and Cdk13$^{tm1b/tm1b}$ (HOMO) are compared to log$_2$FC of "zero" in Cdk13$^{+/+}$ (WT). The reference genes used were Pgk1 and Rpl4. n.s = not significant. SE = standard error.

3.3.9.4 Gene expression analysis of *Cdk13* in hearts at E15.5 shows no significant change in HET compared to WT hearts

The data for *Cdk13*$^{+/+}$ (WT) (W = 0.8808, *P* = 0.3268) and *Cdk13*$^{tm1b/+}$ (HET) (W = 0.9451, *P* = 0.5482) groups were normally distributed. No *Cdk13*$^{tm1b/tm1b}$ (HOMO) hearts were available for analysis. Comparing the two groups using unpaired t test, it was found that there was no significant difference between the means of *Cdk13* expression (log_2FC) of *Cdk13*$^{+/+}$ (WT) and *Cdk13*$^{tm1b/+}$ (HET) hearts (*P* = 0.1903) at E15.5 (Figure 3:31, Table 3:10).

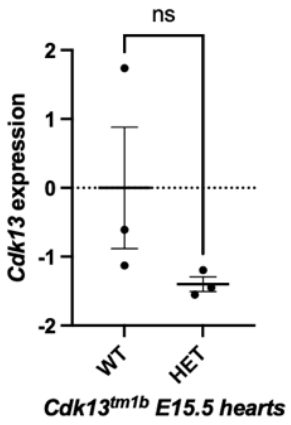


Figure 3:31 Transcript expression of Cdk13 in E15.5 hearts from Cdk13^{tm1b} *mouse line by RT-qPCR. Scatter plot showing mean values of* log_2FC *(with standard error) of Cdk13 in Cdk13*$^{tm1b/+}$ *(HET) hearts collected at E15.5 compared with Cdk13*$^{+/+}$ *(WT) using modified Pfaffl method [198]. There was no significant change in the expression of Cdk13 in Cdk13*$^{tm1b/+}$ *(HET) compared with Cdk13*$^{+/+}$ *(WT) hearts (P = 0.1903). ns: not significant.*

Groups' comparison	Mean *Cdk13* expression (log_2FC)		Mean diff. in log_2FC	SE of diff.	95% CI of difference	Unpaired t test
WT Vs HET	WT 0.000	HET -1.398	-1.398	0.8876	-3.863 to 1.066	0.1903 (n.s.)

Table 3:10 Comparative mean Cdk13 expression in E15.5 hearts from Cdk13^{tm1b} *mouse line. Unpaired t test gave no statistically significant difference between Cdk13*$^{+/+}$ *(WT) and Cdk13*$^{tm1b/+}$ *(HET) hearts (P = 0.1903). The reference genes used were Pgk1 and Rpl4. n.s = not significant, SE: Standard error; diff.: Difference, CI: Confidence interval.*

3.3.9.5 Gene expression analysis of *Cdk13* in adult mouse hearts shows no significant change in HET compared to WT hearts

The *Cdk13* expression data for adult *Cdk13*$^{+/+}$ (WT) (W= 0.9540, *P* = 0.5870) and *Cdk13*$^{tm1b/+}$ (HET) (W = 0.9977, *P* = 0.9076) mice were normally distributed. No adult *Cdk13*$^{tm1b/tm1b}$ (HOMO) mouse hearts were available for this analysis. Comparing the two adult mouse groups using unpaired t test, it was found that there was no significant difference between the means of *Cdk13* expression (log_2FC) in *Cdk13*$^{tm1b/+}$ (HET) hearts compared with *Cdk13*$^{+/+}$ (WT) (*P* = 0.1214) (Table 3:11, Figure 3:32).

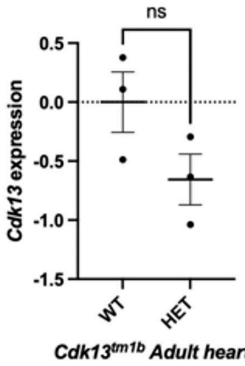


Figure 3:32 Transcript expression of Cdk13 in adult hearts from Cdk13^{tm1b} mouse line by RT-qPCR. Scatter plot showing mean values of log_2FC (with standard error) of Cdk13 in adult Cdk13$^{tm1b/+}$ (HET) hearts collected compared with adult Cdk13$^{+/+}$ (WT) hearts using modified Pfaffl method [198]. There was no significant change in the expression of Cdk13 in Cdk13$^{tm1b/+}$ (HET) compared with Cdk13$^{+/+}$ (WT) hearts (P = 0.1214). ns: not significant.

Groups' comparison	Mean *Cdk13* expression (log_2FC)		Mean diff. in log_2FC	SE of diff.	95% CI of difference	Unpaired t test
WT Vs HET	WT 3.333e-010	HET -0.6554	-0.6554	0.3342	-1.583 to 0.2725	0.1214 (n.s.)

Table 3:11 Comparative mean Cdk13 expression in adult hearts from Cdk13^{tm1b} mouse line. Unpaired t test gave no statistically significant difference between Cdk13$^{+/+}$ (WT) and Cdk13$^{tm1b/+}$ (HET) hearts (P = 0.1214). The reference genes used were Pgk1 and Rpl4. n.s = not significant, SE: Standard error of mean; diff.: Difference, CI: Confidence interval.

3.3.10 Immunoblot for CDK13 protein expression in adult mouse tissues

With the initial aim to identify the specific antibody to analyse *CDK13* protein expression, heart, brain and skeletal muscle tissues from adult WT and *Cdk13* $^{tm1b/+}$ (HET) mice were used. Different antibodies were tested at different time points and following the standard protocol used for other proteins as in this thesis. An example of blot image of one such antibody used is shown in Figure 3:33. It showed different non-specific bands in all tissues. In brain a 220 kDa band in the adult brain tissue was detected in WT and its intensity was reduced in HET brain. However, even this band was of higher size than the expected (164 kDa). Despite all possible efforts, no specific and effective antibody could be identified. A potentially promising antibody previously used by others [211] was discontinued by the supplier. Our group is working on designing a specific antibody for CDK13 in collaboration with others but until now, no breakthrough has been achieved.

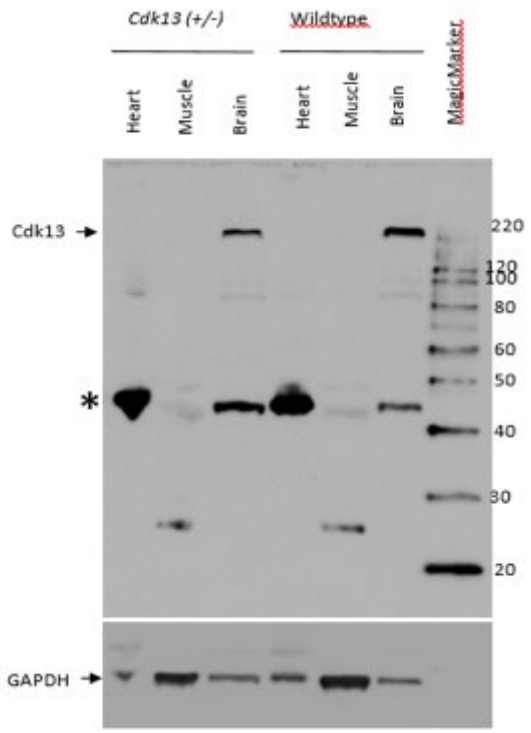


Figure 3:33 Trial for CDK13 protein detection in mouse tissues. Different non-specific bands were seen in all tissue samples. The antibody detected a higher size band of 220 kDa instead of the expected (164kDa) in the adult brain tissue and its intensity was reduced in HET brain. Asterisk denotes one of the non-specific bands. GAPDH was used as a loading control. Cdk13$^{+/-}$ denotes HET (Cdk13$^{tm1b/+}$) samples.

3.3.11 RNA-Sequencing on whole hearts from E12.5 mouse

There is very little information about the role that CDK13 plays during development. In order to obtain further information, targets of *Cdk13* were determined by carrying out transcriptome sequencing analysis. In this regard, RNA was extracted from individual hearts, without pooling, using the RNeasy micro kit as described in the methods section (2.12).

3.3.11.1 RNA-Sequencing results

RNA-Seq (3' end seq - 20 million reads) was carried out to compare WT (n = 5) and HOMO (n = 4) hearts from *Cdk13*^{tm1b} mouse at E12.5 stage. E12.5 was chosen since *Cdk13* is expressed at this time and key events

in heart morphogenesis such as septation of atria, ventricles and outflow tract have just started (at E11.5) and outlet septum, AV valves and semilunar valves start developing at this time [92]. Valvular structures also undergo significant maturation during this period [239] which continues until birth [92]. Moreover, this stage was expected to give enough material for our analysis without pooling them. We sought to explore the role of *Cdk13* in these key developmental events/stages which were susceptible to CHD.

To assess variability within the dataset, principal component analysis (PCA) was carried. Differential expression of genes (DEGs) was analysed by using DESeq2 package in R (done by Dr Fei Sang in Deep sequencing facility, School of Life Sciences, University of Nottingham). PCA showed that the intergroup (WT vs. HOMO) variability (25%) was more than the intragroup (14%) variability which is considered preferable (Figure 3:34). PCA helped us to identify one biological outlier which was later found to be HET (*Cdk13*$^{tm1b/+}$) on repeat genotyping and was thereby excluded from downstream analyses.

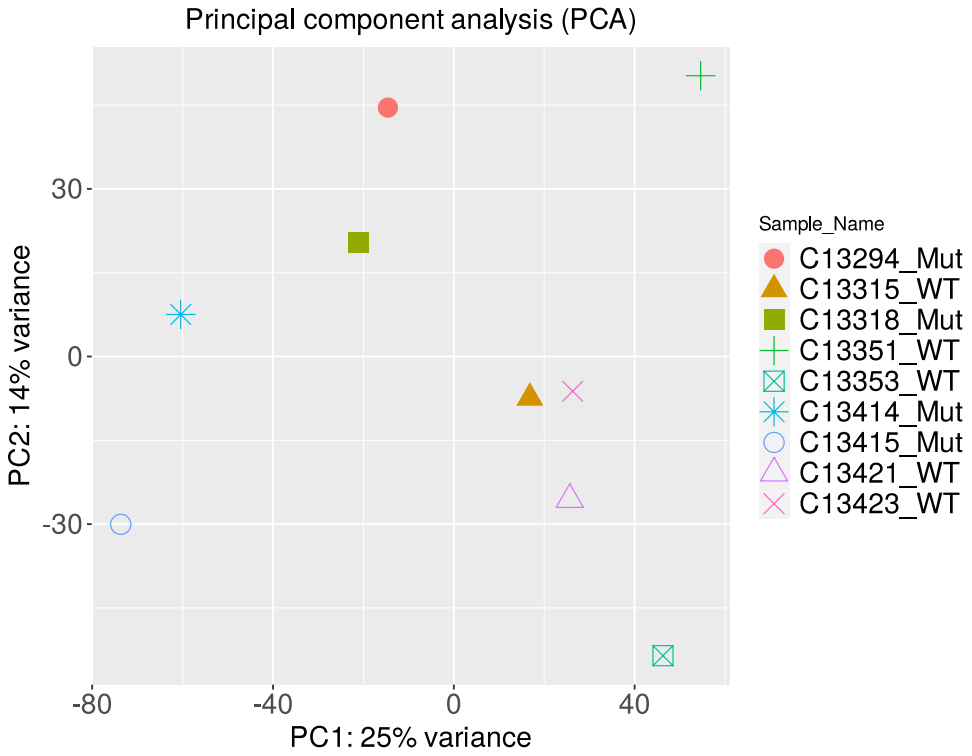


Figure 3:34 Assessment of intra- and intergroup variability. Principal component analysis (PCA) plot showing all 9 samples along the two PCs i.e., PC1 and 2. Within the expression dataset, there is 25% variability along PC1 and 14% along PC2. The expression data for this analysis was normalised (i.e., RPKM) and log transformed. "Mut" denotes Cdk13$^{tm1b/tm1b}$ (HOMO) samples.

3.3.11.2 Differential expression of genes in RNA-Sequencing data from *Cdk13^{tm1b}* mouse at E12.5

1626 genes were found to be differentially expressed (DEGs), using a cut off value of $P < 0.05$. 771 DEGs were upregulated ($log_2FC > 0$) whereas 855 were downregulated ($log_2FC < 0$) (Figure 3:35).

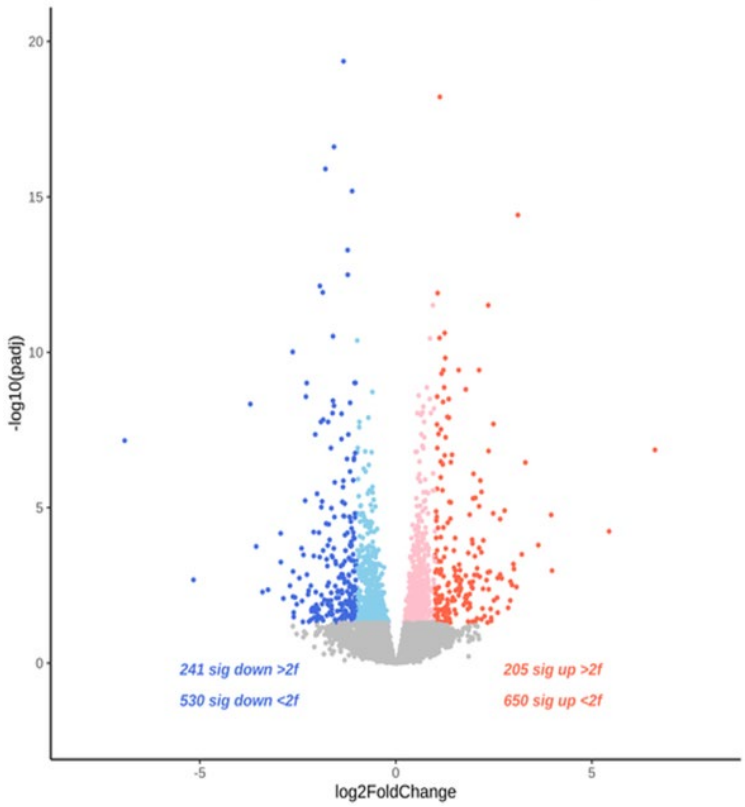


Figure 3:35 Differentially expressed genes in hearts from Cdk13^{tm1b} mouse comparing WT with HOMO. Volcano plot showing the log2 fold change against the −log10 adjusted P value for comparisons between the WT (n = 5) versus HOMO (n = 4) mutant heart samples. Up- and downregulated differentially expressed genes with a false discovery rate less than 0.05 are shown in red and blue, respectively. Total of 771 genes were downregulated (241 with greater than and 530 with less than two-fold change) and 855 genes were upregulated (205 with greater than two-fold change and 650 with less than two fold change). The coloured points are DEGs with FDR = 0.05.

3.3.11.3 *Cdk13* mutation is associated with enrichment of heart related GO terms

Gene ontology (GO) enrichment analysis was performed to explore functional profile of the differentially expressed genes (DEGs). A total of 22 GO terms related to cardiovascular system morphogenesis were enriched, represented by 77 DEGs (41 DR and 36 UR) genes in *Cdk13*$^{tm1b/tm1b}$ (HOMO) hearts samples (Figure 3:36).

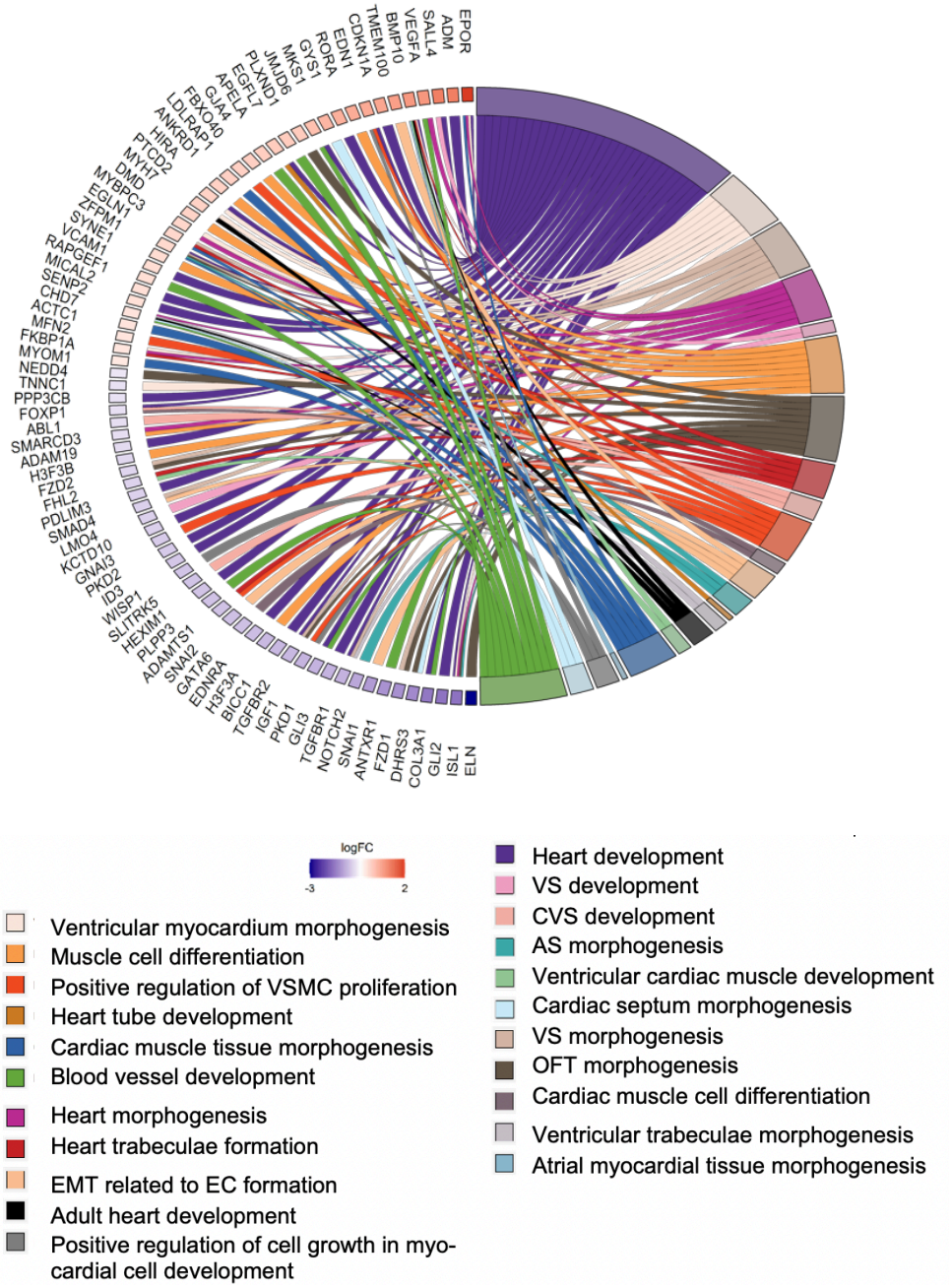


Figure 3:36 Chord diagram showing functional enrichment analysis of the DEGs. The top 41 up- and 36 downregulated genes are shown. GO terms related to heart development are enriched in Cdk13tm1b/tm1b (HOMO) hearts. Varying shades of orange and purple colours denote up- and downregulated genes respectively. A colour code (shown as bar) is proportional to the log_2FC ($P < 0.05$). DEGs are shown on the left half of the chord diagram whereas the heart related GO terms are on the right half (as colour coded regions), connecting with the respective DEG. Colour coded key below the diagram denotes the different GO terms. VSMC: Vascular smooth muscle cell; EMT: epithelial-mesenchymal transition; EC: endocardial cushions formation; AS: atrial septum; VS: ventricular septum; CVS: cardiovascular system; OFT: outflow tract; VSMC: vascular smooth muscle cell.

3.3.11.4 *Cdk13* mutation is associated with suppression of the morphogenetic pathways

Based on RNA-Seq data comparing WT with *Cdk13*$^{tm1b/tm1b}$ (HOMO) hearts at E12.5, it's evident that various pathways related to morphogenesis of various body tissues are suppressed in HOMO (*Cdk13*$^{tm1b/tm1b}$) hearts compared with WT. The pathways related to development of cerebellum and its different layers (even hindbrain), photoreceptor cells in the retina, and hind gut are suppressed in case of homozygous LOF of *Cdk13* (*Cdk13*$^{tm1b/tm1b}$). Pathways related to placenta development are also modulated (activated) in case of *Cdk13* LOF-mutation (Figure 3:37).

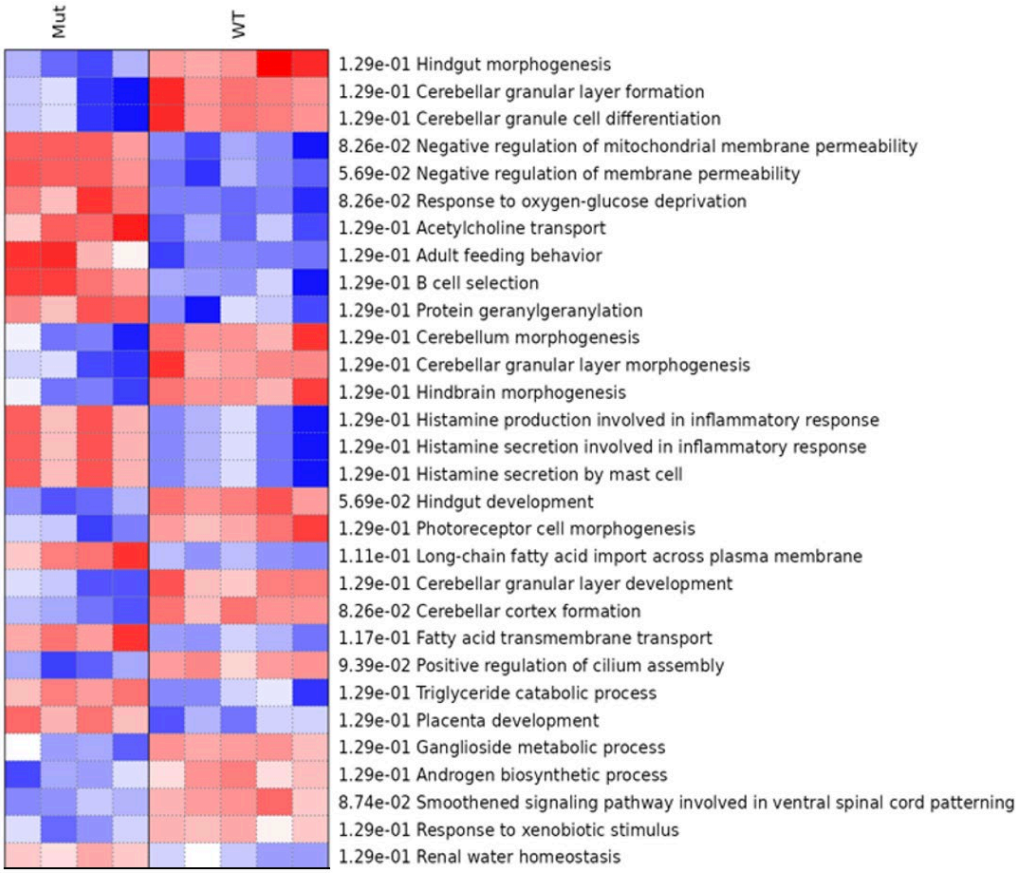


Figure 3:37 Heatmap showing results of gene set enrichment analysis for all samples using gene set of GO biological processes. The pathways for the development of different parts of the body such as brain (cerebellum, hindbrain), eyes (photoreceptor cells of retina) and hind gut are suppressed in Cdk13 HOMO (Mut) samples. Mut: mutant (Cdk13$^{tm1/tm1b}$). Red colour denotes UR whereas blue colour represents DR processes [196].

3.3.11.5 *Cdk13* mutation is associated with suppression of kinase activity at RNA polymerase-II

RNA-Seq data comparing WT with *Cdk13*$^{tm1b/tm1b}$ (HOMO) hearts at E12.5 shows enrichment of various biological processes with high fold change ($P < 0.05$). An interesting finding in this analysis is the downregulation of kinase activity at the CTD of RNA polymerase-II in case of *Cdk13* mutation (Figure 3:38). This is expected in case of LOF of *Cdk13* as in our *Cdk13*$^{tm1b/tm1b}$ (HOMO) mouse.

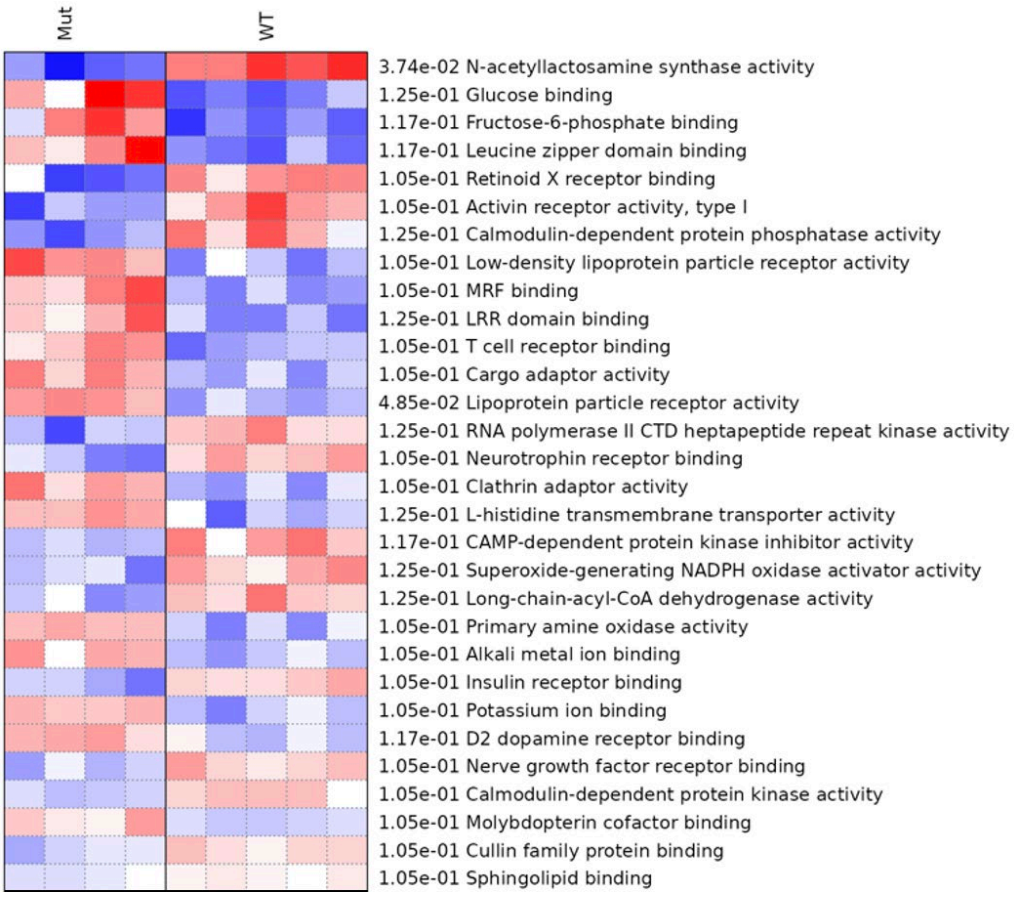


Figure 3:38 Heatmap showing results of gene set enrichment analysis for all samples using gene set of GO molecular processes. Various molecular processes are enriched in case of Cdk13 mutation, including kinase activity at RNA polymerase II at its C-terminal domain which is downregulated in the mutant heart. Mut: mutant (Cdk13$^{tm1b/tm1b}$). Red colour denotes UR whereas blue colour represents DR processes [196].

3.3.11.6 *Cdk13* mutation is associated with downregulation of processes related to RNA processing

RNA-Seq results show that *Cdk13* mutation is associated with significant downregulation ($P < 0.05$) of body processes related to ribosome biosynthesis, ribosomal RNA processing and metabolism. Moreover, the pathways for extracellular structure/matrix organisation are significantly upregulated (Figure 3:39).

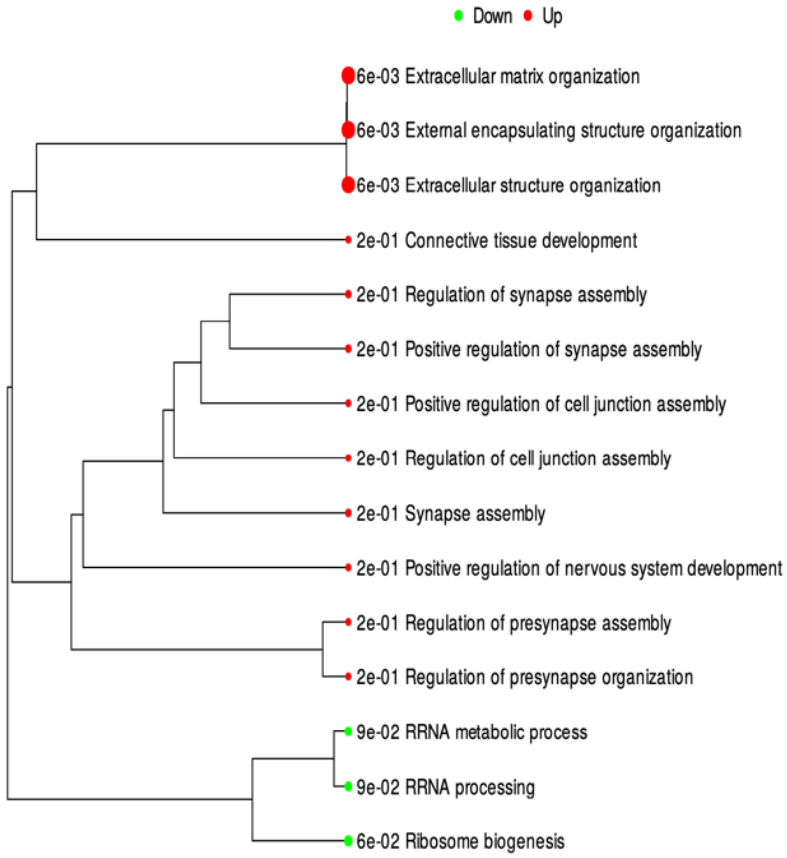


Figure 3:39 Visual tree representation of the effects of the differential expression of GO terms for cellular processes. Red dots denote up- whereas green dot represents down regulation. Size of the dot corresponds to the value of adjusted P value [196].

3.3.11.7 Selecting potential targets from RNA-Seq data for qPCR validation

To study the downstream targets of *Cdk13*, top 10 candidate genes from both up- and downregulated categories were selected based on $\log_2$fold change ($P < 0.05$) and GO terms related to heart development. These were then analysed using STRING [240] to determine their protein-protein interaction networks to know their interaction (direct or indirect) with known heart related developmental pathways. Moreover, their expression profile at different developmental stages of mouse was determined using *Bgee* [241] and *MGI* [242] to know their expression score/level at

E12.5. Additionally, a literature review was carried out to find if GOI have been associated with any CHD phenotype in mouse studies.

Using all these filters and taking into account the time constraints, six genes from the upregulated and six from the downregulated genes' list were selected for downstream analysis. However, five of these 12 genes had to be excluded from further analysis due to failure at the primer optimisation stage. Hence, the final list of selected genes for downstream qPCR validation narrowed down to 4 (*Sall4*, *Vegfa, Cdkn1a* & *Edn1*) from the UR and 3 (*Eln*, *Notch2* & *Ednra*) from the DR categories (Figure 3:40) out of the total 77 heart related-differentially expressed genes in the RNA-Seq data.

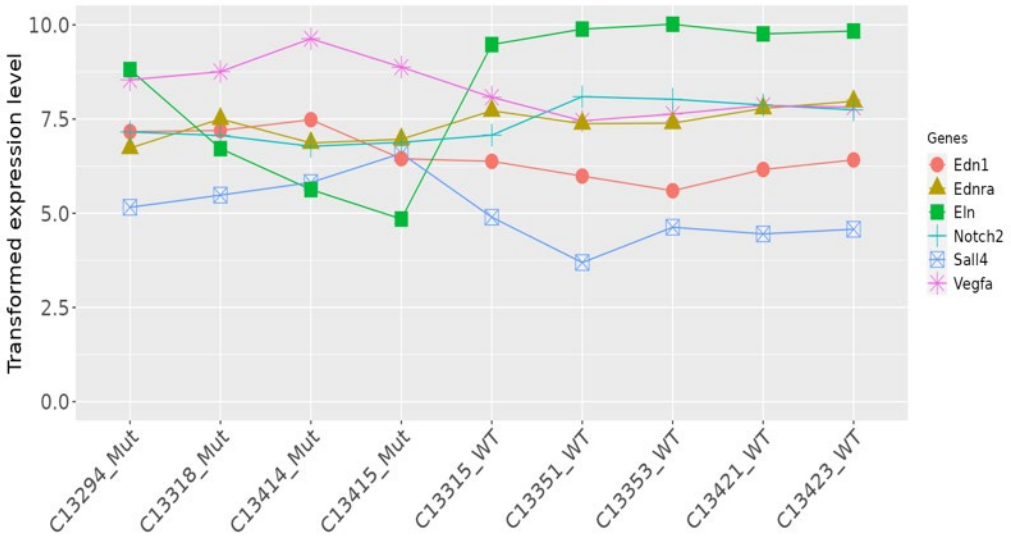


Figure 3:40 Differential expression of the genes in Cdk13^{tm1b} RNA-Seq data, selected for downstream analyses. From the list of heart related genes in the RNA-Seq data, the transformed expression level of these genes from RNA-Seq data is shown along y-axis whereas the x-axis shows individual biological replicates from the two groups. Sall4 (blue), Vegfa (pink) and Edn1 (red) were significantly upregulated whereas Ednra (brown), Eln (green) and Notch2 (turquoise) were downregulated [196]. Cdkn1a is not shown here as its modulated expression was not validated by qPCR.

3.3.12 qPCR for genes related to morphogenesis of cardiovascular system

3.3.12.1 qPCR primer efficiency optimisation for GOI

For qPCR validation of GOI selected, primers were designed and optimised as described in the "methods" section of this thesis (Table 2:7).

3.3.12.2 Comparative qPCR for GOI

For comparative qPCR, RNA was isolated from 3 *Cdk13*$^{+/+}$ (WT) and 3 *Cdk13*$^{tm1b/tm1b}$ (HOMO) mouse hearts at E12.5. RNA was reverse transcribed to cDNA to use as a template for qPCR. *Pgk1* and *Rpl4* were used as reference genes for normalisation to calculate the fold change. Out of the 7 genes selected from the RNA-Seq data, 3 up- and 3 downregulated genes were validated by qPCR. *Cdkn1a* was the only one in this list which was not validated by qPCR (Table 3:12, Figure 3:41).

DEGs	Effect on expression level	log_2FC RNA-Seq (*P* < 0.05))	log_2FC qPCR (*P* value)	qPCR validation
Sall4	UR	+1.52	+0.82 (*P* = 0.02)	validated
Vegfa	UR	+1.12	+0.92 (*P* = 0.02)	validated
Cdkn1a	UR	+1.07	+0.2, (*P* = 0.60)	not validated
Edn1	UR	+1.02	+0.25 (*P* = 0.03)	validated
Ednra	DR	-0.63	-1.034 (*P* = 0.05)	validated
Notch2	DR	-0.83	-1.136 (*P* = 0.03)	validated
Eln	DR	-2.53	-1.67 (*P* = 0.03)	validated

Table 3:12 qPCR validation of the differentially expressed GOI from RNA-Seq data of Cdk13^{tm1b} mouse hearts. The selected up- and downregulated heart-related genes as reported by RNA-Seq data (P < 0.05) were subjected to qPCR validation. Three out of four selected upregulated-GOI and all 3 downregulated-GOI were validated by qPCR (P < 0.05). Positive and negative signs with log_2FC denote up- and downregulation respectively. DEGs: differentially expressed genes.

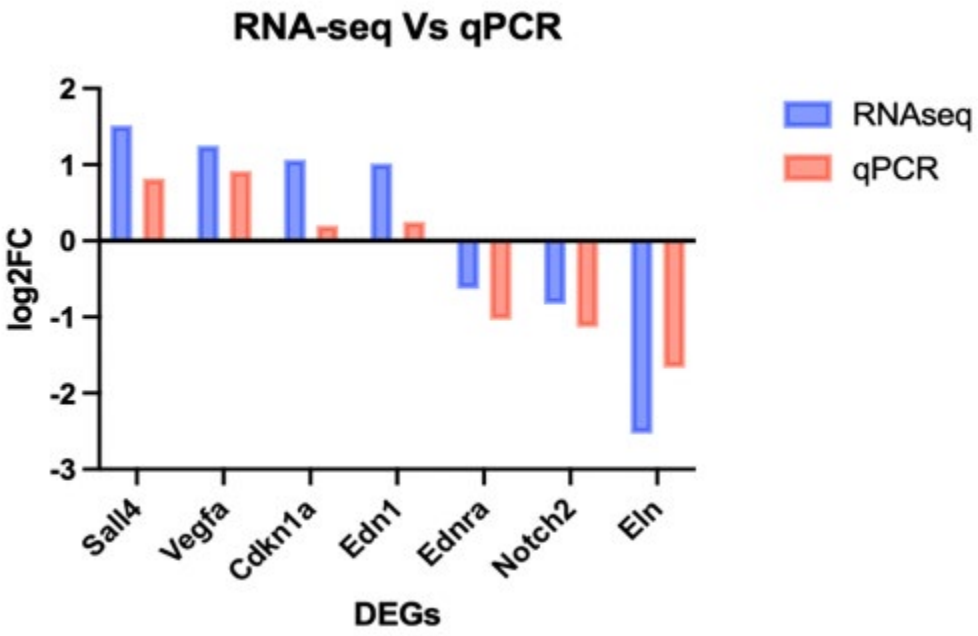


Figure 3:41 qPCR validation of the log_2FC of the differentially expressed genes from RNA-Seq data of $Cdk13^{tm1b}$ mouse, comparing $Cdk13^{+/+}$ (WT) with $Cdk13^{tm1b/tm1b}$ (HOMO) hearts. Bar graphs showing the log_2FC of the differentially expressed genes (P < 0.05) shown along x-axis reported by RNA-Seq (blue bars) and validated by qPCR (red bars). The log_2FC in case of Cdkn1a and Edn1 were quite less on qPCR than that on RNA-Seq data.

3.3.13 Whole mount *in Situ* hybridization (W-ISH) for GOI

Whole mount *in situ* hybridization (W-ISH) is considered as a quite reliable technique to assess spatial and temporal RNA expression pattern of genes in whole embryos or their tissues/organs [243]. In order to understand the potential role of these GOI in CHD, *in situ* hybridization was carried out to locate expression of their transcribed sequences in the developing mouse heart at E12.5, using non-radioactive DIG-labelled RNA probes designed in-house.

3.3.13.1 Differential expression of GOI related to heart development

Cdk13 ^{tm1b} WT and HET embryos (n = 3 each) were collected at E12.5 for W-ISH for each GOI. The GOI selected for W-ISH were 2 DR (*Notch2* and *Eln*) and 1 UR (*Sall4*). The riboprobes for each of these GOIs were used for hybridization with the embryo's RNA in mouse heart. The uracil nucleotide of the riboprobe was conjugated to digoxigenin (DIG) which enabled semiquantitative visualisation of mRNA due to anti-DIG antibody and chromogenic substrate, BM purple. Focus of the analysis was to assess differential expression of the selected GOIs in the areas of the heart related to the morphologic phenotypes observed in the HREM analysis. There was limitation to collect HOMO hearts in the available time for experiment and hence comparative W-ISH based analysis was carried out between WT and HET hearts.

The E12.5 developmental stage was selected since the key structural features of the embryonic hearts are forming at this time [32] and expression pattern of *Cdk13*-targets at this stage would be useful to explain the phenotypes observed in the hearts of these mice at E15.5. Moreover, the heart size and tissue architecture at E12.5 compared to earlier stages (e.g., E10.5) were appropriate to sustain extensive manipulation during processing. Nevertheless, E12.5 stage heart were still very delicate to manipulate and photographing these for expression analysis was quite challenging. For the same reason, some extracardiac tissues were left adhering to the heart so as to avoid damaging the heart. The sense control for W-ISH experiments are given in appendix-1.

***Elastin* (*Eln*):**

Eln was the topmost heart-related downregulated gene in our RNA-Seq dataset (Table 3:12, Figure 3:41). *In Situ* experiments at E12.5 localise its expression in the outflow region of the heart, as well as in aorta and pulmonary trunk (and its branches). Outflow region of the heart in mouse undergoes septation during E11.5 to E13.5 to become aorta and pulmonary trunk [32]. *Eln* expression was strong in the primitive aorta and pulmonary trunk at this stage in WT heart (yellow arrows in Figure 3:42-A). Moreover, some expression was observed in the area inferior to them in the outflow region of the heart (Figure 3:42-B).

Comparing *Eln* expression in WT with HET hearts (n = 3 each), there was reduced expression in HET hearts compared to WT in the outflow region of the heart, specifically at the site of septum between the two vessels (black arrow in Figure 3:42-B' compared with A'). Further, following the pulmonary trunk distally and to some of its branches, the expression appeared reduced in case of HET mutation. Identifying a differential expression, if any, in aorta of HET heart was challenging to identify. However, the fading of expression (faint blue) in pulmonary trunk and its branches in HET hearts could be seen (blue arrows in Figure 3:42 B' compared to A'). Distal extension of aorta and its associated different pharyngeal arch arteries were severed during harvesting.

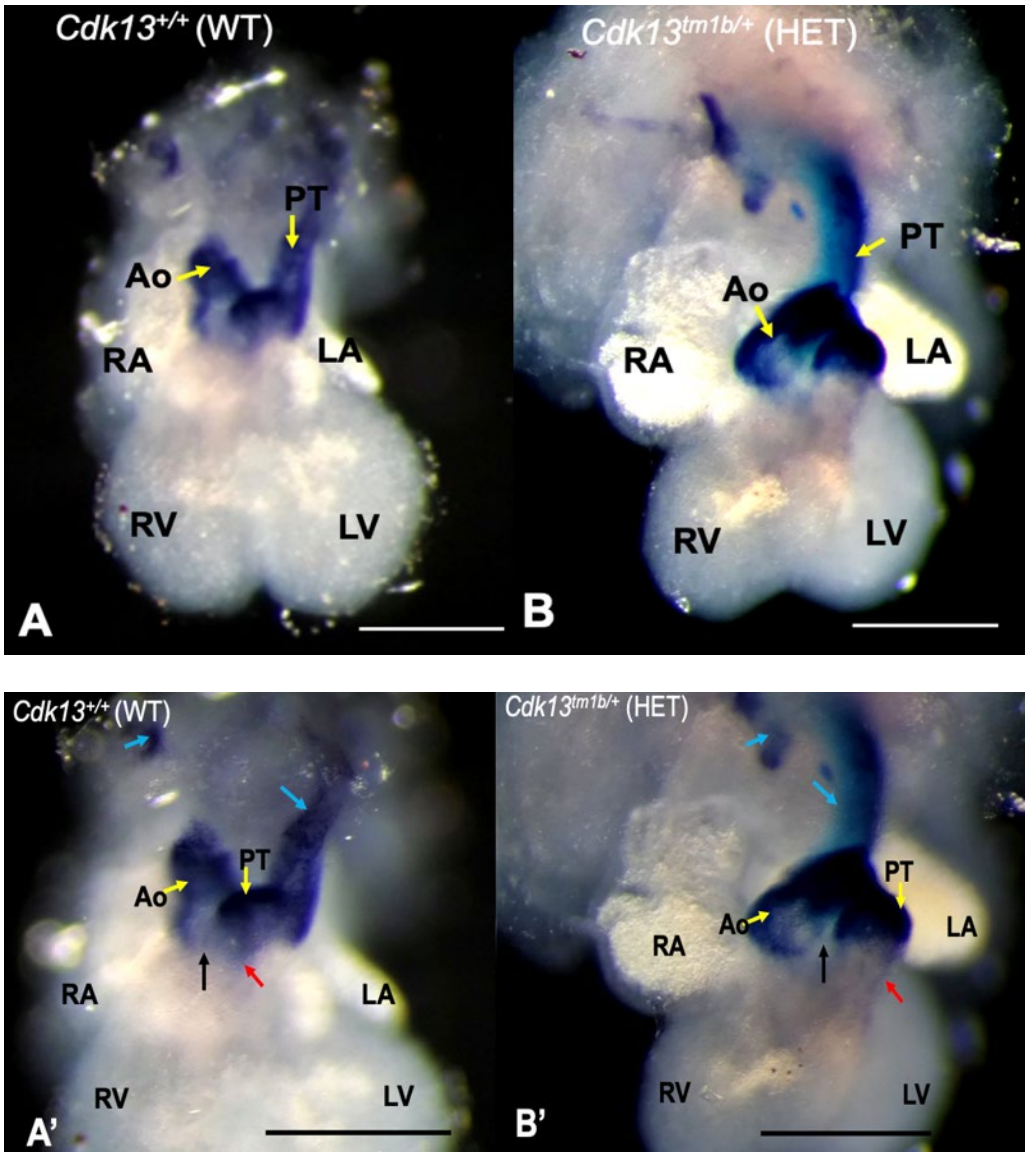


Figure 3:42 Whole mount In Situ hybridization for Eln expression in E12.5 mouse heart. W-ISH was carried on whole Cdk13^{tm1b} hearts at E12.5 comparing transcript expression of Eln in WT with Cdk13$^{tm1b/+}$ (HET) hearts. The comparison showed reduced expression in Cdk13$^{tm1b/+}$ (HET) hearts (n = 3) compared to WT (n = 3) in the outflow region of the heart, specifically in the OFT septation complex (black arrow). Further following the pulmonary trunk distally (blue arrows), the expression appeared reduced in case of HET (Cdk13$^{tm1b/+)}$ mutation. The colour shade in HET, appeared brighter mainly due to overlap of the dyed structures, giving additive/stronger colour effect in the proximal part of pulmonary trunk. Scale bar 200um for all images. RA: right atrium; LA: left atrium; RV: right ventricle; LV: left ventricle; VS: ventricular septum; Ao: aorta; PT: pulmonary trunk.

***Sall4 (Spalt Like Transcription Factor 4)**:*

Sall4 was one of the top UR genes in *Cdk13*$^{tm1b/tm1b}$ (HOMO) hearts in the RNA-Seq data (Table 3:12, Figure 3:41). W-ISH was carried out to locate the expression of *Sall4* in *Cdk13*^{tm1b} hearts at E12.5, and to compare *Cdk13*$^{+/+}$ (WT) (n = 3) with *Cdk13*$^{tm1b/+}$ (HET) hearts (n = 3). *Sall4* expression was observed in E12.5 hearts in ventricular myocardium (red arrows in Figure 3:43 A-C), aorta and pulmonary trunk (yellow arrows in Figure 3:43 A & B), including outflow/conotruncal cushions (black arrows in Figure 3:43-C) and this expression was increased in HET hearts (Figure 3:43 B & C compared to A).

As a limitation of the technique, some liquids can be seen as possibly trapped within the ventricular chambers (Figure 3:43 A-B). In future experiments, ISH on tissue (heart) sections would prevent this to happen. Moreover, that would help localising exact expression of the transcript in specific areas of the heart.

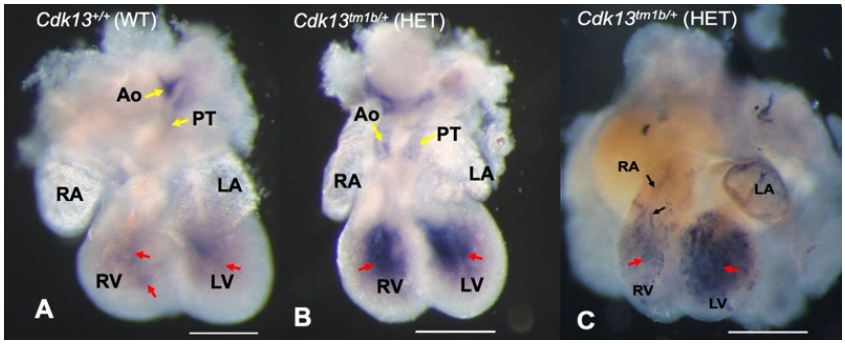


Figure 3:43 W-ISH to locate transcript expression of Sall4 in E12.5 Cdk13^{tm1b} *heart. Sall4 expression was observed in ventricular myocardium (red arrow in A-C), aorta and pulmonary trunk (yellow arrows in A-B), including outflow/conotruncal cushions (black arrows in C) and this expression was increased in HET hearts (n = 3) (B-C) compared with WT (n = 3) (A). Image in panel C is a different HET biological replicate. Scale bar: A= 100μm, B-C = 200μm. RA: right atrium; LA: left atrium; RV: right ventricle; LV: left ventricle; VS: ventricular septum; Ao: aorta; PT: pulmonary trunk.*

***Notch2 (Notch Receptor 2)*:**

Notch2 was one of the top downregulated genes in *Cdk13*$^{tm1b/tm1b}$ (HOMO) hearts in the RNA-Seq data (Table 3:12, Figure 3:41). W-ISH of *Cdk13*^{tm1b} hearts at E12.5 with in-house designed *Notch2* RNA probe showed its expression (denoted by yellow arrows in Figure 3:44 A-D) in atrioventricular endocardial cushions (denoted by asterisks in Figure 3:44 A-D) and in the outflow region (blue arrows pointing at the outflow cushions in Figure 3:44 A,B & D). Between and superior to the two sets of blue arrows, obliquely, there was dense area of *Notch2* expression where the colour intensity was more due to overlap of the aorta and PT in there (Figure 3:44 A). Overall, it showed *Notch2* expression in the outflow region of both ventricles (blue arrows in Figure 3:44 A,B & D). Expression was also observed in left atrioventricular region and in the (anterolateral leaflet of) left AV valve (black arrows in Figure 3:44 B&D). However, origin of aorta was not apparent in this view. Right AV canal being deeply located was not visible, nevertheless, expression in endocardial cushions (*) (denoted by yellow arrows in Figure 3:44 A-D) supports its role in atrioventricular valve development [244]. Some expression was also visible inferior to endocardial cushions in the upper part of muscular VS, facing the two ventricular cavities (white arrows in Figure 3:44-B). *Notch2* expression was also observed in the trabeculae (red arrows in Figure 3:44 A-D). Expression in HET hearts (n = 3) was decreased (Figure 3:44 B & D) compared with WT (n = 3) (Figure 3:44 A&C).

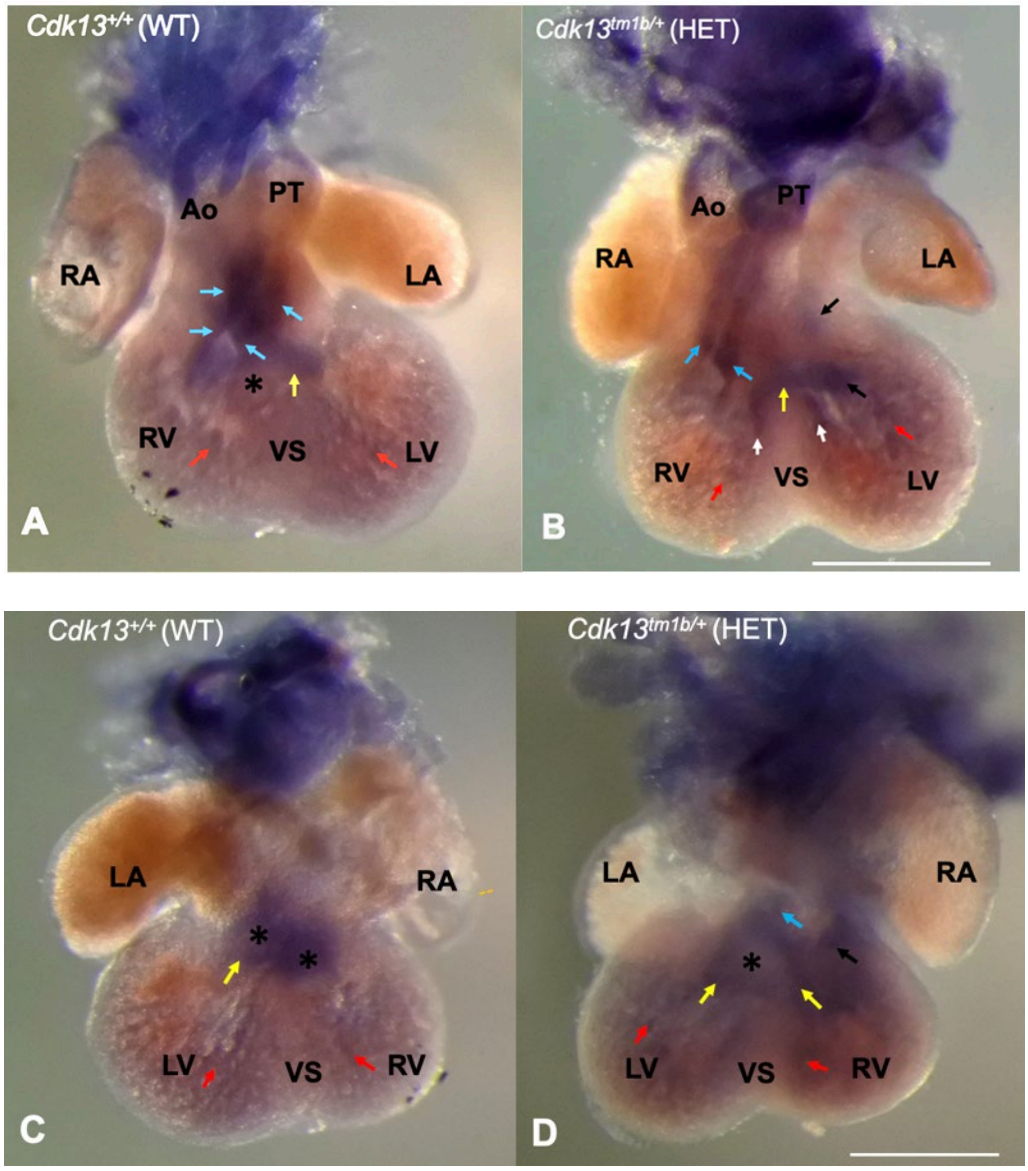


Figure 3:44 Transcript expression of Notch2 in E12.5 Cdk13^{tm1b} mouse heart. A-B: anterior view, and C-D: posterior views of WT (n = 3) and HET hearts (n = 3). In E12.5 heart, Notch2 seems active. Expression of Notch2 is observed in endocardial cushions (asterisk and yellow arrow in A-D) and in the outflow region (blue arrows pointing at outflow tract cushions in A,B & D). Superior to the two blue arrows, obliquely, there is a dense area of Notch2 expression possibly due to overlap of the aorta and PT in there. The lower blue arrow in Fig B is sitting on the outflow cushion. Black arrow (in B, D) are pointing at the site of left atrioventricular canal deeply located and expressing Notch2 in the anterolateral leaflet of mitral valve. Right AV valves being deeply located are not visible. The yellow arow (in A) in the LV is also where LVOT is. However, origin of aorta was not clearly discernible. Some expression is also visible inferior to the AV endocardial cushions in the upper part of muscular VS, facing the two ventricular cavities (denoted by white arrows in B). Posterior view of the WT heart (C) shows increased Notch2 expression in the outflow regions

of both ventricles (superolateral to the yellow arrow and between the endocardial cushions). Image C also shows quite prominent expression in the atrioventricular endocardial cushions (*). There is also expression of Notch2 in the trabeculae (red arrows in A-D). Expression in HET hearts is decreased (B & D) compared with WT (A&C). All the images shown are representative of at least three embryos from each group. Scale bar 200μm for all images. RA: right atrium; LA: left atrium; RV: right ventricle; LV: left ventricle; VS: ventricular septum; Ao: aorta; PT: pulmonary trunk.

3.4 DISCUSSION, CONCLUSIONS AND PERSPECTIVES FOR FUTURE WORK

In order to characterise the role of *Cdk13* in heart development and congenital heart disease, a mouse model with *Cdk13*-LOF mutation was used in this study.

Survival ratios in mouse embryos and neonates

The genotype distribution of the collected embryos at E12.5 and E15.5 shows that the ratios obtained were less than the expected Mendelian ratios and there was a statistically significant difference between the observed and expected ratios at both of these stages, analysed separately. This manifests that *Cdk13*$^{tm1b/tm1b}$ (homozygous) mice are embryonically lethal, with E15.5 worse than E12.5 (Table 3:2). Nevertheless, both of the selected stages (E12.5 and E15.5) for our experiments constitute part of the potential survival window for *Cdk13*$^{tm1b/tm1b}$ (homozygous) embryos at which we collected them for our experiments. A recently reported study states that heart failure might be the reason for embryonic lethality in the *Cdk13*$^{tm1a/tm1a}$ mice and hence advocates for the potentially crucial role of CDK13 for normal heart development [211]. In the data presented in this thesis, hearts with pericardial effusion, as happens in heart failure [245], were observed in some mice on gross phenotypic analysis at the time of harvest (Table 3:3). Effects of *Cdk13* mutation on downstream targets such as *Gata6* can also cause embryonic lethality due to its effect on extraembryonic endoderm [246]. *Gata6* was one of

the significantly downregulated genes in our *Cdk13*^{tm1b} RNA-Seq data (-0.60, P = < 0.05).

Gross morphologic analysis

At the time of collection at E12.5 and E15.5, 9 out of 245 *Cdk13*$^{tm1b/+}$ (HET) and 21 out of 41 *Cdk13*$^{tm1b/tm1b}$ (HOMO) embryos were growth retarded and/or dead (Table 3:3 and Figure 3:6). Placental defects have been associated with intrauterine growth retardation (IUGR) [247], mostly with genetic basis. Such genetic defects in addition to causing placental abnormalities also can cause congenital defects such as CHD [247, 248]. This is because both placenta and heart develop in parallel as "placenta-heart axis" and possess shared ontogeny [249-251]. CHD can result in circulatory changes, affecting the placenta and leading to IUGR, whereas placental insufficiency, if there, can cause IUGR and affect intrauterine developmental programs leading to congenital defects such as CHD [249]. In this study, penetrance of growth retardation as well as CHD was more in case of homozygous (*Cdk13*$^{tm1b/tm1b}$) mutation. This might suggest that genetic mutation might have caused placental defects resulting in IUGR as well as CHD. Placental assessment was not the aim of this study as we focussed on heart defects in relation to *Cdk13* mutation. However, if we correlate the penetrance of CHD with probable placental defects (potentially causing IUGR), we see that in only ~50% homozygous (*Cdk13*$^{tm1b/tm1b}$) cases, there was IUGR and probably the placental defect. So that means that high CHD penetrance in rest of the 50% HOMO mice cannot be explained solely by any potential placental defects (and hence IUGR) leading to CHD. Also, the dam was HET and

hence maternal decidua contribution ideally stays same/uniform for both HET and HOMO embryos unless the cause lies in the trophoblast. Since congenital defects themselves as fetal factors (others being maternal, placental, genetic) can also cause IUGR [248], it seems plausible in case of high CHD penetrance in homozygous (*Cdk13*$^{tm1b/tm1b}$) hearts. However, only one HET heart (C13.57.8) with CHD as analysed at E15.5 had growth retardation in our study. The rest of those labelled as growth retarded at the time of collection were at E12.5 and hence not analysed by HREM for cardiac phenotyping. Placental assessment is something worth doing in any future work to relate *Cdk13* mutation with CHD either as its direct effect, consequence of placental defect or primarily placental defect resulting secondarily as CHD.

CDK13 mutations in human subjects were associated with facial dysmorphism (FD), in association with CHD and intellectual disability (ID), collectively called as CHDFIDD disorder [213]. The *Cdk13*^{tm1b} mouse model used in this study showed that mid-facial aplasia/cleft was observed in 13 homozygous (*Cdk13*$^{tm1b/tm1b}$) embryos (Figure 3:7-D,D'), whereas in only one heterozygous (*Cdk13*$^{tm1b/+}$) embryo, there was a groove at the site of fusion of medial nasal prominences. We noticed that presence of midfacial aplasia/cleft (not groove) was always associated with homozygous (*Cdk13*$^{tm1b/tm1b}$) mutation. Our *LacZ* expression study showed ubiquitous expression of *Cdk13* in craniofacial structures and hence its deficiency could relate to the facial cleft phenotype. Moreover, interference with the key genes and pathways involved in craniofacial development in case of homozygous (*Cdk13*$^{tm1b/tm1b}$) mutation are also

expected to contribute. The pathways related to craniofacial development are shared and those particularly relevant are BMPs [252] WNTs [253], Hedgehog [254] and FGFs [255]. In our RNA-Seq data, expression of *Bmp10*, *Bmp2k*, *Wnt4*, *Wnt5b*, *Fgfr2*, *Fgf11* were dysregulated in homozygous (*Cdk13*$^{tm1b/tm1b}$) mice. In general, there is scarcity of data regards the genes involved in craniofacial development. Genome-wide association studies (GWAS) have reported some genes with potential role in craniofacial development [256-258]. By looking for these genes in our RNA-Seq data, we found that some of the genes are dysregulated in our homozygous (*Cdk13*$^{tm1b/tm1b}$) mouse such as *Cacna2d3*(↑), *Prdm16*(↓) [256], *Gli3*(↓) [257], *Snai1*(↓), *Abca4*(↑), *Arhgap29*(↑) [258]. Craniofacial development involves well-coordinated sequence of events and cranial neural crest cells (NCC) have key role in it [259]. The close and well-patterned interaction between brain and face is vital for normal craniofacial development [260]. The area involving facial defect is derived from NCCs [259], but NCC markers like *Sox2* and *Sox9* were not affected though in our heart transcriptome data. However, this does not exclude NCCs involvement in the abnormal craniofacial development as we noted above that not only presence but proper coordination of sequential events of different factors including NCCs is important. Nevertheless, *Sox12*, expressed in palatal epithelium and mesenchyme [261], was downregulated in our dataset. Since the RNA-Seq transcriptome data is from heart, future studies looking into expression of these key genes related to craniofacial development in craniofacial tissues would be more appropriate.

Hydrocephaly was observed in one adult female heterozygous (*Cdk13*$^{tm1b/+}$) (Figure 3:8) and one E12.5 homozygous (*Cdk13*$^{tm1b/tm1b}$) embryo (with sex unknown). No further analysis of any adult tissues was carried out on this mouse so we are unsure of any other associated defect. Mutation in L1 cell adhesion molecule (*L1cam) with* X-linked inheritance [262], as well as in Kinesin family member 6 (*Kif6)* have been previously associated with congenital hydrocephalus [263]. *L1cam* gene encodes a protein important for neuron guidance as well function [264] whereas knock-out of *Kif6* is associated with dysfunction of cilia of ependymal cells in cerebral ventricles [265]. In our RNA-Seq data, both these genes were upregulated in homozygous (*Cdk13*$^{tm1b/tm1b}$) samples (though not significant; $P > 0.05$). The sex of the E12.5 homozygous (*Cdk13*$^{tm1b/tm1b}$) embryo was unknown and hydrocephalus in this embryo was associated with midfacial aplasia/cleft too, making it a syndromic form of hydrocephalus. This is supported by a recent study suggesting hydrocephalus as part of a syndrome caused by mutations in such genes which are known for causing syndromic defects [266].

In one heterozygous (*Cdk13*$^{tm1b/+}$) and one WT (*Cdk13*$^{+/+}$) E15.5 embryo, unilateral anophthalmia (right and left respectively) with absent palpebral fissure was noted (Figure 3:10). This seemed to be a spontaneous finding. However, ocular abnormalities are common in wild type C57BL/6N mice [267].

HREM analysis of hearts

In humans, the most common CHD is BAV which affects approximately 2% of the population [268] but might stay asymptomatic until later in life

and can complicate into aortic stenosis, coarctation or aortic dissection [269]. In this study, two E15.5 heterozygous hearts had a fused type of BAV which accounts for 90-95% of cases in humans [270, 271]. There were fused left and non-coronary cusps having a single raphe and two commissures (Figure 3:13 B & B' compared with A & A'). The coronary arteries were patent, and both were emerging correctly from their respective sinuses (red arrows in Figure 3:13 A', B' & C'). In another heterozygous heart, type 2 BAV (i.e., 2-sinus BAV) was seen which accounts for 5-7% of cases in humans [235]. This had two cusps and sinuses, two commissures and absent raphe (Figure 3:13 C & C' compared with A & A' and B & B'). Gene mutations have been implicated in the aetiology of BAV [268] which supports our observations. Many of those earlier reported genes associated with BAV were dysregulated in the *Cdk13*^{tm1b} mouse RNA-Seq data such as *Slc2a3* (+1.88), *Timp3* (-0.49) (both on X chromosomes), *Tgfbr1*(-0.73), *Tgfbr2* (-0.67), *Hira* (+0.55) (associated with velofaciocardial syndrome), *Notch3* (-1.15), *Notch2* (-0.84), *Jarid2* (+0.27) (a Notch pathway gene), *Exoc4* (+0.27), *Gata6* (-0.60) [268]. These findings from literature and RNA-Seq data from this project suggest that *Cdk13* mutation results in BAV (and other heart defects) through its various downstream targets.

After BAV, the next most common CHDs in humans are ASDs and VSDs [108]. Cardiac phenotypic analysis showed that in case of *Cdk13* mutation, perimembranous type of VSD was the most common CHD observed (Table 3:5 & Table 3:6). In heterozygous (*Cdk13*$^{tm1b/+}$) hearts, isolated perimembranous VSDs were seen in two whereas muscular VSD

was seen in one of them. In other heterozygous (*Cdk13*$^{tm1b/+}$) hearts, there were associated DORV and BAV. In homozygous (*Cdk13*$^{tm1b/tm1b}$) hearts, AVSD was commonly present, always in association with other defects such as DORV, muscular VSD, BAV in varying combination. AVSD occurs in approximately 0.05% of live-births in humans [112]. Variants of VEGF-A and genes in its pathway (*COL6A1*, *COL6A2*, *CRELD1*, *FBLN2*, *FRZB*, and *GATA5)* have previously been associated with the occurrence of AVSD in both syndromic and non-syndromic cases [272]. Out of these, *Fbln2* (-0.51) and *Frzb* (-0.99), as well as *Vegfa* (+1.25) were dysregulated in the *Cdk13*^{tm1b} mouse RNA-Seq data. Moreover, *Gata6* described above in relation to BAV is another downstream target of *Cdk13* which was downregulated in the RNA-Seq (-0.60). This gene is considered to have direct role not only in aortic valve development through cardiac neural crest cells but also in the development and patterning of the OFT, aortic arch and infundibulum of heart [273]. Moreover, *Rara*, *Rarb* and *Rarg* deficiency in mouse models have been associated previously with PTA through neural crest cells deficiency [274]. In the *Cdk13*^{tm1b} mouse RNA-Seq data, *Rara* (+0.58) and *Rarb* (-0.95) were dysregulated which explains the phenotypes such as AVSD, DORV and deficiency of the septum of outflow tract (Table 3:6). Moreover, FGF signalling is considered vital for remodelling of OFT [275, 276] and is implicated in the development of cardiac valves' leaflets as well [277]. In case of its inhibition/absence, myocardium at OFT will fail to produce extracellular matrix and BMP and TGFβ signalling, resulting in failure of transformation of endothelial cells and invasion

of neural crest cells [278]. Some of these genes such as *Fgfr2* (-0.83), *Smad4* (-0.44) and *Zfpm1* (+0.46) were dysregulated in the *Cdk13*^{tm1b} mouse RNA-Seq data and are suggested to be associated with the observed phenotypes such as DORV, deficient OFT's septum and dysplastic valves.

Myocardial thinning with coarse trabeculation/spongy myocardium was observed in all homozygous (*Cdk13*$^{tm1b/tm1b}$) hearts (n = 4) in this study (Figure 3:16-B compared with A and Figure 3:17-B compared with A). A recent work of Nováková *et al* supported findings from this study by showing that mice with homozygous (*Cdk13*$^{tm1a/tm1a}$) mutation had thinner myocardia, resulting in increased embryonic lethality, probably due to heart failure as a result of compromised myocardial contractility [211]. Moreover, this could be secondary to downregulation of genes encoding structural proteins such as *MYH6 [*279*,* 280*]* or others such as *MYH7*, *MYH11*, *MYBPC3*, *ACTC1* and *ELN* which have a role in different types of CHDs [170, 281]. Singh et al reports that loss of even one functional allele of *Gata4* and *Gata5*, which encode key transcription factors related to heart development, results in thin walled myocardium as well as septal defects such as ASD and VSD [282]. Defective NOTCH signalling in heart [283] and upregulation of *TBX5* and *TBX20* can also result in myocardial thinning [284]. Our RNA-Seq data confirmed modulated expression of some of these genes as downstream targets of *Cdk13* and hence explain this cardiac phenotype e.g. *Actc1*, *Myh7*, *Mybpc3* were up- whereas *Eln* and *Notch2* were downregulated in homozygous hearts ($P < 0.05$).

Pulmonary stenosis (PS) is another heart phenotype reported to occur in 8% of individuals with a CHD [107]. Genetic aetiology of isolated cases are not known however in most cases it is part of the syndrome(s) such as Noonan, LEOPARD or Costello involving *PTPN11* mutations or Holt-Oram syndrome due to *TBX5* mutations [285]. PS is classified as the infundibular, valvular and supravalvular PS [286]. In human studies, various abnormalities of the pulmonary valve including the stenoses at these different levels were seen in 11 cases with *Cdk13* mutations (Table 3:1). In this study, 2 out of 5 heterozygous (*Cdk13*$^{tm1b/+}$) hearts with CHD analysed had narrowing at pulmonary annulus and four out of five had reduced diameters at infundibulum level. In case of homozygous (*Cdk13*$^{tm1b/tm1b}$) hearts, all four hearts had narrowing at infundibular levels and one out of three had narrowing at the annulus level. In one more HOMO heart, the narrowing of pulmonary trunk was apparent on gross analysis however, poor resolution due to presence of clotted blood in the PT did not allow us to measure the diameter of the pulmonary annulus (Figure 3:20-C&C').

There could be cases when the pulmonary annulus diameters are normal but the commissures are fused resulting in a narrowed orifice [287]. Determining pressure gradient readings via echocardiography or through trans-catheterization in beating heart is the gold standard to reliably identify pulmonary stenosis [286, 288]. Our analysis, however, has got limitation being on culled mice. However, future studies can be planned to look at this aspect in relation to PS. In one heterozygous (*Cdk13*$^{tm1b/+}$) heart, quadricuspid pulmonary valve was also seen. This is a rare congenital

anomaly which can be associated with pulmonary stenosis and regurgitation [289]. On STRING based protein-protein interaction analysis among *Cdk13*, our selected significantly dysregulated heart development-related GOI (*Eln, Notch2, Sall4, Vegfa*) and some of the previously reported genes associated with PS such as *PTPN11* (associated with RAS-opathy) and others [237] [290], we found that these different proteins have high confidence interactions (FDR < 50%) with each other and hence share key developmental pathways and processes in the context of heart development with possible association with PS (Figure 3:45). For example, *Sall4* by encoding transcription factor acts synergistically with *Tbx5* in heart and limb development [290]. Since the role of *Cdk13* in heart development and CHD is still being explored, it is not connected to any of these targets in the Figure 3:45. These interactions suggest some unifying mechanism in the aetiology of these syndromes. Moreover, out of the eleven selected genes (excluding *Cdk13*) shown in the Figure 3:45, five (*Sall4, Vegfa, Chd7, Eln, Notch2*), were significantly modulated in case of *Cdk13* mutation in our RNA-Seq data which suggests the potential role of *Cdk13* in PS through these and possibly some other targets. Moreover, the different downstream targets identified are all related to CHD, being a genetically heterogenous condition [291]. High CHD penetrance in case of mutation of these other genes implicate shared pathways in transcriptional regulation, supporting the role of *Cdk13* in this transcription regulation which seems vital for normal heart development.

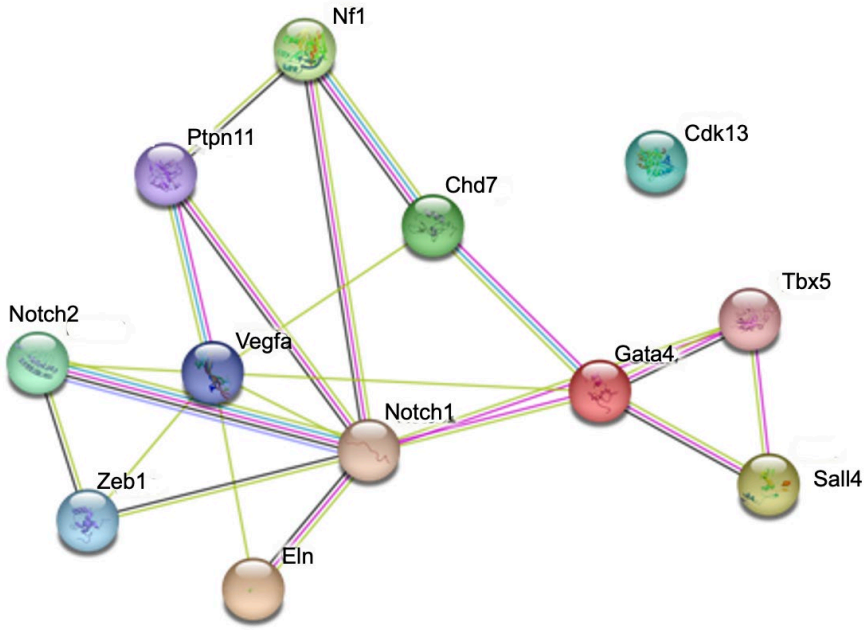


Figure 3:45 Interactions among proteins of some key heart related genes in relation to pulmonary stenosis. High-confidence protein-protein interactions was seen among the top order CHD-associated genes (FDR < 50%) of the Cdk13^{tm1b} mouse RNA-Seq dataset and reported genes associated with PS [237, 290], as found in the STRING database. All the individual proteins in the network show that they are related to heart development and PS, a CHD. Each node in the network represents a protein whereas the coloured edges represent associations among proteins. The turquoise edge shows association determined from curated databases whereas the violet edges denote associations which were experimentally determined. The light green edges are associations determined on text mining whereas the black edges represent associations based on co-expression data. Cdk13, being less characterised gene/protein is not connected to any of these targets. There is statistically significantly more interaction among proteins in this network (P-value for this interaction is 3.34e-06). PS: pulmonary stenosis; Eln: Elastin; Sall4: Sal-like protein 4; Vegfa: Vascular endothelial growth factor A; Ptpn11: Tyrosine-protein phosphatase non-receptor type 11;Tbx5: T-box transcription factor TBX5; Gata4: Transcription factor GATA-4; Notch1:Neurogenic locus notch homolog protein 1; Notch2: Neurogenic locus notch homolog protein 2; Zeb1: Zinc finger E-box-binding homeobox 1; Chd7: Chromodomain-helicase-DNA-binding protein 7; Nf1: Neurofibromin [240].

Since trabeculae carneae are the source of the papillary muscles [236], and homozygous hearts had spongy myocardium, papillary muscles in them were dysplastic. In heterozygous (*Cdk13$^{tm1b/+}$*) hearts,

thickening of papillary muscle was seen in 4/8 hearts (with CHD) analysed (Figure 3:18B&C compared with A, Figure 3:19B&C compared with A). Papillary muscles thickening can happen in response to increased afterload [292]. Though we had limitation to assess afterload in these (culled) mice, these heterozygous (*Cdk13*$^{tm1b/+}$) hearts with CHD were expected to have altered hemodynamics.

***Cdk13* expression analysis**

Based on reported patients with *Cdk13* mutations and the phenotypes, especially in heart, observed in our mouse morphologic study, it was highly pertinent to explore its expression in the developing heart. Using X-Gal staining technique, interestingly, the expression in E10.5 mouse embryo was localised to pericardium including heart as well as the pharyngeal arches (**Error! Reference source not found.**B&C) compared with A). At E12.5 and E15.5, the expression in heart was ubiquitous (Figure 3:26-B&C compared with A, Figure 3:27-B compared with A), suggesting a vital role for *Cdk13* in heart development and CHD. This observation is supported by Nováková et al [211]. X-Gal staining on adult tissues was carried out using spare breeders (both male and female) with cognizance of the 3Rs related to mouse welfare. In adult mouse heart, the expression was mainly localised to the atria and the outflow vessels of heart (Figure 3:28). The reduced uptake of X-Gal stain in adult heart's ventricular tissue most likely is due to the firm nature of cardiac tissue at that stage [293]. qPCR study on RNA extracted from adult mouse heart (including ventricular tissue) showed *Cdk13* expression in WT and heterozygous (*Cdk13*$^{tm1b/+}$) hearts. Nevertheless, with regards to heart

development, the intrauterine stages were more of interest to us to assess if the expression pattern of *Cdk13* translated into the phenotypes observed. *Cdk13* expression in the above-mentioned embryonic stages associate well with the various phenotypes in *Cdk13* mutant mice (mid-facial cleft, CHD) as well human cases (CHD, facial dysmorphism). By RT-qPCR, *Cdk13* transcript's differential expression analysis was done to compare WT with heterozygous (*Cdk13*$^{tm1b/+}$) and homozygous (*Cdk13*$^{tm1b/tm1b}$) hearts at different embryonic stages. Homozygous (*Cdk13*$^{tm1b/tm1b}$) hearts were available for this comparison at E10.5 and E12.5 which showed significant reduction of *Cdk13* transcripts in homozygous (*Cdk13*$^{tm1b/tm1b}$) hearts compared to WT (Figure 3:29, Figure 3:30). This difference was not significant between WT and heterozygous (*Cdk13*$^{tm1b/+}$) hearts at all the selected mouse developmental stages (including E10.5 and E12.5) (Figure 3:29 - Figure 3:32). This suggests that one normal allele can give normal CHD phenotype as was seen in ~86% cases in our mouse study, hence resulting in incomplete penetrance in HET (*Cdk13*$^{tm1b/+}$) hearts. Protein expression analysis for CDK13 was not successful for want of a specific antibody for western blot. However, the significant *Cdk13* transcript reduction in homozygous (*Cdk13*$^{tm1b/tm1b}$) hearts seems to translate into 100% CHD penetrance in them, mostly with complex phenotype.

RNA-Seq transcriptome analysis

CDK13 is involved in phosphorylation of CTD of RNAPII and studies report its interaction with various members of splicing complex [208, 294, 295]. Hence loss of CDK13 could potentially result in improper

splicing of mRNAs for the proteins which are vital for the normal heart development. Human patients with CHD have been causally associated with CDK13 mutations [176, 216, 296]. In order to understand the mechanism by which CDK13 exerts its effect during normal heart development and CHD, RNA-Seq data from E12.5 hearts gave us key downstream targets regulated by CDK13 which have been discussed in relation to the different phenotypes in this study. Some of these key targets related to heart development were validated by RT-qPCR. Among these, two downregulated (*Eln, Notch2*) and one upregulated gene (*Sall4*) were further assessed for pattern of their transcript expression in heart in WT and heterozygous hearts at E12.5 which related with the HREM phenotypes seen. The number of genes selected for qPCR validation and W-ISH had to be limited keeping in view the limitations in terms of time and resources. The WT (*Cdk13*$^{+/+}$) and HOMO (*Cdk13*$^{tm1b/tm1b}$) RNA samples selected for RNA-Seq were from embryonic hearts collected at E12.5 and hence age-matched, but not litter-matched. This was due to aiming for getting samples with best quality and highest RNA integrity number (RIN), after collection from several litters. Moreover, with the aim for a minimum “n” of 3 for the compared groups, litter matching was not possible, particularly due to increased lethality of HOMO (*Cdk13*$^{tm1b/tm1b}$) mice. Another limitation of RNA-Seq analysis was that the dead or necrotic HOMO (*Cdk13*$^{tm1b/tm1b}$) embryos were missed from this analysis for not qualifying due to poor RIN and those included (with best RIN) might be possibly associated with milder phenotype(s). Embryologic hallmarking/staging [297] was not carried out during sample collection for RNA-

Seq but is worth considering in future experiments so to exclude the role of developmental delay impacting on RNA-Seq results or even some phenotype(s). Nevertheless, PCA component analysis distinctly grouped the individual samples of the two comparative groups quite well (Figure 3:34).

Phenotypic characterization, combined with *Cdk13* expression analysis and transcriptomics to identify its downstream targets has produced irrefutable initial evidence regards the potential role of *Cdk13* in heart development and CHD. The work carried out as part of this project has furthered our insight into CDK13 function in heart development and CHD. RNA sequencing transcriptome analysis has enhanced our understanding regards the various potential signalling pathways through which CDK13 can carry out its regulatory role on downstream targets during normal heart development and in case of CHD. Knowledge of these key CDK13-related development pathways and their partners can be used for their detailed analysis in future experiments. This will identify key partners which if manipulated, in case of *Cdk13* mutation, during the course of developmental events through the potential use of agonists/antagonists, as appropriate, can prevent the congenital defects including CHD [298].

CONCLUSIONS

Cdk13$^{tm1b/tm1b}$ (HOMO) mutation is embryonically lethal with stage E12.5 being more deleterious than E15.5. Heterozygous and homozygous *Cdk13*-LOF mutations result in CHD, with complete penetrance in homozygous but incomplete in heterozygous mice. Moreover, one normal allele of *Cdk13,* as in case of heterozygous mutation, can support normal

heart development in more than ~82% cases. *Cdk13* expression studies show its vital role at different developmental stages, especially in the intrauterine ones. *Cdk13* mutation results in significant ($P < 0.05$) dysregulation of downstream heart related targets. The expression pattern and sites of these downstream targets, as well as of the *Cdk13* itself in the heart explain the phenotypes identified in human cases and in this mouse work. Furthermore, extrapolating the discovery of these genes to the signalling pathways they are related to gives a greater insight into the heart development and etiopathogenesis of the different congenital heart defects.

FUTURE RECOMMENDATIONS

This study has systematically characterised the vital role of *Cdk13* in heart development and CHD. However, further research is warranted aiming to understand its role more discretely by designing more focussed interventions against the occurrence of CHD and potentially other congenital defects. Moreover, the potential effect of *Cdk13* mutation on heart phosphoproteome would be quite useful. It was planned for this PhD work but due to limited time and resources, only tissues could be collected for this which are stored in -80C.

Determining the expression profile of CDK13 in specific cardiac progenitor cells will unfold its role at quite an early embryonic stage. Furthermore, single-cell RNA sequencing (scRNA-Seq) can prove to be phenomenal by revealing distinct cell populations and their relation to heart development and CHD. Samples for RNA-Seq were not age or litter matched which can be considered in any future work. Further experiments can be

designed and executed to make targeted interventions on *Cdk13* targets (involving pathways they work in) for therapeutic purposes in cases with *CdK13* mutations. Recently, placenta has been reported to have an important role in causing increased lethality associated with vascular insufficiency in the gene knockout mouse models and can affect cardio genesis as well. In case of some genes, it can be more detrimental than others [299]. Therefore, it will be highly pertinent to plan experiments for analysis of placenta histologically as well as by RNA-Seq and other experiments in order to understand if genetic mutation results in placental defects and in case they do, then to find out if they translate into increased lethality and congenital defects such as CHD.

4 CHARACTERIZATION OF THE ROLE OF *Prkd1* IN HEART DEVELOPMENT AND CHD IN A MOUSE MODEL WITH LOSS OF FUNCTION (LOF) MUTATION

4.1 INTRODUCTION

Protein kinase D1 (PRKD1) is a 912 amino acids serine/threonine kinase enzyme. It is one of the three paralogues, PRKD1-3, each encoded by a specific gene. PRKD1 was discovered in 1994 [300] whereas PRKD2 and 3 were reported for the first time in 2001 [301] and 1999 [302] respectively. The three different paralogues of PRKD have great structural similarity with more than 90% homology in catalytic domain (Figure 4:1) and transcripts of all these PRKDs have been identified in human heart [301-303] . PRKD1 is the predominant of the three paralogues in heart [304]. The homology among the different PRKD paralogues means that they can be activated by the same stimuli [305]. However, based on their tissue specificity, differential expression in different tissues and their interacting partners/targets, each of them has distinct functions [305].

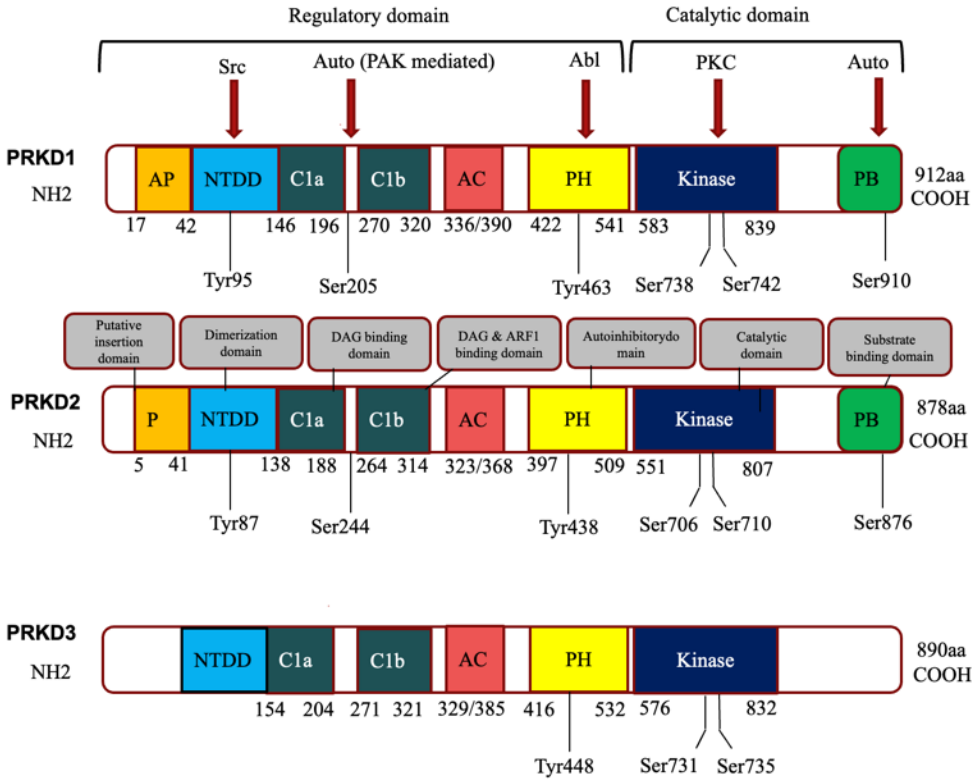


Figure 4:1 Schematic structure of the three paralogues of human PRKD. The three protein kinases (PRKD1, PRKD2, and PRKD3) of the PRKD family have a similar domain structure, however, an alanine-proline or proline-rich region at the N-terminus and a PDZ binding domain at the C-terminus are present only in PRKD1 and PRKD2. They have an N-terminal regulatory region and a C-terminal catalytic domains. PRKD1 has 912 amino acids; PRKD2 contains 878 amino acid residues, and PRKD3 contains 890 amino acids. The numbers denote position of amino acids to locate the different domains/regions of the PRKDs. Functions of major domains along with the main regulatory phosphorylation sites are also shown. Sites for tyrosine phosphorylation in NTDD are conserved in PRKD1 and PRKD2 and the PH domain is conserved in all three PRKDs; the kinase-domain activation loop phosphorylation motif is conserved in all three PRKDs whereas the C-terminal autophosphorylation site is conserved in PRKD1 and PRKD2 but not in PRKD3. Red arrows pointing at the sites of phosphorylation by upstream kinases or by autophosphorylation. NTDD, N terminal dimerization domain, AP, alanine proline–rich region; P, proline–rich region; C1a and C1b, cysteine-rich motifs 1a and 1b; AC, acidic amino acid domain; PH, pleckstrin homology domain (responsible for autoinhibition); kinase, kinase domain; PB, PDZ binding motif; Src & Abl, tyrosine kinases; PKC, Protein Kinase C, PAK, p21-activated kinases; DAG, Diacyl glycerol; ARF1, ADP-ribosylation factor 1. Adapted from [306-308]

PRKDs have quite a complex mechanism of enzymatic and regulatory functions. PRKD1 regulates the different cellular functions in health and disease via gene transcription, intracellular transport and through its role as a kinase on downstream targets [307, 309-311]. It has a role in diverse biological processes such as cellular growth, differentiation and migration, apoptosis, angiogenesis, as well as cardiac hypertrophy in response to sustained stress [312]. Overexpression of this enzyme has been associated with cancers such as pancreatic [313, 314], breast [315] and others. In cancers, it positively regulates cellular proliferation and migration of tumor cells and also prevents their apoptosis [316, 317]. Upregulation of PRKD1 is associated with pathological cardiac remodeling/hypertrophy when enhanced PRKD1 signaling in response to sustained cardiac stress results in activation of fetal gene program [318, 319].

4.1.1 Expression of PRKD1

PRKD1 is expressed throughout the human body including heart [320] (Figure 4:2). Normally, its expression declines with developmental age, with increased expression in embryonic and new-born ventricular myocardium and declines in adult heart [321]. Nevertheless, PRKD1 is the main paralogue expressed in adult heart [310]. Whole mount in-situ hybridization (W-ISH) on mouse embryos at E9.5 and E10.5 showed very strong expression of *PRKD1* in cardiac atria and ventricles [322]. Moreover, its expression increases ectopically in conditions causing increased cardiac stress leading to hypertrophy, dilated cardiomyopathy, and heart failure [319].

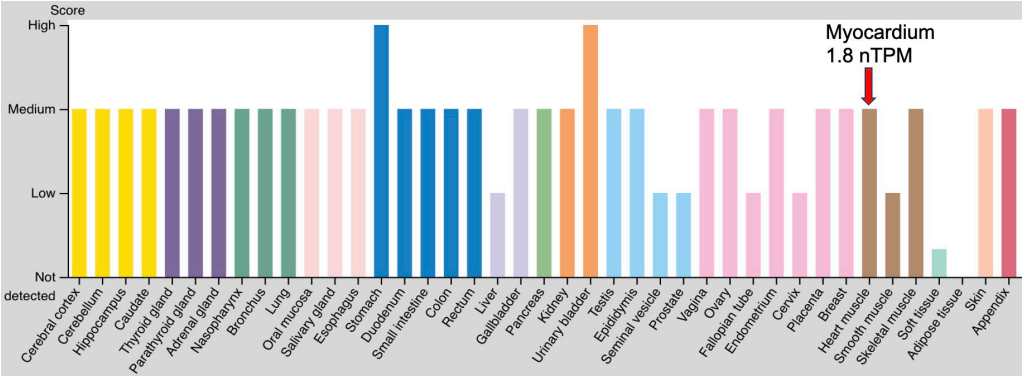


Figure 4:2 The protein expression pattern of PRKD1 in different body tissues in human. The expression score is based on immunohistochemical data manually scored regarding staining intensity (negative, weak, moderate or strong) and fraction of stained cells (<25%, 25-75% or >75%).The expression is very high in stomach and urinary bladder whereas in most of the tissues, including brain, gastrointestinal tract, urinary system, muscles (myocardium and skeletal muscles), its expression score is medium. In myocardium, its expression is 1.8 nTPM (denoted by red arrow). Expression score for PRKD1 in smooth muscle is low as in liver and prostate [320]. nTPM: normalised transcripts per million (https://www.proteinatlas.org).

According to *Bgee* multispecies' expression database (version 15.0) (https://bgee.org/gene/ENSMUSG00000002688/, accessed Sept 28, 2022), which involves genes ranking based on normalised expression score ranging from 0 to 100 (expression score in parenthesis), *Prkd1* is highly expressed in cardiovascular system such as atria (82.53), ventricular myocardium (72.63), endocardium (88.05), aorta and its different parts (85.37), pulmonary valve (86.24) and aortic valve (79.45). In addition, expression was seen to the cardiovascular precursors such as endocardial cushions (88.05), cardiac mesenchyme derived from splanchnic mesoderm (88.05), and neural crest derived mesenchyme (87.99) [241].

Our lab is collaborating with two other research groups (Cuello and Hitz), which were part of the WES on humans, in order to explore the role of

PRKD1 in heart development in a mouse model. Preliminary data from this collaborative research showed that *PRKD1* is expressed in epicardial, atrial and ventricular myocardial cells at E14.5 and there was a significant reduction of *PRKD1* expression at E16.5. Moreover, the expression studies on primitive embryonic cells at E8.5 showed that highest expression of *PRKD1* was observed in mesodermal tissue including heart progenitor cells.

4.1.2 Structure of PRKD1 and mechanism of its activation

Structure of human PRKD1 protein is characterized to have a C-terminus (catalytic) and N-terminus (regulatory) domains (Figure 4:1). The C-terminus comprises protein kinase (catalytic) domain and a PDZ-binding (PB) domain which bind substrates [306]. The N-terminal regulatory domain comprises of a small region rich in alanine and proline (aa17-146) which has a role in membrane insertion [323, 324]. A recent study reported that deletion of this alanine-proline (AP) region only or of the entire cysteine rich domain (including C1a & C1b) in PRKD2 results in reduced interaction of the protein with PKC [325], thereby compromising its activation to act on downstream targets. Based on homology between PRKD1 and PRKD2, loss of AP or cysteine rich domain in PRKD1 is likely to compromise PKC-mediated PRKD1 activation [326].

The two cysteine-rich (C1a/C1b) motifs, both (C1a more than C1b) are responsible for anchoring PRKD1 to membranes containing diacylglycerol (DAG)-/phorbol ester. The C1b also mediates the interaction of PRKD1 with the small G protein ADP-ribosylation factor-1 (ARF1) [327].

The pleckstrin homology (PH) domain inhibits catalytic activity of PRKD1 [328] (Figure 4:1) and is also vital for nuclear export of PRKD1 to cytosol [329] from where it is translocated to the cell membrane for activation. Between AP region and C1a&b motifs, there is an N-terminal dimerization domain (NTDD) which has a role in DAG-mediated dimerization and thereby activation of PRKD1 (Figure 4:1).

PRKD1 integrates signals from both diacylglycerol (DAG) and from protein kinase C (PKC) [330]. DAG directly activates PRKD1 by binding to C1 domain which is in addition to its role to recruit PRKD1 to membranes [331]. DAG production at membranes leads to accumulation of PRKD1 at membranes [330]. The NTDD of the accumulated PRKD1 undergoes DAG-mediated dimerization as a prerequisite step for activation of the kinase domain of PRKD1, whereas as monomer, this NTDD stabilizes the autoinhibitory state of the kinase domain of PRKD1 (Figure 4:3-A). The dimerization of NTDD (also called as ubiquitin-like domain – ULD) can be homo- with another PRKD1 or hetero- with other PRKD paralogues [332]. Dimerised NTDD (turquoise ovals in Figure 4:3-B) then facilitates homo- or heterodimerization of the kinase domain (pink boxes in Figure 4:3-B)[332]. The dimerised kinase domains trans-autophosphorylate Ser^{742} (mainly) and Ser^{738} in the activation loop (AL) of the kinase domain, rendering the kinase domain active[332]. After activation, the dimerised kinases dissociate (separated pink boxes in (Figure 4:3-C) so they are available to phosphorylate their downstream targets (denoted by black arrows in Figure 4:3-C) [332].

Protein kinase C (PKC) activates PRKD1 through transphosphorylation of conserved serine residues (Ser^{738} and Ser^{742}) in its activation loop in the catalytic (CAT)/kinase domain [333] (Figure 4:1). This PKC mediated phosphorylation relieves PRKD1 of auto inhibition by the regulatory PH domain [334].

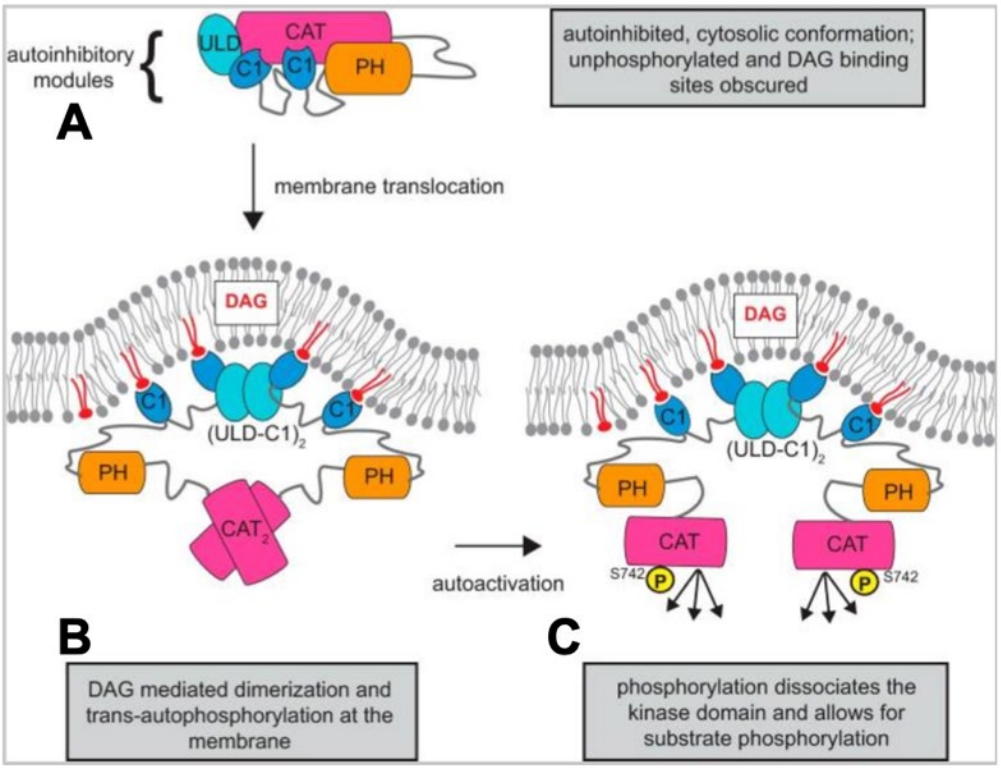


Figure 4:3 Dimerization of PRKD1. The figure depicts the process of dimerization of ULD/NTDD in PRKD1 which leads to trans-autophosphorylation and thereby activation of the catalytic/kinase domain, followed by monomerization of the kinase domains which are then able to phosphorylate downstream targets. CAT: catalytic or kinase domain of PRKD1; PH: pleckstrin-homology domain; ULD: ubiquitin like domain/N-terminal dimerization domain (NTDD). Reproduced from [332].

Additionally, another upstream kinase such as p21-activated kinase (PAK) regulates PRKD1's subcellular localization by causing PRKD1 phosphorylation at Ser^{203} which is a highly conserved site between the two cysteine-rich motifs, C1a & C1b [335] (Figure 4:1). This

PAK-mediated action occurs in response to activation by other G protein-coupled receptor (GPCR) agonists such as angiotensin II and bombesin [335]. Phosphorylation of Ser^{203} (corresponding to Ser^{205} in humans) causes dissociation and thereby translocation of PRKD1 from the plasma membrane to the nucleus where it would phosphorylate its nuclear targets such as class IIa histone deacetylases (HDACs), followed by extrusion of these HDACs (HDAC5) to the cytoplasm – making PAK/PRKD1/HDAC signalling pathway [335]. PRKD1 also undergoes autophosphorylations at Ser^{910} in a PB motif at C-terminus of PRKD1 which is required to cause AL phosphorylation mainly at Ser^{742} [307] (Figure 4:1).

Under conditions of oxidative stress, PRKD1 can also be activated by phosphorylation at distinct tyrosines in a sequential manner. The first tyrosine to get phosphorylated (by tyrosine kinase Abl) is Tyr^{463} located in the PH Domain [336], followed by phosphorylation (mediated by Src) at Tyr^{95} in the NTDD region (17-146aa) [325, 337] (Figure 4:1) However, oxidative stress can also directly activate PKC which thereby activates PRKD1 through phosphorylation of its activation loop ($Ser^{738/742}$) [336]. One of the downstream effector pathways of PRKD1 activation during oxidative stress is NF-κB pathway contributing to the survival of cells faced with oxidative stress [338].

4.1.3 Activity of PRKD1 in ventricular myocardium and its role in cardiac hypertrophy

Cardiac hypertrophy is initially an adaptive response but prolongation of this response leads to chamber dilatation and reduced cardiac contractility [319]. Involvement of PRKD1 in cardiac hypertrophy involves class II histone deacetylases (HDACs) (HDAC4, 5, 7 and 9). Class II HDACs are known to suppress cardiac hypertrophy and remodelling in response to pressure overload [339, 340]. This function of HDACs is due to their association with MEF2 transcription factor, a known activator of heart disease. [341]. In times of increased cardiac stress, PRKD1, being a kinase, phosphorylates the HDACs which results in dissociation of MEF2 from HDACs. Phosphorylated HDACs get exported from the nucleus into the cytoplasm, and the dissociated MEF2 will activate its downstream targets, resulting in cardiac hypertrophy and pathological cardiac remodelling in response to the pressure overload [240, 342].

4.1.4 Regulatory role of PRKD1 in various clinical conditions

The PRKDs through their regulatory role have been linked to a variety to human diseases/clinical conditions such as cancers [343, 344], inflammatory [345, 346] and cardiovascular disorders [311, 347], as depicted in Figure 4:4.

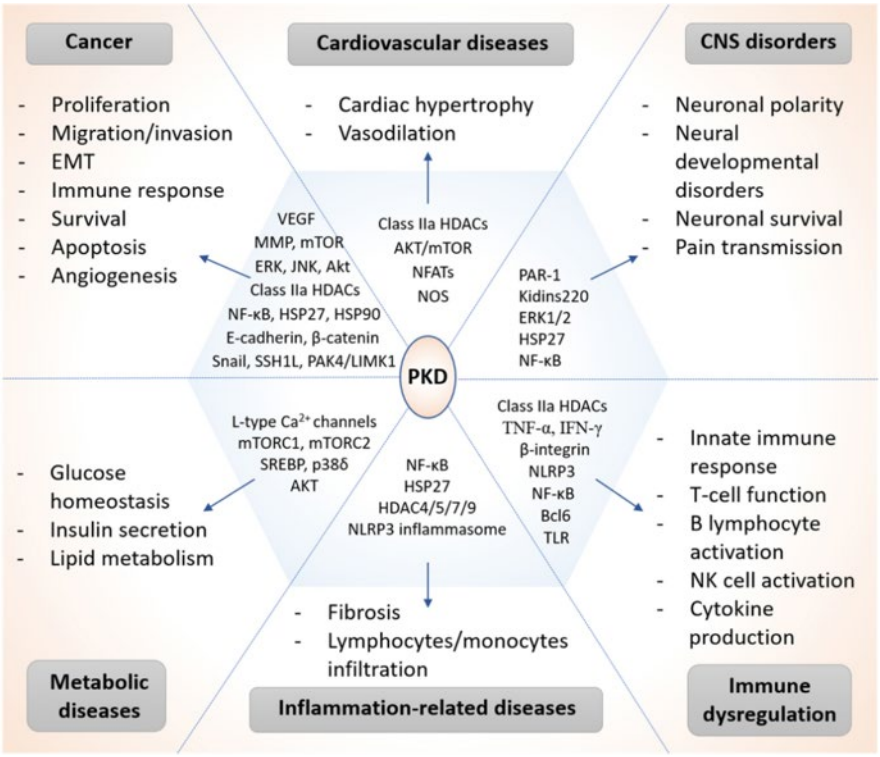


Figure 4:4 Role of PRKDs in various conditions. Schematic representation of major roles and key signalling targets of the different PRKDs in the pathogenesis of cancer, cardiovascular and metabolic, immunologic and inflammatory diseases. Abbreviations: central nervous system (CNS), epithelial-to-mesenchymal transition (EMT), natural killer (NK) cell, Toll-like receptor (TLR), nuclear factor of activated T cells (NFATs), sterol regulatory element binding protein (SREBP). Reproduced from [333].

4.1.5 Reported PRKD1 mutations in patients

In a large multicentre WES study of 1891 probands, in which our lab also participated, two types of *de novo* missense mutations (DNMs) in *PRKD1* were identified in 3 unrelated probands [176] (Figure 4:5). Two of these probands had the same missense mutation (i.e., Gly592Arg) whereas the third one had Leu299Trp. These mutations manifested as CHD, along with other abnormalities affecting head and neck structures including nervous system. Developmental delay, ectodermal and limb defects were noted in two of the three probands [176].

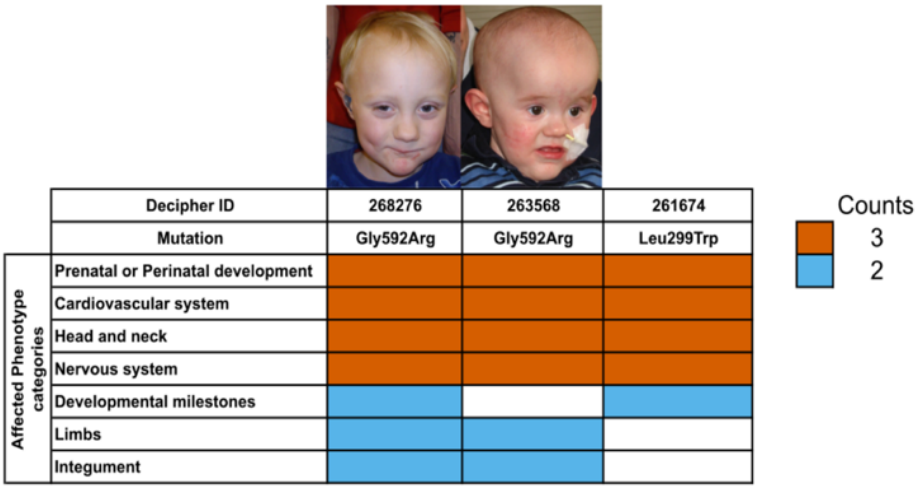


Figure 4:5 Missense mutations of PRKD1. All cases were having CHD along with other abnormalities affecting head and neck, craniofacial structures and nervous system. Two of the three patients had developmental delay and ectodermal defects. Each column represents an individual proband. The orange colour shade of the cells denotes if all three probands share a particular phenotype whereas blue shade represents if only two of the three probands share that specific phenotype. The photos of two of the probands are shown for which prior consent was obtained from parents before publication in the article. Reproduced from [176].

The dataset from this WES study showed that the top order genes have association with the known CHD genes (FDR<50%) shown in blue using STRING database [240] (Figure 4:6). *PRKD1* was discovered as a novel gene in this study to be associated with CHD and STRING analysis predicts its association with the known CHD genes through various interconnected pathways.

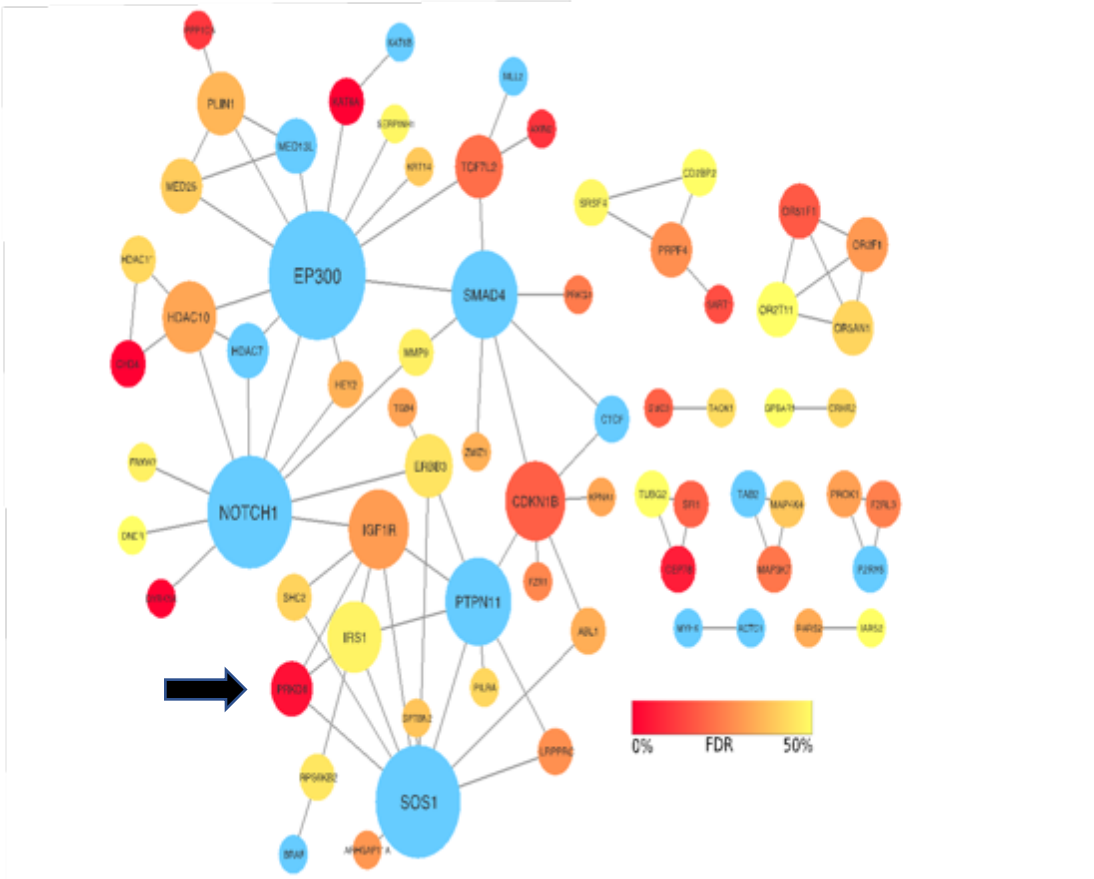


Figure 4:6 High-confidence protein-protein interactions among the top order CHD-associated genes (FDR < 50%) of the WES dataset as found in the STRING database. Nodes for genes known to be associated with CHD are coloured blue whereas other nodes' colours are scaled according to the FDR regarding association. The size of the nodes is according to the degree of association. Reproduced from [176].

Subsequently, a few other studies have also reported *PRKD1* mutations in patients with CHD [175, 176, 348-350]. Moreover, few more yet unpublished *Prkd1* mutations have been reported in ClinVar [351], DECIPHER's databases (https://www.decipherge-nomics.org/gene/PRKD1/overview/clinical-info) [352] and by personal communication (Professor Marc-Phillip Hitz). Those pathogenic, likely pathogenic, VoUS and/or associated with CHD are given in the Table 4:1; Figure 4:7. There is a mutational spectrum including both missense and

loss of function (LOF) variants. Using gnomAD [226], the constraint metric (i.e., *observed / expected* metric) for missense and LOF type of SNVs in *PRKD1* was 0.92 and 0.6 respectively which means that *PRKD1* is under great selective pressure against missense and LOF type of SNV, increasing the probability that any missense and LOF SNV will be deleterious. 34 out of 85 single nucleotide variants (SNVs) in coding region were associated with CHD in 36 patients, with G592R being the most common and identified in 3 patients. Moreover, all mutations (seven) in noncoding region were associated with CHD in 12 patients (six as HET and six as HOMO). This ended up with total of 48 patients with CHD having SNVs of *PRKD1*. Information regards gender was available for only 21 of these patients and 10 male (10/21) and 10 females had CHD whereas one male with LOF variant (Gln143Term) had normal phenotype. The most common CHD in these was pulmonary stenosis, present in 7/48 (14.6%) cases followed by individual septal defects (4 each of ASD and VSD). However, collectively septal defects were present in 10/48 (20.8%) cases (after adding the unspecified septal defects) (Table 4:2). The data from the patients with *PRKD1* mutations suggest a potentially vital role of *PRKD1* in body development including heart morphogenesis. However, the evidence regarding this is scarce and requires further studies in order to fully characterise its role in heart development and CHD.

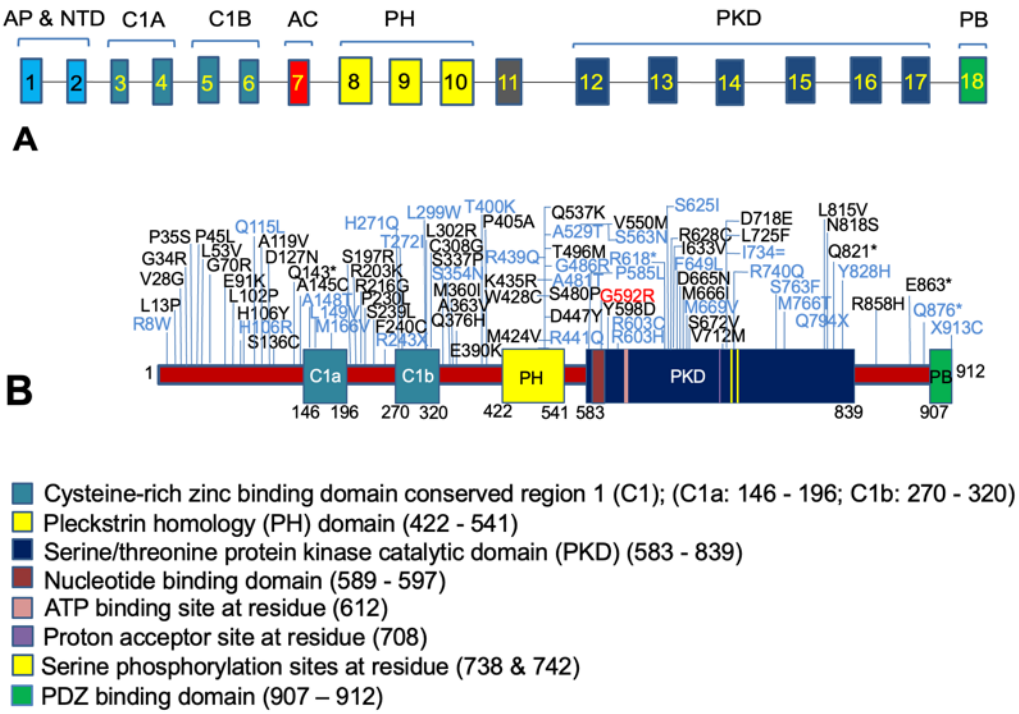


Figure 4:7 Schematic structure of the human protein kinase D1 (PRKD1) gene and protein and location of the reported PRKD1 mutations. A) The eighteen exons of human PRKD1 gene (denoted by coloured boxes with respective numbers) are shown. The domain/region of the PRKD1 protein encoded by respective exon(s) is also shown above the exons. Exon 3 & 4 encode C1a whereas 5 & 6 encode C1b; PH domain is encoded by exon 9-11 whereas PKD is encoded by exon 13-18 (based on exon information from Ensembl and Uniprot's domain structure/sequence information) (https://www.ensembl.org/Homo_sapiens & https://www.uniprot.org/uniprotkb/Q15139). B) The location of reported mutations in the human PRKD1 protein. Benign mutations are excluded. The coloured boxes denote important regions/domains of PRKD1 and the numbers denote position of amino acids to locate the different domains/regions of the PRKDs. The most common mutation, G592R (3 cases), is denoted in red; this mutation is associated with congenital heart defects, as are those denoted in blue. Protein kinase (PK) domain is the catalytic domain located at the C-terminal end, and C1A and C1B located at N-terminal end act as regulatory domain along with PH domain. The coding of amino acids by exons does not necessarily map exactly to each domain, i.e. exon 1 encodes 1-88 aa, exon2 encodes 89-135, exon 3 encodes 135-179 aa, exon 4 179-232, exon 5 233-303, exon 6 303, exon 7 329-397, exon 8 397-438, exon 9 encodes 439-464, exon 10 encodes 465-558, exon 11 encodes 558-575, exon 12 encodes 576-600, exon 13 encodes 600-635, exon 14 encodes 636-689, exon 15 encodes 690-722, exon 16 encodes 723-812, exon 17 encodes 812-840 and exon 18 encodes 841-912. AP: alanine-proline rich region; AC: acidic-amino acid domain; PK: protein kinase domain; C1(a & b): Cysteine-rich zinc binding domain conserved region 1; PH: Pleckstrin homology domain; PB: PDZ binding domain.

No.	Mutation	Study ID	Gender	Molecular consequence	Clinical significance	Location	Cardiac phenotype/others	Ref
1.	p.Arg8Trp (5.56e-6)	-	M	MS	Pathogenic*	Before AP region	PS, FD, coronal craniosynostosis, mild GDD	PC
2.	p.Leu13Pro (5.36e-5)	-	-	MS	VoUS	Before AP region	Inborn genetic diseases	ClinVar 4 Aug 23
3.	p.Val28Gly	-	-	MS	VoUS	AP	Inborn genetic diseases	ClinVar 4 Aug 23
4.	p.Gly34Arg (3.00e-6)	-	-	MS	VoUS	AP	Inborn genetic diseases	ClinVar 4 Aug 23
5.	p.Pro35Ser (6.69e-6)	-	-	MS	VoUS	AP	Inborn genetic diseases	ClinVar 4 Aug 23
6.	Pro45Leu (1.99e-5)	-	-	MS	VoUS/likely benign	NTDD	Normal	PC
7.	p.Leu53Val	-	-	MS	VoUS	NTDD	Inborn genetic diseases	ClinVar 4 Aug 23
8.	p.Gly70Arg (7.05e-6)	-	-	MS	VoUS	NTDD	-	ClinVar 4 Aug 23
9.	p.Asp86Tyr (8.85e-6)	-	-	MS	VoUS	NTDD	Inborn genetic diseases	ClinVar 4 Aug 23
10.	p.Glu91Lys	-	-	MS	VoUS	NTDD	-	ClinVar, 3 June 23
11.	p.Leu102Pro	-	-	MS	VoUS	NTDD	-	ClinVar, 20 Aug 22
12.	p.His106Tyr (4.61e-5)	-	-	MS	Conflicting	NTDD	Inborn genetic diseases	ClinVar 4 Aug 23
13.	p.His106Arg (2.05e-6)	1032083	-	MS	VoUS	NTDD	CHD and ectodermal dysplasia	ClinVar, 20 Aug22
14.	p.Gln115His (1.20e-6)	2435245	-	MS	VoUS	NTDD	CHD and ectodermal dysplasia	ClinVar, 3 June 23
15.	p.Ala119Val (3.10e-5)	-	-	MS	VoUS	NTDD	Inborn genetic diseases	ClinVar 4 Aug 23
16.	p.Asp127Asn (1.98e-5)	-	-	MS	VoUS	NTDD	Inborn genetic diseases	ClinVar 4 Aug 23
17.	p.Ser136Cys (3.48e-6)	-	-	MS	Pathogenic*	- NTDD	Normal	PC
18.	p.Gln143Term (6.92e-7)	272461	M	Stop_gained (LOF)	VoUS	NTDD	No CHD or limb defects	DDD study

19.	p.Arg145Cys (4.84e-6)	-	-		VoUS	NTDD	-	ClinVar, 3 June 23
20.	p.Ala148Thr (1.38e-6)	1696583	-	MS	VoUS	C1a	CHD and ectodermal dysplasia	ClinVar, 20 Aug 22
21.	p.Leu149Val (2.49e-6)	1032084	-	MS	VoUS	C1a	CHD and ectodermal dysplasia	ClinVar, 20 Aug 22
22.	p.Met166Val (1.38e-6)	982667	-	MS	VoUS	C1a	CHD and ectodermal dysplasia	ClinVar, 20 Aug 22
23.	p.Ser197Arg (4.96e-6)	-	-	MS	VoUS	Between C1a & C1b	Inborn genetic diseases	ClinVar 4 Aug 23
24.	p.Arg203Lys (9.29e-6)	-	-	MS	VoUS	Between C1a & C1b	Inborn genetic diseases	ClinVar 4 Aug 23
25.	p.Arg216Gly (1.24e-4)	-	-	MS	VoUS/conflicting	Between C1a & C1b	No CHD, premature ovarian failure	ClinVar, 20 Aug 22
26.	p.Pro230Leu	-	-	MS	VoUS	Between C1a & C1b	Inborn genetic diseases	ClinVar 4 Aug 23
27.	p.Ser239Leu (1.97e-5)	-	-	MS	VoUS	Between C1a & C1b	Inborn genetic diseases	ClinVar 4 Aug 23
28.	p.Phe240Cys	-	-	MS	VoUS	Between C1a & C1b	Inborn genetic diseases	ClinVar 4 Aug 23
29.	p.Arg243Term (2.49e-6)	-	HET	Stop gain (LOF)	Pathogenic	Between C1a & C1b	Ebstein malformation of the left AV valve, NDD	Jin et al, 2017
30.	p.His271Gln	-	-	MS (De novo)	Pathogenic	C1b	ASD (Secundum), VSD (sub pulmonary or Conal), PS (Valvar), single ventricle com-prised of mostly left ventricle, TS	Jin et al, 2017
31.	p.Thr272Ile (1.80e-5)	1805316	-	MS	VoUS	C1b	CHD and ectodermal dysplasia	ClinVar, 3 June 23
32.	p. Leu299Trp	Patient 2	M	MS	Pathogenic	C1b	AVSD, microcephaly	Sifrim et al, 2016
33.	p.Lys302Arg (1.81e-4)	-	-	MS	VoUS	C1b	Inborn genetic diseases	ClinVar 4 Aug 23
34.	p.Cys308Gly	-	-	MS	VoUS	C1b	-	ClinVar, 4 Aug 2023
35.	p.Ser337Pro (4.96e-6)	-	-	MS	VoUS	AC	Inborn genetic diseases	ClinVar 4 Aug 23
36.	p.Ser354Asn (6.57e-6)	2435244	-	MS	VoUS	AC	CHD and ectodermal dysplasia	ClinVar, 3 June 23
37.	p.Met360Ile (2.05e-6)	-	-	MS	VoUS	AC	Inborn genetic diseases	ClinVar 4 Aug 23

38.	p.Ala363Val (1.18e-5)	-	-	MS	VoUS	AC	Inborn genetic diseases	ClinVar 4 Aug 23
39.	p.Gln376His (7.68e-6)	-	-	MS	VoUS	AC	Inborn genetic diseases	ClinVar 4 Aug 23
40.	p.Glu390Lys (2.91e-5)	-	-	MS	VoUS	AC	Inborn genetic diseases	ClinVar 4 Aug 23
41.	p.Thr400Lys (4.34e-6)	-	M	MS	Benign*	Between AC & PH	PS	PC
42.	p.Pro405Ala	-	-	MS	VoUS	Between AC & PH	-	ClinVar 4 Aug 23
43.	p.Met424Val (3.97e-5)	-	-	MS	VoUS	PH	Inborn genetic diseases	ClinVar 4 Aug 23
44.	p.Trp428Cys (3.41e-5)	-	-	MS	VoUS	PH	Inborn genetic diseases	ClinVar 4 Aug 23
45.	p.Lys435Arg	-	-	MS	VoUS	PH	Inborn genetic diseases	ClinVar 4 Aug 23
46.	p.Arg439Gln (2.06e-6)	803014	-	MS	Likely pathogenic	PH	CHD and ectodermal dysplasia	ClinVar, 20 Aug 22
47.	p.Arg441Gln (1.86e-6)	1032079	-	MS	VoUS	PH	CHD and ectodermal dysplasia	ClinVar, 20 Aug 22
48.	Asp447Tyr (5.58e-6)	-	-	MS	Pathogenic*	PH	Normal	PC
49.	p.Ser480Pro (5.47e-6)	-	-	MS	VoUS	PH	Inborn genetic diseases	ClinVar 4 Aug 23
50.	p.Ala481Thr (1.80e-4)	732997	-	MS	Likely benign	PH	CHD and ectodermal dysplasia	ClinVar, 03 June 23
51.	p.Gly486Arg (1.60e-4)	931739	-	MS	VoUS	PH	CHD and ectodermal dysplasia	ClinVar, 20 Aug 22
52.	p.Thr496Met (6.63e-5)	-	-	MS	VoUS	PH	Inborn genetic diseases	ClinVar 4 Aug 23
53.	p.Ala529Thr (5.12e-6)	2435246	-	MS	VoUS	PH	CHD and ectodermal dysplasia	ClinVar, 03 June 23
54.	p.Gln537Lys (8.05e-6)	-	-	MS	VoUS	PH	Inborn genetic diseases	ClinVar 4 Aug 23
55.	p.Val550Met (3.04e-5)	-	-	MS	VoUS	Between PH & PK	Inborn genetic diseases	ClinVar 4 Aug 23
56.	p.Ser563Asn (6.84e-6)	-	F	MS	Pathogenic*	Between PH & PK	Coarctation of aorta	unknown

57.	p.Pro585Leu (2.57e-6)	1804122	-	MS (De novo)	Benign	PK	CHD and ectodermal dysplasia; unaffected twin brother	ClinVar, 03 June 23
58.	p.Gly592Arg	Patient 1	M	MS	Pathogenic	ATP binding site of PK	Pulmonary valvar abnormality	Sifrim et al, 2016
59.	p.Gly592Arg	Patient 3 (263568)	M	MS	Pathogenic	ATP binding site of PK	AVSD	Sifrim et al, 2016
60.	p.Gly592Arg	Patient B	M	MS (LOF	Pathogenic	ATP binding site of PK	PS (congenital)	Alter et al 2021
61.	p.Tyr598Asp	-	-	MS	VoUS	ATP binding site of PK	Not provided	ClinVar 4 Aug 23
62.	p.Arg603His	-	-	MS	VoUS	PK	AVCD; PAS; PDA; Cleft palate; IUGR	DDD study
63.		Patient A	F	MS	VoUS	PK	ASD with a spontaneous closure at 7years, PS and a mild tricuspid insufficiency. mild maxillary and mandibular hypoplasia and high palate,	Alter et al, 2021 and ClinVar, 03 June 23
64.	p.Arg603Cys	-	F	MS	VoUS	PK	AVSD	PC
65.	p.Arg618Term (3.18e-5)	Patient in family 2	F – homo	NS	VoUS	PK	VSD with overriding TA	Shaheen et al 2015
66.	p.Ser625Ile (1.87e-6)	1805098	-	MS	VoUS	PK	CHD and ectodermal dysplasia	ClinVar, 03 June 23
67.	p.Arg628Cys (3.44e-6)	-	-	MS	VoUS	PK	Inborn genetic diseases	ClinVar 4 Aug 23
68.	p.Ile633Val (5.63e-6)	-	-	MS	VoUS	PK	Inborn genetic diseases	ClinVar 4 Aug 23
69.	p.Phe649Leu (4.62e-5)	1032081	-	MS	VoUS	PK	CHD and ectodermal dysplasia	ClinVar, 20 Aug 22
70.	p.Asp665Asn			MS	VoUS	PK	Malignant tumor of prostate	ClinVar, 20 Aug 22
71.	p.Met666Ile (1.59e-6)		-	MS	Pathogenic*	PK	Normal	PC
72.	p.Met669Val (5.58e-6)	-	M	MS	Benign*	PK	Abnormal CS,CDH, anal atresia	PC
73.	p.Ser672Leu	-	-	MS	VoUS	PK	-	ClinVar 4 Aug 23

74.	p.Val712Met	1700150	-	MS	Likely pathogenic	PK	NDD	ClinVar, 20 Aug 22
75.	p.Asp718Glu (4.77e-6)	-	-	MS	VoUS	PK	Inborn genetic diseases	ClinVar 4 Aug 23
76.	p.Leu725Phe	-	-	MS	VoUS	PK	-	ClinVar 4 Aug 23
77.	p.Ile734=	1327446	-	Synonymous SNV	Benign	PK	CHD and ectodermal dysplasia	ClinVar, 20 Aug 22
78.	p.Arg740Gln (4.34e-6)	998171	-	MS	VoUS	PK	CHD and ectodermal dysplasia	ClinVar, 20 Aug 22
79.	p.Ser763Phe	-	M	MS	-	PK	Aortic coarctation, BAV	PC
80.	p.Met766Thr (2.40e-6)	-	M	MS	-	PK	TGA & intact VS	PC
81.	p.Gln794Term	1-00762	HET - Sex un-known	stop gain (LOF)	VoUS	PK	ASD (secundum), PDA, PS (valvar)	Jin et al, 2017
82.	p.Leu815Val (6.87e-7)	-	-	MS	VoUS	PK	-	ClinVar, 20 Aug 22
83.	p.Asn818Ser (6.83e-5)	-	-	MS	VoUS	PK	Inborn genetic diseases	ClinVar 4 Aug 23
84.	p.Gln821Term (6.86e-7)	-	-	NS	VoUS	PK	Normal	PC
85.	p.Tyr828His (1.71e-5)	-	M	MS	Pathogenic*	PK	VSD, cryptorchidism, horseshoe kidney, hy-dronephrosis, sacral dimple, motor delay, mild IUGR	PC
86.	p.Arg858His (1.49e-5)	-	-	MS	VoUS	Between PK & PB	Inborn genetic diseases	ClinVar, 4 Aug 23
87.	p.Glu863Term	-	-	NS	VoUS	Between PK & PB	-	PC
88.	p.Gln876Term (6.20e-6)	1698759	-	NS	VoUS	Between PK and PB	CHD and ectodermal dysplasia	ClinVar, 20 Aug 22
89.	p.X913Cys (1.61e-5)	1-07451	HET - Sex un-known	Stop loss (LOF)	VoUS	PB	VSD (single), AS (subvalvar), BAV, DORV, tubular hypoplasia of aorta + coarctation, ab-errant right subclavian artery, abnormal branching of left aortic arch	Jin et al, 2017
90.	c.2166+39A>C (4.05e-1)	1327448	Unknown	SNV (noncoding)	Benign	-	CHD and ectodermal dysplasia	ClinVar, 20 Aug 22
91.	c.2167-12T>A (3.92e-1)	1327447	Unknown	SNV (noncoding)	Benign	-	CHD and ectodermal dysplasia	ClinVar, 20 Aug 22

92.	c.2435-14G>A (7.31e-1)	1327445	Unknown	SNV (noncoding)	Benign	-	CHD and ectodermal dysplasia	ClinVar, 20 Aug 22
93.	c.1905+2T>A	1691270	Unknown	Splice mutation	Likely pathogenic	-	CHD and ectodermal dysplasia	ClinVar, 20 Aug 22
94.	c.265-5T>C (2.49e-3)	717322	Unknown	SNV (noncoding)	Benign/likely Benign	-	CHD and ectodermal dysplasia	ClinVar, 20 Aug 22
95.	c.265-1G>T (no disease in HETS male/female and in homo males)	II-3	F – homo	Splice mutation	Pathogenic	Canonical splice acceptor of exon 2 of PRKD1-> exon 2 skipping producing premature stop codon	Septal defects (not specified)- Healed spontaneously	Massadeh et al, 2021
96.		II-4	F – homo	Splice mutation	Pathogenic		Septal defects (not specified)- Healed spontaneously	Massadeh et al, 2021
97.		III-1	F – homo	Splice mutation	Pathogenic		PS & TR	Massadeh et al, 2021
98.		III-2	F – homo	Splice mutation	Pathogenic		PS,, TA and VSD	Massadeh et al, 2021
99.		III-3	F – homo	Splice mutation	Pathogenic		ASD – healed spontaneously	Massadeh et al, 2021
100		III-5	F – homo	Splice mutation	Pathogenic		Minor CHD anomalies - Healed spontaneously	Massadeh et al, 2021
101	c.2068-11C>A	1032082	Unknown	SNV (noncoding)	VoUS		CHD and ectodermal dysplasia	ClinVar 20 Aug 2022

Table 4:1 Reported patients with SNVs in Prkd1. This data of 102 patients was collected from published literature, ClinVar [351], DECIPHER's databases (https://www.deciphergenomics.org/gene/PRKD1/overview/clinical-info) [352] and by personal communication (Professor Marc-Phillip Hitz).The reference for each reported mutation is mentioned against each along with the ID. Some main congenital defect(s) (where known) with or without CHD are mentioned. Those mutations which are predicted to be pathogenic, likely pathogenic, VoUS (when there is insufficient evidence to relate the mutation to a disease) or even benign but associated with developmental anomaly/CHD are given in the table. Mutations which were predicted to be benign and were not associated with any congenital anomaly as well, were excluded. 34 out of 85 coding SNVs were associated with CHD in 36 patients. All mutations (seven) in noncoding region were associated with CHD in 12 patients. This ended up with total of 48 patients having SNVs of Prkd1. Clinical significance of new SNVs reported via personal communication (Professor Marc-Phillip Hitz), denoted by asterisk (*), were

determined by PredictSNP [353]. Allele frequency for the variants on gnomAD, where available, is given in parentheses in the "mutation" column. CHD: congenital heart disease; TR: tricuspid regurgitation; TA: truncus arteriosus; PS: pulmonary stenosis; PAS: pulmonary artery stenosis; DORV: double outlet right ventricle; CS: cardiac septum; AV: atrioventricular; BAV: bicuspid aortic valve; TGA: transposition of great arteries; TA: truncus arteriosus; TS: tricuspid stenosis; FD: facial dysmorphism; CDH: congenital diaphragmatic hernia; IUGR: intrauterine growth retardation; LOF: loss of function; ASD: atrial septal defect; VSD: ventricular septal defect; GDD: growth development disorder; NDD: neurodevelopmental disorder; SNV: single nucleotide variant (i.e., variation of a single nucleotide in genome); MS: missense mutation; NS: nonsense mutation; AP: alanine -proline rich region; AC: acidic-amino acid domain; PK: protein kinase domain; C1(a & b): Cysteine-rich zinc binding domain conserved region 1; PB: PDZ binding domain. PC: personal communication by Prof Marc-Philip Hitz.

CHD in patients (n = 48) with *Prkd1* mutations	Prevalence
Pulmonary stenosis/abnormality	7
Atrial septal defect	4
Ventricular septal defect	4
Septal defects – (not specified)	2
Atrioventricular septal defect (AVSD) and AV canal defect	3
Bicuspid aortic valve (BAV)	2
Aortic stenosis	1
Coarctation of aorta	3
Double outlet right ventricle (DORV)	1
Abnormality of tricuspid valve	3
Abnormality of mitral valve	1
Patent ductus arteriosus (PDA)	2
Truncus arteriosus (TA)	2
CHD – not specified	25

Table 4:2 The prevalence of different types of CHD in humans with SNVs in Prkd1. Pulmonary stenosis is the most common defect followed by septal defects. This data was collected from published literature, ClinVar [351], DECIPHER's databases (https://www.decipher-genomics.org/gene/PRKD1/overview/clinical-info) [352] and by personal communication (Professor Marc-Phillip Hitz).

4.1.6 Previous *Prkd1* mouse models

In order to study the role of PRKD1 in heart development, different mouse models have been studied in the past. The Olson lab generated a mouse with exon 12-14 deleted, resulting in disruption of the catalytic domain of PRKD1. They showed that *Prkd1* knockout mice are lethal embryonically with incomplete penetrance (1% surviving to term) however, interestingly, they showed that mice with cardiac-specific *Prkd1* deletion were viable [318]. Matthews *et al* also reported that homozygous mutation of *Prkd1* resulting in inactive protein kinase domain was not compatible with life (~1% penetrance) with reduced Mendelian ratios. They however reported that mice with homozygous mutation of *Prkd2* with resultant

inactivation of their catalytic domain were not lethal and produced litters with normal Mendelian ratios [326]. Moreover, another study aiming to look for role of *Prkd3* and using a mouse model with a gene trap deletion of *Prkd3* reported that loss of function of *Prkd3* was not lethal except with a milder phenotype in terms of skeletal abnormality [354] (http://www.informatics.jax.org/knockout_mice/lexicon/1574.html). This means that PRKD2 and PRKD3 are not indispensable for embryonic development unlike PRKD1. Moreover, it was previously reported that homozygous mutation of PRKD1 is lethal after E9.5 resulting in reduced Mendelian ratios after this stage [326]. This indicates that PRKD1 is vital for normal embryogenesis to take place.

4.1.7 *Prkd1* mouse models used in this work

In order to characterise the role of *Prkd1* in heart development and CHD, two novel mouse models were used in this work: one was "*Prkd1*-deletion" and another being "*Prkd1*-humanised mutation/point mutation" mouse models. Details about the mouse models are mentioned in the methods (chapter 2, section 2.1). Both mice had allele carrying mutation according to International Mouse Phenotyping Consortium (IMPC) and were generated by endonuclease mediated (*em*) mutation at Wellcome Trust Sanger Institute (*Wtsi*) UK and bred at the University of Nottingham. One of them (*Prkd1*$^{em1(IMPC)Wtsi}$ abbreviated as *Prkd1*^{em1} for the rest of this thesis) was a loss of function (LOF) mutation model with exon 2 of the gene deleted whereas the other one (*Prkd1*$^{em2(IMPC)Wtsi}$ abbreviated as *Prkd1*^{em2} for the rest of this thesis) had a point mutation in exon 13

(humanised mutation, HM), corresponding to the PK-domain resulting in a protein with G598R substitution (which corresponds to G592R in human PRKD1). This chapter describes the characterization of the role of PRKD1 in heart development and CHD in case of LOF of *Prkd1*, using the *Prkd1*-mutant mouse model with exon 2 deleted. The next chapter (Ch. # 5) is based on the role of PRKD1 in heart development and CHD using *Prkd1*^{em2}*-HM* mouse model.

4.2 HYPOTHESIS AND AIM OF THIS PROJECT

HREM technology had been in use in life sciences research for years but its application in the Deciphering the Mechanisms of Developmental Disorders (DMDD) program (https://dmdd.org.uk) [355] to study developmental disorders in mutant mouse models made a significant impact on developmental research [356]. With regard to heart development, it is capable to produce high resolution 3D images for phenotypic analysis [357]. Therefore, in order to explore the role of PRKD1 in heart development and CHD, this project was designed to examine the heart morphology in genetically engineered mouse model carrying a deletion (LOF)-mutation of *Prkd1* using in-house HREM technology, which was recently acquired by Siobhan Loughna and David Brook.

4.2.1 Specific aim of this project

The specific aim of this project was to characterise, phenotypically (by HREM), the role of PRKD1 in heart morphogenesis and CHD, and to determine the effects of LOF of *Prkd1* on embryos' survival. Moreover,

external phenotyping would be carried out at the time of embryo collection at E12.5 and E15.5.

4.2.2 Hypotheses for the project:

Hypotheses for this project were:

1. The deletion of both alleles of *Prkd1* would not be compatible with life whereas mice with a single allele would be viable.
2. Deletion of one *Prkd1* allele would result in incomplete penetrance, whereas loss of both alleles would result in 100% CHD-penetrance.

4.3 RESULTS

4.3.1 Mice with heterozygous (*Prkd1*$^{em1/+}$) mutation are viable and fertile, but homozygous mutation (*Prkd1*$^{em1/em1}$) is embryonically lethal

My goal for this project was to set up HET X HET crosses to get homozygous null (*Prkd1*$^{em1/em1}$) embryos in addition to wild type (*Prkd1*$^{+/+}$) and heterozygous (*Prkd1*$^{em1/+}$) null embryos. Help with genotyping of these mice was provided by Sophie Rochette (Siobhan Loughna's lab). In *Prkd1*^{em1} mouse line, having bred 660 pups and genotyped 331 of these, we have noted that heterozygous (*Prkd1*$^{em1/+}$) mice are viable and fertile, whereas homozygous (*Prkd1*$^{em1/em1}$) mutation is lethal. Figure 4:8 is a representative image of a typical result of genotyping of the *Prkd1*^{em1} mouse line. In the case of *Prkd1*^{em1} genotyping, two different PCR reactions were performed for each sample, a WT reaction for the WT allele,

a MUT reaction for the detection of mutant allele. In WT sample, only the WT band was visible whereas in case of HET (*Prkd1*$^{em1/+}$), WT as well as MUT bands were seen (Figure 4:8). From the HET X HET matings, the obtained number of HOMO (*Prkd1*$^{em1/\ em1}$) embryos was 8/170 (4.7%) versus the expected 42.5/170 (25%). On the other hand, the number of obtained WT was 54/170 (31.8% versus expected 25%) whereas that of HET (*Prkd1*$^{em1/+}$) was 108/170 (63.5% versus expected 50%) (Table 4:3). In order to determine the difference between the observed and expected ratios of the collected embryos, a Chi-square test was applied which showed a statistically significant difference ($P < 0.05$) between the observed and expected Mendelian ratios. This indicates that homozygous (*Prkd1*$^{em1/\ em1}$) embryos are not compatible with life and die early during intrauterine life, whereas *Prkd1*$^{em1/+}$ (HET) embryos are viable and fertile, though we have found that the *Prkd1*^{em1} homozygous embryo can survive to E15.5, they are at reduced frequency compared to controls, with just 4.7% of embryos being homozygous (*Prkd1*$^{em1/em1}$) (Table 4:3). We have never had a homozygous (*Prkd1*$^{em1/em1}$) mouse survive to genotyping stage, which we perform at around P10-12. However, in the postnatal study in this mouse, one of the P7 mouse was homozygous (Table 4:8).

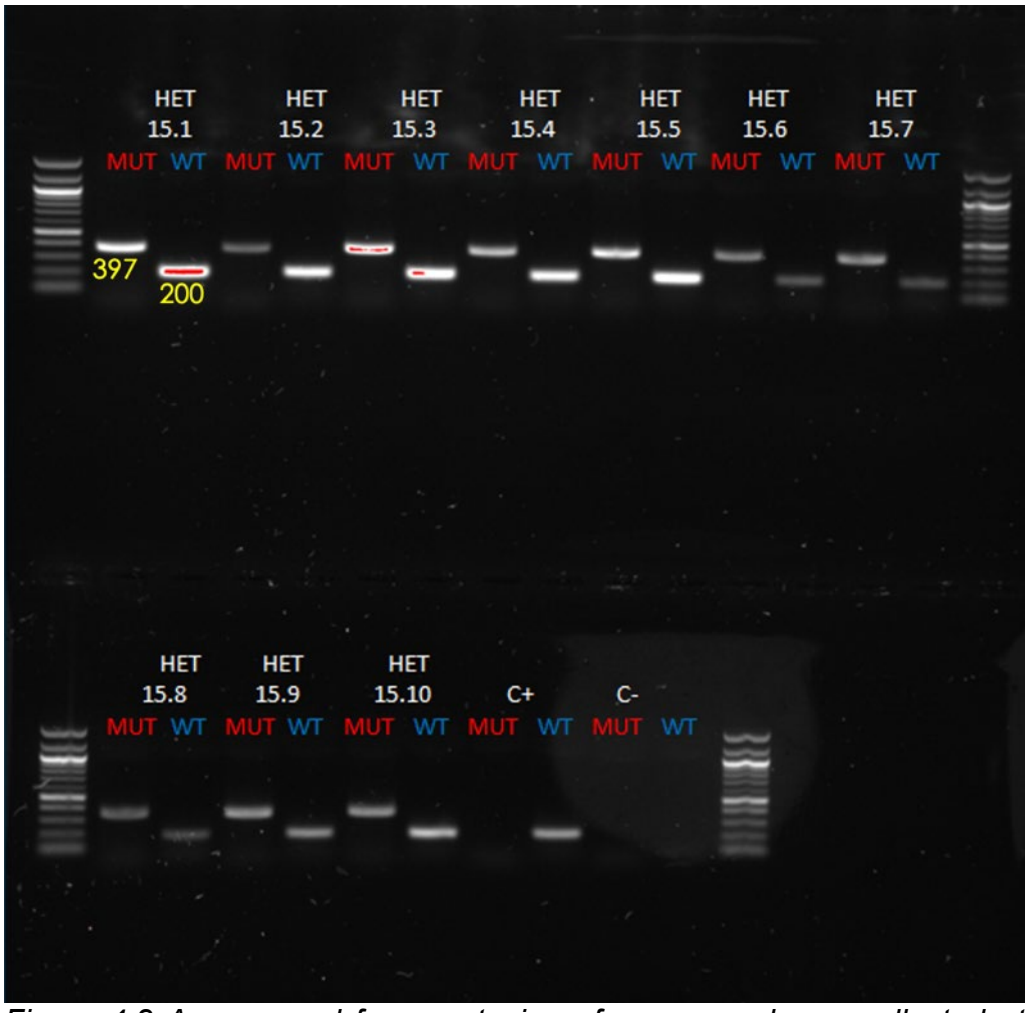


Figure 4:8 Agarose gel for genotyping of mouse embryos collected at E15.5. The wild type (WT) and mutant (MUT) bands are of expected size (shown in yellow) in respective lanes but not in the negative control (C-). Positive control (C+) is a WT sample. Ladder: 100bp (Invitrogen®).

***Prkd1*^{em1} (HET X HET)**	**WT**	**HET**	**HOMO**	**Chi-square test**
Expected	49/196 (25%)	98/196 (50%)	49/196 (25%)	P = 0.000000002
Observed	58/196 (29.59%)	129/196 (65.82%)	9/196 (4.59%)	

Table 4:3 Genotype distribution of Prkd1em1 embryos from HET X HET crosses, collected at E15.5. The observed ratios of embryos with homozygous mutation are significantly lower than the expected (Mendelian) ratios which means that homozygous (Prkd1em1/ em1) LOF-mutation of Prkd1 is incompatible with life.

4.3.2 External phenotyping of E12.5 and E15.5 embryos collected from *Prkd1*^{em1} mouse line

External phenotyping of E12.5 and E15.5 embryos was carried out at the time of tissue collection (n = 105 WT, 155 HET and 15) (Table 4:4). This phenotyping was carried out before genotyping. WT from *Prkd1*^{em1} and *Prkd1*^{em2} lines were pooled.

#	ID	Age	Geno-type	External Phenotype
1	P1.3.3	E15.5	HOMO	Oedema at the back
2	P1.6.2	E15.5	HET	Oedema at the back
3	P1.13.1	E15.5	HOMO	Growth retarded with mandibular hypo-plasia; abnormal overall appearance and lying outside the amniotic sac
4	P1.15.1	E15.5	HET	Oedema at the back
5	P1.22.2	E15.5	HET	Hemopericardium
6	P1.40.5	E12.5	HOMO	Growth retarded
7	P1.40.6	E12.5	HOMO	Growth retarded
8	P1.59.2	E12.5	HOMO	Growth retarded /dead
9	P1.59.3	E12.5	HOMO	Growth retarded /dead
10	P1.59.8	E12.5	HOMO	Growth retarded /dead
11	P1.59.9	E12.5	HOMO	Growth retarded /dead
12	P1.65.6	E12.5	HOMO	Growth retarded
13	P1.65.8	E12.5	HOMO	Growth retarded
14	P1.66.8	E12.5	HET	Growth retarded
15	P1.66.11	E12.5	HOMO	Growth retarded /dead
16	P1.67.1	E12.5	HOMO	Growth retarded /dead

Total WT (E12.5 & E15.5)		Total HET (E12.5 & E15.5)		Total HOMO (E12.5 & E15.5)	
105		155		15	
Normal WT	Abnormal WT	Normal HET	Abnormal HET	Normal HOMO	Abnormal HOMO
105	0	151	4	3	12

Table 4:4 Abnormal external phenotypes of Prkd1^{em1} *embryos. Table showing abnormal phenotypes as noted at the time of harvesting Prkd1*^{em1} *mouse embryo at E12.5 & E15.5. WT from Prkd1*^{em1} *and Prkd1*^{em2} *lines were pooled.*

At the time of collection at E12.5 and E15.5, abnormal external phenotype was observed in 12 out of total 15 (80%) *Prkd1*$^{em1/em1}$ (HOMO) and 4 out of total 155 (2.6%) *Prkd1*$^{em1/+}$ (HET) mice (Table 4:4). Growth

retardation was seen in 11 out of 15 (73.3%) *Prkd1*$^{em1/em1}$ (HOMO) and in 1 out of 155 *Prkd1*$^{em1/+}$ (HET*)* embryos (Figure 4:9 C compared with A-B, and F compared with C-D).

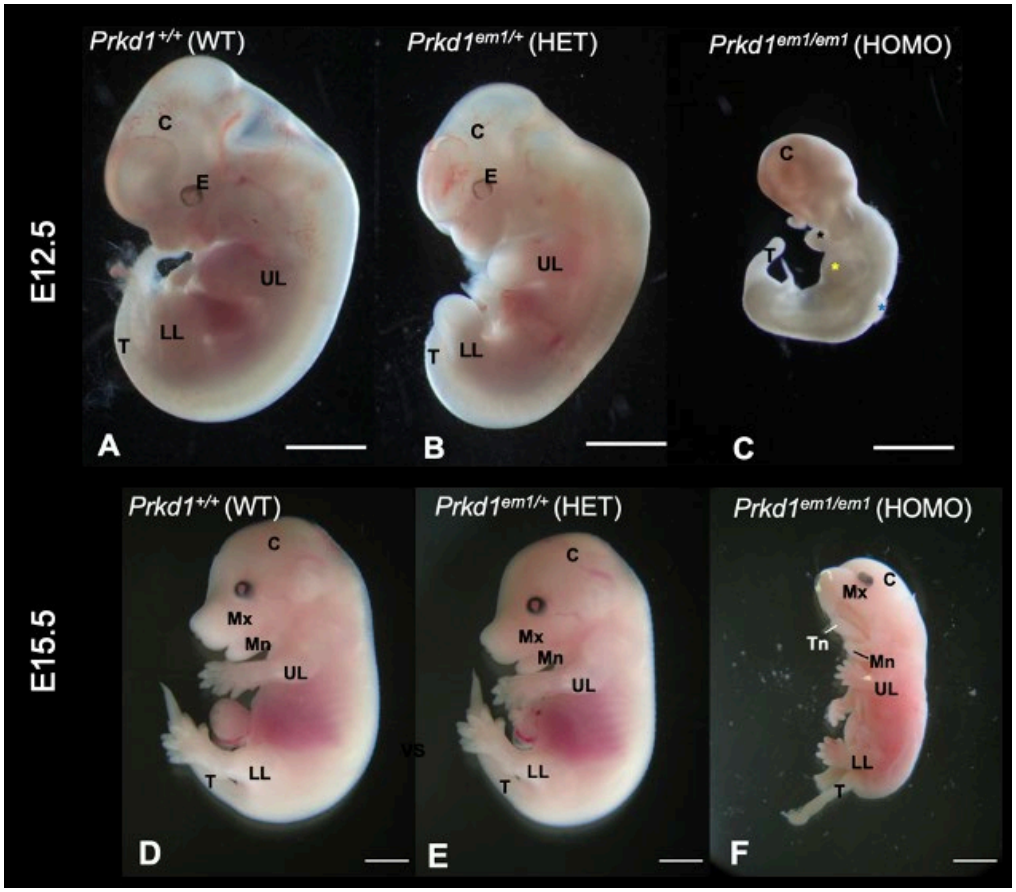


Figure 4:9 Intrauterine growth retardation in Prkd1$^{em1/em1}$ *(HOMO) mice at E12.5 and E15.5. Representative images of WT (A), Prkd1*$^{em1/+}$ *(HET) (B) and Prkd1*$^{em1/em1}$ *(HOMO) embryos (C), collected at E12.5 (A-C) and E15.5 (D-F). The embryos in C and F have severely restricted growth. In "C", blue asterisk denotes upper limb bud; black asterisk is on mandibular primordia and yellow asterisk is on pericardium and heart. In F, mandibular (Mn) hypoplasia is apparent. ULB: upper limb bud; LLB: lower limb bud; T: tail; E: eye; C: cranium; Mx: maxilla; Mn: mandible; Tn: tongue. Scale bar = 2mm for all images.*

Moreover, oedema of the back was seen in one *Prkd1*$^{em1/em1}$ (HOMO) and two *Prkd1*$^{em1/+}$ (HET*)* hearts (Figure 4:10 B and C compared with A).

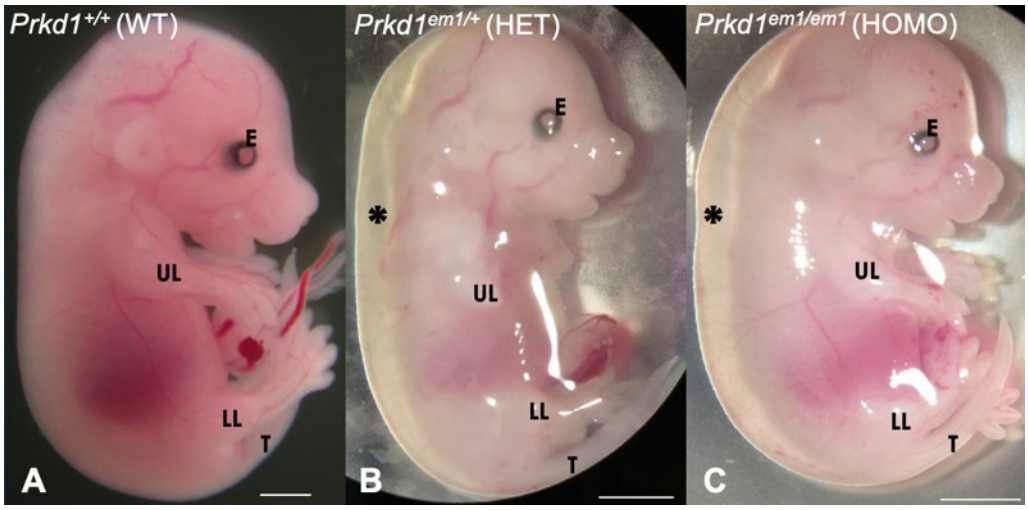


Figure 4:10 Oedema of the back at E15.5. Representative images of the oedema of the back in Prkd1$^{em1/+}$ (HET) (B) and HOMO mice (C) compared with WT (A). UL: upper limb; LL: lower limb; T: tail; E: eye. Asterisk (*) denotes oedema skin of the back. Scale bar for fig. A=1mm; fig B&C=2mm.

In one *Prkd1$^{em1/+}$* (HET*)* heart at E15.5, hemopericardium (blood in pericardium) was seen as well (Figure 4:11).

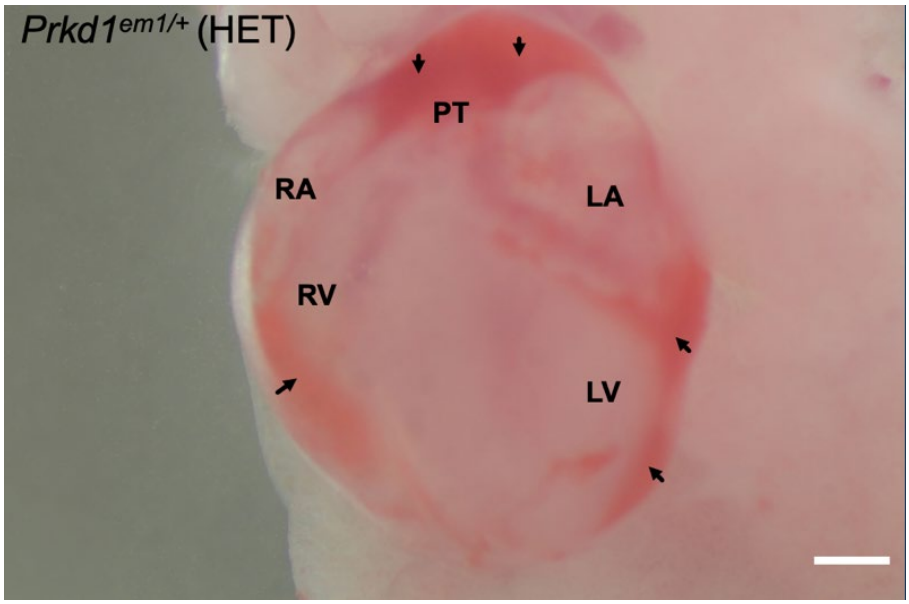


Figure 4:11 Hemopericardium in Prkd1$^{em1/+}$ (HET) mouse. The figure is showing one of the Prkd1$^{em1/+}$ (HET) hearts having blood in pericardium (back arrows) which can happen in heart failure. LA, left atrium; LV, left ventricle; PT, pulmonary trunk; RA, right atrium; RV, right ventricle. Scale = 0.5mm.

4.3.3 HREM based phenotypic analysis

E15.5 hearts from *Prkd1*^{em1} mice were analysed after generating their 3D models from a z-stack of high resolution 2D images. The greater flexibility and ability to analyse the heart in different planes rendered by this new technique enabled analysis of the different parts of the heart such as its different surfaces, the interior including the cardiac musculature, valves as well as the outflow tract (OFT). Interatrial (IA) communication was present in all embryos at E15.5 as open-foramen-ovale and was not related with the mutation since it should close only after birth under physiological conditions.

A total of 135 hearts were analysed by HREM which included 55 HET (*Prkd1*$^{em1/+}$), and 6 HOMO (*Prkd1*$^{em1/em1}$). The WT control hearts were from mice from the same C57BL/6N background and were pooled for all HREM analysis in this thesis (Table 4:5). The analysis of hearts on HREM was done while being blind to the genotype.

Genotype	WT	HET	HOMO	Total
Prkd1*^{em1} *(LOF)				
Number (n)	74	55	6	135

Table 4:5 Prkd1^{em1} *mouse hearts collected at embryonic age E15.5 and analysed by HREM. In case of Prkd1em1, HET (n = 55) and HOMO (n = 6) hearts were analysed and compared with WT (n = 74) hearts. All the mice were on the same (C57BL/6N) background.*

4.3.3.1 CHD penetrance and heart phenotypes in HET (*Prkd1*$^{em1/+}$) hearts

The penetrance of congenital heart disease was quite low in HET (*Prkd1*$^{em1/+}$) hearts as the structural heart defect was noted in only one

(1.82%) case out of the total (n = 55) analysed (Table 4:6, Figure 4:12). Internal examination of this heart showed that there was a small muscular ventricular septal defect (VSD; an opening between the right and left ventricular chambers) (arrows in Figure 4:12B), a defect that was not seen in any of the 56 WT hearts (Figure 4:12 A). In addition, the myocardial trabeculae appear coarser and hypertrophic compared to control.

Prkd1^{em1+} hearts at E15.5 with phenotype		
Sample ID	**Phenotype**	**Penetrance**
NID29_C	Musc. VSD	1/55 (1.82%)

Table 4:6 Ventricular septal defect (VSD) in one Prkd1$^{em1/+}$ (HET) heart at E15.5. One heart from mouse with heterozygous mutation of Prkd1 (Prkd1$^{em1/+)}$ in the loss of function (LOF)/deletion type of mutation model showed muscular VSD. The penetrance of structural heart defects was very low in HET hearts. Musc: Muscular; VSD: Ventricular septal defect.

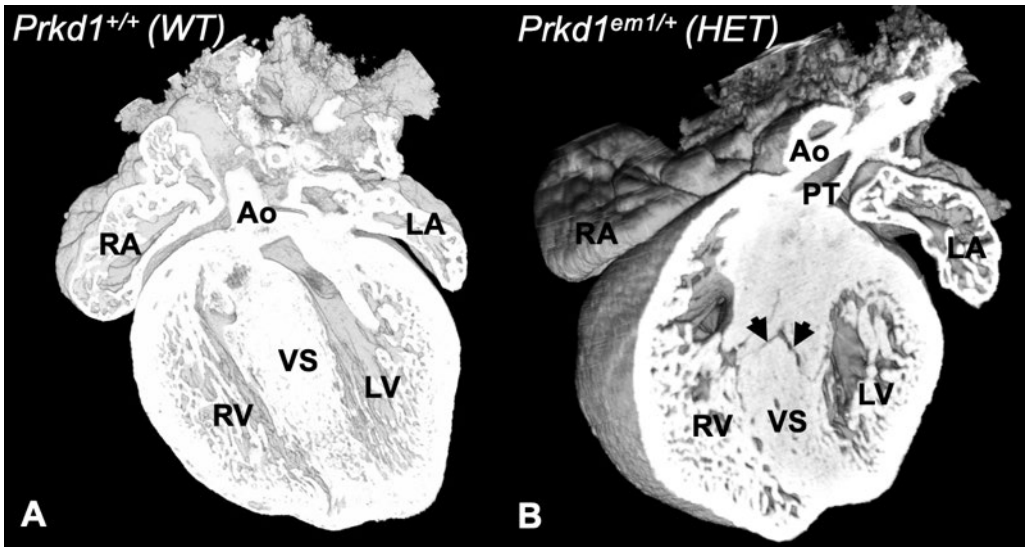


Figure 4:12 One heterozygous Prkd1^{em1} E15.5 heart had a congenital heart defect. A small muscular ventricular septal defect can be seen in a Prkd1$^{em1/+}$ heart (arrows in B), in comparison to WT control (A) where a normal ventricular septum (VS) can be seen. Myocardial trabeculae appear coarser and hypertrophic in the Prkd1em1/+ (HET) heart (B). Ao, Aorta; LA, left atrium; LV, left ventricle; PT, pulmonary trunk; RA, right atrium; RV, right ventricle.

4.3.3.2 CHD penetrance and heart phenotypes in HOMO (*Prkd1*$^{em1/em1}$) hearts and the observed phenotypes

In contrast to the heterozygotes, of the six E15.5 homozygous (*Prkd1*$^{em1/em1}$) hearts, five had structural heart defects (83.3%). The abnormalities seen in these five CHD affected hearts were variable, from isolated anomalies to more complex defects (Table 4:7).

***Prkd1*$^{em1/em1}$ (HOMO)**			
No.	**Sample ID**	**Phenotype**	**Penetrance**
1.	NID42_A	AVSD, DORV, Musc VSD	5/6 = **83.33%**
2.	NID42-B	Dysplastic PV (left dysplastic leaflet)	
3.	NID42_C	BAV (fused type, with three sinuses)	
4.	NID43_B	pMem. VSD (outlet)	
5.	NID76_C	AVSD, DORV	

Table 4:7 Phenotypes in Prkd1$^{em1/em1}$ *(HOMO) mice. The phenotypic analysis of E15.5 hearts from mice with deletion of both alleles of Prkd1 (Prkd1*$^{em1/em1}$*) showed quite high penetrance of CHDs, varying from isolated anomalies to more complex defects. pMem, perimembranous; Musc, muscular; AVSD: atrioventricular septal defect; DORV: double-outlet right ventricle; BAV: bicuspid aortic valve; PV: pulmonary valve.*

4.3.3.3 Isolated defects in HOMO (*Prkd1*$^{em1/em1}$) hearts

One of the isolated defects was a perimembranous VSD, with two involving the outflow valves i.e., a dysplastic pulmonary valve and a bicuspid aortic valve (BAV) were seen in one heart each (Table 4:7). A normal pulmonary valve should have 3 leaflets i.e., right, left, and anterior leaflets (Figure 4:13 A and A'). In the heart with a dysplastic pulmonary valve, the anterior and right leaflets were present, but the left leaflet was deficient (Figure 4:13 B and B'). With regards the aortic valve, however, three normal leaflets (right, left and non-coronary) could be seen in both the

HOMO and control hearts (Figure 4:13 A' and B'). In addition, one HOMO heart had BAV, where it appeared that the right and non-coronary leaflets were fused. Three sinuses were discernible (Figure 4:13 E', boxed area in E). The long black arrow in Figure 4:13-E' indicates the site (raphe) where the two leaflets had fused. In contrast, normal leaflets were seen in the WT controls (right, left and non-coronary) (Figure 4:13 D', boxed area in D).

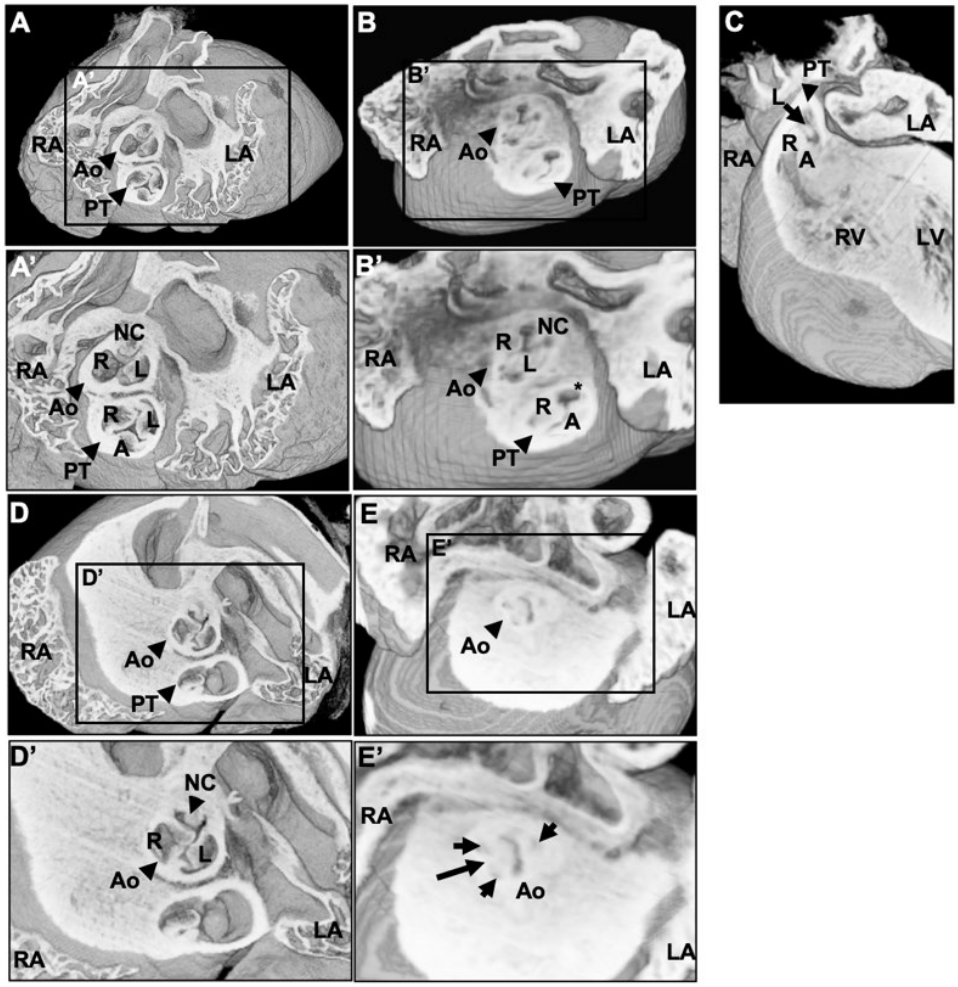


Figure 4:13 Morphology of abnormal valves in outflow vessels in E15.5 Prkd1$^{em1/em1}$ (HOMO) hearts. A-B. Superior views of a Prkd1$^{+/+}$ (WT) (A&A') and Prkd1$^{em1/em1}$ (HOMO) hearts (B&B'). The WT heart has normal valves in the outflow region, with 3 valve leaflets (right, left and anterior) seen in the pulmonary trunk (A', boxed area in A). In contrast, the HOMO heart has an incompetent pulmonary valve (B', boxed area in B); a right and anterior leaflet could be discerned, but the left leaflet was deficient (asterisk), indicating a dysplastic leaflet in the pulmonary valve. Three leaflets (right, left and non-coronary) can be seen in the aortic valve in both hearts. C. The HOMO heart in B, shown from an anterolateral aspect, to show the 2 normal (right (R) and anterior (A) and one dysplastic (left (L) – indicated by the arrow) pulmonary valve leaflets. D-E. A second E15.5 WT heart (D&D') and HOMO (E&E') heart from the superior aspect. The WT heart has normal leaflets (right, left and non-coronary) in the aortic valve (D', boxed area in D). In contrast, the HOMO heart had a non-functional aortic valve (E', boxed area in E); the aortic valve was bifoliate trisinuate. There were three sinuses (denoted by small black arrows), but there were only two leaflets. The long black arrow pointing at the site of raphe, where the two leaflets had fused. A, anterior; Ao, aorta; L, left; LA, left atrium; LV, left ventricle; NC, non-coronary; PT, pulmonary trunk; R, right; RA, right atrium; RV, right ventricle.

4.3.3.4 Complex defects were seen in HOMO (*Prkd1*$^{em1/em1}$) hearts

More complex defects were seen in other homozygous *(Prkd1*$^{em1/em1}$*)* hearts (Table 4:7). In two hearts, there were complete atrioventricular septal defects (AVSD) with shunting above (as interatrial communication) and below the common AV valve (as interventricular communication) (Figure 4:14). In one of these hearts (Figure 4:14 B), septum primum was present (black asterisk in Figure 4:14 C), but there was an interatrial communication inferior to the lower margin of the atrial septum (denoted by black oval in Figure 4:14 C compared with A). The dorsal endocardial cushion could be seen (white asterisk in Figure 4:14 C) and there was an associated deficiency of the inlet septum on the ventricular side which extended into the outlet region of the heart (denoted by black asterisk in Figure 4:14 D). In addition, the aortic valve overrode the crest of the ventricular septum of this heart by more than 50%, with the pulmonary trunk arising normally from the RV more anteriorly. The degree of aortic override (confirmed in different planes) is such to be described as double outlet right ventricle (DORV). Furthermore, at the dorsal aspect, the right ventricle appeared to be subdivided by either a large papillary muscle or prominence of the septomarginal trabeculation (asterisk in Figure 4:14 E), although the trabeculae in this homozygous heart in general seemed coarse and thick (Figure 4:14 C-E compared to A).

In the second homozygous *(Prkd1*$^{em1/em1}$*)* heart with complete AVSD (Figure 4:14 F), the lower part of the septum primum was entirely absent (black asterisk in Figure 4:14 F). There was a large deficiency of the inlet septum on the ventricular side (white asterisk in Figure 4:14 F) which

extended into the outlet of the heart. Both aorta and pulmonary artery originated from right ventricle to result in DORV. The ventricular myocardium of both ventricles and the interventricular septum in this heart appeared spongy, with a number of openings present in the muscular septum (Figure 4:14-F) in comparison to the normally septated WT heart (Figure 4:14-A). There was only a thin layer of compact myocardium present (Figure 4:14-F).

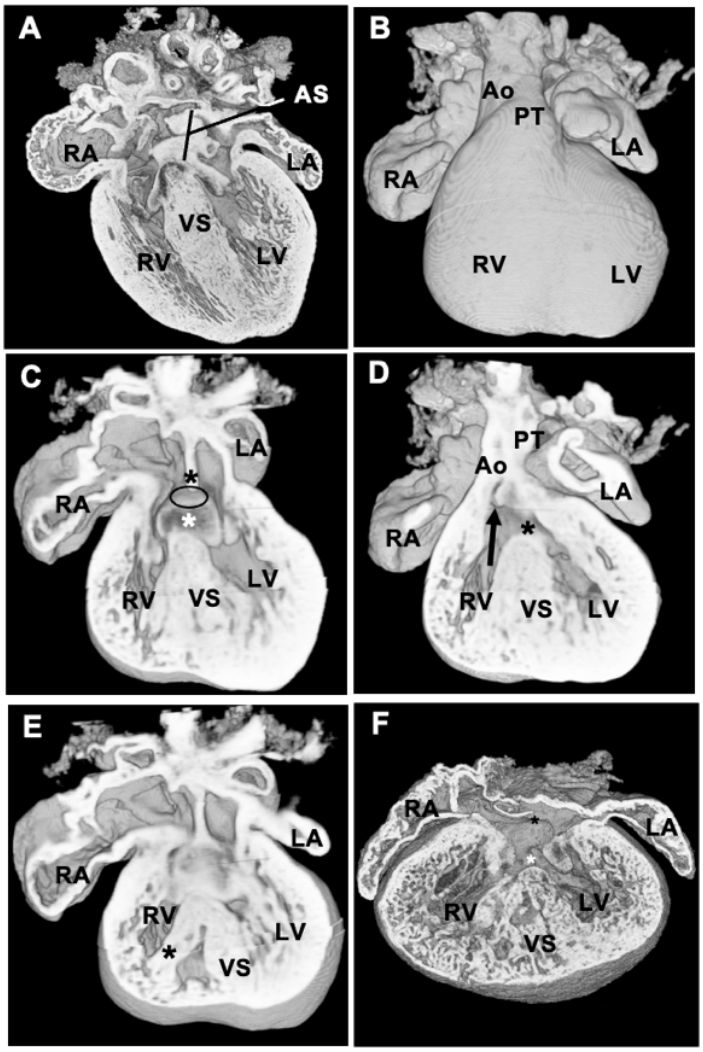


Figure 4:14 AVSD is seen in two E15.5 Prkd1$^{em1/em1}$ (HOMO) hearts. A. A WT control heart with normal atrial septum. B. An external ventral view of a Prkd1$^{em1/em1}$ heart with AVSD. C. Same heart as in B, a complete AVSD, with a lack of fusion of the dorsal endocardial cushion (denoted by white asterisk) with the septum primum (lack of fusion denoted by black oval); the septum primum is indicated (black asterisk). The VSD was of inlet type. D. A view of a more ventral plane shows a perimembranous VSD with outlet extension (black asterisk), with the aortic valve sitting over the right ventricle (RV) (black arrow). E. A ventral view of the deeper plane through the same heart as in B-D shows the right ventricle to be divided by either a large papillary muscle or a prominent septomarginal trabecula (black asterisk). F. Second homozygous heart with a complete AVSD (black asterisk for atrial part and white asterisk for the inlet VSD). The raised area between black and white asterisks is dorsal endocardial cushion. Myocardium of both ventricles and the interventricular septum in this heart appeared spongy, with several openings present in the muscular septum. There is thinning of ventricular wall as well. AS: atrial septum; Ao, aorta; LA, left atrium; LV, left ventricle; PT, pulmonary trunk; RA, right atrium; RV, right ventricle; VS, ventricular septum.

4.3.4 Morphological changes in sub valvular apparatus of right and left) AV valves in E15.5 hearts from *Prkd1^{em1}* mice

Papillary muscles originate from the trabeculae carneae [236] and are vital for the atrioventricular valves' functioning. Their anomalies can happen in association with CHD [358]. Moreover, the myocardium was spongy in case of homozygous *(Prkd1$^{em1/em1}$)* mutation and hence the papillary muscles can be expected to be affected as well. Therefore, papillary muscles of mitral and tricuspid valves were analysed in all the HET *(Prkd1$^{em1/+}$)* (n = 1) and HOMO *(Prkd1$^{em1/em1}$)* (n = 5) hearts with CHD compared with WT (n = 3) and HET hearts without CHD (n = 6). The single HET *(Prkd1$^{em1/+}$)* with CHD (Figure 4:15 Ab and Bb) and 4 out of 5 HOMOs *(Prkd1$^{em1/em1}$)* with CHD (Figure 4:15 Ac and Bc) had thickening of papillary muscles compared with control (Figure 4:15 Aa and Ba). No papillary muscle thickening was observed in the 6 HET hearts without CHD, suggesting that papillary muscle thickening is likely secondary to CHD.

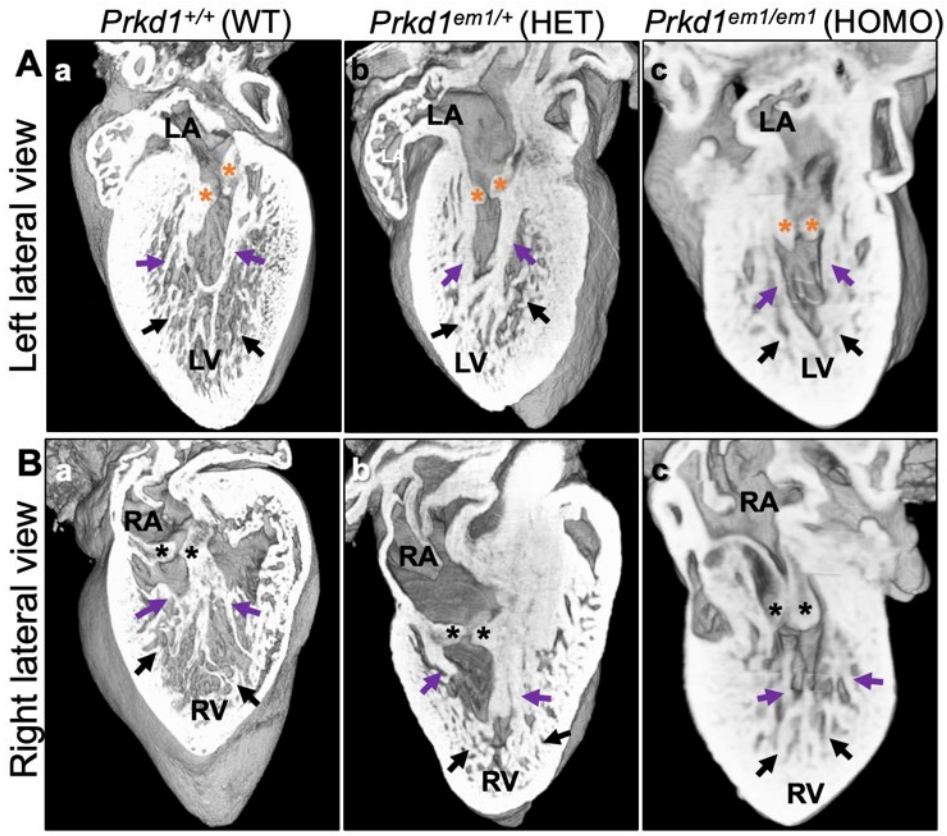


Figure 4:15 Comparison of trabeculae and papillary muscles in E15.5 Prkd1^{em1} hearts. For both A and B, WT are left column, HET middle and HOMO right. Aa-c. Left lateral view to show the papillary muscles (purple arrows) and trabeculae (black arrows) are thin and clearly defined in the WT and become progressively thicker and coarser from HET to HOMO. The mitral valve leaflets are denoted (orange asterisk). Ba-c. Right lateral view to show the papillary muscles (purple arrows) and trabeculae (black arrows). As seen from the left, again both the trabeculae and papillary muscles are more elongated and finer in the WT, in contrast to the HET and HOMO hearts where these muscles appear thicker. The tricuspid valve is denoted (black asterisk). LA, left atrium; LV, left ventricle; RA, right atrium; RV, right ventricle.

4.3.4.1 Abnormality of heart shape in *Prkd1$^{em1/em1}$* (HOMO) mice

Heart shape and size seemed quite different/abnormal in four *Prkd1$^{em1/em1}$* (HOMO) mice (Figure 4:14-A & Figure 4:16 B), compared to WT (n = 74) (Figure 4:16 A). Interior of these hearts showed coarse and/or spongiform trabeculation coupled with changes in chambers'

sizes and shapes, and thinning of compact layer of myocardium compared to WT (Figure 4:14 C-F & Figure 4:16 B' compared to A').

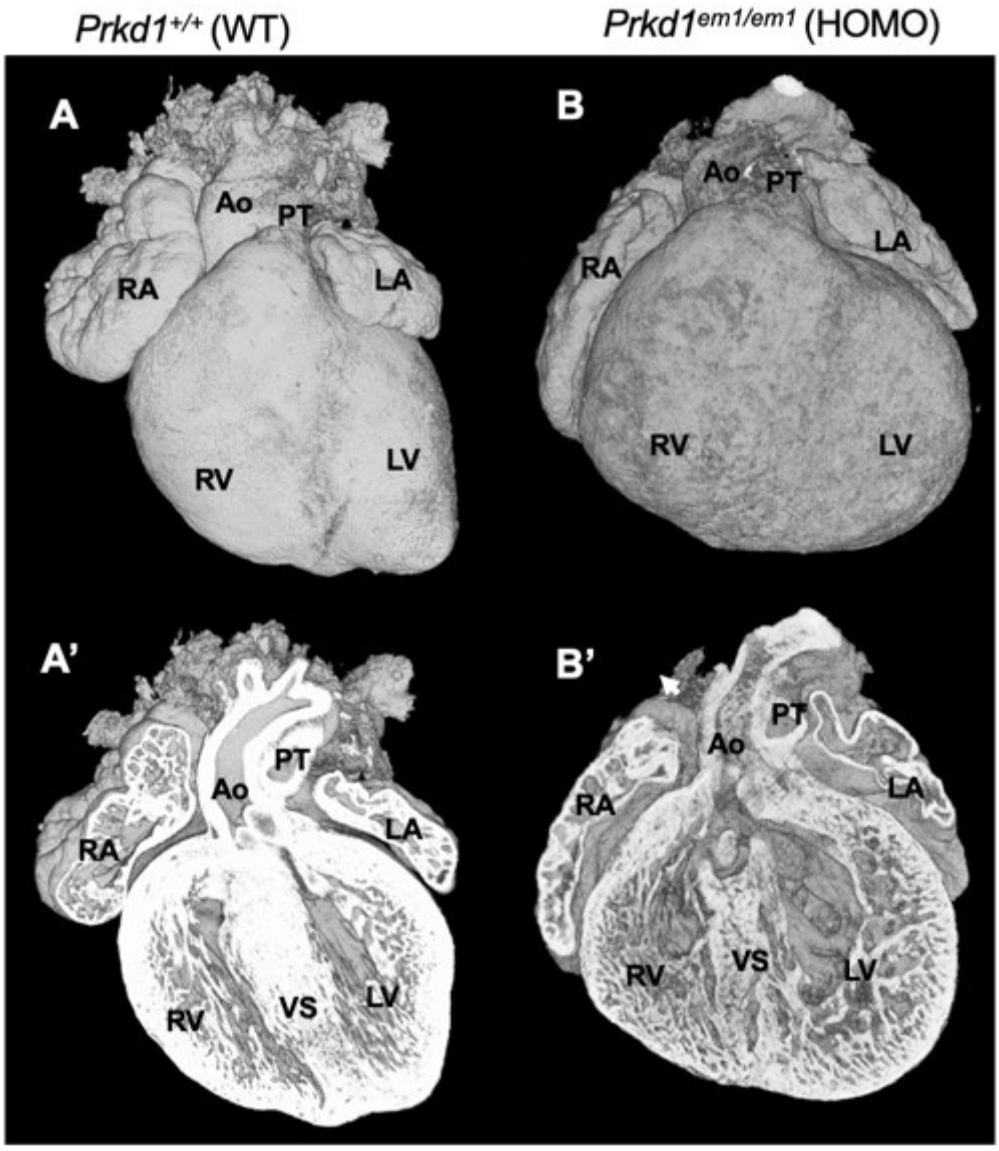


Figure 4:16 Abnormal external appearance of Prkd1$^{em1/em1}$ (HOMO) hearts. A-B: External appearance of HOMO heart (B) is abnormal being globular/bulkier compared to the WT heart (A). A'-B': Interior views of the hearts A and B. The HOMO heart (B') shows spongiform myocardium with recesses and thinning of compact layer of myocardium (along with structural CHD) compared with WT heart (A'). Ao, aorta; LA, left atrium; LV, left ventricle; PT, pulmonary trunk; RA, right atrium; RV, right ventricle; VS, ventricular septum.

4.3.4.2 Quantitative analyses of Prkd1^{em1} mouse hearts at E15.5

By using 3D-slicer program [192], volumes of atria, and ventricles (wall and chamber) as well as total heart muscle volume were measured in mouse hearts at E15.5 (n = 10 WT, 10 HET and 6 HOMO). These measurements were carried out in order to exclude any relation of the deletion of *Prkd1* with changes in these parameters of the heart.

Total right atrial (RA) volume:

The total right atrial volume data for WT (W = 0.9200, *P* = 0.3570), HET (W = 0.8876, *P* = 0.1594) and HOMO (W = 0.9345, *P* = 0.6152) hearts were normally distributed. One-way ANOVA (*P* = 0.3413), and Tukey's multiple comparison test showed that there was no significant difference in WT versus HET (*P* = 0.5892), in WT versus HOMO (*P* = 0.3352), and between HET and HOMO (*P* = 0.8288) (Figure 4:17-A).

Right ventricular (RV) chamber volume:

The right ventricular chamber volume data for WT (W = 0.9107, *P* = 0.2856), HET (W = 0.9357, *P* = 0.5059) and HOMO (W = 0.9227, *P* = 0.5252) hearts were normally distributed. One-way ANOVA (*P* = 0.4614), and Tukey's multiple comparison test showed that there was no significant difference in WT vs. HET (*P* = 0.7516), in WT vs. HOMO (*P* = =0.8103), and between HET and HOMO (*P* = 0.4378) (Figure 4:17-B).

Right ventricular (RV) muscle volume:

The total right volume data for WT (W = 0.9225, *P* = 0.3785), HET (W = 0.9691, *P* = 0.8828) and HOMO (W = 0.9185, *P* = 0.4948) hearts were normally distributed. One-way ANOVA (*P* = 0.0599), and Tukey's multiple comparison test showed that there was no significant difference in WT

vs. HET (*P* = 0.1227), in WT vs. HOMO (*P* = 0.8992), and between HET and HOMO (*P* = 0.0895) (Figure 4:17-C).

Total right ventricular (RV) volume:

The total right ventricular volume data for WT (W = 0.9169, *P* = 0.3314) and HET (W = 0.9593, *P* = 0.7776) and HOMO (W = 0.9879, *P* = 0.9833) hearts were normally distributed. One-way ANOVA showed that there was significant difference among the three groups (*P* = 0.0124). Tukey's multiple comparison test showed that there was significant difference between WT and HET (*P* = 0.0253) and between HET and HOMO (*P* = 0.0320), however the difference was not significant between WT and HOMO (*P* = 0.9606), (Figure 4:17-D).

Total left atrial (LA) volume:

The total left atrial volume data for WT (W = 0.9481, *P* = 0.6466), HET (W = 0.9259, *P* = 0.4083) and HOMO (W = 0.9250, *P* = 0.7561) hearts were normally distributed. One-way ANOVA (*P* = 0.6500), and Tukey's multiple comparison test showed that there was no significant difference in WT vs. HET (*P* = 0.7070), in WT vs. HOMO (*P* = 0.7149), and between HET and HOMO (*P* = 0.9951) (Figure 4:17-E).

Left ventricular (LV) chamber volume:

The data for WT (W = 0.8982, *P* = 0.2092), HET (W = 0.8584, *P* = 0.0731) and HOMO (W = 0.8666, *P* = 0.2131) hearts were normally distributed. One-way ANOVA (*P* = 0.1001), and Tukey's multiple comparison test showed that there was no significant difference in WT vs. HET (*P* = 0.0845), in WT vs. HOMO (*P* = 0.7266), and between HET and HOMO (*P* = 0.4778) (Figure 4:17-F).

Left ventricular (LV) muscle volume:

The total left ventricular volume data for WT (W = 0.9446, *P* = 0.6052), HET (W = 0.8557, *P* = 0.0679) and HOMO (W = 0.9344, *P* = 0.6147) hearts were normally distributed. One-way ANOVA showed that there was significant difference among the groups (*P* = 0.0394). Tukey's multiple comparison test showed that there was no significant difference in WT vs. HET (*P* = 0.5261), in WT vs. HOMO (*P* = 0.1977), but the difference between HET and HOMO was significant (*P* = 0.0308) (Figure 4:17-G).

Total left ventricular (LV) volume:

The data for WT (W = 0.9234, *P* = 0.3858), *Prkd1*$^{em1/+}$(HET) (W = 0.8762, *P* = 0.1180) and HOMO hearts (W = 0.8914, *P* = 0.3256) were normally distributed. One-way ANOVA showed significant difference among the groups (*P* = 0.0401). Tukey's multiple comparison test showed that there was no significant difference in WT vs. HET (*P* = 0.2391), in WT vs. HOMO (*P* = 0.4535) but the HET and HOMO were significantly different from each other (*P* = 0.0356) (Figure 4:17-H).

Total heart muscle volume:

The total heart muscle volume data for WT (W = 0.9285, *P* = 0.4333), and HOMO (W = 0.9606, *P* = 0.8245) hearts were normally distributed but for HET hearts, it was not (W = 0.8382, *P* = 0.0420).

Kruskal-Wallis test (*P* = 0.0449) and Dunn's multiple comparison test showed that there was no significant difference in HET vs. WT (*P* = 0.2666), in HOMO vs. WT (*P* > 0.9999), but the difference was significant between HET and HOMO (*P* = 0.0519) (Figure 4:17-I).

Total heart volume:

The data for total heart volume for WT (W = 0.8822, *P* = 0.1383), HET (W = 0.9695, *P* = 0.8864) and HOMO (W = 0.9741, *P* = 0.9190) hearts were normally distributed.

One-way ANOVA (*P* = 0.0855), and Tukey's multiple comparison test showed that there was no significant difference in WT vs. HET (*P* = 0.3960), in WT vs. HOMO (*P* = 0.4842), and between HET and HOMO (*P* = 0.0738) (Figure 4:17-J).

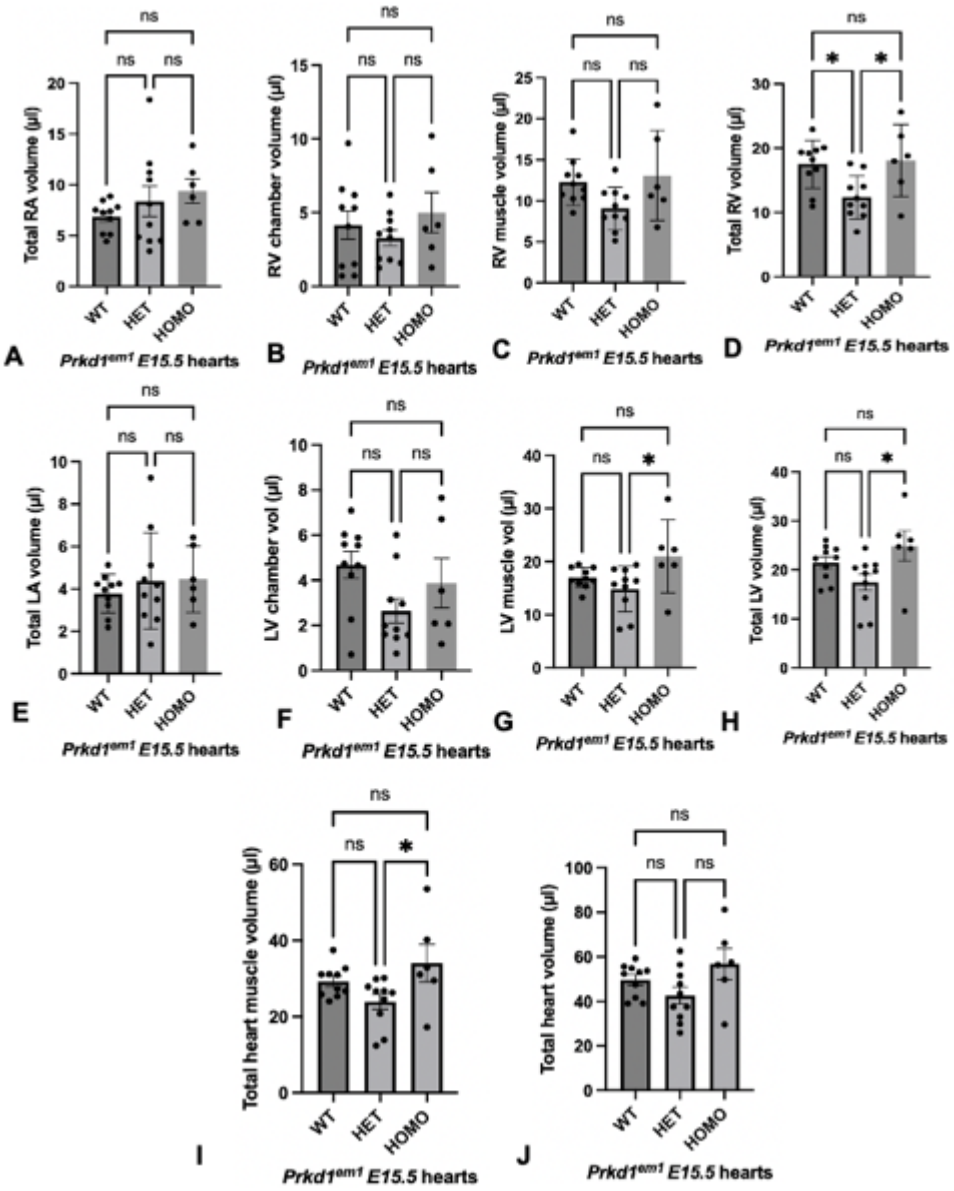


Figure 4:17 Volumetric analyses of Prkd1^{em1} mouse hearts at E15.5. Figures showing the findings from the quantitative analysis of Prkd1em1 mouse hearts collected at E15.5. There was no statistically significant difference (P > 0.05) among WT, HET and HOMO hearts in terms of RA (A), RV (B), RV muscle (C), LA (E), LV chamber (F), LV muscle volume (G) volumes. However, with regard to the total RV (D), LV muscle (G), total LV (H), and total heart muscle volumes (I), HOMO hearts were significantly different than HET hearts (P < 0.05). In case of RV total volume (D), HET hearts were significantly different than WT as well (P < 0.05), in addition to HOMO hearts (n = 10 WT, 10 HET and 6 HOMO hearts).

4.3.4.3 Heart defects were seen in P6/P7 neonates of *Prkd1^{em1}* mice

Postnatal hearts were isolated in order to determine the phenotypes present after birth. Ten P6/P7 heterozygous hearts were analyzed by HREM, with one showing CHD (Table 4:8). This heart clearly showed a BAV with two sinuses, best visualized from a superior view of the heart (asterisks in Figure 4:18 B) in comparison to the WT control where the normal 3 leaflets (right, left and non-coronary) can be seen (Figure 4:18 A).

HREM analysis of Prkd1^{em1} P6/P7 neonatal hearts				
Geno-type	**Total**	**N with CHD (%)**	**Sample ID**	**Phenotype**
WT	10	0	-	-
HET	10	1/10 (10%)	NID0172_B	BAV (two-sinus type)
HOMO	1	1	NID0178_A	Abnormal RV axis with widely spread bilateral apices, small RV and LV cavities, thickened myocardium, likely biventricular outflow tract narrowing.

Table 4:8 HREM analysis of hearts collected from Prkd1^{em1} mouse neonates at P6/P7. BAV: bicuspid aortic valve; ASD: atrial septal defect.

The origin of the right and left coronary arteries from the two sinuses can be seen to be patent (open arrows in the inserted B' in Figure 5B). Both coronary arteries were followed until they curved to the posterior aspect of the heart for the right coronary artery, and until the left coronary artery branched into the circumflex and anterior interventricular arteries. As described above, BAV is a defect that can be seen during development and was seen in this analysis in an E15.5 HOMO hearts (Table 4:7,Figure 4:13 E and E').

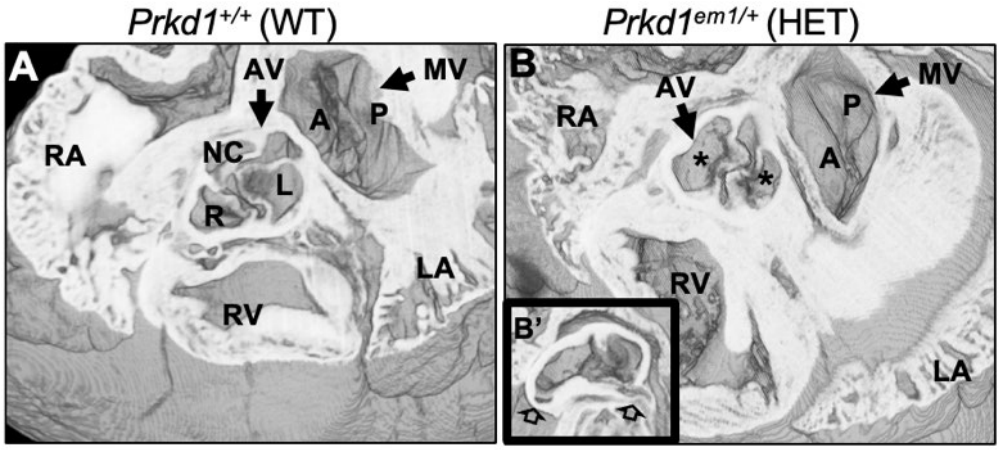


Figure 4:18 Bicuspid aortic valve is seen in P7 Prkd1$^{em1/+}$ (HET) heart. A: Axial view of a Prkd1$^{+/+}$ (WT) heart at P7 showing a normal aortic valve with three sinuses of the three leaflets. B. A Prkd1$^{em1/+}$ (HET) heart with a bicuspid aortic valve (AV), with 2 sinuses from the two leaflets (right and left) denoted by an asterisk. The mitral valve (MV) is also denoted, with normal appearing anterior (A) and posterior (P) leaflets. B'. Inset in B is taken at a slightly different angle to show that the right and left coronary arteries are patent (open arrows). R, right; L, left; NC, non-coronary; Ao, aorta; LA, left atrium; LV, left ventricle; RA, right atrium; RV, right ventricle.

Although it was found that the *Prkd1$^{em1/em1}$* (HOMO) embryo could survive to E15.5, they were at reduced frequency compared to controls, with just 4.7% of embryos being homozygous (Table 4:3). No homozygous mouse was found surviving to P10-12. (the approximate age used for genotyping in this study). However, in this postnatal study, one heart at P7 was homozygous (Table 4:8). On external examination, this heart had a prominent and separate right and left ventricular apices (Figure 4:19 B) in comparison to WT (Figure 4:19 A). Although dual apices are seen in the normal developing heart [359], the position of the right ventricular apex in this heart was abnormal. This heart was processed with other hearts which were found to be morphologically normal and there was no suggestion that this heart had acquired a separate processing artefact;

this heart was also not mechanically damaged. Therefore, we believe that the abnormal morphology of this P7 heart was due to its genotype.

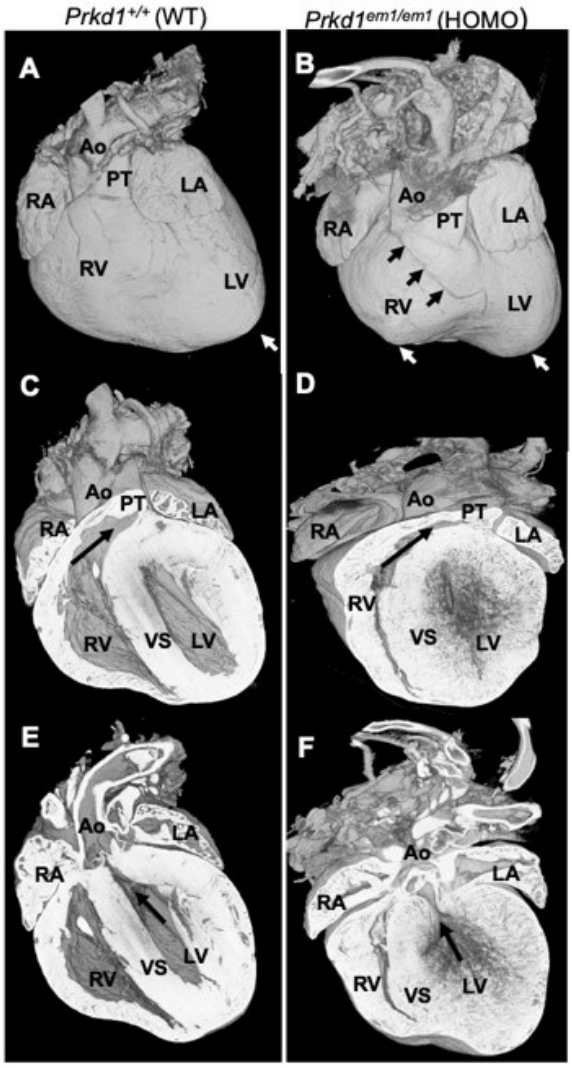


Figure 4:19 Comparison of Prkd1$^{+/+}$ and Prkd1$^{em1/em1}$ hearts at P7. A-B. External view of Prkd1$^{em1/em1}$ (HOMO) heart showing bifid apices (white arrows), in comparison to Prkd1$^{+/+}$ (WT) control where one apex is denoted. The anterior interventricular coronary artery can be seen crossing across the right ventricle (black arrows), instead of in the anterior interventricular sulcus. C-D. Four chamber view showing normal atrial and ventricular septation in the homozygous heart, comparable to WT control. However, the RV outflow tract in homozygous heart seems narrowed compared to WT (black arrow) E-F: Coronal sections (ventral view) of the same WT and the homozygous hearts oriented in a plane appropriate to show the left ventricular outflow tract (left ventricle leading into the ascending aorta, denoted by black arrow). There seems subaortic narrowing of the LV outflow tract in the homozygous heart compared to WT (black arrow). Ao, aorta; LA, left atrium; LV, left ventricle; PT, pulmonary trunk; RA, right atrium; RV, right ventricle; VS, ventricular septum.

The course of the anterior interventricular coronary artery was also abnormal in this homozygous heart (black arrows in Figure 4:19 B, compared to control Figure 4:19 A). It is seen to originate from the right coronary artery rather than, as is more usual, from the left coronary artery; it then traverses across the right ventricular outflow tract and runs between the right and left ventricular chambers in the anterior interventricular groove. Additionally, the right and left ventricular cavity sizes appear small with marked thickening and poorly defined trabeculation of both ventricles (Figure 4:19 D&F) compared to control (Figure 4:19 C and E). The axis of the right ventricle was much more vertical than usual, consistent with the position of the right ventricle apex. Although the left and right ventricular cavities connected anatomically correctly with the aorta and pulmonary trunk respectively, there is much more subaortic (and subpulmonary) crowding than usual consistent with biventricular outflow tract narrowing (Figure 4:19 D and F in comparison to C and E). Septal defects were not apparent (Figure 4:19 D&F compared to control Figure 4:19 C&E).

Phenotypically this heart could be viewed as having some features resembling the bilateral outlet obstruction and cardiomyopathy seen in severe (and often lethal) Noonan's syndrome or other RAS-opathies [360] [361].

4.3.4.4 Het null mutation of *Prkd1* (*Prkd1*$^{em1/+}$) is associated with no change in heart volumes in P6/P7 neonates

3D-slicer program was used to calculate volumes of atria, and ventricles (wall and chamber), the total heart muscle and total heart. These measurements were carried out in order to exclude any relation of mutation of *Prkd1* with changes in these parameters of heart and thereby contribution to/association with the phenotype observed. There was no statistically significant difference between WT (*Prkd1*$^{+/+}$) and HET (*Prkd1*$^{em1/+}$) hearts in terms of these parameters (Figure 4:20, Table 4:9).

Parameters	Normality (Shapiro-Wilk) test		P value (Unpaired T-test/Mann-Whitney test)
	WT W (*P* value)	HET W (*P* value)	
RA vol	0.9553 (0.5929)	0.8318 (0.0351)	0.0734 (n.s)*
LA vol	0.9982 (0.9191)	0.8230 (0.0276)	0.2797 (n.s)*
RV total vol	0.8038 (0.1237)	0.8707 (0.1018)	0.3934 (n.s)
LV total vol	0.9975 (0.9052)	0.9901 (0.9933)	0.9466 (n.s)
RV muscle vol	0.7507 (0.0015)	0.8224 (0.0271)	0.2835 (n.s)*
LV muscle vol	0.9808 (0.7346)	0.9953 (0.9952)	0.8948 (n.s)
RV chamber vol	0.8333 (0.1967)	0.8974 (0.2051)	0.6751 (n.s)
LV chamber vol	0.9423 (0.5368)	0.9222 (0.4863)	0.1333 (n.s)
Total heart muscle vol	0.9398 (0.5265)	0.9613 (0.8298)	0.9893 (n.s)
Total heart vol	0.9885 (0.7949)	0.9157 (0.4368)	0.4238 (n.s)

Table 4:9 Volumetric analysis of Prkd1em1 neonatal hearts comparing WT with HET hearts. There was no statistically significant difference between WT and HET hearts at this stage. The distribution of data for normality was assessed using Shapiro-Wilk test (P value in parenthesis), using GraphPad Prism 9.2.0 (www.graphpad.com). For normal distribution, commonly, the value of W should be close to 1 and P value be >0.05

(however very high P value also denotes that data is not normally distributed). Comparison of the two groups was carried out using Unpaired T-test (two-tailed) for normally distributed data, and Mann-Whitney Test for non-normally distributed data (denoted by asterisk).

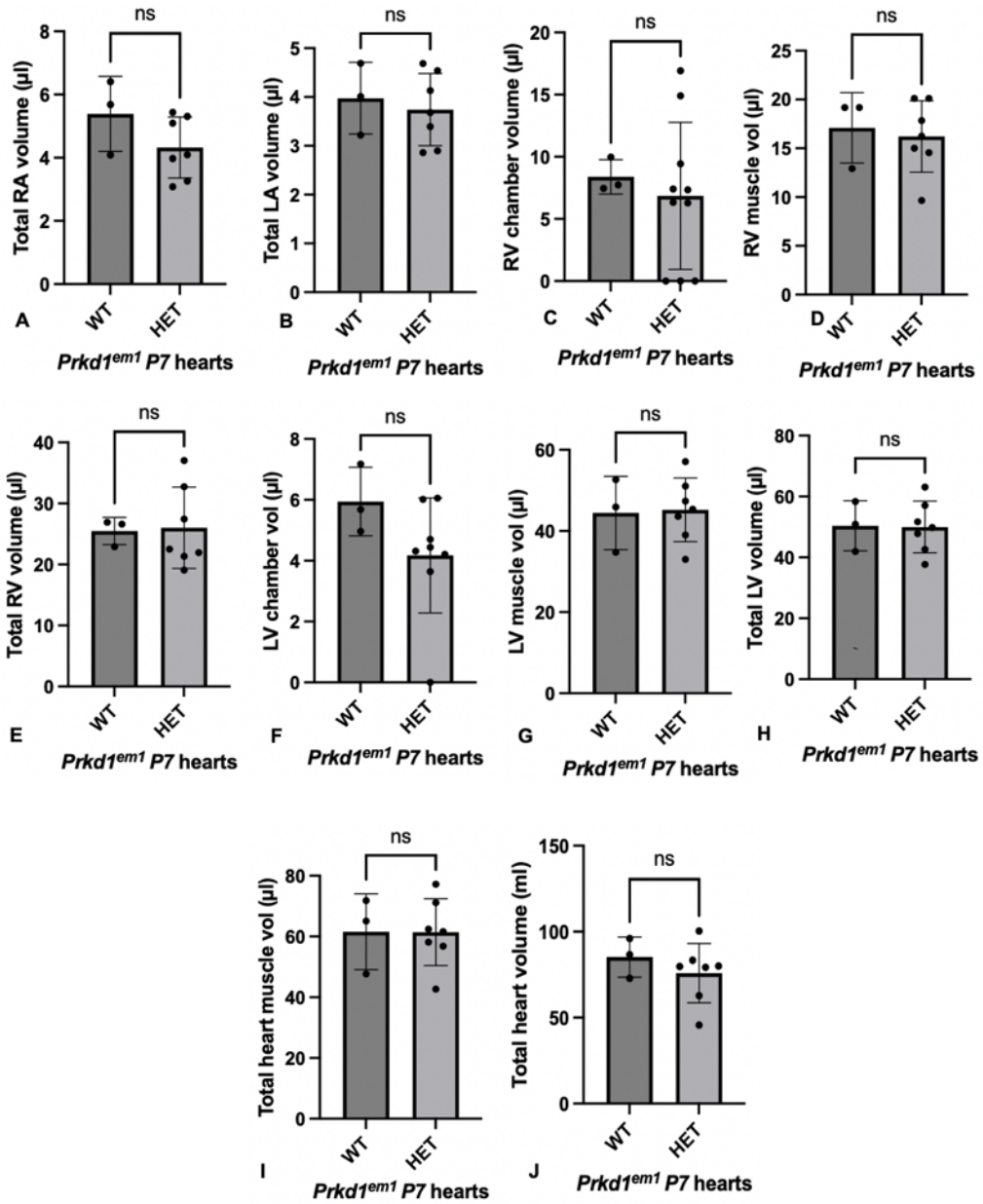


Figure 4:20 Volumetric analysis of Prkd1^{em1} neonatal hearts. Figures showing the findings from the quantitative analysis of Prkd1^{em1} mouse hearts collected at P6/7. There was no statistically significant difference in the heart muscle and chambers' volume as well as the total heart muscle volume in HET (Prkd1$^{em1/+}$) (n = 7) versus WT (Prdk1$^{+/+}$) hearts (n = 3) which means that loss of one allele of Prkd1 generally does not seem to have any significant impact on the heart muscle mass and the volumes of its chambers at this stage of embryonic development.

4.3.5 Expression analysis of *Prkd1, Prkd2* and *Prkd3* in E12.5 hearts by RT-qPCR

Quantification of the transcript of *Prkd1* was carried out by reverse transcriptase- quantitative polymerase chain reaction (RT-qPCR) technique comparing WT (*Prkd1*$^{+/+}$) with HET (*Prkd1*$^{em1/+}$) and HOMO (*Prkd1*$^{em1/em1}$) heart samples collected at E12.5. This stage was selected for tissue collection so as to increase the chances to get more HOMO (*Prkd1*$^{em1/em1}$) samples in order to compare the modulation of *Prkd1* expression in HOMO (*Prkd1*$^{em1/em1}$) and HET (*Prkd1*$^{em1/+}$) hearts with WT (*Prkd1*$^{+/+}$) hearts.

The other PRKDs such as PRKD2 and PRKD3 are structurally homologous to PRKD1[326] and previous studies suggest a potential redundancy between the different PRKD paralogues [362]. In our phenotypic data, some of the features such as hypertrophic changes and or hypertrabeculation (with abnormally rounded heart), were observed in HET (Figure 4:12-B) and HOMO hearts (Figure 4:19 B, D, F compared to A, C and E) despite the earlier research reports that LOF of PRKD1 was cardioprotective with no cardiac hypertrophy in response to pressure overload [318]. On this basis, the apparent hypertrophic response in HOMO heart (Figure 4:19 B, D, F compared to A, C and E) seemed a bit exaggerated. In order to explore if this feature was due to exaggerated activation of the potential redundant role of *Prkd2* and *Prkd3*. Expression of *Prkd2* and *3* was explored at transcript level by qPCR in the same E12.5

mouse heart samples, comparing WT with *Prkd1*$^{em1/+}$ (HET) and *Prkd1*$^{em1/em1}$ (HOMO hearts.

4.3.5.1 Significant reduction of *Prkd1* expression in HOMO (*Prkd1*$^{em1/em1}$) compared to WT (*Prkd1*$^{+/+}$) and HET (*Prkd1*$^{em1/+}$) hearts

In order to determine *Prkd1* expression in E12.5 mouse hearts, RNA was extracted from nine individual E12.5 *Prkd1*^{em1} mouse hearts (i.e., n = 3 WT; n = 3 HET; n = 3 Homo) which was reverse transcribed to cDNA in order to use as a template for the qPCR. The reference genes used for normalisation were *Pgk1* and *Rpl4.*

In order to compare the log_2FC across the three groups, one-way ANOVA was applied on the data which showed that there was a significant difference among the means (P = 0.0395). Multiple comparisons were then performed to find out what those differences were between the groups by performing the post hoc Tukey (multiple comparisons) test ($P \leq 0.05$).

In case of *Prkd1*, using Pfaffl method [363], log_2FC in E12.5 HET heart was -0.003 (P = 0.936 – not significant) whereas in HOMO hearts it was -2.033 (P = 0.013 - significant), compared to WT E12.5 heart (log_2FC=0). The log_2FC in E12.5 HOMO heart compared to HET heart was -2.030 (P = 0.008 - significant) (Table 4:10 and Figure 4:21).

Groups comparison	Mean difference in log_2FC	SE of difference	95% CI of difference	Adjusted p-value
WT vs. HET	-0.002917	0.4415	-1.352 to 1.358	>0.9999 (n.s.)
WT vs. HOMO	-2.033	0.4415	0.6783 to 3.388	0.0088 (sig)
HET vs. HOMO	-2.030	0.4415	0.6753 to 3.385	0.0088 (sig)

Table 4:10 Comparison of Prkd1 expression in Prkd1^{em1}hearts. Multiple comparisons of log_2FC of Prkd1 among the three groups (n = 3 for each group, with three technical repeats) was carried out using Post-hoc (multi-comparisons) Tukey test. There was a statistically significant difference between WT and HOMO (0.0088), and between HET and HOMO (P = 0.0088). However, the difference was not significant between WT and HET heart (P = > 0.9999). The log_2FC in HET and HOMO are compared to log_2FC of "zero" in WT. The reference genes used were Pgk1 and Rpl4. n.s = not significant; sig = significant.

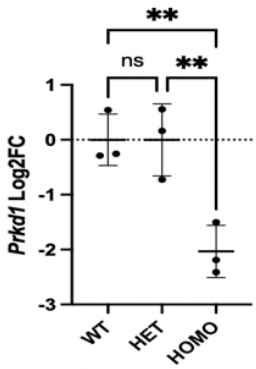


*Figure 4:21 Comparison of Prkd1 expression in Prkd1^{em1}hearts. The log_2FC of Prkd1 in Prkd1$^{em1/+}$ (HET) and Prkd1$^{em1/em1}$ (HOMO) hearts collected at E12.5, compared to WT hearts of the same stage (n = 3 for each group, with three technical repeats). As shown in the scatter plot, using one way-ANOVA and posthoc-Tukey test, statistically significant difference in expression of Prkd1 was noted in HOMO hearts compared to WT (P = 0.0088) as well as Prkd1$^{em1/+}$ (HET) hearts (P = 0.0088). The difference in log_2FC was not significant comparing WT with HET (P > 0.999). ** P < 0.001.*

4.3.5.2 No significant change in expression of *Prkd2* was observed in *Prkd1$^{em1/+}$* (HET) and *Prkd1$^{em1/em1}$* (HOMO) hearts at E12.5

In order to find out if there was any change in the expression of *Prkd2* (a paralogue of *Prkd1*) in the *Prkd1$^{em1/+}$* (HET) and *Prkd1$^{em1/em1}$* (HOMO) hearts collected at E12.5 stage, comparative qPCR was carried out on

the same heart samples as used for the quantification of *Prkd1* transcript. Data obtained from all the three groups (WT, HET and HOMO) were normally distributed as it passed the Shapiro-Wilk normality test (*P* value = 0.3881, 0.0587 and 0.8870 respectively). In order to compare the log_2FC of *Prkd2* across the three groups, one-way ANOVA was applied to the data which showed that there was no significant difference among the means (*P* = 0.3115). Posthoc-Tukey (multiple comparisons) test also showed that the comparisons resulted in no significant difference between WT & HET (*P* = 0.9693), between WT & HOMO (*P* = 0.4317) and between HET & HOMO (*P* = 0.3287) (Figure 4:22, Table 4:11).

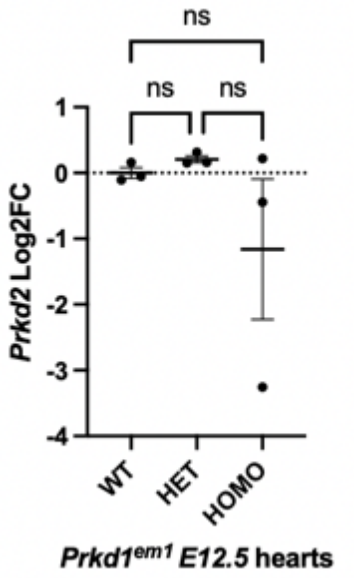


Figure 4:22 Comparison of Prkd2 expression in Prkd1^{em1}hearts. The log_2FC of Prkd2 in Prkd1$^{em1/+}$ (HET) and Prkd1$^{em1/em1}$ (HOMO) hearts collected at E12.5, compared to WT of the same stage (n = 3 for each group, with three technical repeats). As shown in the scatter plot, using one way-ANOVA and posthoc-Tukey test, there was no statistically significant difference in the expression of Prkd2 in Prkd1$^{em1/em1}$ (HOMO) hearts compared to WT (P = 0.4317) as well as HET (P = 0.3287). The difference in log_2FC was also not significant comparing WT with HET (P = 0.9693). n.s: not significant.

Groups comparison	Mean difference in log_2FC	SE of difference	95% CI of difference	Adjusted p-value
WT vs. HET	-0.2081	0.8732	-2.887 to 2.471	0.9693 (n.s.)
WT vs. HOMO	1.160	0.8732	-1.519 to 3.839	0.4317 (n.s.)
HET vs. HOMO	1.368	0.8732	-1.311 to 4.047	0.3287 (n.s.)

Table 4:11 Comparison of Prkd2 expression in Prkd1^{em1}hearts. Multiple comparisons of log_2FC of Prkd2 among the three Prkd1^{em1} groups (n = 3 for each group, with three technical repeats) was carried out using Post-hoc (multi-comparisons) Tukey test. There was no statistically significant difference in the expression of Prkd2 in Prkd1$^{em1/em1}$ (HOMO) hearts compared to WT (P = 0.4317) as well as HET (P = 0.3287). The difference in log_2FC was also not significant comparing WT with HET (P = 0.9693). The log_2FC in HET and HOMO were compared to log_2FC of "zero" in WT. The reference genes used were Pgk1 and Rpl4. n.s = not significant; SE: Standard error; CI: Confidence interval.

4.3.5.3 No significant change in the expression of *Prkd3* was observed in *Prkd1$^{em1/+}$* (HET) and *Prkd1$^{em1/em1}$* (HOMO) hearts at E12.5

In order to find out if there was any change in the expression of *Prkd3* (one of the *Prkd1* paralogues) in the *Prkd1$^{em1/+}$* (HET) (n = 3) and *Prkd1$^{em1/em1}$* (HOMO) hearts (n = 3) compared with WT (n = 3) collected at E12.5 stage, comparative qPCR was carried out on the same heart samples as used for quantification of the *Prkd1* transcript. Data obtained from all the three *Prkd1^{em1}* groups (WT, HET and HOMO) were normally distributed as it passed the Shapiro-Wilk normality test (*P* value = 0.2575, 0.5254 and 0.1416 respectively). The log_2FC of *Prkd3* across the three groups was compared using one-way ANOVA which showed no significant difference among the means (*P* = 0.3445). Posthoc-Tukey (multiple comparisons) test also showed that the comparisons resulted in no significant difference between WT & HET (*P* = 0.9177), between WT &

HOMO (*P* = 0.5252) and between HET & HOMO (*P* = 0.3389) (Figure 4:23, Table 4:12).

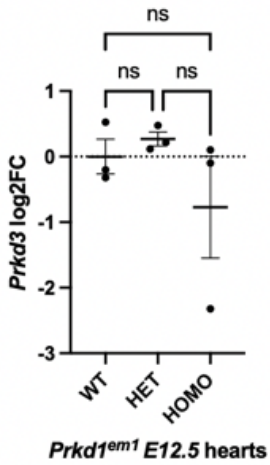


Figure 4:23 Comparison of Prkd3 expression in Prkd1^{em1}hearts. The log$_2$FC of Prkd3 in Prkd1$^{em1/+}$ (HET) and Prkd1$^{em1/em1}$ (HOMO) hearts collected at E12.5, compared to WT of the same stage (n = 3 for each group, with three technical repeats). As shown in the scatter plot, using one way-ANOVA and posthoc-Tukey test, there was no statistically significant difference in the expression of Prkd3 in Prkd1$^{em1/em1}$ (HOMO) hearts compared with WT (P = 0.5252) as well as HET (P = 0.3389). The difference in log$_2$FC was also not significant comparing WT with HET (P = 0.9177). n.s: not significant. The log$_2$FC in HET and HOMO were compared to log$_2$FC of "zero" in WT. The reference genes used were Pgk1 and Rpl4. n.s = not significant; SE: Standard error; CI: Confidence interval.

Groups comparison	Mean difference in log$_2$FC	SE of difference	95% CI of difference	Adjusted p-value
WT vs. HET	-0.2686	0.6755	-2.341 to 1.804	0.9177 (n.s.)
WT vs. HOMO	0.7721	0.6755	-1.300 to 2.845	0.5252 (n.s.)
HET vs. HOMO	1.041	0.6755	-1.032 to 3.113	0.3389 (n.s.)

Table 4:12 Comparison of Prkd3 expression in Prkd1^{em1}hearts. The table shows multiple comparisons of log$_2$FC of Prkd3 among the three Prkd1em1 groups (n = 3 each) as carried out using Post-hoc (multi-comparisons) Tukey test. There was no statistically significant difference in the expression of Prkd3 in Prkd1$^{em1/em1}$ (HOMO) hearts compared to WT (P = 0.5252) as well as HET (P = 0.3389). The difference in log$_2$FC was also not significant comparing WT with HET (P = 0.9177). The log$_2$FC in HET and HOMO were compared to log$_2$FC of "zero" in WT. P-value < 0.05 was considered as statistically significant. The reference genes used were Pgk1 and Rpl4. n.s = not significant; SE: Standard error; CI: Confidence interval.

4.3.6 Significant reduction in PRKD1 protein expression was observed in *Prkd1*$^{em1/em1}$ (HOMO) hearts compared with WT

In order to compare PRKD1 protein expression in the three groups, western blotting was carried out after extracting protein from individual hearts (n = 3 per group). The data obtained from all the three groups (WT, HET and HOMO) was normally distributed as it passed the Shapiro Wilk's normality test (*P* = 0.529, 0.775 and 0.110 respectively). The relative expression of PRKD1 across the three groups was compared, applying one-way ANOVA on the data which showed that there was significant difference among the means (*P* = 0.197). Post hoc-Tukey (multiple comparisons) test showed that statistically significant difference was present between WT & HOMO (*P* = 0.017), however, no significant difference was observed between WT & HET (*P* = 0.117), and between HET & HOMO (*P* = 0.312) (Figure 4:24, Figure 4:25, Table 4:13).

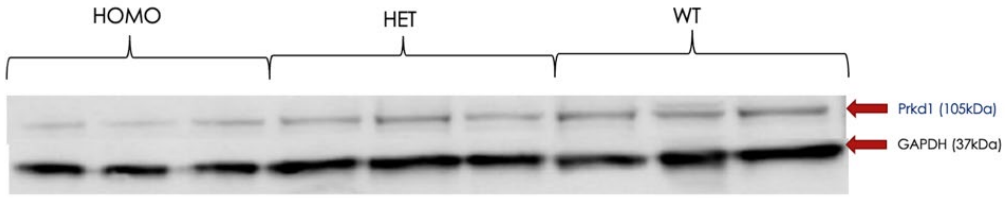


Figure 4:24 Immunoblot of E12.5 Prkd1^{em1}*mouse heart. A: The representative immunoblot (from the three biological and three technical replicates) is showing bands of PRKD1 and GAPDH proteins (used as loading control) in mouse heart samples compared across the three groups (WT, HET and HOMO). Each band in each group represents an individual biological sample, and hence the immunoblot is a single technical replicate. Data not shown for the other two technical replicates. Western blots were cropped for clarity.*

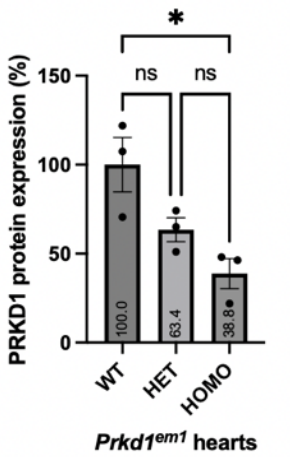


*Figure 4:25 Expression of PRKD1 protein in Prkd1^{em1} hearts. Column bar graph showing mean normalised PRKD1 protein expression in percentage (with standard error bars) from three independent experiments in Prkd1$^{em1/+}$ (HET) and Prkd1$^{em1/em1}$ (HOMO) hearts compared to WT (100%) using GAPDH as the reference protein. There was significant change in the expression of PRKD1 in Prkd1$^{em1/em1}$ (HOMO) hearts (P = 0.017) however the reduction in PRKD1 expression in HET compared to WT (P = 0.117) and HOMO hearts (P = 0.312) was not statistically significant (n = 3 for each group, with three technical repeats). n.s: not significant; * significant P value).*

Groups' comparison	Relative expression (%)		Mean difference (%)	SE of difference	95% CI of difference	P-value
WT vs. HET	WT 100	HET 63.42	36.59	15.30	-10.35 to 83.53	0.1172 (n.s)
WT vs. HOMO	WT 100	HOMO 38.78	61.22	15.30	14.29 to 108.2	0.0167 (sig)
HET vs. HOMO	HET 63.42	HOMO 38.78	24.63	15.30	-22.30 to 71.57	0.3121 (n.s)

Table 4:13 Expression of PRKD1 protein in Prkd1^{em1} hearts. Table showing normalised expression of PRKD1 in Prkd1$^{em1/+}$ (HET) and Prkd1$^{em1/em1}$ (HOMO) hearts, compared with WT (100%) and normalised to GAPDH loading control. There was significant reduction in the expression of PRKD1 in Prkd1$^{em1/em1}$ (HOMO) (P = 0.017) hearts compared to WT, however the reduction in PRKD1 expression in HET hearts compared to WT (P = 0.117) and HOMO (P = 0.312) was not statistically significant. (n = 3 for each group, with three technical repeats). n.s: not significant; sig: significant; SE: Standard error; CI: Confidence interval.

The reduction in PRKD1 protein is ~37% (*P* = 0.1172, not significant) in *Prkd1$^{em1/+}$* (HET) heart and ~61% (*P* = 0.0167, significant) in *Prkd1$^{em1/em1}$*

(HOMO) heart compared to WT. The reduction in *Prkd1*$^{em1/em1}$ (HOMO) heart was ~25% compared to *Prkd1*$^{em1/+}$ (HET) (P = 0.3121, not significant).

4.4 Discussion, conclusions, and perspectives for future work

The broader aim of this part of the project was to elucidate the role of PRKD1 in heart development and CHD. Specifically, it aimed to look for the CHD penetrance, change in PRKD1 expression and embryonic lethality in heterozygous (*Prkd1*$^{em1/+}$) and homozygous (*Prkd1*$^{em1/em1}$) null mouse in comparison to WT.

Survival ratios and lethality

The genotype distribution of the *Prkd1*^{em1} embryos collected at E15.5 shows that homozygous null mutation of *Prkd1 is* embryonically lethal with incomplete penetrance, as reported by others [326, 341]. PRKD1 is involved in cellular proliferation and apoptosis which are key aspects of embryogenesis [322]. The results of preliminary work by Cuello and Hitz (our research collaborators) on induced pluripotent stem cells (iPSC) show that PRKD1 has important role in earlier stages of heart development when there is highest expression in mesodermal tissue including cardiac progenitor cells, along with its expression in epicardial cells, atrial and ventricular myocardial cells at E14.5 but this expression of PRKD1 decreases with growing developmental stage. In our mouse model, the loss of exon 2 encoding protein part involving alanine-proline (AP) region would result in loss of this part of the protein ending up with potentially reduced interaction of PRKD1 with PKCδ [325], thereby compromising its activation to act on downstream targets. In case of homozygous null mutation of *Prkd1,* it is proposed that the role of PRKD1 in

the cellular proliferation and apoptosis [322], vasculogenesis and angiogenesis [364] as well as its role as a kinase to phosphorylate vital factors [304] including cardiac troponin I [365, 366] would have been lost or compromised, resulting in incompatibility with life. However, we have found six *Prkd1*$^{em1/em1}$(homozygous) embryos at E15.5 and one at Postnatal (P) day 7. It is therefore proposed that some residual amounts of PRKD1 in homozygous null mouse (as seen in Figure 4:24, Figure 4:25) are sufficient to permit some survival. Nevertheless, six out of the seven homozygous null mice collected at E15.5 and P7 had CHD, mostly of the complex variety. This contrasts with the heterozygotes, where 2 out of 65 had a CHD (Table 4:6, Table 4:8).

Looking at the **survival of the neonates** from *Prkd1*^{em1} (Prkd1-deletion) mouse line, it was noticed that the overall mortality in HET mice was 12.12%. Near the weaning stage, mortality of *Prkd1*$^{em1/+}$ (HET) mice was only 0.57% compared to no mortality in WT mice. Based on this, it can be suggested that *Prkd1* is quite crucial in embryonic development, more so in cardiogenesis and the significance of PRKD1 in some vital body processes and/or body development decreases in neonatal or adult stages. Earlier study also reported that expression of PRKD1 declines with age [321] which indicates functional significance of PRKD1 decreases after birth and in adult. Nevertheless, PRKD1 has a role in cardiac hypertrophy in response to pressure overload followed by heart failure with reduced contractility [319].

Abnormal external phenotype in embryos

At the time of collection at E12.5 and E15.5, abnormal external phenotype was observed mainly in *Prkd1*$^{em1/em1}$ (HOMO) mice with 12 out of 15 (80%) affected. Most of these (11/15 = 73.3%) were growth retarded (Table 4:4, Figure 4:9 C compared with A,B and F compared with C,D). Abnormal external phenotype was seen in only 4 out of total 155 (2.6%) *Prkd1*$^{em1/+}$ (HET*)* mice. This denotes that deletion of both alleles of *Prkd1* is highly deleterious whereas presence of one normal allele could support normal growth and development in >87% cases.

CHD penetrance in case of heterozygous mutation of PRKD1

At protein level, there was almost ~37% reduction of PRKD1 protein in HET (*Prkd1*$^{em1/+}$) hearts at E12.5 (as seen in Figure 4:24, Figure 4:25) but CHD was seen in one out of total 55 cases. This suggests that the other normal allele is enough to ensure the normal functioning of PRKD1 in the heart development in >98% (n = 54) cases. However, we cannot exclude congenital defects of other systems at this stage as that was not the aim of the current project to determine. Nevertheless, oedema of the back (Figure 4:10B), hemopericardium (Figure 4:11) and occasionally growth retardation (Figure 4:9) were seen in HET (*Prkd1*$^{em1/+}$) mice at E15.5. In HET (*Prkd1*$^{em1/+}$) mouse, the ULD/NTDD region and AP regions of the remaining N-terminal part of the protein would probably still be able to carry out heterodimerization (involving other PRKDs) of NTDD region and thereby heterodimerization and activation of the kinase domain of the PRKD1 which can then act on downstream targets to ensure normal heart development [332]. Another possible explanation for

reduced penetrance in HET was potential functional redundancy by other PRKDs [362]. However, at transcript level, we found no change in the levels of *Prkd2* and *3*. This suggests a unique role for PRKD1 at this stage, as reported by others [367], which is not compensated by PRKD2 and 3. However, to address the issue of samples' variability and limitation of smaller sample size (n = 3 for each group) for this analysis, future work with bigger sample size is worth doing. Due to time constraints, I could not look for protein levels of PRKD2 and PRKD3 to assess any compensation by these at protein level and can be considered for future work.

CHD penetrance in case of homozygous mutation of PRKD1

The loss of both alleles of PRKD1 resulted in CHD in five out of six mice at E15.5 and in the only neonate at P7. This might be explained by the protein structure (Figure 4:1). In case of deletion of both alleles, there wouldn't be any remaining functional PRKD1 protein with regulatory region (including the AP, NTDD and PH parts) as well as the kinetic domain. The absence of the NTDD region (since encoded by exon 2 which is deleted in *Prkd1*$^{em1/em1}$) means there is no chance of even heterodimerization with other PRKDs (PRKD2 & 3) involving NTDD region and obviously no subsequent heterodimerization and thereby activation of the catalytic domain [332]. The also excludes the scope of functional redundancy by PRKD2 & 3 in homozygous mice through this heterodimerisation mechanism. This likely explains the 83.3% penetrance of CHDs and significantly lower Mendelian ratios in homozygous mutant mice at E15.5.

HREM based phenotypic analysis of *Prkd1*^{em1} hearts

BAV is the most common CHD, occurring in at least 2% of the population. Although it may actually never cause symptoms, in more severely affected individuals it is associated with aortic valve stenosis and/or regurgitation, aortic coarctation and a more generic 'aortopathy' for which the understanding of the genesis is still evolving [269, 360]. In such individuals it can require repeated surgeries or lead to heart failure, aortic dissection and sudden death. There is an inherited component to the occurrence of BAV [268]. This is consistent with our findings; of the 72 *Prkd1*^{em1} heterozygous and homozygous hearts analyzed, two had a BAV (Table 4:6, Table 4:7, Table 4:8). There are three main types of BAV, which vary in the morphology of the leaflets and number of sinuses [111]. In our study, one P7 heterozygous heart had a two-sinus type of BAV, with a patent left and right coronary arteries emerging correctly from the left and right aortic sinuses respectively. This type of BAV accounts for 5-7% of cases in humans [111]. The absent leaflet was the non-coronary one. The non-coronary leaflet is derived from the intercalated leaflet swellings (sometimes called intercalated valve cushions); it has been proposed that it is a lack of these structures that results in the two-sinus type of BAV [368]. The other heart with BAV was seen in an E15.5 homozygote; the aortic valve appeared to be of the fused type, with the right and non-coronary leaflets fused, making a trisinuate and bifoliate type of BAV (Figure 4:13, Table 4:7). The fused type of BAV is the most common in humans, accounting for 90-95% of cases [111]. In addition, one homozygous E15.5 heart had a dysplastic pulmonary valve; this could result in pulmonary stenosis (PS) (or incompetence, or both), reported to occur in

8% of individuals with a CHD [107, 369], and as described below is the most common defects in individuals with a *PRKD1* mutation.

Aside from BAV, the next two most common CHDs in humans are VSDs and ASDs [108]. When isolated these are usually at the less severe end of the CHD spectrum, as even if haemodynamically significant they can usually get closed at low risk with a good long-term prognosis [370-372]. Two E15.5 embryos had an isolated VSD, one each of outlet perimembranous and mid-muscular type in a homozygous and a heterozygous *Prkd1*^{em1} heart respectively (Table 4:6 Table 4:7).

In two homozygous E15.5 hearts, an AVSD was seen (Table 4:7, Figure 4:14). AVSD is a CHD known to be associated with abnormality in the development of AV endocardial cushions and DMP [373, 374]. It occurs in approximately 0.05% of live human births; approximately 50% of these are found in individuals with Trisomy 21 [112]. It is also associated with Holt-Oram and Noonan syndromes [375]. Variants of VEGFA and genes in its pathway have previously been associated with the occurrence of AVSD in both syndromic and non-syndromic individuals [376, 377]. PRKD1 has been shown to be a target of VEGFA by mediating VEGF-induced endothelial cell proliferation and migration [378, 379]. Interestingly, both of the mouse hearts with AVSD had outlet extension of the VSD and overriding of the aorta to the extent of producing DORV. DORV is a conotruncal defect and mutations in genes such as *TBX5* (Holt Oram syndrome), *GATA4*, *NKX2-5*, and others have been associated with it [380-382].

In addition, one E15.5 heart had a dysplastic pulmonary valve leaflet (black arrow in Figure 4:13C). This would likely result in pulmonary stenosis (PS) [369] which is reported to occur in >7% of individuals with a CHD [383]. In patients with *PRKD1* mutation, pulmonary stenosis was the most common CHD present in 7 out of 48 cases (Figure 4:5, Table 4:2). Other syndromes associated with PS include Noonan and LEOPARD syndromes [384]. Interestingly, both Noonan and LEOPARD syndromes involve mutations in genes associated with RAS signalling [384]; PRKD1 is also associated with regulating RAS signalling [385]. Intriguingly, many of the congenital heart defects seen in Noonan syndrome, have been seen in the *Prkd1*^{em1} mutant hearts in this study; aside from PS these include AVSD and VSDs [384, 386]. The single P7 HOMO neonate obtained by us had narrower outflow tracts bilaterally, resembling biventricular outlet obstruction which occurs in lethal form of Noonan syndrome in infants [387].

Interestingly, RAS/MAPK regulates MEF2 resulting in hypertrophic cardiomyopathy in RAS-opathies in some individuals [388]. Further, RAS-opathies are associated with specific cancers (benign or malignant) [389]. PRKD1 has been shown to be downregulated in some types of cancers and overexpressed in others, and is associated with many cancer-related signaling pathways [308]. Many of the CHD's and myocardial differences seen in Noonan syndrome and other RAS-opathies were seen in the *Prkd1*^{em1} hearts, including likely PS, AVSDs, VSDs and thickened/hypertrophied myocardium [384, 386].

Therefore, taking together all these factors, we suggest that *Prkd1* may be another gene associated with RAS-opathy type phenotypes [389]. However, although we have seen a dysplastic pulmonary valve in one heart which could lead to PS, a limitation of this study has been our inability to determine the full postnatal penetrance of PS in the *Prkd1*^{em1} hearts. In life, diagnosis of PS is made by 2D-transthoracic echocardiography with Doppler imaging which is the gold standard technique [390]. This was beyond the scope of this study and so confirmation of functional PS was not performed. In addition, optimal resolution was not achievable for all hearts, in particular the homozygous hearts with complex defects, making a detailed analysis of some structures in these hearts more challenging. This might have been due to some blood remaining within the ventricular chamber (possibly related to the increased trabeculation) despite numerous washing steps, which had effectively been cleared in other hearts processed at the same time.

Abnormal external appearance of *Prkd1*$^{em1/em1}$ (HOMO) hearts

Since the external appearance of homozygous hearts (4/6) appeared abnormal and/or large, (Figure 4:16 B & B' compared to A & A'). On quantitative analysis, we found significant increase in total heart volume in homozygotes at E15.5 ($P < 0.05$, Figure 4:17-J). The LV muscle, LV total as well as total heart muscle volumes significantly increased in these hearts contributing to the total increase in heart volume ($P < 0.05$) (Figure 4:17 D,H-I). Muscle mass/volumes might change secondary to the defects i.e., heart having to work harder against increased peripheral resistance to compensate for the different defects [391]. There was one

HOMO (*Prkd1*$^{em1/em1}$) heart at E15.5 which was labelled as normal in terms of CHD. However, conduction defects and others such as coarctation were not analysed. Loss of PRKD1 is associated with arrhythmias and abnormally increased contraction as observed in iPSC by our research collaborators, in preliminary experiments (Cuello and Hitz, personal communication). Nevertheless, according to Bossuyt *et al*, PRKD1 inhibition should prevent arrythmias and hypertrophy in heart failure though it cannot prevent the progression of heart failure itself [392]. Carrying out ECG on embryonic/neonatal hearts in order to diagnose conduction defects/arrhythmias and some others such as coarctation of aorta (of a later stage), would be interesting in any future work.

Looking at the protein-protein interaction of PRKD1 in humans, Figure 4:26 shows the predicted functional partners of PRKD1 and that it has statistically significantly more protein-protein interactions (PPI) than would happen by chance, with *P* - value = 3.18e-05 [240]. Enrichment analysis showed significant enrichment of Gene Ontology (GO) terms related to embryonic developmental processes including heart morphogenesis, neural crest differentiation (related to septum formation in outflow tract), atrial septal defect (ASD), ventricular septal defect (VSD), abnormal cardiac septum morphology, patent foramen ovale, cardiomyopathy, abnormal heart valve morphology and cardiac hypertrophy [240]. There was also significant enrichment of GO terms for biological processes (in both human and mouse) such as regulation of anatomical structure morphogenesis, regulation of vascular system development, regulation of cell signalling, regulation of protein phosphorylation and kinase activity

[240]. These interactions show that PRKD1 participate with various other proteins as part of the complex cellular networks related to development of embryo in general and cardiovascular system in particular. For cardio-vascular system development, the strength of this interaction ranged from 0.52-1.26 (FDR 0.0017 – 0.393), whereas the highest strength of interaction for any process was 2.61 (FDR 1.72E-06) [240].

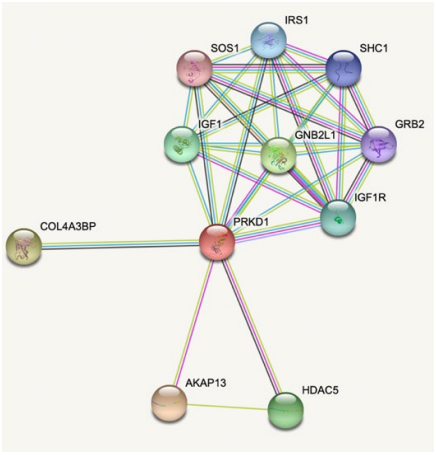


Figure 4:26 The protein-protein interaction of PRKD1 with others using the STRING database. The protein-protein interaction (PPI) of human PRKD1 with other proteins such as HDAC5, IRS1, SHC1, IGF1, IGF1R, GNB2L1, GRB2, COL4A3BP, AKAP13 and SOS1 was of a statistically significant strength (P value = 3.18e-05). The strength of this interaction ranged from 0.52-1.26 (FDR 0.0017 – 0.393), whereas the highest strength of interaction for any process was 2.61 (FDR 1.72E-06). The individual proteins in the network show that they were related to heart development and CHD. Each node in the network represents a protein whereas the coloured edges represent associations among proteins. The turquoise edge shows association determined from curated databases whereas the violet edges denote associations which were experimentally determined. The light green edges are associations determined on text mining whereas the black edges represent associations based on co-expression data. HDAC5: Histone deacetylase5; SHC1: SHC-transforming protein 1; IGF1: Insulin-like growth factor I; IGF1R: Insulin-like growth factor 1 receptor; GNB2L1: Receptor of activated protein C kinase 1; GRB2, Growth factor receptor-bound protein 2; COL4A3BP, Collagen type IV alpha-3-binding protein; AKAP13: A-kinase anchor protein 13; SOS1: Son of sevenless homolog 1. [240].

Conclusions

PRKD1 plays a number of critical roles in the adult heart, as described in Steinberg's recent review [307], such as cardiac remodelling. This study has been pivotal in phenotypically characterising the role of *Prkd1* in embryonic heart development and CHD. The phenotypic characterization of *Prkd1* using HREM, which forms major part of this project, has provided us with encouraging results to support our hypothesis that LOF mutation of *Prkd1* can have adverse effects on heart development, resulting in CHD. This study also demonstrates that other *Prkd1* related genes (*Prkd2* and *Prkd3*) do not compensate for the deletion of *Prkd1*. Even in heterozygotes, cardiac differences occur, albeit at low penetrance, whereas, in homozygous *Prkd1* deleted mice, more complex CHDs occur with high penetrance and myocardial abnormalities are also seen. However, in order to strengthen this notion, further studies aiming to identify the signalling pathways through which PRKD1 exerts its effects on other downstream signalling pathways/key target genes by carrying out transcriptome sequence analysis (RNA-Seq) followed by phosphoproteomics will highly be pertinent as a way forward. Moreover, further research needs to be conducted to determine if *Prkd1* can be truly considered as a gene associated with RAS-opathies or simply bears some similarities. Furthermore, determining the expression profile of PRKD1 in specific cardiac progenitor cells will prove to be very valuable in determining its specific role in cardiac development and CHD at cellular level. Single-cell RNA sequencing (scRNA-Seq) can also be quite useful as a mean to reveal distinct cell populations/lineages and their trajectories related to

heart development and CHD. Moreover, it can unfold the regulatory networks *Prkd1* can have with other genes on the roadmap of heart development. scRNA-Seq will give important clues to cell specific effects of PRKD1 and its mutation and thereby its role in heart development and CHD. These and other experiments to look for the downstream targets will be quite helpful in order to design and execute targeted interventions for therapeutic purposes in CHD.

5 CHARACTERIZATION OF THE ROLE OF *Prkd1* IN HEART DEVELOPMENT AND CHD IN A MOUSE MODEL WITH HUMANISED MUTATION (HM)

5.1 INTRODUCTION

Protein kinase D1 (PRKD1) is a 912 amino acids serine/threonine kinase enzyme which has been implicated in CHD in human patients [176, 348-350]. The mutations in *PRKD1* can occur in both dominant and recessive manner [348].

5.1.1 Rationale for the study

The study which formed basis for this project was the large multicentre WES study of 1891 probands, to which our lab was part of. This study identified that the most common type of de novo missense mutation in *PRKD1* was G592R, identified in two out of the three probands [176]. These mutations manifested as syndromic type of CHD, where in addition to CHD, abnormalities of other systems such as developmental delay and those affecting craniofacial structures, limbs, ectodermal structures and nervous system were noted in two of the three unrelated probands (Figure 4:5) [176]. Later on, more clinical studies about human patients with *PRKD1* mutations also showed that G592R is the most common *PRKD1* mutation [348-350]. This project aimed at characterizing the role of PRKD1 in heart development and CHD in case of

missense/humanised mutation (HM) of *Prkd1*, using the *Prkd1*-mutant mouse model with G598R corresponding to G592R mutation in humans.

5.1.2 The *Prkd1* mouse model with humanised mutation

The *Prkd1* mouse model with point mutation (*Prkd1*$^{em2(IMPC)Wtsi}$) I worked on was novel and replicated the most commonly reported mutation in human patients with CHD [176, 348-350]. This mouse model had point mutation in exon 13 (humanised mutation, HM) corresponding to PK-domain resulting in a protein with G598R substitution (from now on referred to as *Prkd1*^{em2}). It was generated by endonuclease mediated (*em*) mutation at Wellcome Trust Sanger Institute (*Wtsi*) UK and bred at the University of Nottingham.

5.2 HYPOTHESIS AND AIM OF THIS PROJECT

Prkd1 mutation is associated with CHD in humans. We aimed to explore the in vivo role of *Prkd1* in heart development and CHD using mouse model.

5.2.1 Hypotheses for the project:

Hypotheses for this project were:

1. Missense (humanised) mutation in one or both alleles of *Prkd1* would result in CHD with variable penetrance.
2. Missense mutation of *Prkd1* in heterozygous state would be compatible with life, whereas the homozygous missense mutation of *Prkd1* would be embryonically lethal.

5.3 RESULTS

5.3.1 In silico analysis of PRKD1-G592R mutation

In order to predict the possible effect of amino acid substitution (G592R) on the structure and function of the PRKD1, a free web-based application "MutationTaster®" (www.mutationtaster.org) was employed. The program is designed to calculate the probabilities if an amino acid alteration is disease-causing or a harmless polymorphism. According to this, the G592R missense mutation is "disease causing" resulting in splice-site changes and possible effect on protein features (https://www.mutationtaster.org/MT69/MutationTaster69.cgi). Conservation of the amino acid glycine (at position 592 in human) across different species was also analysed using the same program. As shown in Table 5:1-B, it is conserved in PRKD1 orthologues across the different species. The PRKD1-G592R missense mutation involves ATP binding site (589-597aa) in the protein kinase (PK) domain of PRKD1 (583-839aa) [393]. Glycine is a non-polar amino acid with neutral charge whereas arginine is a positively charged polar (hence basic) amino acid. Both have different R groups. Interaction of R groups gives rise to 3D structure of a protein (Figure 5:1). Substitution of amino acids can possibly interfere with 3D structure of a protein. PRKD1 structure was reported recently (https://alphafold.ebi.ac.uk/entry/Q15139) (Figure 5:1). Prediction of pathogenicity was also carried out using other tools (Table 5:1) as part of the PredictSNP® tool which is a combination of six best performing disease-prediction tools [353]. This consensus classifier serves to predict

pathogenicity of SNPs more accurately than individual tools. All the tools, as part of this program, predicted G592R mutation of PRKD1 to be deleterious with expected accuracy ranging from 74-88%. Additionally, a bioinformatics tool/program "*STRUM (Structure-based stability change prediction upon single-point mutation)"* [394] was utilised to determine the effect of this missense mutation on protein stability. According to this program, the difference in Gibbs free energy of a protein between its unfolded and folded states, ΔG, determines its stability. In case of mutation, protein stability is liable to change due to change in the Gibbs free energy in the mutant state. The *STRUM* program computationally determines the difference in Gibbs free energy between the wild type and mutant protein as delta-delta G (DDG). In case of PRKD1-G592 missense mutation, the DDG value calculated by *STRUM* was 1.17 kcal/mol which means that the missense mutation was destabilising.

Based on *in silico* analysis and location of this missense mutation in kinase domain, it is predicted that this mutation will interfere with the catalytic function of PRKD1 as well destabilise the protein structure.

Gene mutation	Type	Domain	Site	DDG (kcal/mol)
PRKD1 - G592R	Missense	PK	ATP binding	1.17
Prediction of pathogenicity of PRKD1-G592R missense mutation				
Tool used	**Prediction**	**Expected accuracy**		
PredictSNP	Deleterious	87%		
MAPP		88%		
PhD-SNP		88%		
PolyPhen-1		74%		
PolyPhen-2		81%		
SIFT		79%		
SNAP		87%		
MutationTaster	Disease causing	-		

A



B

Table 5:1 In silico analysis of PRKD1-G592R point mutation. A) Prediction of pathogenicity of G592R mutation. The different prediction tools suggest that the G592R mutation in PRKD1 is pathogenic. Since it involves ATP binding site in the PK domain of PRKD1, the protein function is predicted to be affected resulting in a disease. B) The site of mutation is conserved across different species as shown in the PRKD1-amino acids alignment (MutationTaster®). Any mutation at this site is expected to result in compromising protein function. DDG was determined using STRUM program [395]. SIFT: Sorting Intolerant From Tolerant; MAPP: Multivariate Analysis of Protein Polymorphism; SNAP: Screening for analysis of Non-acceptable Polymorphism.

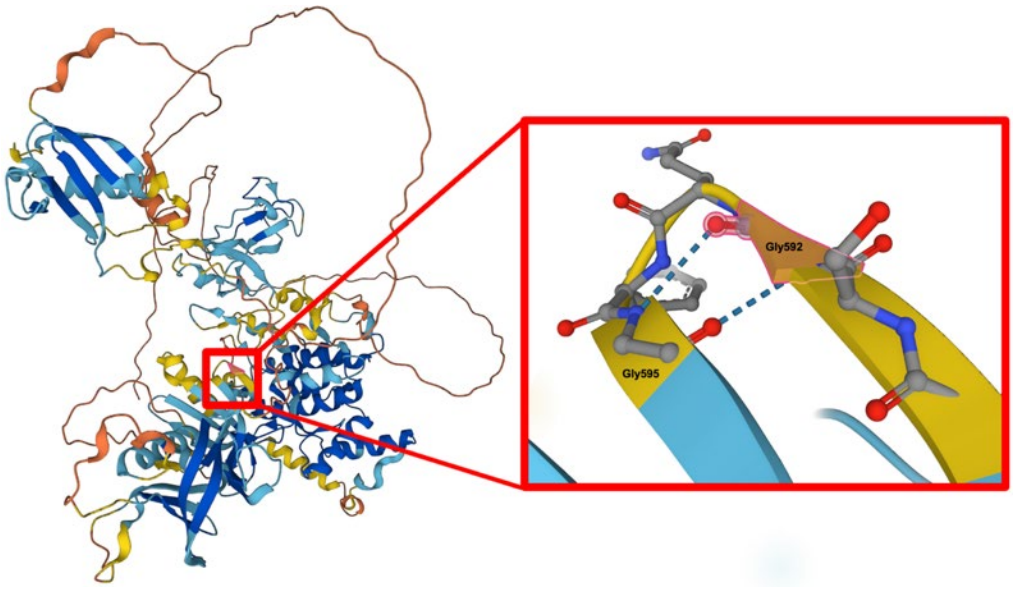


Figure 5:1 The 3D structure of human PRKD1. Interaction between different R groups of the amino acids giving rise to tertiary structure of PRKD1. The zoomed in image (A`) shows hydrogen bonding (shown as dotted lines) between Gly592 and Gly595. The missense mutation at position 592 is predicted to affect the protein structure and hence function. This structure was taken from the AlphaFold system (https://alphafold.ebi.ac.uk/entry/Q15139) which involves artificial intelligence (AI) - based prediction of protein structure.

5.3.2 Mice with heterozygous (*Prkd1*$^{em2/+}$) mutation are viable and fertile, but homozygous mutation (*Prkd1*$^{em2/em2}$) is embryonically lethal

The goal for this project was to set up HET X HET crosses to get homozygous null (*Prkd1*$^{em2/em2}$) embryos in addition to wild type (*Prkd1*$^{+/+}$) and heterozygous (*Prkd1*$^{em2/+}$) embryos. In this mouse line, 581 pups were bred and 250 out of these were genotyped. Genotyping for these mice was done by Sanger sequencing after DNA extraction. Figure 5:2 represents a representative image of a typical result of genotyping of the *Prkd1*^{em2} mouse line in the form of chromatogram.

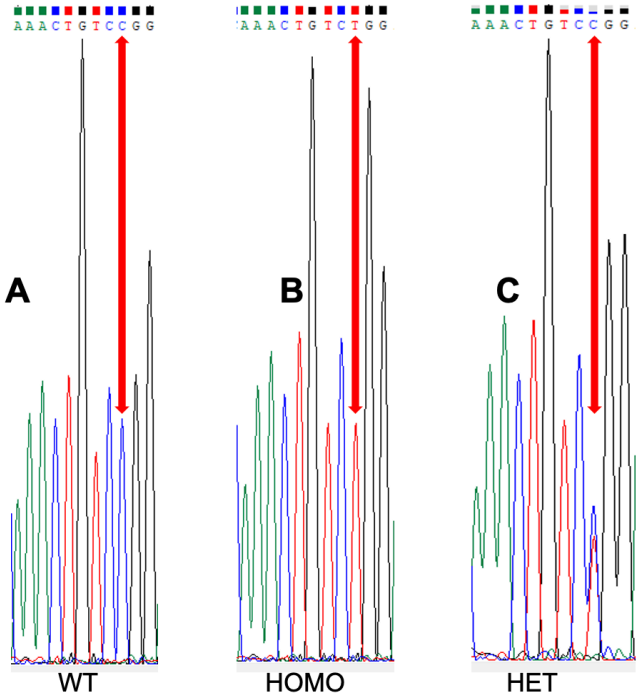


Figure 5:2 Prkd1^{em2} genotyping. Comparison of three chromatograms from Prkd1+/+ (WT) (A), Prkd1$^{em2/em2}$ (HOMO) (B) and Prkd1$^{em2/+}$ (HET) (C) samples. Prkd1^{em2} mouse carries G598R point mutation and genotyping was done by sequence-verification with the screening primers. As shown in top row, in case of homozygous mutation (B), the second 'Cytosine' in the series -TGTCCG in WT (A) is changed to 'Thymine' to have the sequence -TGTCTG in HOMO (B) giving two distinct & specific peaks in both WT and HOMO samples (corresponding to the respective nucleotides), whereas two overlapping peaks in HET sample (C) at the site of missense mutation can be seen. The site of missense mutation and the corresponding peaks are denoted by red arrows in the respective chromatograms from the three samples.

Genotype distribution of the collected embryos at E15.5 for HREM is shown in Table 5:2. A statistically significant difference was present between the observed and expected Mendelian frequencies (Chi square test, *P* = 0.0061). Embryos with homozygous mutation of *Prkd1* (*Prkd1*$^{em2/em2}$) die early during intrauterine life, though those with heterozygous mutation (*Prkd1*$^{em2/+}$) are viable and fertile. However, fifteen viable homozygous mutant (*Prkd1*$^{em2/em2}$) embryos were also collected at

E15.5. Moreover, we obtained 7 live-born *Prkd1*$^{em2/em2}$ (HOMO) mice from HET X HET matings in this line, six of which survived into adulthood an one was culled at P0 (Table 5:3).

***Prkd1*^{em2} (HET X HET)**	**WT**	**HET**	**HOMO**	**Chi-square test**
Expected	42/168 (25%)	84/168 (50%)	42/168 (25%)	P = 0.0016
Observed	47/168 (28%)	99/168 (58.9%)	22/168 (13.1%)	

Table 5:2 Genotype distribution of Prkd1^{em2} *embryos from HET X HET crosses, collected at E15.5. The observed ratios of embryos with homozygous mutation are significantly less than the expected (Mendelian) ratios which means that point mutation - G598R of Prkd1 (G592R in human) in homozygous state is incompatible with life.*

Live-born *Prkd1*$^{em2/em2}$ (HOMO) pups			
#	**ID**	**Gender**	**Comment**
a.	227376	Female	Pregnant twice but lost litter
b.	229279	Male	Mated to HET female but no pregnancy
c.	204289	Female	Never got pregnant
d.	203022	Female	Never got pregnant and culled due to ill health
e.	200978	Female	Never got pregnant
f.	236779	Female	Did get pregnant and litter collected
g.	P2.24.5	-	Collected at P0

Table 5:3 Prkd1$^{em2/em2}$ *live-born pups from HET X HET crosses. Prkd1*$^{em2/em2}$ *mostly die in utero but seven live-born pups including one neonate at P0 were obtained from this mouse line. One of them (#227376) got pregnant twice but cannibalised its litter on both occasions.*

Necrotic/resorbed embryos' (Figure 5:3) material was also collected at E15.5 for genotyping. These constituted 11.11% (n = 11) of total 99 HETs

and 13.64% (n = 3) of total 22 HOMOs. In case of WT, only one out of 47 embryos (2.13%) collected was found necrotic.

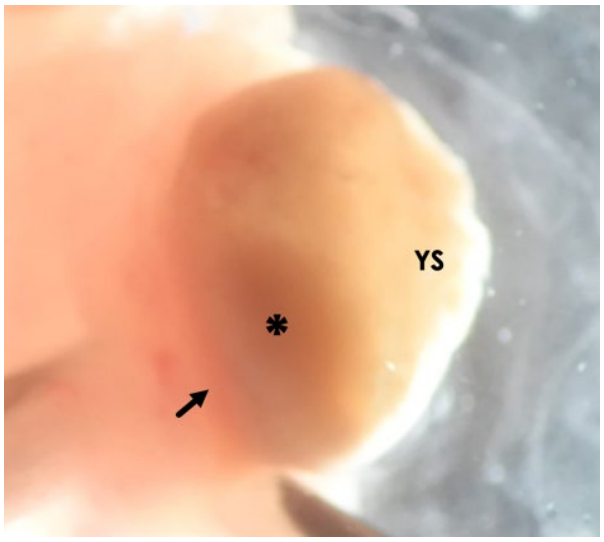


Figure 5:3 Resorbed embryo. The image shows the resorbed embryo still within the yolk sac and undergoing necrosis, visible as brownish necrotic material (*) through the yolk sac. Arrow is pointing at placenta. YS: yolk sac.

5.3.3 Pups' survival ratios at pre-weaning (pre-genotyping) and post weaning stages

In order to look for the effect of HM of PRKD1 on the survival of the liveborn neonates/pups and/or adults, the data were obtained from the *LabTracks* (lab animal data management software) of the animal facility at the University of Nottingham. Looking at the survival ratios of the neonates from *Prkd1*^{em2} mouse line, it was noticed that the overall mortality in this mouse line in the pre-weaning period was higher (22.89%) in comparison to the *Prkd1*^{em1} mouse line (12.12%). After genotyping at or near the weaning stage, mortality of *Prkd1*$^{em2/+}$ (HET) mice was nil as in WT.

Genotyping-based association and hence systematic analysis (involving applying statistics) was not possible. This data was a snapshot and did not involve systematic following due to limitation of the LabTracks program of the BioSupport Unit (BSU).

5.3.4 External phenotyping of E15.5 embryos collected from *Prkd1*^{em2} mouse line

External phenotyping of E15.5 embryos (n = 105, 99 HETs, 22 HOMOs) was carried out at the time of tissue collection (Table 5:4). This phenotyping was carried out before genotyping.

ID	Geno-type	Gross Phenotype	Cardiac phenotype
P2.5.5	HET	Retarded/dead - delicate heart	NA
P2.9.1	HOMO	Oedema of the back (cranio-spinal region)	Inlet & outlet VSD with DORV
P2.11.1	HET	Oedema of the back (cranio-spinal region)	Musc. VSD
P2.11.2	HOMO	Oedema of the back (cranio-spinal region)	Outlet VSD with DORV
P2.12.8	HOMO	Retarded/dead - delicate heart	NA
P2.13.8	WT	Oedema of the back (cranio-spinal region)	N
P2.14.10	HET	Oedema of the back (cranio-spinal region); embryo size seemed smaller, but rest looked normal	N
P2.15.5	HOMO	Oedema of the back (cranio-spinal region); embryo size seemed smaller, but rest looked normal	Outlet VSD with DORV & infundib-ular PS
P2.41.8	HET	Exencephaly, brain hyper-trophy and unilateral anoph-thalmia; alive at collection	-
P2.47.6	HOMO	Oedema of the back (cranio-spinal region)	-
P2.47.7	WT	Oedema of the back (cranio-spinal region)	-
P2.50.5	HET	Retarded/dead	-
P2.54.4	HOMO	Retarded/dead	-
P2.54.5	WT	Retarded/dead – quite early on as was disintegrating while collecting	-
P2.55.3	HET	Oedema of the back	
P2.55.4	WT	Oedema of the back	
P2.56.5	WT	Oedema of the back (cranio-spinal region)	-

Table 5:4 Abnormal external phenotypes of Prkd1^{em2} embryos at E15.5. The abnormal external phenotypes as shown in the table were noted at the time of Prkd1^{em2} embryos collection at E15.5, whereas the cardiac phenotype was determined by HREM. N: normal, NA: non-analysable, "-" : samples used in other experiments, DORV: double outlet right ventricle; PS: pulmonary stenosis; Musc.: muscular; VSD: ventricular septal defect.

Oedema at the back was noted in 3 *Prkd1*$^{em2/+}$ (HET) and 4 *Prkd1*$^{em2/em2}$ (HOMO) mice (black asterisk in Figure 5:4-B). In terms of genotype distribution, HET and WT were very similar in terms of oedema at the back with 3 out of 99 *Prkd1*$^{em2/+}$ (HET) and 4 out of 105 WT embryos affected.

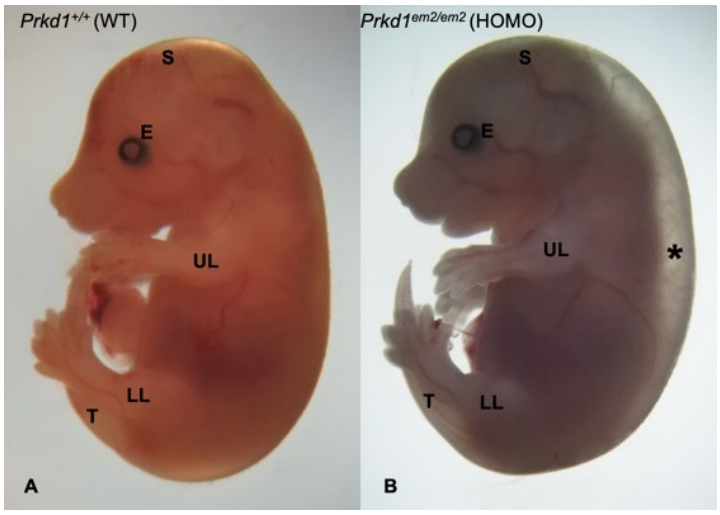
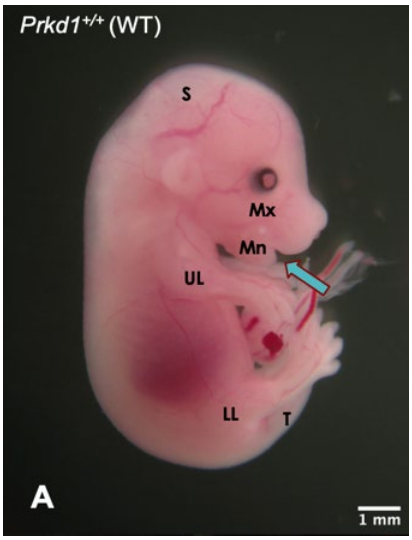


Figure 5:4 Oedema at the back. Comparison of Prkd1$^{+/+}$ *(WT) and Prkd1*$^{em2/em2}$ *(HOMO) embryos collected at E15.5. There is fluid accumulation at the back (*) in HOMO embryo extending from the region above the occiput to lower back. S: skull, E: eye, UL: upper limb, LL: lower limb, T: tail.*

In one *Prkd1*$^{em2/+}$ (HET) embryo, exencephaly along with hypertrophy of the brain were noted when the brain was not covered by cranial vault (Figure 5:5 B-C compared with A). Facial skeleton was maldeveloped, with absent orbits. Primitive and maldeveloped maxillae (Mx) and mandible (Mn) were also present (Figure 5:5 B-C compared with A). In addition, there was oedema of the back in this embryo (white asterisk in Figure 5:5 B-C). However, the embryo was alive at the time of collection, with heart beating and blood coming off the umbilical vessels (after resecting umbilical cord) with each heartbeat (Figure 5:5 B).



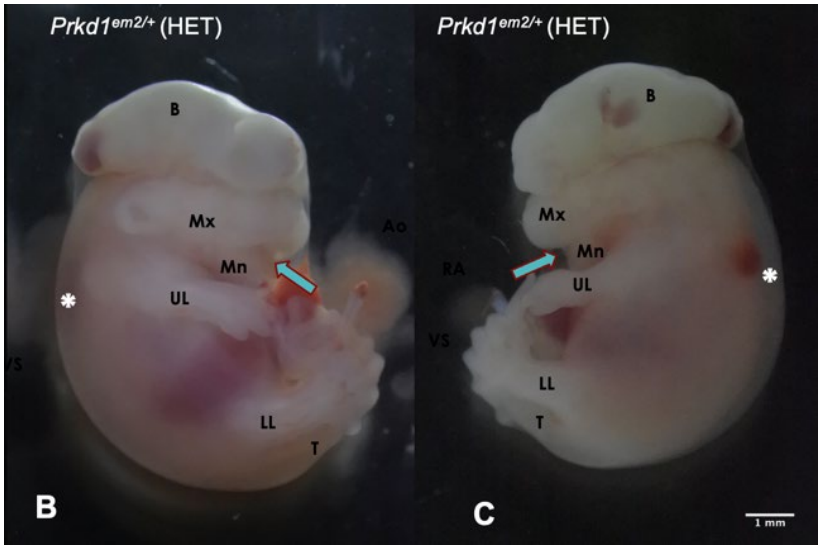


Figure 5:5 Exencephaly, brain hypertrophy, anophthalmia and oedema at the back in Prkd1$^{em2/+}$ (HET) embryo collected at E15.5. (A) WT embryo with (primitive) skull covering the brain. (B-C) Images from right and left handsides, respectively, of a Prkd1$^{em2/+}$ (HET) embryo with the brain present without cranial vault. Frontal bones including orbits are also not developed, along with absence of both eyes (anophthalmia). However, maxillary (Mx) and mandibular (Mn) processes are present. Oedema of the back (white asterisk in B-C) can be seen as well. Arrow is pointing at the oral orifice. S: skull, B: brain, Mx: maxilla, Mn: mandible, UL: upper limb, LL: lower limb, T: tail.

At the time of collection at E15.5, 3 *Prkd1$^{em2/+}$* (HET) and 3 *Prkd1$^{em2/em2}$*

(HOMO) embryos were growth retarded and/or dead (Table 5:4, Figure

5:6). One WT embryo was also retarded and dead with its tissues necrotic.

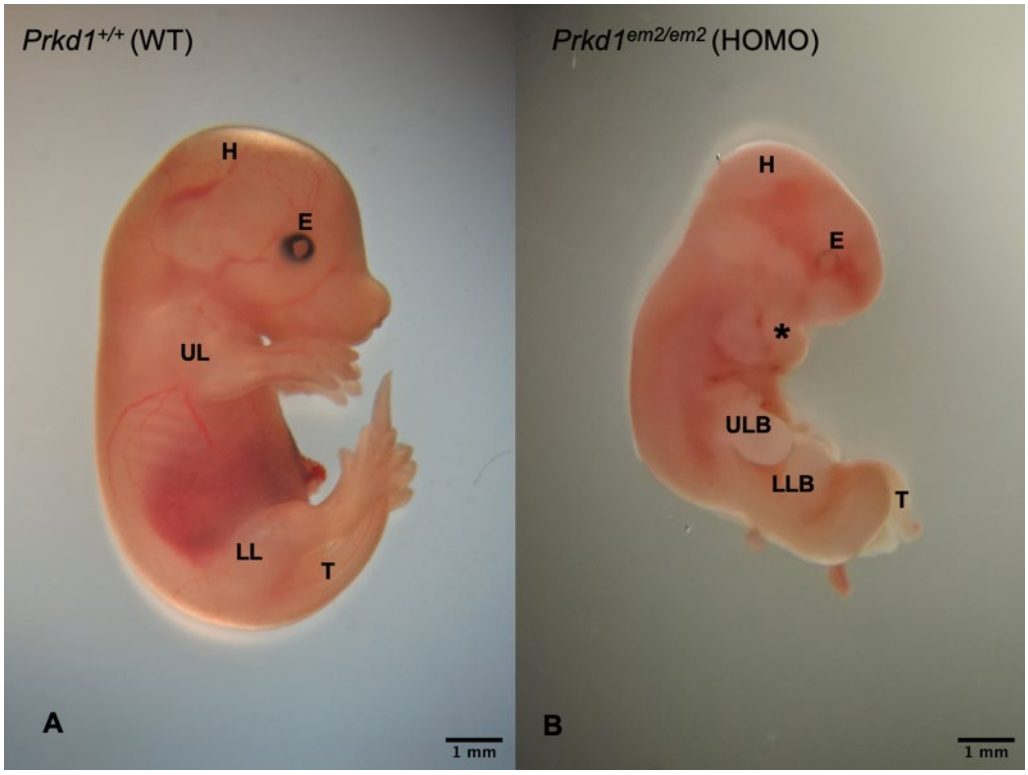


Figure 5:6 Intrauterine growth retardation. Representative images of WT (A) and Prkd1$^{em2/em2}$ (HOMO) embryo (B) collected at E15.5. The Prkd1$^{em2/em2}$ (HOMO) embryo was retarded and probably died quite early. UL: upper limb; ULB: upper limb bud; LL: lower limb; LLB: lower limb bud; T: tail; H: head; Asterisk (*) denotes heart without covering of thoracic cage.

5.3.5 HREM-based phenotypic analysis of E15.5 hearts collected from *Prkd1^{em2}* mouse line

5.3.5.1 The penetrance of CHD was quite high in case of heterozygous (*Prkd1$^{em2/+}$*) humanised mutation in *Prkd1^{em2}* mouse

E15.5 hearts from *Prkd1^{em2}* mice were analysed after generating their 3D models from the z-stack of high resolution 2D images. The analysis of HREM hearts was done while being blind to the genotype. By using

HREM, both external and internal aspects of each heart were analysed in different planes. All chambers including the valves were analysed to exclude any morphological abnormality such as an abnormal communication between the different chambers or any pathology related to the valves structure. Interatrial (IA) communication as open-foramen-ovale was expected to be present as normal finding in all embryos at E15.5 unless there was partial or complete deficiency of the septum primum and/or secundum.

The *Prkd1*^{em2} mouse hearts collected at E15.5 and analysed by HREM are detailed in Table 5:5.

Genotype	WT	HET	HOMO	Total
***Prkd1*^{em2} (HM)**				
Number (n)	74	64	15	153

Table 5:5 Prkd1^{em2} hearts collected at embryonic stage E15.5 and analysed by HREM. In case of Prkd1^{em2}, HET (n = 64) and Homo (n = 15) hearts were analysed. HETs and HOMOs were compared with WT (n = 74) hearts from mice bred on the same (C57BL/6N) background.

The penetrance of CHD in case of missense mutation in one allele of *Prkd1* (*Prkd1*$^{em2/+}$) was 17.19% (11/64) (Table 5:6) which was high, compared to the heterozygous (*Prkd1*$^{em1/+}$) mutation (1/55, 1.82%) in *Prkd1*-deletion mouse model (Chapter 4, section 4.3.3.1).

Prkd1$^{em2/+}$ hearts with phenotype			
No.	**Sample ID**	**Phenotype**	**Penetrance**
1.	SID8083_A	Musc. VSD	11/64 (17.19%)
2.	NID0030_A	Musc. VSD with PS (infundibular & annular)	
3.	NID0031_B	pMem. (outlet) VSD with OA & PS (infundibular & annular)	
4.	NID0087_A	pMem. VSD (outlet) with PS (annular)	
5.	NID0087_B	pMem. (outlet) VSD	
6.	NID0138_B	Musc. VSD	
7.	NID0138_C	pMem. (outlet) VSD with OA	
8.	NID0148_A	Musc. & pMem. (outlet) VSD and DORV	
9.	NID0148_B	Musc. & pMem.VSD (outlet) VSD	
10.	NID0150_B	pMem. (outlet) VSD with PS (annular)	
11.	NID0151_A	pMem. (outlet) VSD with OA with PS (infundibular)	

Table 5:6 Phenotypes of the E15.5 mouse hearts with heterozygous (Prkd1em2/+) mutation. Phenotypic analysis of hearts from mice with humanised (missense) mutation in one of the alleles of Prkd1 (Prkd1em2/+) showed very high penetrance of CHDs, with pMem. type of VSD being the most common type of CHD along with other defects such as muscular VSD, OA, DORV and PS observed in the same or different hearts. However, ~83% hearts with heterozygous missense mutation did not show any CHD. pMem, perimembranous; Musc, muscular; DORV: double-outlet right ventricle; PS: pulmonary stenosis; OA: overriding aorta.

5.3.5.2 VSD was the most common phenotype in *Prkd1$^{em2/+}$* (HET) hearts at E15.5

CHD was noted in 11 out of 64 *Prkd1$^{em2/+}$* (HET) hearts and VSD was present in all of them. In 8 out of the 11 HET hearts with CHD, the VSD was of perimembranous type, present as isolated defect (1/11) or in combination with muscular VSD (2/11), PS (2/11), OA (1/11) (Figure 5:7 B) or OA and PS (2/11).

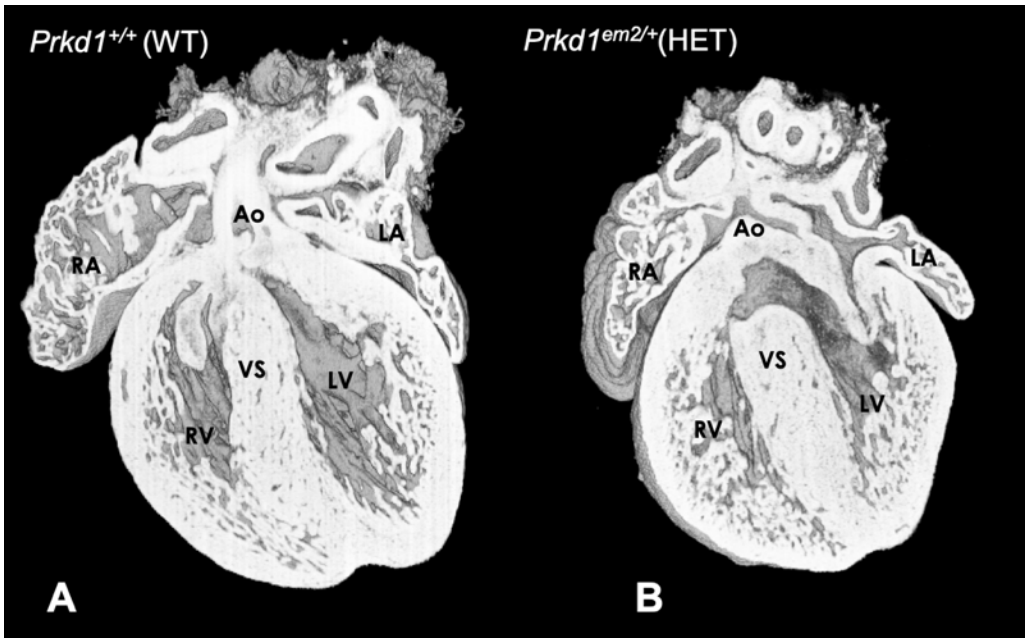


Figure 5:7 Perimembranous VSD with OA. (A) Coronal section of E15.5 WT mouse heart showing the left and right ventricular chambers separated from each other by VS and aorta originating from LV. (B) Anterior view of a Prkd1$^{em2/+}$ (HET) mouse heart collected at E15.5 showing membranous VSD and overriding aorta. Aorta is receiving blood from both ventricles. RA: right atrium, RV: right ventricle, LA: left atrium, LV: left ventricle, VS: interventricular septum, Ao: aorta.

Out of the two cases in which perimembranous VSD (denoted by black arrow in Figure 5:8-B) was noted in conjunction with muscular VSD (denoted by yellow arrow in Figure 5:8-D,d), DORV was observed in one of them when >50% of diameter of the annulus of aortic valve was connecting to the morphologic RV instead of LV (based on the orange line extending from ventricular septum in Figure 5:8-B compared with A).

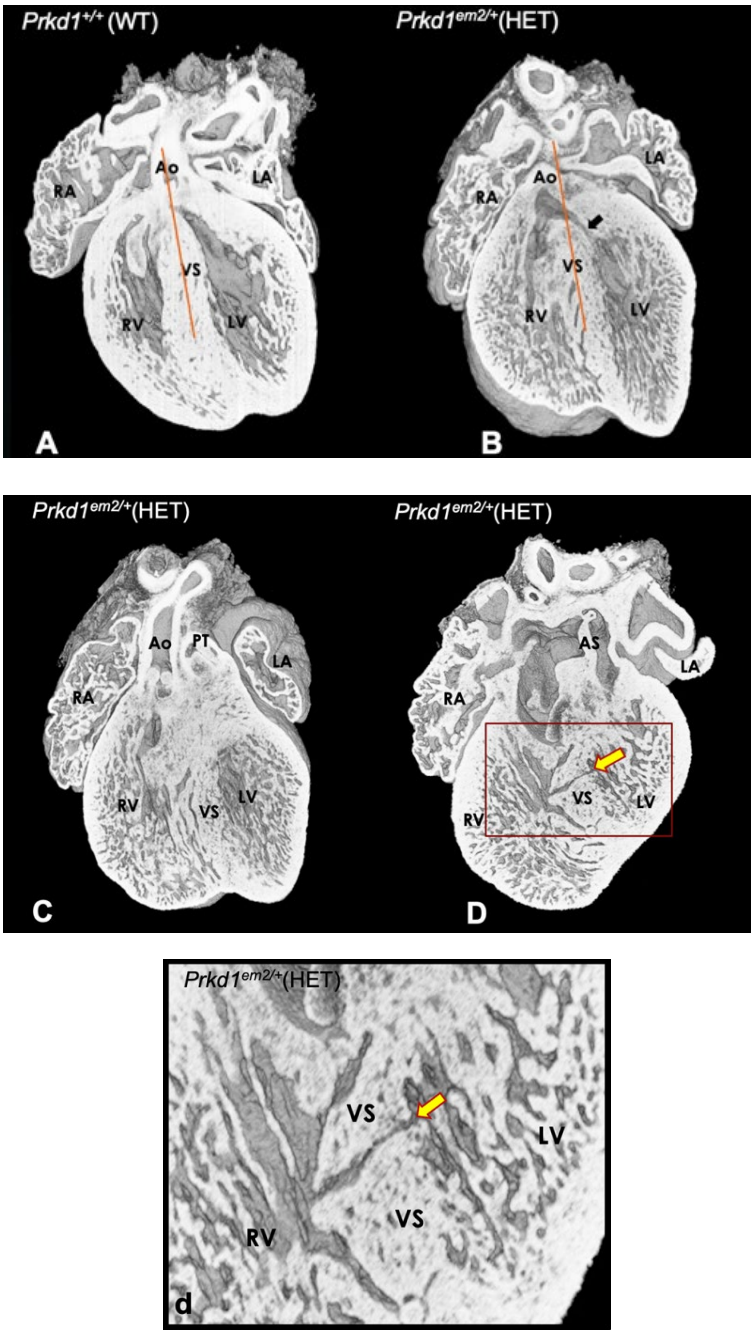


Figure 5:8. Perimembranous VSD with DORV and muscular VSD. (A) A coronal section of E15.5 WT mouse heart showing the left and right ventricular chambers separated from each other by VS and aorta originating from LV. (B) Coronal section of a Prkd1$^{em2/+}$ (HET) mouse heart collected at E15.5 showing pMem. VSD (denoted by black arrow) and >50% of diameter of annulus of aortic valve connecting to morphologic RV instead of LV (based on the line extending from VS). (C) More anterolateral view of the heart in (B) showing Ao originating predominantly from RV. Ao is lodged parallel to PT (PV leaflets visible). (D, d) Images of anterolateral view of the hearts in (B) and (C) taken at a much deeper plane showing Musc. VSD (yellow arrow). "d" is the boxed area in "D". RA: right atrium, RV: right ventricle, LA: left atrium, LV: left ventricle, VS: interventricular septum, Ao: aorta, PT: pulmonary trunk.

Out of the eleven *Prkd1*$^{em2/+}$ (HET) hearts, two were having an isolated muscular VSD (yellow arrow in Figure 5:9-B) whereas one was associated with PS. CHD was not seen in WT (control) hearts collected at E15.5.

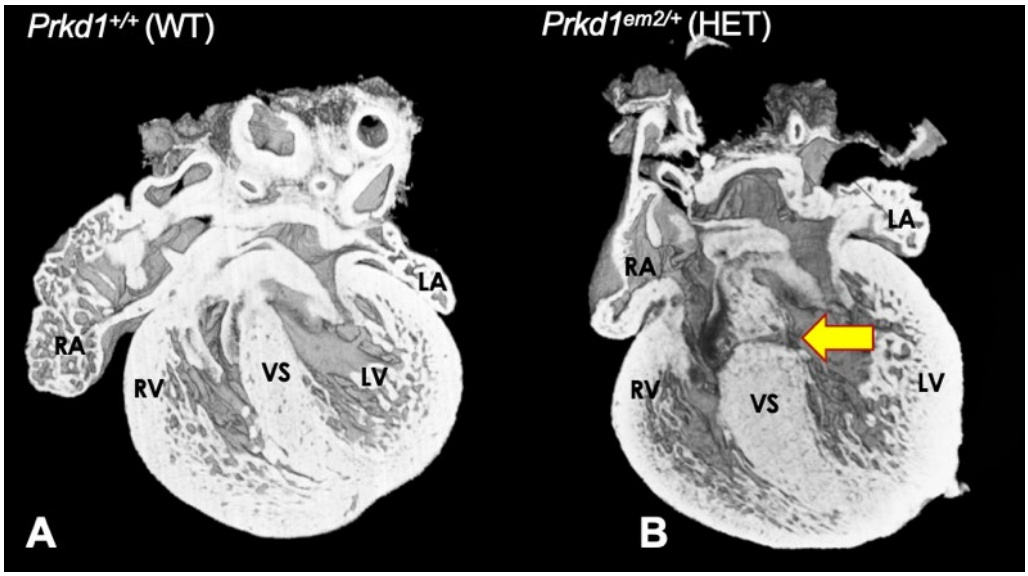


Figure 5:9 Muscular VSD as an isolated defect. (A) Coronal section of E15.5 WT mouse heart showing the left and right ventricular chambers separated from each other by VS. (B) Anterior view of a Prkd1em2/+ (HET) mouse heart collected at E15.5 showing interventricular communication in the muscular part of VS (arrow). RA: right atrium, RV: right ventricle, LA: left atrium, LV: left ventricle, VS: interventricular septum.

5.3.5.3 The penetrance of CHD at E15.5 was higher in case of homozygous (*Prkd1*$^{em2/em2}$) humanised mutation compared with heterozygous (*Prkd1*$^{em2/+}$) mutation

In case of homozygous missense mutation of *Prkd1* (*Prkd1*$^{em2/em2}$), CHD penetrance was 66.6% (10/15). There were 5 out of 10 hearts with homozygous mutation which did not have any CHD based on this initial analysis (Table 5:7). However, quantitative analysis (Figure 5:17 A-J) was carried out to explore other potential effects of these mutations on heart size/volume.

Prkd1$^{em2/em2}$ hearts with phenotype			
#	**Sample ID**	**Phenotype**	**Penetrance**
1.	NID088_A	pMem. VSD (outlet) with OA	10/15 (66.67%)
2.	NID097_A	Inlet VSD (unfused EC) & outlet pMem. VSD with DORV	
3.	NID0120_A	pMem. (outlet) VSD	
4.	NID0120_B	pMem. (outlet) VSD with DORV	
5.	NID0121_B	pMem. (outlet) VSD with DORV with infundibular PS	
6.	NID0123_A	pMem. (outlet) VSD with OA & small Musc. VSD	
7.	NID0123_B	pMem. (outlet) VSD	
8.	NID0129_B	pMem. (outlet) VSD with OA	
9.	NID0130_A	pMem. (outlet) VSD with OA	
10.	NID0130_B	Musc. VSD	

Table 5:7 Phenotypic analysis of hearts from mice with humanised (missense/point) mutation in both alleles of Prkd1 (Prkd1em2/em2). There was ~4 times higher penetrance of CHDs in case of homozygous G598R mutation in comparison to heterozygous (Prkd1em2/+) mutation. pMem. VSD was the most common type of CHD along with other defects such as Musc. VSD, OA, and DORV observed in the same or different hearts. VSD: ventricular septal defect; pMem: Perimembranous; Musc: muscular; DORV: double-outlet right ventricle; BAV: bicuspid aortic valve.

5.3.5.4 Perimembranous VSD was the most common of the phenotypes observed in case of homozygous (*Prkd1$^{em2/em2}$*) humanised mutation at E15.5

As in HET *(Prkd1$^{em2/+}$*) hearts, pMem. VSD was the most common type of CHD, observed in 90% of these mice with HOMO *(Prkd1$^{em2/em2}$*) mutation (Table 5:7), found either singly (n = 2) or in combination with DORV (n = 3) (Figure 5:10), muscular VSD (n = 1) (Figure 5:11), or OA (n = 4) (Figure 5:12). Muscular VSD as an isolated anomaly was noted in one of the 10 HOMO cases with CHD. Out of the three cases with DORV, PS was noted in one of them. So, the prominent CHD observed in case of homozygous *(Prkd1$^{em2/em2}$)* humanised mutation is perimembranous VSD, either as an isolated anomaly or accompanied by other types of

CHD. When the CHD is of complex type, it is hard to understand the primary and the secondary heart defects.

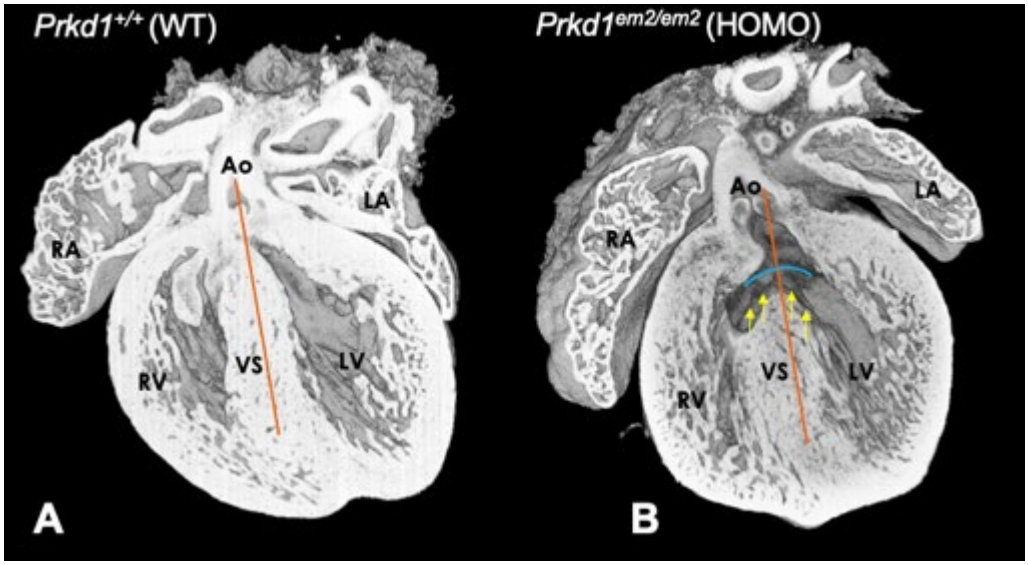


Figure 5:10 Perimembranous VSD with DORV. (A) Coronal section of E15.5 WT mouse heart showing the left and right ventricular chambers separated from each other by VS. (B) Prkd1$^{em2/em2}$ (HOMO) mouse heart collected at E15.5 showing inlet pMem. VSD (pointed by yellow arrows), outlet VSD (blue curved line) and DORV in a coronal section. >50% of diameter of annulus of aortic valve connecting to morphologic RV instead of LV (based on the orange line extending from VS). (PT is not shown here due to the image taken in a (deeper) plane more appropriate to show the DORV). RA: right atrium, RV: right ventricle, LA: left atrium, LV: left ventricle, VS: interventricular septum, Ao: aorta.

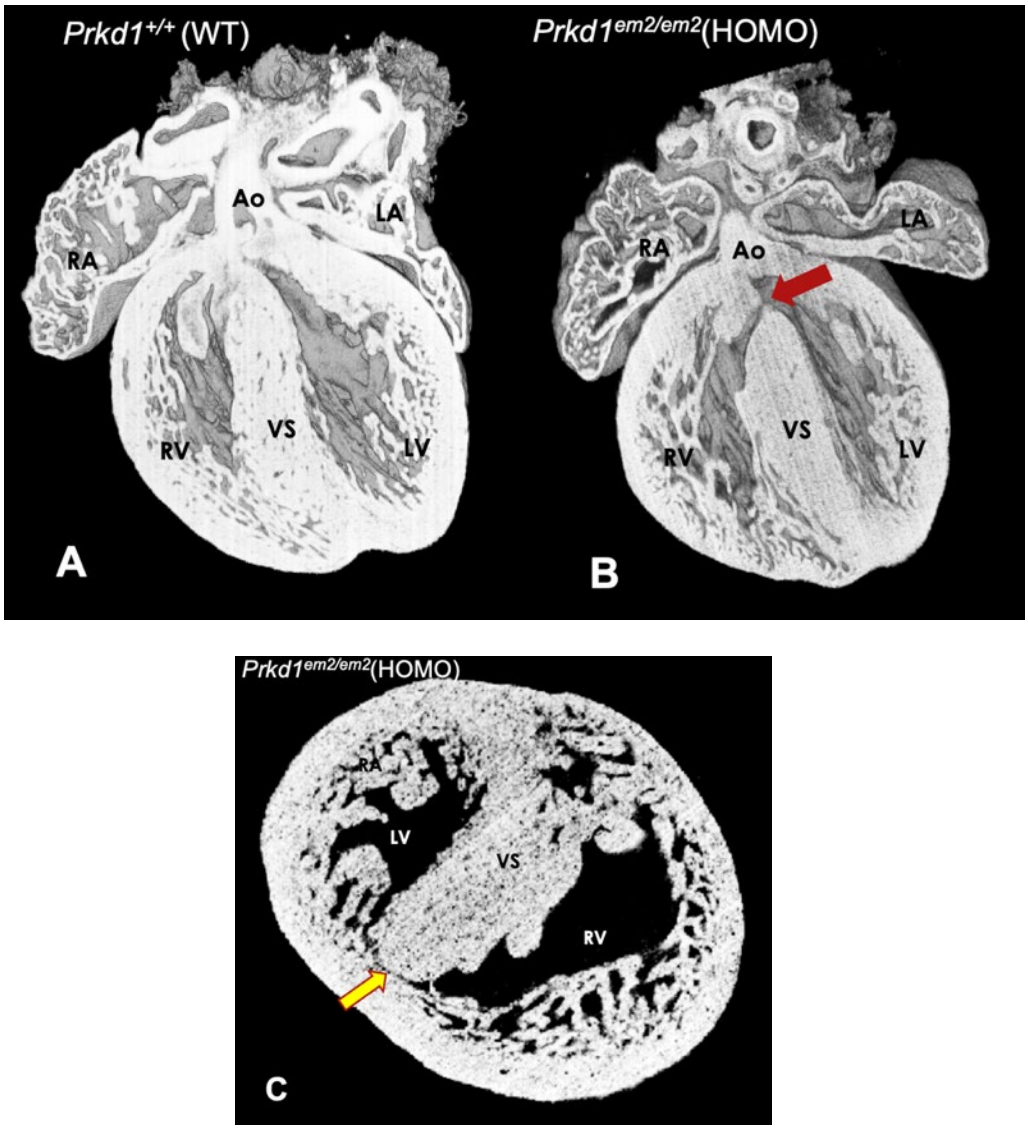


Figure 5:11 Perimembranous and muscular VSD. (A) Coronal section of E15.5 WT mouse heart showing the left and right ventricular chambers separated from each other by VS. (B) Anterior view of a Prkd1em2/+ (HOMO) mouse heart collected at E15.5 showing pMem (outlet) VSD (red arrow). (C) Transverse section through the upper part of heart 'B' showing a tiny VSD in the muscular part of the ventricular septum (yellow arrow). This narrow opening was only discernible in 2D image as shown. RA: right atrium, RV: right ventricle, LA: left atrium, LV: left ventricle, VS: ventricular septum, Ao: aorta.

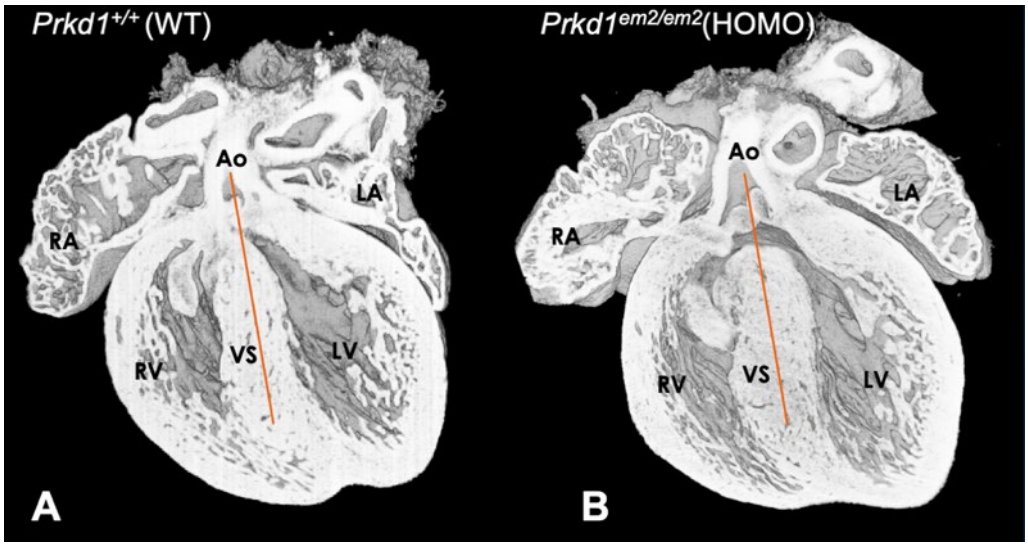


Figure 5:12 Perimembranous VSD with OA. (A) Coronal section of E15.5 WT mouse heart showing the left and right ventricular chambers separated by VS. (B) Anterior view of a Prkd1em2/em2 (HOMO) mouse heart collected at E15.5 showing pMem. (outlet) VSD with OA. The aorta seems to receive 50% blood from each ventricle as there is a biventricular attachment of the aortic valve. The orange line extending from VS is passing through the root of aorta as a straight line. RA: right atrium, RV: right ventricle, LA: left atrium, LV: left ventricle, VS: interventricular septum, Ao: aorta.

5.3.6 Morphological changes in sub valvular apparatus of right (tricuspid) and left (mitral) atrioventricular valves in hearts from mice with HM mutation of PRKD1 (*Prkd1^{em2}*)

In case of both *Prkd1$^{em2/+}$* (HET) and *Prkd1$^{em2/em2}$* (HOMO) hearts, most (7/11 & 7/10 respectively) had thickening or dysplasia of papillary muscles **(**Figure 5:13 & Figure 5:14).

Papillary muscles related to tricuspid valve:

The papillary muscles in WT were attached at one end directly to the leaflets of tricuspid valve (red and black asterisk in Figure 5:13) without intervening chordae tendineae and at the other end to the ventricular wall through trabeculae carneae (black arrows in Figure 5:13). However, in

mutant hearts, (as on visual/qualitative analysis), the papillary muscles (anterior and inferior) were thicker (denoted by redline for anterior and blue arrow for inferior, in Figure 5:13, B-C compared with A) and extending from the TV to ventricular septum (VS).

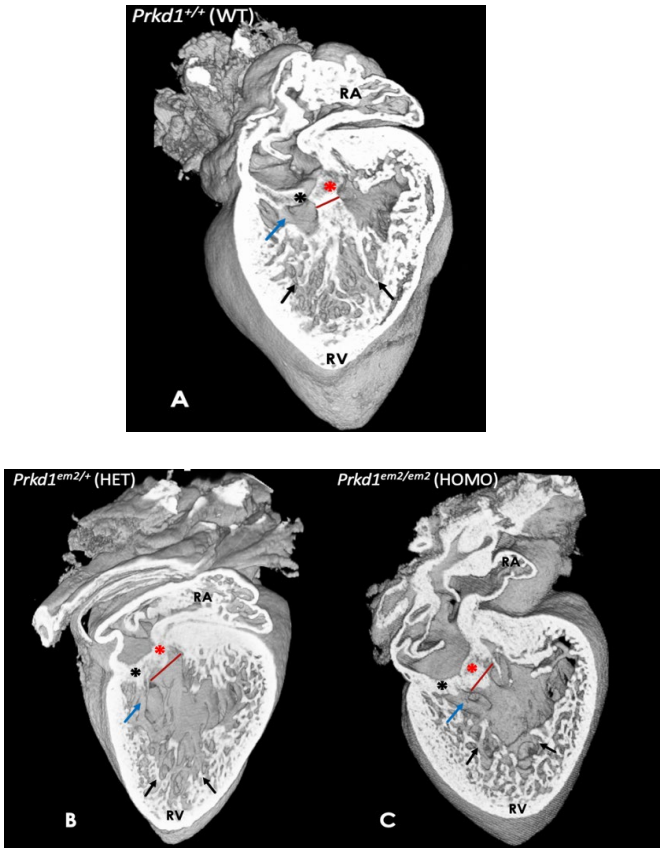


Figure 5:13 Papillary muscles of tricuspid valve, their morphology, and attachments in Prkd1^{em2} hearts at E15.5. Representative images of right sagittal sections of Prkd1^{em2} hearts (right ventricular view) showing papillary muscles which are directly attached to leaflets of tricuspid valve (red and black asterisk) without intervening chordae tendineae. The papillary muscles are thicker (red line and blue arrow) in Prkd1$^{em2/+}$ (HET) (B) and Prkd1$^{em2/em2}$ (HOMO) hearts (C) compared to Prkd1$^{+/+}$ (WT) (A). The inferior papillary muscle (blue arrow) in Prkd1$^{em2/+}$ (HET) heart is slenderer and has visible few strands resembling chordae tendineae too, unlike in Prkd1$^{+/+}$ (WT) and Prkd1$^{em2/em2}$ (HOMO). In Prkd1$^{em2/em2}$ (HOMO) heart (C), the inferior papillary muscle is extending quite obliquely towards the ventricular septum, instead of being more vertical as in WT and HET hearts. RA: right atrium, RV: right ventricle, red asterisk (*): anterior leaflet, black asterisk (*): inferior (aka posterior) leaflet, blue arrow: inferior papillary muscle, black arrow: distal attachment of the papillary muscles as trabeculae carneae to the ventricular wall. Redline denotes the thickness of the anterior papillary muscle.

Papillary muscles related to mitral valve:

The anterolateral and posteromedial papillary muscles (as in valentino position of the heart) related to mitral valve are directly attached to the two leaflets of the mitral valve at this stage (denoted by asterisks in Figure 5:14). Inferiorly, the ends of two types of papillary muscles fuse to form an arcade and the trabeculae carneae extend from this towards the ventricular walls. The papillary muscles as well as the arcade they form were thicker in *Prkd1*$^{em2/+}$ (HET) and *Prkd1*$^{em2/em2}$ (HOMO) hearts compared to *Prkd1*$^{+/+}$ (WT) (red and blue arrows in Figure 5:14 B-C compared to A).

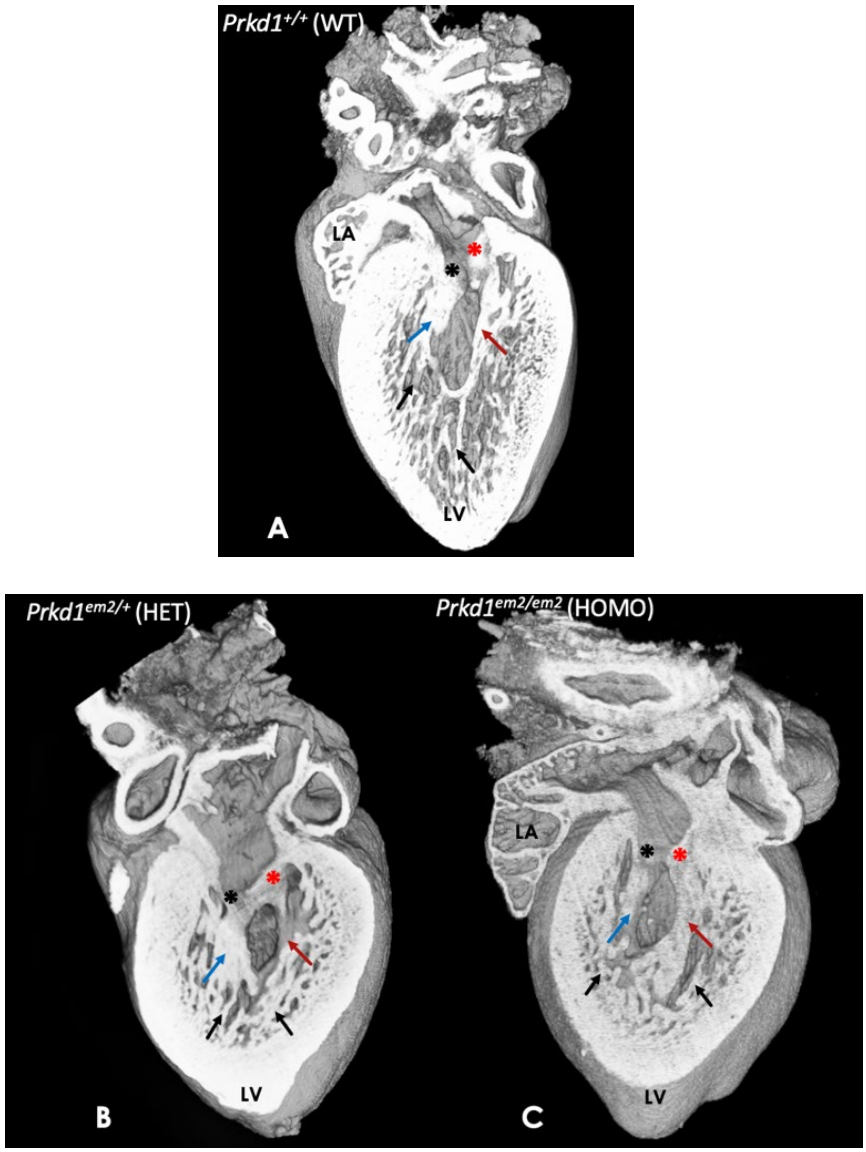


Figure 5:14 Papillary muscles of mitral valve, their attachments and morphology in Prkd1^{em2} hearts at E15.5. Representative images of left sagittal sections of Prkd1^{em2} hearts (left ventricular view) showing thicker papillary muscles in Prkd1$^{em2/+}$ (HET) (B) and Prkd1$^{em2/em2}$ (HOMO) hearts (C) compared to Prkd1$^{+/+}$ (WT) (A). The papillary muscles are directly attached to the mitral valve leaflets without intervening chordae tendineae at this stage. Inferiorly, the papillary muscles form arcade when the two types of papillary muscles fuse, and from this arcade, trabeculae extend towards their insertion into the ventricular walls. LA: left atrium, LV: left ventricle, red asterisk (*): posterior leaflet, black asterisk (*): anterior leaflet, blue arrow: posteromedial papillary muscle, red arrow: anterolateral papillary muscle, black arrow: distal attachments of the papillary muscles as trabeculae carneae to the ventricular wall.

5.3.7 Dimensions of RVOT and pulmonary annulus in *Prkd1^{em2}* hearts with CHD

Since reported patients with PRKD1-G592R mutations had abnormality of the pulmonary valve and was the most common CHD in these patients (Table 4:1), all the hearts with CHD were analysed for any obstruction of the right ventricular outflow tract (RVOT). The RVOT dimensions were measured at sub-pulmonary/infundibular as well as the pulmonary annular levels. Hearts from all the three groups (WT=3, HET=11, HOMO=10) were quantitatively analysed for any associated obstruction to the outflow of right ventricle at pulmonary valvular as well as infundibular levels, selecting the widest diameter in coronal view, using the measurement tool in Osirix™. All *Prkd1$^{em2/+}$* (HET) and *Prkd1$^{em2/em2}$* (HOMO) hearts had narrowing (diameter less than mean $\pm$ SD = 0.56mm $\pm$ 0.07 in WT) at the infundibular level (yellow arrow in Figure 5:15B-C compared with A) but the difference was significant only between WT and *Prkd1$^{em2/em2}$* (HOMO) (P = 0.0361, Dunn's multiple comparison test) (Figure 5:15-D & Table 5:8). There was no significant difference among WT, *Prkd1$^{em2/+}$* (HET) and *Prkd1$^{em2/em2}$* (HOMO) hearts regarding the pulmonary annulus diameter (P > 0.05, one way ANOVA) (Figure 5:15-E & Table 5:8), though ten out of eleven *Prkd1$^{em2/+}$* (HET) and five out of ten *Prkd1$^{em2/em2}$* (HOMO) hearts had pulmonary annulus diameter less than the mean $\pm$ SD of 0.55mm $\pm$ 0.13 in WT (black arrow in Figure 5:15B-C compared with A).

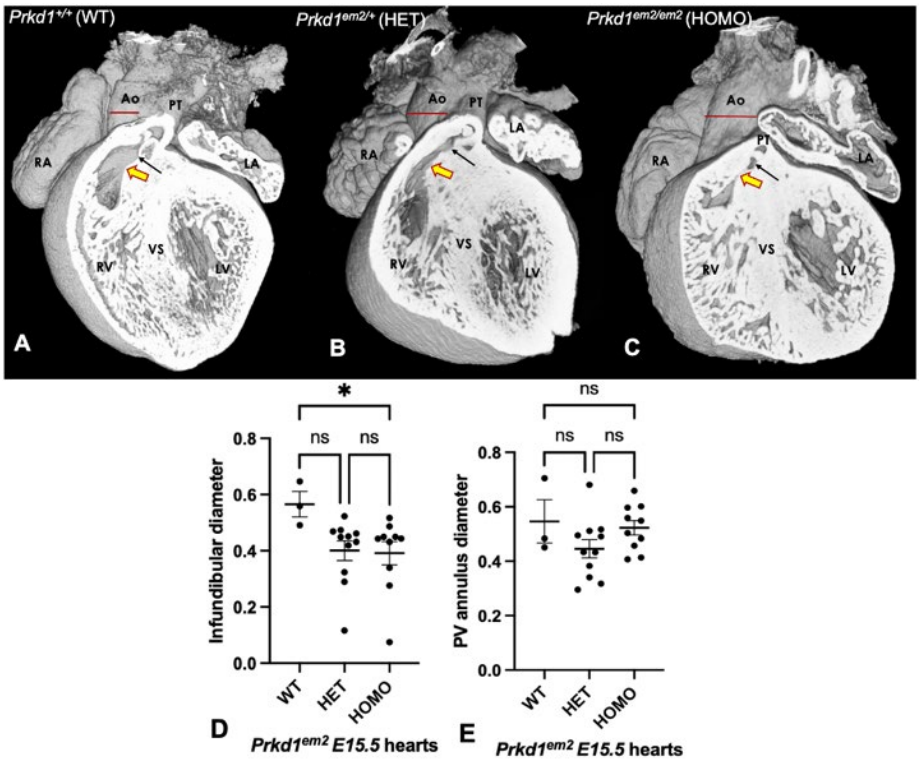


Figure 5:15 Right ventricular outflow tract obstruction and pulmonary stenosis. In some Prkd1$^{em2/+}$ (HET) (B) and Prkd1$^{em2/em2}$ (HOMO)(C) hearts, narrowing at infundibular (sub valvular) region (yellow arrow) and at pulmonary annulus levels (black arrow) were observed, compared with WT (A). However, the difference was significant between WT and Prkd1$^{em2/em2}$ (HOMO) hearts in terms of infundibular diameter (Kruskal-Wallis test, P = 0.0361) (D) whereas, at annulus level, it was not significant in Prkd1$^{em2/+}$ (HET) and Prkd1$^{em2/em2}$ (HOMO) compared with WT (Tukey's test, P > 0.05) (E). In the Prkd1$^{em2/em2}$ (HOMO) heart (C), in addition to severe narrowing at infundibular and pulmonary valve-annulus regions, the size of aorta was quite massive compared to Prkd1em2/+ (HET) (B) and WT (A) (denoted by red line). This homo heart had VSD and DORV as well.

Pulmonary valve annular diameter					
Groups comparison	**Mean**		**Mean diff.**	**SE of diff.**	**Adjusted *P* - value (Tukey's test)**
WT Vs HET	WT 0.5467	HET 0.4455	0.1011	0.06744	0.3114 (n.s.)
WT Vs HOMO	WT 0.5467	HOMO 0.5232	0.02347	0.06816	0.9369 (n.s.)
HET Vs HOMO	HET 0.4455	HOMO 0.5232	-0.07765	0.04524	0.2226 (n.s.)
ANOVA = 0.1635 (n.s)					

Infundibular diameter				
Groups comparison	**Mean rank (Mean value)**		**Mean rank diff.**	**Adjusted *P*-value (Dunn's test)**
WT Vs HET	WT = 22.33 (0.5657)	HET 11.50 (0.4008)	10.83	0.0558 (n.s.)
WT Vs HOMO	WT = 22.33 (0.5657)	HOMO 10.65 (0.3914)	11.68	0.0361 (sig)
HET Vs HOMO	HET 11.50 (0.4008)	HOMO 10.65 (0.3914)	0.8500	>0.9999 (n.s.)
ANOVA = 0.0349 (sig)				

Table 5:8 Comparison of pulmonary valvular and infundibular diameters. Table showing pulmonary valvular and infundibular diameters in Prkd1$^{em2/+}$ (HET) and Prkd1$^{em2/em2}$ (HOMO) hearts compared with WT. With data normally distributed for pulmonary valvular diameter, there was no significant difference among the three groups (P > 0.05, Tukey's test). However, at infundibular level, there was significant narrowing in Prkd1$^{em2/em2}$ (HOMO) hearts compared with WT (P = 0.0361, Dunn's multiple comparison test). Data was not normally distributed for infundibular diameter. sig: significant; SE: standard error.

5.3.8 HM mutation of *Prkd1* causes significant change in total heart and left ventricular volumes at E15.5

5.3.8.1 Volumetric analysis of WT, HET and HOMO hearts from *Prkd1^{em2}* mouse at E15.5

Volumetric analysis of *Prkd1^{em2}* hearts (n = 8 WT, 6=HET, 6=HOMO) was carried out to explore if humanised mutation in *Prkd1* results in change in the size and volumes of the heart and its different heart chambers (Figure 5:17). The HOMO (*Prkd1$^{em2/em2}$*) hearts were those with CHD.

Results of volumetric analyses are as follows:

Right atrial (RA) chamber volume:

The total RA volume data for *Prkd1$^{+/+}$*(WT) (W = 0.9558, *P* = 0.7986), *Prkd1$^{em2/+}$*(HET) (W = 0.8762, *P* = 0.1733) and *Prkd1$^{em2/em2}$* (HOMO) (W = 0.9588, *P* = 0.7867) hearts were normally distributed. There was significant difference among the three groups on on one way ANOVA (*P* = 0.0021). Tukey's multiple comparison test showed that there was no significant difference in HET vs. WT (*P* = 0.8724). However, the difference was significant between WT and HOMO (*P* = 0.0075) and between HET and HOMO hearts (*P* = 0.0027) (Figure 5:17-A).

Left atrial (LA) chamber volume:

The total LA volume data for *Prkd1$^{+/+}$*(WT) (W = 0.9545, *P* = 0.7567), *Prkd1$^{em2/+}$*(HET) (W = 0.9591, *P* = 0.8011) and *Prkd1$^{em2/em2}$* (HOMO) (W = 0.8053, *P* = 0.0656) hearts were normally distributed. One way ANOVA showed significant difference among the three groups (*P* = 0.0018).

Tukey's multiple comparison test showed that there was no significant difference in WT vs. HET hearts (P = 0.9724). However, the difference was significant between WT and HOMO (P = 0.0029) and between HET and HOMO hearts (P = 0.0046) (Figure 5:17-B).

RV chamber volume:

The data for RV chamber/lumen volume for *Prkd1*$^{+/+}$(WT) (W = 0.9501, P = 0.7121) and *Prkd1*$^{em2/+}$(HET) hearts (W = 0.9754, P = 0.9365) were normally but for *Prkd1*$^{em2/em2}$ (HOMO) (W=0.7617, P = 0.0259) hearts abnormally distributed. There was no significant difference among the three groups (Kruskal-Wallis test, P = 0.0722) (Figure 5:17-C). Dunn's multiple comparison test showed that there was no significant change in the right ventricular chamber volume in *Prkd1*$^{em2/+}$(HET) (P = 0.2935) and *Prkd1*$^{em2/em2}$ (HOMO) (P > 0.999) compared to WT, and *Prkd1*$^{em2/+}$(HET) compared to *Prkd1*$^{em2/em2}$ (HOMO) (P = 0.0974). (Figure 5:17-C).

RV muscle volume:

The data for *Prkd1*$^{+/+}$(WT) (W = 0.8637, P = 0.1308), *Prkd1*$^{em2/+}$(HET) (W=0.9511, P = 0.7219) hearts were normally but for *Prkd1*$^{em2/em2}$ (HOMO) hearts were abnormally distributed (W=0.6907, P = 0.0049). There was significant difference among the means of the three groups (Kruskal-Wallis test, P = 0.0244). Dunn's multiple comparison test showed that there was no significant change in RV muscle volume in HET versus WT (P > 0.999) and HOMO versus WT (P = 0.2019) hearts. However, significant difference was observed in HET versus HOMO hearts (P = 0.0269) (Figure 5:17-D).

Total right ventricular (RV) volume:

The data for *Prkd1*$^{+/+}$(WT) (W = 0.9737, *P* = 0.9253), *Prkd1*$^{em2/+}$(HET) (W = 0.8850, *P* = 0.2100) hearts were normally distributed but for *Prkd1*$^{em2/em2}$ (HOMO) hearts were abnormally distributed (W = 0.7027, *P* = 0.0066).

There was significant difference among the means of the three groups (Kruskal-Wallis test, *P* = 0.0004). Dunn's multiple comparison test showed that there was significant difference in terms of total RV volume in HET versus WT (*P* = 0.0412), HOMO versus HET (*P* = 0.0023) hearts. However, no significant difference was observed in HOMO versus WT hearts (*P* = 0.8388) (Figure 5:17-E).

LV chamber/cavity volume:

The data for *Prkd1*$^{+/+}$(WT) (W = 0.9434, *P* = 0.6450) and *Prkd1*$^{em2/em2}$ (HOMO) (W = 0.8595, *P* = 0.1875) hearts were normally distributed but not for *Prkd1*$^{em2/+}$(HET) (W = 0.8107, *P* = 0.0372). Statistically significant difference was observed among the means (Kruskal-Wallis test, *P* = 0.0003). Dunn's multiple comparison test showed that there was significant reduction in the left ventricular chamber volume in *Prkd1*$^{em2/+}$(HET) (*P* = 0.0021) and *Prkd1*$^{em2/em2}$ (HOMO) (*P* = 0.0391). However, the difference was not significant in *Prkd1*$^{em2/+}$(HET) versus *Prkd1*$^{em2/em2}$ (HOMO) (*P* > 0.9999) (Figure 5:17-F). In HET hearts, the reduction of left ventricular chamber volume without increased in wall thickness was due to excessive number of trabeculae (Figure 5:16 E,H compared with D,G).

LV muscle volume:

The LV muscle volume data for *Prkd1*$^{+/+}$(WT) (W = 0.9328, *P* = 0.5418), *Prkd1*$^{em2/+}$(HET) (W = 0.9737, *P* = 0.9252) and *Prkd1*$^{em2/em2}$ (HOMO) (W = 0.8584, *P* = 0.1838) hearts were normally distributed. One-way ANOVA showed that there was significant difference among the means (*P* = 0.0003). Tukey's multiple comparison test showed that there was significant increase in LV muscle volume in HOMO versus WT (*P* = 0.0153). The difference was also significant between HET and HOMO (*P* = 0.0164) hearts. However, no significant difference was observed in HET compared to WT hearts (*P* = 0.9994) (Figure 5:17-G).

Total left ventricular (LV) volume:

The data for *Prkd1*$^{+/+}$(WT) (W = 0.9077, *P* = 0.3383), *Prkd1*$^{em2/+}$(HET) (W = 0.9761, *P* = 0.9411) and *Prkd1*$^{em2/em2}$ (HOMO) (W = 0.8717, *P* = 0.2331) hearts were normally distributed. One-way ANOVA showed that there was significant difference among the means (*P* = 0.0071). Tukey's multiple comparison test showed that there was significant increase in LV total volume in HOMO versus WT (*P* = 0.0219). The difference was also significant between HET and HOMO (*P* = 0.0084) hearts. However, no significant difference was observed in HET versus WT hearts (*P* = 0.8823) (Figure 5:17-H).

Total heart muscle volume:

The data for *Prkd1*$^{+/+}$(WT) (W = 0.9706, *P* = 0.9024), *Prkd1*$^{em2/+}$(HET) (W = 0.9794, *P* = 0.9601) and *Prkd1*$^{em2/em2}$ (HOMO) (W = 0.8036, *P* = 0.0633) hearts were normally distributed. One-way ANOVA showed that there was significant difference among the means (*P* = 0.0133). Tukey's

multiple comparison test showed that there was significant increase in total heart muscle volume in *Prkd1*$^{em2/em2}$ (HOMO) versus WT (*P* = 0.0296) (Figure 5:16). The difference was also significant between HET and HOMO (*P* = 0.0175) hearts. However, no significant difference was observed in HET versus WT hearts (*P* = 0.9612). (Figure 5:17-I).

Total heart volume:

The data for total heart volume for *Prkd1*$^{+/+}$(WT) hearts (W = 0.8384, *P* = 0.0725), *Prkd1*$^{em2/+}$(HET) hearts (W = 0.8707, *P* = 0.1530) and *Prkd1*$^{em2/em2}$ (HOMO) (W = 0.8069, *P* = 0.0677) hearts were normally distributed. Using ordinary one-way ANOVA, significant difference (*P* = 0.0050) was observed among the means of the three groups. Multiple comparison test showed no significant difference in *Prkd1*$^{+/+}$(WT) versus *Prkd1*$^{em2/+}$(HET) (*P* = 0.9561). However, the difference was significant between *Prkd1*$^{+/+}$(WT) versus *Prkd1*$^{em2/em2}$ (HOMO) (*P* = 0.0127), and between *Prkd1*$^{em2/+}$(HET) and *Prkd1*$^{em2/em2}$ (HOMO) hearts (*P* = 0.0071) (Figure 5:16, Figure 5:17-J).

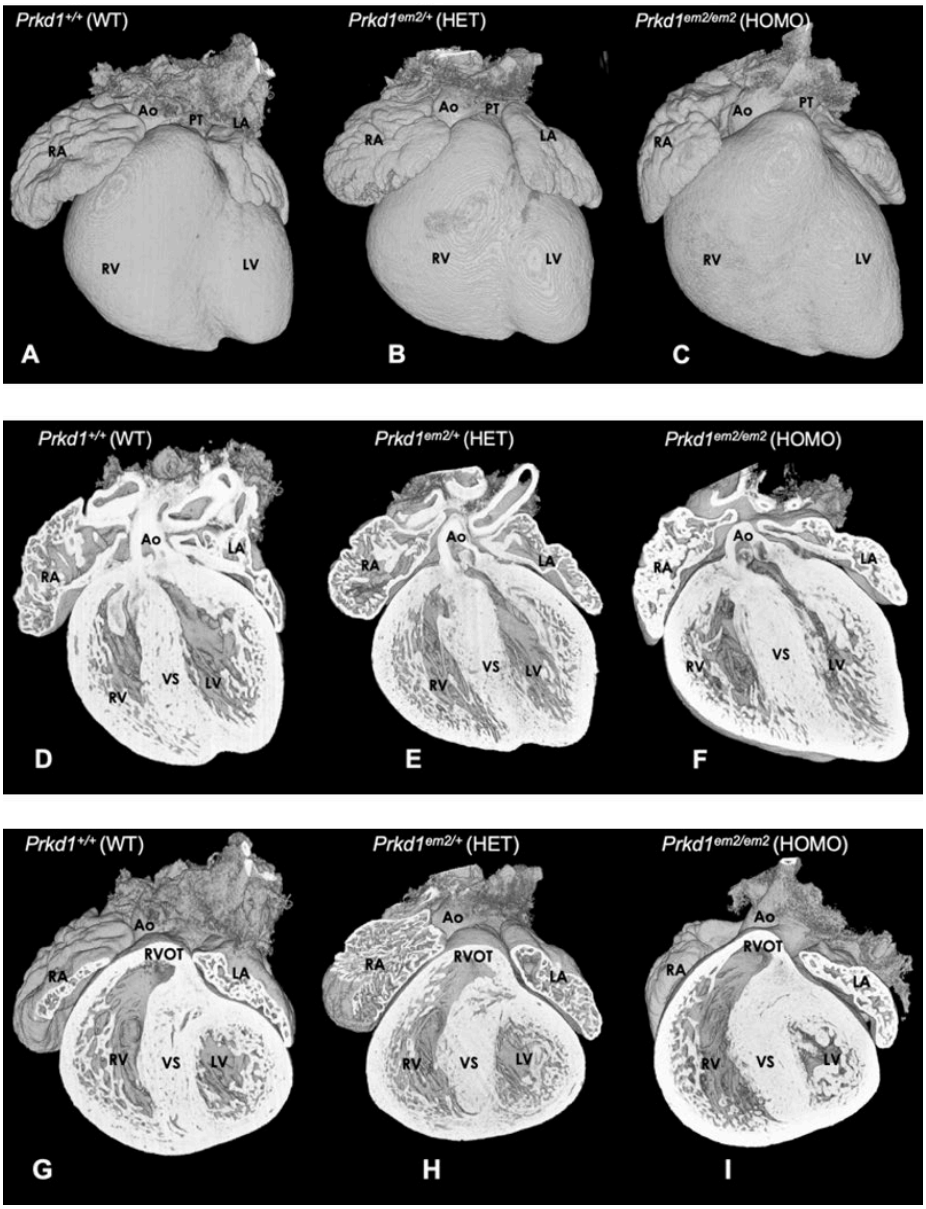


Figure 5:16 Comparison of heart size and muscle volume in E15.5 Prkd1^{em2} hearts. The Prkd1$^{em2/em2}$ (HOMO) hearts have increased heart muscle volume compared to Prkd1$^{+/+}$(WT) (P = 0.0296) as well as Prkd1$^{em2/+}$ (HET) (P = 0.0175). Moreover, the total heart volume (size) in Prkd1$^{em2/em2}$ (HOMO) is significantly increased compared to Prkd1+/+(WT) (P = 0.0127) and Prkd1$^{em2/+}$ (HET) hearts (P = 0.0071). However, the Prkd1$^{em2/+}$ (HET) hearts are not different from Prkd1$^{+/+}$ (WT) in terms of these two parameters (P = 0.9612 and 0.9561 respectively). The LV's total and muscle volumes are increased whereas the LV chamber volume is reduced in Prkd1$^{em2/em2}$ (HOMO) hearts compared with Prkd1$^{+/+}$ (WT) (P < 0.05). Representative images of anterior view of heart exterior (A-C), coronal sections (D-F), and sections from hearts A-F taken in anteroinferior planes (G-I). RA: right atrium; LA: left atrium; RV: right ventricle; LV: left ventricle; VS: ventricular septum; RVOT: right ventricular outflow tract; Ao: aorta.

Summary of the quantitative analysis of E15.5 *Prkd1*^{em2} hearts:

Total heart size (volume) increases significantly in *Prkd1*$^{em2/em2}$ (HOMO) E15.5 heart whereas in *Prkd1*$^{em2/+}$ (HET) hearts, the change is not statistically significant. The increase in total heart size in *Prkd1*$^{em2/em2}$ (HOMO) E15.5 heart is due to increased total heart muscle volume, with contribution of increased LV (i.e., total and muscle) and RV volumes. The increased LV total and muscle volumes in *Prkd1*$^{em2/em2}$ (HOMO) hearts seem to be at the expense of LV chamber/lumen volume which significantly reduces in both *Prkd1*$^{em2/+}$ (HET) and *Prkd1*$^{em2/em2}$ (HOMO) hearts (Figure 5:16, Figure 5:17).

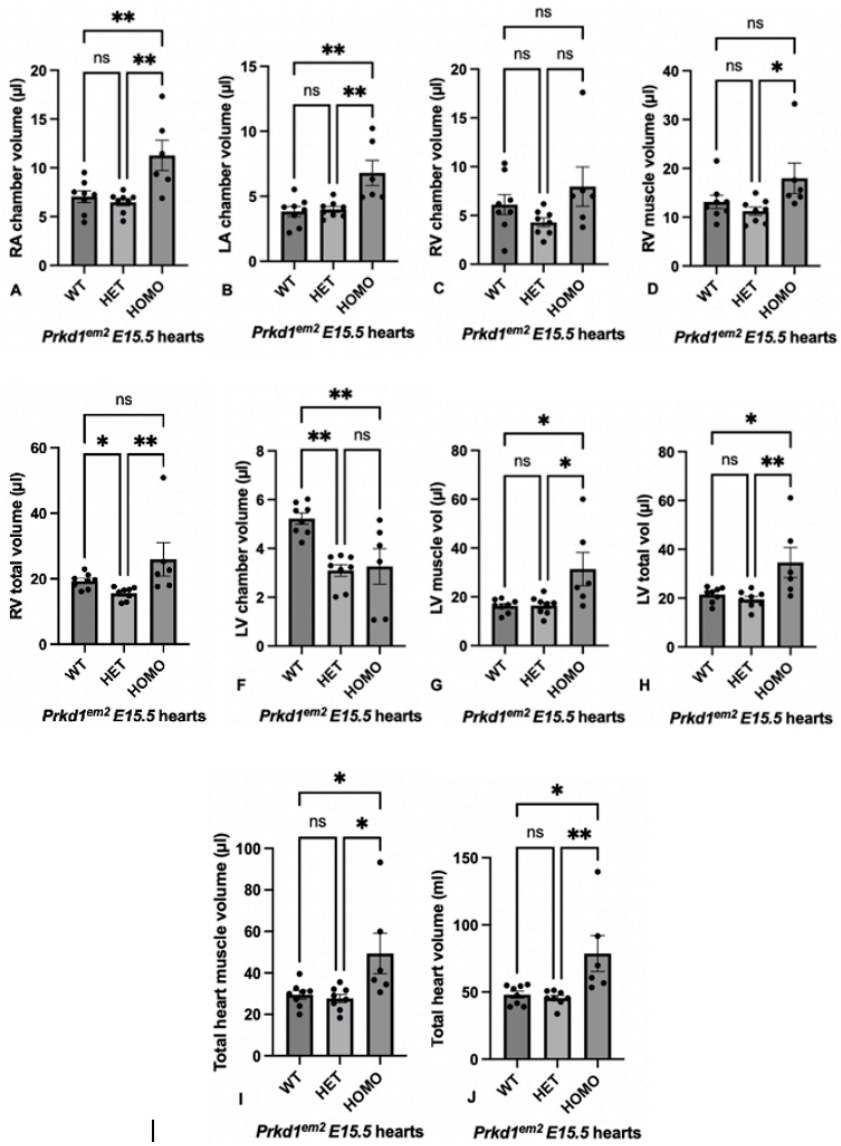


Figure 5:17 Volumetric analyses of Prkd1^{em2} hearts collected at E15.5. Figures showing the findings from the volumetric analysis of Prkd1^{em2} mouse hearts collected at E15.5 (n = 8 WT, 8 HET and 6 HOMO hearts). There was no statistically significant difference in Prkd1$^{em2/+}$ (HET) and Prkd1$^{em2/em2}$ (HOMO) vs. Prkd1$^{+/+}$ (WT) hearts regarding right ventricular chamber (C) and right ventricular total volume (E). However, the difference was significant in terms of left ventricular total (H), chamber (F) and muscle volume (G), RA volume (A), LA volume (B), total heart muscle volume (I) and total heart volume (J) in homozygous (Prkd1$^{em2/em2}$) hearts compared with WT hearts. The difference was also significant between HET and HOMO hearts in terms of RV muscle (D), RV total (E), LV total (H), LV muscle (G), total heart muscle (I) and total heart (J) volumes. There was a trend of increase in the left ventricular total and muscle volume (G-H) and RV chamber, muscle and total volumes (C-E) and increase in atria size (A-B) in Prkd1$^{em2/em2}$ (HOMO) hearts leading to significant increase in the total heart muscle content (I) as well as total heart volume/size (J) at E15.5 stage.

5.3.8.2 Volumetric analysis of E15.5 *Prkd1*$^{em2/em2}$ (HOMO) hearts without CHD

On HREM analysis, we observed that there were 5 out 15 *Prkd1*$^{em2/em2}$ (HOMO) hearts which had no CHD. However, their shape did not seem normal. To analyse them quantitatively, dimensions of three of these normal *Prkd1*$^{em2/em2}$ (HOMO) hearts were compared with WT hearts (n = 8), using unpaired t-test, with data being normally distributed (except for RV dimensions where Mann-Whitney test was applied for data being not normally distributed).

Measuring the different parameters of the three *Prkd1*$^{em2/em2}$ (HOMO) hearts (without CHD) versus WT (n = 8) showed that the mean value of RA volume was 11.02μl versus 7.05μl, LA volume was 7.161μl versus 3.83μl, RV lumen volume was 8.739μl versus 6.116μl, RV muscle volume was 20.08μl versus 13.16μl, RV total volume was 28.82μl versus 19.27μl, LV's chambers volume was 2.885μl versus 5.22μl, LV muscle volume was 34.70μl versus 16.29μl, LV total volume was 37.581μl versus 21.51μl, total heart muscle volume was 54.78μl versus 29.44μl, and total heart volume was 84.58μl versus 48.07μl, respectively. From this comparison, it was found that *Prkd1*$^{em2/em2}$ (HOMO) hearts which did not have any structural CHD were significantly larger in size than their WT counterparts (P = 0.0465) (Figure 5:18-J). LA chambers were enlarged in HOMO (P = 0.0136) (Figure 5:18-B). However RA chamber volume was not significantly changed (P = 0.0827) (Figure 5:18-A).The difference was also not statistically significant in case of RV's (total, lumen, and muscle)

volumes (P > 0.05) (Figure 5:18, C-E). Moreover, the LV's total volume (P = 0.0422) and muscle volume (P = 0.0310) were significantly increased, resulting in significant narrowing of the LV cavity (P = 0.0053) in these *Prkd1$^{em2/em2}$* (HOMO) hearts (Figure 5:18, F-H).

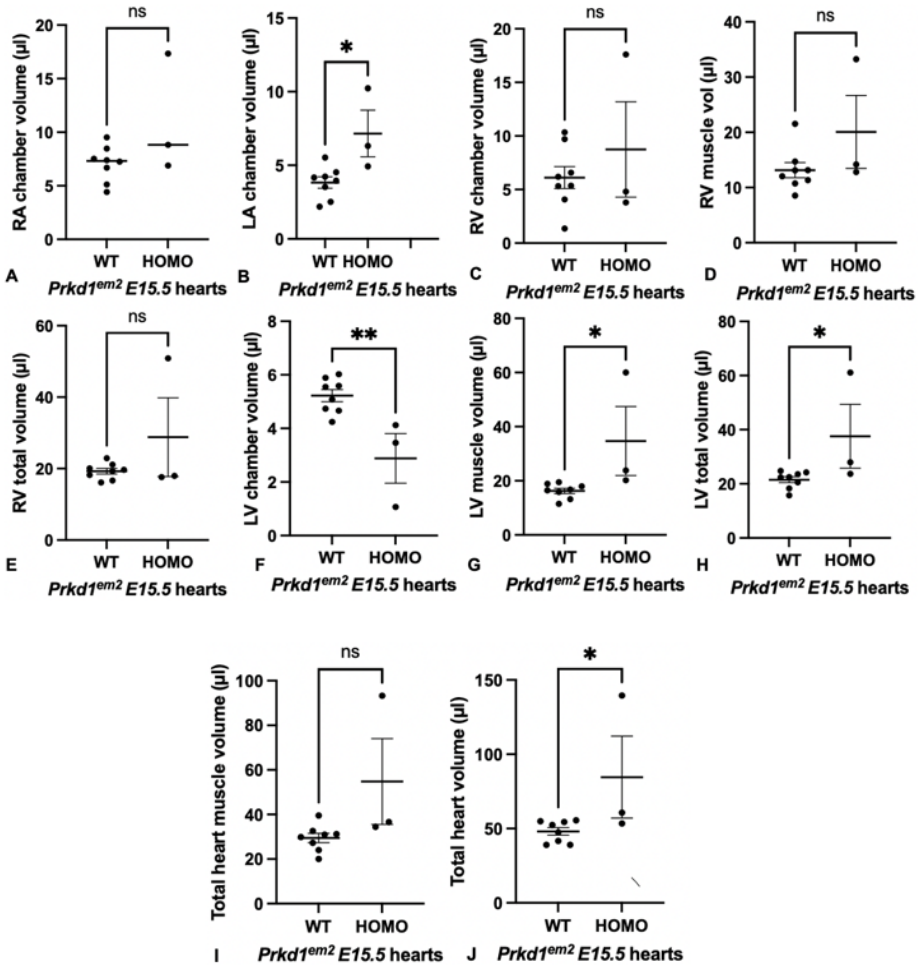


Figure 5:18 Volumetric analysis of Prkd1$^{em2/em2}$ (HOMO) hearts without CHD collected at E15.5. Figures showing the findings from the volumetric analysis of E15.5 Prkd1$^{em2/em2}$ (HOMO) mouse hearts without CHD (n = 3) and compared with WT (n = 10). Volumes of both atrial chambers (A-B) was higher in these HOMO hearts. Moreover, LV muscle volume (G), total volume (H), total heart muscle volume (I) as well as total heart volume (J) were significantly increased in these HOMO hearts. There was no statistically significant difference in case of RV's chamber (C), muscle (D) and total volumes (E) compared with WT (P > 0.05). From this comparison, it was found that Prkd1$^{em2/em2}$ (HOMO) hearts which did not have any structural CHD were significantly larger in size than their WT counterparts (P = 0.0241).

Comparing the results of volumetric analysis of *Prkd1*$^{em2/em2}$ (HOMO) hearts with CHD (Figure 5:17), and those without CHD (Figure 5:18), it was found that the heart size increases in case of *Prkd1*$^{em2/em2}$ (HOMO) mutation with or without CHD (panel “J” in Figure 5:17 & Figure 5:18), due to increase in left ventricular total (H) and muscle volumes (G) correspondingly resulting in reduced LV chamber volume (panel “F” in Figure 5:17 & Figure 5:18). Furthermore, in *Prkd1*$^{em2/em2}$ (HOMO) hearts with and without CHD, there was increase in LA volumes (panel B in both Figure 5:17 & Figure 5:18). The RA volume did not show significant change in *Prkd1*$^{em2/em2}$ (HOMO) hearts without CHD (panel “A” in Figure 5:18) though was significantly increased in *Prkd1*$^{em2/em2}$ (HOMO) hearts with CHD (like LA volume) (panel A in Figure 5:17). Atrial enlargement can occur due to pressure and volume overload, possibly due to increased resistance to blood flow through atrioventricular canals or the outflow tract of heart [396, 397]. In the absence of any CHD such as VSD, PDA, back pressure created due to obstruction to blood flow e.g. due to RVOTO transmits to RA and LA resulting in possible enlargement of the atria [396, 397].

5.3.9 Exploring CHD phenotypes in mouse neonates

5.3.9.1 Selection of sixth postnatal day (P6) for exploring CHD phenotypes postnatally

By P6/P7, interatrial communication should have closed off normally in the region of foramen ovale due to fusion of septum primum and secundum [238]. This mouse neonatal stage was selected to explore if *Prkd1*

mutation results in non-fusion of the two septa of atria in the region of fossa ovalis. Nevertheless, these hearts were also analysed morphologically for all the structures including ventricular septum (VS), aortic valve (AV), pulmonary valve (PV), mitral valve (MV), tricuspid valve (TV), in addition to the atrial septum (AS).

5.3.9.2 CHD phenotypes in *Prkd1^{em2}* neonatal hearts at P6 by HREM analysis

Neonatal hearts at P6 (n = 6 HET, 4 WT) from *Prkd1^{em2}* mice were analysed after generating their 3D models from a z-stack of high resolution 2D images. Neonates (n = 10) at P6 were analysed to explore the CHD phenotypes (mainly closure of the interatrial communication) in neonates in case of *Prkd1$^{em2/+}$*(HET) mutation. Utilising HREM, the phenotypes observed in these P6 *Prkd1$^{em2/+}$* (HET) hearts are shown in the Table 5:9:

Prkd1$^{em2/+}$ (HET) neonatal hearts at P6 with phenotype		
Sample ID	**Phenotype**	**CHD Penetrance**
NID0184-A	• Spontaneously closed muscular VSD	2/6 (33.33%)
NID0184-B	• Spontaneously closing muscular VSD near apex	

Table 5:9 Phenotypes in hearts collected from Prkd1$^{em2/+}$ (HET) mouse neonates at P6. In the two Prkd1$^{em2/+}$ (HET) hearts, spontaneously closed muscular VSDs noted. Persistent interatrial communication was seen in these two HET hearts as well. VSD: Ventricular septal defect.

In hearts from mice with *Prkd1$^{em2/+}$* (HET) mutation (n = 6), two had the septum primum which was not fused with septum secundum, resulting in persistent communication between the two atria at this stage i.e., patent foramen ovale (PFO) (yellow arrows in Figure 5:19 B & D, Figure 5:21 B). In 2 out of 4 WT hearts collected at P6, these two septa were fused

to close the oval foramen (denoted by black arrow in Figure 5:19 A). However, in the remaining two P6 WT hearts, these two septa were not fused. This suggests that such analysis for PFO be carried at a much later stage in future studies e.g., around weaning.

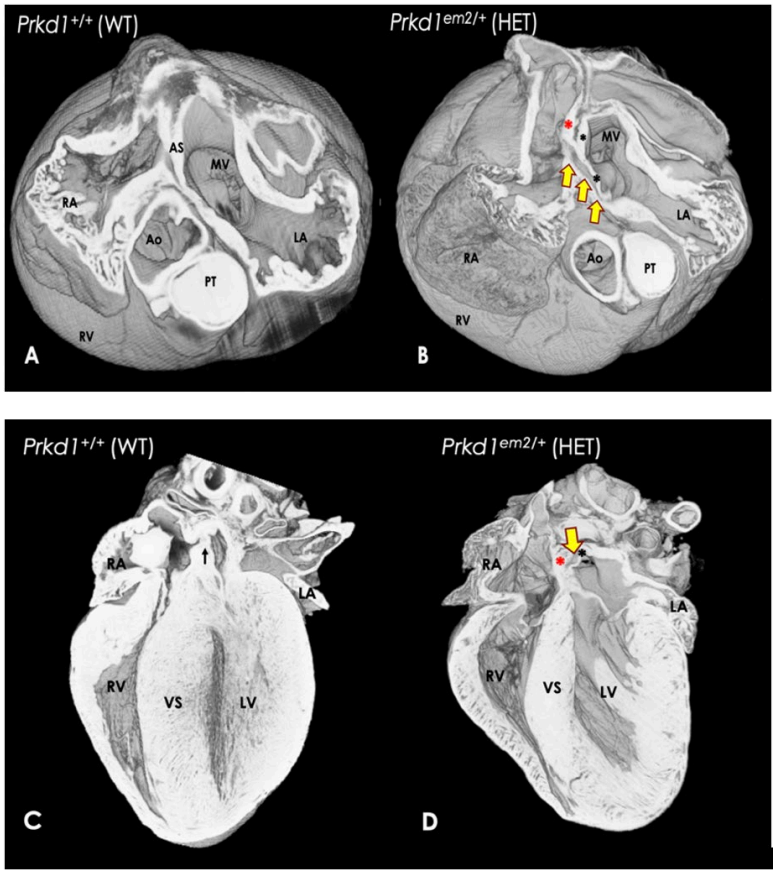


Figure 5:19 Patent foramen Ovale (PFO). A&B - Axial views of the outflow region of Prkd1$^{+/+}$ (WT) and Prkd1$^{em2/+}$ (HET) hearts at P6. A: Prkd1$^{+/+}$ (WT) mouse heart showing the closed interatrial communication after the fusion of septum primum and septum secundum to give rise to atrial septum; B: Prkd1$^{em2/+}$ (HET) heart showing non-fusion of septum primum (black asterisk),) and septum secundum (red asterisk), leaving a gap (yellow arrow in B) to allow abnormal interatrial communication when it should have closed-off at this stage; C-D: Anterior/coronal sectional view of the same Prkd1$^{+/+}$ (WT) (C) and Prkd1$^{em2/+}$ (HET) (D) hearts showing closed IA communication in Prkd1$^{+/+}$ (WT) heart (black arrow in C), and unfused septum primum (black asterisk) and secundum (red asterisk) in Prkd1$^{em2/+}$ (HET) heart with persistent IA communication as patent foramen ovale (yellow arrow in D). RA: right atrium; LA: left atrium; RV: right ventricle; LV: left ventricle; VS: ventricular septum.

In the same *Prkd1*$^{em2/+}$ (HET) heart, a narrow muscular VSD near the heart apex was present, which could have been in the process of closing spontaneously (red arrow in Figure 5:20-C) as tissue seemed less dense than the rest of the ventricular septum. However, through and through communication with clear margins was not discernible.

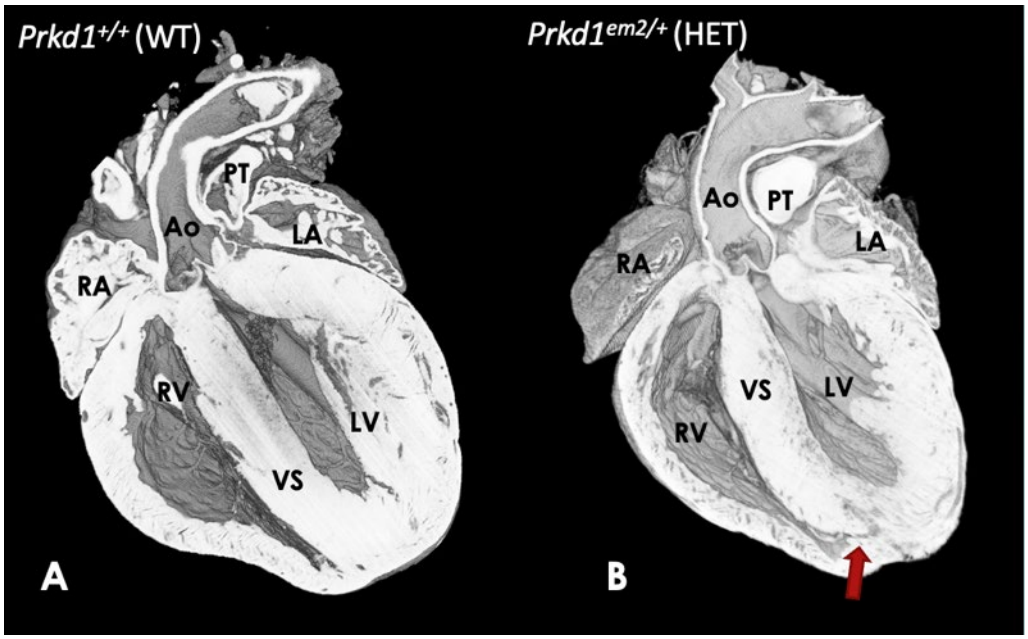


Figure 5:20 Spontaneous correction of ventricular septal defect in P6 Prkd1^{em2} *neonates. A: A wild type heart having normal ventricular septum. B: In Prkd1*$^{em2/+}$ *(HET) heart, less dense area of ventricular septum near the apex (red arrow) was observed with the possibility of being a spontaneously closing muscular VSD. For this reason, it was not labelled as CHD at this stage since not through and through communication between the two ventricles could be established. RA: right atrium; LA: left atrium; RV: right ventricle; LV: left ventricle; VS: ventricular septum; Ao: aorta; PT: pulmonary trunk.*

In another *Prkd1*$^{em2/+}$ (HET) heart, there was probe patency of foramen ovale (Figure 5:21 A-B**,** yellow arrow). In the same *Prkd1*$^{em2/+}$ (HET) heart, a possibly spontaneously closed muscular VSD was observed as well (red arrow in Figure 5:21 C-D) though it was not labelled as CHD. No other congenital heart defects were observed in these *Prkd1*$^{em2/+}$

(HET) neonatal hearts (Table 5:9). *Prkd1*$^{+/+}$(WT) hearts (n = 6) were normal phenotypically.

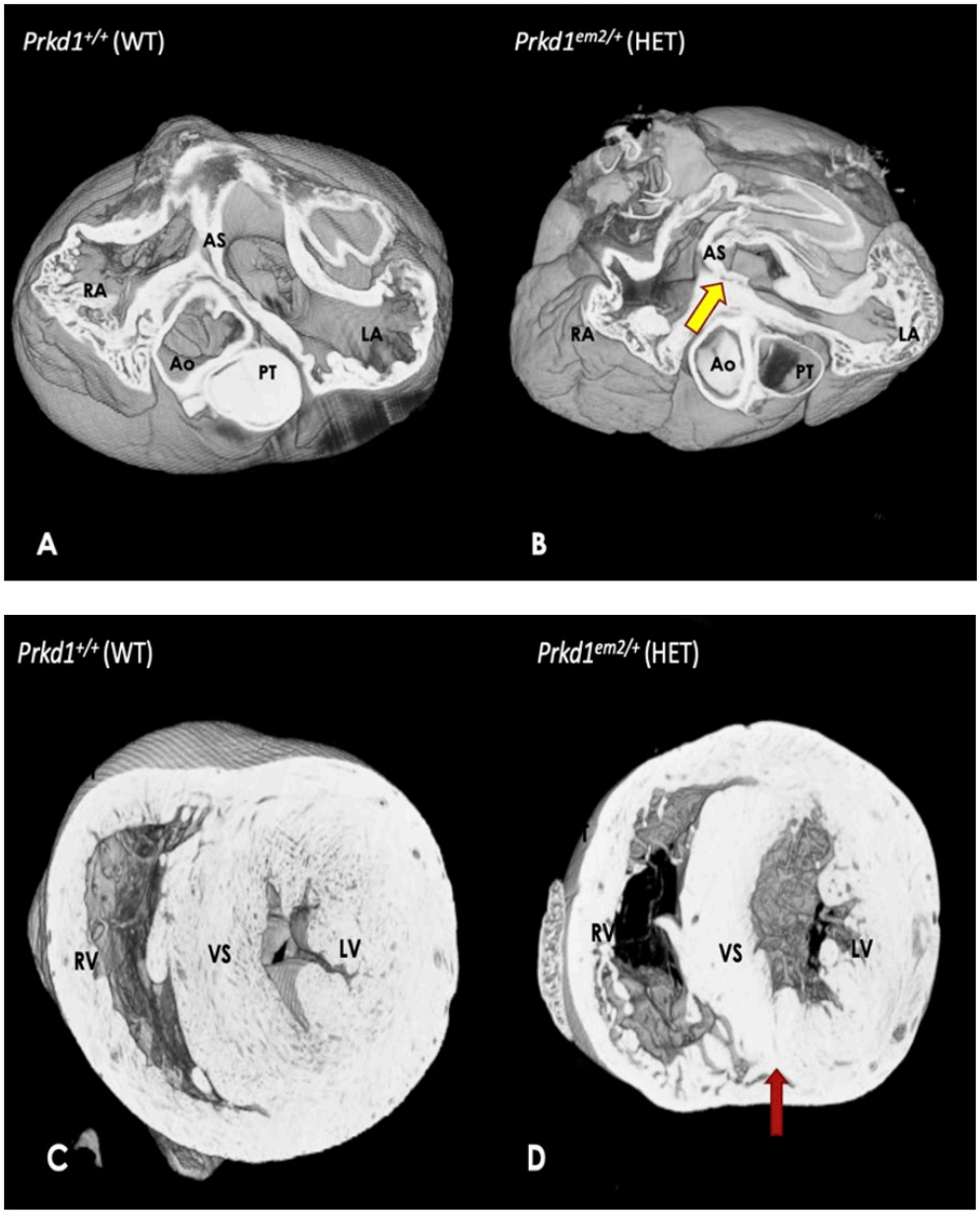


Figure 5:21 Probe patency of foramen Ovale and spontaneously closed muscular VSD. A: P6, in Prkd1$^{+/+}$ *(WT) mouse heart the atrial septum has formed to close-off interatrial communication after the fusion of septum primum and secundum; B: Prkd1*$^{em2/+}$ *(HET) heart showing tiny interatrial communication (yellow arrow) seemingly in the process of spontaneous closure. C-D: Images from the same heart showing a site of probably spontaneously closed muscular VSD, being less dense than the rest of VS (red arrow) though it is not labelled as CHD. RA: right atrium; LA: left atrium; RV: right ventricle; LV: left ventricle; VS: interventricular septum; AS: atrial septum; Ao: aorta; PT: pulmonary trunk.*

No *Prkd1*$^{em2/em2}$ (HOMO) mutant pups at P6 were available for heart morphological analysis due to resources and time constraints.

5.3.10 Heterozygous humanised mutation of *Prkd1* is not associated with a significant change in heart size and heart chambers' volumes in P6 *Prkd1*^{em2} neonates

P6 neonatal hearts (n = 10) were further analysed quantitatively to find out if *Prkd1* humanised mutation resulted in any change in the dimensions of these hearts. 3D-slicer program [192] was used to calculate volumes of atria, ventricles (wall and chamber), the total heart muscle and of whole heart. These measurements were carried out to exclude any relation of humanised mutation of *Prkd1* with changes in these parameters of heart. This was deemed important to carry out as sometimes the hearts with mutation would not have the common structural CHD such as ASD, VSD and others but would have abnormal shape and/or size compared with WT. To impart objectivity to such observations, quantitative analysis of *Prkd1*$^{+/+}$ (WT) (n = 4) and *Prkd1*$^{em2/+}$ (HET) (n = 6) neonatal hearts was carried out, as follows (Figure 5:22 A-I):

RA chamber volume:

The data for *Prkd1*$^{+/+}$ (WT) (W=0.9852, P = 0.9319) and *Prkd1*$^{em2/+}$ (HET) (W=0.8007, P = 0.0597) hearts was normally distributed. RA volume increased in *Prkd1*$^{em2/+}$ (HET) hearts, however the difference was not statistically significant (P = 0.6880) (Figure 5:22-A).

LA chamber volume:

The data for *Prkd1*$^{+/+}$ (WT) (W = 0.9555, *P* = 0.7507) and *Prkd1*$^{em2/+}$ (HET) (W = 0.8468, *P* = 0.1483) hearts were normally distributed. LA volume did not change significantly in *Prkd1*$^{em2/+}$ (HET) neonatal hearts compared to WT (*P* = 0.4259) (Figure 5:22-B).

RV chamber volume:

The data of RV chamber volume for *Prkd1*$^{+/+}$ (WT) (W = 0.9007, *P* = 0.4347) and *Prkd1*$^{em2/+}$ (HET) (W = 0.9830, *P* = 0.9656) hearts were normally distributed. RV chamber volume was not significantly increased in *Prkd1*$^{em2/+}$ (HET) hearts compared to WT (*P* = 0.5746) (Figure 5:22-C).

RV muscle volume:

RV muscle volume was calculated as a difference between the total and chamber volumes of RV. The data for RV muscle volume for *Prkd1*$^{+/+}$ (WT) (W=0.8991, *P* = 0.4267) and *Prkd1*$^{em2/+}$ (HET) (W = 0.9532, *P* = 0.7662) hearts were normally distributed. RV muscle volume was not significantly different in *Prkd1*$^{em2/+}$ (HET) neonatal hearts compared to WT (*P* = 0.3244) (Figure 5:22-D).

RV total volume:

RV total volume was measured as combined muscle and chamber volumes of right ventricle. The data for total volume of RV in *Prkd1*$^{+/+}$ (WT) (W = 0.9281, *P* = 0.5832) and *Prkd1*$^{em2/+}$ (HET) (W = 0.9044, *P* = 0.4006) hearts were normally distributed. However, the two groups were not significantly different from each other (*P* = 0.7870) (Figure 5:22-E).

LV chamber volume:

The data of left ventricular chamber volume for *Prkd1*$^{+/+}$ (WT) (W = 0.8681, *P* = 0.2902) and *Prkd1*$^{em2/+}$ (HET) (W = 0.9755, *P* = 0.9272) hearts was normally distributed. The differe in LV chamber volume in HET hearts was not significant between the two groups (*P* = 0.6027) (Figure 5:22-F).

LV muscle volume:

LV muscle volume was calculated as a difference between the total and chamber volumes of LV. LV muscle volume data for *Prkd1*$^{+/+}$ (WT) (W = 0.9743, *P* = 0.8678) and *Prkd1*$^{em2/+}$ (HET) (W = 0.8851, *P* = 0.2933) hearts passed the normality tests. There was no significant difference between *Prkd1*$^{+/+}$ (WT) and *Prkd1*$^{em2/+}$ (HET) neonatal hearts in terms of LV muscle volume (*P* = 0.0527) (Figure 5:22-G).

LV total volume:

The total LV volume was combined muscle and chamber volume of LV. The data for *Prkd1*$^{+/+}$ (WT) (W = 0.9334, *P* = 0.6143) and *Prkd1*$^{em2/+}$ (HET) hearts (W = 0.8876, *P* = 0.3058) was normally distributed. There was no significant difference between *Prkd1*$^{+/+}$ (WT) and *Prkd1*$^{em2/+}$ (HET) neonatal hearts in terms of left ventricular total volume (*P* = 0.1408) (Figure 5:22-H).

Total heart muscle volume:

Total heart muscle volume was calculated as sum of the right and left ventricle muscle volumes as they make the bulk of the heart muscle mass. The data for *Prkd1*$^{+/+}$ (WT) (W = 0.9541, *P* = 0.7416) and *Prkd1*$^{em2/+}$ (HET) (W = 0.8776, *P* = 0.2583) hearts was normally

distributed. There was no significant difference between *Prkd1*$^{+/+}$ (WT) and *Prkd1*$^{em2/+}$ (HET) neonatal hearts in terms of total heart muscle volume (P = 0.0744). The atrial walls are too thin to measure dimensions/volumes of their walls separate from their chambers' volumes which is a limitation of the technique. Therefore, total atrial volumes were measured which were then included in the measurement of the whole heart volume, however, the total heart muscle volume measurements did not include any measurement of atrial muscle volume owing to the mentioned limitation (Figure 5:22-I).

Total heart volume:

Total heart volume was calculated as a sum of the total volumes of both atria and both ventricles. The data for *Prkd1*$^{+/+}$ (WT) (W = 0.9267, 0.5752) and *Prkd1*$^{em2/+}$ (HET) (W = 0.8405, P = 0.1315) hearts was normally distributed. There was no significant difference between *Prkd1*$^{+/+}$ (WT) and *Prkd1*$^{em2/+}$ (HET) neonatal hearts in terms of total heart volume (P = 0.3847) (Figure 5:22-J).

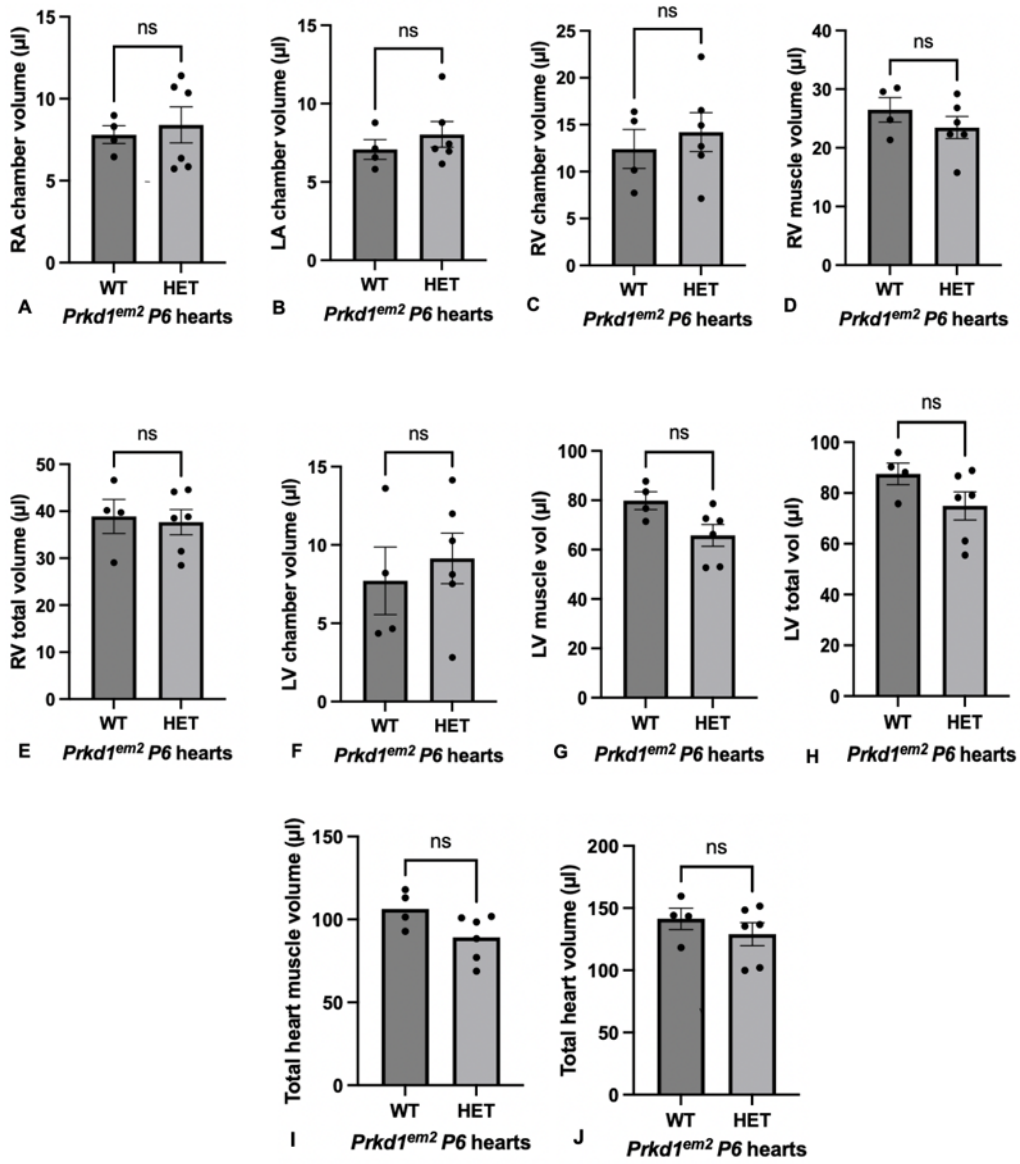


Figure 5:22 Quantitative analysis of the Prkd1^{em2} neonatal hearts collected at P6. Column charts showing the comparative analysis of Prkd1$^{+/+}$ (WT) (n = 4) and Prkd1$^{em2/+}$ (HET) (n = 6) hearts. There was no statistically significant difference in all these parameters between Prkd1$^{+/+}$ (WT) and Prkd1$^{em2/+}$ (HET) hearts (P > 0.05).

5.3.11 Gender determination of *Prkd1^{em2}* mutant mice with CHD

Gender was determined of both *Prkd1$^{em2/+}$* (HET) (n = 7/11) and *Prkd1$^{em2/em2}$* (HOMO) (n = 10) mice with CHD. gDNA sample was not available for 4 out of 11 *Prkd1$^{em2/+}$* (HET) mice (with CHD). Out of the

available total 17 *Prkd1^{em2}* - mutant mice with CHD, 11 (2 HET +9 HOMO) were males and 6 (5 HET + 1 HOMO) were females.

5.3.12 RT-qPCR to explore gene expression of *Prkd1*, *Prkd2* and *Prkd3* in *Prkd1^{em2}* mouse hearts at E15.5

5.3.12.1 Tissue collection for RT-qPCR

Quantification of the transcript of *Prkd1* was carried out by reverse transcriptase-quantitative polymerase chain reaction (RT-qPCR) technique comparing *Prkd1$^{+/+}$* (WT) with *Prkd1$^{em2/+}$* (HET) and *Prkd1$^{em2/em2}$* (HOMO) heart samples collected at E15.5.

The other PRKDs such as PRKD2 and PRKD3 are structurally homologous to PRKD1, and previous studies suggest a potential redundancy between the different PRKD paralogues [398]. In our phenotypic data from *Prkd1-HM (Prkd1^{em2})* mouse model, an increase in LV muscle and total heart volumes were observed in *Prkd1$^{em2/em2}$ (HOMO)* mouse (Figure 5:17 G-I). Upregulation of PRKD1 is associated with pathologic cardiac hypertrophy [318, 399] and its deletion attenuates pathologic cardiac remodelling [392]. Despite significant reduction of PRKD1 protein in HOMO (*Prkd1$^{em2/em2}$*) hearts (Figure 5:26, Figure 5:27), increase in total heart volume/size as well as total heart muscle volume in case of homozygous (*Prkd1$^{em2/em2}$*) mutation raised the question if there was a potential redundancy exhibited by other paralogues (i.e. PRKD2 and 3). To explore this, expressions of *Prkd2* and *3* were analysed at transcript level by qPCR in the same E15.5 mouse heart samples, comparing *Prkd1$^{+/+}$*

(WT) with *Prkd1*$^{em2/+}$ (HET) and *Prkd1*$^{em2/em2}$ (HOMO) hearts (Figure 5:24, Figure 5:25).

5.3.12.2 Gene expression analysis of *Prkd1* in E15.5 *Prkd1*^{em2} hearts by RT-qPCR shows no significant change in HOMO and HET hearts compared to WT

To determine *Prkd1* expression in E15.5 *Prkd1*^{em2} mouse hearts, RNA was extracted from nine individual E15.5 mouse hearts (i.e., n = 3 WT; n = 3 HET; n = 3 HOMO) which was reverse transcribed to cDNA in order to use as a template for the qPCR. Expression data, normalised to *Pgk1* and *Rpl4,* was analysed by using modified Pfaffl method [198]. The data for WT (W = 0.9138, *P* = 0.4308), HET (W = 0.8544, *P* = 0.2522) and HOMO (W = 0.9519, *P* = 0.5777) groups were normally distributed. Comparing the three groups, we found that there was no significant difference among the means of *Prkd1* expression (log_2FC) of these groups (*P* = 0.0675). Multiple comparisons (Tukey) test also showed no significant difference in terms of *Prkd1* expression, comparing WT with HET (*P* = 0.0723), WT with HOMO (*P* = 0.1359) and HET with HOMO (*P* = 0.8757) (Table 5:10, Figure 5:23).

Groups comparison	Mean *Prkd1* expression (log_2FC)		Mean difference in log_2FC	SE of difference	95% CI of difference	Adjusted p-value
WT Vs HET	WT 0.000	HET 0.5019	-0.5019	0.1811	-1.057 to 0.05366	0.0723 (n.s.)
WT Vs HOMO	WT 0.000	HOMO 0.4120	-0.4120	0.1811	-0.9676 to 0.1435	0.1359 (n.s.)
HET Vs HOMO	HET 0.5019	HOMO 0.4120	0.08986	0.1811	-0.4657 to 0.6454	0.8757 (n.s.)

Table 5:10 Comparative mean Prkd1-transcript expression in E15.5 hearts from Prkd1^{em2} mouse line. Multiple comparisons of log_2FC of Prkd1 among the three E15.5 groups (n = 3 each) from Prkd1^{em2} mouse line using Post-hoc (multiple-comparisons) Tukey test. There is no statistically significant difference between WT and HET (P > 0.0723), WT and HOMO (P = 0.1359), and between HET and HOMO hearts (P = 0.8757). The log_2FC in HET and HOMO are compared to log_2FC of "zero" in WT. The reference genes used were Pgk1 and Rpl4. n.s = not significant. SE = standard error.

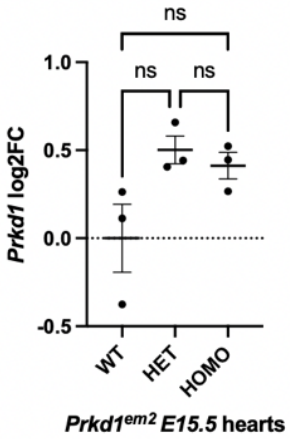


Figure 5:23 Expression of Prkd1 in E15.5 hearts from Prkd1^{em2} mouse. The log_2FC of Prkd1(mean with SE) in Prkd1$^{em2/+}$ (HET) and Prkd1$^{em2/em2}$ (HOMO hearts collected at E15.5, compared to WT (Prkd1$^{+/+}$) hearts of the same stage. As shown in the scatter plot, using one way-ANOVA and posthoc-Tukey test, no statistically significant difference was found in the level of Prkd1 transcript in Prkd1$^{em2/+}$ (HET) and Prkd1$^{em2/em2}$ (HOMO) hearts compared to WT (Prkd1$^{+/+}$). ns = not significant (P > 0.05).

5.3.12.3 No significant difference in the expression of *Prkd2* was observed in *Prkd1*$^{em2/+}$ *(HET)* and *Prkd1*$^{em2/em2}$ (HOMO) mouse hearts at E15.5

To find out if there was any change in the transcript level of *Prkd2* in the *Prkd1*$^{em2/+}$ (HET) and *Prkd1*$^{em2/em2}$ (HOMO) hearts collected at E15.5 stage, comparative qPCR was carried out on the same heart samples as used for *Prkd1* transcript quantification. Data obtained from all the three groups – WT (W = 0.8675, *P* = 0.2883) HET (W = 0.9892, *P* = 0.8012) and HOMO (W = 0.8970, *P* = 0.3761) was normally distributed. One-way ANOVA showed that there was no significant difference among the means (*P* = 0.7161). Post-hoc-Tukey (multiple comparisons) test also showed that the comparisons resulted in no significant difference between WT & HET (*P* = 0.9175), between WT & HOMO (*P* = 0.6940) and between HET & HOMO (*P* = 0.8997) (Table 5:11, Figure 5:24).

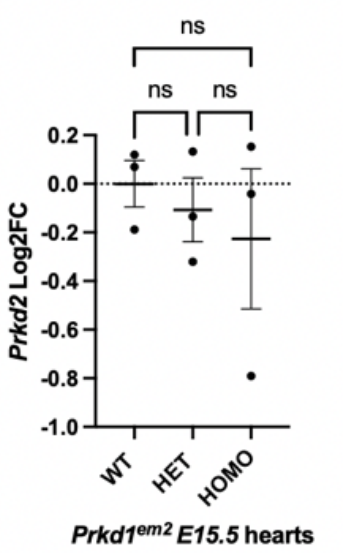


Figure 5:24 Expression of Prkd2 in E15.5 hearts from Prkd1^{em2} mouse line. Scatter plot showing mean values of log$_2$FC (with standard error) of Prkd2 in Prkd1$^{em2/+}$ (HET) and Prkd1$^{em2/em2}$ (HOMO) hearts collected at E15.5 compared with WT (Prkd1$^{+/+}$), using modified Pfaffl method [198]. There was no significant change in the expression of Prkd2 in Prkd1$^{em2/+}$ (HET)) (P = 0.9175) and Prkd1$^{em2/em2}$ (HOMO) hearts (P = 0.6940) compared with WT (Prkd1$^{+/+}$), and Prkd1$^{em1/+}$ (HET) compared with Prkd1$^{em1/em1}$ (HOMO) hearts (P = 0.8997). n.s: not significant.

Groups comparison	Mean *Prkd2* expression (log$_2$FC)		Mean diff. in log$_2$FC	SE of diff.	95% CI of diff.	Adjusted P-value
WT vs. HET	WT -3.333e-010	HET -0.1074	0.1074	0.2697	-0.7200 to 0.9348	0.9175 (n.s.)
WT vs. HOMO	WT -3.333e-010	HOMO -0.2266	0.2266	0.2697	-0.6008 to 1.054	0.6940 (n.s.)
HET vs. HOMO	HET -0.1074	HOMO -0.2266	0.1192	0.2697	-0.7082 to 0.9466	0.8997 (n.s.)

Table 5:11 Comparative mean Prkd2 expression in E15.5 hearts from Prkd1^{em2} mouse line. Multiple comparisons of log$_2$FC of Prkd2 among the three E15.5 groups (n = 3 each) from Prkd1^{em2} mouse line using Post-hoc Tukey test. There was no statistically significant difference between WT and HET heart (P = 0.9175), WT and HOMO (P = 0.6940), and between HET and HOMO (P = 0.8997). The reference genes used were Pgk1 and Rpl4. n.s = not significant, SE: Standard error; diff: difference; CI: Confidence interval.

5.3.12.4 There was no significant change in the expression of *Prkd3* in *Prkd1*$^{em2/+}$ (HET) and *Prkd1*$^{em2/em2}$ (HOMO) hearts at E15.5

Comparing the relative expression of *Prkd3* across the three groups showed that there was no significant difference among the means (*P* = 0.314). Posthoc-Tukey test also showed that the comparisons resulted in no significant difference between WT & *Prkd1*$^{em2/+}$ (HET) (*P* = 0.8178), between WT & HOMO (*P* = 0.5769) and between HET & HOMO (*P* = 0.2932) (Figure 5:25, Table 5:12).

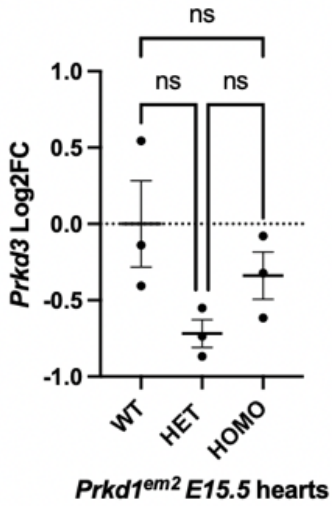


Figure 5:25 Expression of Prkd3 in E15.5 hearts from Prkd1^{em2} *mouse line. Column bar graph showing mean values of log*$_2$*FC (with standard error) of Prkd3 in Prkd1*$^{em2/+}$ *(HET) and Prkd1*$^{em2/em2}$ *(HOMO hearts collected at E15.5 compared with WT (Prkd1*$^{+/+}$*) heart using modified Pfaffl method [198]. There was no significant change in the expression of Prkd3 in Prkd1*$^{em2/+}$ *(HET)) (P = 0.0874) and Prkd1*$^{em2/em2}$ *(HOMO) hearts (P = 0.4759) compared with WT (Prkd1*$^{+/+}$*), and Prkd1*$^{em2/+}$*(HET) compared with Prkd1*$^{em2/em2}$ *(HOMO) hearts (P = 0.4060). n.s: not significant.*

Groups comparison	Mean *Prkd3* expression (log_2FC)		Mean diff. in log_2FC	SE of diff.	95% CI of diff.	Adjusted P-value
WT vs. HET	WT - 3.333e-010	HET -0.7183	0.7183	0.2740	-0.1233 to 1.559	0.0874 (n.s.)
WT vs. HOMO	WT - 3.333e-010	HOMO -0.3392	0.3392	0.2740	-0.5013 to 1.180	0.4759 (n.s.)
HET vs. HOMO	HET - 0.7183	HOMO -0.3392	-0.3791	0.2740	-1.220 to 0.4615	0.4060 (n.s.)

Table 5:12 Comparative mean Prkd3 expression in E15.5 hearts from Prkd1^{em2} mouse line. Multiple comparisons of log_2FC of Prkd3 among the three E15.5 groups (n = 3 each) from Prkd1^{em2} mouse line using Post-hoc Tukey test. There was no statistically significant difference between WT and HET heart (P = 0.0874) WT and HOMO (P = 0.4759), and between HET and HOMO (P = 0.4060). The reference genes used were Pgk1 and Rpl4. n.s = not significant, SE: Standard error; diff.: Difference, CI: Confidence interval.

5.3.13 Immunoblot for PRKD1 protein expression in *Prkd1^{em2}* hearts at E15.5

5.3.13.1 Significant reduction in PRKD1 protein expression was observed in *Prkd1$^{em2/+}$* (HET) and *Prkd1$^{em2/em2}$* (HOMO) hearts compared with WT at E15.5

To compare PRKD1 protein expression in the three groups, western blotting and immunostaining was carried out after extracting protein from individual hearts (n = 3 per group), followed by densitometric analysis. The protein expression data obtained for all the three groups – WT (W = 0.9763, *P* = 0.7046), HET (W = 0.9880, *P* = 0.7900) and HOMO (W = 0.9844, *P* = 0.7606) were normally distributed. Comparison of relative expression of PRKD1 across the three groups, applying one-way ANOVA

showed that there was significant difference among the means of the three groups (*P* = 0.0050). Post hoc-Tukey (multiple comparisons) test showed statistically significant difference between WT & HET, and WT & HOMO (*P* = 0.0058). However, no significant difference was observed between HET & HOMO (*P* = 0.7218) (Figure 5:26**,** Figure 5:27**,** Table 5:13**)**.

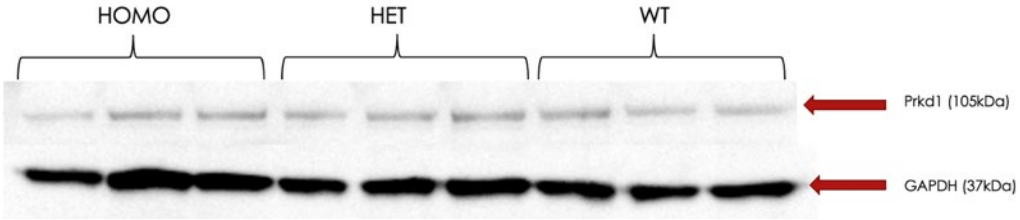


Figure 5:26 Immunoblot of E15.5 mouse heart with point mutation (G598R) in Prkd1 (Prkd1^{em2}). A: The immunoblot is showing bands of PRKD1 and GAPDH (used as loading control) proteins in mouse heart samples (from the three biological and three technical replicates) comparing the three groups (WT, HET and HOMO). Each band in each group represents an individual biological sample, and hence the immunoblot is a single technical replicate. Data not shown for the other two technical replicates. Western blots were cropped for clarity.

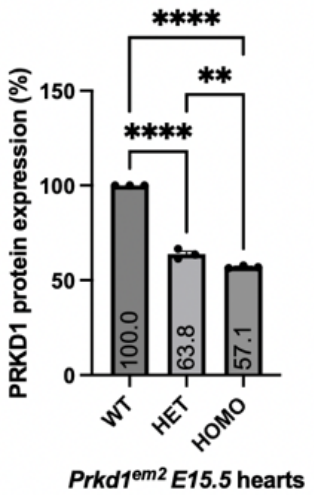


*Figure 5:27 Comparison of normalised protein expression of PRKD1 in E15.5 mouse hearts from Prkd1^{em2} mouse line. The column bar graph showing normalised mean PRKD1 protein expression (n = 3 per group) as percentage (with standard error of means) in Prkd1$^{em2/+}$ (HET) and Prkd1$^{em2/em2}$ (HOMO) hearts compared to Prkd1$^{+/+}$ (WT) (100%), using GAPDH as the reference protein. There was significant reduction in the expression of PRKD1 in Prkd1$^{em2/+}$ (HET) (P < 0.0001) as well as Prkd1$^{em2/em2}$ (HOMO) (P < 0.0001) hearts compared to WT. The reduction was also significant in Prkd1$^{em2/em2}$ (HOMO) hearts compared to Prkd1$^{em2/+}$ (HET) hearts (P = 0.0042). Asterisk = significant P value (**P < 0.005, ****P < 0.0001).*

Groups' comparison	Normalised mean expression (%)		Mean diff. (%)	SE of diff.	95% CI of diff.	P-value
WT vs. HET	WT 100	HET 63.84	36.16	1.263	32.29 to 40.04	<0.0001 (sig)
WT vs. HOMO	WT 100	HOMO 57.06	42.94	1.263	39.06 to 46.81	<0.0001 (sig)
HET vs. HOMO	HET 63.84	HOMO 57.06	6.772	1.263	2.896 to 10.65	0.0042 (sig)

Table 5:13 Comparative mean PRKD1 protein expression in E15.5 hearts from Prkd1^{em2} mouse line. Table showing normalised protein expression of PRKD1 (in percentages) in Prkd1$^{em2/+}$ (HET) and Prkd1$^{em2/em2}$ (HOMO) hearts, compared with Prkd1$^{+/+}$ (WT) and normalised to GAPDH loading control. Expression in WT was taken as 100%. There was significant reduction in the expression of PRKD1 in Prkd1$^{em2/+}$ (HET) (P < 0.0001) and Prkd1$^{em2/em2}$ (HOMO) (P < 0.0001) hearts compared to Prkd1$^{+/+}$ (WT). The reduction in PRKD1 expression in Prkd1$^{em2/em2}$ (HOMO) hearts compared to Prkd1$^{em2/+}$ (HET) was also statistically significant (P = 0.0042). sig: significant; SE: standard error; CI: confidence interval.

The reduction in PRKD1 protein was >36% ($P < 0.0001$) in *Prkd1*$^{em2/+}$ (HET) heart and ~43% ($P < 0.0001$) in *Prkd1*$^{em2/em2}$ (HOMO) heart compared to *Prkd1*$^{+/+}$ (WT). The reduction in HOMO heart was ~7% compared to HET ($P = 0.0042$).

5.4 DISCUSSION, CONCLUSIONS AND PERSPECTIVES FOR FUTURE WORK

In silico analysis

Stable 3D structure of a protein involves interaction among its constituent amino acids as well as with the environment [400-402]. Mutations at the protein surface might have no or least effect in terms of disease causation (though can affect protein-protein interactions [403]) but those present in the core of a protein have been associated with changes in protein stability and hence its conformation/folding and function, resulting in a disease [404, 405]. The G592R mutation is present at ATP binding site in the core of PRKD1 protein in the highly conserved glycine rich loop (G-loop) (with the characteristic consensus GxGxxG sequence) [393] in the kinase domain of PRKD1. Missense mutations at the first and second glycine of this G-loop are more deleterious than those at the third one [406]. In PRKD1, the G592 is the second glycine of this G-loop's consensus sequence. Hence G592R is suggested to be affecting protein stability resulting in potentially adverse effect on its folding and normal function. *In silico* analysis to predict the effect of this mutation also showed that this missense mutation in PRKD1 is pathogenic (Table 5:1). The presence of this missense mutation at the ATP binding site is likely to interfere with the binding and optimal orientation of ATP for catalytic reactions [393, 407]. Replacement of the second glycine of the G-loop in case of G592R possibly results in reduced enzymatic activity as described previously for protein kinases with mutation in this second glycine of the G-

loop [406]. This predicts significant detrimental effect of G592R mutation on the structure and function of the protein, adversely affecting the embryonic survival, growth and normal development as reported in humans [176, 349].

External phenotype of embryos

Skin oedema at the back was noted in 3 *Prkd1*$^{em2/+}$ (HET) and 4 *Prkd1*$^{em2/em2}$ (HOMO) mice (black asterisk in **Figure 5:4**-B). In these seven mice with oedema of the back, CHD was present in 4 of them i.e., 3 *Prkd1*$^{em2/em2}$ (HOMO) and 1 *Prkd1*$^{em2/+}$ (HET) (Table 5:4), whereas the 4th *Prkd1*$^{em2/em2}$ (HOMO) and 2nd *Prkd1*$^{em2/+}$ (HET) with oedema were utilised for experiments other than HREM so they could not subsequently be analysed for the presence of CHD. The third HET with oedema was normal on HREM analysis. In terms of genotype distribution, Het and WT were very similar in terms of oedema at the back with 3 out of 99 *Prkd1*$^{em2/+}$ (HET) and 4 out of 105 WT embryos affected. Previous studies have associated oedema of the skin with defective development of lymphatic vessels in the dermis in different knockout mouse models [408-411]. WNT signalling has been implicated in the differentiation of lymphatic vessels and *Wnt5a* null mouse developed oedema of the dermis due to abnormal development of the dermal lymphatics [408]. PRKD1 inhibition results in inhibition of Wnt5a dependent cellular migration as needed for development of lymphatic vessels [412]. Moreover, VEGF-A has been involved in the development of blood vessels and lymphatics [413]. PRKD1 has been shown to be a target of VEGF-A by mediating

VEGF-induced endothelial cell proliferation and migration [378, 414] whereas inhibition of VEGF-A results in inhibition of proliferation of the lymphatic endothelial cells [415].

Growth retardation was seen in only two HETs and two HOMOs and one WT embryo (Table 5:4).

Survival ratios in mouse embryos and neonates

The *Prkd1*^{em2} mouse model used in this study carried the humanised mutation (HM) - G598R. Survival ratios of *Prkd1*^{em2} mouse embryos at E15.5 showed that PRKD1-HM in homozygous state (*Prkd1*$^{em2/em2}$) is embryonically lethal with incomplete penetrance, as reported earlier too where loss of exons 12-14 in homozygous state, eliminating catalytic domain of PRKD1, resulted in embryonic lethality with incomplete penetrance [341]. PRKD1 is reported to be quite crucial after E9.5 [326] and its loss of function in homozygous state explains the increased lethality at E15.5 in our mouse model.

PRKD1 is ubiquitously expressed in body tissues, beginning as early as E8.5 and is strongly expressed in atria and ventricles at E14.5 [322] as well as in early postnatal heart [321]. This suggests its important role in body systems' development including CVS. The increased lethality in case of these mutations might be due to its adverse effects not only on CVS but other organs/tissues such as brain, since PRKD1 has been associated with disorders of other systems in addition to CHD in patients [176, 349]. PRKD1 has a role in angiogenesis and vasculogenesis, by upregulating transcription of vascular endothelial growth factor receptor – 2 (VEGFR-2) [364]. In case of compromised PRKD1 function due to

this G598R (G592R in humans) missense mutation, the cellular proliferation and regulation of apoptosis, vasculogenesis, angiogenesis, as well as its activity as kinase [304] [365, 366] are likely to be compromised or lost. This also suggests that its role to regulate other signalling pathways [328] would be affected as well. PRKD1 has a role in maintenance of normal cardiac contractility [319, 365] and increased lethality after E12 could be due to cardiac structural defects or conduction problems [239]. Preliminary work from our research collaborators (Cuello and Hitz – personal communication) reports that loss of PRKD1 is associated with arrhythmias and abnormally increased contraction of myocardium. All such potential effects could result in incompatibility with life in case of loss of PRKD1 activity due to this missense mutation. Nevertheless, we were able to collect fifteen *Prkd1*$^{em2/em2}$ (HOMO) embryos at E15.5, with CHD present in 10 of them.

Genotyping of the necrotic/resorbed embryos' material collected at E15.5 showed that the ratios were almost the same in HET (*Prkd1*$^{em2/+}$) (11.11%, n = 11/99) versus HOMO *(Prkd1*$^{em2/em2}$) (13.64%, n = 3/22) mice, suggesting causes other than *Prkd1* mutation in embryos for these earlier embryonic deaths or that HET and HOMO are not different in terms of early death. This could be explained by the possible deleterious effects of PRKD1-mutation on placenta, as PRKD1 is expressed in placenta [416] and mothers were HET. PRKD1 through its role via VEGFR-3 in angiogenesis might have a role in early embryonic lethality in case of PRKD1 mutation [417].

Survival ratios of the neonates from *Prkd1*^{em2} mouse line shows that in the pre-weaning period the overall mortality in this *Prkd1*$^{em2/+}$ mouse line was 22.89%. After genotyping at or near the weaning stage, mortality of *Prkd1*$^{em2/+}$ (HET) mice was nil as in WT. Based on these observations, it seems that PRKD1 has (more) crucial role in early embryonic and neonatal developmental stages which declines with age [321].

Penetrance of CHD

The CHD penetrance in *Prkd1*$^{em2/+}$ (HET) (17.19%) hearts is less than in *Prkd1*$^{em2/em2}$ (HOMO) (66.67%) hearts suggesting that one normal allele is enough to produce normal phenotype in ~83% cases. The presence of more severe phenotype in case of *Prkd1*$^{em2/+}$ (HET) mutation compared to HET mutation in case of LOF of PRKD1 (*Prkd1*$^{em1/+}$) suggests that the G598R mutation (corresponding to G592R in human) alters the function of PRKD1 protein and that the other WT allele is not enough to ensure the normal functioning of PRKD1 as required for normal heart development. It might be due to other factors as well such as modifier genes, epistasis or environment which can potentially modulate the normal copy of the gene in heterozygous (*Prkd1*$^{em2/+}$) state [418]. Despite one normal allele, the allele with missense mutation seems to be very toxic and probably negatively affects the functioning of the normal allele in HET state. Moreover, in PRKD1-G598R mutation in homozygous state, though the decrease in protein level is comparable to that in heterozygous state, the protein produced in case of heterozygous G598R mutation might be quite unstable leading to more damaging phenotype/higher CHD penetrance (compared to *Prkd1*$^{em1/+}$).

Moreover, morphologic analysis showed >33% of *Prkd1*$^{em2/em2}$ (HOMO) hearts had no structural CHD. This led us to speculate that probably other members of PRKD family (PRKD1 & 3), being homologous to PRKD1, [308] might compensate for PRKD1 deficiency.

Expression study for *Prkd1* and its paralogues

Expression studies showed that there was no significant change in *Prkd1* transcript in *Prkd1*$^{em2/+}$ (HET) and *Prkd1*$^{em2/em2}$ (HOMO) hearts at E15.5 (Table 5:10, Figure 5:23). However, the missense mutation of *Prkd1* (G598R) resulted in significant reduction of PRKD1 protein expression in *Prkd1*$^{em2/+}$ (HET) as well as *Prkd1*$^{em2/em2}$ (HOMO) hearts (Figure 5:26, Figure 5:27, Table 5:13). Missense mutations can negatively impact DNA-transcription factors which can result in reduced protein expression [419]. In order to exclude if decreased transcription or unstable mRNA was the cause of reduced protein expression, mRNA transcript analysis was carried by RT-qPCR which showed no significant change in the *Prkd1* transcript in HET and HOMO hearts (Table 5:10, Figure 5:23). This suggests that the missense mutation probably causes production of abnormal PRKD1 protein which stays within the cell, resulting in its reduced expression on western blot [420]. The level of protein reduction in HET and HOMO hearts was comparable (36% versus 43%) (Figure 5:26, Figure 5:27) which indicates that G598R missense mutation in one allele is almost as deleterious as the same involving both alleles.

Expression analysis for transcripts of *Prkd1* paralogues, carried out by qPCR, showed that the other *Prkd* paralogues did not compensate for the deficiency of *Prkd1* (Figure 5:24, Table 5:11, Figure 5:25, Table 5:12).

This suggests that each specific *Prkd* paralogue has a specific and functionally exclusive role(s) [421], working through possibly unique cellular networks [240].

Phenotypes observed on HREM analysis

In this project, CHD was observed in 11/64 (17.19%) *Prkd1*$^{em2/+}$ (HET) hearts (Table 5:6) and 10/15 (66.67%) *Prkd1*$^{em2/em2}$ (HOMO) hearts (Table 5:7) at E15.5 and VSD was present in all of them. Generally, VSD is the most common type of CHD with prevalence of 20-30% in patients [422]. PRKD1 upon activation phosphorylates class II histone deacetylases (HDACs) which results in their dissociation of the myocyte enhancer factor-2 (MEF2) transcription factor, leading to relief of MEF2 repression which would then activate its downstream targets [423]. MEF2C is an important regulator of cardiac myogenesis and right ventricular development [304]. *Mef2c* null mice die at E10 [424] due to defects of cardiac looping, endocardium and myocardium such as cardiomyopathies [425]. KO of *Mef2c* in secondary heart field causes VSDs and defects of the outflow tracts including semilunar valves ([426]. Therefore, loss of relief of MEF2 repression due to *Prkd1* mutation could possibly be one of the mechanisms of VSD or other CHD occurrence in these mice.

TBX5 is a well-established gene related to heart development and its knock out in mouse studies result in VSD [427]. PRKD1, through phosphorylation of HDAC4/5, is known to relieve repression of TBX5 to activate its downstream targets [428]. PRKD1 deficiency preventing TBX5 mediated downstream effects is another potential mechanism of causing CHD.

Our quantitative analysis on E15.5 *Prkd1*^{em2} embryos showed that whole heart and LV wall and IVS underwent thickening in *Prkd1*$^{em2/em2}$ (HOMO) hearts. PRKDs regulate cell motility and migration through their interaction with cofilins which are actin-binding proteins. PRKD, through phosphorylating and activating p21-activated kinase 4 (PAK4), results in phosphorylation of cofilin (rendering it inactive) through activation of LIMK pathway, resulting in decreased directed cellular migration due to no interaction between phosphorylated/inactive cofilin and actin [429]. However, this migration is restored when cofilins are dephosphorylated by slingshot 1L (SSH1L) – a protein phosphatase. SSH1L is a substrate of PRKD and PRKD negatively regulates/inhibits it. PRKD phosphorylation of SSH1L makes it inactive and hence prevents interaction of SSH1L with phosphorylated/inactive cofilin and F-actin [430] (panel A in Figure 5:28). In case of deficiency or absence of PRKD1, this negative regulatory effect of PRKD1 would be deficient. Therefore, PRKD1 mutation is expected to have the role of PRKD1 to be diminished or absent, probably resulting in (abnormally) increased and disorganized directed cellular migration/cell crawling (panel B in Figure 5:28), due to potential impact on dynamics of actin cytoskeleton and actin-associated proteins, resulting in the abnormal gross appearance of *Prkd1*$^{em2/em2}$ (HOMO) hearts. However, a change in heart dimensions was not seen in HET (*Prkd1*$^{em2/+}$) state in both E15.5 and neonates suggest that one normal *Prkd1* allele is sufficient to normally regulate cellular migration during heart development. *Prkd1*$^{em2/em2}$ (HOMO) hearts could not be obtained at neonatal stage for comparative analysis due to time/study limitations.

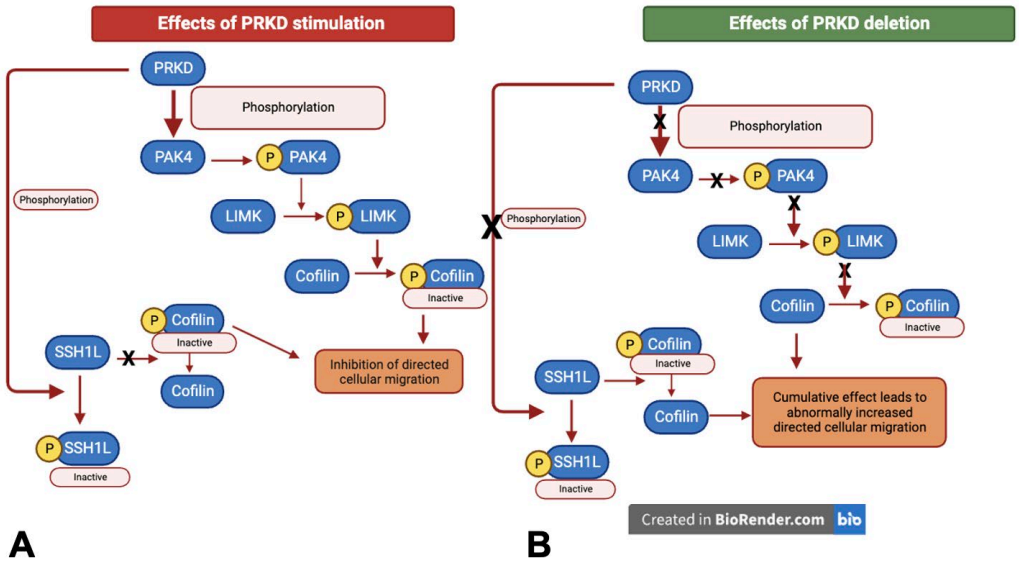


Figure 5:28 Interaction between PRKDs and actin cytoskeleton to regulate directed cellular migration. A: PRKD, through phosphorylating and activating p21-activated kinase 4 (PAK4), results in phosphorylation of cofilin (rendering it inactive) through activation of LIMK pathway, resulting in decreased directed cellular migration due to no interaction between phosphorylated/inactive cofilin and actin. However, this migration is restored when cofilins are dephosphorylated by slingshot 1L (SSH1L) – a protein phosphatase. PRKD phosphorylation makes SSH1L inactive and hence prevents its interaction with phosphorylated/inactive cofilin and F-actin, resulting in inhibition of directed cellular migration. B: PRKD1 mutation is expected to have the role of PRKD1 to be diminished or absent, probably resulting in (abnormally) increased and disorganized directed cellular migration/cell crawling, when the activated cofilins would be increased leading to potential impact on dynamics of actin cytoskeleton and actin-associated proteins. The "x" in the figure denotes the inhibited/absent steps due to upstream changes in normal (A) and mutated (B) states [429, 430]. Figure created in BioRender.com.

As mentioned before, there were 5 out of 10 *Prkd1*$^{em2/em2}$ (HOMO) hearts in which no CHD was identified. However, on quantitative analysis, it was observed that these 5 *Prkd1*$^{em2/em2}$ (HOMO) hearts were also not normal as they had increased heart size as compared to WT hearts (P = 0.0241) (Figure 5:16). The LV total and its muscle volume increased significantly whereas the LV cavity volume decreased (P < 0.05) (Figure 5:17 F-H). Abnormal increase in heart musculature and overall heart size

happens due to upregulation of PRKD1 when the heart must pump against increased peripheral resistance [431]. Absence of PRKD1 should prevent development of pathologic cardiac remodelling/hypertrophy in the face of increased peripheral resistance [318]. However, a recent study reports that PRKD1-KO can still result in hypertrophy and increased heart weight in response to increased peripheral resistance, but the effect is attenuated [392]. It reports further that the loss of PRKD1 is unable to prevent against heart failure and associated arrythmias due to K+ channels downregulation [392]. Moreover, other PRKD paralogues such as PRKD2 and 3 do not compensate for the deficiency or loss of PRKD1 (Figure 5:24, Figure 5:25). However, to address the issue of samples' variability and limitation of smaller sample size (n = 3 for each group) for this analysis, future work with bigger sample size is worth doing.

Even though G598R missense mutation is embryonically lethal, we did get seven liveborn pups which were fertile as well. Their hearts were not analysed. However, extrapolating findings from embryonic study, it could be assumed that they might have some of these CHDs and/or abnormalities of heart size and shape. But since most of these defects are not necessarily and absolutely lethal, some of these *Prkd1*$^{em2/em2}$ (HOMO) pups survived to adulthood.

CONCLUSIONS

Homozygous missense/humanised mutation of *Prkd1* (G598R) is embryonically lethal resulting in reduced Mendelian ratios. Moreover, heterozygous (*Prkd1*$^{em2/+}$) and homozygous (*Prkd1*$^{em2/em2}$) G598R mutations of *Prkd1* result in CHD with incomplete penetrance. Embryonic lethality

and CHD occur probably due to deleterious effect of missense mutation on PRKD1 protein's structural stability and its catalytic activity. Missense mutation probably results in producing abnormal protein, which is retained by the cell, resulting in reduced protein expression in both hetero- (*Prkd1*$^{em2/+}$) and homozygous (*Prkd1*$^{em2/em2}$) hearts. However, one normal allele of *Prkd1,* as in case of heterozygous (*Prkd1*$^{em2/+}$) mutation, can support normal heart development in more than 83% cases. Furthermore, in case of homozygous (*Prkd1*$^{em2/em2}$) mutation with no structural CHD, hypertrophic changes can still occur, possibly due to the residual PRKD1 protein. In case of loss/deficiency of function of PRKD1 at E15.5, there is no compensation by other PRKD paralogues.

FUTURE RECOMMENDATIONS

This study has been pivotal in phenotypically characterising the role of *Prkd1* in heart development and CHD in case of humanised mutation, using HREM. However, further research is warranted aiming to identify the downstream targets of PRKD1 and the signalling pathways through which PRKD1 exerts its effects. Therefore, carrying out transcriptome sequence analysis (RNA-Seq) followed by phosphoproteomics will highly be pertinent as a way forward.

Moreover, determining the expression profile of PRKD1 in specific cardiac progenitor cells will determine its specific role in cardiac development and CHD at cellular level.

Additionally, Single-cell RNA sequencing (scRNA-Seq) can reveal distinct cell populations/lineages and their trajectories related to heart development and CHD. It can unfold the regulatory networks *Prkd1* can

have with other genes on the roadmap of heart development. These and other experiments to look for the downstream targets will be quite helpful to design and execute targeted interventions for therapeutic purposes in cases with *Prkd1* mutations.

6 SUMMARY AND IMPLICATIONS FOR FURTHER RESEARCH

Congenital heart defects occur in ~1% of live-births, making it the most common cause of mortality due to congenital anomalies [132, 159] [101]. One out of 150 babies born in the United Kingdom have CHD with an average of 13 cases per day [160]. Mutations in more than 500 genes have been associated with CHD affecting transcription, cell signalling and chromatin modification (http://www.informatics.jax.org) [170]. Aetiology remains undetermined in about 60% CHD cases due to heterogeneity related to CHD [170, 171, 432, 433], genetic diversity [433] and possibly the role of environment [434]. Recurrence risks of CHD are relatively low, such that it is reasonable to consider CHD as a complex trait to which both genetic and environmental factors contribute [434-436]. In case of CHD, maternal diabetes mellitus, phenylketonuria, and certain medications taken by the mother [434, 437] as well as maternal obesity might have a role [183, 434, 438, 439]. With increase in global trend towards obesity and increased incidence and prevalence of diabetes mellitus, amongst others, future work on these (or even other) transgenic mice should also look at the role of these and the relation of genetic and environmental factors (particularly diabetes mellitus and obesity) in the causation of CHD.

Several studies have focussed on whole exome sequencing (WES) of large cohorts having CHD, aiming to find some novel genes [172, 440]. A similar WES of 1891 probands with NS-CHD and S-CHD was carried

out through widespread collaboration under the umbrella of the Deciphering Developmental Disorders (DDD) study to which our lab was part of [176]. This study reported that there was a role of inherited mutations in the occurrence of NS-CHD. This study came up with the identification of three novel human S-CHD genes such as cyclin dependant kinase 13 (*CDK13),* chromodomain helicase DNA binding protein 4 *(CHD4)* and protein kinase D1 (*PRKD1)* [176] [171]. The main goal of this thesis was to characterise the role of CDK13 and PRKD1 in heart development and CHD in mouse models.

In the first part of thesis, transgenic mouse model carrying loss of function (LOF) mutation in *Cdk13* was studied. It was generated by the European Conditional Mouse Mutagenesis (EUCOMM) program and bred at the University of Nottingham. The results from this study revealed that mice with heterozygous (*Cdk13*$^{tm1b/+}$) mutation of *Cdk13* were viable and fertile. Lethality assessment at E12.5 and E15.5 showed that the homozygous (*Cdk13*$^{tm1b/tm1b}$) mutation of *Cdk13* is embryonically lethal. i.e., they die at an early embryonic stage. Stage E15.5 was more deleterious than E12.5. On HREM-based phenotypic analysis, the penetrance of CHD was 17% (8/47) in *Cdk13*$^{tm1b/+}$ (HET) and 100% (4/4) in *Cdk13*$^{tm1b/tm1b}$ (HOMO) mouse. Almost fifty percent of the embryos with *Cdk13*$^{tm1b/tm1b}$ (HOMO) mutation were growth retarded compared with only 3.6% in case of *Cdk13*$^{tm1b/+}$ (HET) mutation. Expression studies using X-Gal staining and qPCR showed *Cdk13* expression at different stages. At E10.5, was quite distinctly localised and ubiquitous in heart/pericardium and in the 1st pharyngeal arch area (mandibular and maxillary processes/facial

skeleton), neck structures including laryngeal cartilages and trachea. In our mouse, midfacial aplasia was seen only in *Cdk13*$^{tm1b/tm1b}$ (HOMO) mice at both E12.5 and E15.5. Studies in humans already associated CDK13 mutation with developmental disorders affecting heart, brain and facial skeleton but with incomplete penetrance [176, 213, 214]. At E12.5, *Cdk13* expression was ubiquitous as well as very strong throughout the embryo including heart. *Cdk13* expression was ubiquitous in heart/pericardium at E15.5 as well. X-Gal staining of adult *Cdk13*$^{tm1b/+}$ (HET) hearts showed that there was a strong expression of *Cdk13* in atria, pulmonary trunk and aorta whereas no expression in ventricles probably was due to firmer adult ventricular tissue. Transcript expression analysis by qPCR showed that there was significant reduction of *Cdk13* expression in *Cdk13*$^{tm1b/tm1b}$ (HOMO) compared to WT and HET hearts. The change was not significant in HET hearts at all stages (E10.5, E12.5, E15.5 and adult). These findings correspond with the non-viability and complete CHD penetrance in case of *Cdk13*$^{tm1b/tm1b}$ (HOMO) mutation. RNA sequencing transcriptome analysis also showed significant modulation of expression of genes related to heart development i.e., there was significant enrichment of heart related GO terms in *Cdk13*$^{tm1b/tm1b}$ (HOMO) compared to WT hearts at E12.5. Some of the key targets were further validated by qPCR and W-ISH. This study gives systematic insight into the role of CDK13 in heart development and CHD which will inform planning for further characterization of its role at molecular level.

In the second and third parts of thesis, role of PRKD1 in heart development and CHD was investigated. The phenotype associated with PRKD1

mutation was less characterized though recent studies associate it with characteristic facial features, CHD and ectodermal dysplasia [175, 176, 349]. There is a mutational spectrum including both missense and loss of function variants in case of PRKD1 (Fig 3.7 & Table 3.1). The most common CHD in these was pulmonary stenosis, present in 7/49 (14.3%) cases followed by individual septal defects (4 each of ASD and VSD). In the second part of the thesis, transgenic mouse model carrying loss of function (LOF) mutation in *Prkd1* was studied. It was generated at Wellcome Trust Sanger Institute (*Wtsi*) UK and bred at the University of Nottingham. Although we have found that the *Prkd1*^{em1} homozygous embryo can survive to E15.5, they are at reduced frequency compared to controls, with just 4.7% of embryos being homozygous (*Prkd1*$^{em1/em1}$) (Table 4:3). We have never had a homozygous (*Prkd1*$^{em1/em1}$) mouse survive to notching, which we perform at around P10-12. However, in the postnatal study in this mouse, one of the P7 mouse was in fact homozygous (Table 4:8). Most (12 out of 15, 80%) *Prkd1*$^{em1/em1}$ (HOMO) embryos had abnormal external phenotype at the time of collection (Table 1:4), with 11/15 (73.3%) being growth retarded (Figure 4:9 C compared with A,B and F compared with C,D) and another having oedema of the back (Fig 4:10C). On the other hand, only 4 heterozygous (*Prkd1*$^{em1/+}$) embryos had abnormal external phenotype at the time of collection, with oedema of the back in two (Fig 4:10B), and growth retardation and hemopericardium (Fig 4:11) in two other different heterozygous hearts. On HREM analysis, CHD penetrance in heterozygous (*Prkd1*$^{em1/+}$) hearts was just 1.82% (i.e., muscular VSD in one out of the 155 hearts), whereas 5 out of 6 (83.3%)

homozygous (*Prkd1*$^{em1/em1}$) hearts had CHD. The one P7 homozygous heart had features resembling bilateral outlet obstruction, smaller ventricular cavity sizes and poorly defined trabeculation of the myocardium (Figures 4:20D and F compared to C and E), resembling those seen in severe and often lethal Noonan's syndrome or other RAS-opathies [360, 361]. Pulmonary stenosis (PS) was the most common phenotype seen in patients (Table 1:4). Mutations in RAS/MAPK cell signalling pathway, or 'RAS-opathies', are associated with PS; these include Noonan and Leopard syndromes [384, 386]. PRKD1 is also associated with the regulation of RAS signalling [441]. Interestingly, RAS/MAPK regulates MEF2 resulting in hypertrophic cardiomyopathy (HCM) in some individuals with RAS-opathies [388]. PRKD1 also regulates MEF2c [442] [318]. Further, RAS-opathies are associated with specific cancers (benign or malignant) [389]. PRKD1 has been shown to be downregulated in some types of cancers and overexpressed in others and is associated with many cancer-related signaling pathways [308]. Many of the CHD's and myocardial differences seen in Noonan syndrome and other RAS-opathies, were seen in the *Prkd1*^{em1} hearts, including likely PS, AVSDs and VSDs [384, 386]. Taking together all these factors, we suggest that *Prkd1* may be another gene associated with RAS-opathy type phenotypes [389]. Investigating the potential effects of PRKD1 on its various downstream targets (and possibly upstream regulators) could explain reliably the potential role of PRKD1 in the specific phenotypes seen in our HREM based phenotypic analysis.

In the third part of the thesis, mouse model with PRKD-point mutation (G598R) was studied. This corresponded to G592R mutation in humans which was the most common type of coding SNV in patients (Fig 3.7 & Table 3.1). Having very few patients with mutation, it was quite interesting to characterise the role of this SNV in CHD in a mouse model. *In silico* analysis and location of this missense mutation in kinase domain, it is proposed that this mutation would interfere with the catalytic function of PRKD1. Embryos with homozygous mutation of *Prkd1* (*Prkd1*$^{em2/em2}$) died early during intrauterine life (Chi square test, P = 0.0061), though those with heterozygous mutation (*Prkd1*$^{em2/+}$) were viable and fertile. However, fifteen viable homozygous (*Prkd1*$^{em2/em2}$) mice at E15.5 and six live-born pups surviving into adulthood were seen (Table 5:3). Skin oedema at the back was noted in 3 *Prkd1*$^{em2/+}$ (HET) and 4 *Prkd1*$^{em2/em2}$ (HOMO) mice (black asterisk in Figure 5:4-B). Skin oedema has been attributed to defective development of lymphatic vessels in the dermis as seen in different knockout mouse models [408-411]. In these seven mice with oedema of the back, CHD was present in 4 of them (Table 5:5). This suggests involvement of some key targets having shared impact on heart and lymphatic system development *[*413, 443*]*. Loss of PRKD1 results in inhibition of WNT5A dependent cellular migration as needed for development of lymphatic vessels [412]. Moreover, loss of PRKD1 would cause dysregulated development of second heart field through WNT5A along with WNT11 *[*443*].* Further, VEGF-A has got a critical role in heart as well as blood vessels and lymphatics development [413]. PRKD1 has been shown to be a target of VEGF-A [378, 414] and hence loss of PRKD1

could possibly prevent the role of VEGF-A in heart and lymphatic development [415]. Growth retardation was seen in only two hetero- and two homozygotes and one WT embryo which suggests that intrauterine growth retardation is not a main phenotype associated with *Prkd1*-HM. The CHD penetrance in *Prkd1*$^{em2/+}$ (HET) (11/64, 17.19%) hearts (Table 5:6) was less than in *Prkd1*$^{em2/em2}$ (HOMO) (10/15, 66.67%) hearts (Table 5:7) suggesting that one WT allele was enough to produce normal phenotype in ~83% cases. However, the presence of more severe phenotype in case of *Prkd1*$^{em2/+}$ (HET) mutation compared to HET mutation in case of LOF of PRKD1 (*Prkd1*$^{em1/+}$) suggests that the G598R mutation (corresponding to G592R in human) is more deleterious. At transcript level in *Prkd1*^{em2} mouse, no significant difference among the three experimental groups (WT, HET, HOMO) was seen (Figure 5:23, Table 5:10). However, at protein level, there was significant reduction in HET (*Prkd1*$^{em2/+}$) and HOMO (*Prkd1*$^{em2/em2}$) hearts compared to WT (*Prkd1*$^{+/+}$) as well as HOMO (*Prkd1*$^{em2/em2}$) compared to HET (*Prkd1*$^{em2/+}$) hearts (Table 5:13, Figure 5:26, Figure 5:27), with no compensation by *Prkd2* and *Prkd3* (Figure 5:24*,* Figure 5:25*)*. Our quantitative analysis on E15.5 *Prkd1*^{em2} embryos showed that the RV & LV walls, underwent thickening in *Prkd1*$^{em2/em2}$ (HOMO) hearts with (Figure 5:17) and without CHD (Figure 5:18), resulting in increased heart size in *Prkd1*$^{em2/em2}$ (HOMO) mice (panel “J” in Figure 5:17 & Figure 5:18). This finding was quite surprising and future work could focus on looking if humanised mutation in PRKD1 (G598R) is associated with cardiac hypertrophy. Looking at the protein-protein interaction of PRKD1 in humans, Figure 4:26 shows the predicted

functional partners of PRKD1 with significant protein-protein interactions (PPI) (*P* - value = 3.18e-05) [240]. Moreover, significant enrichment of Gene Ontology (GO) terms related to developmental processes including heart morphogenesis, neural crest differentiation, abnormality of cardiac septa and valves, patent foramen ovale, cardiomyopathy and cardiac hypertrophy was seen [240]. Single-cell RNA sequencing (scRNA-Seq) can reveal distinct cell lineages related to heart development and CHD. Moreover, it can unfold the networks in which *Prkd1* plays its role on the roadmap of heart development.

The mothers (dams and breeders) used for the experiments in the three mouse lines were mostly HET (occasionally WT for colony maintenance) but fertile - being possibly mild HET. No apparent gross phenotypic abnormality was seen in these breeders too, except one pregnant *Cdk13* HET mouse which developed severe hydrocephaly while pregnant (Figure 3:8) and had to be culled before littering down. Moreover, ~82% of mice with *Cdk13*-LOF (n = 39/47) and *Prkd1*-HM (n = 53/64), and 98% of mice with *Prkd1*-LOF mutation (n = 54/55) had no CHD. This suggests that presence of one normal *Cdk13* and *Prkd1* alleles respectively seemed enough to ensure normal function of CDK13 and PRKD1, as in the HET mothers as well in HET embryos of these respective lines which had normal Mendelian ratios (Table 3:2, Table 4:3, Table 5:2) and incomplete CHD penetrance (Table 3:5, Table 4:6, Table 5:6).

Based on gender distribution (where reported) of *Cdk13* (section 3.1.2) and *Prkd1* patients (section 4.1.5), male and females were alike, whereas in *Prkd1*^{em2} *and Cdk13*^{tm1b} mice with CHD, more males were affected (11

males versus 6 females in *Prkd1*^{em2}, and 6 males versus 3 females in *Cdk13*^{tm1b}) (sections 5.3.11& 3.3.7 respectively). This suggests the possibility that female mice with severe disease especially with homozygous mutation might have died quite early on. Future experiments could do gender-genotyping of the necrotic/resorbed embryos as well to get better information in this regard. Female HET mice with possibly milder phenotype could breed almost normally hence enabling such HET mothers to be used for HET X HET matings in this study. In humans, most of the adults with CHD are detected incidentally having milder phenotype and among them, > 63% are female [444]. Therefore, true prevalence of CHD in female might be higher.

In mice and some other mammals, females are promiscuous (to mate with multiple males) which is expected to increase genetic variability, reproductive success, and increased litter size [445-447], the latter is partly due to confused paternity and hence acceptability by the infanticidal males [448]. Nevertheless, according to some, multi-male mating (MMM) would reduce effective population size because of fewer offspring per male (reviewed in [449]. The pups in any litter therefore might differ (both in number and genetic variability) from those in a different litter where chances of MMM and number of males involved might vary. Another idea in support of this is that littermates share possibly the same genetic background and same environment with possible effect on developmental outcome [450]. Therefore, offspring from different litters might differ from each other though even littermates can differ in genetic make-up [451]. This potentially makes it relevant and useful to analyse the genotype

ratios and lethality in an individual litter rather than as collective ratios for all litters. In our case, this variability was at least partially controlled by mating two females with a single stud for couple of matings. However, it was beyond the scope of this study to assess the effects of paternity on genetic variability and hence survival.

Overall, the results of these *in vivo* characterisation studies support the critical roles of *Cdk13* and *Prkd1* in heart development and CHD. To our knowledge, HREM technology has been used for the first time by our group to study heart and CHD phenotypes related to mutations in both *Cdk13* and *Prkd1*. This technology has enabled identification of several specific and complex CHD phenotypes which would add to the phenotypic repertoire of the mutations in these genes. Moreover, the resemblance of some phenotypes to the known syndromes (e.g., Noonan syndrome) provide insight into the key molecular players of those syndromes and their potential relation to these genes. We showed that the most common mutation of *Prkd1* (G592R) in heterozygous state was very deleterious in terms of CHD and the protein was significantly reduced in heterozygous, as in homozygous hearts. Moreover, to our knowledge, there has been only one other study so far [211], after its identification as a novel gene [176], which looked at the role of *Cdk13* in mouse models (which were different to ours though). In addition to HREM-based phenotypic characterisation, we looked at the *Cdk13* expression at different stages by X-Gal staining and RT-qPCR. X-Gal staining gave quite interesting results in terms of varied expression at E10.5 compared to later stages. Moreover, in order to identify downstream targets of *Cdk13* as related to

heart development and CHD, RNA-Seq was carried out for the first time in any *Cdk13*-mutant mouse model which identified key targets related to heart development and CHD. These targets would help understand the molecular basis of heart development and CHD and would open avenues for further research to identify key players on the roadmap to heart development and CHD.

Using mouse models to characterise the role of *Cdk13* and *Prkd1* has provided a useful insight into the role of these genes in heart development and CHD. However, the variability in penetrance and types of CHD phenotypes in the mutant mice could be due to differences in the biology between human and mouse [185]. Moreover, the vital genes in the developmental network related to heart development and the CHD might interact with a different set of genes in mouse compared to humans, resulting in varied CHD phenotypes (with varied prevalence) in the two species [186].

7 APPENDIX

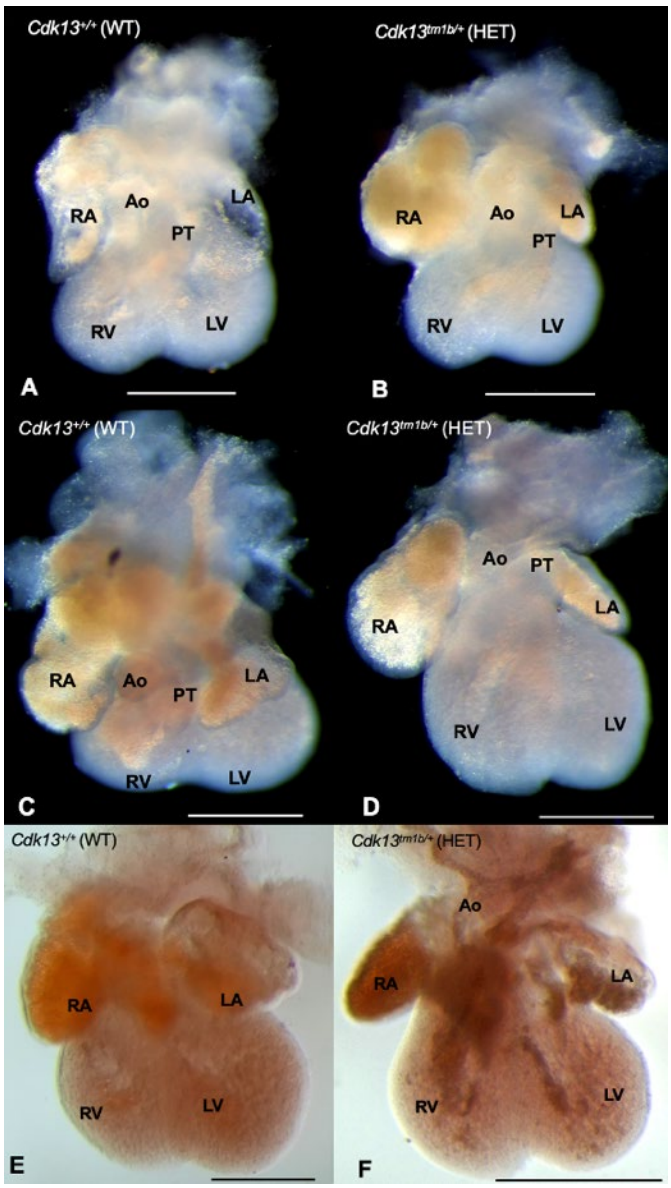


Figure 7:1 Results of sense probes from in situ hybridization experiments on Cdk13^{tm1b} mouse. Wild type and heterozygous(Cdk13$^{tm1b/+)}$ hearts are shown for each sense probes. A-B are wild type and het hearts applied with sense probe for Eln; C-D are for Sall4 and E-F for Notch2. Scale bar for each image = 500μm. RA: right atrium, LA: left atrium, Ao: aorta, PT: pulmonary trunk, RV: right ventricle, LV: left ventricle.

8 REFERENCES

1. Wittig, J.G. and A. Münsterberg, *The Early Stages of Heart Development: Insights from Chicken Embryos.* J Cardiovasc Dev Dis, 2016. **3**(2).
2. Bruneau, B.G., *Signaling and transcriptional networks in heart development and regeneration.* Cold Spring Harb Perspect Biol, 2013. **5**(3): p. a008292.
3. Bruneau, B.G., *The developmental genetics of congenital heart disease.* Nature, 2008. **451**(7181): p. 943-948.
4. Valenti, O., et al., *Fetal cardiac function during the first trimester of pregnancy.* J Prenat Med, 2011. **5**(3): p. 59-62.
5. Brade, T., et al., *Embryonic heart progenitors and cardiogenesis.* Cold Spring Harb Perspect Med, 2013. **3**(10): p. a013847.
6. Buckberg, G.D., et al., *What Is the Heart? Anatomy, Function, Pathophysiology, and Misconceptions.* J Cardiovasc Dev Dis, 2018. **5**(2).
7. Solnica-Krezel, L. and D.S. Sepich, *Gastrulation: making and shaping germ layers.* Annu Rev Cell Dev Biol, 2012. **28**: p. 687-717.
8. Sadler, T.W., *Langman's Medical Embryology*. 14th ed. 2019, Philadelphia, USA.: Wolters Kluwer. 432.
9. Kuhn, E.N. and S.M. Wu, *Origin of cardiac progenitor cells in the developing and postnatal heart.* J Cell Physiol, 2010. **225**(2): p. 321-5.
10. Sylva, M., M.J.B. van den Hoff, and A.F.M. Moorman, *Development of the human heart.* American Journal of Medical Genetics Part A, 2014. **164**(6): p. 1347-1371.
11. Sakabe, M., et al., *Understanding heart development and congenital heart defects through developmental biology: A segmental approach.* Congenital Anomalies, 2005. **45**(4): p. 107-118.
12. Kelly, R.G., M.E. Buckingham, and A.F. Moorman, *Heart fields and cardiac morphogenesis.* Cold Spring Harb Perspect Med, 2014. **4**(10).
13. Meilhac, S.M. and M.E. Buckingham, *The deployment of cell lineages that form the mammalian heart.* Nature Reviews Cardiology, 2018. **15**(11): p. 705-724.
14. Klaus, A., et al., *Wnt/β-catenin and Bmp signals control distinct sets of transcription factors in cardiac progenitor cells.* Proceedings of the National Academy of Sciences, 2012. **109**(27): p. 10921-10926.
15. Ratajska, A., et al., *Vasculogenesis of the embryonic heart: Origin of blood island-like structures.* The Anatomical Record Part A: Discoveries in Molecular, Cellular, and Evolutionary Biology, 2006. **288A**(3): p. 223-232.

16. Kruithof, B.P.T., et al., *Cardiac muscle cell formation after development of the linear heart tube.* Developmental Dynamics, 2003. **227**(1): p. 1-13.
17. Kloesel, B., J.A. DiNardo, and S.C. Body, *Cardiac Embryology and Molecular Mechanisms of Congenital Heart Disease: A Primer for Anesthesiologists.* Anesth Analg, 2016. **123**(3): p. 551-69.
18. Moore, K.L., T.V.N. Persaud, and M.G. Torchia, *The Developing Human - E-Book: Clinically Oriented Embryology*. 2018: Elsevier Health Sciences.
19. Yamagishi, H., et al., *Molecular embryology for an understanding of congenital heart diseases.* Anatomical Science International, 2009. **84**(3): p. 88-94.
20. Schlueter, J. and T. Brand, *Subpopulation of Proepicardial Cells Is Derived From the Somatic Mesoderm in the Chick Embryo.* Circulation Research, 2013. **113**(10): p. 1128-1137.
21. Nahirney, P.C., T. Mikawa, and D.A. Fischman, *Evidence for an extracellular matrix bridge guiding proepicardial cell migration to the myocardium of chick embryos.* Developmental Dynamics, 2003. **227**(4): p. 511-523.
22. Männer, J., *Does the subepicardial mesenchyme contribute myocardioblasts to the myocardium of the chick embryo heart? A quail-chick chimera study tracing the fate of the epicardial primordium.* The Anatomical Record, 1999. **255**(2): p. 212-226.
23. Mikawa, T. and R.G. Gourdie, *Pericardial Mesoderm Generates a Population of Coronary Smooth Muscle Cells Migrating into the Heart along with Ingrowth of the Epicardial Organ.* Developmental Biology, 1996. **174**(2): p. 221-232.
24. Dettman, R.W., et al., *Common Epicardial Origin of Coronary Vascular Smooth Muscle, Perivascular Fibroblasts, and Intermyocardial Fibroblasts in the Avian Heart.* Developmental Biology, 1998. **193**(2): p. 169-181.
25. Tallquist, M.D., *Developmental Pathways of Cardiac Fibroblasts.* Cold Spring Harb Perspect Biol, 2020. **12**(4).
26. Haack, T. and S. Abdelilah-Seyfried, *The force within: endocardial development, mechanotransduction and signalling during cardiac morphogenesis.* Development, 2016. **143**(3): p. 373-386.
27. Quijada, P., M.A. Trembley, and E.M. Small, *The Role of the Epicardium During Heart Development and Repair.* Circulation Research, 2020. **126**(3): p. 377-394.
28. Stankunas, K., et al., *Endocardial Brg1 represses ADAMTS1 to maintain the microenvironment for myocardial morphogenesis.* Dev Cell, 2008. **14**(2): p. 298-311.
29. Cho, E., et al., *Cardiac-specific developmental and epigenetic functions of Jarid2 during embryonic development.* J Biol Chem, 2018. **293**(30): p. 11659-11673.
30. Moorman, A., et al., *Development of the heart: (1) formation of the cardiac chambers and arterial trunks.* Heart, 2003. **89**(7): p. 806-14.

31. Buijtendijk, M.F.J., P. Barnett, and M.J.B. van den Hoff, *Development of the human heart.* American Journal of Medical Genetics Part C: Seminars in Medical Genetics, 2020. **184**(1): p. 7-22.
32. Krishnan, A., et al., *A detailed comparison of mouse and human cardiac development.* Pediatr Res, 2014. **76**(6): p. 500-7.
33. Männer, J., *The anatomy of cardiac looping: A step towards the understanding of the morphogenesis of several forms of congenital cardiac malformations.* Clinical Anatomy, 2009. **22**(1): p. 21-35.
34. Hirokawa, N., et al., *Nodal Flow and the Generation of Left-Right Asymmetry.* Cell, 2006. **125**(1): p. 33-45.
35. Shiraishi, I. and H. Ichikawa, *Human Heterotaxy Syndrome - From Molecular Genetics to Clinical Features, Management, and Prognosis &ndash.* Circulation Journal, 2012. **76**(9): p. 2066-2075.
36. Ryan, A.K., et al., *Pitx2 determines left–right asymmetry of internal organs in vertebrates.* Nature, 1998. **394**(6693): p. 545-551.
37. Weiss, A. and L. Attisano, *The TGFbeta Superfamily Signaling Pathway.* WIREs Developmental Biology, 2013. **2**(1): p. 47-63.
38. Weninger, W.J., et al., *Cited2 is required both for heart morphogenesis and establishment of the left-right axis in mouse development.* Development, 2005. **132**(6): p. 1337-1348.
39. Breckenridge, R.A., T.J. Mohun, and E. Amaya, *A role for BMP signalling in heart looping morphogenesis in Xenopus.* Dev Biol, 2001. **232**(1): p. 191-203.
40. Ramsdell, A.F., *Left–right asymmetry and congenital cardiac defects: Getting to the heart of the matter in vertebrate left–right axis determination.* Developmental Biology, 2005. **288**(1): p. 1-20.
41. Habib, A., et al., *The anatomy of the coronary sinus venous system for the cardiac electrophysiologist.* EP Europace, 2009. **11**(suppl_5): p. v15-v21.
42. Faber, J.W., et al., *Sinus venosus incorporation: contentious issues and operational criteria for developmental and evolutionary studies.* J Anat, 2019. **234**(5): p. 583-591.
43. Wolters, R., et al., *Role of the Epicardium in the Development of the Atrioventricular Valves and Its Relevance to the Pathogenesis of Myxomatous Valve Disease.* Journal of Cardiovascular Development and Disease, 2021. **8**(5): p. 54.
44. Annabi, M.R.K., C.C.; Makaryus, A.N. , *Embryology: Atrioventricular Septum*. StatPearls [Internet]. . 2022, Treasure Island, Florida, USA.: StatPearls Publishing LLC.
45. Deepe, R., et al., *The Mesenchymal Cap of the Atrial Septum and Atrial and Atrioventricular Septation.* J Cardiovasc Dev Dis, 2020. **7**(4).
46. Wessels, A. and D. Sedmera, *Developmental anatomy of the heart: a tale of mice and man.* Physiological Genomics, 2003. **15**(3): p. 165-176.
47. Sylva, M., M.J. van den Hoff, and A.F. Moorman, *Development of the human heart.* Am J Med Genet A, 2014. **164a**(6): p. 1347-71.

48. Wessels, A., et al., *The Development of the Atrioventricular Junction in the Human Heart.* Circulation Research, 1996. **78**(1): p. 110-117.
49. Wessels, A., et al., *Epicardially derived fibroblasts preferentially contribute to the parietal leaflets of the atrioventricular valves in the murine heart.* Developmental Biology, 2012. **366**(2): p. 111-124.
50. Lin, C.J., et al., *Partitioning the heart: mechanisms of cardiac septation and valve development.* Development, 2012. **139**(18): p. 3277-99.
51. Wessels, A., et al., *Atrial development in the human heart: An immunohistochemical study with emphasis on the role of mesenchymal tissues.* The Anatomical Record, 2000. **259**(3): p. 288-300.
52. Anderson, R.H., et al., *Development of the heart: (2) Septation of the atriums and ventricles.* Heart, 2003. **89**(8): p. 949-58.
53. Robert, H.A., A.B. Nigel, and W. Sandra, *Development and structure of the atrial septum.* Heart, 2002. **88**(1): p. 104.
54. Snarr, B.S., et al., *A spatiotemporal evaluation of the contribution of the dorsal mesenchymal protrusion to cardiac development.* Developmental Dynamics, 2007. **236**(5): p. 1287-1294.
55. Kim, J.-S., et al., *Development of the Myocardium of the Atrioventricular Canal and the Vestibular Spine in the Human Heart.* Circulation Research, 2001. **88**(4): p. 395-402.
56. Schleich, J.-M., et al., *An overview of cardiac morphogenesis.* Archives of Cardiovascular Diseases, 2013. **106**(11): p. 612-623.
57. Steimle, J.D. and I.P. Moskowitz, *TBX5: A Key Regulator of Heart Development.* Curr Top Dev Biol, 2017. **122**: p. 195-221.
58. Zhang, K.K., et al., *Gene network and familial analyses uncover a gene network involving Tbx5/Osr1/Pcsk6 interaction in the second heart field for atrial septation.* Hum Mol Genet, 2016. **25**(6): p. 1140-51.
59. Zhou, L., et al., *Gata4 potentiates second heart field proliferation and Hedgehog signaling for cardiac septation.* Proc Natl Acad Sci U S A, 2017. **114**(8): p. E1422-e1431.
60. Posch, M.G., et al., *Molecular genetics of congenital atrial septal defects.* Clin Res Cardiol, 2010. **99**(3): p. 137-47.
61. Budde, B.S., et al., *Noncompaction of the ventricular myocardium is associated with a de novo mutation in the beta-myosin heavy chain gene.* PLoS One, 2007. **2**(12): p. e1362.
62. Monserrat, L., et al., *Mutation in the alpha-cardiac actin gene associated with apical hypertrophic cardiomyopathy, left ventricular non-compaction, and septal defects.* Eur Heart J, 2007. **28**(16): p. 1953-61.
63. Briggs, L.E., et al., *Expression of the BMP receptor Alk3 in the second heart field is essential for development of the dorsal mesenchymal protrusion and atrioventricular septation.* Circ Res, 2013. **112**(11): p. 1420-32.

64. Waldo, K., et al., *Cardiac neural crest cells provide new insight into septation of the cardiac outflow tract: aortic sac to ventricular septal closure.* Dev Biol, 1998. **196**(2): p. 129-44.
65. Koshiba-Takeuchi, K., et al., *Reptilian heart development and the molecular basis of cardiac chamber evolution.* Nature, 2009. **461**(7260): p. 95-8.
66. Rana, M.S., V.M. Christoffels, and A.F.M. Moorman, *A molecular and genetic outline of cardiac morphogenesis.* Acta Physiologica, 2013. **207**(4): p. 588-615.
67. Dyer, L.A. and M.L. Kirby, *The role of secondary heart field in cardiac development.* Dev Biol, 2009. **336**(2): p. 137-44.
68. Zaffran, S. and R.G. Kelly, *New developments in the second heart field.* Differentiation, 2012. **84**(1): p. 17-24.
69. Bertrand, N., et al., *Hox genes define distinct progenitor sub-domains within the second heart field.* Developmental Biology, 2011. **353**(2): p. 266-274.
70. Neeb, Z., et al., *Cardiac outflow tract anomalies.* Wiley Interdiscip Rev Dev Biol, 2013. **2**(4): p. 499-530.
71. Anderson, R.H., et al., *Development of the heart: (3) formation of the ventricular outflow tracts, arterial valves, and intrapericardial arterial trunks.* Heart, 2003. **89**(9): p. 1110-8.
72. Robert, H.A., *Anderson - Morphology series*, in *Cradiac development* H.A. Robert, Editor. 2021, Congenital Heart Academy.
73. Jiang, X., et al., *Fate of the mammalian cardiac neural crest.* Development, 2000. **127**(8): p. 1607-1616.
74. Kirby, M.L., T.F. Gale, and D.E. Stewart, *Neural crest cells contribute to normal aorticopulmonary septation.* Science, 1983. **220**(4601): p. 1059-61.
75. Vincentz, J.W., et al., *HAND transcription factors cooperatively specify the aorta and pulmonary trunk.* Dev Biol, 2021. **476**: p. 1-10.
76. Schleich, J.-M., *Development of the human heart: days 15–21.* Heart, 2002. **87**(5): p. 487-487.
77. Kau, T., et al., *Aortic development and anomalies.* Semin Intervent Radiol, 2007. **24**(2): p. 141-52.
78. Anderson, R.H. and S.D. Bamforth, *Morphogenesis of the Mammalian Aortic Arch Arteries.* Frontiers in Cell and Developmental Biology, 2022. **10**.
79. Graham, A., et al., *A reappraisal and revision of the numbering of the pharyngeal arches.* Journal of Anatomy, 2019. **235**(6): p. 1019-1023.
80. Pucéat, M., *Embryological origin of the endocardium and derived valve progenitor cells: From developmental biology to stem cell-based valve repair.* Biochimica et Biophysica Acta (BBA) - Molecular Cell Research, 2013. **1833**(4): p. 917-922.
81. Aikawa, E., et al., *Human Semilunar Cardiac Valve Remodeling by Activated Cells From Fetus to Adult.* Circulation, 2006. **113**(10): p. 1344-1352.

82. Hinton, R.B., et al., *Extracellular Matrix Remodeling and Organization in Developing and Diseased Aortic Valves.* Circulation Research, 2006. **98**(11): p. 1431-1438.
83. Fisher, S.A., B.L. Langille, and D. Srivastava, *Apoptosis During Cardiovascular Development.* Circulation Research, 2000. **87**(10): p. 856-864.
84. MacGrogan, D., et al., *How to make a heart valve: from embryonic development to bioengineering of living valve substitutes.* Cold Spring Harb Perspect Med, 2014. **4**(11): p. a013912.
85. Butcher, J.T. and R.R. Markwald, *Valvulogenesis: the moving target.* Philosophical Transactions of the Royal Society B: Biological Sciences, 2007. **362**(1484): p. 1489-1503.
86. Restivo, A., et al., *Cardiac outflow tract: A review of some embryogenetic aspects of the conotruncal region of the heart.* The Anatomical Record Part A: Discoveries in Molecular, Cellular, and Evolutionary Biology, 2006. **288A**(9): p. 936-943.
87. Okamoto, N., et al., *Formal genesis of the outflow tracts of the heart revisited: Previous works in the light of recent observations.* Congenital Anomalies, 2010. **50**(3): p. 141-158.
88. Mifflin, J.J., et al., *Intercalated cushion cells within the cardiac outflow tract are derived from the myocardial troponin T type 2 (Tnnt2) Cre lineage.* Dev Dyn, 2018. **247**(8): p. 1005-1017.
89. Wu, B., et al., *Nfatc1 coordinates valve endocardial cell lineage development required for heart valve formation.* Circ Res, 2011. **109**(2): p. 183-92.
90. Phoon, C.K., et al., *Embryonic heart failure in NFATc1−/− mice: novel mechanistic insights from in utero ultrasound biomicroscopy.* Circulation research, 2004. **95**(1): p. 92-99.
91. Stankunas, K., et al., *VEGF signaling has distinct spatiotemporal roles during heart valve development.* Dev Biol, 2010. **347**(2): p. 325-36.
92. Krishnan, A., et al., *A detailed comparison of mouse and human cardiac development.* Pediatric Research, 2014. **76**(6): p. 500-507.
93. Tyser, R.C.V., et al., *Calcium handling precedes cardiac differentiation to initiate the first heartbeat.* eLife, 2016. **5**: p. e17113.
94. Finnemore, A. and A. Groves, *Physiology of the fetal and transitional circulation.* Seminars in Fetal and Neonatal Medicine, 2015. **20**(4): p. 210-216.
95. Morton, S.U. and D. Brodsky, *Fetal Physiology and the Transition to Extrauterine Life.* Clin Perinatol, 2016. **43**(3): p. 395-407.
96. Stewart, D.J., et al., *Increased Plasma Endothelin-1 in Pulmonary Hypertension: Marker or Mediator of Disease?* Annals of Internal Medicine, 1991. **114**(6): p. 464-469.
97. Cavaliere, T.A., *From Fetus to Neonate: A Sensational Journey.* Newborn and Infant Nursing Reviews, 2016. **16**(2): p. 43-47.
98. Blum-Johnston, C., et al., *Developmental acceleration of bradykinin-dependent relaxation by prenatal chronic hypoxia*

impedes normal development after birth. American Journal of Physiology-Lung Cellular and Molecular Physiology, 2016. **310**(3): p. L271-L286.
99. Tan, C.M.J. and A.J. Lewandowski, *The Transitional Heart: From Early Embryonic and Fetal Development to Neonatal Life.* Fetal Diagn Ther, 2020. **47**(5): p. 373-386.
100. Nagasawa, H., et al., *Time to spontaneous ductus arteriosus closure in full-term neonates.* Open Heart, 2016. **3**(1): p. e000413.
101. Jarrell, D.K., M.L. Lennon, and J.G. Jacot, *Epigenetics and Mechanobiology in Heart Development and Congenital Heart Disease.* Diseases, 2019. **7**(3).
102. Prall, O.W.J., et al., *An Nkx2-5/Bmp2/Smad1 Negative Feedback Loop Controls Heart Progenitor Specification and Proliferation.* Cell, 2007. **128**(5): p. 947-959.
103. Naito, A.T., et al., *Developmental stage-specific biphasic roles of Wnt/β-catenin signaling in cardiomyogenesis and hematopoiesis.* Proceedings of the National Academy of Sciences, 2006. **103**(52): p. 19812-19817.
104. Lian, X., et al., *Robust cardiomyocyte differentiation from human pluripotent stem cells via temporal modulation of canonical Wnt signaling.* Proceedings of the National Academy of Sciences, 2012. **109**(27): p. E1848-E1857.
105. Srivastava, D., *GENETIC REGULATION OF CARDIOGENESIS AND CONGENITAL HEART DISEASE.* Annual Review of Pathology: Mechanisms of Disease, 2006. **1**(1): p. 199-213.
106. Paige, S.L., et al., *Molecular Regulation of Cardiomyocyte Differentiation.* Circulation Research, 2015. **116**(2): p. 341-353.
107. van der Linde, D., et al., *Birth Prevalence of Congenital Heart Disease Worldwide: A Systematic Review and Meta-Analysis.* Journal of the American College of Cardiology, 2011. **58**(21): p. 2241-2247.
108. Liu, Y., et al., *Global birth prevalence of congenital heart defects 1970-2017: updated systematic review and meta-analysis of 260 studies.* Int J Epidemiol, 2019. **48**(2): p. 455-463.
109. Meberg, A., et al., *Outcome of congenital heart defects–a population-based study.* Acta Paediatrica, 2000. **89**(11): p. 1344-1351.
110. Bédard, E., D.F. Shore, and M.A. Gatzoulis, *Adult congenital heart disease: a 2008 overview.* British Medical Bulletin, 2008. **85**(1): p. 151-180.
111. Michelena, H.I., et al., *International consensus statement on nomenclature and classification of the congenital bicuspid aortic valve and its aortopathy, for clinical, surgical, interventional and research purposes.* European Journal of Cardio-Thoracic Surgery, 2021. **60**(3): p. 448-476.
112. Calkoen, E.E., et al., *Atrioventricular septal defect: From embryonic development to long-term follow-up.* International Journal of Cardiology, 2016. **202**: p. 784-795.

113. Taqatqa, A.S. and J.J. Vettukattil, *Atrioventricular Septal Defects: Pathology, Imaging, and Treatment Options.* Current Cardiology Reports, 2021. **23**(8): p. 93.
114. Burns, T., et al., *The Dorsal Mesenchymal Protrusion and the Pathogenesis of Atrioventricular Septal Defects.* J Cardiovasc Dev Dis, 2016. **3**(4).
115. Anderson, R.H., A. Wessels, and J.J. Vettukattil, *Morphology and Morphogenesis of Atrioventricular Septal Defect With Common Atrioventricular Junction.* World Journal for Pediatric and Congenital Heart Surgery, 2010. **1**(1): p. 59-67.
116. Anderson, R.H., T.J. Mohun, and N.A. Brown, *Clarifying the morphology of the ostium primum defect.* J Anat, 2015. **226**(3): p. 244-57.
117. Anderson, R.H., T.J. Mohun, and N.A. Brown, *Clarifying the morphology of the ostium primum defect.* Journal of Anatomy, 2015. **226**(3): p. 244-257.
118. Romano, V., et al., *Patent Foramen Ovale-A Not So Innocuous Septal Atrial Defect in Adults.* J Cardiovasc Dev Dis, 2021. **8**(6).
119. Homma, S. and R.L. Sacco, *Patent Foramen Ovale and Stroke.* Circulation, 2005. **112**(7): p. 1063-1072.
120. Teshome, M.K., et al., *Patent Foramen Ovale: A Comprehensive Review.* Current Problems in Cardiology, 2020. **45**(2): p. 100392.
121. Handke, M., et al., *Patent Foramen Ovale and Cryptogenic Stroke in Older Patients.* New England Journal of Medicine, 2007. **357**(22): p. 2262-2268.
122. Di Tullio, M., et al., *Patent Foramen Ovale as a Risk Factor for Cryptogenic Stroke.* Annals of Internal Medicine, 1992. **117**(6): p. 461-465.
123. Hexdall, E.J. and J.S. Cooper, *Patent Foramen Ovale In Diving*, in *StatPearls*. 2023, StatPearls Publishing

Copyright © 2023, StatPearls Publishing LLC.: Treasure Island (FL).

124. Shi, Y.-J., et al., *Migraine and percutaneous patent foramen ovale closure: a systematic review and meta-analysis.* BMC Cardiovascular Disorders, 2017. **17**(1): p. 203.
125. Liu, Y., et al., *Global birth prevalence of congenital heart defects 1970–2017: updated systematic review and meta-analysis of 260 studies.* International Journal of Epidemiology, 2019. **48**(2): p. 455-463.
126. Bajolle, F., et al., *Rotation of the Myocardial Wall of the Outflow Tract Is Implicated in the Normal Positioning of the Great Arteries.* Circulation Research, 2006. **98**(3): p. 421-428.
127. Fu, W., et al., *Swiss cheese interventricular septum presenting with catastrophic stroke: the potential role of ECG-gated CTA.* BJR|case reports, 2022. **8**(1): p. 20210069.
128. Houyel, L. and S.M. Meilhac, *Heart Development and Congenital Structural Heart Defects.* Annual Review of Genomics and Human Genetics, 2021. **22**(1): p. 257-284.
129. McDaniel, N., *Ventricular septal defects.* Moss and Adams' heart disease in infants, children, and adolescents, 2001: p. 636-651.

130. McCarthy, K., S. Ho, and R. Anderson, *Categorisation of ventricular septal defects: review of the perimembranous morphology.* Images Paediatr Cardiol, 2000. **2**(2): p. 24-40.
131. Minette, M.S. and D.J. Sahn, *Ventricular Septal Defects.* Circulation, 2006. **114**(20): p. 2190-2197.
132. van der Linde, D., et al., *Birth prevalence of congenital heart disease worldwide: a systematic review and meta-analysis.* J Am Coll Cardiol, 2011. **58**(21): p. 2241-7.
133. Adler, A.C. and R.S. Litman, *3 - Congenital Heart Disease*, in *Litman's Basics of Pediatric Anesthesia (Third Edition)*, R.S. Litman and A.P. Ambardekar, Editors. 2022, Elsevier: New Delhi. p. 13-22.
134. Idrizi, S., et al., *Interventional Treatment of Pulmonary Valve Stenosis: A Single Center Experience.* Open Access Maced J Med Sci, 2015. **3**(3): p. 408-12.
135. Kodliwadmath, A., *Dysplastic pulmonary valve stenosis associated with unilateral absent first metacarpal: A rare association.* SAGE Open Med Case Rep, 2017. **5**: p. 2050313x17726946.
136. Jashari, R., et al., *The incidence of congenital bicuspid or bileaflet and quadricuspid or quadrileaflet arterial valves in 3,861 donor hearts in the European Homograft Bank.* J Heart Valve Dis, 2009. **18**(3): p. 337-44.
137. Vida, V.L., et al., *Preserving the pulmonary valve during early repair of tetralogy of Fallot: Anatomic substrates and surgical strategies.* The Journal of Thoracic and Cardiovascular Surgery, 2015. **149**(5): p. 1358-1363.e1.
138. Yang, J.H., S.W. Park, and Y.H. Choe, *Diagnóstico de válvula pulmonar tetracúspide mediante tomografía computarizada multidetector.* Revista Española de Cardiología, 2013. **66**(5): p. 401.
139. Neeb, Z., et al., *Cardiac outflow tract anomalies.* WIREs Developmental Biology, 2013. **2**(4): p. 499-530.
140. Anderson, R.H., et al., *Development and Morphology of the Ventricular Outflow Tracts.* World Journal for Pediatric and Congenital Heart Surgery, 2016. **7**(5): p. 561-577.
141. Demir, M.T., et al., *The double outlet right ventricle with additional cardiac malformations: an anatomic and echocardiographic study.* Folia Morphol (Warsz), 2009. **68**(2): p. 104-8.
142. Niezen, R.A., et al., *Double outlet right ventricle assessed with Magnetic Resonance Imaging.* The International Journal of Cardiac Imaging, 1999. **15**(4): p. 323-329.
143. Goo, H.W., *Double Outlet Right Ventricle: In-Depth Anatomic Review Using Three-Dimensional Cardiac CT Data.* Korean J Radiol, 2021. **22**(11): p. 1894-1908.
144. Yoo, S.J., et al., *MR anatomy of ventricular septal defect in double-outlet right ventricle with situs solitus and atrioventricular concordance.* Radiology, 1991. **181**(2): p. 501-5.

145. Yoo, S.-J. and G.S. Van Arsdell, *3D printing in surgical management of double outlet right ventricle.* Frontiers in pediatrics, 2018. **5**: p. 289.
146. Yim, D., et al., *Essential Modifiers of Double Outlet Right Ventricle: Revisit With Endocardial Surface Images and 3-Dimensional Print Models.* Circ Cardiovasc Imaging, 2018. **11**(3): p. e006891.
147. Sherrid, M.V., et al., *On the Cardiac Loop and Its Failing: Left Ventricular Outflow Tract Obstruction.* J Am Heart Assoc, 2020. **9**(3): p. e014857.
148. Anderson, R.H.M., T.J., *Cardiology of the Young*. 7th ed. Feigenbaum's Echocardiography, ed. W.F.A.a.T. Ryan. 2015: Lippincott Williams & Wilkins.
149. Anderson, R.H., et al., *What is aortic overriding?* Cardiology in the Young, 2015. **25**(4): p. 612-625.
150. Warnes, C.A., *Transposition of the Great Arteries.* Circulation, 2006. **114**(24): p. 2699-2709.
151. Hornung, T.S., et al., *Transposition complexes in the adult: a changing perspective.* Cardiology Clinics, 2002. **20**(3): p. 405-420.
152. Bhansali, S.P., C., *Truncus Arteriosus.* 2023, StatPearls Publishing: Treasure Island (FL).
153. Patel, D.M., P.D. Maldjian, and C. Lovoulos, *Interrupted aortic arch with post-interruption aneurysm and bicuspid aortic valve in an adult: a case report and literature review.* Radiol Case Rep, 2015. **10**(3): p. 5-8.
154. O'Brien, P. and A.C. Marshall, *Coarctation of the Aorta.* Circulation, 2015. **131**(9): p. e363-e365.
155. Rosenthal, E., *Coarctation of the aorta from fetus to adult: curable condition or life long disease process?* Heart, 2005. **91**(11): p. 1495-1502.
156. Joseph, G., A. Mandalay, and G. Rajendiran, *Percutaneous recanalization and balloon angioplasty of congenital isolated local atresia of the aortic isthmus in adults.* Catheter Cardiovasc Interv, 2001. **53**(4): p. 535-41.
157. Sakellaridis, T., et al., *Latent congenital defect: interrupted aortic arch in an adult—case report and literature review.* Vascular and endovascular surgery, 2010. **44**(5): p. 402-406.
158. O'Brien, P. and A.C. Marshall, *Tetralogy of Fallot.* Circulation, 2014. **130**(4): p. e26-e29.
159. Bouma, B.J. and B.J.M. Mulder, *Changing Landscape of Congenital Heart Disease.* Circulation Research, 2017. **120**(6): p. 908-922.
160. BHF, *CVD STATISTICS –UK Fact Sheet*. 2023, British Heart Foundation (BHF): Oxford, UK. p. 21.
161. Kusner, J.J., et al., *The Natural History of Bicuspid Aortic Valve Disease.* Struct Heart, 2023. **7**(2): p. 100119.
162. Hoffman, J.I.E. and S. Kaplan, *The incidence of congenital heart disease.* Journal of the American College of Cardiology, 2002. **39**(12): p. 1890-1900.

163. Wu, W., J. He, and X. Shao, *Incidence and mortality trend of congenital heart disease at the global, regional, and national level, 1990-2017.* Medicine (Baltimore), 2020. **99**(23): p. e20593.
164. Hoffman, J., *The global burden of congenital heart disease.* Cardiovasc J Afr, 2013. **24**(4): p. 141-5.
165. Warnes, C.A., et al., *ACC/AHA 2008 Guidelines for the Management of Adults With Congenital Heart Disease.* Circulation, 2008. **118**(23): p. e714-e833.
166. Marelli, A.J., et al., *Congenital Heart Disease in the General Population.* Circulation, 2007. **115**(2): p. 163-172.
167. Cowan, J.R. and S.M. Ware, *Genetics and Genetic Testing in Congenital Heart Disease.* Clinics in Perinatology, 2015. **42**(2): p. 373-393.
168. Geddes, G.C., et al., *Genetic Testing Protocol Reduces Costs and Increases Rate of Genetic Diagnosis in Infants with Congenital Heart Disease.* Pediatr Cardiol, 2017. **38**(7): p. 1465-1470.
169. Geddes, G.C. and M.G. Earing, *Genetic evaluation of patients with congenital heart disease.* Curr Opin Pediatr, 2018. **30**(6): p. 707-713.
170. Andersen, T.A., L. Troelsen Kde, and L.A. Larsen, *Of mice and men: molecular genetics of congenital heart disease.* Cell Mol Life Sci, 2014. **71**(8): p. 1327-52.
171. Wilsdon, A., et al., *Recent advances in congenital heart disease genomics.* F1000Research, 2017. **6**(0): p. 869-869.
172. Zaidi, S., et al., *De novo mutations in histone-modifying genes in congenital heart disease.* Nature, 2013. **498**(7453): p. 220-223.
173. Homsy, J., et al., *De novo mutations in congenital heart disease with neurodevelopmental and other congenital anomalies.* Science, 2015. **350**(6265): p. 1262-6.
174. Jin, S.C., et al., *Contribution of rare inherited and de novo variants in 2,871 congenital heart disease probands.* Nature Genetics, 2017. **49**(11): p. 1593-1601.
175. Jin, S.C., et al., *Contribution of rare inherited and de novo variants in 2,871 congenital heart disease probands.* Nat Genet, 2017. **49**(11): p. 1593-1601.
176. Sifrim, A., et al., *Distinct genetic architectures for syndromic and nonsyndromic congenital heart defects identified by exome sequencing.* Nature Genetics, 2016. **48**(9): p. 1060-1065.
177. Vandamme, T.F., *Use of rodents as models of human diseases.* J Pharm Bioallied Sci, 2014. **6**(1): p. 2-9.
178. Lamers, W.H., et al., *Formation of the tricuspid valve in the human heart.* Circulation, 1995. **91**(1): p. 111-21.
179. Dhanantwari, P., et al., *Human Cardiac Development in the First Trimester.* Circulation, 2009. **120**(4): p. 343-351.
180. Mohun, T., W. Weninger, and S. Bhattacharya, *Chapter 11.3 - Imaging Cardiac Developmental Malformations in the Mouse Embryo*, in *Heart Development and Regeneration*, N. Rosenthal and R.P. Harvey, Editors. 2010, Academic Press: Boston. p. 779-791.

181. Dickinson, M.E., et al., *High-throughput discovery of novel developmental phenotypes.* Nature, 2016. **537**(7621): p. 508-514.
182. Shen, Y., et al., *Cardiovascular phenotyping of fetal mice by noninvasive high-frequency ultrasound facilitates recovery of ENU-induced mutations causing congenital cardiac and extracardiac defects.* Physiol Genomics, 2005. **24**(1): p. 23-36.
183. Zhu, Y., et al., *Association between maternal body mass index and congenital heart defects in infants: A meta-analysis.* Congenit Heart Dis, 2018.
184. Liu, F., et al., *A genome-wide association study identifies five loci influencing facial morphology in Europeans.* PLoS Genet, 2012. **8**(9): p. e1002932.
185. Perlman, R.L., *Mouse models of human disease: An evolutionary perspective.* Evol Med Public Health, 2016. **2016**(1): p. 170-6.
186. Ravasi, T., et al., *An atlas of combinatorial transcriptional regulation in mouse and man.* Cell, 2010. **140**(5): p. 744-52.
187. Weninger, W.J., et al., *High-resolution episcopic microscopy: a rapid technique for high detailed 3D analysis of gene activity in the context of tissue architecture and morphology.* Anat Embryol (Berl), 2006. **211**(3): p. 213-21.
188. Skarnes, W.C., et al., *A conditional knockout resource for the genome-wide study of mouse gene function.* Nature, 2011. **474**(7351): p. 337-342.
189. Geyer, S.H., et al., *A staging system for correct phenotype interpretation of mouse embryos harvested on embryonic day 14 (E14.5).* J Anat, 2017. **230**(5): p. 710-719.
190. Soh, Y.Q., et al., *Sequencing the mouse Y chromosome reveals convergent gene acquisition and amplification on both sex chromosomes.* Cell, 2014. **159**(4): p. 800-13.
191. Tunster, S.J., *Genetic sex determination of mice by simplex PCR.* Biol Sex Differ, 2017. **8**(1): p. 31.
192. Fedorov, A., et al., *3D Slicer as an image computing platform for the Quantitative Imaging Network.* Magn Reson Imaging, 2012. **30**(9): p. 1323-41.
193. Mortazavi, A., et al., *Mapping and quantifying mammalian transcriptomes by RNA-Seq.* Nature Methods, 2008. **5**(7): p. 621-628.
194. Anders, S. and W. Huber, *Differential expression analysis for sequence count data.* Genome Biology, 2010. **11**(10): p. R106.
195. Young, M.D., et al., *Gene ontology analysis for RNA-seq: accounting for selection bias.* Genome Biology, 2010. **11**(2): p. R14.
196. Ge, S.X., E.W. Son, and R. Yao, *iDEP: an integrated web application for differential expression and pathway analysis of RNA-Seq data.* BMC Bioinformatics, 2018. **19**(1): p. 534.
197. Ruiz-Villalba, A., et al., *Reference genes for gene expression studies in the mouse heart.* Sci Rep, 2017. **7**(1): p. 24.
198. Pfaffl, M.W., *A new mathematical model for relative quantification in real-time RT-PCR.* Nucleic Acids Res, 2001. **29**(9): p. e45.

199. Hellemans, J., et al., *qBase relative quantification framework and software for management and automated analysis of real-time quantitative PCR data.* Genome Biology, 2007. **8**(2): p. R19.
200. Vandesompele, J., et al., *Accurate normalization of real-time quantitative RT-PCR data by geometric averaging of multiple internal control genes.* Genome Biology, 2002. **3**(7): p. research0034.1.
201. Corpet, F., *Multiple sequence alignment with hierarchical clustering.* Nucleic Acids Res, 1988. **16**(22): p. 10881-90.
202. Loughna, S. and D. Henderson, *Methodologies for Staining and Visualisation of β-Galactosidase in Mouse Embryos and Tissues*, in *Reporter Genes: A Practical Guide*, D.S. Anson, Editor. 2007, Humana Press: Totowa, NJ. p. 1-11.
203. Gierut, J.J., T.E. Jacks, and K.M. Haigis, *Whole-mount X-Gal staining of mouse tissues.* Cold Spring Harb Protoc, 2014. **2014**(4): p. 417-9.
204. Kohoutek, J. and D. Blazek, *Cyclin K goes with Cdk12 and Cdk13.* Cell Div, 2012. **7**: p. 12.
205. Malumbres, M., *Cyclin-dependent kinases.* Genome Biology, 2014. **15**(6): p. 122.
206. Greifenberg, A.K., et al., *Structural and Functional Analysis of the Cdk13/Cyclin K Complex.* Cell Rep, 2016. **14**(2): p. 320-31.
207. Blazek, D., et al., *The cyclin K/Cdk12 complex maintains genomic stability via regulation of expression of DNA damage response genes.* Genes and Development, 2011. **25**(20): p. 2158-2172.
208. Liang, K., et al., *Characterization of Human Cyclin-Dependent Kinase 12 (CDK12) and CDK13 Complexes in C-Terminal Domain Phosphorylation, Gene Transcription, and RNA Processing.* Molecular and Cellular Biology, 2015. **35**(6): p. 928-938.
209. Greifenberg, A.K., et al., *Structural and Functional Analysis of the Cdk13/Cyclin K Complex.* Cell Rep, 2016. **14**(2): p. 320-31.
210. Greifenberg, A.K., et al., *Structural and Functional Analysis of the Cdk13/Cyclin K Complex.* Cell Reports, 2016. **14**(2): p. 320-331.
211. Nováková, M., et al., *Mouse Model of Congenital Heart Defects, Dysmorphic Facial Features and Intellectual Developmental Disorders as a Result of Non-functional CDK13.* Frontiers in Cell and Developmental Biology, 2019. **7**(155).
212. Chen, H.-R., et al., *Cdk12 and Cdk13 regulate axonal elongation through a common signaling pathway that modulates Cdk5 expression.* Experimental Neurology, 2014. **261**: p. 10-21.
213. Bostwick, B.L., et al., *Phenotypic and molecular characterisation of CDK13-related congenital heart defects, dysmorphic facial features and intellectual developmental disorders.* Genome medicine, 2017. **9**(1): p. 73-73.
214. Hamilton, M.J., et al., *Heterozygous mutations affecting the protein kinase domain of CDK13 cause a syndromic form of developmental delay and intellectual disability.* Journal of Medical Genetics, 2018. **55**(1): p. 28-38.

215. Uehara, T., et al., *Redefining the phenotypic spectrum of de novo heterozygous CDK13 variants: Three patients without cardiac defects.* Eur J Med Genet, 2018. **61**(5): p. 243-247.
216. van den Akker, W.M.R., et al., *De novo variants in CDK13 associated with syndromic ID/DD: Molecular and clinical delineation of 15 individuals and a further review.* Clin Genet, 2018. **93**(5): p. 1000-1007.
217. Yakubov, R., et al., *One-month-old girl presenting with pseudohypoaldosteronism leading to the diagnosis of CDK13-related disorder: a case report and review of the literature.* J Med Case Rep, 2019. **13**(1): p. 386.
218. McRae, J.F., et al., *Prevalence and architecture of de novo mutations in developmental disorders.* Nature, 2017. **542**(7642): p. 433-438.
219. Trinh, J., et al., *Novel pathogenic variants and multiple molecular diagnoses in neurodevelopmental disorders.* J Neurodev Disord, 2019. **11**(1): p. 11.
220. Rouxel, F., et al., *CDK13-related disorder: Report of a series of 18 previously unpublished individuals and description of an epigenetic signature.* Genet Med, 2022. **24**(5): p. 1096-1107.
221. Carneiro, T.N., et al., *Utility of trio-based exome sequencing in the elucidation of the genetic basis of isolated syndromic intellectual disability: illustrative cases.* Appl Clin Genet, 2018. **11**: p. 93-98.
222. Cui, D., et al., *Case Report: Hemophagocytic Lymphohistiocytosis Prior to the Onset of Leukemia in a Boy With CDK13-Related Disorder.* Front Genet, 2022. **13**: p. 858668.
223. Acharya, A., et al., *Correction: Wolfram-like syndrome with bicuspid aortic valve due to a homozygous missense variant in CDK13.* J Hum Genet, 2021. **66**(10): p. 1019.
224. Hildebrand, M.S., et al., *Severe childhood speech disorder.* Gene discovery highlights transcriptional dysregulation, 2020. **94**(20): p. e2148-e2167.
225. Morison, L.D., et al., *CDK13-related disorder: a deep characterization of speech and language abilities and addition of 33 novel cases.* European Journal of Human Genetics, 2023.
226. Karczewski, K.J., et al., *The mutational constraint spectrum quantified from variation in 141,456 humans.* Nature, 2020. **581**(7809): p. 434-443.
227. Richards, S., et al., *Standards and guidelines for the interpretation of sequence variants: a joint consensus recommendation of the American College of Medical Genetics and Genomics and the Association for Molecular Pathology.* Genet Med, 2015. **17**(5): p. 405-24.
228. DDDS, T.D.D.D.S., *Prevalence and architecture of de novo mutations in developmental disorders.* Nature, 2017. **542**(7642): p. 433-438.
229. Gibbs, M., et al., *A Prenatal Presentation of CDK13-Related Disorder with a Novel Pathogenic Variant.* Case Reports in Genetics, 2023. **2023**: p. 3437706.

230. Kim, H.E., et al., *Frequent Amplification of CENPF, GMNN and CDK13 Genes in Hepatocellular Carcinomas.* PLoS ONE, 2012. **7**(8): p. 43223-43223.
231. Ahrens-Nicklas, R.C., et al., *Utility of genetic evaluation in infants with congenital heart defects admitted to the cardiac intensive care unit.* Am J Med Genet A, 2016. **170**(12): p. 3090-3097.
232. Pan, J., et al., *Establishment and characterization of a new human acute myelomonocytic leukemia cell line JIH-3.* Leuk Res, 2012. **36**(7): p. 889-94.
233. Andersen, T.A., K.D.L.L. Troelsen, and L.A. Larsen, *Of mice and men: Molecular genetics of congenital heart disease.* Cellular and Molecular Life Sciences, 2014. **71**(8): p. 1327-1352.
234. Lage, K., et al., *Dissecting spatio-temporal protein networks driving human heart development and related disorders.* Mol Syst Biol, 2010. **6**: p. 381.
235. Michelena, H.I., et al., *International consensus statement on nomenclature and classification of the congenital bicuspid aortic valve and its aortopathy, for clinical, surgical, interventional and research purposes.* Eur J Cardiothorac Surg, 2021. **60**(3): p. 448-476.
236. Captur, G., et al., *Morphogenesis of myocardial trabeculae in the mouse embryo.* Journal of Anatomy, 2016. **229**(2): p. 314-325.
237. Weaver, K.N., et al., *Prevalence of Genetic Diagnoses in a Cohort With Valvar Pulmonary Stenosis.* Circ Genom Precis Med, 2022. **15**(4): p. e003635.
238. Cole-Jeffrey, C.T., et al., *Progressive anatomical closure of foramen ovale in normal neonatal mouse hearts.* Anat Rec (Hoboken), 2012. **295**(5): p. 764-8.
239. Savolainen, S.M., J.F. Foley, and S.A. Elmore, *Histology atlas of the developing mouse heart with emphasis on E11.5 to E18.5.* Toxicol Pathol, 2009. **37**(4): p. 395-414.
240. Szklarczyk, D., et al., *STRING v10: protein-protein interaction networks, integrated over the tree of life.* Nucleic Acids Res, 2015. **43**(Database issue): p. D447-52.
241. Bastian, F.B., et al., *The Bgee suite: integrated curated expression atlas and comparative transcriptomics in animals.* Nucleic Acids Research, 2021. **49**(D1): p. D831-D847.
242. Baldarelli, R.M., et al., *The mouse Gene Expression Database (GXD): 2021 update.* Nucleic acids research, 2021. **49**(D1): p. D924-D931.
243. Gross-Thebing, T., A. Paksa, and E. Raz, *Simultaneous high-resolution detection of multiple transcripts combined with localization of proteins in whole-mount embryos.* BMC Biology, 2014. **12**(1): p. 55.
244. Varadkar, P., et al., *Notch2 is required for the proliferation of cardiac neural crest-derived smooth muscle cells.* Developmental Dynamics, 2008. **237**(4): p. 1144-1152.
245. Natanzon, A. and I. Kronzon, *Pericardial and Pleural Effusions in Congestive Heart Failure—Anatomical, Pathophysiologic, and*

Clinical Considerations. The American Journal of the Medical Sciences, 2009. **338**(3): p. 211-216.
246. Koutsourakis, M., et al., *The transcription factor GATA6 is essential for early extraembryonic development.* Development, 1999. **126**(4): p. 723-32.
247. Cosmi, E., et al., *Consequences in infants that were intrauterine growth restricted.* J Pregnancy, 2011. **2011**: p. 364381.
248. Sharma, D., S. Shastri, and P. Sharma, *Intrauterine Growth Restriction: Antenatal and Postnatal Aspects.* Clinical Medicine Insights: Pediatrics, 2016. **10**: p. CMPed.S40070.
249. Andescavage, N.N. and C. Limperopoulos, *Placental abnormalities in congenital heart disease.* Transl Pediatr, 2021. **10**(8): p. 2148-2156.
250. Linask, K.K., *The heart-placenta axis in the first month of pregnancy: induction and prevention of cardiovascular birth defects.* J Pregnancy, 2013. **2013**: p. 320413.
251. Burton, G.J. and E. Jauniaux, *Development of the Human Placenta and Fetal Heart: Synergic or Independent?* Front Physiol, 2018. **9**: p. 373.
252. Alexander, C., et al., *Combinatorial roles for BMPs and Endothelin 1 in patterning the dorsal-ventral axis of the craniofacial skeleton.* Development, 2011. **138**(23): p. 5135-46.
253. Moro, E., et al., *In vivo Wnt signaling tracing through a transgenic biosensor fish reveals novel activity domains.* Dev Biol, 2012. **366**(2): p. 327-40.
254. Schwend, T., E.J. Loucks, and S.C. Ahlgren, *Visualization of Gli activity in craniofacial tissues of hedgehog-pathway reporter transgenic zebrafish.* PLoS One, 2010. **5**(12): p. e14396.
255. Molina, G.A., S.C. Watkins, and M. Tsang, *Generation of FGF reporter transgenic zebrafish and their utility in chemical screens.* BMC Dev Biol, 2007. **7**: p. 62.
256. Shaffer, J.R., et al., *Genome-Wide Association Study Reveals Multiple Loci Influencing Normal Human Facial Morphology.* PLOS Genetics, 2016. **12**(8): p. e1006149.
257. Adhikari, K., et al., *A genome-wide association scan implicates DCHS2, RUNX2, GLI3, PAX1 and EDAR in human facial variation.* Nat Commun, 2016. **7**: p. 11616.
258. Miller, S.F., et al., *Exploratory genotype–phenotype correlations of facial form and asymmetry in unaffected relatives of children with non-syndromic cleft lip and/or palate.* Journal of Anatomy, 2014. **224**(6): p. 688-709.
259. Roth, D.M., et al., *Craniofacial Development: Neural Crest in Molecular Embryology.* Head Neck Pathol, 2021. **15**(1): p. 1-15.
260. Marcucio, R., B. Hallgrimsson, and N.M. Young, *Chapter Twelve - Facial Morphogenesis: Physical and Molecular Interactions Between the Brain and the Face*, in *Current Topics in Developmental Biology*, Y. Chai, Editor. 2015, Academic Press. p. 299-320.

261. Watanabe, M., et al., *Spatio-temporal expression of Sox genes in murine palatogenesis.* Gene Expression Patterns, 2016. **21**(2): p. 111-118.
262. Jackson, S.R., et al., *L1CAM mutation in association with X-linked hydrocephalus and Hirschsprung's disease.* Pediatr Surg Int, 2009. **25**(9): p. 823-5.
263. Konjikusic, M.J., et al., *Mutations in Kinesin Family Member 6 Reveal Specific Role in Ependymal Cell Function and Human Neuro-Cranial Development.* bioRxiv, 2018: p. 350140.
264. Adle-Biassette, H., et al., *Neuropathological review of 138 cases genetically tested for X-linked hydrocephalus: evidence for closely related clinical entities of unknown molecular bases.* Acta Neuropathologica, 2013. **126**(3): p. 427-442.
265. Konjikusic, M.J., et al., *Mutations in Kinesin family member 6 reveal specific role in ependymal cell ciliogenesis and human neurological development.* PLoS Genet, 2018. **14**(11): p. e1007817.
266. Jacquemin, V., et al., *Congenital hydrocephalus: new Mendelian mutations and evidence for oligogenic inheritance.* Hum Genomics, 2023. **17**(1): p. 16.
267. Moore, B.A., et al., *A Population Study of Common Ocular Abnormalities in C57BL/6N rd8 Mice.* Invest Ophthalmol Vis Sci, 2018. **59**(6): p. 2252-2261.
268. Bravo-Jaimes, K. and S.K. Prakash, *Genetics in bicuspid aortic valve disease: Where are we?* Prog Cardiovasc Dis, 2020. **63**(4): p. 398-406.
269. Shah, S.Y., A. Higgins, and M.Y. Desai, *Bicuspid aortic valve: Basics and beyond.* Cleveland Clinic Journal of Medicine, 2018. **85**(10): p. 779-784.
270. Michelena, H.I., et al., *Bicuspid Aortic Valve.* Circulation, 2014. **129**(25): p. 2691-2704.
271. Sabet, H.Y., et al., *Congenitally Bicuspid Aortic Valves: A Surgical Pathology Study of 542 Cases (1991 Through 1996) and a Literature Review of 2,715 Additional Cases.* Mayo Clinic Proceedings, 1999. **74**(1): p. 14-26.
272. Ackerman, C., et al., *An excess of deleterious variants in VEGF-A pathway genes in Down-syndrome-associated atrioventricular septal defects.* Am J Hum Genet, 2012. **91**(4): p. 646-59.
273. Lepore, J.J., et al., *GATA-6 regulates semaphorin 3C and is required in cardiac neural crest for cardiovascular morphogenesis.* J Clin Invest, 2006. **116**(4): p. 929-39.
274. Mendelsohn, C., et al., *Function of the retinoic acid receptors (RARs) during development (II). Multiple abnormalities at various stages of organogenesis in RAR double mutants.* Development, 1994. **120**(10): p. 2749-2771.
275. Vincentz, J.W., et al., *Fgf15 is required for proper morphogenesis of the mouse cardiac outflow tract.* genesis, 2005. **41**(4): p. 192-201.

276. Abu-Issa, R., et al., *Fgf8 is required for pharyngeal arch and cardiovascular development in the mouse.* Development, 2002. **129**(19): p. 4613-4625.
277. Sugi, Y., et al., *Fibroblast growth factor (FGF)-4 can induce proliferation of cardiac cushion mesenchymal cells during early valve leaflet formation.* Developmental Biology, 2003. **258**(2): p. 252-263.
278. Park, E.J., et al., *An FGF autocrine loop initiated in second heart field mesoderm regulates morphogenesis at the arterial pole of the heart.* Development, 2008. **135**(21): p. 3599-610.
279. Ching, Y.H., et al., *Mutation in myosin heavy chain 6 causes atrial septal defect.* Nat Genet, 2005. **37**(4): p. 423-8.
280. Granados-Riveron, J.T., et al., *Alpha-cardiac myosin heavy chain (MYH6) mutations affecting myofibril formation are associated with congenital heart defects.* Hum Mol Genet, 2010. **19**(20): p. 4007-16.
281. Razmara, E. and M. Garshasbi, *Whole-exome sequencing identifies R1279X of MYH6 gene to be associated with congenital heart disease.* BMC Cardiovasc Disord, 2018. **18**(1): p. 137.
282. Singh, M.K., et al., *Gata4 and Gata5 cooperatively regulate cardiac myocyte proliferation in mice.* J Biol Chem, 2010. **285**(3): p. 1765-72.
283. Luxán, G., et al., *Mutations in the NOTCH pathway regulator MIB1 cause left ventricular noncompaction cardiomyopathy.* Nature Medicine, 2013. **19**(2): p. 193-201.
284. Tu, C.T., T.C. Yang, and H.J. Tsai, *Nkx2.7 and Nkx2.5 function redundantly and are required for cardiac morphogenesis of zebrafish embryos.* PLoS One, 2009. **4**(1): p. e4249.
285. Spiridon, M.R., et al., *Holt-Oram Syndrome With Multiple Cardiac Abnormalities.* Cardiol Res, 2018. **9**(5): p. 324-329.
286. Mishra, S. and P. Lele, *Echocardiography to Evaluate Pulmonary Stenosis.* Journal of The Indian Academy of Echocardiography & Cardiovascular Imaging, 2020. **4**(3): p. 276-286.
287. Miga, D.E., *Pulmonary Stenosis*, in *Pediatric Clinical Advisor (Second Edition)*, L.C. Garfunkel, J.M. Kaczorowski, and C. Christy, Editors. 2007, Mosby: Philadelphia. p. 473-474.
288. Kim, D.H., et al., *The Comparison between the Echocardiographic Data to the Cardiac Catheterization Data on the Diagnosis, Treatment, and Follow-Up in Patients Diagnosed as Pulmonary Valve Stenosis.* J Cardiovasc Ultrasound, 2013. **21**(1): p. 18-22.
289. Guijarro-Contreras, A., et al., *Quadricuspid Pulmonic Valve, Pulmonary Artery Aneurysm, and Apical Hypertrophic Cardiomyopathy.* Circulation: Cardiovascular Imaging, 2018. **11**(6): p. e007698.
290. Koshiba-Takeuchi, K., et al., *Cooperative and antagonistic interactions between Sall4 and Tbx5 pattern the mouse limb and heart.* Nature Genetics, 2006. **38**(2): p. 175-183.

291. Yasuhara, J. and V. Garg, *Genetics of congenital heart disease: a narrative review of recent advances and clinical implications.* Transl Pediatr, 2021. **10**(9): p. 2366-2386.
292. Rajiah, P., N.L. Fulton, and M. Bolen, *Magnetic resonance imaging of the papillary muscles of the left ventricle: normal anatomy, variants, and abnormalities.* Insights into Imaging, 2019. **10**(1): p. 83.
293. Shimada, A., et al., *Improved methods for detection of β-galactosidase (lacZ) activity in hard tissue.* Histochem Cell Biol, 2012. **137**(6): p. 841-7.
294. Bartkowiak, B. and A.L. Greenleaf, *Expression, purification, and identification of associated proteins of the full-length hCDK12/CyclinK complex.* J Biol Chem, 2015. **290**(3): p. 1786-95.
295. Davidson, L., L. Muniz, and S. West, *3′ end formation of pre-mRNA and phosphorylation of Ser2 on the RNA polymerase II CTD are reciprocally coupled in human cells.* Genes Dev, 2014. **28**(4): p. 342-56.
296. Firth, H.V. and C.F. Wright, *The Deciphering Developmental Disorders (DDD) study.* Dev Med Child Neurol, 2011. **53**(8): p. 702-3.
297. Geyer, S.H., et al., *Morphology, topology and dimensions of the heart and arteries of genetically normal and mutant mouse embryos at stages S21–S23.* Journal of Anatomy, 2017. **231**(4): p. 600-614.
298. Tian, Y., et al., *Characterization and in vivo pharmacological rescue of a Wnt2-Gata6 pathway required for cardiac inflow tract development.* Dev Cell, 2010. **18**(2): p. 275-87.
299. Radford, B.N., et al., *Defects in placental syncytiotrophoblast cells are a common cause of developmental heart disease.* Nature Communications, 2023. **14**(1): p. 1174.
300. Valverde, A.M., et al., *Molecular cloning and characterization of protein kinase D: a target for diacylglycerol and phorbol esters with a distinctive catalytic domain.* Proceedings of the National Academy of Sciences, 1994. **91**(18): p. 8572-8576.
301. Sturany, S., et al., *Molecular cloning and characterization of the human protein kinase D2. A novel member of the protein kinase D family of serine threonine kinases.* J Biol Chem, 2001. **276**(5): p. 3310-8.
302. Hayashi, A., et al., *PKCν, a new member of the protein kinase C family, composes a fourth subfamily with PKCμ1The nucleotide sequence data reported in this paper have been deposited in the DDBJ, EMBL and GenBank databases under the accession number AB015982.1.* Biochimica et Biophysica Acta (BBA) - Molecular Cell Research, 1999. **1450**(1): p. 99-106.
303. Valverde, A.M., et al., *Molecular cloning and characterization of protein kinase D: a target for diacylglycerol and phorbol esters with a distinctive catalytic domain.* Proc Natl Acad Sci U S A, 1994. **91**(18): p. 8572-6.

304. Avkiran, M., et al., *Protein kinase d in the cardiovascular system: emerging roles in health and disease.* Circ Res, 2008. **102**(2): p. 157-63.
305. Fu, Y. and C.S. Rubin, *Protein kinase D: coupling extracellular stimuli to the regulation of cell physiology.* EMBO Rep, 2011. **12**(8): p. 785-96.
306. Wakana, Y. and F. Campelo, *The PKD-Dependent Biogenesis of TGN-to-Plasma Membrane Transport Carriers.* Cells, 2021. **10**(7).
307. Steinberg, S.F., *Decoding the Cardiac Actions of Protein Kinase D Isoforms.* Molecular Pharmacology, 2021. **100**(6): p. 558-567.
308. Sundram, V., S.C. Chauhan, and M. Jaggi, *Emerging roles of protein kinase D1 in cancer.* Mol Cancer Res, 2011. **9**(8): p. 985-96.
309. Bossuyt, J., et al., *Spatiotemporally Distinct Protein Kinase D Activation in Adult Cardiomyocytes in Response to Phenylephrine and Endothelin.* Journal of Biological Chemistry, 2011. **286**(38): p. 33390-33400.
310. Avkiran, M., et al., *Protein Kinase D in the Cardiovascular System.* Circulation Research, 2008. **102**(2): p. 157-163.
311. Wood, B.M. and J. Bossuyt, *Emergency Spatiotemporal Shift: The Response of Protein Kinase D to Stress Signals in the Cardiovascular System.* Front Pharmacol, 2017. **8**: p. 9.
312. Rozengurt, E., *Protein kinase D signaling: multiple biological functions in health and disease.* Physiology (Bethesda), 2011. **26**(1): p. 23-33.
313. Kisfalvi, K., et al., *Induced overexpression of protein kinase D1 stimulates mitogenic signaling in human pancreatic carcinoma PANC-1 cells.* J Cell Physiol, 2010. **223**(2): p. 309-16.
314. Liou, G.Y., et al., *Protein kinase D1 drives pancreatic acinar cell reprogramming and progression to intraepithelial neoplasia.* Nat Commun, 2015. **6**: p. 6200.
315. Karam, M., et al., *Protein kinase D1 stimulates proliferation and enhances tumorigenesis of MCF-7 human breast cancer cells through a MEK/ERK-dependent signaling pathway.* Exp Cell Res, 2012. **318**(5): p. 558-69.
316. Trauzold, A., et al., *PKCmu prevents CD95-mediated apoptosis and enhances proliferation in pancreatic tumour cells.* Oncogene, 2003. **22**(55): p. 8939-47.
317. Johannes, F.J., et al., *Protein kinase Cmu downregulation of tumor-necrosis-factor-induced apoptosis correlates with enhanced expression of nuclear-factor-kappaB-dependent protective genes.* Eur J Biochem, 1998. **257**(1): p. 47-54.
318. Fielitz, J., et al., *Requirement of protein kinase D1 for pathological cardiac remodeling.* Proc Natl Acad Sci U S A, 2008. **105**(8): p. 3059-63.
319. Harrison, B.C., et al., *Regulation of cardiac stress signaling by protein kinase d1.* Mol Cell Biol, 2006. **26**(10): p. 3875-88.
320. Uhlen, M., et al., *Towards a knowledge-based Human Protein Atlas.* Nature Biotechnology, 2010. **28**(12): p. 1248-1250.

321. Haworth, R.S., et al., *Expression and activity of protein kinase D/protein kinase C mu in myocardium: evidence for alpha1-adrenergic receptor- and protein kinase C-mediated regulation.* J Mol Cell Cardiol, 2000. **32**(6): p. 1013-23.
322. Oster, H., D. Abraham, and M. Leitges, *Expression of the protein kinase D (PKD) family during mouse embryogenesis.* Gene Expr Patterns, 2006. **6**(4): p. 400-8.
323. Malhotra, V. and F. Campelo, *PKD regulates membrane fission to generate TGN to cell surface transport carriers.* Cold Spring Harb Perspect Biol, 2011. **3**(2).
324. Van Lint, J., et al., *Protein kinase D: an intracellular traffic regulator on the move.* Trends in Cell Biology, 2002. **12**(4): p. 193-200.
325. Cobbaut, M., et al., *Differential regulation of PKD isoforms in oxidative stress conditions through phosphorylation of a conserved Tyr in the P+1 loop.* Sci Rep, 2017. **7**(1): p. 887.
326. Matthews, S.A., et al., *Unique functions for protein kinase D1 and protein kinase D2 in mammalian cells.* Biochem J, 2010. **432**(1): p. 153-63.
327. Pusapati, G.V., et al., *Role of the second cysteine-rich domain and Pro275 in protein kinase D2 interaction with ADP-ribosylation factor 1, trans-Golgi network recruitment, and protein transport.* Mol Biol Cell, 2010. **21**(6): p. 1011-22.
328. Steinberg, S.F., *Regulation of protein kinase D1 activity.* Mol Pharmacol, 2012. **81**(3): p. 284-91.
329. Rykx, A., et al., *Protein kinase D: a family affair.* FEBS Lett, 2003. **546**(1): p. 81-6.
330. Kolczynska, K., et al., *Diacylglycerol-evoked activation of PKC and PKD isoforms in regulation of glucose and lipid metabolism: a review.* Lipids in Health and Disease, 2020. **19**(1): p. 113.
331. Van Lint, J.V., J. Sinnett-Smith, and E. Rozengurt, *Expression and characterization of PKD, a phorbol ester and diacylglycerol-stimulated serine protein kinase.* J Biol Chem, 1995. **270**(3): p. 1455-61.
332. Elsner, D.J., et al., *A ubiquitin-like domain controls protein kinase D dimerization and activation by trans-autophosphorylation.* J Biol Chem, 2019. **294**(39): p. 14422-14441.
333. Zhang, X., et al., *Multifaceted Functions of Protein Kinase D in Pathological Processes and Human Diseases.* Biomolecules, 2021. **11**(3).
334. UniProt. *PRKD1 - UniProtKB - Q15139 (KPCD1_HUMAN)*. 2020 October 15, 2019 [cited 2020 June 06, 2020]; Available from: https://www.uniprot.org/uniprot/Q15139.
335. Chang, J.K., et al., *Protein kinase D1 (PKD1) phosphorylation on Ser(203) by type I p21-activated kinase (PAK) regulates PKD1 localization.* J Biol Chem, 2017. **292**(23): p. 9523-9539.
336. Storz, P., et al., *Tyrosine phosphorylation of protein kinase D in the pleckstrin homology domain leads to activation.* J Biol Chem, 2003. **278**(20): p. 17969-76.

337. Döppler, H. and P. Storz, *A Novel Tyrosine Phosphorylation Site in Protein Kinase D Contributes to Oxidative Stress-mediated Activation*.* Journal of Biological Chemistry, 2007. **282**(44): p. 31873-31881.
338. Lingappan, K., *NF-κB in Oxidative Stress.* Curr Opin Toxicol, 2018. **7**: p. 81-86.
339. Vega, R.B., et al., *Protein kinases C and D mediate agonist-dependent cardiac hypertrophy through nuclear export of histone deacetylase 5.* Mol Cell Biol, 2004. **24**(19): p. 8374-85.
340. Han, Y., et al., *Mechanism of histone deacetylases in cardiac hypertrophy and its therapeutic inhibitors.* Front Cardiovasc Med, 2022. **9**: p. 931475.
341. Fielitz, J., et al., *Requirement of protein kinase D1 for pathological cardiac remodeling*. 2008. p. 3059-3063.
342. Breuer, K., et al., *InnateDB: systems biology of innate immunity and beyond--recent updates and continuing curation.* Nucleic Acids Res, 2013. **41**(Database issue): p. D1228-33.
343. Azoitei, N., et al., *Protein kinase D2: a versatile player in cancer biology.* Oncogene, 2018. **37**(10): p. 1263-1278.
344. Roy, A., et al., *Protein kinase D signaling in cancer: A friend or foe?* Biochimica et Biophysica Acta (BBA) - Reviews on Cancer, 2017. **1868**(1): p. 283-294.
345. Youssef, I. and J.-M. Ricort, *Deciphering the Role of Protein Kinase D1 (PKD1) in Cellular Proliferation.* Molecular Cancer Research, 2019. **17**(10): p. 1961-1974.
346. Yuan, J. and S.J. Pandol, *PKD signaling and pancreatitis.* Journal of Gastroenterology, 2016. **51**(7): p. 651-659.
347. Simsek Papur, O., et al., *Acute and Chronic Effects of Protein Kinase-D Signaling on Cardiac Energy Metabolism.* Front Cardiovasc Med, 2018. **5**: p. 65.
348. Massadeh, S., et al., *Novel Autosomal Recessive Splice-Altering Variant in PRKD1 Is Associated with Congenital Heart Disease.* Genes (Basel), 2021. **12**(5).
349. Alter, S., et al., *Telangiectasia-ectodermal dysplasia-brachydactyly-cardiac anomaly syndrome is caused by de novo mutations in protein kinase D1.* J Med Genet, 2021. **58**(6): p. 415-421.
350. Shaheen, R., et al., *Positional mapping of PRKD1, NRP1 and PRDM1 as novel candidate disease genes in truncus arteriosus.* Journal of Medical Genetics, 2015. **52**(5): p. 322-329.
351. Landrum, M.J., et al., *ClinVar: improving access to variant interpretations and supporting evidence.* Nucleic Acids Res, 2018. **46**(D1): p. D1062-d1067.
352. Firth, H.V., et al., *DECIPHER: Database of Chromosomal Imbalance and Phenotype in Humans Using Ensembl Resources.* The American Journal of Human Genetics, 2009. **84**(4): p. 524-533.

353. Bendl, J., et al., *PredictSNP: robust and accurate consensus classifier for prediction of disease-related mutations.* PLoS Comput Biol, 2014. **10**(1): p. e1003440.
354. Lexicon, *Lexicon knockout mice phenotypic data summary: gene name protein kinase D3.* 2005.
355. Mohun, T., et al., *Deciphering the Mechanisms of Developmental Disorders (DMDD): a new programme for phenotyping embryonic lethal mice.* Disease Models & Mechanisms, 2013. **6**(3): p. 562-566.
356. Geyer, S.H. and W.J. Weninger, *High-Resolution Episcopic Microscopy (HREM): Looking Back on 13 Years of Successful Generation of Digital Volume Data of Organic Material for 3D Visualisation and 3D Display.* Applied Sciences, 2019. **9**(18): p. 3826.
357. Weninger, W.J., et al., *Phenotyping structural abnormalities in mouse embryos using high-resolution episcopic microscopy.* Disease Models & Mechanisms, 2014. **7**(10): p. 1143-1152.
358. Bett, J.H. and P.G. Stovin, *Parachute deformity of the mitral valve.* Thorax, 1969. **24**(5): p. 632-6.
359. Leung, C., et al., *Myocardium-Specific Deletion of Rac1 Causes Ventricular Noncompaction and Outflow Tract Defects.* J Cardiovasc Dev Dis, 2021. **8**(3).
360. Lioncino, M., et al., *Hypertrophic Cardiomyopathy in RASopathies: Diagnosis, Clinical Characteristics, Prognostic Implications, and Management.* Heart Fail Clin, 2022. **18**(1): p. 19-29.
361. Marino, B., et al., *Noonan syndrome: structural abnormalities of the mitral valve causing subaortic obstruction.* Eur J Pediatr, 1995. **154**(12): p. 949-52.
362. Johannes, F.J., et al., *PKCu is a novel, atypical member of the protein kinase C family.* J Biol Chem, 1994. **269**(8): p. 6140-8.
363. Pfaffl, M.W., G.W. Horgan, and L. Dempfle, *Relative expression software tool (REST) for group-wise comparison and statistical analysis of relative expression results in real-time PCR.* Nucleic Acids Res, 2002. **30**(9): p. e36.
364. Wang, Y., et al., *Protein kinase D up-regulates transcription of VEGF receptor-2 in endothelial cells by suppressing nuclear localization of the transcription factor AP2beta.* J Biol Chem, 2019. **294**(43): p. 15759-15767.
365. Cuello, F., et al., *Protein kinase D selectively targets cardiac troponin I and regulates myofilament Ca2+ sensitivity in ventricular myocytes.* Circ Res, 2007. **100**(6): p. 864-73.
366. Haworth, R.S., et al., *Protein kinase D is a novel mediator of cardiac troponin I phosphorylation and regulates myofilament function.* Circ Res, 2004. **95**(11): p. 1091-9.
367. Roy, A., et al., *Protein kinase D signaling in cancer: A friend or foe?* Biochim Biophys Acta Rev Cancer, 2017. **1868**(1): p. 283-294.

368. Anderson, R.H., et al., *Myths and Realities Relating to Development of the Arterial Valves.* Journal of Cardiovascular Development and Disease, 2014. **1**(3): p. 177-200.
369. KORETZKY, E.D., et al., *Congenital Pulmonary Stenosis Resulting from Dysplasia of Valve.* Circulation, 1969. **40**(1): p. 43-53.
370. Wang, S.Y., et al., *Spontaneous Closure of a Secundum Atrial Septal Defect.* Methodist Debakey Cardiovasc J, 2018. **14**(1): p. 60-62.
371. Miyake, T., et al., *Spontaneous closure of perimembranous ventricular septal defect after school age.* Pediatr Int, 2008. **50**(5): p. 632-5.
372. Scully, B.B., et al., *Current expectations for surgical repair of isolated ventricular septal defects.* Ann Thorac Surg, 2010. **89**(2): p. 544-9; discussion 550-1.
373. Briggs, L.E., J. Kakarla, and A. Wessels, *The pathogenesis of atrial and atrioventricular septal defects with special emphasis on the role of the dorsal mesenchymal protrusion.* Differentiation, 2012. **84**(1): p. 117-30.
374. Pierpont, M.E., R.R. Markwald, and A.E. Lin, *Genetic aspects of atrioventricular septal defects.* Am J Med Genet, 2000. **97**(4): p. 289-96.
375. Pierpont, M.E.M., R.R. Markwald, and A.E. Lin, *Genetic aspects of atrioventricular septal defects.* American Journal of Medical Genetics, 2000. **97**(4): p. 289-296.
376. Redig, J.K., et al., *Allelic Interaction between CRELD1 and VEGFA in the Pathogenesis of Cardiac Atrioventricular Septal Defects.* AIMS Genet, 2014. **1**(1): p. 1-19.
377. Ackerman, C., et al., *An Excess of Deleterious Variants in VEGF-A Pathway Genes in Down-Syndrome-Associated Atrioventricular Septal Defects.* The American Journal of Human Genetics, 2012. **91**(4): p. 646-659.
378. Wang, S., et al., *Control of endothelial cell proliferation and migration by VEGF signaling to histone deacetylase 7.* Proc Natl Acad Sci U S A, 2008. **105**(22): p. 7738-43.
379. di Blasio, L., et al., *Protein kinase D1 regulates VEGF-A-induced alphavbeta3 integrin trafficking and endothelial cell migration.* Traffic, 2010. **11**(8): p. 1107-18.
380. Zhang, Y., et al., *A New TBX5 Loss-of-Function Mutation Contributes to Congenital Heart Defect and Atrioventricular Block.* Int Heart J, 2020. **61**(4): p. 761-768.
381. Liu, J., et al., *Gata4 regulates hedgehog signaling and Gata6 expression for outflow tract development.* PLoS Genet, 2019. **15**(5): p. e1007711.
382. Benson, D.W., et al., *Mutations in the cardiac transcription factor NKX2.5 affect diverse cardiac developmental pathways.* The Journal of Clinical Investigation, 1999. **104**(11): p. 1567-1573.

383. Samánek, M., et al., *Prevalence, treatment, and outcome of heart disease in live-born children: a prospective analysis of 91,823 live-born children.* Pediatr Cardiol, 1989. **10**(4): p. 205-11.
384. Tartaglia, M., B.D. Gelb, and M. Zenker, *Noonan syndrome and clinically related disorders.* Best Pract Res Clin Endocrinol Metab, 2011. **25**(1): p. 161-79.
385. Su, Y., et al., *The protein kinase D1-mediated classical protein secretory pathway regulates the Ras oncogene-induced senescence response.* Journal of Cell Science, 2018. **131**(6).
386. Delogu, A.B., et al., *The heart in RASopathies.* American Journal of Medical Genetics Part C: Seminars in Medical Genetics, 2022. **190**(4): p. 440-451.
387. Marino, B., et al., *Congenital heart diseases in children with Noonan syndrome: An expanded cardiac spectrum with high prevalence of atrioventricular canal.* The Journal of Pediatrics, 1999. **135**(6): p. 703-706.
388. Yi, J.-S., S. Perla, and A.M. Bennett, *An Assessment of the Therapeutic Landscape for the Treatment of Heart Disease in the RASopathies.* Cardiovascular Drugs and Therapy, 2022.
389. Rauen, K.A., *Defining RASopathy.* Dis Model Mech, 2022. **15**(2).
390. Cuypers, J.A.A.E., et al., *Pulmonary stenosis: update on diagnosis and therapeutic options.* Heart, 2013. **99**(5): p. 339-347.
391. Machackova, J., J. Barta, and N.S. Dhalla, *Myofibrillar remodeling in cardiac hypertrophy, heart failure and cardiomyopathies.* Can J Cardiol, 2006. **22**(11): p. 953-68.
392. Bossuyt, J., et al., *Protein Kinase D1 Regulates Cardiac Hypertrophy, Potassium Channel Remodeling, and Arrhythmias in Heart Failure.* J Am Heart Assoc, 2022. **11**(19): p. e027573.
393. Steinberg, S.F., *Post-translational modifications at the ATP-positioning G-loop that regulate protein kinase activity.* Pharmacol Res, 2018. **135**: p. 181-187.
394. Quan, L., Q. Lv, and Y. Zhang, *STRUM: structure-based prediction of protein stability changes upon single-point mutation.* Bioinformatics, 2016. **32**(19): p. 2936-2946.
395. Quan, L., Q. Lv, and Y. Zhang, *STRUM: structure-based prediction of protein stability changes upon single-point mutation.* Bioinformatics, 2016. **32**(19): p. 2936-46.
396. Cuspidi, C., M. Rescaldani, and C. Sala, *Prevalence of Echocardiographic Left-Atrial Enlargement in Hypertension: A Systematic Review of Recent Clinical Studies.* American Journal of Hypertension, 2013. **26**(4): p. 456-464.
397. Harrigan, R.A. and K. Jones, *ABC of clinical electrocardiography. Conditions affecting the right side of the heart.* Bmj, 2002. **324**(7347): p. 1201-4.
398. Lv, D., et al., *Small-Molecule Inhibitor Targeting Protein Kinase D: A Potential Therapeutic Strategy.* Front Oncol, 2021. **11**: p. 680221.
399. Bossuyt, J., et al., *Ca²⁺/Calmodulin-Dependent Protein Kinase IIδ and Protein Kinase D Overexpression*

Reinforce the Histone Deacetylase 5 Redistribution in Heart Failure. Circulation Research, 2008. **102**(6): p. 695-702.
400. Mojtabavi, S., N. Samadi, and M.A. Faramarzi, *Osmolyte-Induced Folding and Stability of Proteins: Concepts and Characterization.* Iran J Pharm Res, 2019. **18**(Suppl1): p. 13-30.
401. Yoshioka, S., et al., *Effect of Sugars on the Molecular Motion of Freeze-Dried Protein Formulations Reflected by NMR Relaxation Times.* Pharmaceutical Research, 2011. **28**(12): p. 3237-3247.
402. Gruebele, M., *THE FAST PROTEIN FOLDING PROBLEM.* Annual Review of Physical Chemistry, 1999. **50**(1): p. 485-516.
403. Navío, D., et al., *Structural and Computational Characterization of Disease-Related Mutations Involved in Protein-Protein Interfaces.* Int J Mol Sci, 2019. **20**(7).
404. Martelli, P.L., et al., *Large scale analysis of protein stability in OMIM disease related human protein variants.* BMC Genomics, 2016. **17**(2): p. 397.
405. Hartl, F.U., *Protein Misfolding Diseases.* Annual Review of Biochemistry, 2017. **86**(1): p. 21-26.
406. Hemmer, W., et al., *Role of the glycine triad in the ATP-binding site of cAMP-dependent protein kinase.* J Biol Chem, 1997. **272**(27): p. 16946-54.
407. Torkamani, A., et al., *Congenital disease SNPs target lineage specific structural elements in protein kinases.* Proc Natl Acad Sci U S A, 2008. **105**(26): p. 9011-6.
408. Lutze, G., et al., *Non-canonical WNT-signaling controls differentiation of lymphatics and extension lymphangiogenesis via RAC and JNK signaling.* Scientific Reports, 2019. **9**(1): p. 4739.
409. Bui, H.M., et al., *Proteolytic activation defines distinct lymphangiogenic mechanisms for VEGFC and VEGFD.* The Journal of Clinical Investigation, 2016. **126**(6): p. 2167-2180.
410. Coxam, B., et al., *Pkd1 regulates lymphatic vascular morphogenesis during development.* Cell reports, 2014. **7**(3): p. 623-633.
411. Outeda, P., et al., *Polycystin signaling is required for directed endothelial cell migration and lymphatic development.* Cell Rep, 2014. **7**(3): p. 634-44.
412. Yamamoto, H., et al., *Wnt5a signaling is involved in the aggressiveness of prostate cancer and expression of metalloproteinase.* Oncogene, 2010. **29**(14): p. 2036-46.
413. Nagy, J.A., et al., *VEGF-A induces angiogenesis, arteriogenesis, lymphangiogenesis, and vascular malformations.* Cold Spring Harb Symp Quant Biol, 2002. **67**: p. 227-37.
414. Di Blasio, L., et al., *Protein Kinase D1 Regulates VEGF-A-Induced αvβ3 Integrin Trafficking and Endothelial Cell Migration.* Traffic, 2010. **11**(8): p. 1107-1118.
415. Shin, J.W., R. Huggenberger, and M. Detmar, *Transcriptional profiling of VEGF-A and VEGF-C target genes in lymphatic endothelium reveals endothelial-specific molecule-1 as a novel*

mediator of lymphangiogenesis. Blood, 2008. **112**(6): p. 2318-2326.
416. Fagerberg, L., et al., *Analysis of the human tissue-specific expression by genome-wide integration of transcriptomics and antibody-based proteomics.* Mol Cell Proteomics, 2014. **13**(2): p. 397-406.
417. Wang, Y., et al., *Protein kinase D up-regulates transcription of VEGF receptor-2 in endothelial cells by suppressing nuclear localization of the transcription factor AP2β.* J Biol Chem, 2019. **294**(43): p. 15759-15767.
418. Veitia, R.A. and J.A. Birchler, *Dominance and gene dosage balance in health and disease: why levels matter!* The Journal of Pathology, 2010. **220**(2): p. 174-185.
419. Zhang, Z., et al., *Analyzing effects of naturally occurring missense mutations.* Comput Math Methods Med, 2012. **2012**: p. 805827.
420. Boulling, A., et al., *Functional analysis of pancreatitis-associated missense mutations in the pancreatic secretory trypsin inhibitor (SPINK1) gene.* European Journal of Human Genetics, 2007. **15**(9): p. 936-942.
421. Hausser, A., et al., *Protein kinase D regulates vesicular transport by phosphorylating and activating phosphatidylinositol-4 kinase IIIbeta at the Golgi complex.* Nat Cell Biol, 2005. **7**(9): p. 880-6.
422. Kirkland, L.a.K., K. *Ventricular Septal Defect - ACHA*. 2020 2020 [cited 2020 June 07, 2020]; Available from: https://www.achaheart.org/your-heart/health-information/ventricular-septal-defect/.
423. Armstrong, E.J. and J. Bischoff, *Heart valve development: endothelial cell signaling and differentiation.* Circ Res, 2004. **95**(5): p. 459-70.
424. Lin, Q., et al., *Control of mouse cardiac morphogenesis and myogenesis by transcription factor MEF2C.* Science, 1997. **276**(5317): p. 1404-7.
425. Lin, Q., et al., *Requirement of the MADS-box transcription factor MEF2C for vascular development.* Development, 1998. **125**(22): p. 4565-74.
426. Barnes, R.M., et al., *MEF2C regulates outflow tract alignment and transcriptional control of Tdgf1.* Development, 2016. **143**(5): p. 774-9.
427. Bruneau, B.G., et al., *A murine model of Holt-Oram syndrome defines roles of the T-box transcription factor Tbx5 in cardiogenesis and disease.* Cell, 2001. **106**(6): p. 709-21.
428. Ghosh, T.K., et al., *HDAC4 and 5 repression of TBX5 is relieved by protein kinase D1.* Sci Rep, 2019. **9**(1): p. 17992.
429. Spratley, S.J., et al., *Protein kinase D regulates cofilin activity through p21-activated kinase 4.* J Biol Chem, 2011. **286**(39): p. 34254-61.
430. Niwa, R., et al., *Control of actin reorganization by Slingshot, a family of phosphatases that dephosphorylate ADF/cofilin.* Cell, 2002. **108**(2): p. 233-46.

431. Saheera, S. and P. Krishnamurthy, *Cardiovascular Changes Associated with Hypertensive Heart Disease and Aging.* Cell Transplant, 2020. **29**: p. 963689720920830.
432. Zaidi, S. and M. Brueckner, *Genetics and Genomics of Congenital Heart Disease.* Circ Res, 2017. **120**(6): p. 923-940.
433. Williams, K., J. Carson, and C. Lo, *Genetics of Congenital Heart Disease.* Biomolecules, 2019. **9**(12).
434. Patel, S.S. and T.L. Burns, *Nongenetic risk factors and congenital heart defects.* Pediatr Cardiol, 2013. **34**(7): p. 1535-55.
435. Akhirome, E., et al., *The Complex Genetic Basis of Congenital Heart Defects.* Circ J, 2017. **81**(5): p. 629-634.
436. Gelb, B.D. and W.K. Chung, *Complex genetics and the etiology of human congenital heart disease.* Cold Spring Harb Perspect Med, 2014. **4**(7): p. a013953.
437. Jenkins, K.J., et al., *Noninherited risk factors and congenital cardiovascular defects: current knowledge: a scientific statement from the American Heart Association Council on Cardiovascular Disease in the Young: endorsed by the American Academy of Pediatrics.* Circulation, 2007. **115**(23): p. 2995-3014.
438. Persson, M., et al., *Risk of major congenital malformations in relation to maternal overweight and obesity severity: cohort study of 1.2 million singletons.* BMJ, 2017. **357**: p. j2563.
439. Cai, G.J., et al., *Association between maternal body mass index and congenital heart defects in offspring: a systematic review.* Am J Obstet Gynecol, 2014. **211**(2): p. 91-117.
440. Homsy, J., et al., *De novo mutations in congenital heart disease with neurodevelopmental and other congenital anomalies.* Science, 2015. **350**(6265): p. 1262-1266.
441. Su, Y., et al., *The protein kinase D1-mediated classical protein secretory pathway regulates the Ras oncogene-induced senescence response.* J Cell Sci, 2018. **131**(6).
442. Kim, M.S., et al., *Protein kinase D1 stimulates MEF2 activity in skeletal muscle and enhances muscle performance.* Mol Cell Biol, 2008. **28**(11): p. 3600-9.
443. Cohen, E.D., et al., *Wnt5a and Wnt11 are essential for second heart field progenitor development.* Development, 2012. **139**(11): p. 1931-40.
444. Kwag, E.M., J.S. Lee, and S.H. Kim, *The incidentally diagnosed adult congenital heart disease during routine medical health checkups in 27,897 Koreans at a single center over seven years.* BMC Cardiovasc Disord, 2018. **18**(1): p. 223.
445. Kvarnemo, C. and L.W. Simmons, *Polyandry as a mediator of sexual selection before and after.* 2013.
446. Pearse, D.E. and E.C. Anderson, *Multiple paternity increases effective population size.* Mol Ecol, 2009. **18**(15): p. 3124-7.
447. Thonhauser, K.E., et al., *Why do female mice mate with multiple males?* Behav Ecol Sociobiol, 2013. **67**(12): p. 1961-1970.
448. Wolff, J.O. and D.W. Macdonald, *Promiscuous females protect their offspring.* Trends Ecol Evol, 2004. **19**(3): p. 127-34.

449. Karl, S.A., *The effect of multiple paternity on the genetically effective size of a population.* Mol Ecol, 2008. **17**(18): p. 3973-7.
450. Holmdahl, R. and B. Malissen, *The need for littermate controls.* European Journal of Immunology, 2012. **42**(1): p. 45-47.
451. Oey, H., et al., *Genetic and epigenetic variation among inbred mouse littermates: identification of inter-individual differentially methylated regions.* Epigenetics & Chromatin, 2015. **8**(1): p. 54.